# Contribution to the understanding of the linear friction welding technique applied on aeronautical alloys

Xavier Boyat

▶ **To cite this version:**

Xavier Boyat. Contribution to the understanding of the linear friction welding technique applied on aeronautical alloys. Mechanics [physics.med-ph]. Université de Technologie de Compiègne, 2020. English. NNT : 2020COMP2592 . tel-04711387

**HAL Id: tel-04711387**

**https://theses.hal.science/tel-04711387v1**

Submitted on 26 Sep 2024

**HAL** is a multi-disciplinary open access archive for the deposit and dissemination of scientific research documents, whether they are published or not. The documents may come from teaching and research institutions in France or abroad, or from public or private research centers.

L'archive ouverte pluridisciplinaire **HAL**, est destinée au dépôt et à la diffusion de documents scientifiques de niveau recherche, publiés ou non, émanant des établissements d'enseignement et de recherche français ou étrangers, des laboratoires publics ou privés.

Par **Xavier BOYAT**

# *Contribution to the understanding of the linear friction welding technique applied on aeronautical alloys*

Thèse présentée
pour l'obtention du grade
de Docteur de l'UTC

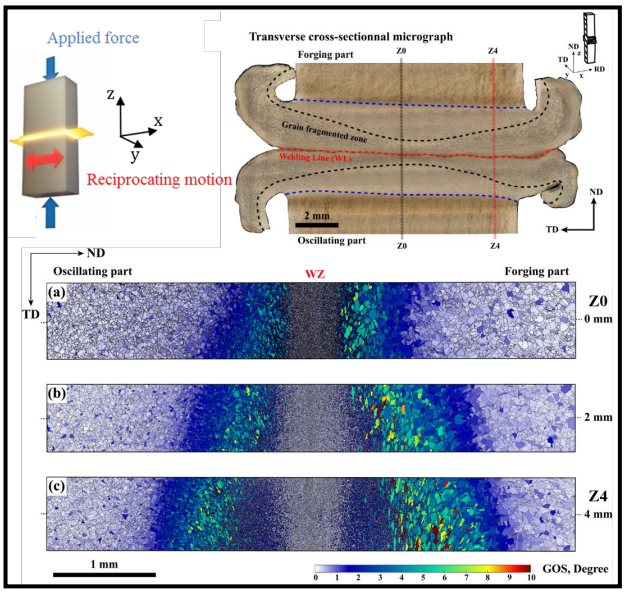


Soutenue le 8 décembre 2020
**Spécialité :** Mécanique et Matériaux : Unité de recherche en Mécanique - Laboratoire Roberval (FRE UTC - CNRS 2012)
D2592

**THESE DE DOCTORAT DE L'UNIVERSITE DE TECHNOLOGIE DE COMPIEGNE**

## *Spécialité : Mécanique & Matériaux*

***ED71 « Sciences pour l'ingénieur »***

***Doctoral dissertation of mechanical and material engineering***

# Contribution to the understanding of the linear friction welding technique applied on aeronautical alloys

*As part of the 'OPTIMUM Project' - ANR-14-CE27-0017*


## BOYAT Xavier

Roberval laboratory, CNRS FRE 2012 – Department of mechanical engineering


Thesis defended on December 8, 2020

**Jury members :**

| | | |
|---|---|---|
| *Rapporteurs* | GERMAIN Lionel | MC HDR, Université de Lorraine, Metz |
| | KERMOUCHE Guillaume | PU, Ecole des mines de Saint-Etienne |
| *Examiners* | RISBET Marion | PU, Université de technologie de Compiègne |
| | CORMIER Jonathan | MC, Université de Poitiers |
| | ANDRIEU Eric | PU, Université de Toulouse |
| *Thesis supervisors* | BOUVIER Salima | PU, Université de technologie de Compiègne |
| | MARTEAU Julie | MC, Université de technologie de Compiègne |
| | FAVERGEON Jérôme | PU, Université de technologie de Compiègne |


The author would like to thank the Hauts-de-France region and the European Regional Development Fund (ERDF) 2014/2020 for the co-funding of this work.

L'allocation doctorale relative au projet «OPTIMUM» est cofinancée par le Fonds européen de développement économique et régional (FEDER)

**Remerciements**

Je tiens tout d'abord à remercier mes encadrants de thèse Salima BOUVIER, Jérôme FAVERGEON et Julie MARTEAU pour m'avoir donné l'opportunité de me lancer dans cette aventure et avec qui les échanges ont toujours été enrichissants et agréables. Je les remercie également pour leur disponibilité, leurs conseils et leur soutien, j'ai beaucoup appris à leur côté à travers cette expérience.

Je tiens à exprimer toute ma gratitude envers les membres du jury avec lesquels je retiens un formidable moment d'échanges lors des discussions. Je remercie notamment chaleureusement Éric ANDRIEU de m'avoir fait l'honneur de présider la défense de ce travail, ses mots de conclusion m'ont beaucoup touché. Un grand remerciement va également aux deux rapporteurs Lionel GERMAIN et Guillaume KERMOUCHE qui ont eu la lourde tâche de lire et évaluer mon travail. Je suis particulièrement reconnaissant de l'intérêt qu'ils ont manifesté à l'égard de ma problématique de recherche. Merci enfin à Marion RISBET, Jonathan CORMIER et François BOURDET d'avoir pris le temps d'examiner mon manuscrit avec soin. C'était un honneur de pouvoir présenter mon travail devant une assemblée d'une telle qualité.

Je remercie chaleureusement toutes les personnes qui m'ont aidé de près ou de loin à l'élaboration de ma thèse et tout particulièrement à Dorick BALLAT-DURAND avec qui j'ai adoré collaborer tout au long de ce projet. Mes remerciements aux collègues et amis du « bureau » pour leur soutien moral, notamment Thibault LESAGE et Guillaume SCHUHLER pour les parties de « katemesu » / « don't starve » endiablées d'after-work. Un grand merci à Corentin GUELLEC pour son formidable travail sur la partie essais mécaniques et à qui je souhaite le meilleur pour sa thèse à venir.

Merci au personnel du laboratoire Roberval pour sa précieuse assistance notamment à Caroline VERDARI pour son écoute et sa bonne humeur, Sabine LOOF pour son implication et sa gentillesse, Brigitte DUCH pour son soutien et sa bienveillance et Isabelle VELLUET pour son aide et sa disponibilité. Merci à François OUDET et Pierre FEISSEL pour leur indéfectible soutien.

Aux différents collègues que j'ai eu l'occasion de côtoyer au labo pour tous les bons moments passés ensemble au labo comme en dehors !

A mes colocs successifs qui ont toujours trouvé les mots pour me soutenir et traverser le doute.

Merci à mes amis de toujours Guillaume, Nicolas, Maxime, Dimitri, Yves, Clément, Thibaud pour le précieux soutien moral.

Je dédie enfin ce travail à mes parents, ma soeur et ma Gougou qui m'ont toujours soutenu, quelles que soient les circonstances, vous avez été la force m'ayant maintenu à flot jusqu'au bout. Une pensée émue pour mon grand-oncle François qui nous a quitté et qui aurait sûrement aimé assister à l'épilogue de ce travail.

# *Index*

**Contents**

# General introduction

## Background

Among the various solid-state assembling techniques, linear friction welding initially emerged as an interesting technical alternative for the manufacturing of bladed disks in aeroengines [1]. Indeed, the conventional fir-tree or dovetailed designs for the attachments of the blades to the disk are notably prone to fatigue fretting damages [2], thus limiting the lifetime and the reliability of the assemblies. The linear friction welding technology advantageously replaces such mechanical joints by allowing direct and accurate assembling of blades parts on the disk through welding. Besides, the elimination of mechanical attachment systems not only enhances in-service life but also noticeably lightens the assembled structure, enabling until 20 to 30 % overall weight reduction in some cases, therefore improving the in-use performances of the bladed disk. In addition to that, damaged blades on engine turbine can be removed and easily replaced by new linear friction welded ones, which is an economically profitable option. Despite these technical qualities, blisk designs integrating friction-welded parts remain currently marginal with regard to integrated designs or mechanical assembling designs. However, commonly used materials in integrated designs, *id est* Ti-alloys and Ni-superalloys, are exceptionally hard to machine materials through conventional milling processes [3]. Besides, the realization of large and complex structural parts out of a solid block of material requires costly and time-consuming machining processes that cause significant material waste. Friction welded designs consequently constitute a consistent alternative to address these technical challenges in blisk manufacturing.

Similarly, the aerospace industry extensively uses massive machining applied on high-cost materials in aircraft parts production. Such fabrication methods are wasteful and result in poor buy-to-fly ratio. In this perspective, design engineers are showing a growing interest on alternative manufacturing technologies as substitutes to subsequent material removal processing. Such requirements notably resulted in the development of near-net-shape designs favoring additive manufacturing processes. Among these, linear friction welding allows incorporating additional parts on already shaped structures with a considerable spatial accuracy. Besides, linear friction welding is an attractive candidate for the realization of complex multi-functional components with high added value materials. In addition to that, a clever utilization of the friction welding technique opens to new design and encourage weight reduction by favoring welding at the expense of mechanical joint in structural part assemblies.

The process execution is quite simple: the weld is obtained by the friction of a moving part in a reciprocating motion on a stationary part under a force. The local heat generation at the interface causes the materials to flow expelling along oxides and surface contaminants with plastically deformed material allowing parts coalescence in a thin metallurgical bond. The processing stage does not necessitate external application of heat nor require much surface preparation and operate in just a few seconds. As the welding takes place below the *liquidus*, typical fusion welding defects are avoided and the resulting joint properties are, in some cases, comparable with the base materials. Post-assembly machining is limited to a flash deburring stage and eventual finishing processes. Furthermore, the possibility of assembling dissimilar alloys is one of the most promising application of the technique. It would notably allow locally tailoring the materials assembly to the in-use functional requirements. For instance, when manufacturing an aeroengine compressor, blades made of fine-grained microstructure, which are suitable for elevated high-cycle fatigue performances, may be joined to a disc displaying a coarse microstructure, the latter being well adapted to low-cycle performances. Nevertheless, such dissimilar joining configurations are often challenging and the effectiveness of the bonding strongly depend on the chemical reactivity of the alloys forced against each. The appearance of multiple intermetallic phases generally results in subsequent degradation of the joint properties at the joint interface and not all combination of material in joining are possible.

The friction welding procedure however results in severe thermo-mechanical loads causing significant modifications on the local microstructure and mechanical properties of the materials in the joint. The present work aims at providing a better understanding of the process's consequences on the microstructural evolution of Ti-alloys and a nickel-based alloy, which are aeronautical alloys commonly used in structural aircraft parts.

## Aims and scope

The present work is part of a multipartite ANR project named OPTIMUM aiming at identifying the causal relationship of varied LFW conditions (i.e. process parameters and materials) on the microstructural changes involved in the weld and their resulting mechanical durability. During the project, butt-weld test campaigns were carried out implying the joining of various aeronautical material combinations. Notably, two Ti-alloy grades, the near-α Ti6242 and the β-metastable Ti17, were linear friction welded in mono then dissimilar configurations. On another note, the precipitation hardenable nickel superalloy Inconel 718 was linear friction welded through two initial metallurgical conditions: a soft solution annealed state and a hard precipitation strengthened state. Finally, prospective tests were realized on the welding of Ti-alloys with Inconel 718. The ACB Company, with the technical support of Airbus, provided the weld samples.

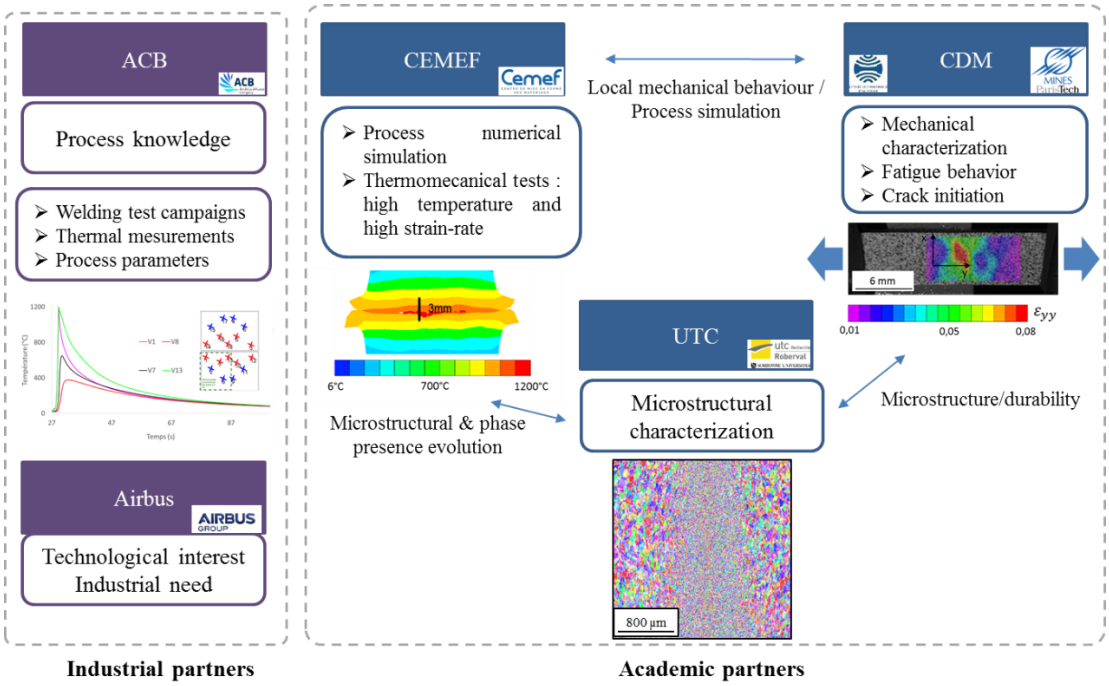


Concerning Ti-alloys, detailed results of the microstructural and mechanical characterizations on the mono-grade Ti6242 and Ti17 configurations are exposed through the thesis work of BALLAT-DURAND Dorick (UTC) [4] and GARCÍA Juan-Manuel (CdM) [5]. A numerical simulation of the process was also developed through the work of POTET Antoine (CEMEF) [6].

The objective of this work is to make an exhaustive description of the microstructural change operating during the linear friction welding of Inconel 718. Indeed, the severe thermo-mechanical loads applied during the procedure resulted in remarkable microstructural changes because of successive phase transformations and through the activation of thermally activated mechanisms of recovery. Once achieved, the joints display significant microstructure heterogeneities in term of phase presence and grain characteristics,

with discontinuous mechanical properties. As many nickel-based alloys controlling the microstructure and the grain size and distribution after Inconel 718 processing is a key factor in the optimization of the mechanical properties of the material. To that end, post-weld heat treatments were applied in an attempt to recover a homogeneous microstructure across the weld with interesting mechanical properties for in-use applications.

The successful realization of Inconel 718 friction welds has been particularly problematic, notably on the solution-annealed condition. An ancillary work focusing on the joining mechanism on the Ti6242 / Ti17 dissimilar weld configuration notably helped clarifying the mechanisms in-play during the solid-state welding process. The latter configuration also gave a comparative study-case to compare with the prospection of a dissimilar: Inconel 718 / Ti-alloys weld configuration. Through that work, a special emphasis is given on the interface evolution on each tested weld couple.

## Structure of the manuscript

The exposed work is divided into five chapters, the summarized content is presented below:

**Chapter 1** gives a general introduction about the physical mechanisms in-play during the linear friction welding procedure. The main issues concerning solid-state welding are reviewed and discussed.

**Chapter 2** focuses on the detailed characterization of the metallurgical mechanisms taking place on a Ti6242 / Ti17 dissimilar weld configuration. The main objective of that work is to understand the effective metallurgical mechanisms leading to the formation of the joint during the linear friction welding procedure.

**Chapter 3** endeavors to detail the microstructural transformations on an Inconel 718 linear friction welded joint. The blocks were butt-welded in a precipitation strengthened metallurgical state. The investigation notably focuses on the phases change and grain fragmentation mechanisms induced by the process. A specific attention is notably given on the weld interface evolution.

**Chapter 4** details the prospection of set of parameters for the welding of Inconel 718 alloy in a solution-annealed state. Again, the microstructural changes induced by the joining process are described. The results are then compared with the precipitation-hardened joints.

**Chapter 5** post-weld heat treatments strategies are prospected on both welded microstructures: the precipitation strengthened and solution annealed, to re-homogenize the microstructure within the joints. The strength of these configurations is eventually comparatively tested *via* monotonous tensile tests followed by a DIC procedure.

The results obtained on the IN718/Ti-alloys weld attempts are briefly detailed in supplementary material (Suppl. Mat. C).

**References**


[1] E. D. Nicholas et W. M. Thomas, « A review of friction processes for aerospace applications », *Int. J. Mater. Prod. Technol.*, vol. 13, nº 1/2, p. 45‑55, 1998.

[2] S.-P. Zhu, P. Yue, Z.-Y. Yu, et Q. Wang, « A Combined High and Low Cycle Fatigue Model for Life Prediction of Turbine Blades », *Materials*, vol. 10, nº 7, p. 698, juin 2017, doi: 10.3390/ma10070698.

[3] F. Klocke *et al.*, « Technological and Economical Assessment of Alternative Process Chains for Blisk Manufacture », *Procedia CIRP*, vol. 35, p. 67‑72, 2015, doi: 10.1016/j.procir.2015.08.052.

[4] D. Ballat-Durand, « Microstructural characterization and optimization of linear friction welded titanium alloys joints through the influence of the process parameters and post-weld heat treatments », Université technologique de Compiègne, 2019.

[5] J.-M. Garcia, « Mechanical characterization of Linear Friction Welded Titanium alloys », p. 293.

[6] A. Potet, K. Mocellin, et L. Fourment, « Numerical simulation of linear friction welding of aeronautical alloys », Penang, Malaysia, 2017, p. 110007, doi: 10.1063/1.5008134.

# Chapter I

## Presentation of the linear friction welding technology

## &

## Physical mechanisms in play during solid-state welding

### Background

This introductive chapter aims at presenting the basic physical mechanisms in play during friction assembling processes. The operational specificities of the linear friction welding technique are first introduced. The notions of friction, which underlies the technology, and in a wider sense dissipation, are then discussed. The highly dissipative aspect of plastic deformation, arising from the imposed mechanical load, notably demonstrates a fundamental role in the weld procedure. Indeed, the subsequent heat generation stemming from these dissipative processes causes the materials to extensively flow allowing parts coalescence in a thin metallurgical bond. The disruption of the native surface oxides with the concomitant establishment of metal-to-metal contacts are widely accepted mechanisms for solid-state joining between metallic materials. Regarding that, a succinct review on the current knowledge concerning the adhesion mechanisms in metallic contacts is brought. The influence of the native surface oxide phases on the bond procedure is finally discussed focusing on the materials studied during the OPTIMUM project *id est*: Ti-alloys & Inconel 718 alloy.

## 1. Solid state assembling & linear friction welding

Solid-state assembling processes refer to a class of joining technologies in which the metallurgical coalescence between workpieces results, in general, from the application of pressure or/and heat during a specific holding time [1]. Its main characteristic is that the joining takes place without fusion at the junction interface between the materials in contact.

These assembling techniques are parts of a wider ensemble of deformation-based welding processes. To do so, various thermomechanical routes are possible. Some will favor long processing time under moderate applied force and high temperature conditions to stimulate creep deformation conditions such as in diffusion bonding techniques; others will favor higher deformation rate and low temperature (for instance in deformation bonding, accumulative roll bonding). Among them, the friction assembling processes usually combine high temperature and high deformation conditions where the local temperature elevation is the consequence of frictional interactions generated at the weld interface. Among them, the most prominent applications are the inertia friction welding, the friction stir welding and the linear friction welding. They all form a class of solid-state joining technologies where engineers exploit in an original manner the consequences of the fundamental processes of friction-dissipation phenomena in order to obtain a metallurgical junction between workpieces.

It is interesting to note that all these processes have in common to stimulate plastic deformation in the junction zone in order to favor a metallurgical coalescence between the workpieces brought in contact.

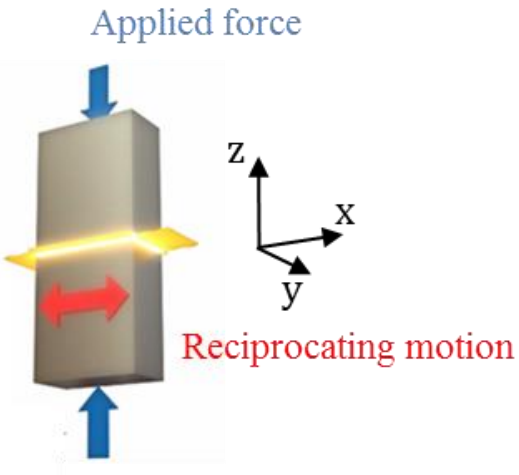


**Figure 1**: *Schematic representation of the linear friction welding procedure on a couple of parallelepipedic workpiece assembled in a butt-configuration on a vertical mounting*, source: https://www.acb-ps.com/.

The operating principle of the Linear Friction Welding (or LFW) technique is quite straightforward. First, the nominally plane surfaces of the workpieces to assemble are brought in contact together; the ensemble forms a classical textbook example of one solid body sliding on another. Then, the weld is obtained by the friction of a moving part in a forced oscillatory motion against a stationary part under the action of a compressive force (see Figure 1). Die-holding parts firmly maintains the assembling workpieces in contact

one another during the process. The harmonic solicitation imposed of the oscillating workpiece yields to a dry sliding friction phenomenon between the rubbing components. The frictional interactions progressively lead to subsequent temperature elevation at the weld interface, which in turn soften the materials to level suitable for forging. Once a sufficient heat generation is provided, an intermediate viscoplastic layer forms and start to flow under the process loadings. The local plastic deformation breaks along former surface oxides/contaminants layers and conducts to the formation of lateral weld expulsion flashes. While the viscoplastic layer collapses and is being expelled under the concomitant action of shear and compressive solicitation, new matter is brought to the weld center zone due to the action of the compressive force. Eventually, the materials flow in the weld interfacial zone yields to a global axial shortening of the LFWed workpieces. The latter is often use as an end criterion to control the process. When it is the case, the friction welding procedure stops once the axial shortening, or measured upset, reaches a pre-set targeted value. Alternatively, the end process criterion may sometimes be set on the total processing time. The ensemble of above-described phenomena results in the coalescence of the rubbing materials in a thin metallurgical bond.

### 1.1 Process parameters of the LFW

Thus, only four essential parameters are necessary to monitor the friction welding procedure: the pressing force P, the oscillation amplitude A, its oscillation frequency f, and a stopping criterion, which is generally driven through the axial shortening parameter u (the stopping criterion is sometimes defined as a total time duration).

The detailed friction welding process is classically decomposed into four distinct phases:

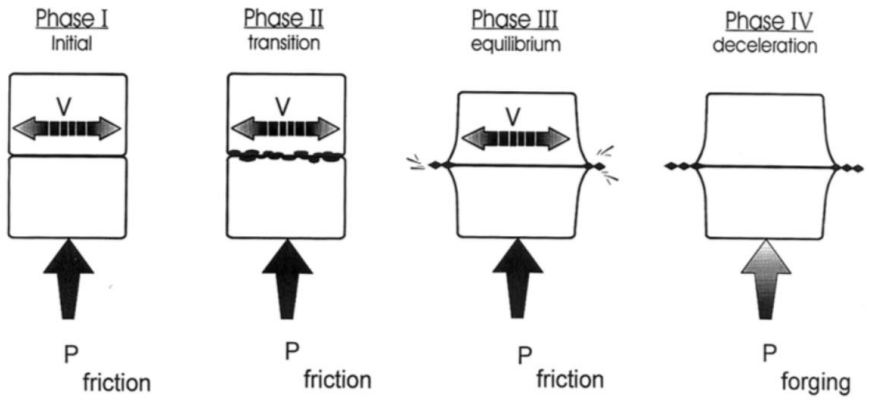


**Figure 2***: Illustration in four acts of the different stages of the linear friction welding process as identified by Vairis and Frost in* [2].

**Phase I** – ***Initiation phase*** – The faying surfaces are brought in contact and start oscillating relative from one another. The surface asperities collide each other and progressively deform, increasing the true area of contact between the workpieces. The axial shortening at this stage is close to negligible.

**Phase II - *Transition phase*** – The frictional interactions emerging from the dry sliding contacts increasingly degrade part of the kinetic energy into thermal energy. These dissipative phenomena result in a temperature elevation in the close interfacial zone. The temperature elevation is then carried away through heat transfer processes (mainly dominated by conduction here). In turn, the matter softens and starts to substantially flow. The progressive collapse of the yield stress increases the true area of contact and an intermediate viscoplastic layer of softened materials progressively forms between the rubbing surfaces. Such thermomechanical load then leads to extensive plastic deformation at the weld interface. The hot matter cannot sustain the mechanical loads yielding to the formation of lateral expulsion flashes. The axial shortening begins.

**Phase III - *Equilibrium phase*** – The temperature profile and thickness developing within the intermediate viscoplastic layer between the rubbing surfaces reaches a quasi-steady state. The plastic deformation induced dissipation phenomena now mainly sustain the heat generation. The expelled material is continuously replaced by new matter under the effect of the compressive force and the burn-off rate also reaches a quasi-steady-state. At this stage of the process, the apparent equilibrium between the thermomechanical loads, the plastic flow of matter and the heat transport mechanisms gives to the viscoplastic deformation process a self-regulated aspect. Simultaneously, the axial shortening rate reaches a constant value.

**Phase IV - *Deceleration phase*** – Once the axial-shortening reaches the targeted pre-set value, the relative motion is ramped down and the workpieces are aligned. In most applications, an additional forging force is also applied to consolidate the junction while the materials cool down until equilibrium with the surrounding heat bath.

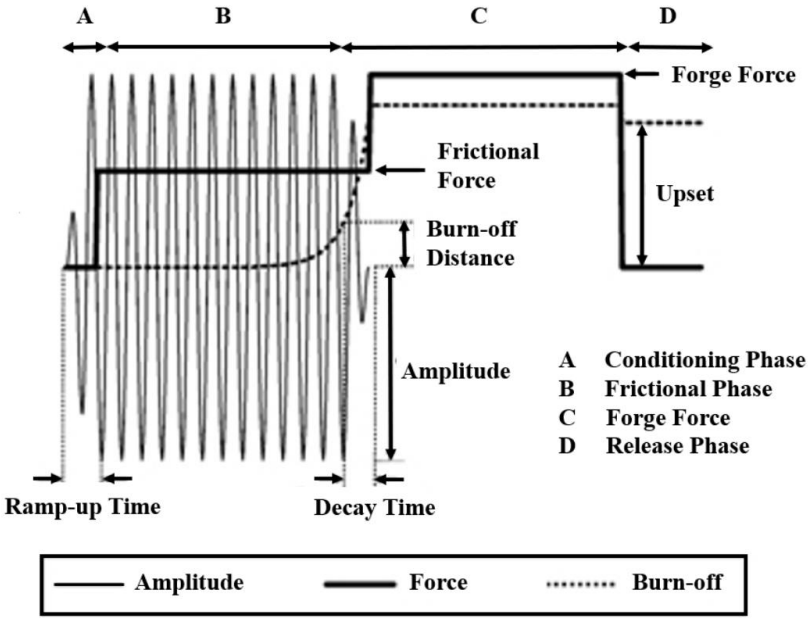


**Figure 3***: Schematic representation of signal evolution of the different monitoring parameters through time during the linear friction welding procedure, extracted from* [2].

### 1.2 In-use applications of the technology

The process is in-use for specific niche applications such as high-value metal component assembly in aero-engines. However, the aerospace industry is showing a growing interest in the potential of LFW technology as a substitute in aircraft parts production to massive machining by material removal and is in concurrence with additive manufacturing processes [3]. Indeed, neither filler metal addition nor shielding gazes are required for the technical realization of the weld. Moreover, solid state welding is an interesting alternative avoiding solidification problems such as grain boundary liquation, detrimental phase formation or micro-cracking problems in fusion zone. Besides, by avoiding melting, solid-state welding enables the joining of advanced metals and dissimilar metal pairs that are often difficult or impossible to join via fusion welding.

**Figure 4***: (Left): Blisk machining by high-speed milling (credit: MTU aeroengines). (Right): Photograph of a blisk demonstrator with linear friction welded bladed extracted from* [3].

## 2. Physical principles behind the linear friction welding procedure

Friction is a familiar and universally experienced phenomenon accompanying our macroscopic everyday life. When rubbing two objects together a force resisting the motion arises. Besides, another experimental observation is that the frictional zones of the rubbed bodies become warmer. We commonly take advantage of that phenomenon by the simple gesture of rubbing our hand together to warm them up. The latter example constitutes an interesting intuitive illustration of the physical effects of the sliding friction. Furthermore, the friction welding processes use the same exact fundamental principle in order to warm up the rubbing interfaces and finally obtain a metallurgical coalescence between workpieces. The cause of these drag phenomena is the resisting forces arising from the frictional interaction between the blocks.

An interesting insight is given by classical experiments on the dissipation of mechanical work carried by Joule [4]. When work is dissipated, the frictional processes result in a change in the thermal state of the system on which the work is done even though no heat is transferred to the system through contact with a higher temperature body. One can calculate the amount of heat transferred that would have produced the same change in state. Experimentally, if the amount of work dissipated is doubled, the amount of heat that would need to be transferred to the enclosed system to produce the same change in state is doubled; that is, there is a linear relation between the two quantities. This is how it came to be recognized that both mechanical and thermal effects could be united under the common and equivalent rubric of "*energy*".

### 2.1 Dry sliding friction from a thermodynamic viewpoint in LFW

In linear friction welding, the surfaces in contact form a classical example of one solid body sliding on another in a forced oscillatory motion. The frictional interactions developing between the sliding surfaces originate from the internal reaction forces that oppose the externally applied forces [5]. A correct way to approach such problem is to consider both blocks in contact as a whole system [6]. In this way, the blocks are deformable bodies that are forced against each other under the external loads imposed by the friction-assembling machine. The application of the first law of thermodynamics on the system allows defining the internal energy of the system: $\Delta U$. The latter includes all the different countable forms of energy *id est* the kinetic energy from the movement of the oscillating block but also the various forms of physical excitations that arise from the frictional interactions during the motion. These excitations notably yield to energy dissipation phenomena that transform part of the mechanical energy into thermal energy and consequently result in an internal heating effect.

### 2.2 Friction and dissipation at microscale

The friction reaction forces arise from the contribution of remarkably complex multi-component and multi-scale processes [7]. The sum of these physical interactions globally acts as a power loss mechanism directed against the motion. In order to better picture the phenomenon without entering into complex details, friction phenomena may be regarded as an irreversible redistribution of the macroscopic mechanical energy among a multitude of microscopic degree of freedom [8]. In other words, the kinetic energy of the macroscopic body in motion is eventually converted into the energy of thermal vibrational motion of atoms. The macroscopic kinetic energy thus converted into heat is then said to be dissipated. However, the frictional response is quantitatively difficult to evaluate in through predictive models.

Indeed, understanding how the mechanical kinetic energy of the oscillating block at macroscale is transferred into various elementary excitations within the surrounding medium at microscale is a complicated issue. Although, considerable advances have been realized in both the theoretical and the experimental fields on the friction energy dissipation mechanisms during the past decades. In crystalline metallic materials, the transport processes such as phononic excitations, electronic effects and bonding/debonding interaction [13] were demonstrated to play key roles in mediating the frictional energy dissipation at a fundamental level. These physical interactions are notably responsible for the thermalization and heat carrying processes in metal. Further detailed developments may be found elsewhere [9]–[12] on these interesting topics. Nevertheless, these works only describe the friction-dissipation mechanisms at the atomic scale; either through theoretical modellings or through experimental sets on nanomaterials, and fail at providing a consistent macroscopic formulation of friction, even at a mesoscale level. Bridging the gap between nanoscale and microscale contact systems probably constitute the most outstanding challenge of the surface science field.

### 2.3 Limits in the prediction of friction related phenomena at the macroscale

Friction assembling technologies are macroscopic tribo-systems where the ‘friction’ terminology actually designates various unrelated effects of different nature such as: adhesion, fracture, or deformation; all these mechanisms imply dissipation phenomena. The interactions between the sliding surfaces are then influenced by multiple factors such as the nature and the intensity of the load, the reactivity of the materials with the environment, the bulk properties of the materials, the physical properties of the sub-surface layers and the surfaces properties and topography. Thus, due to that complexity, no straightforward relationship exists between a considered macroscopic system and the friction dissipation forces that would arise. Despite progresses in the understanding friction-dissipation related phenomena, the Feynman’s observation stating that: “i*t is quite difficult to do quantitative experiments in friction, and the laws of friction are still not analyzed very well, in spite of the enormous engineering value… At the present time (1963), in fact, it is impossible even to estimate the coefficient of friction between two substances*” is still true and the situation has not drastically changed since. Consequently, the development of predictive model on friction stimulated assembling processes

are a challenging task. The set of experimental campaigns appears as the most reliable way to estimate the phenomenological effect of the friction related phenomena on a macroscopic tribo-system.

In the linear friction welding field, most assembling parameters are determined empirically and classified in processing maps related to their ability to efficiently produce axial shortening.

## 3. Plastic flow behavior and thermal softening

While dry sliding friction phenomena initially dominate the first stage of the welding procedure, the increasing onset of plastic deformation progressively prevails over the bulk materials until becoming the dominant operating mechanism through the junction. The thermal energy generation then seems to switch from a friction-dissipation phenomenon restricted to the close surface region to a bulk plastic deformation-dissipation phenomenon. Closer look at different moment of the welding procedure (see example presented in Figure 5) illustrate the progressiveness of the change over a global plastic deformation process.

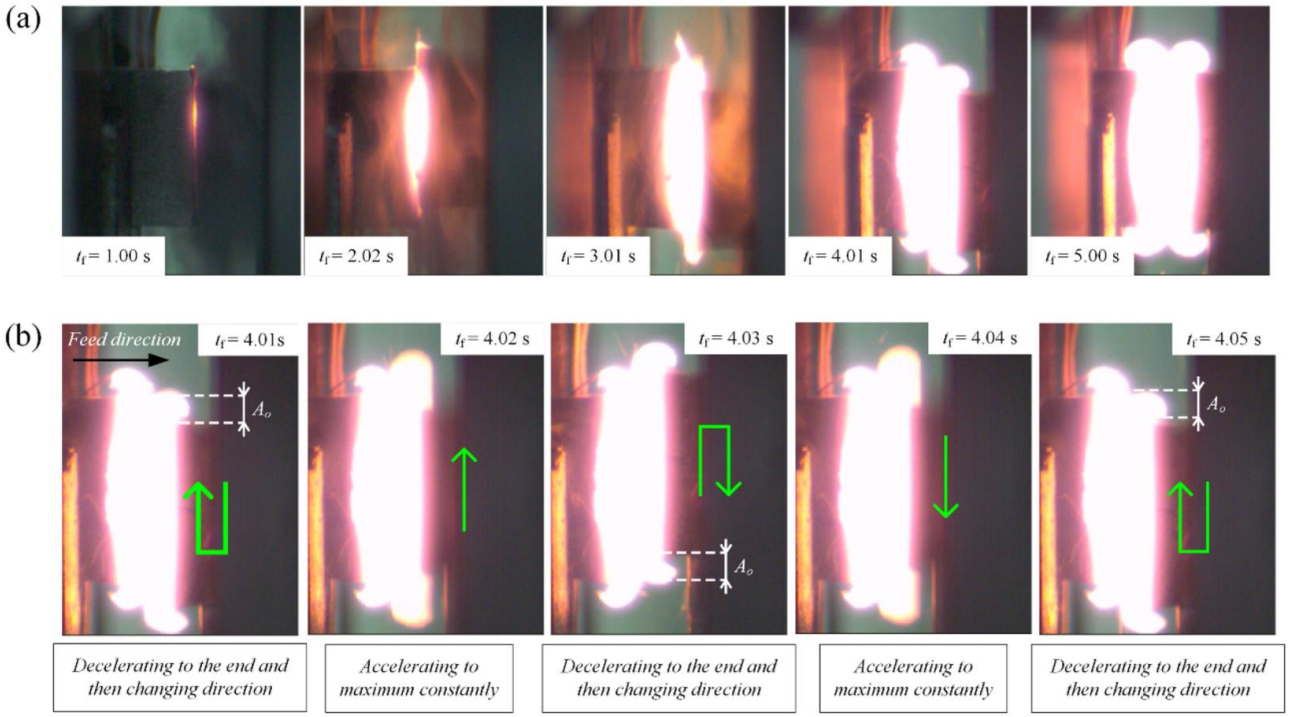


**Figure 5***: Illustration of the linear friction welding procedure captured from* [13] *and applied on a nickel-based alloy:* **(a)** *a high-speed camera filmed the process at different welding times;* **(b)** successive *frames decomposing one oscillation cycle. The blocks dimensions are 15 x 10 x 33 mm and the process parameters are P = 400 MPa, f= 25 Hz and A = 2.9mm.*

### 3.1 Plasticity-induced heating phenomenon

Plasticity-induced heating results from complex internal friction mechanisms that we will try to detail schematically in this section. Pioneer works [14], [15] demonstrated that when metallic materials are deformed plastically, most of the mechanical energy expended in the deformation process degenerates into thermal energy. Therefore, the deformed materials manifest a temperature rise that finally dissipates through heat transfer processes within the surrounding environment. According its intensity, such plasticity-induced temperature elevation may have profound effects on the constitutive behavior of materials [18]–[20]. In deforming metallic materials, this phenomenon generally induces a thermal softening that drastically modify the materials response to mechanical loads. This is specially the case when the deformation is highly localized. For instance, in some extreme events such as shear banding [21], materials experience intense local deformation that may sometimes result in temperature elevation close up to several hundred of Kelvins in barely a tenth of seconds [22]. In such conditions, the sudden thermo-mechanical changes within the deforming zone of the material approach quasi-adiabatic conditions [23].

The proportion of plastic energy effectively dissipated through thermal micro-dynamic excitations is often simplistically modelled by a scalar quantity: the Taylor-Quinney coefficient [24], [25]. It expresses the efficiency of the thermomechanical conversion, defined as the ratio of the thermal dissipation to mechanical work involved in the deformation process. However, modern experimental investigations [17], [26]–[28], [25] tend to revise this interpretation and demonstrate more subtle and complex dependences on the energy partition. The latter notably relies on the thermo-mechanical history, the nature and the rate of the solicitation, the activated plastic deformation mechanisms or prospective phase transformation. These transformations are all susceptible to consume energy and then influence the time-deformation behavior of materials [29]. Furthermore, accurate measurements pose major experimental issues in the field, and the current experimental data are notoriously unreliable. The problem of plasticity-induced heating is nowadays far from understood [20].

### 3.2 Plastic deformation carriers and energy dissipation mechanisms

On another note, the rest of the energy delivered to the material contributes to the effective mechanisms of plastic flow. In crystalline materials, structural defects govern the plastic deformation within the lattice. Among them, the dislocations are the main elementary carriers that mediate crystal plasticity [30]. Indeed, the dynamic motion of dislocations allows shearing the lattice along certain crystallographic plane and certain crystallographic directions eventually leading to the irreversible deformation of crystals [31]. The fundamental elements of dislocation-mediated plasticity theory are well formulated and described in classic solid-state physics textbooks [32]–[34], where dislocations are described as line-like crystal defects moving as elastic strings through a space of lattice periodic potentials: known as the Peierls potentials [35].

In this respect, dislocation motion is a chaotic process that requires overcoming flow-impeding obstacles. Thus, when macroscopic thermo-mechanical loads are applied, the supplied energy stimulates vibrations on the dislocation lines at a microscale level. It occasionally results in the formation of successive kink-pair events that exceeded local energy barriers and propagate through the whole dislocation line eventually yielding its motion across the lattice [36]. Their motion is then statistically favored along crystallographic planes and directions of lower barrier energy therefore, of easier glide. Finally, the collective glide of dislocations through the crystal lattice is responsible for macroscopic plastic flow.

Nevertheless, the crystal lattice is a highly dissipative environment that manifests an important intrinsic resistance to dislocation motion (the Peierls stress) [37]. This mechanism competes with extrinsic resistances exerted by interactions with other lattice defects such as vacancies, interstitials as well as other stored dislocations. Consequently, while mobile dislocations escape their metastable configurations and start moving through the lattice, they ancillary trigger multiple micro-dynamic excitations. The various interactions within the lattice give rise to a friction-dissipation phenomenon where the kinetic energy of the moving and vibrating dislocation is progressively degraded into thermal excitations. It eventually results in local temperature elevation through the passage of dislocations. Hence, the subsequent energy loss slows down the moving defects. The latter consequently experience strong viscous drag effects until they get trapped into the next metastable-equilibrium position within Peierls valleys of the lattice [38]–[40]. The dissipated micro-dynamic excitations enable the relaxation of the dislocation structures. Dislocation are crystal defects are strongly coupled to their atomic environment, they generate thermal energy as they nucleate, move, interact, tangle [41]. At a fundamental level, the interactions of dislocations with phonons [42]–[46], and to lesser extent electrons [47], are pointed out as the key physical ingredients in the process of conversion of the plastic work into thermal energy during deformation; as well as in the process of thermal activation of dislocation glide. Lastly, when the external thermo-mechanical solicitations stop, part of the structural defects remain stored in the lattice. They constitute sources of potential energy for further transformations. These entrapped structural defects are sometimes designated as the stored energy of plastic deformation [16].

Herewith, the elementary mechanisms that govern crystal plasticity give rise to a thermoplastic coupling between the deformation activity and its dissipative side effects. Extensive plastic deformation leads to the multiplication of mobile dislocations by activation of multiple dislocation sources [48], [49] within the lattice. The plastic flow results then from the collective contribution of numerous individual dislocations, each concomitantly contributing to local thermallization of the material. The latter effect may lead to substantial temperature elevation within the deforming matter (the latter may reach several hundred of Kelvins). Eventually, the additional thermal vibrational energy provided during the deformation helps dislocations core to overcome the energy barriers within the lattice, thus resulting in a reduction of the flow stress as the temperature rises. Consequently, the yield stress at a given rate collapses as the temperature increase.

### 3.3 Self-sustained plastic-flow and plasticity-induced heating in linear friction welding

When applied under appropriate rubbing parameters, the operating mechanisms of linear friction welding perfectly exploit the thermoplastic coupling effects on materials. The alternate oscillation motion progressively leads to alternate shear deformation of the junction zone. Simultaneously, the formation of the intermediate viscoplastic layer between the rubbing/adhering surfaces arise from the causal relationship between plastic flow and thermally induced softening. The collapse of yield stress under the influence of the temperature elevation makes the plastic flow easier, which in turn generate additional thermal energy, which further soften the materials… finally resulting in self-sustained thermo-mechanical processing conditions. Lastly, the material is heated up until a malleable state where it cannot hold the constraints imposed by the compressive force it is subjected to. A kinematically admissible plastic flow then develops yielding to the formation of lateral extrusion of matter. An example of thermal field development during the linear friction welding of Ti64 alloy blocks is illustrated in Figure 6.

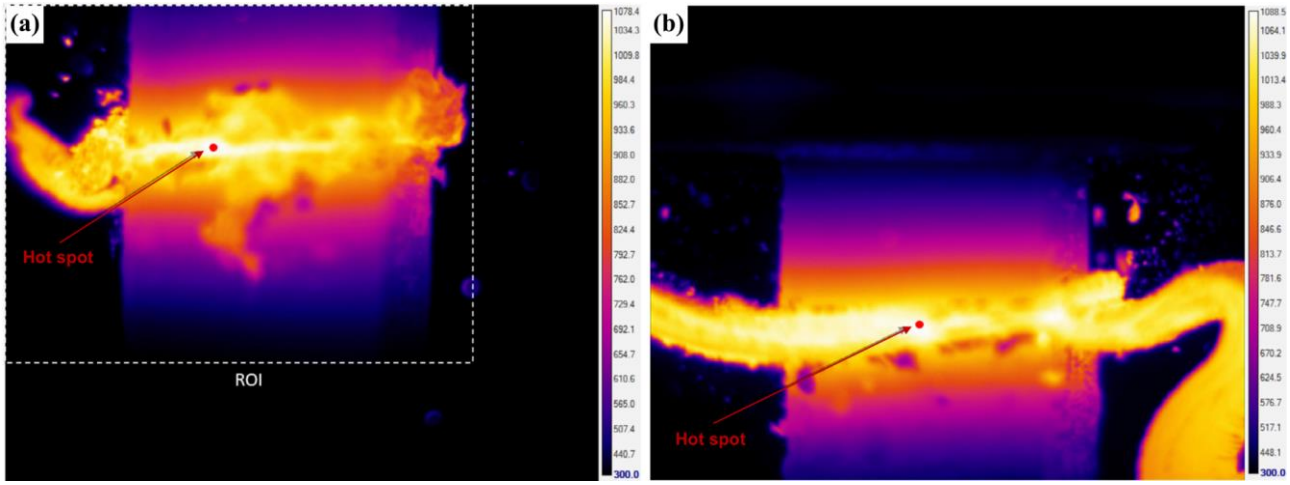


**Figure 6***: Infrared thermography imaging of the temperature field developing during the linear friction welding of Ti64 alloy blocks (20 x 14 mm² x 30 mm). The surface temperature map are displayed in the beginning of the flash formation stage* **(a)***, and during the 'self-sustained' expulsion stage of the equilibrium phase* **(b)***. The weld parameters are: 30 MPa forging pressure, 36 Hz oscillating frequency and 1.5 mm amplitude. The results are extracted from* [50].

Hence, it is presumed that the self-regulated behavior often described in the LFW literature relies on the establishment of a balance between the imposed mechanical solicitation, the resulting extensive plastic formation and its conjugated temperature elevation, the material expulsion rate and the heat flux. The burn-off rate thus reaches a quasi-steady-state.

## 4. Adhesion mechanism between the rubbing surfaces

As in many macroscopic tribological systems, the interactions arising from the linear friction welding procedure between the faying surfaces are complex. The variety of phenomena implied in the surfaces interactions are wide and goes from atomic collisions between surface asperities, chemical reactions, plastic deformation, breaking mechanisms, or potential formation of debris and the resulting influences they present are challenging to quantify. However, when applied under appropriate process parameters, the initial dry sliding friction phenomenon turns into a shear and pressure-driven plastic deformation of the joining zone. The latter phenomenon is a common experimental trend that emerges whenever the necessary conditions for effective solid-state bonding are met.

Paradoxically and despite its fundamental importance, the transition from a close sub-surficial friction-dissipation to bulk deformation driven mechanism currently remains poorly understood. The dynamic aspect of the friction welding procedure notably explains this and limits deeper experimental prospections on the effective bonding mechanisms. Regarding that, adhesive interactions presumably play a key role in the proto-joining mechanism between the rubbing surfaces.

### 4.1 Presumed adhesion mechanisms between real metallic surfaces

Real surfaces may schematically be characterized through two dominant characteristics: their roughness (most often in form of statistical quantities aiming at describing the geometrical characteristics of the surfaces) and their composition (oxide layers, physisorbed and chemisorbed species, contaminants) [51]. On a microscopic scale, surfaces are rough and consist of peaks and asperities with variable morphologies. Consequently, the initial contact area produced when metallic surfaces are brought together are much less than the nominal surface area because of surface roughness. Herewith, under compressive mechanical load, the interfacial contacts are supported by asperities that elastically and plastically deform until the actual area of contact is capable enduring the applied load.

In open air and under standard conditions of temperature and pressure, surface oxide layers are in chemical equilibrium with ambient atmosphere. Similarly as in accumulative roll-bonding processes [52] or in friction stir welding processes [53], the disruption of those oxides is a prerequisite condition to successfully achieve a metallic bond through the establishment of a metal-to-metal intimate contact at the interface. Hence, when the faying surfaces start rubbing each other, a tangential stress arises from the contact interactions. The combination of tangential shear stresses with compressive stresses should favor extensive deformation until breaking of the frail sub-surface oxide layers, thereby promoting metal-to-metal contacts. A strong interfacial cohesion may then take place by the formation of metallic bonds resulting from electron delocalization between the contacting atoms of metallic elements as described in *jellium* model approximations [54]. Ultimately, it may reasonably be expected that the continuous alternate motion the oscillating block conducts

to extensive break up, fragmentation and dispersion of the former surface oxide within plastic flowing material at the interface.

### 4.2 Metallic bond at metal-to-metal contacts

Two metallic surfaces brought together in contact experiences adhesion if a tensile force is required to separate the contacting system [55]. Thus, the fundamental quantity attesting the formation of an adhesive bond is the strength of the chemical bond between the two metals. The latter is evaluated by the definition of an adhesive energy $E_{adh}$.

In deformation welding, the adhesion phenomenon between metallic surfaces constitutes a phenomenon of primary technological importance and probably plays a fundamental role in the joining process. The details of the adhesive bond depend on many factors like surface topography, crystal structure, chemical state, lattice mismatch, interfacial segregation, potential formation of new phases at the interface, *etc* [56].

An intuitive assumption proposes that when two clean metallic surfaces are brought into contact, solid-state bonding occurs. The latter phenomenon was notably observed experimentally on clean single crystals in ultra-high vacuum [57]–[60] or in cold deformation assembling through seizure effects [61]. Indeed, even though the faying surface manifests a boundary defined by the position of surface atoms at the microscopic scale, the electron wave-functions can reach far out of the surface [62]. Hence, interactions due to the overlap of wave-functions may arise eventually yielding to a metallic bond. The bond interactions that held the atomic structures together in metals can best be described as a cloud of free negatively charged electrons enveloping ionized positively charged atoms and forming one unit due to the resulting attractive forces. In this prospective theory, plastic deformation is necessary to break up surface films that preclude intimate metallic contact and weld formation.

Theoretical calculations performed through self-consistent density-functional theory [63], [64] for metal-metal interfaces using *jellium* models gave reasonable modelling for the cohesive interactions in simple metals [65]–[69]. Thus, defining the theoretical background for metallic bonding between contact surfaces. The '*jellium*' formalism consists of thinned atom cores imbedded in a thinned sea of electrons and where the electronic structure of the metal atoms are simplified. The adhesion bond strength at the bimetallic interface is then shown to depend on the free-electron density, the electronic structure of metals ((s, p, d) character of free electrons), and the structure of the Fermi surface.

In the experimental field, different *in-situ* observations of the metallic adhesion and bonding were carried out [70], and notably on nano-contacts made of gold [71]–[73]. Indeed, material made of gold avoids surface oxide issue during the contacting phase since this element is very stable in ambient atmosphere; gold is then an ideal candidate for such 'cold welding' experiments. The latter series of work [71]–[73] gives an

interesting insight about the fundament mechanisms of solid-state bonding between metals. Two nanometer-sized tips are first brought in contact using a piezo-driving specimen holder and followed *in-situ via* high-resolution transmission electron microscopy. Once the contacting done, the mobile tip (A) is retracted back to its initial position. The atomic processes occurring at the contacting point are depicted in Figure 7 and 8.

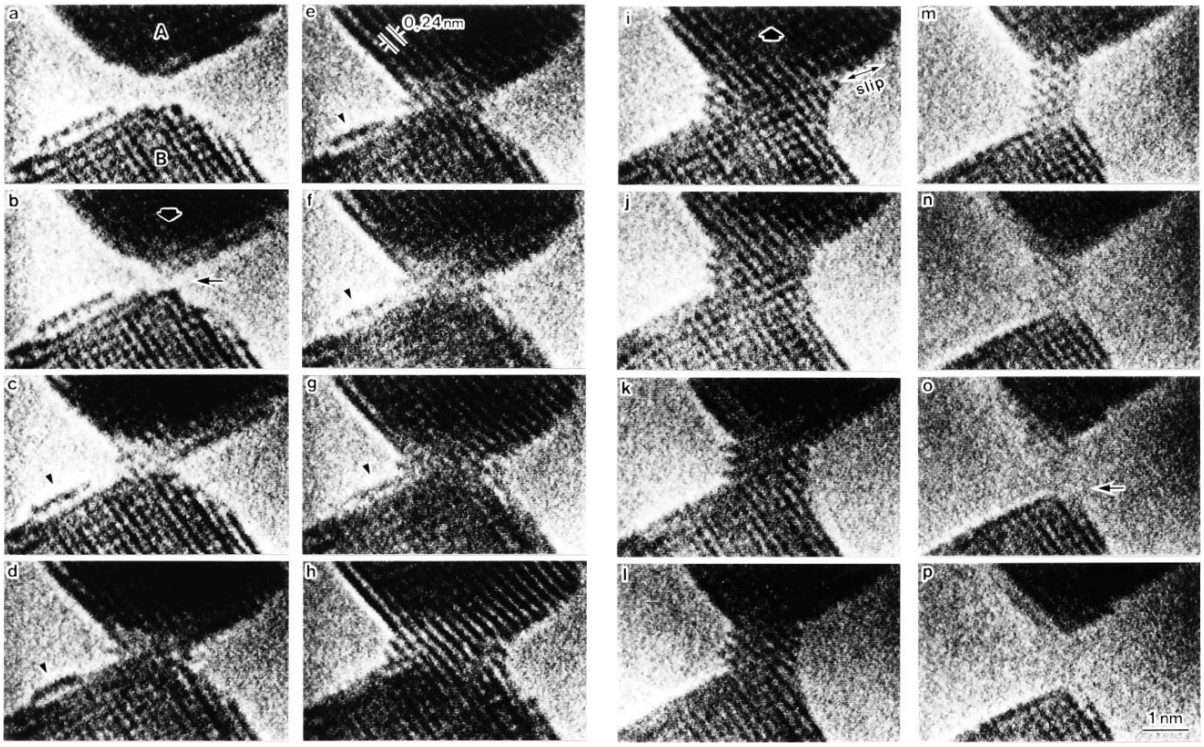


**Figure 7**: *Time-sequence series of HRTEM images of the contact between a mobile gold tip* A *and a fixed gold tip* B, *the* **a-h** *sequence shows the contact formation and neck growth and the* **i-p** *sequence illustrates the retraction phase; the total duration of the contact then retraction sequence is partitionned on 30 s. The results are extracted from* [72].

The results exposed in [72] demonstrated that the formation of the initial contact implies a few atomic columns, then the contact grows until taking a neck shaped configuration. The latter forms under the action of compression and surface diffusion. When the tips are retracted, slip events are observed through the juntion and may help structural relaxation within the intermediate pillar. After fracture, the pillar-like structure are elongated by a few atomic layers.

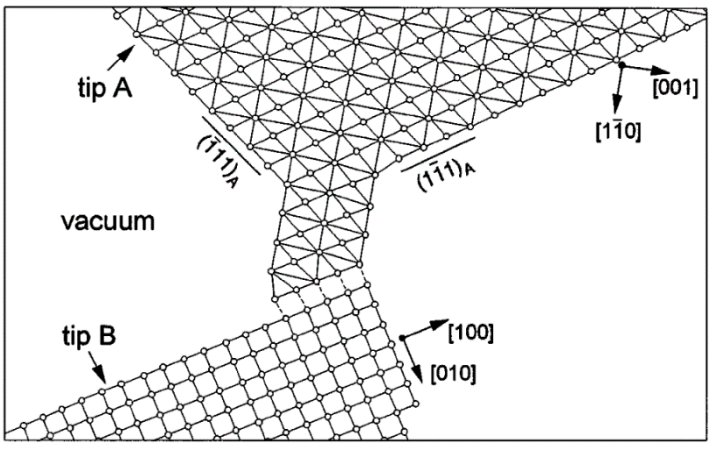


**Figure 8**: *Projected atomic arrangement within the tips* [24].

During the approach phase, the piezoelectric sensor measured an attractive force spontaneously arising for the metal surfaces. The adhesion phenomenon results then from the spontaneous aggregation of the atoms from the faying tips. It finally forms a grain boundary structure within a neck-shaped bonding.

Similarly, other *in-situ* contact welding experiments [74] were carried on gold mono-crystalline nano-wires performed and monitored under high-resolution transmission electron microscopy. A head-to-head assembling sequence between two gold nano-rods is illustrated in the Figure 9 below. Interestingly, the results demonstrated that when the front surfaces of the nano-rods are brought in contact, they spontaneously weld together without significant deformation. By way of qualifying that results, though, the fact that the contacting crystal structures present very close orientation from one another may explain the ease of the bonding process. After welding, the bonded structure do not seems to present extenstive defect density.

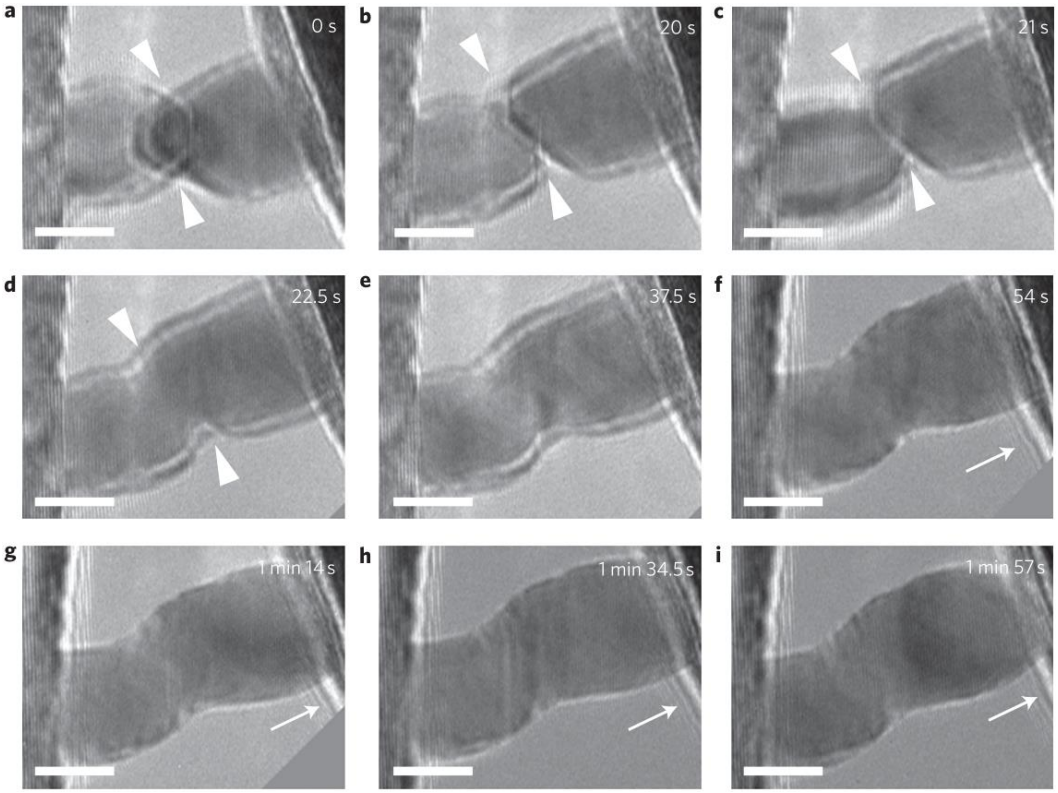


**Figure 9***: In-situ observation of a head-to-head welding between two gold nano-rods extracted from* [74]*, the* **a-c** *sequence presents the approach phase, the front surfaces come into contact at c. The joining process is completed within 1.5 s* **(c, d)** *followed by a relaxation of the structure* **(d, e)**. *The* **f-i** *sequence illustrates the withdrawal of the STM probe along the direction indicated by the arrows. The scale bar in white is of 5 nm.*

The coalescence process discussed through these works highlighted the role of fast atomic diffusion on the metal surface and the loss in surface energy due to the loss in surface area when contracting (or surface relaxation) as the driving force for metal coalescence. Indeed, the diffusion barrier for single atoms on metal surfaces are low with estimated order of magnitude < 1 eV [75], thus providing high mobility to the surface atoms.

Although difficult to transpose at a macroscopic scale, these series of works qualitatively indicate that the intimate metal-to-metal assumption leading to solid state bonding in friction welding technologies seems plausible. The different atomic-scale visualizations of the process highlight the spontaneous bonding of metallic atoms when an intimate metal-to-metal contact is established.

## 5. Reflections on the surface oxide layers evolution

Most metallic alloys are extremely reactive with the ambient atmosphere. Indeed, the intrinsic reaction of metallic elements with oxygen spontaneously yields to the formation of and oxide layer at the solid-gas interface [76]. The transport mechanisms by which the reactants (here metallic elements or/and oxygen element) penetrate the oxide layer constitutes the essential of the field of oxidation kinetic [77].

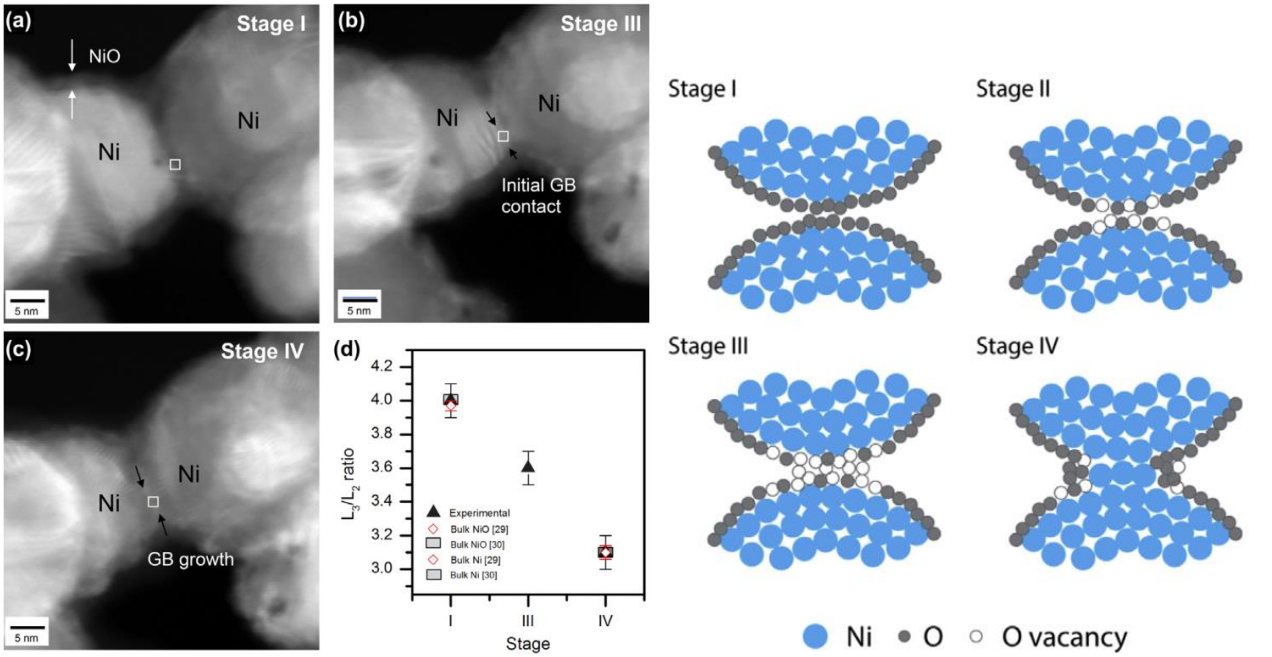


**Figure 10**: H*igh-angle annular dark field-STEM images of two contacting Ni particles extracted from* [78], *the* **(a)-(c)** *sequence shows the progressive oxide removal until necking formation.* **(d)** *The electron energy loss spectroscopy (EELS) results on the $L_3/L_2$ ionization ratio at the contact area is also provided, the ratio decreases and tend to 1 meaning that $L_3$ ionization (oxide) change to $L_2$ corroborating with the progressive oxide disruption. A schematic representation of the surface cleaning mechanism is also displayed.*

Thus, under ambient atmosphere and standard conditions of temperature and pressure, most metals and alloys display stable oxide phases forming a few nanometers thick passive layer at their surface. Oxide layers form with little to no delay on the reaction with oxygen at the solid-gas interface when exposed to ambient atmosphere making their presence unavoidable. Once formed, they generally constitute a protective shield to metal-to-metal contacts and prevents from metal adhesion. The disruption of those oxides is then a prerequisite condition to achieve a metallic bond throughout the successful establishment of intimate metal-to-metal contact at the interface. To illustrate this statement, experimental evidences are provided on the bonding of nano-particles [78] followed by *in-situ* by TEM imaging. Interestingly, the NiO oxide layer covering the nickel particles is found to get disrupted during electric field assisted sintering. The elucidation of the mechanisms responsible for metal-metal contact establishment in this specific case are further developed elsewhere [79].

Therefore, the primary function in all solid-state assembling processes aims at getting rid of these oxide layers in order to favor metal-metal contact points through the weld interface. Linear friction welding, similarly as accumulative roll-bonding processes [52], or friction stir welding processes [53], are all plastic deformation stimulated processes. In this case, it is then reasonably expected that part of the surface oxide layer and adsorbed contaminants are mechanically broken up, fragmented and dispersed with flowing material along the procedure.

Besides mechanical breaking, other oxide disruption mechanisms are conceivable regarding the nature of the friction welding procedure. Indeed, the friction welding induces severe thermo-mechanical change that may have consequences on the phase stability of the former surface oxide. The potential scenarios are enumerated as it follows:

**(1)** The oxide phases remain stable despite the thermo-mechanical load. The action of the mechanical loads fragments the passive layer into oxide particles. The latter are disseminated within the flowing material due to extensive plastic deformation.

**(2)** The oxide phases become unstable under the thermo-mechanical loads and dissolve within the metallic matrix.

**(3)** Similarly, the oxide phases become unstable under the thermo-mechanical loads and dissolve within the metallic matrix. However, the dissolve oxygen oxidizes other elements with which it has higher chemical affinity resulting in an internal oxidation phenomenon.

**(4)** Lastly, residual gaseous species entrapped within surface asperities may also react with metal elements during the assembling process yielding to their oxidation.

The fate of the former surface oxide phases is rarely studied or discussed through the solid-state welding literature. Indeed, experimental procedure to follow the potential transformation of the oxide phases through the assembling procedure are difficult to build up. In order to clarify this aspect of the process, comparison with similar industrial processes would be interesting. In this sense, considering diffusion bonding technique of metals and metal powder sintering is irrelevant here. The latter are often better documented on the surface oxide evolution, while the thermomechanical loads are comparable, to a certain extent.

Indeed, in diffusion assembling technique and in sintering processes the thermodynamic stability of the oxide surface films has a considerable influence on the resulting bond quality. In both processes the materials, massive blocks on the one hand, fine metal powder on another hand, are forced against each other under high temperature conditions and start to plastically flow. A local oxygen-lean atmosphere is then created between the faying surfaces helped by the surface sorption of gas molecules. In diffusion bonding, creep deformation is exploited for the closure of the interfacial voids between the contacting surfaces and imply slow kinetics of deformation with a low applied pressure owing to limited surface oxide mechanical breaking at the assembling interface. While in sintering processes higher isostatic pressure are applied on the hot matter with

comparable holding time (most often a few hours). From a physical point of view, sintering may arguably be seen as a form of diffusion bonding of compressed metal powders. Although the analogy with friction welding is interesting, the thermal cycle duration of the LFW procedure is way quicker with only a few seconds of total duration. The relevance of the comparison then strongly depends on the transformation kinetic of the oxide phases.

Two types of aeronautical grades were examined during the OPTIMUM project: titanium alloys and a nickel-based alloy. In order to better understand the eventual oxide disruption mechanisms in linear friction welding will be review.

### 5.1 Oxide disruption on titanium-based alloys

In the diffusion-bonding field, it is well-established that the metal-metal bond formation depends heavily on the dissociation ability of the oxide film at the contacting surfaces [80]. Because of that, titanium alloys are considered as excellent candidate materials in such assembling techniques. Indeed, under high temperature conditions, the critical chemical activity for oxide reduction by the bulk metallic matrix may result in the complete dissociation of the oxide film and the oxygen bulk-diffusion into the metal lattice. Furthermore, the oxide dissociation rate is temperature dependent and drives considerably the mechanism in diffusion bonding processes [81]. It is the reason why the diffusion bonding of metals is carried at temperature $T_h > 0.5$, (where $T_h$ is the homologous temperature: $T/T_{melting}$).

This property is notably of utmost importance in the diffusion bonding of titanium-based alloys where the dissociation reaction may be described as it follows:

$$Ti_xO_y \rightarrow x.Ti + y.O^* \quad : (1)$$

$$O^* \rightarrow O_{Sol} \quad : (2)$$

The dissolution occurs in series with first (1), the dissociation reaction at the oxide/metal interface which is an energetically activated reaction (1) and second, the solid-state diffusion of the oxygen in the metallic solute matrix which is a diffusion-controlled process. The stability of the oxide layer depends on the oxygen solubility in the metal lattice, the lattice diffusivity of oxygen and the processing temperature [82]. Theoretical calculations developed in the literature [83], [84] on the stability of the titanium oxide layer with the titanium HCP α-phase based on oxygen diffusion equation and considering an instantaneous dissociation process show that for homologous temperature $T_h$ = 0,6 a 10 nm thick oxide layer may be dissolved in a tenth of seconds.

A more advanced model [81] taking into account the dissociation rate and the oxygen solubility limit of the titanium alpha and beta lattice gives a homologous temperature estimation in the same order of magnitude, with $T_h = 0{,}66$ for the dissolution of a 10 nm thick oxide layer in ≈ 0,1 s.

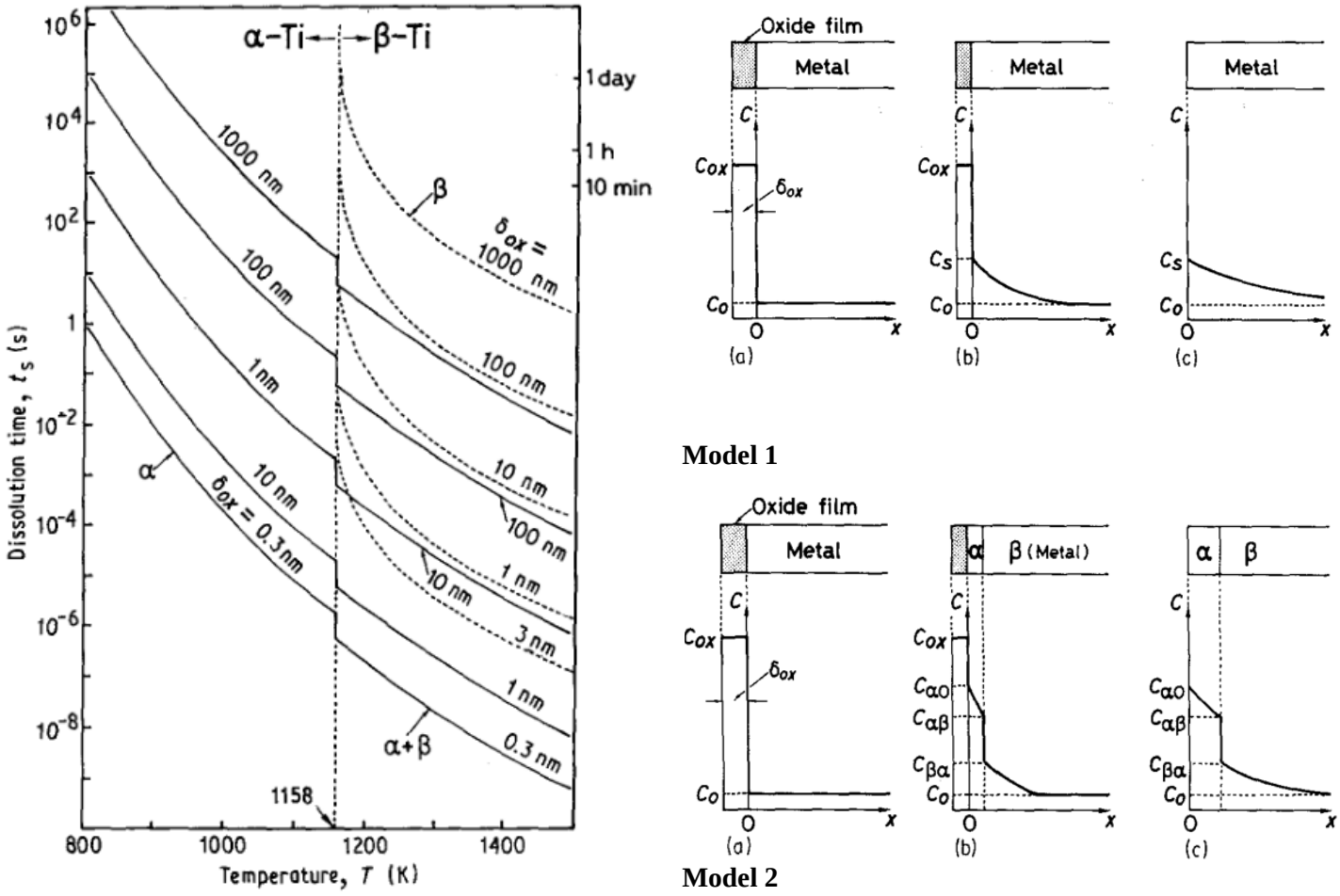


**Figure 11**: *Results of the calculations adapted from* [81]. *Temperature dependence of dissolution time of titanium oxide film on pure titanium. The solid curves for T<1158 K were calculated by model 1 and those for T> 1158 K by model 2. The dotted curve for T> 1158 K denotes the time when the α–phase disappears.*

Despite the technical limitations for experimental verification of such rapid kinetics of dissolution, those approached models offer a plausible explanation for the primal interfacial metal-metal bond formation occurring between the faying surfaces in titanium alloy friction assembling processes. It may also be expected that the mechanical fragmentation in particles lead to faster kinetics for native oxide dissolution.

### 5.2 Oxide disruption on the nickel-based alloy IN718

On the contrary to titanium alloy, very little works are yet available on the diffusion bonding applied on nickel-based alloys in the scientific literature. Most superalloys contain elements that present high intrinsic

affinity for oxygen in their composition *id est*: Ni, Cr, Al, Ti, etc… In addition, this class of alloys is known for its corrosion resistant grades with good performance up to high in-use temperature, meaning that their surface oxide phases are very stable under these extreme conditions. Such oxide film stability is highly problematic in a diffusion-bonding context and probably explain why the scientific literature on the topic is not abundant.

The efforts [85] initiated to investigate the diffusion bonding of IN718 alloy demonstrated incomplete bond and strong microstructural heterogeneities in the interfacial zone. In addition, the joining parameters in such configurations are clearly designed toward a mechanical break of the oxide films by creep deformation. It results in high temperature processing parameter with detrimental consequences on the microstructure (notably in term of phase presence and grain size distribution). Alternative methods are carried out using intermediate coating [86] or transient liquid phases [87] to try improving the performances in such assembling with varying degrees of success.

Diffusion bonding techniques seems inappropriate for the solid-state bonding of IN718 alloy. In the perspective of linear friction welding, it is then important to note the potential problematic aspect of the former surface oxide film on the joint integrity.

## 6. Conclusion

The physical mechanisms in play during the linear friction welding process have been reviewed. The role of dry sliding friction and the importance of the thermo-mechanical coupling arising from the imposed harmonic load have been highlighted. Concerning the latter, the physical origin of the self-sustained plastic flow has been attentively discussed. The fundamental mechanisms of the metal-to-metal adhesion were also succinctly presented, as they presumably play a major role in the onset of the metallurgical coalescence in solid-state assembling processes. Finally, the important problem raised by the unavoidable presence of passive oxide films on the faying surfaces of the parts to assemble was addressed. Indeed, the latter constitute a physical and effective barrier to metallic adhesion. Thus, solid-state welding processes all aims at bringing energy either by deformation or/and through thermal load to disrupt these oxide layers, as they prevent from spontaneous metal-to-metal adhesion. Furthermore, the variety of solid-state welding technologies illustrates the different technological response adopted to answer that issue.

Having all these topics clear will help to contextualize the present work in the LFW field. In light of these elements, the objective of the phD project is to clarify the microstructural evolution at the joining interface of two types of weld configurations. The first configuration concerns the welding of two dissimilar titanium alloy grades. Their dissimilar aspect has been advantageously exploited to elucidate the joining mechanism that takes place at the microstructural level in the weld interface. The second configuration explores the possibility to weld together two blocks made of the nickel superalloy grade IN718. Indeed, nickel-based alloys are known to be challenging to weld through solid-state methods owing to the stability of their native oxide phases.

## 7. References


[1] I. Bhamji, M. Preuss, P. L. Threadgill, et A. C. Addison, « Solid state joining of metals by linear friction welding: a literature review », *Materials Science and Technology*, vol. 27, nº 1, p. 2‑12, janv. 2011, doi: 10.1179/026708310X520510.

[2] A. Vairis et M. Frost, « High frequency linear friction welding of a titanium alloy », *Wear*, vol. 217, nº 1, p. 117‑131, avr. 1998, doi: 10.1016/S0043-1648(98)00145-8.

[3] A. M. Mateo Garcia, « BLISK Fabrication by Linear Friction Welding », in *Advances in Gas Turbine Technology*, E. Benini, Éd. InTech, 2011.

[4] J. P. Joule, « The mechanical equivalent of heat », 1845.

[5] R. Feynman, R. Leighton, et M. Sand, *The Feynman lectures on physics*, Addison-Wesley Pub. Co. 1963.

[6] A. B. Arons, « Development of energy concepts in introductory physics courses », *American Journal of Physics*, vol. 67, nº 12, p. 1063‑1067, déc. 1999, doi: 10.1119/1.19182.

[7] B. N. J. Persson, *Sliding friction: physical principles and applications*. Berlin; London: Springer, 2011.

[8] U. Seifert, « Stochastic thermodynamics, fluctuation theorems and molecular machines », *Rep. Prog. Phys.*, vol. 75, nº 12, p. 126001, déc. 2012, doi: 10.1088/0034-4885/75/12/126001.

[9] I. L. Singer, « Friction and Energy Dissipation at the Atomic Scale: A Review », *J. Vac. Sci. Technol. A*, vol. 12, nº 5, p. 13, 1994.

[10] S. Yu. Krylov et J. W. M. Frenken, « The physics of atomic-scale friction: Basic considerations and open questions: The physics of atomic-scale friction », *Phys. Status Solidi B*, vol. 251, nº 4, p. 711‑736, avr. 2014, doi: 10.1002/pssb.201350154.

[11] J. Y. Park et M. Salmeron, « Fundamental Aspects of Energy Dissipation in Friction », *Chem. Rev.*, vol. 114, nº 1, p. 677‑711, janv. 2014, doi: 10.1021/cr200431y.

[12] R. Hu, S. Yu. Krylov, et J. W. M. Frenken, « On the Origin of Frictional Energy Dissipation », *Tribol Lett*, vol. 68, nº 1, p. 8, mars 2020, doi: 10.1007/s11249-019-1247-7.

[13] P. Geng, G. Qin, L. Chen, J. Zhou, et Z. Zou, « Simulation of plastic flow driven by periodically alternating pressure and related deformation mechanism in linear friction welding », *Materials & Design*, vol. 178, p. 107863, sept. 2019, doi: 10.1016/j.matdes.2019.107863.

[14] W. S. Farren et G. I. Taylor, « The heat developed during plastic extension of metals », *Proc. R. Soc. Lond. A*, vol. 107, nº 743, p. 422‑451, mars 1925, doi: 10.1098/rspa.1925.0034.

[15] G. I. Taylor et H. Quinney, « The latent energy remaining in a metal after cold working », *Proceeding of the Royal Society A*, nº 143, p. 307‑326, 1934, doi: 10.1098/rspa.1934.0004.

[16] A. L. Titchener et M. B. Bever, « THE STORED ENERGY OF COLD WORK », p. 92.

[17] J. J. Mason, A. J. Rosakis, et G. Ravichandran, « On the strain and strain rate dependence of the fraction of plastic work converted to heat: an experimental study using high speed infrared detectors and the Kolsky bar », *Mechanics of Materials*, vol. 17, nº 2‑3, p. 135‑145, mars 1994, doi: 10.1016/0167-6636(94)90054-X.

[18] A. Zubelewicz, « Overall stress and strain rates for crystalline and frictional materials », *International Journal of Non-Linear Mechanics*, vol. 25, nº 4, p. 389‑393, 1990, doi: 10.1016/0020-7462(90)90027-7.

[19] A. Zubelewicz, « Metal behavior in the extremes of dynamics », *Sci Rep*, vol. 8, nº 1, p. 5162, déc. 2018, doi: 10.1038/s41598-018-23566-1.

[20] A. Zubelewicz, « Century-long Taylor-Quinney interpretation of plasticity-induced heating reexamined », *Sci Rep*, vol. 9, nº 1, p. 9088, déc. 2019, doi: 10.1038/s41598-019-45533-0.

[21] P. Landau, S. Osovski, A. Venkert, V. Gärtnerová, et D. Rittel, « The genesis of adiabatic shear bands », *Sci Rep*, vol. 6, nº 1, p. 37226, déc. 2016, doi: 10.1038/srep37226.

[22] A. Eisenlohr, I. Gutierrez-Urrutia, et D. Raabe, « Adiabatic temperature increase associated with deformation twinning and dislocation plasticity », *Acta Materialia*, vol. 60, nº 9, p. 3994‑4004, mai 2012, doi: 10.1016/j.actamat.2012.03.008.

[23] H. C. Rogers, « Adiabatic Plastic Deformation », *Annu. Rev. Mater. Sci.*, vol. 9, nº 1, p. 283‑311, août 1979, doi: 10.1146/annurev.ms.09.080179.001435.

[24] R. Zaera, J. A. Rodríguez-Martínez, et D. Rittel, « On the Taylor–Quinney coefficient in dynamically phase transforming materials. Application to 304 stainless steel », *International Journal of Plasticity*, vol. 40, p. 185‑201, janv. 2013, doi: 10.1016/j.ijplas.2012.08.003.

[25] D. Rittel, L. H. Zhang, et S. Osovski, « The dependence of the Taylor–Quinney coefficient on the dynamic loading mode », *Journal of the Mechanics and Physics of Solids*, vol. 107, p. 96‑114, oct. 2017, doi: 10.1016/j.jmps.2017.06.016.
[26] P. Rosakis, A. J. Rosakis, G. Ravichandran, et J. Hodowany, « A thermodynamic internal variable model for the partition of plastic work into heat and stored energy in metals », *Journal of the Mechanics and Physics of Solids*, vol. 48, nº 3, p. 581‑607, mars 2000, doi: 10.1016/S0022-5096(99)00048-4.
[27] J. Hodowany, G. Ravichandran, A. J. Rosakis, et P. Rosakis, « Partition of plastic work into heat and stored energy in metals », *Experimental Mechanics*, vol. 40, nº 2, p. 113‑123, juin 2000, doi: 10.1007/BF02325036.
[28] P. Knysh et Y. P. Korkolis, « Determination of the fraction of plastic work converted into heat in metals », *Mechanics of Materials*, vol. 86, p. 71‑80, juill. 2015, doi: 10.1016/j.mechmat.2015.03.006.
[29] J. P. Sethna *et al.*, « Deformation of Crystals: Connections with Statistical Physics », *Annu. Rev. Mater. Res.*, vol. 47, nº 1, p. 217‑246, juill. 2017, doi: 10.1146/annurev-matsci-070115-032036.
[30] J. P. Hirth et L. P. Kubin, Éd., *Dislocations in solids. Vol. 16: The 30th Anniversary volume*, 1. ed. Amsterdam: Elsevier North-Holland, 2010.
[31] L. Kubin, *Dislocations, mesoscale simulations and plastic flow*, First edition. Oxford, United Kingdom: Oxford University Press, 2013.
[32] Nabarro, *Theory of crystal dislocation*, Dover Publ. Inc. New York, 1967.
[33] J. Friedel, *Dislocations*. Pergamon, 1964.
[34] P. M. Anderson, J. P. Hirth, et J. Lothe, *Theory of dislocations*, 3rd edition. New York, 2017.
[35] T. Suzuki, S. Takeuchi, et H. Yoshinaga, *Dislocation Dynamics and Plasticity*, vol. 12. Berlin, Heidelberg: Springer Berlin Heidelberg, 1991.
[36] S. P. Fitzgerald, « Kink pair production and dislocation motion », *Sci Rep*, vol. 6, nº 1, p. 39708, déc. 2016, doi: 10.1038/srep39708.
[37] Y. Tang, « Uncovering the inertia of dislocation motion and negative mechanical response in crystals », *Sci Rep*, vol. 8, nº 1, p. 140, déc. 2018, doi: 10.1038/s41598-017-18254-5.
[38] W. P. Mason, « Phonon viscosity and its effect on acoustic wave attenuation and dislocation motion », *The Journal of the Acoustical Society of America*, vol. 32, nº 4, p. 458‑472, avr. 1960, doi: 10.1121/1.1908099.
[39] D. H. Niblett et J. Wilks, « Dislocation damping in metals », *Advances in Physics*, vol. 9, nº 33, p. 1‑88, janv. 1960, doi: 10.1080/00018736000101159.
[40] G. D'Anna, W. Benoit, et V. M. Vinokur, « Internal friction and dislocation collective pinning in disordered quenched solid solutions », *Journal of Applied Physics*, vol. 82, nº 12, p. 5983‑5990, déc. 1997, doi: 10.1063/1.366463.
[41] V. A. Al'shitz et V. L. Indenbom, « Dynamic dragging of dislocations », vol. 18, nº 1, p. 21.
[42] T. Ninomiya, « Dislocation vibration and phonon scattering », *Journal of the physical society of Japan*, vol. 25, nº 3, p. 830‑840, 1968.
[43] T. Ninomiya, « Frictional force acting on a dislocation - Fluttering mechanism », *Journal of the physical society of Japan*, vol. 36, nº 2, p. 399‑405, 1974.
[44] T. Ninomiya, « Equations of Motion of a Dislocation and Interactions with Phonons », in *Treatise on Materials Science & Technology*, vol. 8, Elsevier, 1975, p. 1‑41.
[45] E. P. Roth et A. C. Anderson, « Interaction between thermal phonons and dislocations in LiF », *Phys. Rev. B*, vol. 20, nº 2, p. 768‑775, juill. 1979, doi: 10.1103/PhysRevB.20.768.
[46] A. Maurel, J.-F. Mercier, et F. Lund, « Elastic wave propagation through a random array of dislocations », *Phys. Rev. B*, vol. 70, nº 2, p. 024303, juill. 2004, doi: 10.1103/PhysRevB.70.024303.
[47] H. Kojima et T. Suzuki, « Electron Drag and Flow Stress in Niobium and Lead at 4.2°K », *Phys. Rev. Lett.*, vol. 21, nº 13, p. 896‑898, sept. 1968, doi: 10.1103/PhysRevLett.21.896.
[48] D. Kuhlmann-Wilsdorf, « On the origin of dislocations », *The Philosophical Magazine A*, vol. 3, nº 26, p. 125‑139, 1958, doi: https://doi.org/10.1080/14786435808244398.
[49] J. J. Gilman, « Dislocation sources in crystals », *Journal of Applied Physics*, vol. 30, nº 10, doi: https://doi.org/10.1063/1.1735005.
[50] L. Maio *et al.*, « Infrared thermography for monitoring heat generation in a linear friction welding process of Ti6Al4V alloy », *Infrared Physics & Technology*, vol. 81, p. 325‑338, mars 2017, doi: 10.1016/j.infrared.2017.01.023.
[51] *TRIBOLOGY: Friction and wear of engineering materials*, Second Editions. Cambridge, MA: Elsevier, 2017.

[52] Y. Saito, H. Utsunomiya, N. Tsuji, et T. Sakai, « Novel ultra-high straining process for bulk materials - Development of the accumulative roll-bonding (ARB) process », *Acta mater.*, vol. 47, nº 2, p. 579‑583, 1999.
[53] R. S. Mishra et Z. Y. Ma, « Friction stir welding and processing », *Materials Science and Engineering: R: Reports*, vol. 50, nº 1‑2, p. 1‑78, août 2005, doi: 10.1016/j.mser.2005.07.001.
[54] J. Ferrante et J. R. Smith, « Theory of metallic adhesion », *Physical Review B*, vol. 19, nº 8, p. 3911‑3920, avr. 1979, doi: 10.1103/PhysRevB.19.3911.
[55] H. Czichos, « The mechanism of the metallic adhesion bond », *J. Phys. D: Appl. Phys.*, vol. 5, nº 10, p. 1890‑1897, oct. 1972, doi: 10.1088/0022-3727/5/10/321.
[56] N. Mårtensson, A. Stenborg, Q. Björneholm, A. Nilsson, et J. N. Andersen, « Quantitative studies of metal-metal adhesion and interface segregation energies using photoelectron spectroscopy », *Phys. Rev. Lett.*, vol. 60, nº 17, p. 1731‑1734, avr. 1988, doi: 10.1103/PhysRevLett.60.1731.
[57] H. M. Pollock, P. Shufflebottom, et J. Skinner, « Contact adhesion between solids in vacuum. I. Single-asperity experiments », *J. Phys. D: Appl. Phys.*, vol. 10, nº 1, p. 127‑138, janv. 1977, doi: 10.1088/0022-3727/10/1/014.
[58] H. M. Pollock, « Contact adhesion between solids in vacuum. II. Deformation and interfacial energy », *J. Phys. D: Appl. Phys.*, vol. 11, nº 1, p. 39‑54, janv. 1978, doi: 10.1088/0022-3727/11/1/007.
[59] J. B. Pethica et D. Tabor, « Contact of characterised metal surfaces at very low loads: Deformation and adhesion », *Surface Science*, vol. 89, nº 1‑3, p. 182‑190, janv. 1979, doi: 10.1016/0039-6028(79)90606-X.
[60] V. Keller, « Adhesion between atomically clean surfaces », p. 25.
[61] A. P. Semenov, « The phenomenon of seizure and its investigation », *Wear*, vol. 4, nº 1, p. 1‑9, janv. 1961, doi: 10.1016/0043-1648(61)90236-8.
[62] Sutton, *Electronic structure of materials*. 1993.
[63] P. Hohenberg et W. Kohn, « Inhomogeneous Electron Gas », *Phys. Rev.*, vol. 136, nº 3B, p. B864‑B871, nov. 1964, doi: 10.1103/PhysRev.136.B864.
[64] W. Kohn et L. J. Sham, « Self-Consistent Equations Including Exchange and Correlation Effects », *Phys. Rev.*, vol. 140, nº 4A, p. A1133‑A1138, nov. 1965, doi: 10.1103/PhysRev.140.A1133.
[65] Ferrante et Smith, « A theory of adhesion at a bimetallic interface - Overlap effect », 1973.
[66] J. Ferrante et J. R. Smith, « Theory of metallic adhesion », *Phys. Rev. B*, vol. 19, nº 8, p. 3911‑3920, avr. 1979, doi: 10.1103/PhysRevB.19.3911.
[67] J. H. Rose, J. Ferrante, et J. R. Smith, « Universal Binding Energy Curves for Metals and Bimetallic Interfaces », *Phys. Rev. Lett.*, vol. 47, nº 9, p. 675‑678, août 1981, doi: 10.1103/PhysRevLett.47.675.
[68] J. H. Rose, J. R. Smith, et J. Ferrante, « Universal features of bonding in metals », *Phys. Rev. B*, vol. 28, nº 4, p. 1835‑1845, août 1983, doi: 10.1103/PhysRevB.28.1835.
[69] J. Ferrante et J. R. Smith, « Theory of the bimetallic interface », *Phys. Rev. B*, vol. 31, nº 6, p. 3427‑3434, mars 1985, doi: 10.1103/PhysRevB.31.3427.
[70] U. Dürig, O. Züger, et D. W. Pohl, « Observation of metallic adhesion using the scanning tunneling microscope », *Phys. Rev. Lett.*, vol. 65, nº 3, p. 349‑352, juill. 1990, doi: 10.1103/PhysRevLett.65.349.
[71] Kizuka, Yamada, Degushi, Naruse, et Tanaka, « Time-resolved high-resolution electron microscopy of atomic scale solid-state direct bonding of gold tips », *Microscopy*, vol. 46, nº 2, janv. 1997, doi: 10.1093/oxfordjournals.jmicro.a023502.
[72] T. Kizuka, K. Yamada, et N. Tanaka, « Time-resolved high-resolution electron microscopy of solid state direct bonding of gold and zinc oxide nanocrystallites at ambient temperature », *Appl. Phys. Lett.*, vol. 70, nº 8, p. 964‑966, févr. 1997, doi: 10.1063/1.118312.
[73] T. Kizuka, « Atomic Process of Point Contact in Gold Studied by Time-Resolved High-Resolution Transmission Electron Microscopy », *Phys. Rev. Lett.*, vol. 81, nº 20, p. 4448‑4451, nov. 1998, doi: 10.1103/PhysRevLett.81.4448.
[74] Y. Lu, J. Y. Huang, C. Wang, S. Sun, et J. Lou, « Cold welding of ultrathin gold nanowires », *Nature Nanotech*, vol. 5, nº 3, p. 218‑224, mars 2010, doi: 10.1038/nnano.2010.4.
[75] M. José-Yacamán, C. Gutierrez-Wing, M. Miki, D.-Q. Yang, K. N. Piyakis, et E. Sacher, « Surface Diffusion and Coalescence of Mobile Metal Nanoparticles », *J. Phys. Chem. B*, vol. 109, nº 19, p. 9703‑9711, mai 2005, doi: 10.1021/jp0509459.
[76] D. J. Young, *High temperature oxidation and corrosion of metals*, 2nd edition. Amsterdam Boston Heidelberg London: Elsevier, 2016.

[77] N. Cabrera, « THEORY OF THE OXIDATION OF METALS », p. 23.
[78] C. S. Bonifacio, T. B. Holland, et K. van Benthem, « Evidence of surface cleaning during electric field assisted sintering », *Scripta Materialia*, vol. 69, nº 11 ‑ 12, p. 769 ‑ 772, déc. 2013, doi: 10.1016/j.scriptamat.2013.08.018.
[79] C. S. Bonifacio, T. B. Holland, et K. van Benthem, « Time-dependent dielectric breakdown of surface oxides during electric-field-assisted sintering », *Acta Materialia*, vol. 63, p. 140 ‑ 149, janv. 2014, doi: 10.1016/j.actamat.2013.10.018.
[80] B. Xie, M. Sun, B. Xu, C. Wang, D. Li, et Y. Li, « Dissolution and evolution of interfacial oxides improving the mechanical properties of solid state bonding joints », *Materials & Design*, vol. 157, p. 437‑446, nov. 2018, doi: 10.1016/j.matdes.2018.08.003.
[81] Y. Takahashi, T. Nakamura, et K. Nishiguchi, « Dissolution process of surface oxide film during diffusion bonding of metals », *Journal of Materials Science*, vol. 27, nº 2, p. 485‑498, 1992, doi: 10.1007/BF00543942.
[82] Y. Mizuno *et al.*, « Temperature dependence of oxide decomposition on titanium surfaces in ultrahigh vacuum », *Journal of Vacuum Science & Technology A: Vacuum, Surfaces, and Films*, vol. 20, nº 5, p. 1716‑1721, sept. 2002, doi: 10.1116/1.1500746.
[83] Z. A. Munir, « Analytical treatment of the role of surface oxide layers in the sintering of metals », *Journal of Materials Science*, vol. 14, nº 11, p. 2733‑2740, nov. 1979, doi: 10.1007/BF00610647.
[84] Z. A. Munir, « A Theoretical Analysis of the Stability of Surface Oxides During Diffusion Welding of Metals », p. 4.
[85] G. Zhang, R. S. Chandel, et H. P. Seow, « Solid state diffusion bonding of Inconel 718 », *Science and Technology of Welding and Joining*, vol. 6, nº 4, p. 235‑239, août 2001, doi: 10.1179/136217101101538820.
[86] J. Xiong, L. Yuan, Y. Zhu, H. Zhang, et J. Li, « Diffusion bonding of nickel-based superalloy GH4099 with pure nickel interlayer », *J Mater Sci*, vol. 54, nº 8, p. 6552‑6564, avr. 2019, doi: 10.1007/s10853-018-03274-x.
[87] M. A. Arafin, M. Medraj, D. P. Turner, et P. Bocher, « Transient liquid phase bonding of Inconel 718 and Inconel 625 with BNi-2: Modeling and experimental investigations », *Materials Science and Engineering: A*, vol. 447, nº 1‑2, p. 125‑133, févr. 2007, doi: 10.1016/j.msea.2006.10.045.

# Chapter II

## Understanding the mechanisms yielding to cohesion in solid state assembling processes

### *Interfacial characteristics and cohesion mechanisms of linear friction welded dissimilar titanium alloys: Ti-5Al-2Sn-2Zr-4Mo-4Cr (Ti17) and Ti-6Al-2Sn-4Zr-2Mo (Ti6242)*

### Background

A detailed microstructural examination endeavoring to understand the interfacial phenomena yielding to cohesion in solid-state assembling processes was performed. This study focuses on the transition zone of a dissimilar titanium alloy joint obtained by Linear Friction Welding (LFW) the β-metastable Ti17 to the near-α Ti6242. Indeed, the transition zone delimitating both titanium alloys after welding is interestingly characterized by a sharp microstructure change from acicular HCP (Hexagonal Close-Packed) α' martensitic laths in the Ti6242 to equiaxed BCC β (Body-Centered Cubic) subgrains in the Ti17; these α' plates were shown to precipitate within prior-β subgrains remarkably more rotated than the ones formed in the Ti17.

Both α' and β microstructures were found to be intermingled within transitional subgrains demarcating a limited gradient from one chemical composition to the other. These peculiar interfacial grains revealed that the cohesive mechanisms between the rubbing surfaces occurred in the single-phase β domain under severe strain and high-temperature conditions.

During the hot deformation process, the mutual migration of the crystalline interfaces from one material to another assisted by a continuous dynamic recrystallization process was identified as the main adhesive mechanism at the junction zone. The latter led to successful cohesion between the rubbing surfaces. Once the reciprocating motion stopped, fast cooling caused both materials to experience either a $\beta_{lean} \rightarrow \alpha'$ or $\beta_{lean} \rightarrow \beta_{metastable}$ transformation in the interfacial zone depending on their local chemical composition. The limited process time and the subsequent hindered chemical homogenization at the transition zone led to retaining the so-called intermingled $\alpha'/\beta_m$ subgrains constituting the border between both Ti-alloys.

First, this succinct introductive part aims at presenting the specificities of titanium alloys in order to set the essential notions before getting into the substance of the linear friction welding.

## 1. Brief introductive elements about the physical metallurgy of titanium alloys

The use of titanium alloys for engineering applications gained interest from the late 40' to now. The development of Ti-alloys accompanied the rapid development of the aerospace industry in the second half of the twentieth century. It notably broadened the use of Ti-alloys in other economic sectors such as chemical, cryogenic or medical industries [1]. Indeed, titanium alloys present an interesting combination of good mechanical strength, up to medium temperature (until about 550°C for some specific grades) for a low density and significant corrosion resistance.

Titanium alloys consequently form a class of materials particularly suitable for light structural applications. In addition, the use of titanium alloys in aerospace application beneficiates from compatible thermal properties, notably in term of thermal dilation, with carbon-fiber reinforced plastic materials that are now commonly used in the manufacture of aircrafts.

### 1.1 Pure titanium

Under standard conditions of temperature and pressure, pure titanium displays a Hexagonal Close Packed (HCP, see Figure 1.a) crystal structure a ≃ 0.295 nm and c ≃ 0.468 nm and is commonly referred as the α phase. When heating pure titanium up to 882°C while keeping constant the external pressure constant, it undergoes a displacive phase transformation into a Body-Centered Cubic (BCC, see Figure 1.b). This high temperature phase is referred as the β phase and possesses a lattice parameter of a ≃ 0.332 nm. The temperature of transformation from one allotropic form to the other is called the β-*transus* temperature.

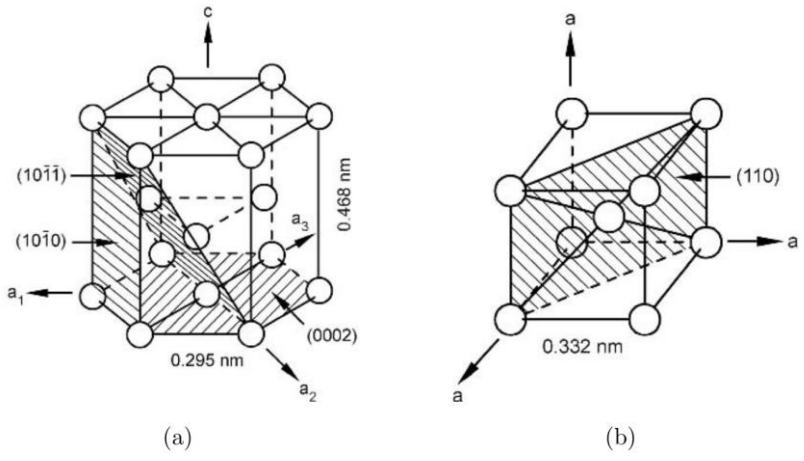


**Figure 1**: *Schematic representation of the elementary crystal structures of* **(a)** *the α phase and* **(b)** *the β phase for pure titanium* [2].

The c/a ratio is smaller than ideal stacking ratio, *id est*: $\sqrt{8/3}$. This particularity has some important consequences on the crystal plasticity of the α phase. Indeed, in ideally stacked HCP structures the basal planes $\{0001\}$ usually correspond to the dense plane; slip is then favored along the $\langle 1120 \rangle_\beta$ directions.

However, the smaller c/a ratio in α titanium is known [3] to favor prismatic slip along the $\{10\bar{1}0\}_{\alpha}$. Slip may also occur the basal planes $\{0001\}_{\alpha}$ and the $\{10\bar{1}1\}_{\alpha}$ pyramidal planes as secondary slip systems. The higher multiplicity of the main available slip systems confers better ductility to the α phase of titanium in comparison to other hexagonal metals such as magnesium. In the BCC β phase, the primary slip plane $\{110\}_{\beta}$, but slip may also take place along the $\{112\}_{\beta}$ and $\{123\}_{\beta}$ planes.

The transformation from β → α follows the Burgers Orientation Relationship (BOR) [4]: $\{110\}_{\beta}$ // $\{0001\}_{\alpha}$ and $\langle 111\rangle_{\beta}$ // $\langle 11\bar{2}0\rangle\alpha$. During phase transformation, the atoms glide along the $\{112\}_{\beta}$ planes following the $\langle 111\rangle_{\beta}$ direction in order to minimize the strain energy of transformation between both crystal structures. A schematic representation of the BOR is given in Figure 2 below:

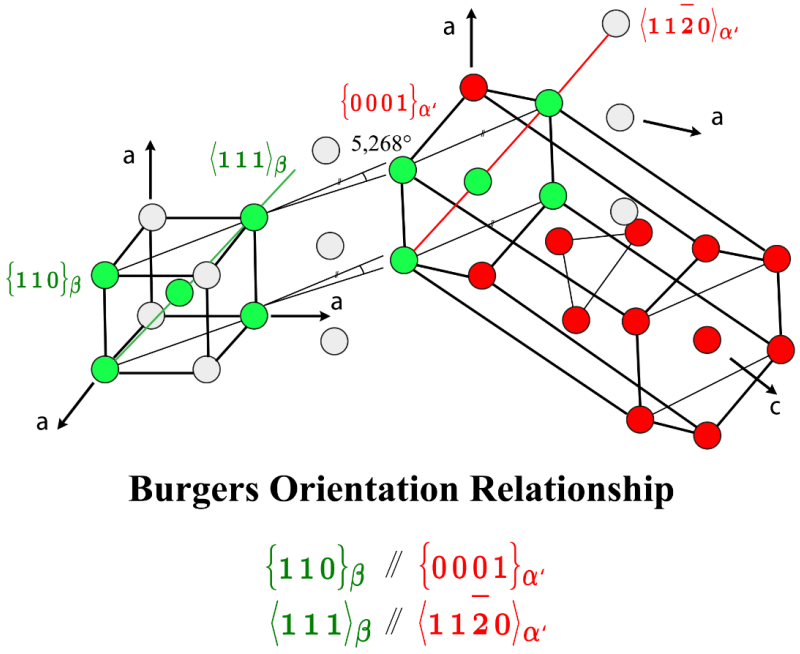


**Figure 2**: *Schematic representation of the classical Burgers orientation relationship* [4], *colorized*.

The ω phase is another allotropic form of titanium that appears under high-pressure conditions. The transformation from α → ω occurs under a 2 GPa to 17 GPa pressure, it depends on the temperature and the β → ω phase boundary has been experimentally determined up to a pressure of 15 GPa. The ω phase presents an hexagonal structure with three atoms per unit cell with a little displayed $AB_2$ type (*structurbericht* notation) that is not really compact (0.57 of compactness, considering atoms as hard spheres), which is quite uncommon for a high-pressure phase. The ω phase displays an hysteretic behavior regarding the ω → α transformation and may remain under standard conditions of temperature and pressure in a metastable state. However, the importance of the ω phase in that work is secondary.

The triple point at which the α, β and ω phases meet occurs at about 9.0 GPa and 940 K.

### 1.2 Effect of alloying elements & alloys classification

The addition of alloying element modifies the phase stability domain of Ti-alloys. A classification of the alloying elements is then established in accordance to how they affect the temperature of α to β-phase transformation (see Figure 3). The elements that stabilize the α-phase by raising the β-*transus* temperature are classified as α-stabilizers, while elements that lower the allotropic transformation are designated as β-stabilizers.

The classical α-stabilizer elements commonly found generally are non-transition metals like aluminum (Al) or interstitial elements like carbon (C), nitrogen (N) and oxygen (O) [5].

The β-stabilizers generally are transition metals and noble metals with unfilled or just filled d-electron bands. Among them, the β-isomorphs are perfectly miscible in the β-phase, it notably concerns: vanadium (V), molybdenum (Mo), niobium (Nb) or the interstitial element hydrogen (H). On another note, the β-eutectoids are able to form intermetallic precipitates in the β-phase, it is the case for: iron (Fe), manganese (Mn), chrome (Cr), Silicon (Si), nickel (Ni) or copper (Cu) [5].

Some are considered as neutral, or with little effect on phase stability like tin (Sn) or zirconium (Zr).

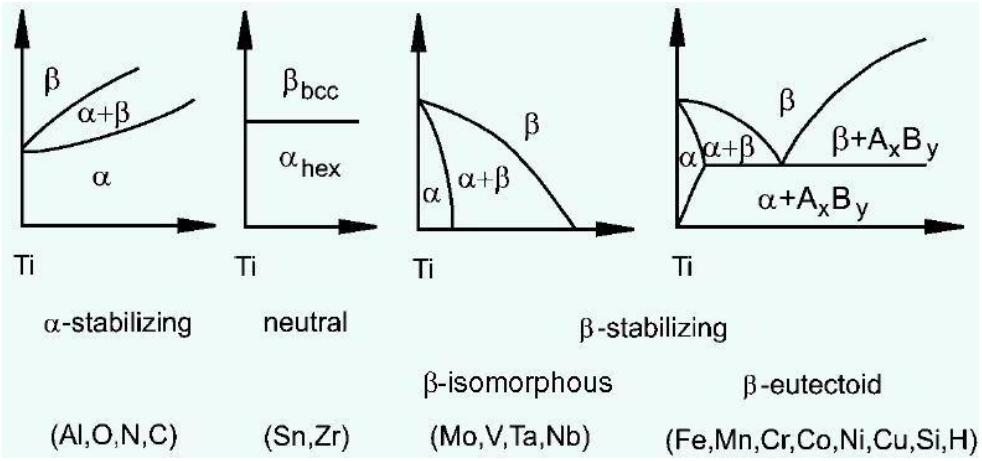


**Figure 3**: *Alloying elements effects on phase transformation in Ti-alloys, schematic representation, extracted from the web page of D. Raabe:* http://www.dierk-raabe.com/titanium-alloys/.

Unlike in pure titanium where only single-phase domains exist. In alloyed titanium, the single-phase domains in the temperature versus composition phase diagram are separated by a bi-phase domain α+β [6]. The width of this region increases with increasing solute content. Two *equilibrium* temperatures then appear: the α-*transus* temperature, below which the alloy contains only the α-phase, and the β-*transus* temperature, above which the alloy contains only the β-*transus*. At intermediate temperature between these two, both phases are present yielding to an α+β *equilibrium*. Technical Ti-alloys are generally multicomponent and contain a mixture of α-stabilizing as well as β-stabilizing elements adapted to the specifications of the application.

Ti-alloys are then classified regarding their phase stability under standard conditions of pressure and temperature: α-alloys do present 100% of α phase and β-alloys display 100% of β phase. However, the majority of technical Ti-alloys commonly used for industrial applications present a mixture of α and β phases: the α+β alloys. Among these, different subcategories are often distinguished, for instance: quasi-α alloys that possess small portion of β-phase and properties close to the α-alloys or β-metastable alloys that can retain β phase at room temperature under certain cooling conditions thanks to the addition of adequate amounts of β-stabilizing elements.

### 1.3 Effect of alloying elements on microstructure morphologies

Although diffusional mechanisms dominate during the phase transformation of alloyed titanium, the Burgers orientation relationship is conserved during β → α transformation. In addition, the cooling rate heavily influences the transformation kinetics from the β domain in Ti-alloys. Various morphologies of microstructure are therefore obtainable upon cooling. Under appropriate cooling conditions, it is then possible to shape the microstructure and optimize its characteristics for in-use application. Schematically, a high cooling rate from the β domain would generally result in thin needle-like morphologies, while reducing the rate of cooling would tend to form *lamellae*-like morphologies [7]. With the help of mechanical processing it is then possible to break such *lamellae* structures to form nodular structures [8] (a classic thermo-mechanical processing route for *lamellae* breakdown for is schematized in figure 4).

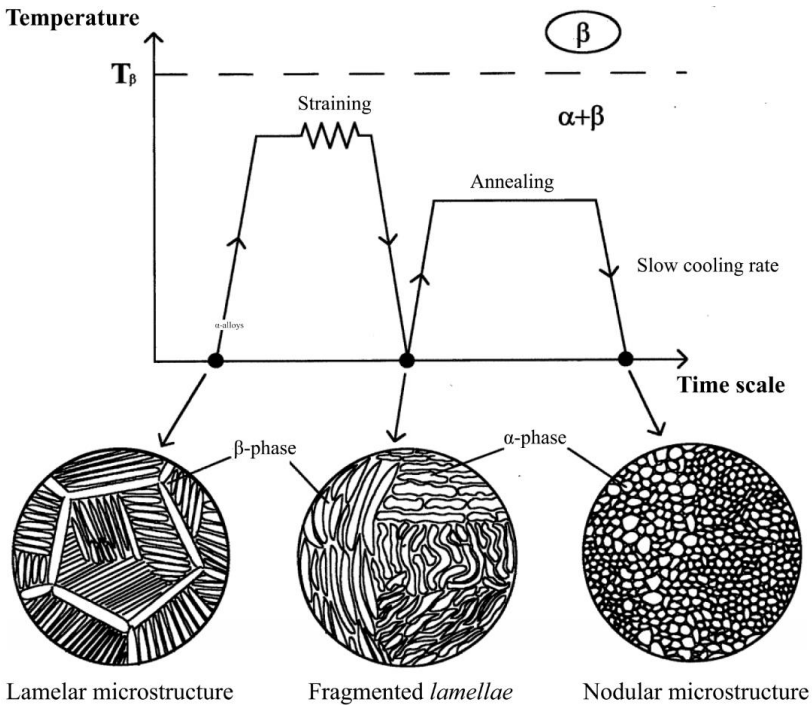


**Figure 4**: *Lamellae breakdown through thermomechanical processing, schematic representation from* [9].

A wide variety of microstructures is then achievable *via* more or less complex thermomechanical processing routes[10]–[12].

### 1.4 Metastable phases in Ti-alloys

Besides their influence on the α or β *equilibrium* phase, alloying elements may also favor the appearance of metastable phases. The latter may notably precipitate under the influence of thermo-mechanical processing procedures. The existence of metastable phases rely on a thermodynamic compromise where the systems tends to reach a lower Gibbs free energy state and its associated the transformation kinetics [13]. Their appearance generally necessitates a smaller driving force making them dynamically unstable to change in temperature, pressure or differences in chemical potential. Metastable phase precipitation strongly depends on the composition of the alloy and may usually be triggered through critical cooling or induced by application of an external stress.

In titanium alloys, various metastable phases may exist (Figure 5):

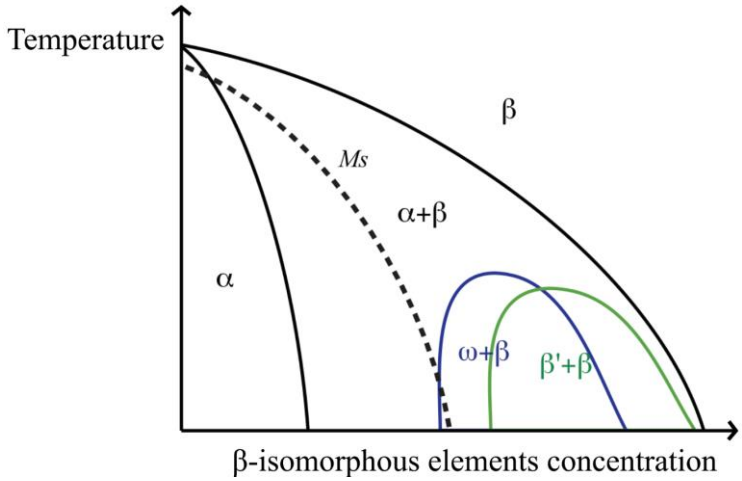


**Figure 5**: *Schematic representation of a 'concentration in β-isomorphs versus temperature' phase diagram with the approximate position of the metastable phase precipitation domains.*

**The α' phase** is a type of martensitic structure that forms upon fast cooling from the β domain in near-α titanium alloys (such as Ti6242). The α' phase may be regarded as a s*uper*-saturated α phase, as the α' keeps the original β composition. It displays a HCP crystal structure close to the *equilibrium* α phase. The β → α phase transformation follows the Burgers orientation relationship: $\{110\}_{\beta}$ // $\{0001\}_{\alpha'}$ and $\langle 111\rangle_{\beta}$ // $\langle 11\bar{2}0\rangle_{\alpha'}$ [14]. Depending on the nature and the portion of solute elements, the α' phase may exhibit various morphologies however, plate-like or needle like shapes are the most current occurrences.

Although close to the hexagonal unit cell, **the α" phase** presents an orthorhombic crystallographic structure and usually displays an acicular morphology. often with numerous internal twins. The commonly reported orientation relationship with the β phase is: $\{110\}_{\beta}$ // $\{001\}_{\alpha''}$ and $\langle 111\rangle_{\beta}$ // $\langle 101\rangle_{\alpha''}$ [14]. In α+β alloys, the α" phase may precipitate upon quenching in the place of α' phase when the portion of β-stabilizing elements passes a critical value. However, the martensite starts temperature (Ms) deceases rapidly when increasing the amount of β-phase stabilizer in alloys, the α"-phase is consequently less prone to precipitate beyond a certain

concentration. On another note, the appearance of α" phase when deforming β-metastable phase stabilized at room temperature *via* stress induced precipitation in β-metastable alloys is also well documented. The transformation is here driven by mechanical energy. These features are notably reported on classical β-metastable grades, such as: Ti17, β-CEZ or Ti-10-2-3. Thermally induced precipitation of α" phase was nevertheless reported during annealing on β-metastable grades.

It is important to highlight here that when quenched under the right conditions **β-metastable** alloys (such as Ti17) retain an undercooled β-phase at room temperature; it is their defining feature.

Lastly, in titanium alloys displaying particularly high concentration of β phase stabilizers, **ω phase** precipitation may occur rather than α" phase upon quenching. The ω phase exhibits a hexagonal structure and may be viewed as an intermediate phase between the α and β phases. Even though the role of ω phase and its relationship with the formation of the α phase is still an open to debate in the metallurgy field [15]–[17]. The ω phase is often divided into two varieties: the ω-athermal phase and the ω-isothermal (sometimes noted β'). In such highly alloyed β titanium, the ω-athermal is an unavoidable diffusionless transformation that always appears when cooling from the β domain. The lattice correspondence between the β phase and the ω phase is: $\{111\}_{\beta}$ // $\{0001\}_{\boldsymbol{\omega}}$ and $\langle 1\bar{1}0\rangle_{\beta}$ // $\langle 11\bar{2}0\rangle_{\boldsymbol{\omega}}$ and the details about the complex transformation mechanisms are well spelt out elsewhere [18]. In term of phase morphology, the ω-athermal phase forms dispersed nanometric particles of about 20 nm. Similarly to α", plate-like ω phase can be produced upon deformation through stress-induced martensitic transformation in the β-alloys. On the contrary, the ω-isothermal forms, as its name suggests, during isothermal aging (often between 100°C to 500°C) and consequently implies long range diffusion in its formation process. The ω-isothermal phase precipitation may form nanometric cuboidal or ellipsoidal morphologies depending on the coherency relation with the parent β phase. Nevertheless, the ω phase do not appear in the following the study-case.

### 1.5 Valuable information about the welded Ti-alloys

The phase transformation features above exposed aimed at clarifying the, sometimes confusing, classification logic concerning Ti-alloys. Now, regarding the welded grades, it is important to notify that:

→ Ti6242 in a 'near-α' alloy, it is then important to keep in mind that fast cooling from the β domain may provoke the formation of the metastable α' phase.

→ Ti17 is classified as β-metastable alloy meaning that fast cooling β domain retains a 'β-metastable' phase at room temperature.

## 2. Linear friction welding applied on dissimilar Ti-alloys: aim and context

The mechanisms leading to cohesion in solid-state assembling processes of mutually soluble metallic alloys are observed, studied and applied with success in various industrial joining techniques. An intuitive assumption states that bringing together metal atoms from the faying in-contact surfaces within the range of interatomic distance would result in the formation of a metallic bond by mutual sharing of non-localized electrons. Yet, the oxide films or extraneous adsorbed species which interfere as a physical barrier to the material coalescence must inevitably be preliminary disrupted or decomposed [19].

In forge and large deformation based assembling processes such as accumulative roll bonding or in various forms of pressure welding techniques, the asperities between the faying surfaces are collapsed by means of important plastic deformation, while the contaminants are breakdown by the local strain in the joining zone [20], [21], [22]. In diffusion bonding processes, macroscopic deformations are avoided and the bond formation is mainly obtained by the material transport phenomena taking place across the materials being joined. The applied pressure and the high-temperature conditions facilitate local contaminant break-up and dispersion at the contact points. However, the thermal dissolution of oxides and surface contaminants was demonstrated as a significant thermo-chemical mechanism to achieve the bond formation [23]–[26]. Besides, the physical mechanisms induced by local plastic creep deformation, such as grain sliding and restoration/recrystallization mechanisms, were also outlined in the literature as key phenomena favoring cohesion in diffusion assembling techniques [27], [28].

Linear Friction Welding (LFW) is a solid-state assembling process in-between these categories. Indeed, the LFW process combines the features of frictional heating in dry tribological contacts [29] with the ones of plastic-deformation induced assembling processes and solid-state diffusion bonding techniques. In linear friction welding, the weld is obtained by pressing a work-piece (forging part) into another one that describes a linear reciprocating motion (oscillating part). The control of the friction process is ensured through three independent parameters as: the contact pressure, the oscillating amplitude and the frequency. With adapted process parameters, the local heat generation by friction at the interface and the consequent thermal softening cause the materials to plastically flow and lead to the coalescence of the rubbing parts into a thin metallurgical bond.

The ability to assemble dissimilar alloys is one of the most promising applications of LFW technology. Indeed, the latter is of high technological interest for replacing mechanical assemblies and to produce innovative multi-material and multi-functional parts. In addition, this class of processes is also highly appreciated in the aircraft industry for producing/repairing blade-disk assemblies as well as to obtain near-net-shape parts. Recent studies involving the successful assembling of dissimilar titanium alloys [30]–[34] demonstrated viable configurations which exhibited satisfying mechanical strengths for practical applications. Assembling Ti-alloys can be done using dissimilar microstructures or different grades. Detailed descriptions of the central weld zone are often given but without identifying the phenomena at the origin of the bonds

between materials. As an example, Guo *et al.* [32] gave a detailed description of the microstructure of a LFW joint between Ti-6Al-4V and Ti-6Al-2Sn-4Zr-6Mo and thoroughly characterized the texture of the central weld zone. However, they did not clarify the interfacial mechanisms responsible for solid state bonding. The underlying mechanisms leading to the bond formation in friction assembling processes and, more broadly, on mutually soluble solid-state assembling processes are still debated in the literature [35], [36].

**Hence, in an attempt to clear up the interfacial mechanisms responsible for solid-state joining, extensive observations and chemical analyses were performed in the close vicinity of the transitional zone of such a joint.**

The present work endeavors to clarify the operating phenomena contributing to the bond formation at a microstructural scale between two dissimilar, but mutually soluble, Ti-alloys: the β-metastable Ti-5Al-2Sn-2Zr-4Mo-4Cr (Ti17) and the near-α Ti-6Al-2Sn-4Zr-2Mo (Ti6242).

These alloys were chosen because of their strong differences in microstructures formed under rapid cooling from the Solution-Treated (ST) configurations: acicular HCP (Hexagonal Close Packed) α' martensitic laths in the Ti6242 and BCC (Body-Centered Cubic) $\beta_{metastable}$ equiaxed grains in the Ti17. The former will help to identify the welding interfacial zone as it will lead to a sharp α'/ $\beta_m$ phase contrast.

## 3. Materials & methods

A butt-welding test campaign was carried out using the commercial standard titanium alloy grades: Ti-6Al-2Sn-4Cr-2Mo and the Ti-5Al-2Sn-2Zr-4Mo-4Cr. Pairs of solid blocks of 15 x 80 x 70 $mm^3$ were cut by electrical-discharge machining from 250 mm diameter and 570 mm length standard forged billets of (TIMETAL®6-2-4-2 or commonly denominated Ti6242) and (TIMETAL®17, Ti17) provided by TIMET Savoie S.A., France.

The extracted specimens were linear friction welded in an open-air environment on the 15 x 80 $mm^2$ surface with the 80 mm edge parallel to the oscillation direction $\langle x \rangle$ as depicted in Figure 6. It is also noted that the 80 mm edge is parallel with the billet axis.

Prior to the welding procedure, the raw assembling surfaces were polished with P120 SiC grinding paper. The Ti6242 block was used as the oscillating part whereas the Ti17 block was used as the forging part. The machine used to obtain the linear friction weld is an MDS-30 developed by the ACB Company, Nantes, France. The process parameters selected in this study were: a forging pressure of 90 MPa, a frequency of 50 Hz and a 2 mm amplitude. The process lasted about 3 s using a 5 mm axial shortening; a forging pressure of 90 MPa was maintained for a duration of 10 s after the end of the oscillating motion.

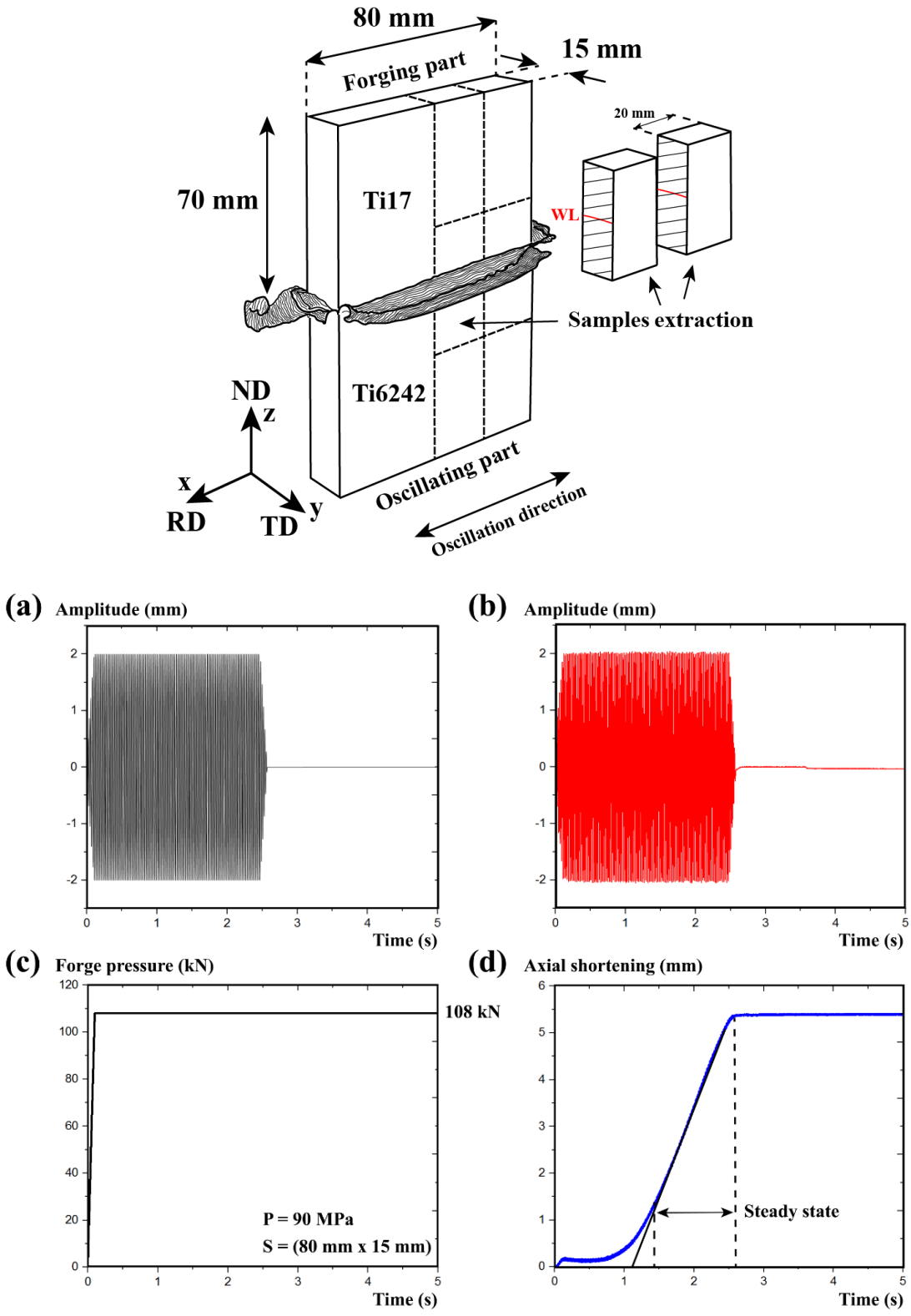


**Figure 6**: *Schematic illustration of a Ti17 – Ti6242 linear friction weld assembly and the sampling strategy; process parameters evolution during the linear friction assembling procedure with* **(a)** *the set amplitude,* **(b)** *the amplitude response signal,* **(c)** *the set forge pressure and* **(d)** *the axial shortening signal.*

The microstructural characterization of the transition zone of the dissimilar joint was carried out on representative samples collected from cross-sectional cuts in the welded work-pieces, orthogonal to the friction direction of the welding process. A schematic representation of the extraction procedure is illustrated in Figure

6. The microstructural observations were then carried out on the (Y, Z) plane of the extracted samples, close to the central section of the weld joint. For surface preparation, the specimens were mechanically polished through standard abrasive polishing procedures using SiC abrasive grinding papers (P80, P220, P1200, P2400 and finally P4000 grit sizes). The final grinding procedures were performed using successive polishing with standard diamond solutions down to 1 µm mean diameter on a polyester cloth. Finishing was done using a 40% oxide polishing suspension (OPS) solution and 60% in volume of $H_2O$ on a Buehler VibroMet™ 2 vibratory polisher.

Microstructural observations were performed using a tungsten Field Emission Gun Zeiss Σigma Scanning Electron Microscope (FEG-SEM). The Electron Back-Scattered Diffraction (EBSD) mapping was obtained using a Nordiff OptiPlex 7040 detector for Kikuchi pattern image capture. The specimens were mounted onto a 70° tilted holder and a 20 mm working distance was used. The measurement steps were chosen according to the resolution required for the analyses. The orientation maps were then calculated using the TSL OIM data collection™ software and the EBSD post-processing procedures were finally performed on the Matlab© open-source toolbox Mtex [37], [38] v5.1.1. The high-current beam voltage was equal to 15 kV for imaging and to 25 kV for EBSD mapping.

The sample reference used to formulate the EBSD orientation data is defined with the "rolling direction" RD parallel with the friction direction $\langle x \rangle$. The "normal direction" ND is parallel with the forge direction $\langle z \rangle$ and the "transverse direction" TD is orthogonal to the (RD, ND) plane and corresponds to the $\langle y \rangle$ direction (Figure 6). Clean-up procedures were applied on the EBSD orientation cartographies: before grain detection, a first correction was applied on the isolated non-indexed pixels with a median filter procedure taking into account the orientations of the adjacent neighboring pixels. Besides, the pixels with a confidence index lower than 0.1 were deleted from the analyses.

The atomic force microscopy (AFM) imaging was done using a Bruker acquisition system in tapping mode. The metallographic sample for AFM imaging was mechanically polished then chemically etched with a Struers-A3 electrolytic solution at 6 °C.

For Transmission Electron Microscopy (TEM), 1 mm thick slices of cross-sectioned weld samples were cut in the (X, Z) plane using a micro-cutting machine. The slices were then contoured down to 3 mm diameter disc-shaped foils. Afterward, the extracted thin foils were mechanically pre-thinned to reach a 100 µm thickness. The resulting slices were finally polished using a conventional twin-jet polishing technique at 20 V and -30°C with a solution of 10% (in vol.) perchloric acid diluted in a 20% 2-butoxyethanol. TEM observations were carried out with a FEI Tecnai OSIRIS S/TEM equipped with the Super-X SDD EDX detector and a second FEI Tecnai F20 TEM combined with the NanoMegas ASTAR system for automated phase/orientation mapping of nanocrystals materials. Both microscopes were operated at an accelerating voltage of 200kV. For orientation data acquisition, the condenser aperture was equal to 30 µm, the spot size was 8 nm and the scan step size was equal to 5 nm.

Both the Ti17 and the Ti6242 are conventional Ti-alloys widely used in the aircraft industry for structural parts or intermediate-temperature compressor disks respectively. The materials were provided in the solution treated then aged configuration (STA).

The Ti6242 used in this study is characterized by an initial microstructure consisting mainly of coarse α nodules presenting an ellipsoid shape with interspersed residual intergranular β matrix. On another note, the Ti17 exhibited an as-received Widmanstätten α+β microstructure formed by the intragranular precipitation of fine entangled hardening α laths within large prior-β grains. Their respective β-transus temperatures specified by the manufacturer are of approximately: 995°C for the Ti6242 and 890°C for the Ti17. Both microstructures are presented in Figure 7.

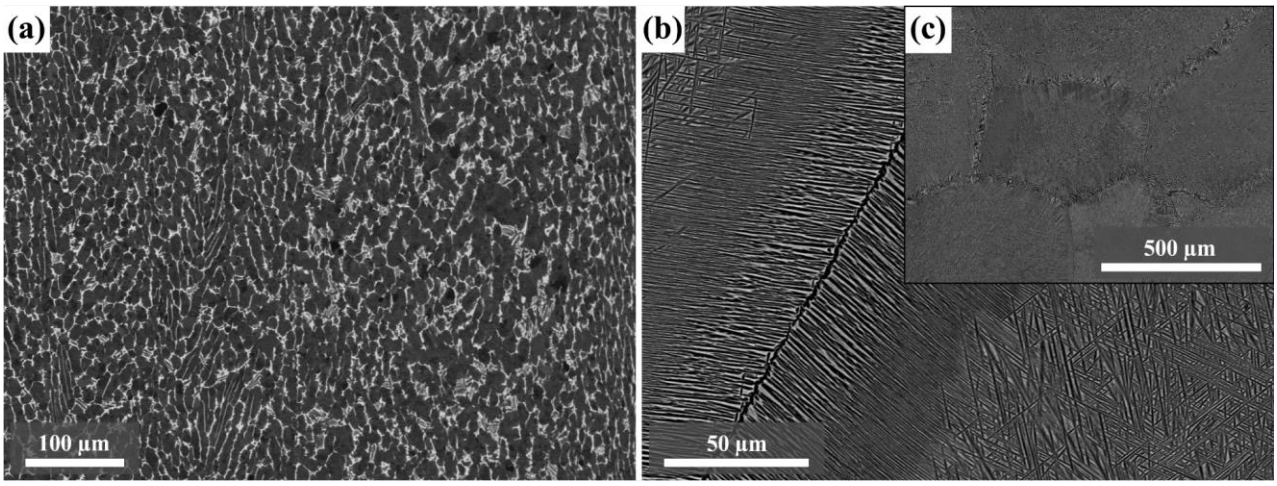


**Figure 7**: **(a)** *SE-SEM image of the Ti6242 base material*, **(b)-(c)** *SE-SEM image of the Ti17 base material*.

Concerning the base Ti6242 material, some microstructural specificities have to be further detailed. A primary microstructural alignment is observed along the billet axis plane (here corresponding to the TD, RD plane, see Figure 8). In addition to that, visible macrozones presenting close-oriented α-nodules are distinguishable in the associated inverse pole figure maps presented in Figure 8. Such features are quite common in α/β titanium and quasi-α alloy semi products (billets) after standard thermomechanical processing. The main objective of such procedure is to convert a coarse millimetric β microstructure containing colonies of α into a fine equiaxed α microstructure in a transformed β [39]. Indeed, such product are usually elaborated via vacuum-arc or cold-hearth melting followed by casting in round mold. Following the casting stage, the ingot structure is then broken down through series of thermomechanical processing comprising hot working above the β-*transus* temperature to fragment the casted β-microstructure into fine equiaxed β grains in order to eventually control the microstructure. Then, secondary α/β hot working is applied to spheroidize the α (or α') colonies thereby producing the observed Ti6242 microstructure (Figure 7.a) of fine equiaxed globular α particles in a matrix of single-phased β.

Such thermomechanical processing requires quite high effective strain levels (in the order of magnitude of 1 to 1.5) to complete the spheroidization process [10], [11]. After such procedure, it is not unusual

that the billet products contain quite large regions characterized by many α crystallites presenting crystallographic orientation close from one another (see Figure 8). Although fully spheroidized, the latter characteristic is notably observed in the present Ti6242 microstructure. The close-oriented features encompass several neighboring grains forming macrozones known as microtextured region (MTRs). Connections between MTRs presence and deleterious consequences on fatigues properties were notably established on such microstructures [40].

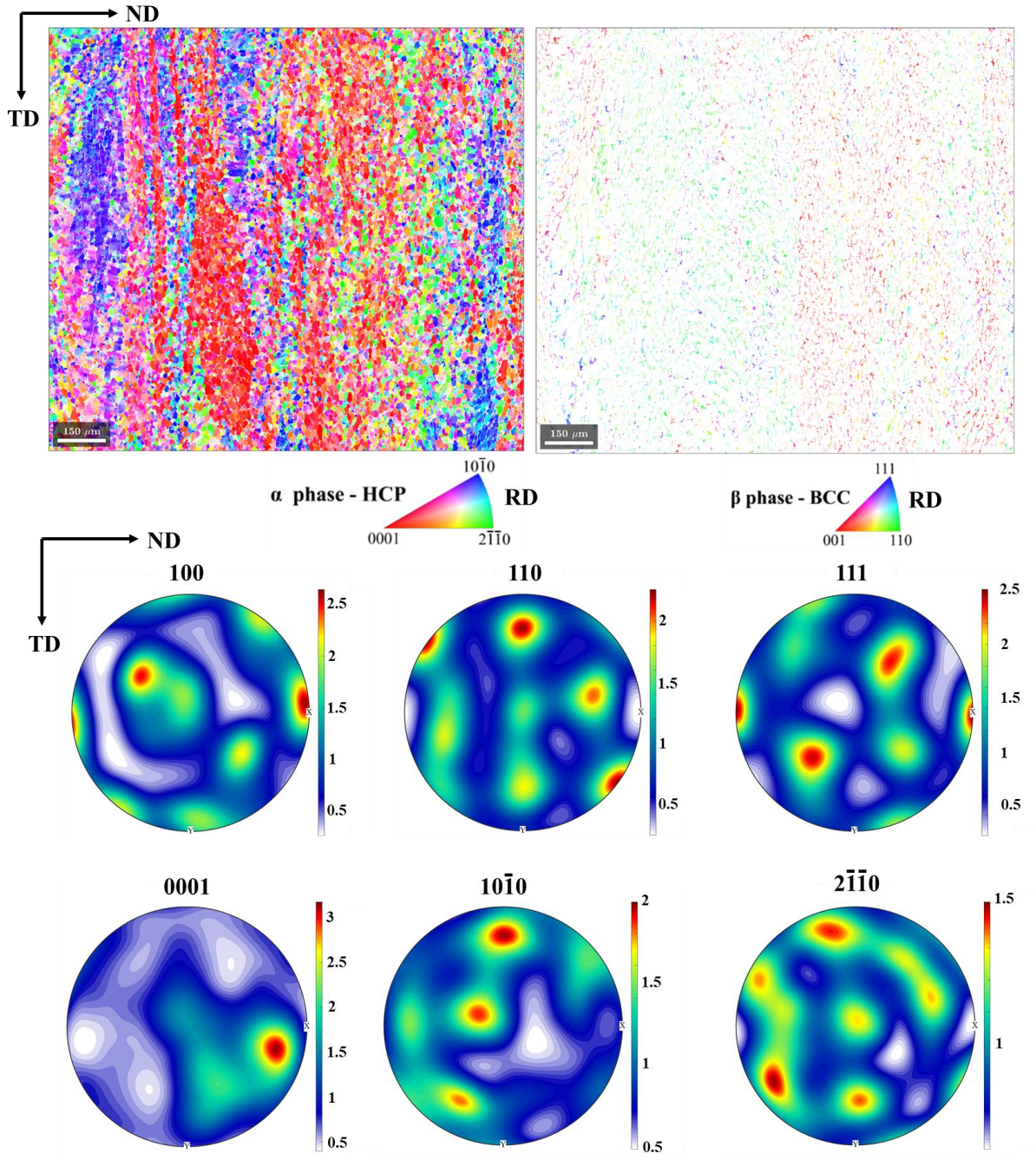


**Figure 8**: *Inverse pole figures obtained from EBSD analysis (0.5 µm step size) of the Ti6242 base microstructure, the α and β phase are displayed, the colors represent the crystallographic direction of the indexed lattice along RD direction (friction direction of the linear friction process). The associated pole figures are also represented.*

MTRs primarily results from specific colonies which have received relatively limited deformation notably in orientation configurations relative to the applied stress where prism or basal slip is limited, consequently the neighboring colonies generally share close c-axes orientations [41]. In the present case, a dominant alignment of the c-axes close to the ND is noticed (Fig. 8 and 9).

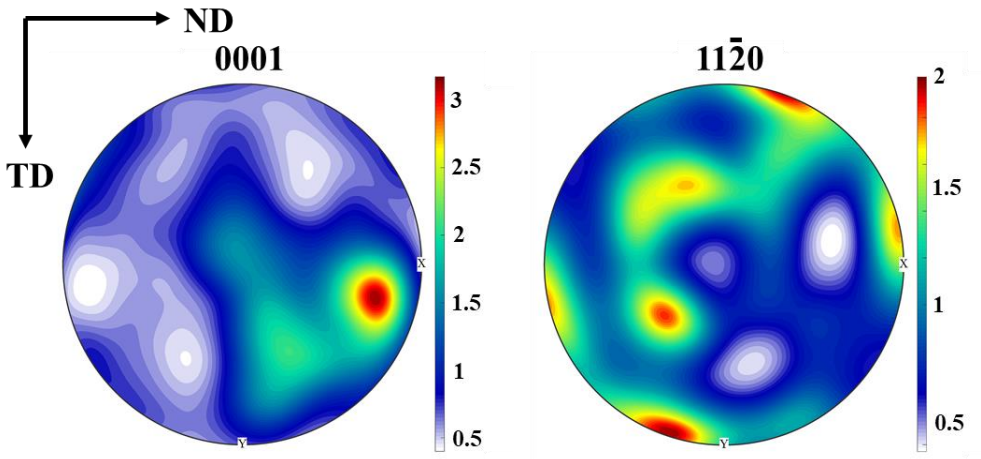


**Figure 9**: *α 0001/11$\bar{2}$0 pole figures.*

## 4. Results

### 4.1 Overview of the microstructural changes

The microstructure of the dissimilar LFW joint was preliminary observed by SEM in Back-Scattered Electron (BSE) mode, the corresponding micrographs are presented in Figure 10. The Welding Line (WL) is easily identifiable due to the glaring differences in microstructural features (i.e. morphologies, phases) with both Ti6242 and Ti17 former starting microstructures (i.e. fully-equiaxed and Widmanstätten respectively). Indeed, a significant microstructure refinement can be noted in this zone that exhibits a remarkable fragmentation of the β matrix phase accompanied, in the Ti6242, by the intragranular precipitation of discernible acicular α' martensitic laths (Figure 10.b-c). Neighboring the fully-transformed WL, an apparent Thermo-Mechanically Affected Zone (TMAZ) was revealed in the form of gradually plasticized grains and dissolved morphologies (i.e. smeared former β matrix in the Ti6242 and α precipitates dissolution in the Ti17). Seemingly unaffected microstructures were recovered at approximately 1 mm and 2.5 mm in the Ti6242 and Ti17 respectively.

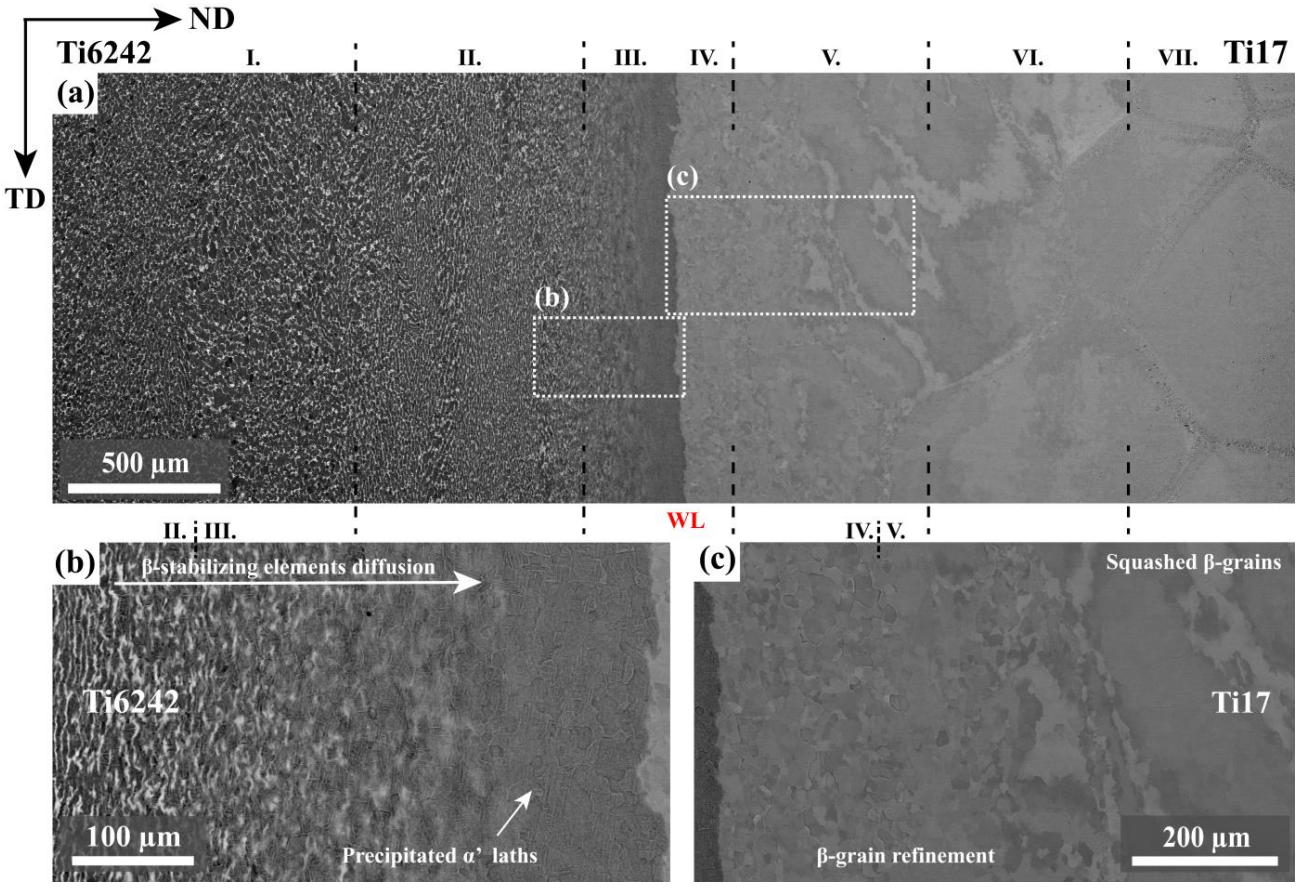


**Figure 10**: *BSE-SEM micrographs of the dissimilar Ti6242/Ti17 LFW joint*. **(a)** *Overview of the weld interface*; **(b)** *zoom at the Ti6242 TMAZ*; (c) *zoom at the Ti17 TMAZ.*

In complement to imaging, orientation data measurements were carried out by EBSD technique to further investigate the microstructural changes across the joint. The resulting HCP and BCC orientation maps superimposed with the calculated grain boundaries are shown in Figure 11. Yet, since the crystal structures of α phase and α' martensitic phase (space group $P6_3/mmc$) are very similar, the EBSD indexing software was unable to distinguish the difference. Consequently, the α' phase would be indexed as α.

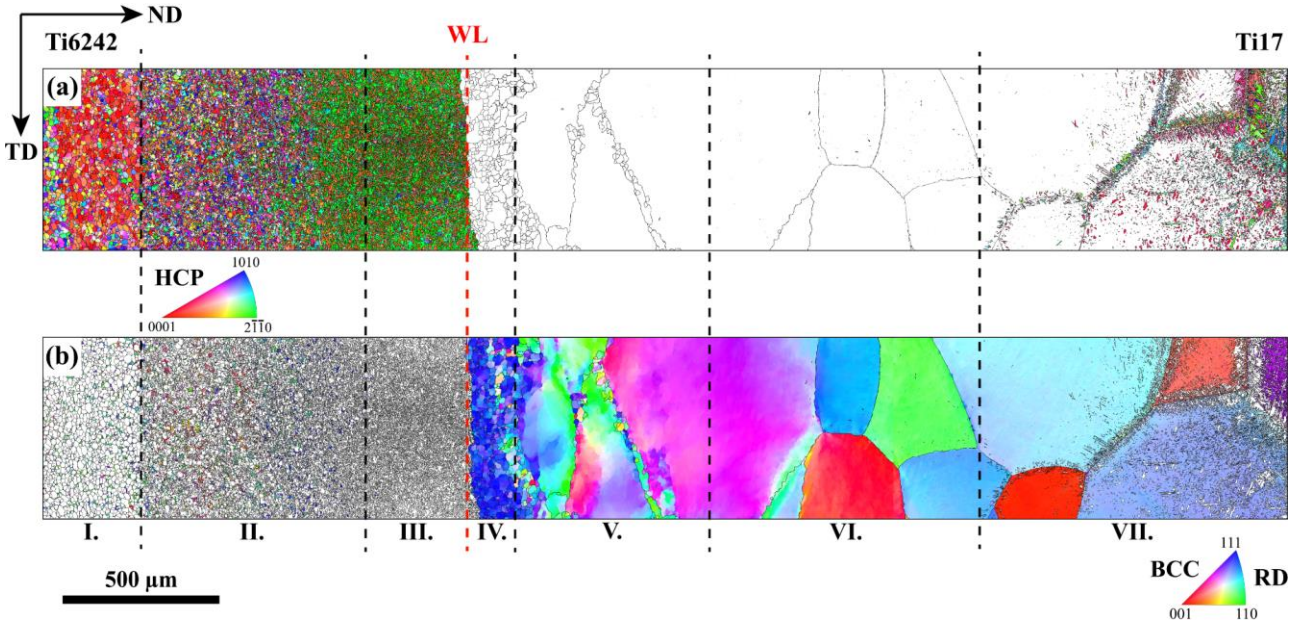


**Figure 11**: *Inverse pole figures obtained from EBSD analysis (0.5 µm step size) of the Ti6242/Ti17 LFW joint showing* (a) *the HCP and* (b) *BCC indexed data superimposed with the grain boundaries (5° orientation angle threshold); the colors represent the crystallographic direction of the indexed lattice along RD direction.*

Seven main areas showing noteworthy differences in microstructure were identified in Figure 10 and Figure 11 which complement with each other. The different microstructural zone will be subjected to separated analyses. Starting from the WL and going to the left (*i.e.* Ti6242 side), an about 400 µm thick band of HCP indexed microstructure can be observed (Zone III). A detailed examination of the morphologies constituting the local microstructure by SEM imaging in Figure 10.b shows the probable precipitation of acicular α' laths within seemingly refined equiaxed prior-β grains (of 10 µm mean grain size). No distinct retained β phase was identified within this acicular microstructure. In the near-WL zone of the Ti6242 (i.e. II./III. border in Figure 10 and 11), the corresponding micrographs revealed a gradual distribution of the β stabilizers. The latter extends from the initially interspersed intergranular $\beta_{rich}$ matrix (i.e. former equilibrium β matrix enriched in β-stabilizing elements) to the adjacent plasticized α nodules resulting in a white cloudy aspect on BSE imaging signal (Figure 10.b). These features blur away as approaching the weld center zone, which might indicate that an extensive chemical composition homogenization occurred in this zone during the frictional process. Thereafter (Zone II in Figure 11.a), a fragmented-like microstructure was observed with a progressive apparition of the initial β matrix as moving further away from the WL. Then, a sharp delimitation can be identified from the fragmented-like α nodules to a seemingly unaffected microstructure (Zone I).

Now, starting from the WL and going to the right side (i.e. Ti17), Zone IV is characterized by a 200 µm thick band of refined equiaxed β grains (10 µm mean grain size). Then, one can notice the presence of squashed large β grains on an about 1 mm thick band (zone V) originating from the starting Widmanstätten microstructure of the base material. These grains exhibit an elongated aspect in the direction of the material expulsion (i.e. RD & TD) and noteworthy intragranular misorientation gradients. The apparent grain refinement in the zone V is preferentially located in the vicinity of the coarse β grains boundaries forming necklace structures [17]; this phenomenon is more pronounced near Zone IV. Further on, just plasticized β grains are observed in zone VI. Then in zone VII, the starting Widmanstätten α+β mixture is progressively recovered, first with the presence of α Grain-Boundary layers ($\alpha_{GB}$) followed by the α intragranular laths ($\alpha_{WI}$).

In addition to that, a remarkable texture development is present in both the Ti17 and the Ti6242 indicating a significant crystal reorientation to the deformation conditions during the process. This reorientation appeared to be rather limited to the WL in the Ti17 but extended to 700 µm from the weld center line in the Ti6242; in the latter, both, the α fragments and the retained β matrix, were subjected to this reorientation. In order to visually highlight the local crystal preferred orientation development within the weld, the IPF color code has been chosen to represent the crystallographic direction of the indexed lattice along the RD direction (friction direction) on the orientation maps depicted in Figure 11 and Figure 19 (which corresponds to the normal direction of these maps). Similar microstructure morphologies, phase presence, and texture were reported in Ballat-Durand *et al.* [42] and [43] for single-material joints using analogous LFW conditions.

### 4.2 Chemical investigations at the transition zone

The SEM imaging carried out in the interfacial zone reveals the side-by-side coexistence of sharp needle-like α' structures with a β microstructure (Figure 12.a and 12.b). The latter observation offers a stark microstructural contrast from one side to the other. Closer observations of the junction zone showed the presence of round-shaped porosities with diameters that do not exceed 1 µm. In the transition zone, both phases appeared to be intermingled within seemingly common β subgrains. Besides, AFM topographic imaging revealed a close interpenetration of the in-contact microstructures along the transition zone (Figure 12.c). Deeper analyses were therefore performed in SEM and TEM in an attempt to understand the phenomena that could form such a peculiar structure as well as to thoroughly characterize the interfacial zone.

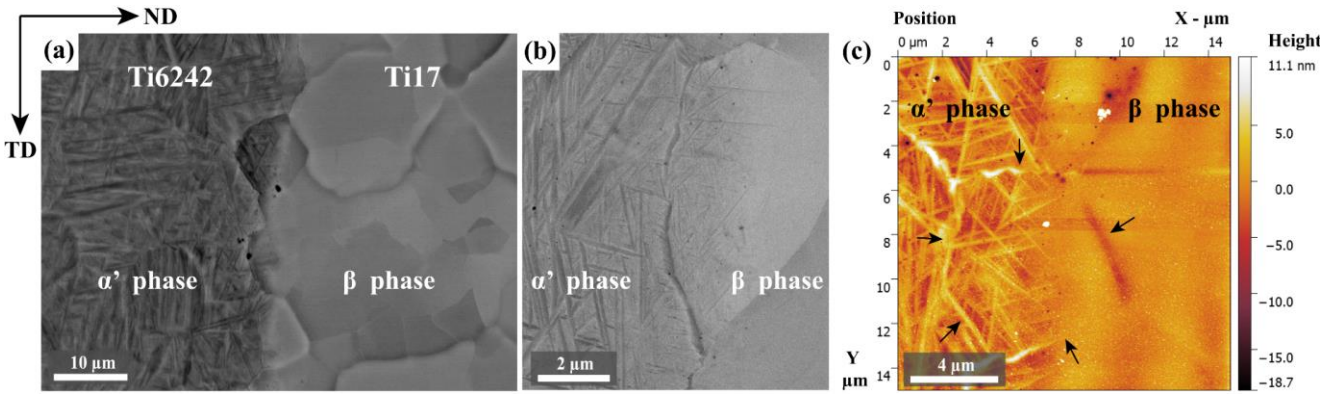


**Figure 12**: **(a)**, **(b)** *BSE-SEM image of the interfacial zone*, **(c)** *AFM tapping mode imaging of the interfacial zone, the black arrows highlight an intermingled interfacial subgrain.*

First, the local distribution of substitutional elements across the interfacial zone was investigated through energy-dispersive X-ray spectroscopy in TEM; the corresponding qualitative element cartographies are presented in Figure 13. The gradual signal intensity in the near interfacial zone around the apparent heterophase interface is easily noticeable on the Cr signal (Figure 13.d) due to the absence of the latter among the alloying elements of the Ti6242.

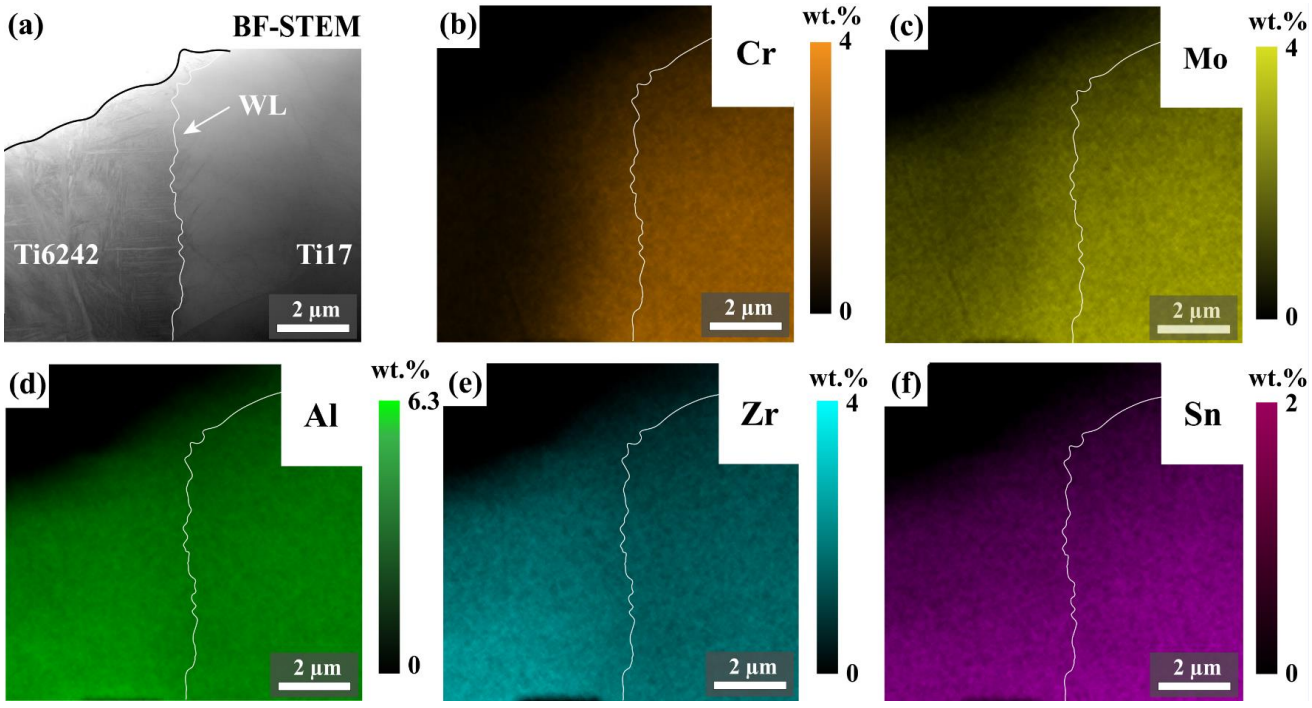


**Figure 13**: **(a)** *BF-STEM image of an intermingled prior-β subgrain and the corresponding EDX intensity maps of the solute elements*: **(b)** *Cr*, **(c)** *Mo*, **(d)** *Al*, **(e)** *Zr*, **(f)** *Sn (intensity bar scaled on the wt.%).*

A detailed chemical analysis was conducted along with a cross-line profile shown in Figure 14.a. The resulting interdiffusion profiles across the interface present a typical error-function aspect and an interdiffusion band of approximately 4 µm in thickness is discernable in the transition zone.

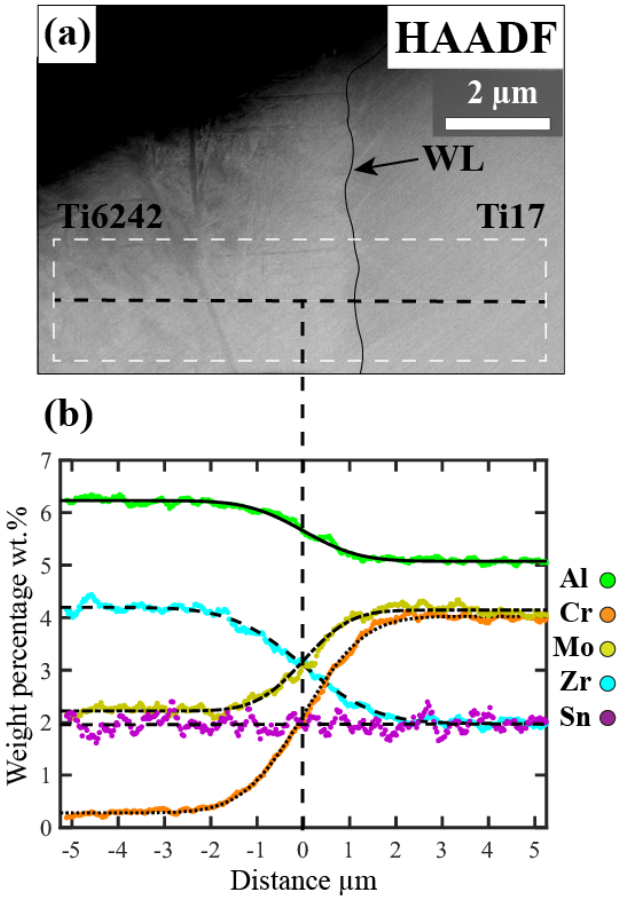


**Figure 14**: **(a)** *HAADF image of the interfacial zone for EDX profile analysis*; **(b)** *line profile of element composition distribution across the Ti6242/Ti17 interface in wt.%*.

A basic one-dimension model was applied from the experimental data (Figure 14) with the aims of roughly estimate the order of magnitude of the interdiffusion phenomenon during the high-temperature processing time. The plateau-like aspect on both sides of the element diffusion profiles seems to corroborate the hypothesis of a local homogeneous partition of the solute elements in the adjacent microstructures on either side of the transition zone. The latter hypothesis was notably speculated after back-scattered electron microscopy observations (Figure 10.b-c). Equation (1) is then the error-function solution of the classic 1D semi-infinite manifolds diffusion model considered; where C is the concentration of an element at a distance equal to x; C1 and C2 are the solute limits in the Ti6242 and the Ti17 alloys respectively. The values of C1 and C2 were determined from the alloys standard composition, considering the homogeneous solute partition assumption formulated above. The duration (t) was set as the steady-state axial shortening stage which is about 1.3 s.

The estimated diffusion coefficients $D_{fit}$ of the different elements were then computed by fitting the following error-function to the measured data. The estimated values of the diffusion coefficient $D_{fit}$ for the substitutional elements in Ti-alloys are listed in Table 1:

$$C(x)=\frac{C_1-C_2}{2}.\,\mathrm{erf}\left(\frac{x}{2\sqrt{D_{fit}t}}\right)+\frac{C_1+C_2}{2}$$

**Table 1**: Estimated diffusion coefficient $D_{fit}$ of the substitutional elements.

| **Alloying element** | **Al** | **Mo** | **Cr** | **Zr** |
|---|---|---|---|---|
| **$D_{fit}$ [µm$^2$.s$^{-1}$]** | 0.35 | 0.25 | 0.41 | 0.59 |

The Sn element variation was excluded from the analysis since both alloys contain equivalent quantities in mass proportion. One should also note that the centers of the error-function profiles do not actually correspond with the visible limit of the interface: a slight shift of the fitted curves towards the martensitic side was observed.

Lastly, local substitutional elements repartition cartographies were realized at high magnification in TEM focusing on the close interfacial zone. The results are displayed in Figure 15. Thin pile-ups of Cr and Mo elements are observed in the in-contact β phase around the α'/β heterophase bounds while important depletions of the latter are observed within the precipitated α' laths. A slight but similar trend seems to appear on the Zr signal as well, even though the intensity contrast on the cartography remains unclear. This phenomenon is not clearly discernible on the other elements at such a measurement scale.

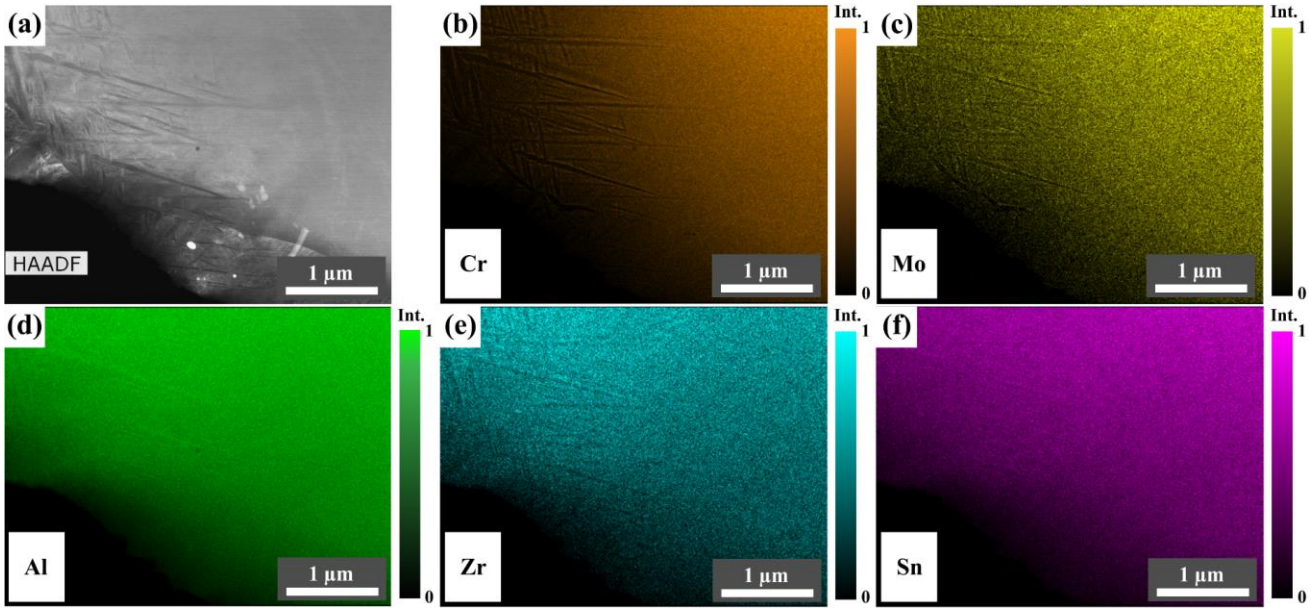


**Figure 15**: **(a)** *High magnification HAADF image of the close interfacial zone; local EDX intensity maps of the solute elements*: **(b)** *Cr*, **(c)** *Mo*, **(d)** *Al*, **(e)** *Zr*, **(f)** *Sn*.

### 4.3 Microstructural investigations by crystal orientation analyses at the transition zone

Additional crystal orientation investigations were carried out in the vicinity of the interfacial zone. The aims for such an approach are twofold: first, to clarify a prospective relationship between the in-contact β-metastable phase and the adjacent precipitated α' phase in the transitional zone and second; to reconstruct the

microstructure history from the final state observations considering the thermo-mechanical processing conditions relating to the friction assembling process.

EBSD analyses were first carried out in the vicinity of the interfacial zone. The resulting HCP and BCC inverse pole figures are shown in Figure 16.a and 16.b respectively; superimposed grain boundaries are also provided.

The change in crystallographic structure that operates under external constraints from the high-temperature β-parent lattice to the α' (or α) product crystal structure is known to theoretically follow coordinated rules minimizing the strain energy of phase transformation [44], [5]. Consequently, a self-developed subroutine detailed by authors in [43] using the Matlab toolbox Mtex v5.1.1 and based on the work of Germain *et al* [45], [46] permitted to reconstruct the parent β orientation prior to the $\beta_{lean} \rightarrow \alpha'$ among clusters of entangled HCP laths relying on the following Burgers Orientation Relationship (BOR) [4]: $\{110\}_{\beta}$ // $\{0001\}_{\alpha'}$ and $\langle 111\rangle_{\beta}$ // $\langle 11\bar{2}0\rangle_{\alpha'}$.

The approach may be summarized as it follows: for each precipitated α' needle, the algorithm first computed every possible theoretical β parent orientations using the ideal Burgers orientation relationship (taking into account the 5.268° rotation shift around the $(0001)_{\alpha'}$ zone-axis between β and α' phases). A cross-check comparative procedure was then applied between groups of three neighboring laths surrounding the considered α' needle and separated by high angle grain boundaries (>15° threshold). The β-reconstructed parent grain was then computed as the common BCC orientation solution triplet that minimized the misorientation between the tested laths while respecting a 5° misorientation threshold. This algorithm was then repeated for all the spatial lath combinations of the maps. The reconstructed β orientations are shown in Figure 16.c. and a schematic representation depicting the BOR is provided in Figure 16.e.

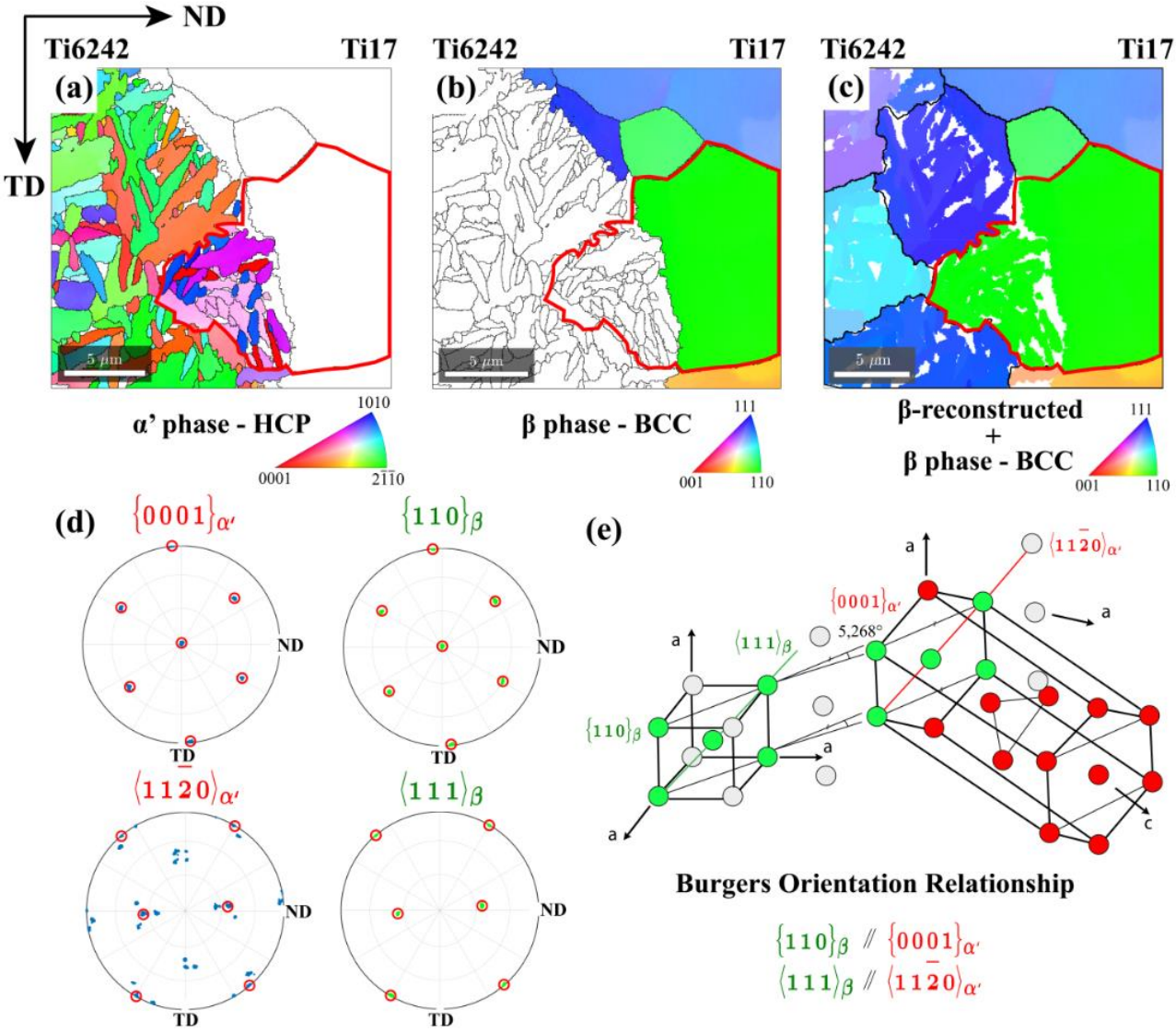


**Figure 16**: *Inverse pole figure from EBSD analysis at the Ti6242/Ti17 transition zone for* **(a)** *the HCP*, **(b)** *BCC indexed data and* **(c)** *the BCC reconstructed orientations*; **(d)** *110-111 and 0001-11$\bar{2}$0 pole figures for, respectively, the HCP and BCC indexed data within the selected subgrain (red boundary)*; **(e)** *Schematic representation of the Burgers Orientation Relationship*; *a step size of 40 nm was used for the EBSD data acquisition and solely the points with a confidence index higher than 0.1 were considered in this analysis; a threshold of 2° misorientation was used for grain boundary detection*.

The high-temperature β-reconstructed map confirms unequivocally the occurrence of a mutual β-phase intermingling of the materials in the interfacial zone. Closer examinations of the orientation relationship correspondences were then carried out on the interfacial subgrain outlined in red in Figure 16.(a, b, c). In order to clearly illustrate the BOR, the orientations of the map presented in Figure 16 were shifted to align the {110} plane direction of the red-highlighted parent β subgrain with the RD direction corresponding to the out-of-plane normal direction of the map. The stereographic projections of each individual α' lath orientations formed in the Ti6242 side of the selected subgrain were superimposed to the β orientation of the latter (i.e. Ti17 side), the resulting 110-111 and 0001-11$\bar{2}$0 pole figures are shown in Figure 16.d. The red circles on these pole figures indicate that the BOR is actually resolved which confirms the existence of a β microstructural

continuity between both alloys during the LFW configuration presently studied. Additional investigations by TEM and the corresponding ASTAR analysis supported as well this statement plus showed that the α' martensitic laths at the juncture between the materials are directly embedded within the β matrix (Figure 17 and Figure 18). The BOR is systematically shown on the needle-like formations. However, since at the tip of the embedded needles their width as seen in the TEM image is only around 10 nm, the thickness of the sample can be expected to be around 50 nm or higher and no overlapping of diffraction patterns is seen in the central pixels of the needle, these needles should be considered as 2D cross-sections of thin plate structures (Figure 18).

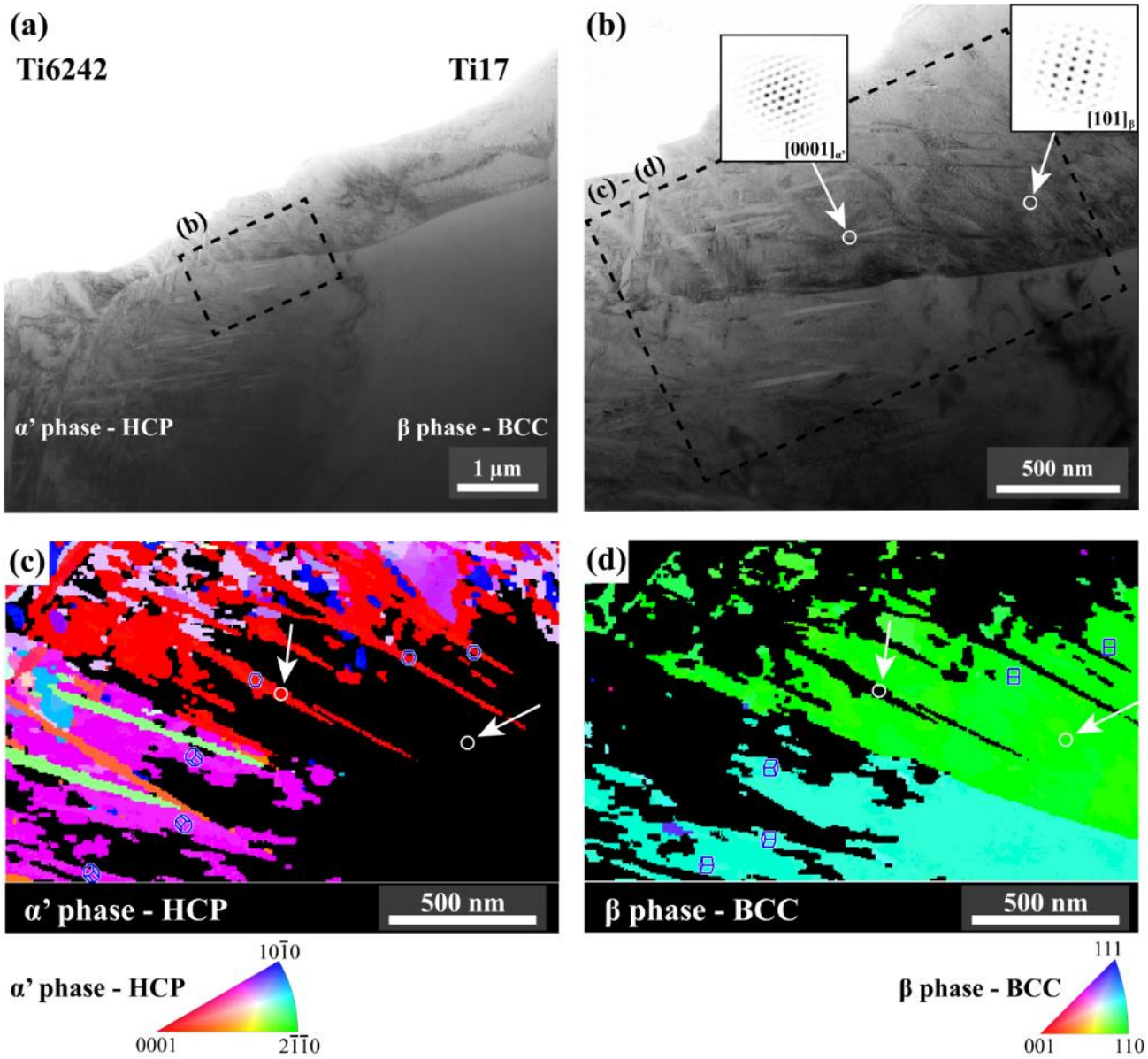


**Figure 17**: **(a)** *TEM bright field imaging of the interfacial zone along the welding line*, **(b)** *High magnification image of the interface combined with diffraction spots obtained in an α' lath and in the β phase; ASTAR inverse pole figure of* **(c)** *the HCP and* **(d)** *the BCC crystals, the white circles represent the positions of the diffraction spots used in* (b).

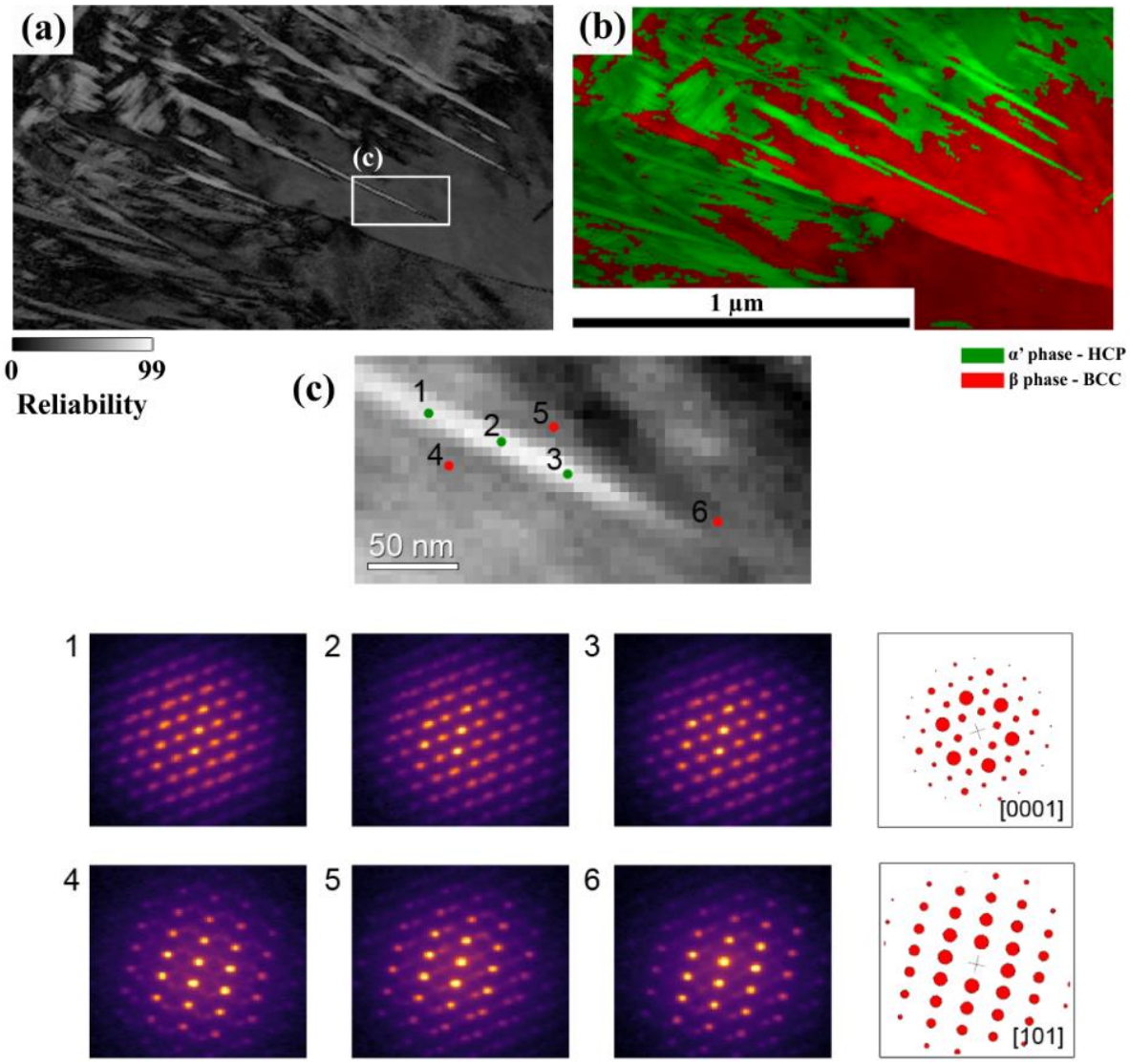


**Figure 18**: **(a)** *Reliability map of the ASTAR orientation acquisition in TEM*, **(b)** *α'-HCP and β-BCC phase map*; **(c)** *experimental diffraction patterns obtained on local spots on an α' needle-like formation embedded within β phase matrix comparison with simulated patterns for the* [0001] *α' and* [101] *β phase, correspondly*.

### 4.4 Grain fragmentation and texture development

An overview of the near-interfacial zone from EBSD investigations is presented in Figure 19.(a, b, c). A classification of the grain boundary misorientations is also provided combined with a Kernel Average Misorientation (KAM) cartography in Figure 19.d; the KAM procedure was solely applied to the Ti17 side. A fragmented microstructure is discernible in both materials characterized by a remarkably high fraction of low-angle grain boundaries arranged in mosaic patterns. Such a microstructure would indicate that extensive grain fragmentation occurred accompanied by substantial crystallite rotations. These apparent crystallites constitute substructures with low internal misorientations formed within deformed large β grains. Some local interpenetrations of materials are also readily observable despite the presence of a notable β microstructural continuity revealed in the β-reconstructed configuration.

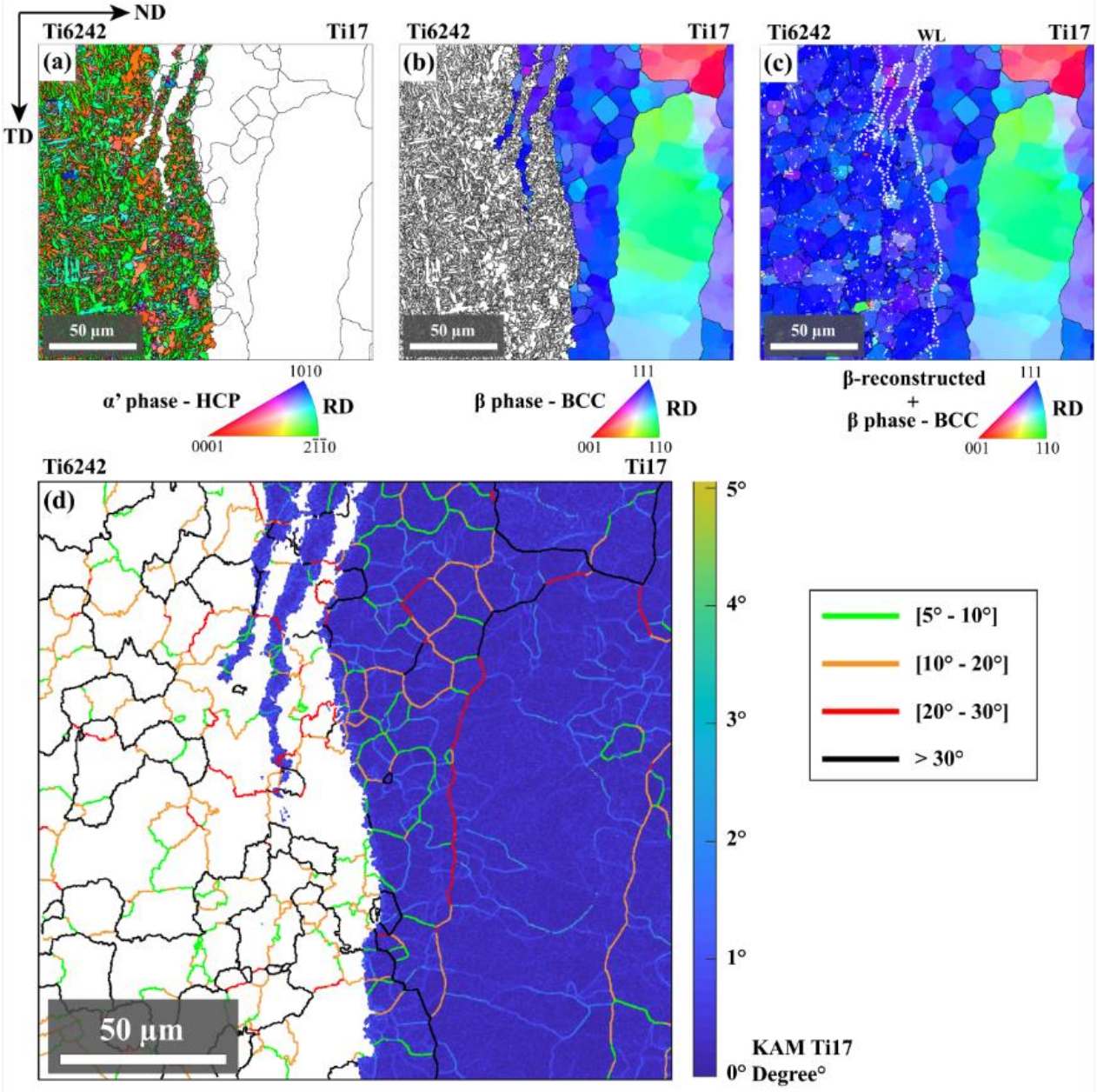


**Figure 19**: *Inverse pole figure from EBSD analysis (step-size 0.2 µm) at the extended Ti6242/Ti17 interfacial zone for* **(a)** *the HCP,* **(b)** *BCC indexed data and* **(c)** *the BCC reconstructed orientations superimposed with the grain boundary detection (5° misorientation threshold); the IPF color code corresponds to crystallographic direction of the indexed lattice along the RD (friction) direction.* **(d)** *The corresponding Kernel Average Misorientation (KAM) cartography combined with the grain boundary misorientation classification.*

The distributions of the misorientation angles in the BCC Ti17 (Figure 20.a) and the reconstructed BCC Ti6242 microstructures (Figure 20.b) corroborate the occurrence of a significant grain fragmentation and a subsequent texture development. Indeed, in both microstructures, the spatially correlated and uncorrelated misorientation distributions revealed the presence of a noteworthy statistical peak at the low angle boundaries; the former being significantly higher than the latter. Such a feature would indicate that a reorientation of the

grains towards a specific direction occurred during LFW accompanied by gradual rotation of the crystallites from low-angle to high-angle grain boundaries. The mechanism forming such textured recrystallized-like microstructures is often referred to as a Continuous Dynamic Recrystallization (CDRX) process [47] and appeared to be more pronounced in the Ti6242 than in the Ti17. In addition, a secondary peak at 60° could be noted in the Ti6242 and is presumably due to the formation of a twin-symmetric texture component. The latter was not as readily visible in the Ti17.

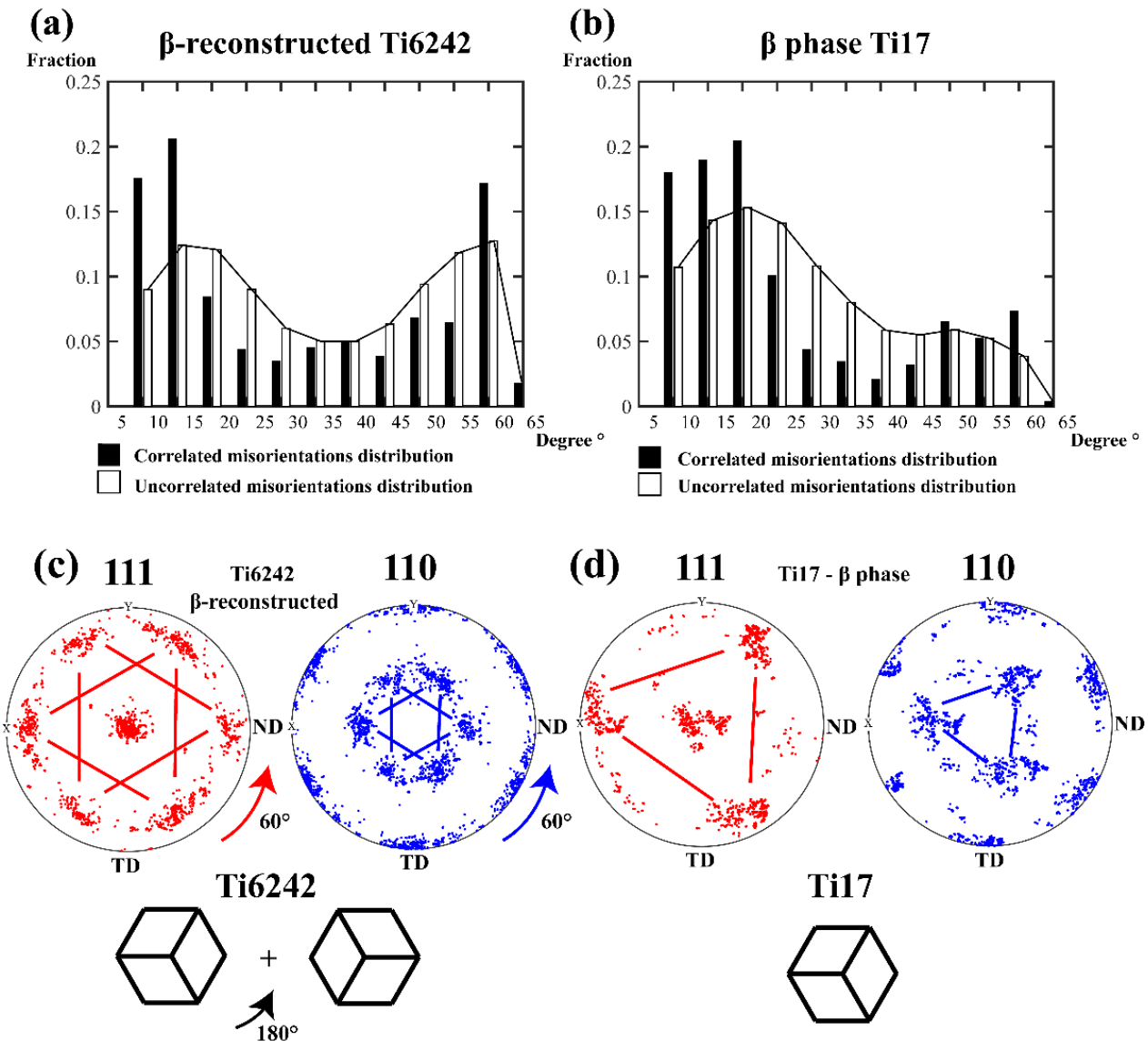


**Figure 20**: *Spatially correlated and spatially uncorrelated misorientation angles distributions for* **(a)** *the Ti6242 β-reconstructed and* **(b)** *the Ti17 β microstructures*; *the corresponding 111 and 110 pole figures for* **(c)** *the Ti6242 and* **(d)** *the Ti17, the equal-area stereographic projections of the orientations are done along the RD (friction) direction in the (TD, ND) plane.*

The 111 and 110 pole figure projections of the individual orientations from the EBSD orientation data presented in Figure 17 are plotted in Figure 20.c and 20.d. The stereographic projections were first realized on

the (TD, ND) cross-sectional plane, along the friction direction RD and according to the Schmidt equal-area convention. The 111 and 110 pole figure representations highlight the formation of a common two-component β texture development in the near-thermomechanical affected zone of both titanium alloys. A strong crystallites reorientation is notably observed and resulted in the alignment of the BCC <111> crystal direction with the RD. Where the RD also corresponds to the friction direction of the welding process. Furthermore, the texture components manifest a twin-symmetry from one another that is characterized by a 180° rotation around <111>/RD, eventually resulting in a misorientation angle of 60° towards each other. In the Ti6242, both twin texture components are developed with equivalent observable intensities. While a limited but discernible development of the second twin-symmetric texture component was noted in the Ti17.

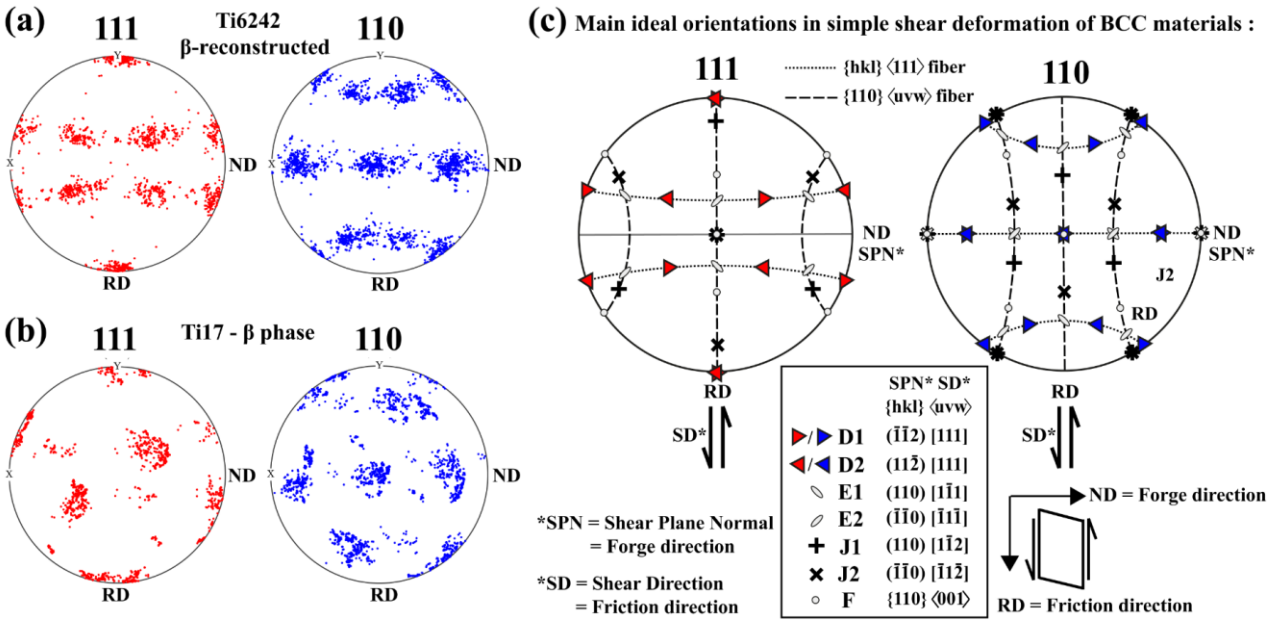


**Figure 21**: *Equal-area 111 and 110 pole figure projections in the (RD, ND) shear frame reference and along the TD for*: **(a)** *the Ti6242 β-reconstructed and* **(b)** *the Ti17 β phase*; *the schematic representation of the main ideal orientations in simple shear deformation of BCC materials is illustrated in* **(c)** *after* [48] *and* [49] *for the ideal shear orientations convention*.

Regarding the mechanical load produced by the alternate friction motion, it is interesting to reposition the problem on the longitudinal cross-section of the welded assembly. The latter corresponds to the (RD, ND) plane in the sample reference system. Indeed, the deformation process is ideally comparable with a classic case of simple shear deformation, where the predominant shear deformation would be introduced by the movement of the lower block rubbing against the upper block along the friction direction RD. By analogy, the friction direction would consequently correspond to the shear direction SD, and the shear plane would correspond to the friction plane (RD, TD). Finally, the shear plane normal (SPN) would hence be aligned with the ND. The corresponding 111 and 110 equal-area pole figure projections in the above-defined shear frame reference (SD, SPN) (or also (RD, ND)) are presented in Figure 21.a and 21.b. The ideal shear texture components that may

develop in BCC materials were reported in the literature by Baczynski and Jonas [48]. They identified four ideal preferred orientations: D, E, F and J, that develop along two partial fibers: $\{110\}\langle uvw\rangle$ and $\{hkl\}\langle 111\rangle$, during torsion tests realized on α-BCC iron alloys. A schematic representation of these ideal texture components is depicted in Figure 21.c.

The preferred orientation components developing in the near thermo-mechanical affected zone of the weld were then compared with the ideal orientations of the texture components developing in simple shear deformations (Figure 21). The comparative identification analyses consequently exhibited a predominant development of the D1 and D2 twin-symmetric texture components in Ti6242 during the LFW process. In Ti17, only limited development of the D2 component was observed, while a strong crystal preferred reorientation developed towards the D1 component. Both ideal orientations D1 $(\bar{1}\bar{1}2)[111]$ and D2 $(11\bar{2})[111]$ lie on the $\{hkl\}\langle 111\rangle$ fiber and tend to align the $\langle 111\rangle$ crystal direction with the shear/friction direction (SD and RD). As previously remarked, the D1 and D2 component display a 180° rotation symmetry around the shear direction, which also corresponds to the <111>/RD partial fiber. These findings are consistent with the texture developments observed in the LFW literature on the residual β phase of Ti64 alloy [30], [50] and reported on the texture analyses of a β-metastable alloy [51].

# 5. Discussion

## 5.1 Microstructural changes upon thermo-mechanical loading

The overviews of the microstructure in the joint (Figure 10 and Figure 11) showed that both Ti17 and Ti6242 alloys present markers of an extensive α→β phase transformation that occurred during the process.

In the Ti6242, these markers are present within a band of approximately 1 mm in thickness (corresponding to the Zones II and III). On the one hand, the former α nodules of the near WL area (Zone III) first underwent a β phase transformation during the hot deformation process. The observed redistribution of the Ti6242 alloying elements was most likely caused by the progressive diffusion of the β stabilizing elements from the initially interspersed intergranular $\beta_{rich}$ matrix to the adjacent β transformed nodules. The gradual aspect of the diffusion phenomena is directly related to the local temperature distribution which lowers as moving away from the WL. The close WL area rather experienced the highest temperature values. As a result, the rates of the transport phenomena in the latter zone were important enough to lead to substitutional elements partitioning close to a local $\beta_{lean}$ composition on a 100 µm thick band of grain refined β microstructure. Where the $\beta_{lean}$ composition consequently stems from the homogeneous partition of the alloy elements above the β transus. Besides, the alleged extensive chemical homogenization corroborates with the observation of α' martensitic phase in the Zone III. Indeed, the precipitation of the metastable phase α' can only result from the decomposition of a $\beta_{lean}$ (or quasi-$\beta_{lean}$) phase upon rapid cooling to room temperature [1] when the cooling rates are high enough to hinder long-range diffusion phenomena.

On the other hand, in the TMAZ (Zone II) the former α nodules were similarly subjected to above β transus temperatures and consequently underwent β phase transformation as well. However, the limited dwell time in the β domain restrained the diffusion of the β stabilizers from the matrix to the solute lean $\beta_{transformed}$ zones, which resulted in retaining intergranular β matrix upon quenching. The decomposition of these $\beta_{transformed}$ nodules upon cooling led to the precipitation of intertwining α plates (often referred to as $\alpha_{secondary}$) presenting a fragmented-like appearance. The fragmented aspect was attributed by authors in a previous study [43] to a nucleation-shear mechanism leading to the precipitation of various α plates following different crystallographic variants within former $\beta_{transformed}$ parent nodules. This transformation-induced process finally resulting in such fragmented-like α microstructure, with the progressive presence of intergranular β matrix.

In the Ti17, the markers of α→β transformation are present within a 2.5 mm thick band from the WL (Zone IV, V, VI, VII), the cooling rates from the β domain were high enough to result in the stabilization of a single β-metastable phase at room temperature. The afore-mentioned descriptions are in conformity with the ones previously reported by Ballat *et al.* [42], [43] for Ti17 and Ti6242 single-material LFW configurations using the same block geometries and analogous process parameters. Furthermore, Ballat *et al.* [42], [43] also performed *in situ* temperature measurements in the vicinity of the rubbing surfaces and reported that the local

interfacial temperature reached about 1200°C. The observed microstructural changes on the Ti17-Ti6242 dissimilar joint are in agreement with these measurements.

To identify the mechanisms resulting in bond formation, the β-grain boundaries of both materials were closely observed at the vicinity of the interfacial junction. In Figure 19.d, the features of β-grain fragmentation and rotation are clearly discernible in both materials with the presence of subgrain structures exhibiting low intragranular misorientation levels. These subgrains subdivide the prior-deformation β-parent grains in smaller crystallites. As illustrated in Figure 12 and, more closely in Figure 16, the interfacial zone exhibits an apparent continuity characterized by the presence of intermingled α'/β grains. The comprehension of the origin of those intermingled grains is a crucial element for the extensive understanding of the creation of the bond.

To this end, the hypothetic parent crystallographic relationship between the α' phase and the β phase has been prospected *via* EBSD and TEM investigations in the junction zone (Figure 16, 17 and 18). A perfect verification of the specific BOR was demonstrated in these peculiar intermingled structures between the precipitated α' laths of the Ti6242 and the corresponding β-metastable structure of the Ti17. Such findings reveal that both structures unequivocally shared the same β-parent crystallographic orientation above β-transus temperature conditions, and indicates that the cohesion mechanisms actually occurred between single-phase β structures.

### 5.2 Grain fragmentation mechanisms & texture formation

β titanium is a BCC high stacking fault energy structure, under such hot working conditions, the appearance of a significant dynamic recovery is a characteristic feature [52]–[54]. High-temperature conditions promote the mobility of dislocations and the mutual interaction of their associated elastic fields yield to their self-organization into dislocation wall structures. The result of those complex many-body interactions is the progressive building of new grain boundaries to geometrically accommodate the strain with respect to the mechanical interactions between neighboring grains [55]. In recovery processes, the dislocation generation is balanced by the rate of dislocation annihilation, while a fraction is consumed by the formation of geometrically necessary and incidental boundaries that progressively subdivide the parent grains into smaller crystallites with low dislocation density [53]. Those structures correspond to the reported observations (Figure 19.d) with the progressive and continuous transformation of the geometrically necessary boundaries into low angle grain boundaries and finally to high angle grain boundaries.

Globally, the Ti17 was shown to exhibit a larger amount of low angle to medium angle grain boundaries than the Ti6242. The higher proportion of high angle grain boundaries in the latter observed in Figure 19.d and Figure 20 is probably caused by advanced crystallite rotations and the subsequent development of the two-component D1/D2 simple shear texture (Figure 21). These components are the result of the progressive grain rotation occurring in the near-thermomechanical affected zone in order to tend to the most

favorable active slip configuration regarding the imposed plastic flow during the process. Indeed, the usual features of crystal plasticity in BCC structures essentially occur by slip on the {110}, {112} and {123} planes, which all contain the $\frac{1}{2}\langle 111\rangle$ Burgers vector (dominant slip direction) [56]. As a consequence, during the hot deformation process, the continuous lattice rotation favored the alignment of the $\langle 111\rangle$ BCC primary slip direction with the shear/friction direction. The dominant alignment of the {112} slip planes with the friction plane finally led to the observed D1/D2 twin-texture development. It was notably noted that the D1 component development was greatly favored in the Ti17 part. One possible explanation for the asymmetric fragmentation-rotation behavior between Ti6242 and Ti17 may be due to the smaller β grains ($D \approx 20$ μm) forming in the TMAZ of the Ti6242 compared to ones present in the Ti17 side (millimetric). Indeed, smaller grains imply higher density of grain boundaries which are favored nucleation sites for subgrain formation; the former are also more prone to grain fragmentation by GDRX (Geometric Dynamic Recrystallization) in the zones subjected to severe plastic deformation. These mechanisms would result in an enhanced fragmentation process in the Ti6242 that softened the latter compared to the work-hardened β grains of Ti17 rendering the Ti6242 more prone to plastic deformation and subsequent fragmentation-rotation. Eventually, the dominant development of BCC simple shear texture components observed in the thermomechanical affected zone of the weld joint is an additional argument that tends to confirm that the deformation process predominantly took place in the β domain.

In such severe thermo-mechanical processing conditions, β-titanium exhibits high recovery rates. Due to that fact, the increase in misorientation between the fragmented rotating sub-structures generally manifests slow kinetics that allegedly does not imply long-range motion of the crystalline interfaces. Nevertheless, the microstructural observations reported in Figure 16 and Figure 19 in the vicinity of the interfacial junction revealed that mutual β-grain boundary motions occurred across the interfacial junction between the β fragmenting grains belonging to the Ti17 and the Ti6242. This phenomenon led to a remarkable β microstructure continuity in the transition zone between the two alloys, regardless of the local alloying composition differences between the in-contact materials. As mentioned in [57], a recrystallization process is "the formation of new grain structures in a deformed material by the generation and the migration of high angle grain boundaries driven by the stored energy of deformation". Consequently, the previously described β-fragmentation process can be requalified as a recrystallization process. Recovery and recrystallization are competitive processes that are both driven by the stored energy of deformation. As a result, the interfacial migration mechanism was presumably mainly caused by differences in defect density and interfacial energy between the in-contact crystalline interfaces. The latter locally resulted in a driving force for the migration of the grain boundaries. This type of grain refinement process is often referred to as a Continuous Dynamic Recrystallization (CDRX) process in the literature [47], [58]. Therefore, such CDRX process led to the progressive transformation of the initial β boundaries, delimiting both contacting alloys as homophase crystalline interfaces [59], in favor of interfacial β grains by mutual grain boundary motion.

### 5.3 Phase precipitation upon cooling in the interfacial zone

The local repartition of substitutional elements across the interfacial zone manifests clear evidence of a global interdiffusion phenomenon on an approximately 4 µm thick band along the transition zone. The latter probably mainly arose at high-temperature and under BCC crystal structure, when the interfacial zone became cohesive. The fitting of the element diffusion profiles (Figure 14) through Gaussian error-functions showed a slight shift of the center of the fitted error-function away from the WL towards Ti17. This slight shift can be explained based on the effects of the alloying elements on phase stability: Mo and Cr elements are strong β-stabilizers while Al element is an α-stabilizer [60]. Zr is known as a neutral element, but it was demonstrated to increase the β-stabilizing effects (propensity to suppress the metastable α"/ ω phases in favor of single β phase) when associated with other β-stabilizing elements in β-titanium alloys [61]. Sn is also considered as a neutral element, but it acts as an α stabilizer in the presence of other α stabilizers [60]. The concentration of α-stabilizer elements was still large enough to facilitate the precipitation of the α' laths between the WL and the center of the fitted error-functions. The estimated diffusion coefficients deduced from the fitting of the experimental profiles with error-functions displayed an order of magnitude of $10^{-1}$ µms$^{-1}$. Such values are consistent with the order of magnitude of the β-titanium lattice diffusivity, which is around $10^{-1}$ µm$^2$.s$^{-1}$ [62], [63] under the presumed interfacial temperature values reached during the steady-state rubbing process *id est* 1200°C. Contrary to measured diffusion values in similar solid-state assembling processes [64], no short-circuit diffusion features caused by large strains were noticed in the present configuration. The absence of observable dislocation-pipe assisted diffusion as described in [42] or [43] may be explained by the occurrence of continuous dynamic recrystallization in the junction zone. The balance between the dislocation generation and the rate of dislocation annihilation might have inhibited the assisted diffusion along short-circuiting paths because of the low resulting dislocation density inside the forming subgrain structures [67].

When the motion of the oscillating part stopped, the near interfacial zone between the alloys locally underwent a critical cooling. On the one hand, α' laths spanned across the parent refined β subgrains of the Ti6242 presenting a slab-like morphology in self-similarity pattern arrangements [68]. The textured aspect of the α' precipitates (see orientations data in Figure 11) is most likely due to the variants selections according to the BOR from the strong high-temperature β preferred orientation that developed during the hot deformation process.

In principle, the phase transformation reaction for the α' phase precipitation should be partitionless and the α' laths should locally inherit the local chemical composition of the parent β phase. However, in practice, it is rarely possible to completely avoid diffusion phenomena. In the close interfacial zone, a strong partitioning between the α' and β phase was notably revealed. Indeed, a remarkable depletion in β stabilizing elements (Cr, Mo and arguably Zr) was observed within the precipitated α' plates, accompanied with thin pile-ups of the latter along the α'/β interfaces (Figure 15). The phenomenon is notably clearly perceptible on the chrome element which is the strongest β stabilizer among the alloys components (Figure 15.b). This finding suggests that during the phase transformation, which operates throughout the progressive and coordinate

collapse of the β crystal planes, an important portion of β stabilizer atoms crossed the migrating interphase boundary. The latter observation consequently indicates an element partitioning at the moving phase boundary probably controlled by a local equilibrium condition [69]. The low solubility of the Cr and Mo components in the HCP phase [70] presumably led to the diffusion of these elements towards the adjacent β-BCC phase upon phase transformation and consequently caused the continuous accumulation of these migrating elements in front of the α'/β interfaces. A local equilibrium condition at the moving phase boundary would push the local elements pile-ups forward the transformation front, which would finally result in the observed gradient-aspect pile-ups of rejected elements along the phase boundary. Besides, the local boundary conditions and notably the high concentration of misfit dislocations between the phase boundaries might have enhanced the transport phenomena by pipe-assisted diffusion. Similar element partitioning features were notably reported and are described in details by authors [71] in precipitation-hardened Mn-enriched TRIP-steel at the martensite/austenite phase boundaries. On the other hand, a full retention of the high temperature BCC β phase is detected at ambient temperature in the β-metastable alloy Ti17 forming the observed intermingled α'/β interfacial structures (Figures 16, 17 and 18).

### 5.4 Bond formation & joining mechanisms

Based on the previous results, the scenario presented in Figure 22 is proposed to describe the formation of the cohesive junction between the studied dissimilar alloys:

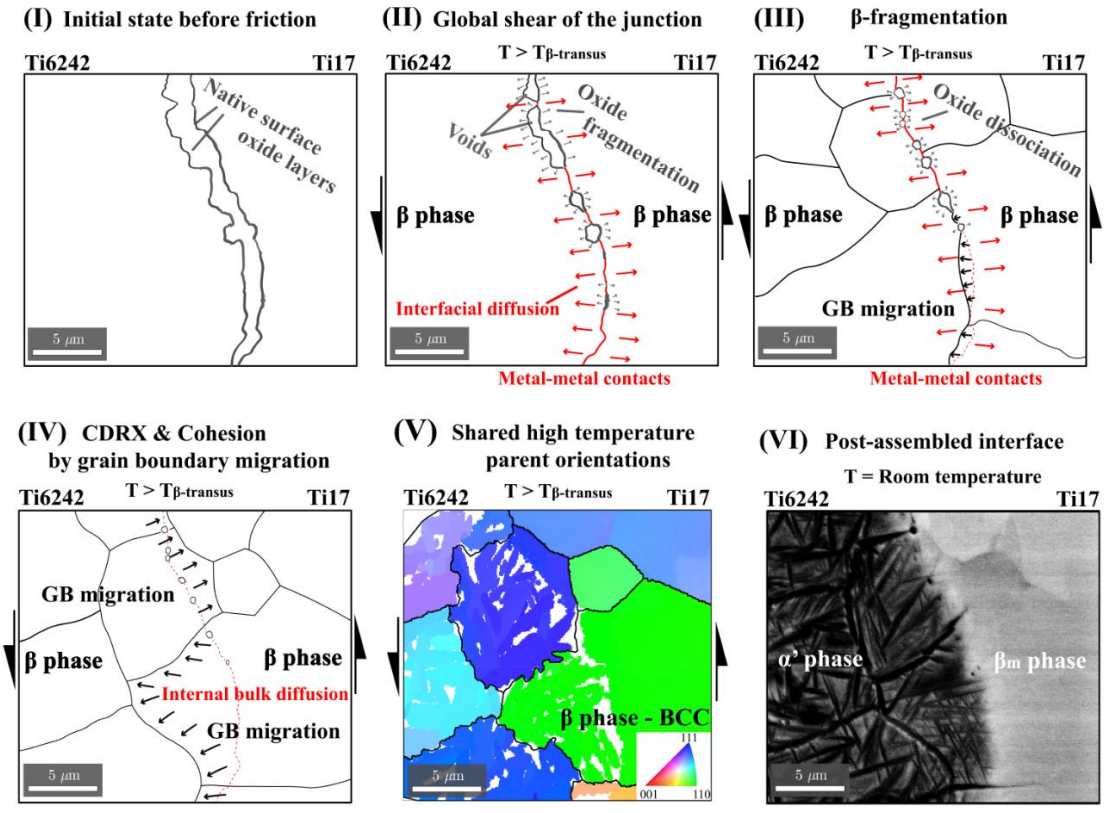


**Figure 22**: *Schematic representation of the stages leading to interface bonding during LFW.*

**(Step I)** Before friction, stable $Ti_xO_y$ oxide layers of a few nanometers in width are initially present on the ground surfaces of the titanium alloy work-pieces. Similarly as in other solid-state joining processes, the disruption of those oxides is a prerequisite condition for successfully forming a metallic bond [28], [72]. During the friction process, the energy dissipation originating from the contact friction interactions was substantially transformed into thermal energy. The increase in temperature at the vicinity of the faying/reciprocating surfaces led to the thermal softening of the materials. The plastic flow resulting from this softening might have enhanced the fragmentation, breaking up and/or dispersion of the oxide layers.

**(Step II)** The thermal energy arising from the irreversibility of such a frictional process caused the materials to be subjected to high-temperature values (higher than the β-*transus* temperature in both materials). The latter would favor a progressive closure of the voids between the faying surfaces by mutual plastic deformation. As well described by authors in diffusion bonding processes [23], [25], such local high-temperature conditions promote the fast dissociation of the titanium oxides at the oxide/metal interface ; followed by bulk-diffusion of the reaction products in the metallic solute matrix. The round-shapes porosities observed in Figure 10 may be explained by the incomplete mechanical closure of the interfacial voids. The latter might be formed by entrapped gaseous species resulting from the incomplete reduction reaction of the oxides.

**(Step III – Step V)** Such thermomechanical processing conditions led to a β-fragmentation process through a progressive reorganization of the geometrically necessary dislocations into low angle boundaries and then to high angle boundaries. Likewise other solid-state assembling processes, it was already shown by the authors in [73], [74], [75] that, in metal-to-metal contacts, fast surface atomic diffusion and surface relaxation are key factors yielding to the primal solid-state bonding between crystalline materials. When a sufficient adhesion occurred between the frictional parts, a migration of the crystalline interfaces assisted by a continuous dynamic recrystallization process is demonstrated across the junction zone. The grain boundary migration kinetics were probably caused by differences in defect density and interfacial energy between the in-contact crystalline interfaces, ultimately leading to the formation of the cohesive junction depicted in Step V. Once the cohesive junction established, the thermal source is eventually mainly sustained by internal dissipative processes (*id est* by the degeneration of the plastic deformation energy in the form of thermal energy). The thermomechanical coupling under the imposed deformation conditions yields to the apparent self-regulated behavior of the process during the axial shortening phase.

**(Step VI)** Under high cooling rate, the composition differences between the alloys resulted in the formation of different detected phases in the transitional zone (α' martensitic laths in the Ti6242 side and room temperature single β-metastable phase in the Ti17 side). Intermingled grain-refined structures sharing both α' and β phase structures were observed in the interfacial zone.

## 6. Conclusion

**(1)** The interfacial features of linear friction welding between two dissimilar but mutually soluble titanium alloys (Ti17 and Ti6242) were examined. The thorough analysis of the interface and its surrounding allowed identifying the underlying microstructural mechanisms leading to the successful cohesion between the assembled work-pieces.

**(2)** The joining phenomenon occurred in the single-phase β domain by the active migration of the crystalline interfaces from one grain to another across the junction zone assisted by a continuous dynamic recrystallization process. Besides, the motion of the interfacial grain boundaries arose despite the chemical composition difference between the examined titanium alloys. It was shown that the resulting interfacial β grains present a common β-parent crystallographic orientation and an internal diffuse interface.

**(3)** Once the reciprocating motion stopped, both materials experienced rapid cooling from the β domain. Under these β quenching conditions, the chemical composition heterogeneity across the diffuse interfaces caused a strong difference in local phase precipitation. It resulted in the formation of intermingled grains of HCP phase in the Ti6242-dominant side and of stabilized $\beta_{metastable}$ structure in Ti17-dominant side. It was shown that these intermingled structures perfectly verified the Burgers orientation relationship, which finally confirmed the common crystallographic origin of their high-temperature β parent grains.

Eventually, this work outlines the role of grain boundary motion as a crucial metallurgical mechanism for solid-state bond formation between mutually soluble alloys. The plasticity-induced phenomena activated during the hot deformation process stimulated crystal interface migration, notably in the weld center zone, and favored the materials coalescence in a thin metallurgical bond.

# 7. Prospects

## 7.1 Technical limitations for dissimilar weld configurations

The possibility to weld dissimilar alloys is an attractive application of the friction welding technology and may offer interesting alternatives in the functional design of technical workpieces. Nevertheless, it must be highlighted that the effective implementation of such assembling in engineering design must be carefully treated. From a metallurgical viewpoint, the assembling of dissimilar materials may pose extremely constraining issues. It seems consequently important to qualify the technical possibilities of the linear friction welding process. Through this section, we will try to set out the different limiting issues of the technology.

First, the materials to bond together must be chemically compatible from one another in order to avoid detrimental phase precipitation at the weld interface. Then, it is worth reiterating that the friction welding procedure intrinsically results in intense and highly localized thermomechanical loads in the junction zone. The latter generally yield to severe microstructural changes in the welding zone and considerably affect the materials properties in the joint. In dissimilar configurations, these changes may result in significantly diverging microstructures eventually emphasizing the differences between the joined microstructures. Last, the local heterogeneities in term of chemical composition or microstructure may pose challenging issues concerning post-weld heat treatment strategies. Indeed, the applied thermal load must meet the requirements for both without negatively affecting one. Furthermore, the chemical composition difference at the weld interface may result in unusual phase morphologies formation or phase transformations *via* diffusion. The latter phenomena may exacerbate local heterogeneities in the joint and have detrimental consequences on the assembly.

Regarding that, dissimilar welding does not appear as positive as it seems on paper. The complete development of viable dissimilar assemblies has to fill out demanding conditions that severely restrict their applicability in concrete engineering problems. Thus, dissimilar configurations yield to complex issues that must be intently evaluated in order to determine the viability of potential assembly.

## 7.2 Post-weld heat treatment on the Ti17 / Ti6242 weld couple

The studied Ti17/Ti6242 weld configuration is an excellent example illustrating such problematic. Despite elements interdiffusion at the weld interface, the local concentration in each alloy remained below the solubility limit within the titanium phases. The absence of miscibility gap between the joined alloyed prohibited detrimental intermetallic phase precipitation at the joining interface. Both alloys are consequently chemically compatible.

The thermo-mechanical loads resulted in an intense shear-texturation of the refining microstructure in the β domain under elevated conditions and resulted in metastable microstructures upon cooling with on the

one hand: β metastable phase, and on another hand: α' martensitic phase. Furthermore, the latter were found to be shared within the same parent crystal in the close interfacial region. The resulting as-welded microstructure is then unusable in such state without further appropriate post weld heat treatment strategy.

A homogenization strategy was then prospected on the welded Ti17/Ti6242 dissimilar microstructure. The main idea behind the post-weld heat treatment strategy was to provoke grain growth and determine whether the 'shared' character on the interfacial grains (illustrated in the Figure 21) is conserved after the triggering of grain growth.

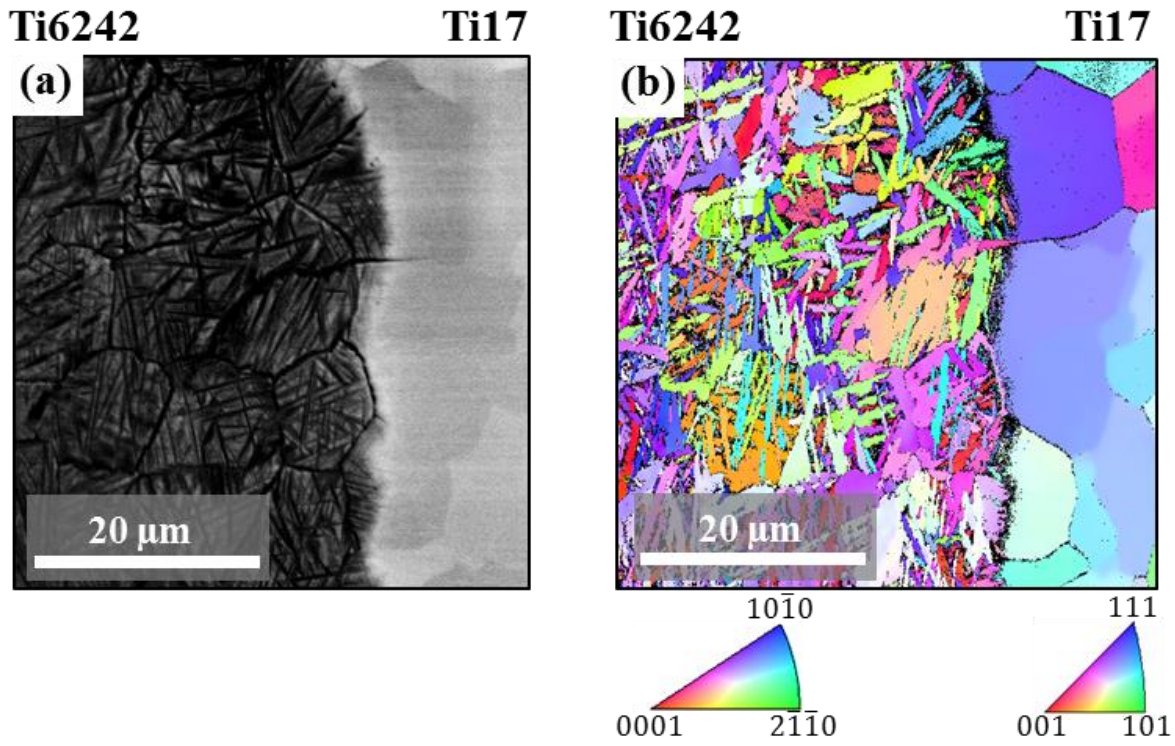


**Figure 21**: **(a)** *BSE-SEM image of the interfacial zone;* **(b)** *EBSD mapping of the interfacial zone corresponding to the BSE-image presented in (a), α'-HCP (Ti6242 side) and β-BCC phase (Ti17 side) IPF map are plotted.*

The Post-Weld Heat Treatment (PWHT) procedure is then divided into two stages. First a *super*-β-*transus* annealing procedure for the complete dissolution of α' and α phase and to initiate the growth of the β-recrystallized microstructure in the joint. Second, an annealing treatment for the re-precipitation of α phase to strengthen and confer the assembly interesting properties. Ti6242 presents the highest β-*transus* temperature, it is the limiting alloy for the choice of annealing temperature. The latter was then fixed 10°C above the β-*transus* temperature (estimated at about 900°C).

The PWHT finally consisted of an annealing at 910 °C for 2h followed by furnace cooling to 635 °C in 2h, such choice was motivated by the interesting microstructural & mechanical characteristics obtained on Ti17 and Ti6242 mono-material configurations on previous work developed in [76].

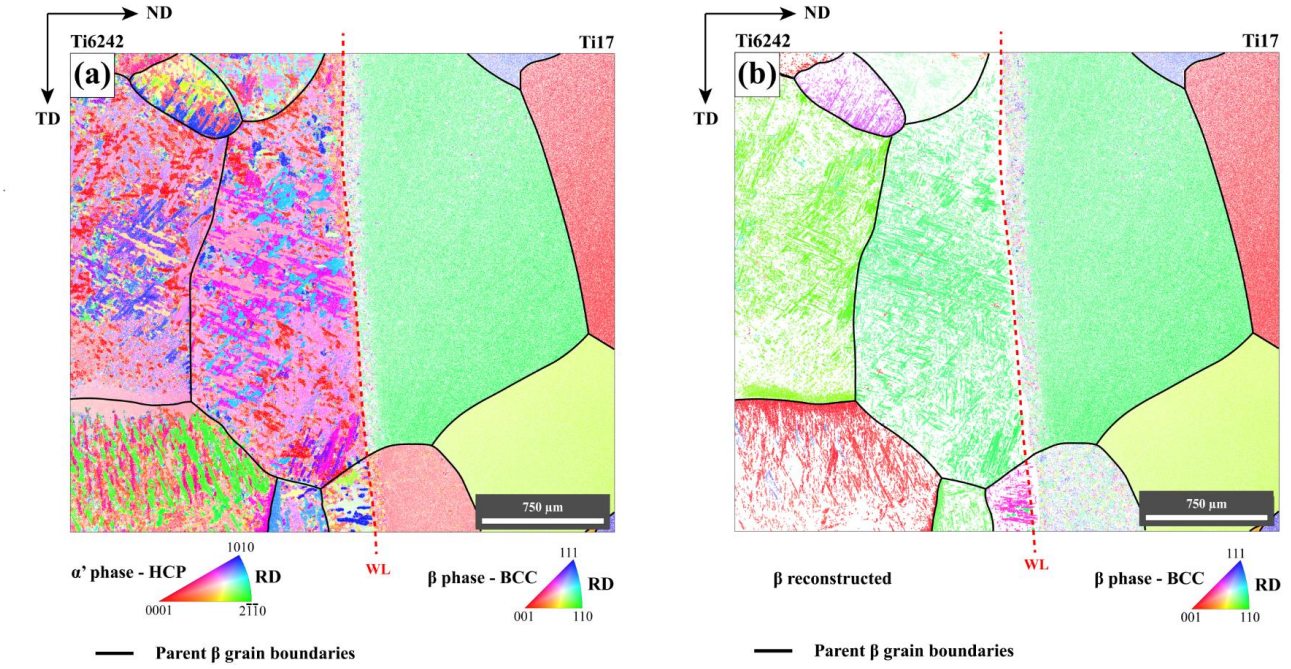


**Figure 22**: **(a)** *EBSD-IPF imaging of the annealed microstructure at the Ti17 / Ti6242 interface after 2h annealing at 910°C followed by air-quenching;* **(b)** *EBSD-IPF map of the β-reconstructed map. On both maps, black continuous lines delineate the former high-temperature β-parent grain boundaries.*

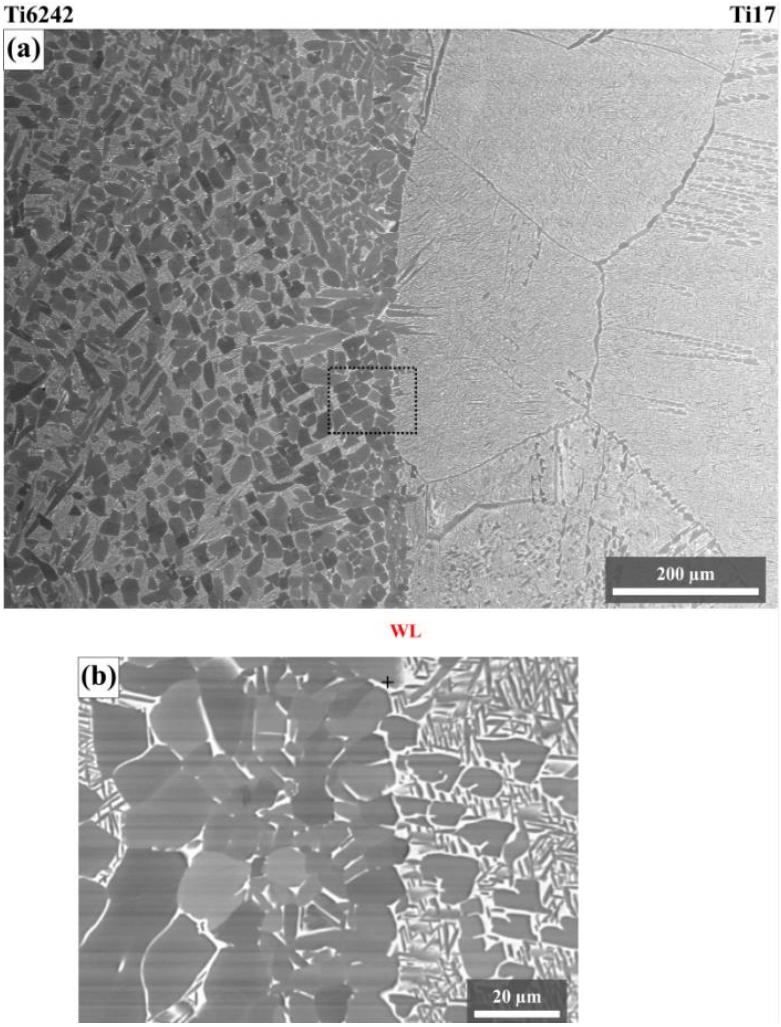


**Figure 23**: **(a)** *SE2-SEM image of the interfacial zone after PWHT: 2h annealing at 910°C* followed by furnace cooling *to 635°C, the sample was then held 2h at 635°C followed by air-quenching;* **(b)** *high magnification SE2-SEM micrograph at the materials weld interface.*

As illustrated in Figure 22, coarse 'shared' β-grain structures developed across the welding line after 2h annealing treatment in the β-domain. This result demonstrates that the interfacial "intermingled" grain structures that were observed to take place during the friction welding procedure continued to grow regardless the compositional differences between the alloys. Such exhausted grain migration from one material to the other presumably have beneficial effect on the bonding characteristics in term of material continuity. However, it is not certain that such microstructural features would result in a beneficial effect on the global mechanical strength of the assembly, notably after α phase precipitation.

Indeed, the treatment are proceeded at the same temperature on the whole assembly, which may create incompatibility issues because of the dissimilar nature of the bonded alloys. In the present case the α re-precipitation upon annealing eventually led to a sharp microstructure contrast with a nodular / close to a bi-modal microstructure in the Ti6242 and a plate-like microstructure embedded in coarse millimetric β grain. If the microstructure characteristics in the Ti6242 side are fairly close to the original microstructure (Figure 7.a), the ones of the Ti17 side are rather far from the initial Widmanstätten microstructure (Figure 7.b). Both microstructures co-exist side-by-side at the weld interfacial, sometimes sharing the same β matrix. Such brutal change between these adjacent morphologies forms a heterogeneous transition between the alloys that may result in deleterious effect on the mechanical response of the weld assembly. Further prospections on this latter point would be interesting to carry out.

At last, the presented results are only one of a number of strategies for PWHT and treatments resulting in better matching microstructural morphologies may exist. It might be advisable that the available post-weld heat treatment strategies should be considered in advance regarding the potential microstructural evolution of the alloys after joining.

To conclude, a critical perspective on the interest and the applicability of dissimilar welding by friction has been developed through that section. Even if technically possible, dissimilar joined configurations often present only a limited functional interest in the as-welded state. Therefore, post-weld heat treatment strategies have to be adapted to match both: alloys compatibility in term of developed microstructure and technical requirement for the in-use function of the assembly. These last points may be technically challenging. Thus, although appealing at first sight some significant operational limitations arise from the application of the linear friction welding technique on dissimilar alloys configurations.

### 7.3 Interfacial porosities

Detailed inspections at the weld interfacial zone exhibited the presence of evenly distributed round-shaped nanometric porosities (see Figure 24 below). Such formations are often classically reported in solid-state welding. However, at present time, no reasonable mechanism or satisfactory explanation supported with experimental or modelling *data* give tangible clue about their formation. All hypotheses are still possible (entrapped gaseous species? Gaseous products following oxide dissociation? Condensation into voids of excess vacancies generated during phase transformation? Incomplete joining formation? Expansion differences between phases?).

Nevertheless, these features were not observed after PWHT suggesting that a resorption mechanism might have taken place upon thermal loading.

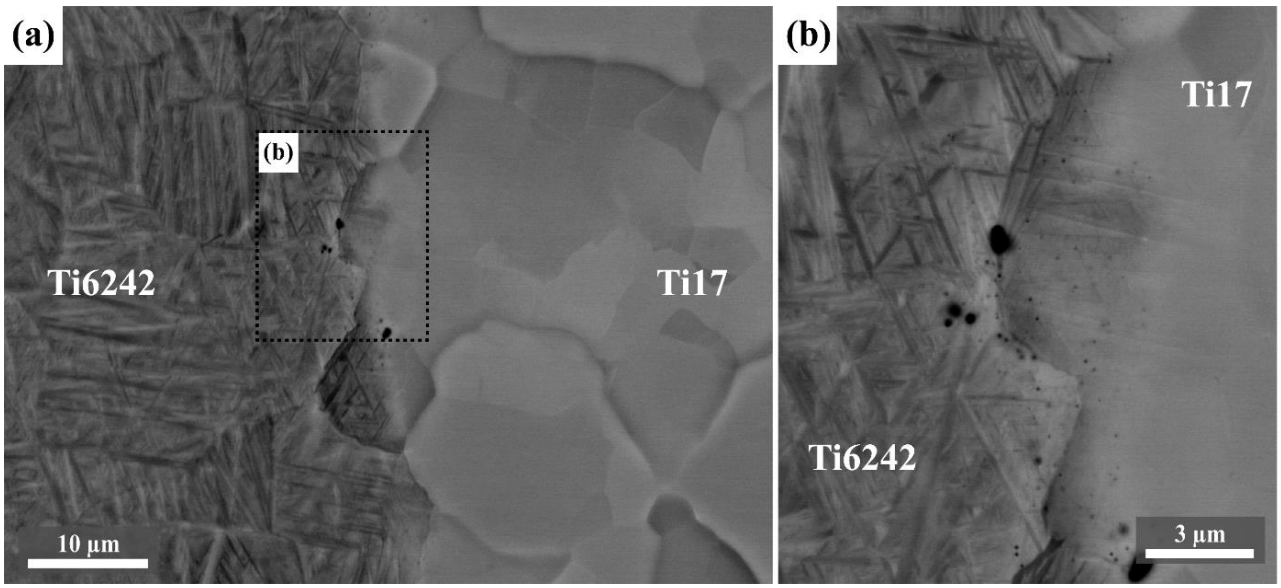


**Figure 24**: *BSE-SEM image of the interfacial zone* **(a)**; *the presence of round-shaped porosities is depicted in* **(b)** *in the junction zone.*

## 8. References


[1] G. Lütjering et J. C. Williams, *Titanium*, 2nd edition. Berlin; New York: Springer, 2003.

[2] J. Wen, « Effet de l'Hydrogène sur la Microstructure et la Déformation en Laminage à Froid du Titane de Pureté Commerciale et d'un Alliage de Titane β Métastable », p. 275, 2017.

[3] A. Akhtar et E. Teghtsoonian, « Prismatic slip in α-titanium single crystals », *Metallurgical Transactions A*, vol. 6A, p. 2001-2208, 1975.

[4] W. G. Burgers, « On the process of transition of the cubic-body-centered modification into the hexagonal-close-packed modification of zirconium », *Physica*, vol. 1, nº 7-12, p. 561-586, mai 1934, doi: 10.1016/S0031-8914(34)80244-3.

[5] Banerjee S., Mukhopadhyay P., *Phase Transformations - Examples fromTitanium and Zirconium alloys*, vol. 12. Elsevier Science, 2007.

[6] F. H. Froes, Éd., *Titanium: physical metallurgy processing and applications*. Materials Park, Ohio: ASM International, 2015.

[7] S. L. Semiatin, S. L. Knisley, P. N. Fagin, D. R. Barker, et F. Zhang, « Microstructure evolution during alpha-beta heat treatment of Ti-6Al-4V », *Metall and Mat Trans A*, vol. 34, nº 10, p. 2377-2386, oct. 2003, doi: 10.1007/s11661-003-0300-0.

[8] G. Lütjering, « Influence of processing on microstructure and mechanical properties of (α+β) titanium alloys », *Materials Science and Engineering A*, nº 243, p. 32-45, 1998.

[9] B. Dumanowski, « Simulation de traitements thermomécaniques de l'alliage de titane Ti-6% Al-4% V dans le domaine biphasé alpha + bêta », Ecole nationale supérieure des mines de Saint-Etienne, 1997.

[10] I. Weiss et S. L. Semiatin, « Thermomechanical processing of alpha titanium alloys—an overview », *Materials Science and Engineering: A*, vol. 263, nº 2, p. 243-256, mai 1999, doi: 10.1016/S0921-5093(98)01155-1.

[11] S. L. Semiatin, V. Seetharaman, et I. Weiss, « The thermomechanical processing of alpha/beta titanium alloys », *JOM*, vol. 49, nº 6, p. 33-39, juin 1997, doi: 10.1007/BF02914711.

[12] I. Weiss et S. L. Semiatin, « Thermomechanical processing of beta titanium alloys—an overview », *Materials Science and Engineering: A*, vol. 243, nº 1-2, p. 46-65, mars 1998, doi: 10.1016/S0921-5093(97)00783-1.

[13] D. Turnbull, « Metastable structures in metallurgy », *METALLURGICAL TRANSACTIONS B*, p. 14.

[14] H. Y. Kim et S. Miyazaki, « Martensitic Transformation Characteristics », in *Ni-Free Ti-Based Shape Memory Alloys*, Elsevier, 2018, p. 1-52.

[15] F. Prima, P. Vermaut, G. Texier, D. Ansel, et T. Gloriant, « Evidence of α-nanophase heterogeneous nucleation from ω particles in a β-metastable Ti-based alloy by high-resolution electron microscopy », *Scripta Materialia*, vol. 54, nº 4, p. 645-648, févr. 2006, doi: 10.1016/j.scriptamat.2005.10.024.

[16] S. Nag, R. Banerjee, R. Srinivasan, J. Y. Hwang, M. Harper, et H. L. Fraser, « ω-Assisted nucleation and growth of α precipitates in the Ti–5Al–5Mo–5V–3Cr–0.5Fe β titanium alloy », *Acta Materialia*, vol. 57, nº 7, p. 2136-2147, avr. 2009, doi: 10.1016/j.actamat.2009.01.007.

[17] Y. Zheng *et al.*, « Role of ω phase in the formation of extremely refined intragranular α precipitates in metastable β-titanium alloys », *Acta Materialia*, vol. 103, p. 850-858, janv. 2016, doi: 10.1016/j.actamat.2015.11.020.

[18] D. De Fontaine, N. E. Paton, et J. C. Williams, « The omega phase transformation in titanium alloys as an example of displacement controlled reactions », *Acta Metallurgica*, vol. 19, p. 1153-1162, 1971.

[19] J. L. Jellison, « The Role of Surface Contaminants in the Solid-State Welding of Metals », in *Treatise on Clean Surface Technology*, Boston, MA: Springer US, 1987, p. 205-234.

[20] N. Bay, « Mechanisms producing metallic bonds in cold welding », *Welding research supplement*, p. 137-142, mai 1983.

[21] H. A. Mohamed et J. Washburn, « Mechanism of Solid State Pressure Welding », *Welding research supplement*, p. 9.

[22] Y. Saito, H. Utsunomiya, N. Tsuji, et T. Sakai, « Novel ultra-high straining process for bulk materials - Development of the accumulative roll-bonding (ARB) process », *Acta mater.*, vol. 47, nº 2, p. 579-583, 1999.
[23] Z. A. Munir, « Analytical treatment of the role of surface oxide layers in the sintering of metals », *Journal of Materials Science*, vol. 14, nº 11, p. 2733-2740, nov. 1979, doi: 10.1007/BF00610647.
[24] Y. Takahashi, K. Inoue, et K. Nishiguchi, « Identification of void shrinkage mechanisms », *Acta Metallurgica et Materialia*, vol. 41, nº 11, p. 3077-3084, nov. 1993, doi: 10.1016/0956-7151(93)90036-R.
[25] Y. Takahashi, T. Nakamura, et K. Nishiguchi, « Dissolution process of surface oxide film during diffusion bonding of metals », *Journal of Materials Science*, vol. 27, nº 2, p. 485-498, 1992, doi: 10.1007/BF00543942.
[26] N. F. Kazakov, Éd., *Diffusion Bonding of materials*. Oxford: Oxford Scientific Press, 1985.
[27] M. Lagos et C. Retamal, « An alternate theoretical approach to solid-state bonding », *Scripta Materialia*, vol. 64, nº 5, p. 402-405, mars 2011, doi: 10.1016/j.scriptamat.2010.10.044.
[28] A. A. Shirzadi, H. Assadi, et E. R. Wallach, « Interface evolution and bond strength when diffusion bonding materials with stable oxide films », *Surface and Interface Analysis*, vol. 31, nº 7, p. 609-618, juill. 2001, doi: 10.1002/sia.1088.
[29] J. Bos et H. Moes, « Frictional Heating of Tribological Contacts », *Journal of Tribology*, vol. 117, nº 1, p. 171, janv. 1995, doi: 10.1115/1.2830596.
[30] J. Romero, M. M. Attallah, M. Preuss, M. Karadge, et S. E. Bray, « Effect of the forging pressure on the microstructure and residual stress development in Ti–6Al–4V linear friction welds », *Acta Materialia*, vol. 57, nº 18, p. 5582-5592, oct. 2009, doi: 10.1016/J.ACTAMAT.2009.07.055.
[31] Y. Ji, Z. Chai, D. Zhao, et S. Wu, « Linear friction welding of Ti–5Al–2Sn–2Zr–4Mo–4Cr alloy with dissimilar microstructure », *Journal of Materials Processing Technology*, vol. 214, nº 4, p. 979-987, avr. 2014, doi: 10.1016/J.JMATPROTEC.2013.11.006.
[32] Y. Guo, Y. Chiu, M. M. Attallah, H. Li, S. Bray, et P. Bowen, « Characterization of Dissimilar Linear Friction Welds of α-β Titanium Alloys », *Journal of Materials Engineering and Performance*, vol. 21, nº 5, p. 770-776, mai 2012, doi: 10.1007/s11665-012-0129-z.
[33] G. D. Wen, T. J. Ma, W. Y. Li, S. Q. Wang, H. Z. Guo, et D. L. Chen, « Strain-controlled fatigue properties of linear friction welded dissimilar joints between Ti–6Al–4V and Ti–6.5Al–3.5Mo–1.5Zr–0.3Si alloys », *Materials Science and Engineering: A*, vol. 612, p. 80-88, août 2014, doi: 10.1016/J.MSEA.2014.06.010.
[34] P. Zhao et L. Fu, « Strain hardening behavior of linear friction welded joints between TC11 and TC17 dissimilar titanium alloys », *Materials Science and Engineering: A*, vol. 621, p. 149-156, janv. 2015, doi: 10.1016/J.MSEA.2014.10.044.
[35] A. A. Ward, Y. Zhang, et Z. C. Cordero, « Junction growth in ultrasonic spot welding and ultrasonic additive manufacturing », *Acta Materialia*, vol. 158, p. 393-406, 2018, doi: https://doi.org/10.1016/j.actamat.2018.07.058.
[36] L. X. Sun, M. Q. Li, et H. Li, « Interface characteristics and recrystallization mechanism of dissimilar titanium bonds », *Journal of Materials Science*, vol. 53, nº 7, p. 5380-5388, avr. 2018, doi: 10.1007/s10853-017-1950-4.
[37] F. Bachmann, R. Hielscher, et H. Schaeben, « Texture Analysis with MTEX – Free and Open Source Software Toolbox », *Solid State Phenomena*, vol. 160, p. 63-68, févr. 2010, doi: 10.4028/www.scientific.net/SSP.160.63.
[38] F. Bachmann, R. Hielscher, et H. Schaeben, « Grain detection from 2d and 3d EBSD data—Specification of the MTEX algorithm », *Ultramicroscopy*, vol. 111, nº 12, p. 1720-1733, déc. 2011, doi: 10.1016/j.ultramic.2011.08.002.
[39] S. L. Semiatin, « An Overview of the Thermomechanical Processing of α/β Titanium Alloys: Current Status and Future Research Opportunities », *Metall Mater Trans A*, vol. 51, nº 6, p. 2593-2625, juin 2020, doi: 10.1007/s11661-020-05625-3.
[40] A. L. Pilchak, C. J. Szczepanski, J. A. Shaffer, A. A. Salem, et S. L. Semiatin, « Characterization of Microstructure, Texture, and Microtexture in Near-Alpha Titanium Mill Products », *Metall and Mat Trans A*, vol. 44, nº 11, p. 4881-4890, nov. 2013, doi: 10.1007/s11661-013-1804-x.

[41] L. Germain, N. Gey, M. Humbert, P. Vo, M. Jahazi, et P. Bocher, « Texture heterogeneities induced by subtransus processing of near α titanium alloys », *Acta Materialia*, vol. 56, nº 16, p. 4298-4308, sept. 2008, doi: 10.1016/j.actamat.2008.04.065.
[42] D. Ballat-Durand, S. Bouvier, M. Risbet, et W. Pantleon, « Multi-scale and multi-technic microstructure analysis of a linear friction weld of the metastable-β titanium alloy Ti-5Al-2Sn-2Zr-4Mo-4Cr (Ti17) towards a new Post-Weld Heat Treatment », *Materials Characterization*, vol. 144, p. 661-670, oct. 2018, doi: 10.1016/J.MATCHAR.2018.08.013.
[43] D. Ballat-Durand, S. Bouvier, M. Risbet, et W. Pantleon, « Through analysis of the microstructure changes during linear friction welding of the near-α titanium alloy Ti-6Al-2Sn-4Zr-2Mo (Ti6242) towards microstructure optimization », *Materials Characterization*, vol. (Under peer-review).
[44] H. M. Otte, « Mechanism of the martensitic transformation in titanium and its alloys », in *The Science, Technology and Application of Titanium*, Elsevier, 1970, p. 645-657.
[45] L. Germain, S. R. Dey, M. Humbert, et N. Gey, « Determination of parent orientation maps in advanced titanium-based alloys », *Journal of Microscopy*, vol. 227, nº 3, p. 284-291, sept. 2007, doi: 10.1111/j.1365-2818.2007.01812.x.
[46] L. Germain, N. Gey, R. Mercier, P. Blaineau, et M. Humbert, « An advanced approach to reconstructing parent orientation maps in the case of approximate orientation relations: Application to steels », *Acta Materialia*, vol. 60, nº 11, p. 4551-4562, juin 2012, doi: 10.1016/j.actamat.2012.04.034.
[47] S. Gourdet et F. Montheillet, « A model of continuous dynamic recrystallization », *Acta Materialia*, vol. 51, nº 9, p. 2685-2699, mai 2003, doi: 10.1016/S1359-6454(03)00078-8.
[48] J. Baczynski et J. J. Jonas, « Texture development during the torsion testing of α-iron and two IF steels », *Acta Materialia*, p. 4273-4288, 1996.
[49] S. Li, I. J. Beyerlein, et M. A. M. Bourke, « Texture formation during equal channel angular extrusion of fcc and bcc materials: comparison with simple shear », *Materials Science and Engineering: A*, vol. 394, nº 1-2, p. 66-77, mars 2005, doi: 10.1016/j.msea.2004.11.032.
[50] M. Karadge, M. Preuss, C. Lovell, P. J. Withers, et S. Bray, « Texture development in Ti–6Al–4V linear friction welds », *Materials Science and Engineering: A*, vol. 459, nº 1-2, p. 182-191, juin 2007, doi: 10.1016/j.msea.2006.12.095.
[51] E. Dalgaard, P. Wanjara, J. Gholipour, X. Cao, et J. J. Jonas, « Linear friction welding of a near-β titanium alloy », *Acta Materialia*, vol. 60, nº 2, p. 770-780, janv. 2012, doi: 10.1016/j.actamat.2011.04.037.
[52] T. Sakai, A. Belyakov, R. Kaibyshev, H. Miura, et J. J. Jonas, « Dynamic and post-dynamic recrystallization under hot, cold and severe plastic deformation conditions », *Progress in Materials Science*, vol. 60, p. 130-207, mars 2014, doi: 10.1016/j.pmatsci.2013.09.002.
[53] D. Kuhlmann-Wilsdorf et N. Hansen, « Geometrically necessary, incidental and subgrain boundaries », *Scripta Metallurgica et Materialia*, vol. 25, nº 7, p. 1557-1562, juill. 1991, doi: 10.1016/0956-716X(91)90451-6.
[54] W. Pantleon et N. Hansen, « Dislocation boundaries—the distribution function of disorientation angles », *Acta Materialia*, vol. 49, nº 8, p. 1479-1493, mai 2001, doi: 10.1016/S1359-6454(01)00027-1.
[55] R. Sedláček, W. Blum, J. Kratochvíl, et S. Forest, « Subgrain formation during deformation: Physical origin and consequences », *Metallurgical and Materials Transactions A*, vol. 33, nº 2, p. 319-327, févr. 2002, doi: 10.1007/s11661-002-0093-6.
[56] D. Raabe, « Investigation of contribution of {123} slip planes to development of rolling textures in bcc metals by use of Taylor models », *Materials Science and Technology*, p. 455-460, mai 1995.
[57] R. D. Doherty *et al.*, « Current issues in recrystallization: a review », *Materials Science and Engineering A*, p. 56, 1997.
[58] K. Huang et R. E. Logé, « A review of dynamic recrystallization phenomena in metallic materials », *Materials & Design*, vol. 111, p. 548-574, déc. 2016, doi: 10.1016/j.matdes.2016.09.012.
[59] A.P. Sutton et R. W. Balluffi, *Interfaces in crystalline materials*, Oxford University Press. 1995.
[60] S. (Srikumar) Banerjee et P. (Pradip) Mukhopadhyay, *Phase transformations : examples from titanium and zirconium alloys*. Elsevier, 2007.
[61] M. Abdel-Hady, H. Fuwa, K. Hinoshita, H. Kimura, Y. Shinzato, et M. Morinaga, « Phase stability change with Zr content in β-type Ti–Nb alloys », *Scripta Materialia*, nº 57, p. 1000-1003, 2007.
[62] G. Neumann et C. Tuijn, *Self-diffusion and impurity diffusion in pure metals: Handbook of experimental data*. Amsterdam: Pergamon, 2009.

[63] H. Nakajima et M. Koiwa, « Diffusion in Titanium. », *ISIJ International*, vol. 31, nº 8, p. 757-766, août 1991, doi: 10.2355/isijinternational.31.757.
[64] I. E. Gunduz, T. Ando, E. Shattuck, P. Y. Wong, et C. C. Doumanidis, « Enhanced diffusion and phase transformations during ultrasonic welding of zinc and aluminum », *Scripta Materialia*, vol. 52, nº 9, p. 939-943, mai 2005, doi: 10.1016/J.SCRIPTAMAT.2004.12.015.
[65] A. L. Ruoff et R. W. Balluffi, « Strain-Enhanced Diffusion in Metals. II. Dislocation and Grain-Boundary Short-Circuiting Models », *Journal of Applied Physics*, vol. 34, nº 7, p. 1848-1853, juill. 1963, doi: 10.1063/1.1729698.
[66] A. L. Ruoff, « Enhanced Diffusion during Plastic Deformation by Mechanical Diffusion », *Journal of Applied Physics*, vol. 38, nº 10, p. 3999-4003, sept. 1967, doi: 10.1063/1.1709056.
[67] M. Cohen, « Self-diffusion during plastic deformation ». Commemorative lecture by the fifteenth gold medalist of the japan institute of metals.
[68] J. W. Elmer, T. A. Palmer, S. S. Babu, W. Zhang, et T. DebRoy, « Phase transformation dynamics during welding of Ti–6Al–4V », *Journal of Applied Physics*, vol. 95, nº 12, p. 8327-8339, juin 2004, doi: 10.1063/1.1737476.
[69] M. Hillert, *Phase Equilibria, Phase Diagrams and Phase Transformations*, Second edition. Cambridge university press, 2007.
[70] H. Nakajima, K. Ogasawara, S. Yamaguchi, et M. Koiwa, « Diffusion of Cromium in alpha titanium and its alloys », *Materials Transactions, JIM*, vol. 31, nº 4, p. 249-254, 1990.
[71] O. Dmitrieva *et al.*, « Chemical gradients across phase boundaries between martensite and austenite in steel studied by atom probe tomography and simulation », *Acta Materialia*, vol. 59, nº 1, p. 364-374, janv. 2011, doi: 10.1016/j.actamat.2010.09.042.
[72] S. Koyama, M. Takahashi, et K. Ikeuchi, « Behavior of Superficial Oxide Film at Solid-State Diffusion-Bonded Interface of Tin », *MATERIALS TRANSACTIONS*, vol. 45, nº 2, p. 300-302, 2004, doi: 10.2320/matertrans.45.300.
[73] Y. Lu, J. Y. Huang, C. Wang, S. Sun, et J. Lou, « Cold welding of ultrathin gold nanowires », *Nature Nanotechnology*, vol. 5, nº 3, p. 218-224, mars 2010, doi: 10.1038/nnano.2010.4.
[74] T. Kizuka, K. Yamada, et N. Tanaka, « Time-resolved high-resolution electron microscopy of solid state direct bonding of gold and zinc oxide nanocrystallites at ambient temperature », *Applied Physics Letters*, vol. 70, nº 8, p. 964-966, févr. 1997, doi: 10.1063/1.118312.
[75] T. Kizuka, « Atomic Process of Point Contact in Gold Studied by Time-Resolved High-Resolution Transmission Electron Microscopy », *Physical Review Letters*, vol. 81, nº 20, p. 4448-4451, nov. 1998, doi: 10.1103/PhysRevLett.81.4448.
[76] D. Ballat-Durand, S. Bouvier, et M. Risbet, « Contributions of an innovative post-weld heat treatment to the micro-tensile behavior of two mono-material linear friction welded joints using: The β-metastable Ti–5Al–2Sn–2Zr–4Mo–4Cr (Ti17) and the near-α Ti–6Al–2Sn–4Zr–2Mo (Ti6242) Ti-alloys », *Materials Science and Engineering: A*, vol. 766, p. 138334, oct. 2019, doi: 10.1016/j.msea.2019.138334.

# Chapter III

## Microstructural characterization of an IN718 weld – Precipitation Hardened (PH) state

***Detailed microstructure analyses on a Ni-Cr-Fe-Nb-Al nickel-based alloys: Inconel 718.***

### Background

The present chapter follows on from previous investigations of the dissimilar titanium alloys linear friction assembling of the β-metastable Ti17 with the quasi-α Ti6242. The previous chapter endeavored to understand and demonstrate the close relationship between hot plasticity phenomena and the cohesive junction formation involving grain boundary migration from one material to the other. The latter strain-induced mechanisms were shown to play a significant role in the junction establishment in Ti-alloys during the β-hot deformation process.

In this work, butt-weld test campaigns were carried out implying the joining of the Ni-Fe-Cr superalloy Inconel 718, a γ" ($Ni_3Nb$) precipitation hardenable materials, *via* linear friction welding. Specifically, a weld configuration between two precipitation-hardened blocks has been extensively studied. During the welding process, the severe thermo-mechanical loads applied on the materials resulted in significant microstructure changes, with important consequences on the mechanical properties of the joint. Detailed characterizations of the post-welded microstructures were carried out on selected cross-sectioned weld samples.

The hot deformation process gave rise to a discontinuous dynamic recrystallization phenomenon in the junction zone. The resulting thermo-mechanical affected zone (TMAZ) consists of: first, a thick band of uniform dynamically recrystallized grains presenting equiaxed grain morphology surrounding the welding line. Then, a partially recrystallized zone composed of fine recrystallized grains distributed along the grain boundaries of strained and elongated grains extends. Lastly, a zone made of visibly deformed grains marks the end of the TMAZ. Phase and microstructure changes across the joint were shown to have a significant influence on the micro-hardness properties across the weld.

Finally, precipitated nano-oxide particles made of titanium and aluminum were identified in the weld center zone. These dispersed weld defects were likely generated *via* selective internal oxidation during the welding procedure. The elevated thermal load presumably yielded to the dissociation of the former native oxide layer, thus providing the excess oxygen in the austenitic matrix for internal oxidation.

## 1. Introductive elements about nickel base alloys

In the field of physical metallurgy of nickel-based alloys, a popular legend speculates that the terminology “superalloy” would originate from the late 1940s, when the famous comic-book character Superman had become a familiar fictional figure [1]. It finally passed into the common parlance as a household word among metallurgists. The identification of the materials properties of nickel-based alloys to the exceptional abilities of the superhero notably highlights the high interest of material scientists and engineers from that time for such alloys and their potential field of applications.

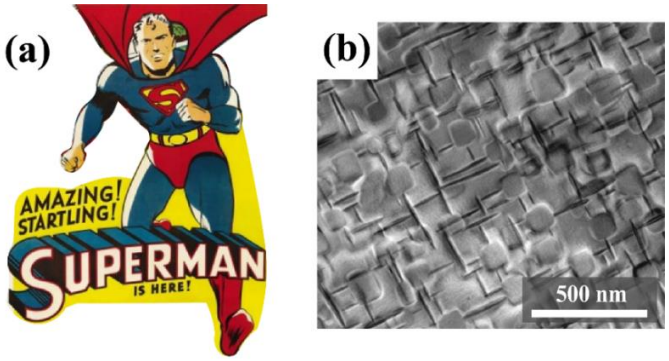


**Figure 1**: **(a)** *Comic book cover of Superman character from the 50’s;* **(b)** *STEM bright-field image of the cuboidal γ′ and acicular γ″ phase nanoprecipitations in an Alloy 718 after heat treatment at 1200°C for 4h followed by 700°C for 1000h, extracted from* [2].

The materials characteristics of nickel-based superalloys are generally designed for high-temperature applications. This class of materials notably displays excellent mechanical properties and good resistance to chemical degradation and corrosion, notably under elevated thermal loads in atmospheric environments [3]. Since their common appearance in industrial applications in the late 1940s, the uses of nickel-based alloys are multiples and varied. Nevertheless, their original engineering interest was in the design of the high-temperature parts of modern aeroengines. Indeed, the efficiency of heat engines is intrinsically connected with the temperature of the hot reservoir; the higher is the difference in temperature between the hot reservoir and the cold reservoir, the better would the efficiency be [4].

To illustrate the latter characteristic, let us consider the theoretical thermodynamic cycle of Carnot. The Carnot cycle describes the ideal heat engine and is divided into 4 sequences:

- (1 → 2): Isothermal expansion *i.e.* reversible heat transfer from the high temperature reservoir to the heat engine system.
- (2 → 3): Reversible adiabatic expansion *i.e.* work output gas expansion, isolated from the heat bath.
- (3 → 4): Isothermal compression *i.e.* reversible heat transfer from the engine system to the cold reservoir (generally in a classical motor, the surrounding environment).
- (4 → 1): Reversible adiabatic compression *i.e.* frictionless work done by the surrounding on the system to compress back the heat engine, the working medium stay isolated from the external heat bath (no exchange of heat across the system boundaries) and start a new cycle.

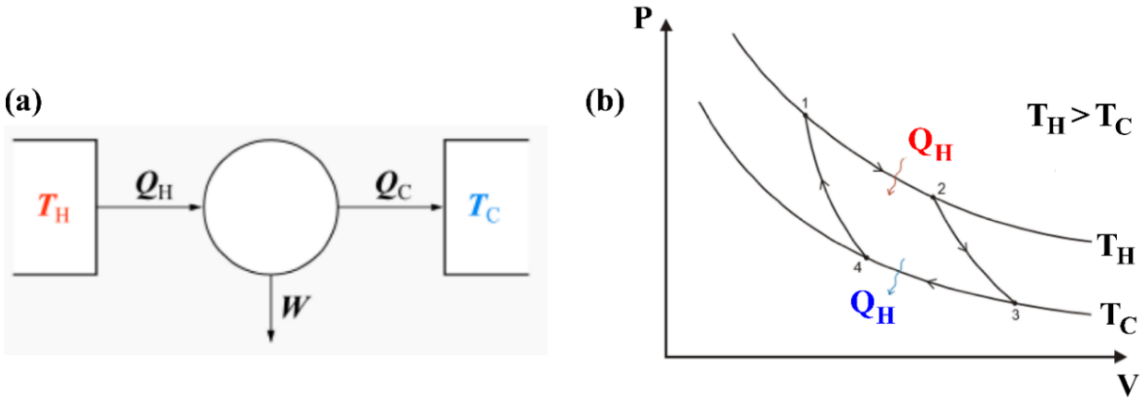


**Figure 2**: **(a)** *Schematic representation of a thermodynamic heat engine with respectively $T_H$ and $T_C$ the hot and cold reservoirs on the engine, $Q_H$ and $Q_C$ the heat exchanges between the engine and the reservoirs and W the total converted work;* **(b)** *Carnot thermodynamic cycle on a PV diagram.*

The 2nd law of thermodynamic applied on the system yields to the *Clausius-Carnot equality* (1):

$$\frac{Q_H}{T_H} + \frac{Q_C}{T_C} = 0$$

The efficiency of the ideal heat engine is deduced from the previous expression and states (2):

$$\eta_{Carnot} = 1 - \frac{T_H}{T_C}$$

The Carnot cycle efficiency is maximized with the highest possible heat source temperature and the lowest possible heat sink temperature. Therefore, the higher is the operating temperature of a considered heat engine; the better would the engine efficiency be in terms of performances. Thus, the materials constituting the hottest sections of modern aeroengine parts must operate at the higher working temperature possible.

The magnitude of the melting temperature $T_m$ of nickel is not particularly high ($T_m \approx 1455°C$) compared to other alternative candidate alloys made of either iron or titanium. In that perspective, nickel and nickel-based alloys do not appear as excellent candidates for such high temperature use at first sight. Herewith, the physical characteristics that give rise to the high-performances of these alloys for applications under elevated temperature conditions depend on material specific factors.

First, nickel-based alloys present a Face-Centered Cubic (FCC) austenitic crystal structure that is stable from ambient temperature to the melting point. Second, various alloying elements are substantially soluble in the austenitic matrix. This property notably allows reinforcing the nickel base matrix by the addition of various elements. It is then possible to shape the alloy properties in order to make it suitable for different engineering applications. For instance, the addition of chrome Cr and cobalt Co demonstrates improvement in the resistance of the nickel alloys to oxidation and corrosion. The addition of aluminum Al, titanium Ti, and tantalum Ta is known to improve the flow-stress resistance and ultimate tensile strength. In FCC crystal structure, the

thermally activated processes controlling creep deformation are low [5]. The latter property makes nickel alloys suitable against creep damage. Furthermore, the addition of molybdenum Mo, rhenium Re and tungsten W sometimes associated with some classical grain boundary strengtheners such as carbon C or bore B generally improves the creep performances and the time-dependent flow behavior of the nickel based alloys. [6] A wide range of possibilities exists for the design of new nickel base alloys making them extremely versatile and functional. Their elaboration generally relies on series of complex experimental works based on trials and errors methodology. Such empirical researches are sometimes fruitful and lead to interesting grades regarding specific technical requirements. Consequently, nickel-based alloys often display complex chemical compositions implying various alloying elements.

Nevertheless, the utmost characteristic of Nickel superalloys comes from their ability to be strengthened by phase precipitation in the FCC matrix [7]. Those structures are thermally stable and form dense nano-precipitates in the FCC matrix as illustrated in the Figure 1.b. The precipitation of those phases not only strongly arise the yield stress but also increase the flow stress with temperature, an important property exploited for high-temperature applications. The physical origin of those properties will be discussed further below.

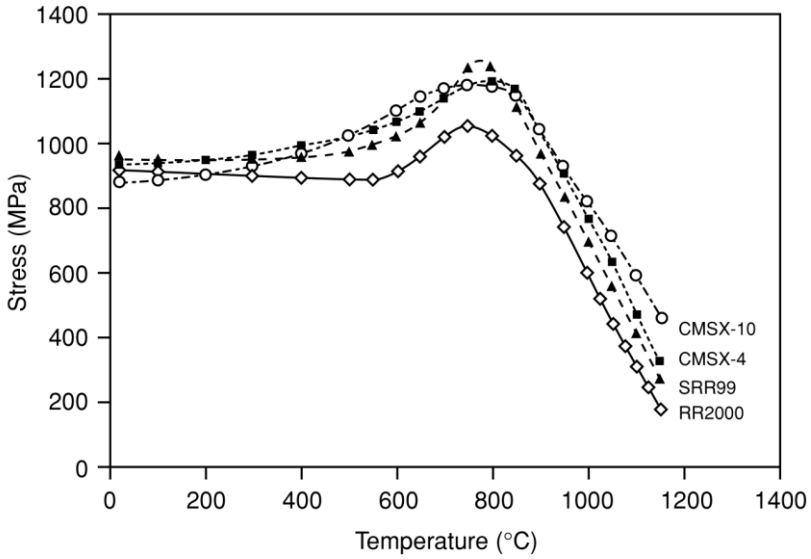


**Figure 3**: *Variation of the yield stress of single-crystal superalloys with temperature (from* [3]).

Lastly, nickel alloys exhibit a remarkable characteristic: the yield stress, by which, one means the stress necessary to cause the onset of a macroscopic plastic flow. Indeed, in superalloys, the yield stress usually remains fairly unaltered while increasing temperature (see Figure 3), contrary to most other alloy systems. In fact, for many superalloys the yield stress can even increase with temperature (see Figure 3), typically until about 750°C to 800°C values are reached.

## 2. Physical metallurgy of the IN718 alloy

### 2.1 General features

Polycrystalline Inconel 718 (or IN718) is a classical nickel-iron-chrome based precipitation strengthened alloy. The alloy 718 has already been extensively studied in the scientific literature due to its interesting properties for industrial applications [8]. IN718 was initially developed in the late 50s by the Huntington alloy products division of INCO (hence its name) and is widely used as wrought alloy for structural applications up to 650°C such as high temperature components (gas turbine disks in in airplane engines or power generation installations) [3]. Indeed, alloy 718 advantageously exhibits a combination of excellent mechanical properties (high yield strength up to high temperature conditions and good fatigue properties), good formability (interesting thermomechanical processing map for hot forming procedures) and high oxidation resistance [10], [11]. IN718 is still nowadays a prevalent material for high temperature applications in the aerospace industry notably in jet engines due to its moderate price compared with other competing materials and space applications due to its not less favorable properties at cryogenic temperatures [12].

As well designated, IN718 is a precipitation-strengthened alloy, *id est* its outstanding high temperature strength is largely attributed to the presence of fine precipitates of a few dozen of nanometers dimensions disseminated in the FCC austenitic matrix γ. The later precipitates are formed of two types of crystallographic ordered intermetallic phases denominated γ' and γ". They respectively present a rough cuboidal to spherical interfacial shape for γ' and ellipsoidal disc-interfacial shape for γ" with the γ matrix [13]–[16]. Both present superlattice crystallographic structures close to the FCC structure constituting the γ matrix which usually lead to quasi-coherent relationships equivalent to several percent of coherency strains with the austenitic matrix. Because of their coherency with the matrix, these precipitates are known to interfere with the motion of dislocations through the austenitic matrix due to the energy penalty associated with their interfacial energy and the additional energy necessary for the faulting of the precipitates following the passage of dislocations *via* complex crystal plasticity mechanisms [17], [18].

### 2.2 Element composition of the studied IN718 alloy

Iron, chromium, niobium, titanium, aluminum, and molybdenum are the main chemical components of IN718 alloy [19]. They notably lead to significant property enhancements [12], [13]. Other trace elements are commonly present, but most display marginal upgrading role or even detrimental on the alloy properties (see Table 1). The solute elements can be classified according to three main function: γ' formers, γ" formers and solid solution strengtheners [20].

Iron is a cheap additional element; it is here used as a solid solution strengthener to adjust lattice parameter within the matrix. Chromium is added to increase oxidation resistance and promote solid solution

strengthening within the matrix; but it also presents detrimental effects to the workability of the material. Molybdenum is added as a solid solution strengthener. Niobium is the most important alloying element. Niobium is the greatest γ" former and strengthener. Titanium partition between γ' and γ" phases. Aluminum is a γ' and γ" former, its effect on the mechanical properties is complex with carbon concentration as well.

Small amounts of carbon, silicon nitrogen and bore are present 718. Carbon tends tied up niobium in a stable NbC phase which decreases the amount of Nb available to form the γ" phase. Silicon is detrimental to hot workability which is likely due to the embrittlement of the matrix [21]. TiN formation decreases the quantity of secondary phases.

The alloy 718 grade standard composition is detailed in the Table 1 below:

| Element | Ni | Cr | Fe | Nb+Ta | Mo | Ti | Al | Co | Si | Mn | Cu | C | S | B |
|---|---|---|---|---|---|---|---|---|---|---|---|---|---|---|
| wt.% | 53.80 | 17.96 | Bal. | 5.25 | 2.95 | 1.03 | 0.50 | 0.11 | 0.04 | 0.02 | 0.02 | 0.026 | 0.0015 | 0.0033 |

**Table 1***: Element composition of the used IN718 grade, provided by the Aubert&Duval Company.*

The complete composition of the 718 alloy is complex (more than 15 different elements). It is often suggested in the literature that the terminology of superalloy comes from that compositional complexity.

### 2.3 Phase composition & strengthening mechanism of IN718 alloy

The FCC matrix phase, noted γ, is essentially composed of nickel Ni in solid solution enriched with various additional elements randomly dispersed in the lattice. The reported lattice parameter of the γ matrix is about a ≃ 0.352 nm. The γ phase, often referred as the austenitic phase with reference to steel metallurgy, is reinforced by additional elements such as iron Fe, chrome Cr, cobalt Co, molybdenum Mo and tungsten W in order to optimize the mechanical resistance of the matrix. In usable condition, the γ phase is strengthened by secondary phase precipitations: the γ' and most importantly γ" phases.

The understanding of the physical origin of the strengthening contribution of those nanoprecipitations in γ" / γ' alloys such as IN718 or IN706 was a controversial topic in the early literature [22], [23], [16]. Since then, it has been clarified that if IN718, like most of the Ni-based superalloys, is effectively strengthened by the precipitation of the cubic $Ni_3(Al, Ti)$ γ' phase, the additional strengthening conveyed by the Body-Centered Tetragonal (BCT) $Ni_3(Nb, Ta)$ γ" nanophases is the major strengthening contribution to these alloys [17], [24], [25].

| Phase | Crystal system | Space group | Unit cell | Reference |
|---|---|---|---|---|
| $\gamma$ Ni-base solid solution | Ordered cubic | F m −3 m | $a_\gamma = 3.524$ nm | Suh *et al.* (1988) |
| $\gamma'$ $Ni_3Al$ | Ordered cubic | P m −3 m | $a_{\gamma'} = 3.5718$ nm | Mohan Rao *et al.* (1989) |
| $\gamma''$ $Ni_3Nb$ | Tetragonal | I 4/m m m | $a_{\gamma''} = b_{\gamma''} = 3.62$ nm, $c_{\gamma''} = 7.41$ nm | Kaufman *et al.* (1969) |

**Table 2**: *Crystallographic unit-cell parameters of the main phases in IN718: γ, γ', γ", listed by* [26].

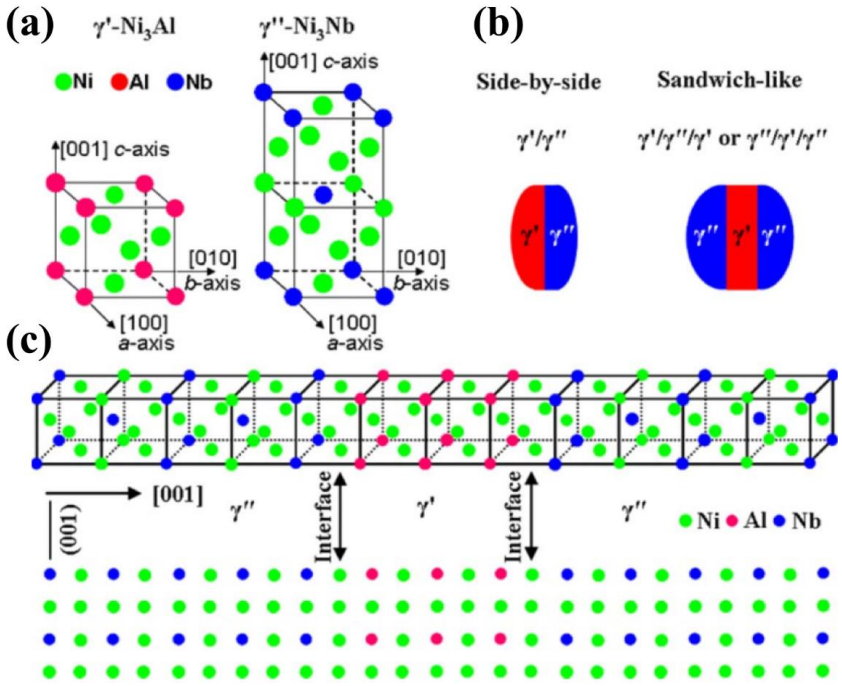


**Figure 4**: *Schematic representation of the IN718 crystal lattice and co-precipitation lattice configurations from* [27].

**The γ' phase** is a classical precipitation strengthening structure that exists in most of nickel-based superalloys. The γ' phase constitutes an ordered intermetallic compound that presents a $L1_2$-FCC crystal structure made of $Ni_3$(Al, Ti, Ta). The latter structure may be regarded as interpenetrating simple cubic structures of Ni on the one hand, and (Al, Ti or Ta) on another hand, forming two ordered sublattices translated by a vector $a/2\ \langle\bar{1}01\rangle$ from one another (see illustration Figure 4.a-c). The lattice parameter of γ′ is slightly larger than that of the matrix at a ≃ 0.357 nm and both structures are quasi-coherent.

In γ' ordered phase, the Ni atoms preferentially surround themselves with Al, Ti or Ta atoms occupying the sublattice points, thus generating a long-range order. In such secondary phase structures, the order degree is defined by a parameter η:

$$\frac{1+\eta}{2} = \text{Probability that Ni atom is on the sublattice 1}$$

$$\frac{1-\eta}{2} = \text{Probability that Ni atom is on the sublattice 2}$$

If the long-range order is complete, the probability is either 1 or 0, consequently the order parameter η is either +1 or -1. The interphase boundary that separates region with long-range $L1_2$ order from the matrix zone forms a diffuse boundary of a few nanometer in thickness where the probability to find ordered Ni-Al, Ni-Ti or Ni-Ta bonds is substantially reduced.

When the temperature increases and reaches the second-order phase transition, such ordered sublattices systems lose its spatial coherency until complete breakdown of the long-range order. The critical decomposition temperature for the γ' system is estimated at about 895°C [28].

In term of morphology, γ' precipitates in IN718 form spheroid to cuboid nano-particles dispersed in the matrix (see Figure 5). Since the lattice parameters between the disordered γ phase and the ordered γ' are close, they display a cube-cube orientation relationship *id est*: $\{100\}_{\gamma}$ // $\{100\}_{\gamma'}$ and $\langle 010\rangle_{\gamma}$ // $\langle 010\rangle_{\gamma'}$. The γ / γ' interface is fairly coherent, though, an interfacial energy barrier arises due to the local strain field generated by the interfacial misfit combined with the chemical bonding difference between these structures.

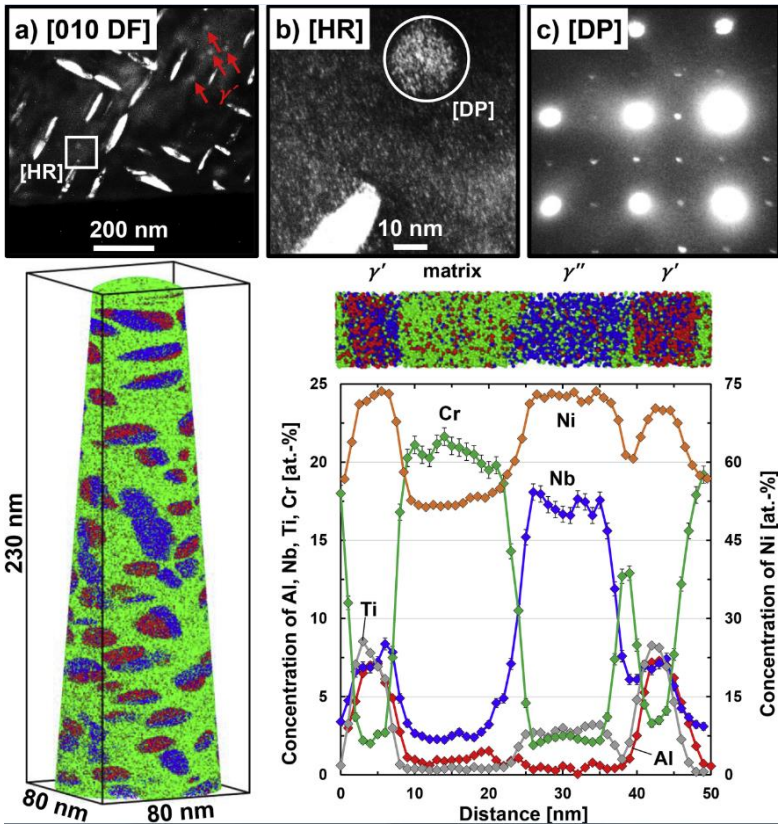


**Figure 5**: *Phase identification of γ'- phase in a IN718 alloy by TEM extracted from* [29], *the observed grain is tilted to the [001]-zone axis:* **(a)** *Dark-Field (DF) imaging using a (010)-reflection shows large γ'' precipitates and small γ' precipitates indicated by red arrows.* **(b)** *High-resolution image according to the squared zone indicated in figure (a).* **(c)** *Diffraction pattern associated with the area highlighted in (b).* **(d)** *Reconstruction of an extracted tip-sample of IN718 (left), where only Cr (green), Al (red) and Nb (blue) atoms are visualized; (right) a 1D composition profile along a cylinder placed inside the tip indicating Cr rich regions (>20 at.-%) belong to the matrix, Nb rich regions (>16 at.-%) to γ''- precipitates and Al rich regions (>5 at.-%) to γ'- precipitates.*

The superior high-temperature performance of the superalloys (Figure 3) stems from the complex interactions of the ordered secondary phases with the fundamental plasticity carriers within the lattice *id est*: dislocations. In FCC structures, perfect dislocations ideally glide along the primary $a/2\,\langle 1\bar{1}0\rangle\{111\}$ slip system. Incoming dislocations travelling in the γ phase cannot enter the γ' and remain locked in the phase boundary region due to the energy penalty associated with the presence of the heterophase interface. To pass such obstacles, incoming dislocations generally form pairs of identical dislocations $a/2\,\langle 1\bar{1}0\rangle$ where the leading dislocation create an anti-phase boundary (APB) by reversing the atomic order in the $\{111\}$ plane of the $L1_2$ particles while the trailing dislocation removes the anti-phase boundary, thus restoring the order [30],

[31]. The associated anti-phase boundary energy, $\gamma_{APB}$, represents a barrier that must be overcome for particle cutting occurrence.

However, such picture is a bit simplistic and the situation in real crystal structures is considerably more complicated. Indeed, the actual shear distortion associated with perfect dislocations $a/2\ \langle 1\bar{1}0\rangle$ is energetically costly. In response to that, dislocations usually dissociate into structures that are energetically more advantageous. The reaction classically generates pairs of partial dislocations $a/6\ \langle 112\rangle$ connected by a Superlattice Intrinsic Stacking Fault (SISF) on the $\{111\}$ plane or a complex stacking fault (CSF) when the stacking sequence in the $L1_2$ structure is broken [32], [33]. When coupled, such dislocations configurations can shear the precipitates without leaving a planar fault in their wake. Beyond this simplified description, several mechanisms govern the dislocations/precipitates interaction, depending upon the size of the precipitates [34], available dissociation configurations [35], the triggered shearing mechanisms [36], the APB energy [37], the equilibrium spacing of paired dislocations and the nature of the coupling between dislocation pairs (weak, strong) [38].

Lastly, the detailed mechanisms explaining the increase of the yield-stress with temperature generated intense debate in the field of physical metallurgy [39]–[42], summarized in [3], [43]. In brief, the consensus points out the increasing role of cross-slip events from the $\{111\}$ planes to the $\{100\}$ with temperature, trapping the $a/2\ \langle 1\bar{1}0\rangle$ dislocations pairs into locked-configurations. The macroscopic yielding is then governed by the stress to expand the dislocation loops between such pinning points. The detailed mechanisms behind the locking and unlocking processes are sometimes unclear and still to be elucidated. Beyond the peak temperature (~800°C, Figure 3), cube-slip on $\{001\}$ planes become activated and the more favorable $\langle 101\rangle\{010\}$ slip system prevails finally leading to a decrease of the yield stress with temperature.

Nevertheless, the fraction of the γ′ phase represents about 5 to 6 percent of the total volume fraction in alloy 718 and consequently on provides a small strengthening effect on the microstructure. The major strength contribution in alloy 718 is as achieved by the precipitation of another finely dispersed nanoscale ordered phase: the γ" phase.

**The γ" phase** presents a Body-Centered Tetragonal (BCT) crystallographic structure with a $D0_{22}$ $Ni_3$(Nb, Ta) order. Compared with the γ' phase, the γ" phase displays a more complicated crystal structure with a lower symmetry because of the lattice distortion induced the c-axis of the tetragonal crystal structure (a schematic representation of the lattice unit-cell for the γ' and γ" phase is depicted in Figure 4.a-c). The lattice parameters classically reported are: a ≃ 0.362 nm and c a ≃ 0.741 nm (Table 2).

The γ" phase nucleates directly from the matrix as an ordered intermetallic component with the following orientation relationship: $\{100\}_\gamma$ // $\{001\}_{\gamma"}$ and $\langle 100\rangle_\gamma$ // $\langle 100\rangle_{\gamma"}$. The γ" phase displays a significant coherency with the austenitic matrix, but also with the γ' phase particles. In standard IN718 alloys, they form dispersed disk-shaped particles (see Figure 6.a) oriented along three variants: the $[001]_{\gamma"}$ directions of the

precipitates are aligned with the three $\langle 100 \rangle_{\gamma}$ γ directions, and the $[001]_{\gamma''}$ is the normal to the face of the precipitate disk. Interestingly, compositional modifications on the standard IN718 chemistry can lead to remarkable composite structures giving rise to γ' / γ" co-precipitations (illustrated in Figure 4.b and Figure 5.b-c), and notably constitute an active research topic on alloy 718 [27], [44], [45]. Such sandwich-like structures exist in conventional IN718 in a much lesser extent.

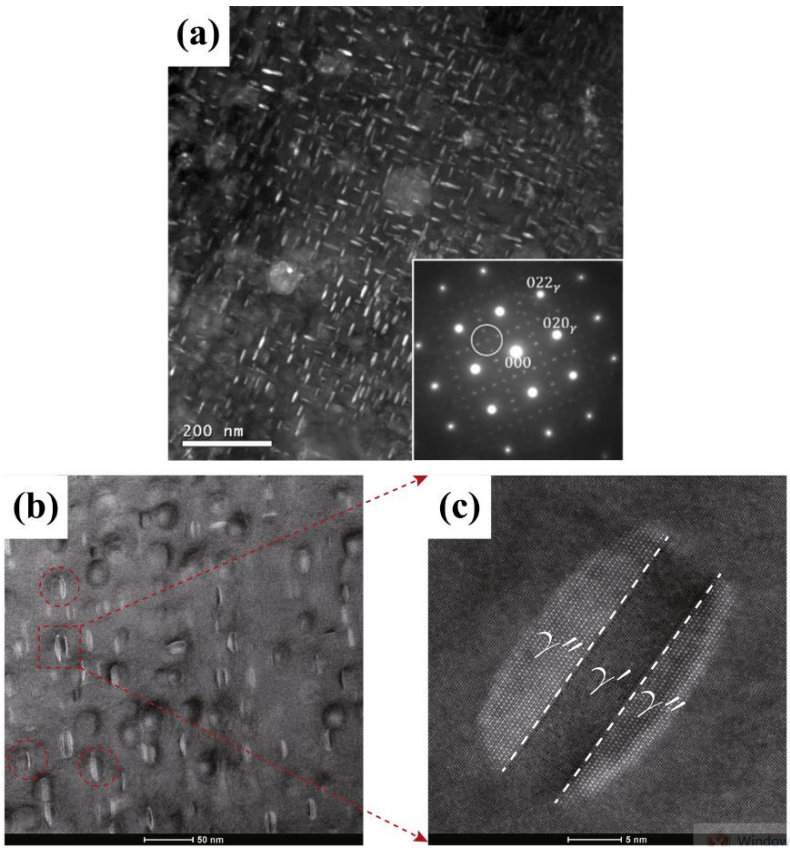


**Figure 6**: **(a)** *TEM-Dark-Field imaging of in a standard double aged IN718 alloy showing lenticular γ" precipitates, from* [46], *the selected area diffraction pattern inset was taken in the [100] zone axis DF-image taken by inserting the objective aperture at the encircled diffraction sport from γ".* **(b)-(c)** *Bright-field STEM imaging of γ'/ γ" co-precipitations inset in he selected area diffraction pattern viewed along the [001] direction, extracted from* [47].

The estimated volume fraction γ" after application of the conventional two-staged heat treatment at 720°C and 620°C on alloy 718 is about ~15 percent. The *solvus* temperature of the γ" is estimated at about 960°C [28].

Similarly to the γ' phase, the γ" particles strengthen alloy 718 primarily through ordering and coherency strengthening mechanisms [16], [17], [48]. However, contrary to γ' phase, the γ" particles display a less symmetric tetragonal crystallographic structure. The latter limits the number of available slip systems operating in the γ" phase and lead to more complicated deformation mechanisms. Such characteristics lead to complex available shear mechanisms within the γ" precipitates, which consequently provides the majority of the bulk yield strength improvements. Nevertheless, there is still little consensus about the active deformation

mechanisms across the temperature range in which alloy 718 is employed [49]. The understanding of the microstructure–property relationships in γ”-strengthened alloys is still partial and lack of details on the active mechanisms at stake. Thence, these complex interactions between matrix, secondary phases are matter of intense scientific prospections in the field of crystal plasticity modelling [49]–[52].

Accordingly, γ” strengthened alloys are critically dependent on the stability of their major strengthening phase γ”. It is noted that above 650°C the γ” phase undergoes important coarsening leading to the progressive loss of coherency of the precipitates with the matrix until the γ” precipitates decompose into the more stable and incoherent δ orthorhombic phase finally resulting in a substantial degradation in mechanical properties of the alloy [53], [54]. The thermal stability of the γ” phase thus defines the limiting temperature of application for such γ” / γ’ reinforced alloys, *id est* 650°C for IN718. Indeed, γ”-precipitation strengthened alloys present lower temperature applications than γ’-precipitate based alloys because of the higher ability of the γ’ to remain stable until temperatures up to ≈750°C.

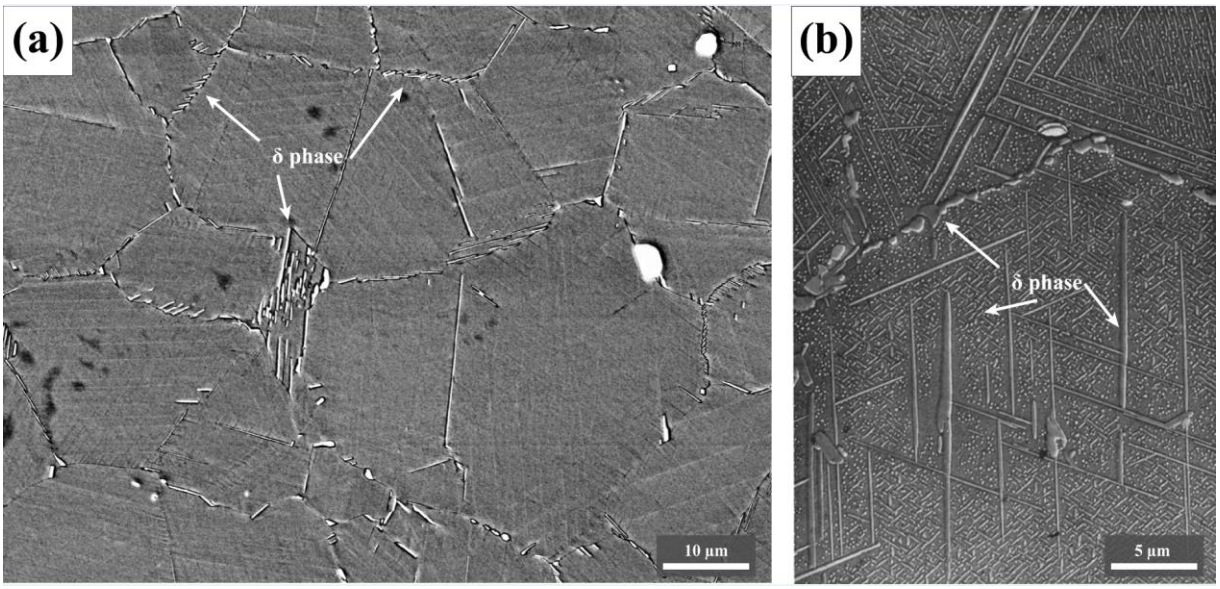


**Figure 7**: **(a)** *SEM-SE2 micrograph showing the intergranular-δ phase morphology in a standard IN718 deformed microstructure (LFWed IN718 from this work).* **(b)** *Overaged microstructure demonstrating overgrown γ” precipitate finally transformed into intragranular δ phase after 6048h at 704°C, micrograph extracted from* [55].

**The δ phase** is a thermodynamically stable intermetallic precipitation product displaying an orthorhombic crystallographic structure with a $D0_a$ order ($Ni_3Nb$). In IN718 polycrystalline alloy, the δ phase preferentially nucleates at the grain boundaries of the austenitic phase between 700°C and 1000°C, but it can also nucleate within the γ matrix notably starting from structural defects or *via* γ” overgrowth events at elevated temperature (see Figure 7.a-b). δ phase precipitates often tends to grow along the {111} planes into the γ matrix, forming needle-like or platelet structures; nonetheless, they do not present any orientation relationship with the γ phase.

The formation of the δ phase was initially considered as detrimental to the alloys performances as it is a brittle and incoherent intermetallic compound. However, its ability to control grain growth and grain boundary sliding when nucleated at the grain boundaries in small quantities demonstrated beneficial effects. Consequently, conventional IN718 microstructures generally display some grain boundary δ phase. The δ phase precipitation treatment is usually done between 950°C to 1000°C. The dwelling time for the δ precipitation is adapted according to the niobium content of the IN718 grade. Over-precipitation of niobium element would deteriorate the mechanical properties of the alloy in-service by consuming the important niobium element. The latter is absolutely necessary for the formation of γ" nanoprecipitates.

When an important volume fraction of δ orthorhombic phase is displayed within the bulk phase composition of a γ"-strengthened superalloy, the material is often designated as in the overaged condition (Figure 7.b). The scientific literature clearly demonstrates that the formation of extensive amount of δ phase induces severe degradation of the mechanical properties among the overaged γ" alloys and must absolutely be avoided during in-service conditions. Nevertheless, the presence of δ phase within such materials is not an exclusively undesirable phenomenon. On the contrary, it has to be emphasized that the controlled presence of δ phase may even confer beneficial consequences on the mechanical properties of the material.

Indeed, when forging procedures are applied under the δ solvus temperature, it is then possible to control and optimize the final grain size and grain distribution of the microstructure *via*:

- (1) the use of the residual fragmented δ, that remains along the grain boundary zones of the grain refined microstructure, that can serve as pining points allowing to inhibit detrimental uncontrolled grain growth and to limit grain size distribution heterogeneity that would deteriorate the tensile and fatigue properties of the material, and *via;*

- (2) adapted heat treatment procedures avoiding overgrowth of the δ phase (overaging) but allowing grain restoration and controlled growth of the γ austenitic grains.

**MC-type carbides** precipitation primarily occurs after casting stages, during the solidification phase. In alloy 718 (Nb, Ti)C types carbides are specifically reported [56]. MC-phases preferentially appear in the grain boundary zones and are suspected to play a role for grain size control during alloy elaboration by hindering grain boundary motion. They are uniformly distributed in the final microstructure and display a cube-to-cube orientation relationship. Their formation is indicative of a very restricted carbon solubility in the γ phase and MC-carbides form very stable phases up until temperature close to the melting point [57]. Their existence has little influence on the mechanical properties of the alloys, even though carbide clusters are sometimes pointed out as preferential crack initiation sites in low-cycle fatigue failures [57]. MC-precipitation yields to concomitant depletion in alloying elements in the surrounding zones, thus impeding γ'/γ" intermetallic precipitations. The appearance of $M_6C$-type carbides is possible, notably with Mo or Co, and depends on the alloys specific composition. Same for borides $M_3B_2$ with Mo [58]. Lastly, **TiN nitride particles**

may also be observed. They form in the melt from the dissolve nitrogen in the liquid bath. IN718 casting is generally done under vacuum conditions to avoid their detrimental appearance.

### 2.4 Forging and conventional heat treatments of the alloy 718

Friction welding procedure usually leads to thermomechanical loads comparable with hot forging processes. Given that, a review of the different heat treatment strategy after conventional forging procedures may help understanding the evolution of strained microstructures through further thermal loads.

Forging cycles are important parts of the total thermomechanical-processing route of superalloys, the aim is to introduce energy in the alloy *via* temperature (thermal energy) and controlled deformation procedures to generate the desired component with an adapted shape (forming) and optimized mechanical properties regarding the desired specification for the in-use application. For instance, some applications would require high tensile properties and high rupture stress behavior; while others would accord preference to significant creep strength or even privilege high performances in low-cycle fatigue life. These criteria require generating spatially homogeneous microstructures presenting well-defined grain size and shape statistics, with adapted phase composition. Such microstructures are generally obtained after successive thermomechanical processing sequences until the desired characteristics are obtained in the material. Grain fragmentation and recovery phenomena triggered during hot straining procedures notably play a key role in such objective.

The forging domain of the iron-nickel 718 alloy is conventionally composed of two sub-domains (Figure 8.a) located on either side of the δ phase *solvus* temperature, the latter is estimated around T ≈1027°C (variations on the δ *solvus* temperature are essentially related with the Nb content of the alloy). When δ phase is dissolved, the microstructure is then solely composed of austenitic grains with dispersed MC-carbides. The temperature of the forging procedure is selected with respect to the final properties targeted for in-service application.

→ The δ *subsolvus* domain is situated below the δ phase *solvus* temperature. In such forging domain, the grain size statistics are notably controlled by the boundary pinning exerted by the δ precipitates on the fragmented microstructure [59]. Forging in the δ-*subsolvus* domain normally aimed at obtaining a fine resulting austenitic microstructure.

→ The δ-*supersolvus* domain above the δ phase *solvus* temperature. It generally results in a coarser austenitic microstructure [60].

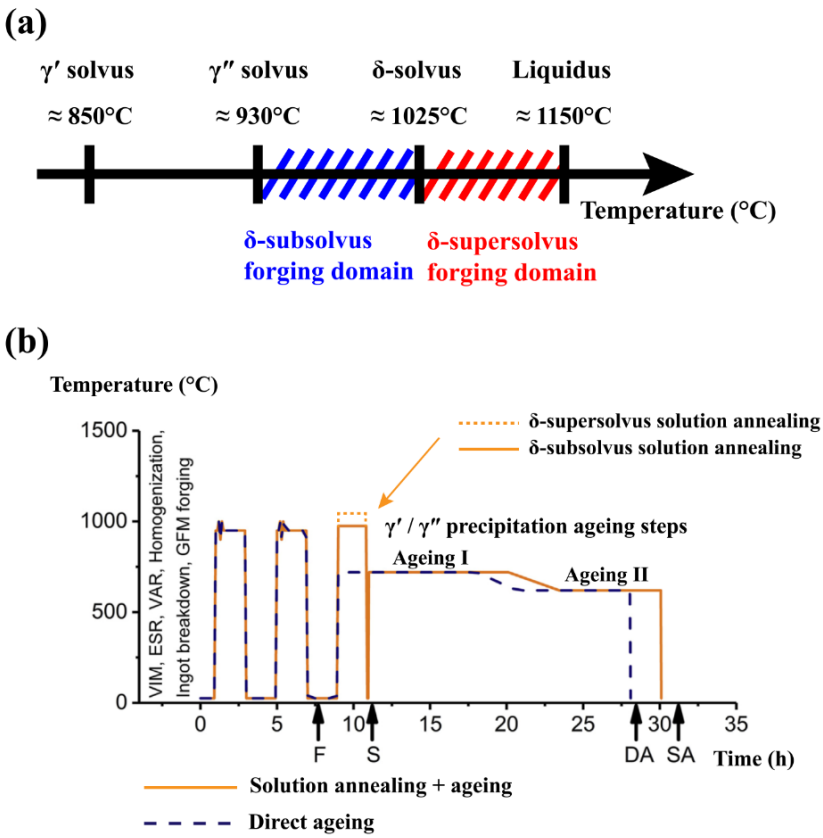


**Figure 8**: ***(a)*** *Forging temperature domains,* ***(b)*** *standard thermo-mechanical temperature-time processing procedures for in-service IN718 alloy, extracted from* [61].

After hot forging procedures, wrought IN718 alloy is generally submitted to a two-steps heat treatment constituted by a solution annealing hold performed within the 950°C to 1050°C temperature range and maintained at constant temperature for a 30 min to 2 hours duration. This step is then followed by a precipitation ageing heat treatment for the progressive formation of the γ' and γ" precipitates.

Two heat treatment strategies are classically possible for the solution annealing steps. They are adapted according to the final functional use of the material. Their specificities are detailed below:

→ On the one hand, standard δ *subsolvus* heat treatments are applied in most of the industrial applications. The principle is to obtain a fine γ-austenitic microstructure with a limited grain size allowing obtaining a high-strength material with good fatigue properties. To that end, the hot-forged material is solution treated in order to precipitate a residual intermetallic δ phase which preferentially nucleates and develops along the grain boundaries. The objective for such a treatment is to inhibit further grain boundary motions by δ-particle assisted pining. In most of the cases, the treatment is performed within a 950°C to 1020°C temperature range and adapted in function of the desired final microstructure and the chemical composition of the alloy (notably with regards to the precipitation kinetic of the in δ phase which is highly Nb.w% content dependent).

→ On another hand, when the hot-forged material is solution treated above the δ phase solvus temperature that procedure is denominated: δ *supersolvus* heat treatment. Such heat treatment yields to

important coarsening of the wrought recrystallized microstructure because of the complete dissolution of the δ intermetallic phase into the γ-FCC matrix. The objective is here to obtain a coarse grain-sized microstructure adapted for interesting creep properties. Such super δ solvus treatments are rarely performed beyond a 1050°C temperature. If necessary, a δ precipitation procedure may thereafter be applied, according to the application requirements.

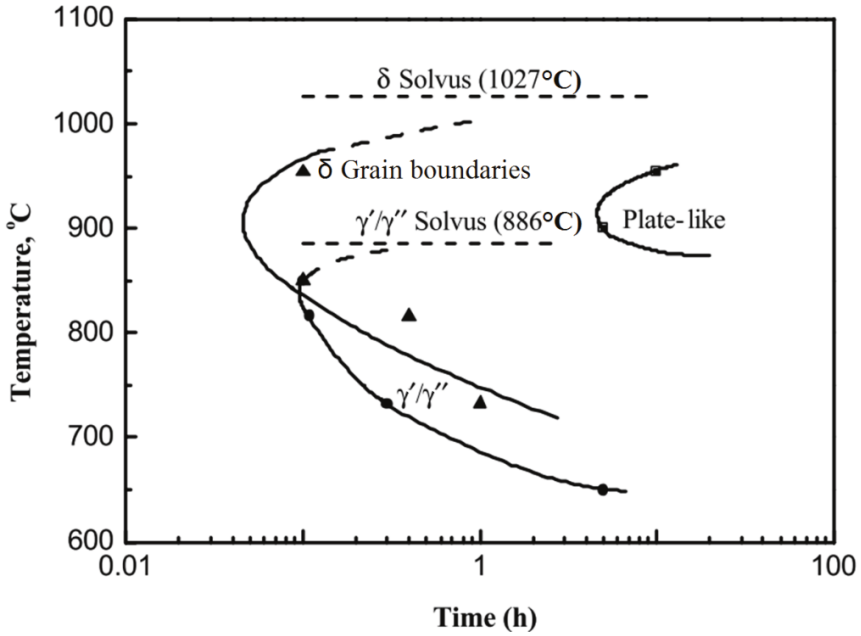


**Figure 9**: *Time-temperature-transformation diagram of alloy 718.*

Both heat solution annealing processes are eventually followed by the classical two-step aging procedure: holding at 720°C for an 8h duration, then furnace cooling at a 50°C/h cooling rate to a 620 °C temperature, for a final 8h holding at 620°C finally followed by air cooling (Figure 8.b). Such heat treatment procedure aims at maximizing the strengthening effect through the progressive formation of the dispersed γ' / γ" precipitates in the austenitic matrix. The definition of the double-staged ageing procedure originally results from empirical works seeking to optimize the materials characteristics [62].

## 3. Linear friction welding applied on alloy 718: aim and context

Nickel-based alloys are key structural materials commonly used in aerospace and power generation industries due to their high temperature strength, fatigue and creep resistance, as well as satisfactory resistance to corrosion and oxidation under aggressive environments. Solid-state friction welding processes are considered as promising for joining Ni-based superalloys as solidification problems, inherent to fusion welding-based technologies, such as grain boundary liquation, detrimental phase formation, elements segregation or micro-cracking problems in the heat affected zone can be avoided. In addition, Ni-alloys are high value materials particularly challenging to weld via conventional techniques while obtaining consistent mechanical properties for demanding in-use applications. Thus, the aerospace is showing a growing interest in

the potential of the Linear Friction Welding (LFW) technology initially interested in applications for the assembly of bladed disks on certain modern aero-engines in place of mechanical insertion systems.

Linear friction welding implies complex and severe thermo-mechanical loads resulting in profound microstructural changes on the welded microstructures once the materials coalescence obtained. Contrary to Ti-alloys, solid-state welding applied on Ni-alloys are not extensively documented in the scientific literature and only limited number of study cases are described. The scientific works generally focuses on three aspects: describing the microstructural changes in the joining zone, applying simple post-weld heat treatment procedures then carry out mechanical tests to evaluate the strength of the assembly. Early works on Inertia Friction Welding (IFW) or Linear Friction Welding (LFW) mainly focused on providing descriptions of the microstructure evolution at the weld interface after processing [63]–[65]. The 'solid-state' character of IFW/LFW was subjected to debate [66], [67]. Notably, the eventual occurrence of detrimental liquation due to the elevated temperature reached in joining zone constitutes an important issue concerning the solid-state assembling Ni-based superalloys [68]. However, the occurrence of liquation events were not reported to date in the scientific literature [69]. Studies on dissimilar Ni-alloys configurations remain rather marginal and show some interesting insight on some weld couples, notably *via* IFW [70]–[72].

Concerning the solid-state wending on IN718 alloy, only basic microstructural descriptions were done on an inertia friction welded configuration [73], post-weld heat treatment strategies were also prospected with success *via* monotonic tensile properties of the obtained assemblies [74]. The first microstructure evolution observations on a LFWed IN718 couple were realized on a solution annealed configuration [75], [76], a thin layer of defects was identified at the weld interface but not characterized. Residual stress characterizations were also realized on different LFWed configurations [77] associating different metallurgical states: solution annealed and precipitation hardened and post-weld heat treatments.

**The present work consequently aims at clarifying the microstructural changes induced by the linear friction welding procedure on IN718 alloy blocks. The microstructure evolution on a specific precipitation hardened weld couple will exhaustively described and discussed**. In addition, careful inspections in the close bonding zone are carried out aiming at identifying the nature of potential weld defects in the junction zone.

## 4. Materials & methods - IN718 – Precipitation Hardened (PH) configurations

The material used in this work is a commercial grade of Inconel 718 polycrystalline nickel-based superalloy in the precipitation hardened metallurgical state (PH). Parallelepipedic solid blocks were extracted by electrical-discharge machining from Ø115 mm diameter and 390 mm length standard wrought IN718 billets provided by Aubert&Duval, Les Ancizes, S.A., France. The dimensions of the blocks are: 10 x 80 x 70 $mm^3$.

### 4.1 Friction assembling procedure

The extracted specimens were linear friction welded in an open-air environment on the 10 x 80 mm² surface with the 80 mm edge parallel to the oscillation direction $\langle x \rangle$ as depicted in Figure . It is also noted that the 80 mm edge is parallel with the billet axis. The friction-assembling machine for the present welding campaign is a MDS-30 model, developed by the ACB Company, Nantes, France. The first welding campaign sets of process parameters on Inconel 718 alloy are detailed bellow in Table 3.

Before the welding procedure, the raw assembling surfaces, which underwent marked surface oxidation during the electrical discharge cutting process, were manually polished by means of P120 grade SiC grinding paper in order to remove the polluted oxidized layer and avoid perturbations and limit adverse effects during the friction phase of the assembling procedure.

| Parameters (Units) | Pressure (MPa) | Frequency (Hz) | Amplitude (mm) | Axial shortening (mm) | Total oscillations duration (s) | |
|---|---|---|---|---|---|---|
| **'Centre'** | 270 | 50 | 1 mm | 3,13 | 5,68 | Nominal weld |
| **P+1** | 300 | 50 | 1 | 3,07 | 6,23 | Nominal weld |
| **P-1** | 240 | 50 | 1 | 3,07 | 5,97 | Nominal weld |
| **A+1** | 270 | 50 | 1,5 | 3,07 | 5,97 | Nominal weld |
| **A-1** | 270 | 50 | 0,5 | 0 | 10 (limit time) | No weld |
| **F+1** | 270 | 70 | 1 | 0 | 10 (limit time) | No weld, an observed cohesive start, then a fracture of the bond |
| **F-1** | 270 | 30 | 1 | 3,11 | 6,49 | Nominal weld |

**Table 3**: *Window of process parameters explored during the study*.

For clarity purpose, the in-depth microstructural characterization of the consequences of the linear friction welding process on the precipitation-hardened material will focus on the "Centre" denominated configuration. The "Centre" configuration selection is based on a rate efficiency criterion and relies on the shortest processing time to reach the 3 mm axial shortening set.

Indeed, among the tested sets of parameters for the precipitation hardened metallurgical state, the 'Centre' configuration: **270 MPa** of forging pressure, **1 mm** of friction amplitude at a **50 Hz** frequency stood out by its ability to reach the 3 mm targeted axial shortening value with the shortest friction processing time. This 'Centre' friction welding conditions was consequently chosen as a 'reference' set of parameters because it led to the most-efficient axial-shortening rate, thus plastic expulsion rate, among the tested sets of parameters.

Nevertheless, the results obtained on the other process parameter configurations are summed up and discussed in a supplementary material part (Sup. Mat. A). The reasons for that decision are two-fold: first, the 'Centre' welding parameter conditions present an excellent study-case in order describe the microstructural changed induced by the linear friction welding procedure within the microstructures. Second, because there is not much difference in term of physical mechanisms implied between the different successfully welded

conditions. Indeed, they all resulted in comparable induced phenomena on the microstructures, with comparable general characteristics, which make a global phenomenological description transposable from one configuration to another. The changes observed between the different welded configurations and the non-welded configuration are then discussed in supplementary material (Sup. Mat. A).

### 4.2 Materials & methods for microstructural description

The microstructural characterization of the assembling interfaces has been carried out on selected cross-sectioned metallographic weld samples. The sample extraction strategy for further characterization is detailed in Figure 10.

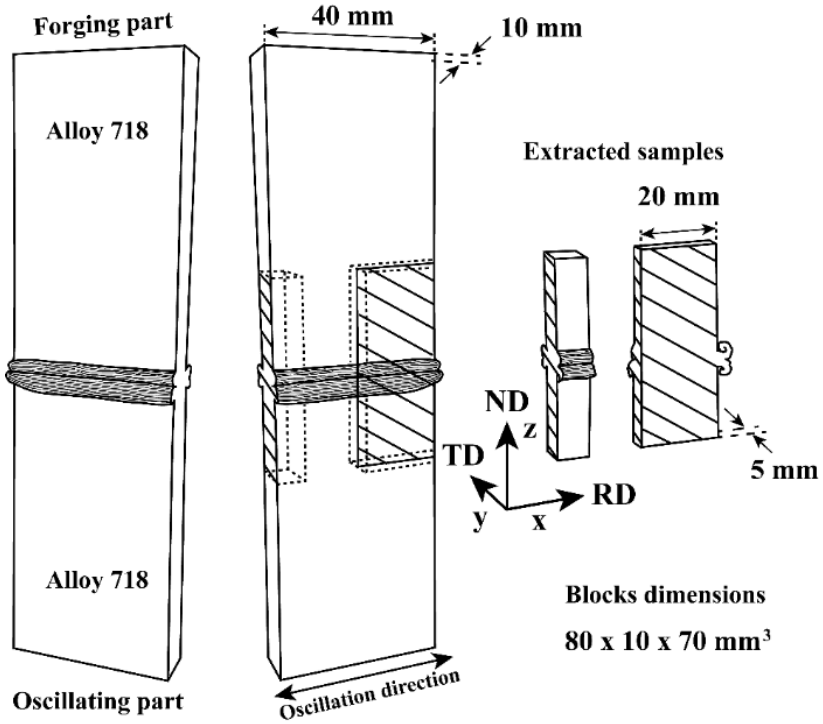


**Figure 10**: *Schematic illustration of the extraction sample strategy on linear friction assembled blocks of alloy 718 for further microstructural characterizations.*

For microstructural examinations the specimen was first mechanically polished through standard abrasive polishing procedures using SiC abrasive grinding papers until a P4000 grit size. The grind finishing procedure is done using successive polishing with standard diamond solution from 3 µm to 1 µm particle mean diameter on a polyester cloth. The final surface finishing is done using a 50% oxide polishing suspension (OPS) solution and 50% in volume of $H_2O$ on a Buehler VibroMet™ 2 vibratory polisher.

Microstructural observations were done using a tungsten field emission gun Zeiss Σigma scanning electron microscope (FEG-SEM). The orientation maps were obtained by electron back-scattered diffraction (EBSD) technique. A Nordiff OptiPlex 7040 detector was used for the Kikuchi pattern images capture and the

orientation maps were calculated through the use of the TSL OIM data collection™ software. During the acquisition, the specimens were mounted onto a 70° tilted holder fixed at a 20 mm working distance from the electron gun outlet. The Matlab© open source toolbox Mtex [78] v5.1.1 is used for the EBSD post-processing procedures. The results of the chemical analysis in SEM are obtained with energy dispersive X-ray spectrometry (EDX) and SAMx IDfix™ software for spectra acquisition. The spectra acquisition duration is 2 minutes with a 1 µm diameter spot approximated measurement area. The high-current beam voltage used for imaging and EDX analysis is 20 kV and 25 kV for EBSD mapping.

Vickers microhardness testing were carried out under a 300 kgF load by means of a Zwick micro-indentation system. In terms of characterization method, the microhardness values on the realized profiles are averaged on three measured points.

The metallographic sample for the atomic for the microscopy (AFM) imaging was first smoothly mechanically polished until vibratory polishing then attacked using a 5% in volume sulfuric acid electrolytic solution at 0°C with the following parameters: a 2V voltage for a targeted intensity value raging between 30 mA to 40 mA for a 20s duration. The electro-polishing machine utilized for that procedure was a Struers Tenu-Pol 4.

# 5. Results on the IN718 - PH 'CENTRE' configuration

## 5.1 Base microstructure characteristics of the IN718 nickel base alloy grade

The initial microstructure of the used IN718 alloy consists of face-centered cubic (FCC) γ austenitic grains presenting an equiaxed grain shape decorated with δ phase micron-sized platelets of $Ni_3Nb$. This microstructure was obtained after a 2h05 isothermal solution annealing treatment at 990°C, which followed the wrought procedures on the IN718 billet. Such solutionning heat treatment favored the uniform precipitation and development of the orthorhombic δ platelets $DO_a$ as observed in the grain boundary region of the γ matrix grains presented in Figure 11.a. The presence of δ phase in the grain boundary zone is notably reported to hinder grain growth and increase creep resistance of the alloy [79], [80]. The solution annealing treatment was followed by water quench on the billet.

Lastly, the final metallurgical state of the material was achieved by the precipitation of the finely inter-dispersed nanoscale intermetallic compounds: $L1_2$-ordered γ' $Ni_3$(Al, Ti) and $D0_{22}$-ordered γ'' $Ni_3$(Nb, Ta) within the γ austenitic matrix grains. The latter were formed during a classical dual ageing procedure at 720 °C and 620°C holding temperatures for 8h each with a controlled cooling rate of 50°C/h in-between the ageing stages. A final air-cooling to room temperature followed the latter step. The microstructure also presents MC carbides and carbonitrides, these metal-carbon phases are well distinguishable on SEM imaging. This material state will from now be denominated as the precipitation hardened (PH) state in the following sections of the work.

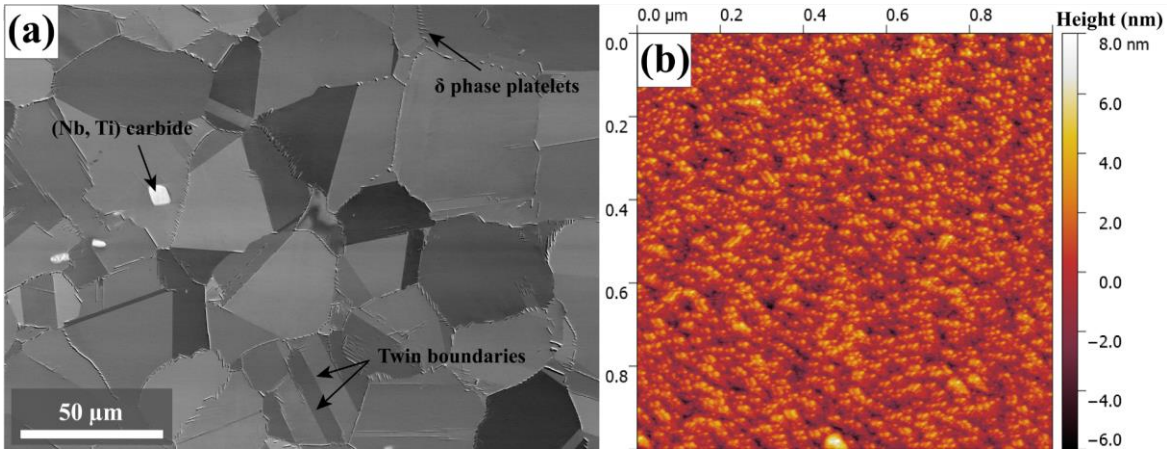


**Figure 11**: **(a)** *SEM-BSE imaging of the base material microstructure composing the forging part;* **(b)** *AFM topography imaging of the γ' and γ'' interdispersed precipitates of the in-use precipitation strengthened IN718 base material after a surface etching procedure*.

An imaging attempt was carried out by AFM technique, in order to illustrate the distribution of those second phase particles within the FCC matrix. The results of the AFM topographic measurements are presented in Figure 11.b. They confirm the expected order of magnitude of a few tens of nanometers in length for the precipitated particles size. Nevertheless, it should be noted that those results were obtained through a classical

AFM measurement method implying tapping mode in open air environment using a standard scanning probe. These experimental conditions imply a lateral resolution of 5 nm at best to 10 nm for the AFM tip, which is significant compared with the characteristic length of the secondary particles (~30 nm) within the matrix. Consequently, the relevance for further accurate evaluation of shape and size for the second phase precipitates is limited.

The main elements nominal composition of the alloy 718 grade used during the different friction welding campaigns covered through this work is recalled in the Table below:

| Element | Ni | Cr | Fe | Nb+Ta | Mo | Ti | Al | Co | Si | Mn | Cu | C | S | B |
|---|---|---|---|---|---|---|---|---|---|---|---|---|---|---|
| wt.% | 53.80 | 17.96 | Bal. | 5.25 | 2.95 | 1.03 | 0.50 | 0.11 | 0.04 | 0.02 | 0.02 | 0.026 | 0.0015 | 0.0033 |

**Table**: *Nominal composition of the welded IN718 alloy grade in weight percentage*.

In term of grain size distribution and statistics, the billets characteristics data sheet provided by the manufacturer indicates that the austenitic microstructure should present a grain distribution with an average equivalent grain size diameter microstructure ranging from <D>=22,5 µm to <D>=63,5 µm values (ASTM 5 - 8) [81] which is quite a wide extent. An important grain size distribution difference is notably observed among the extracted solid blocks from the initial billets. The latter appear to present a spatially dependent grain size distribution that would require additional clarifications. Indeed, the extracted IN718 alloy blocks used for the "Centre" set parameters study case present an obvious difference in grain size statistics between the denominated "oscillating" block and "forge" workpiece.

For that reason, the size distribution of the γ matrix grains in the assembling blocks was evaluated from 2 x 2 $mm^2$ electro back-scattered diffraction (EBSD) scans. As an example, the resulting map and complementary results on the oscillating part are shown in Figure 12. The grain boundary character distribution was first calculated from the orientation map (Figure 12.a), the results are shown in Figure 12.b. A grain boundary character classification was carried out and differentiates low-angle grain boundaries (LAGB) from high-angle grain boundaries (HAGB) by a color code. In addition, among the HAGB type the special angle boundaries: Σ3 60°/<111> and Σ9 38,94°/<110> originating from primary and secondary recrystallization were highlighted with a 5° deviation angle from the ideal twin orientation relationship. Eventually, the grain orientation distribution was evaluated using the harmonic method [82], the corresponding 100, 110 and 111 pole figures indicates weak initial texture near to a random orientation distribution value among the base material blocks (Figure 12.c).

Both microstructures present similar numbers in term of grain boundary type length fraction with 2-3% of LAGB for 97-98% of HAGB. Both also present high and similar proportion of Σ3 twin boundary of about 44% in length fraction. Those results are illustrated in Figure 13.

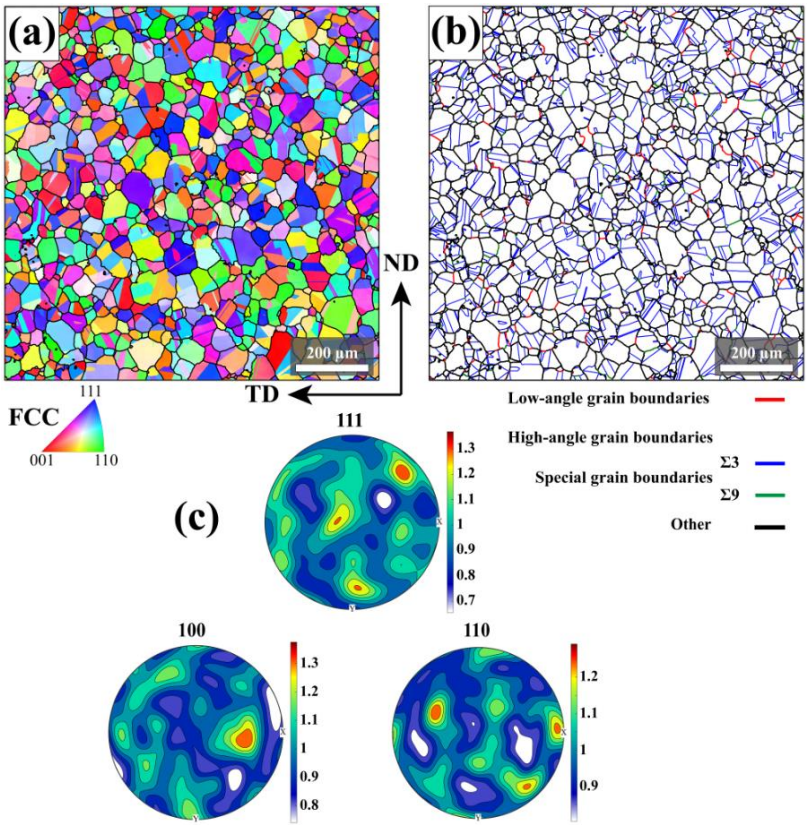


**Figure 12: (a)** *IPF orientation map of the base material composing the oscillating part; the colors represent the crystallographic direction of the indexed lattice along the normal of the (ND, TD) plane;* **(b)** *grain boundary delineations are drawn with a 2° to 15° disorientation threshold for low-angle grain boundaries, beyond 15° degrees of disorientation the boundary is an high-angle grain boundary, Σ3 and Σ9 type special boundaries are highlighted among the high-angle boundary with a 5° threshold;* **(c)** *111, 110, 100 pole figures.*

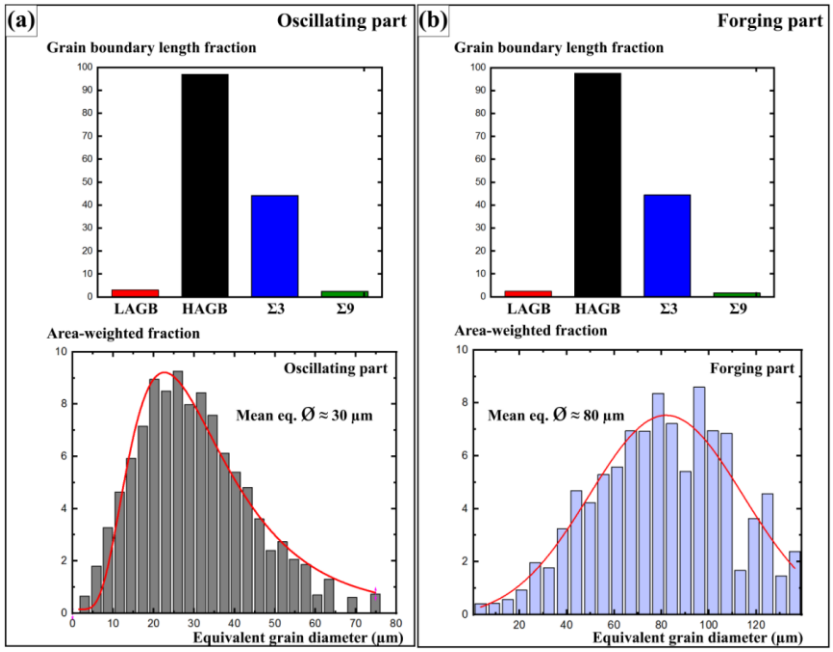


**Figure 13**: *Base material microstructure grains boundary types; and grain size statistics (excluding Σ3 60°/<111> and Σ9 38,94°/<110> twin boundaries types) for* **(a)** *the oscillating and* **(b)** *forging part.*

The average grain size distribution was then determined by area-weighted statistics on the orientation maps excluding the Σ3 and Σ9 twin boundaries. The average equivalent grain diameter of the base austenitic microstructure is of about 30 µm for the oscillating part and of about 80 µm for the forging part. In the grain size analysis, the grains intersecting the delimitating window were excluded from the statistical counts, and the area fraction statistical distribution were fitted with lognormal repartition function. The detailed equivalent grain diameter statistical repartitions are presented in Figure 13.

### 5.2 Friction assembling procedure and control signal of the machine

The linear friction welding process involves the solid state joining of the workpieces by means of the relative reciprocating motion between the oscillation part (here the inferior part) and the forging part (the superior part). The forging part is submitted to a constant vertical axial force. It is recalled that the applied process parameters on the herewith work are: a **forging pressure** of **270 MPa**, a **frequency** of **50 Hz**, an **amplitude** of **1 mm**. The set and aimed **axial shortening** correspond to a **3 mm** material burn-off width. The total oscillation phase duration was of 5,68 s, then; when the relative motion between the blocks stopped, the forging pressure of 270 MPa was maintained for a total process duration of 10 s (set from the starting of the oscillation till the cessation of the forge pressure action). A comparison between the set-signals and the response signals of the MDS30 welding machine is examined and presented in Figure 14.

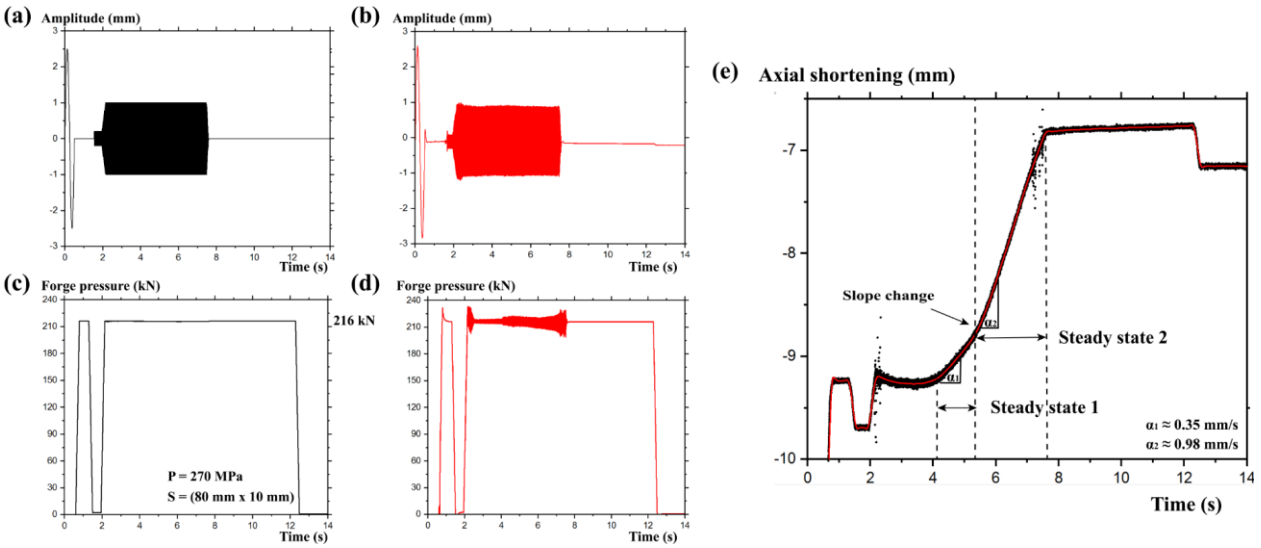


**Figure 14**: ***(a)*** *Amplitude set-point signal (± 1mm),* ***(b)*** *amplitude response signal,* ***(c)*** *pressing force application set-point (kN),* ***(d)*** *pressing force machine signal,* ***(e)*** *Z-axial shortening evolution during the processing time*

The friction assembling process may schematically be divided into the following steps: first (1), a quick progressive amplitude acceleration phase with the progressive application of the pressure force *via* a ramp signal. Then, (2) a steady state was both oscillation amplitude and axial forging force are maintained at constant values. Once the axial shortening set value is reached, (3) the oscillation amplitude progressively

decreases but the forging forge is sustained until (4) the processing time reaches a 10 s value to consolidate the junction.

The axial shortening trend over the steady state processing time demonstrates three main regimes with first a slight initial decline between 2.4 s to 4 s processing time, then the axial shortening increases and reaches a first quasi-linear trend (noted steady state 1). After an about 1,2 s duration, the axial shortening trend experiences an abrupt change in slope to reach another quasi-linear evolution (notes steady state 2) over time until the set axial shortening value is reached marking the end of the alternate friction motion.

### 5.3 Macroscale description of the thermomechanical changes in the joining zone

The resulting microstructure obtained after the linear friction joining procedure was in the first instance prospected by visible light microscopy. These observations are illustrated in the following Figure 15.

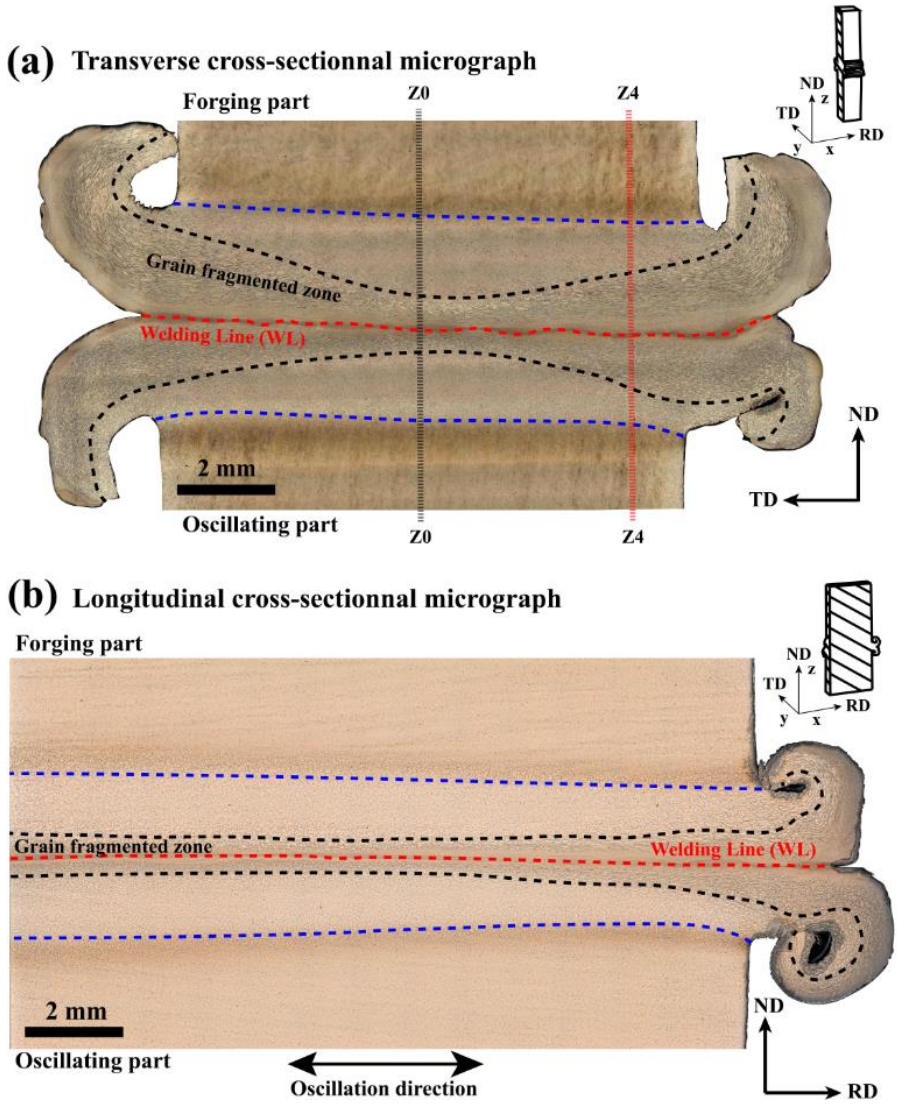


**Figure 15**: *Visible light microscope imaging of selected cross-sectioned weld samples with,* **(a)** *transverse cross sectional micrograph;* **(b)** *longitudinal cross-sectional micrograph.*

In an attempt to describe as well as possible the global microstructural changes across joining zone, two representative cross-sectional views were chosen. The latter were defined regarding the parallelepipedal geometry and the symmetries of the friction assembled workpieces. On the one hand, Figure 15.a. is representative of the global changes along the transverse plane, the sectional plane cuts the weld assembly in half along the (TD, ND) plane, the friction direction (RD) is here normal to the micrograph. On another hand, Figure 15.b depicts the microstructural changes along the longitudinal direction near the expulsion flashes, the cross section was conducted along the (RD, ND) symmetry plane, so the TD is normal to the micrograph. The schematic representation of the sample extraction procedure and cutting method is detailed in Figure 10. Additionally, a detailed close-up micrograph was carried out in complement with the global micrograph presented above. Those results are presented in Figure 16.

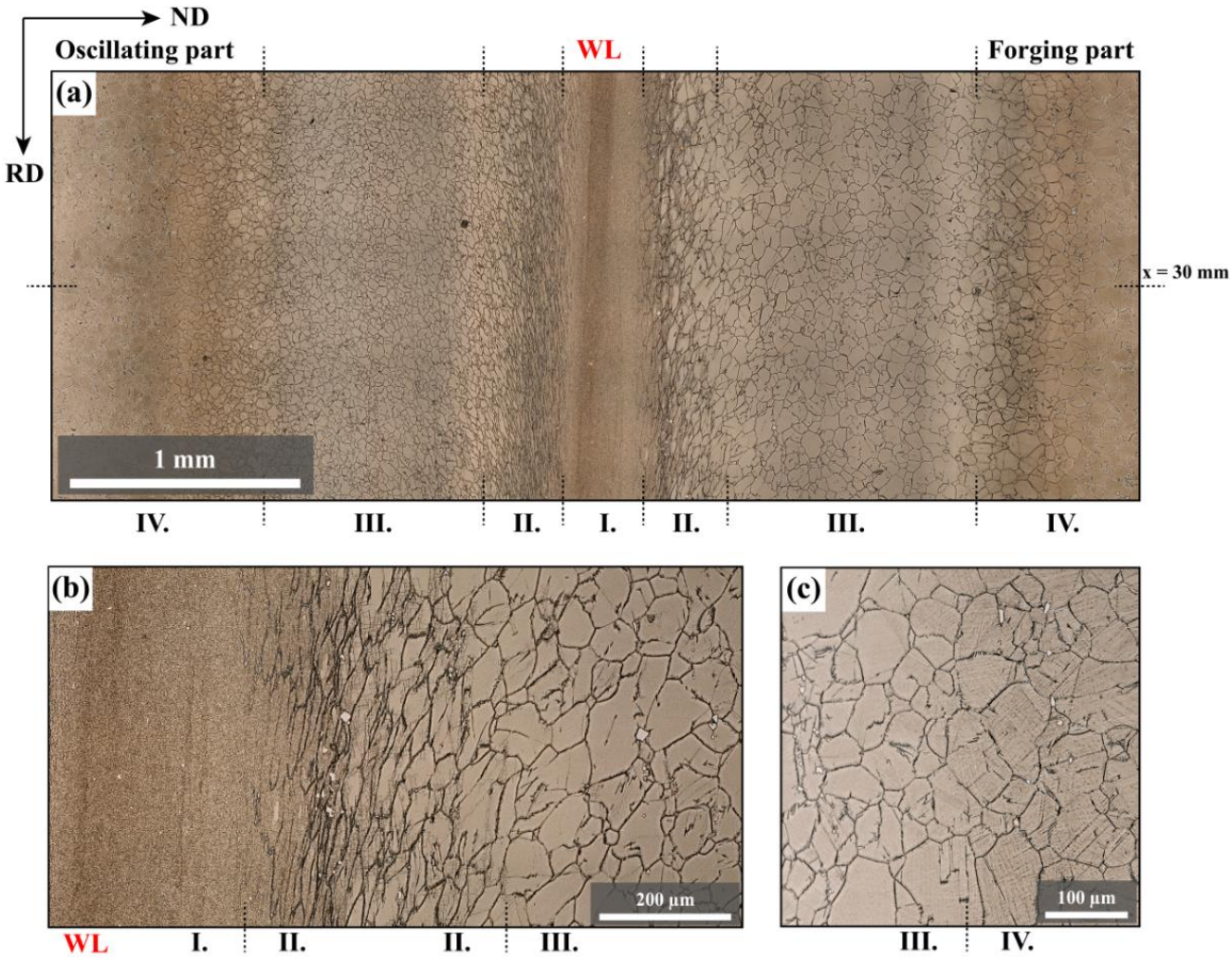


**Figure 16**: *Detailed visible light microscope imaging of the microstructural change at x=30 mm away from the weld geometric center, in the (TD, ND) plane and moving along the RD friction direction;* **(a)** *global cross-sectional micrograph;* **(b)** *focus on the grain fragmentation zone;* **(c)** *focus on the color-contrast zone.*

After the application of a chemical etching, the observation of the joint by visible light microscopy revealed strong microstructure heterogeneities in the assembling zone. The apparent morphological differences between the base material microstructure and the affected microstructure make the junction zone of the weld

easily identifiable. Four main areas demonstrating specific microstructural characteristics were identified: the detailed micrograph highlighting those induced microstructural changes is shown in Figure 16.

It is first remarked that the extruded transverse and lateral material flashes present a dissociated aspect. The welding line (WL) connects one point of divergence of the flashes to the other and its position is highlighted by red broken lines in the optical micrographs presented in Figure 15.a and b. In terms of microstructural markers, the WL is characterized by a slightly finer grain size than the neighboring one composed of a fine band of refined equiaxed microstructure in the Zone I, Figure 16.a. The total disappearance of the δ phase presence markers (white platelets predominantly distributed in grain boundary zones) as approaching the WL zone marks the border between the Zone I and the Zone II.

Then, one can notice a progressive evolution from a completely grain-refined microstructure into a partially refined one as getting away from the junction zone. Starting from the WL, the morphological aspect of the microstructure evolves with the progressive appearance of: first, a grain-fragmented microstructure, then an alternate microstructure made of elongated grains neighboring fine refined equiaxed grains and eventually, grain with a slightly flattened aspect along the forge direction (Z). The grain fragmentation is readily visible inside the grains originating from the base microstructure due to the glaring contrast made by the presence of δ phase platelets marking the grain boundaries prior deformation (Figure 16.b). Furthermore, important variations in thickness for the grain-fragmented zones therefore identified are noticeable. This fact is particularly remarkable along the TD direction on the transverse micrograph (Figure 15.a), where the grain fragmented zone near the expulsion zone is more than twice as thick (about 2 mm thick) that the one in the central section. However, the thickness of the grain fragmentation zone along the longitudinal direction (RD) remains regular until an observed progressive thickening 5 mm away from the expulsion zone. In addition, the thickness of the grain fragmentation zone is clearly asymmetric between the forging and the oscillating part. All those above-described microstructural markers are specific to the Zone II.

Lastly, a coloration contrast is visible between the apparent base material microstructure, either of the oscillating or the forging side, and the affected microstructure of the junction zone. Such color contrasted appearance after etching would suggest a change in the local chemical composition of the microstructure notably in term of phase presence between these two regions. The frontier between these microstructural features is highlighted in Figure 15 by blue broken lines, a detailed view is also provided in Figure 16.c. The latter emphasizes the presence of parallel crosshatching markers within the zone frontier grains which is a specific local microstructural marker. The color contrast delineations present a quasi-straight shape and are approximately situated at 3 mm away from the junction plane and mark the border between the Zone III and the Zone IV. These delineations also correspond to the starting height of formation of the material expulsion flashes.

The ensemble from Zone I to Zone IV of previously described microstructural features defines the Process Affected Zone (PAZ) of this studied PH-IN718 “Centre” weld junction.

Additional SEM observations were performed in Back-Scattered Electrons (BSE) mode in the PAZ. These observations were carried out on the (TD, ND) transverse plane view; along the Z0 profile and were limited on the forging part. The results are displayed in the Figure 17.

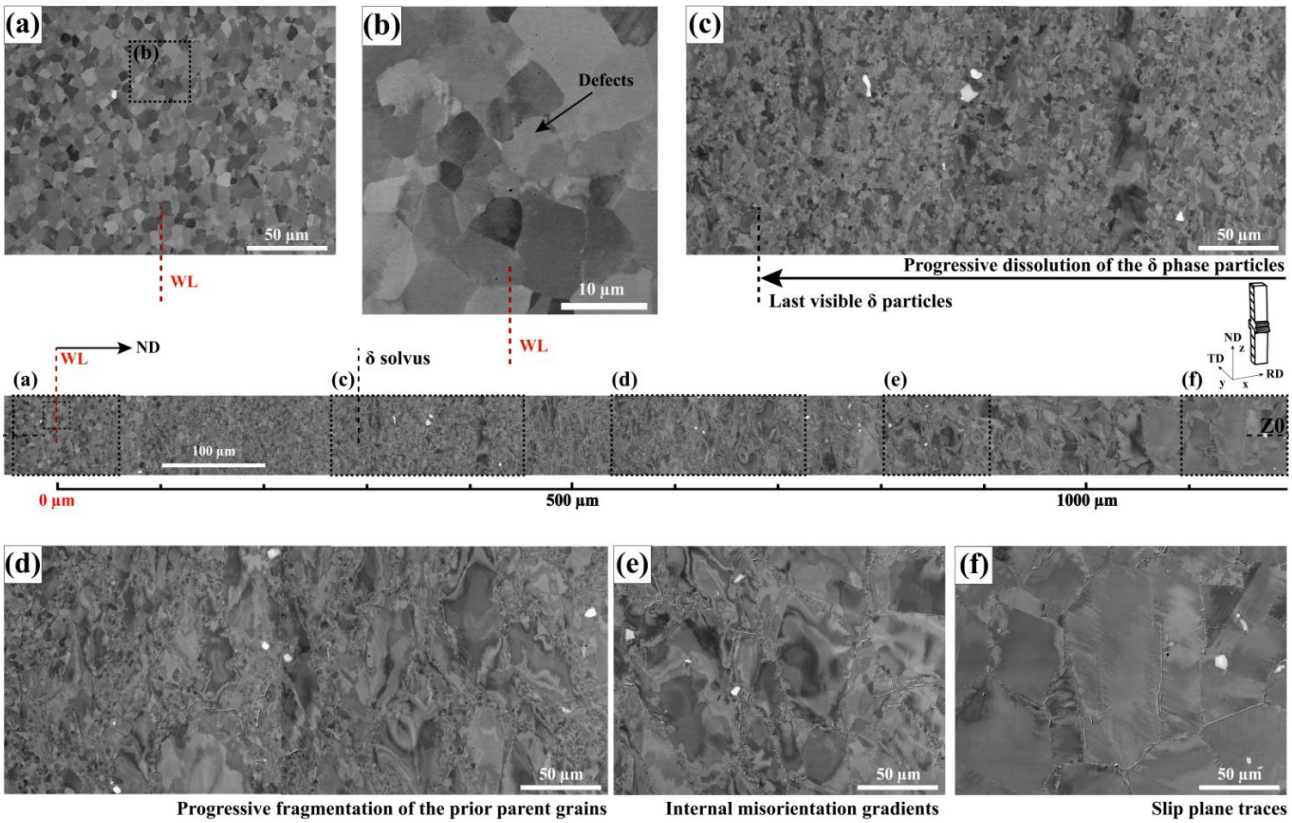


**Figure 17**: *SEM micrographs along the Z0 profile in the (TD, ND) cross-sectional view, forging part side.*

A detailed imaging of the microstructure near the weld junction is shown in Figure 17.a and b, the grain refined microstructure is regular and presents a polygonised aspect. Closer observation highlights the presence of nanometer scale defects, which are expected WL markers in such joints [83]. The latest detectable δ remaining fragments are observed at an about 300 µm distance from the WL, an illustration of the progressive δ phase scattering and dissolution is addressed in Figure 17.c. The internal misorientation gradients inside the plastically deformed grains are highlighted by important grey contrast variations on the BSE signal. Heavily deformed grains surrounded refined grain structures are readily observable in Figure 17.c and d. Then the deformed microstructure goes from grains presenting important internal misorientation gradients (Figure 9.e) to less deformed ones where traces of dense slip plane are distinguishable.

Two microhardness profiles were measured across the joint along the Z direction in the transverse median plane (TD, ND) of the welded specimens. The microhardness tests were carried out on about 16 mm length: one (Z0) evaluated at the median position in the transverse plane (TD, ND) and the other measured at 1 mm near the extrusion zone (Z4). The results are illustrated in the Figure 18 below.

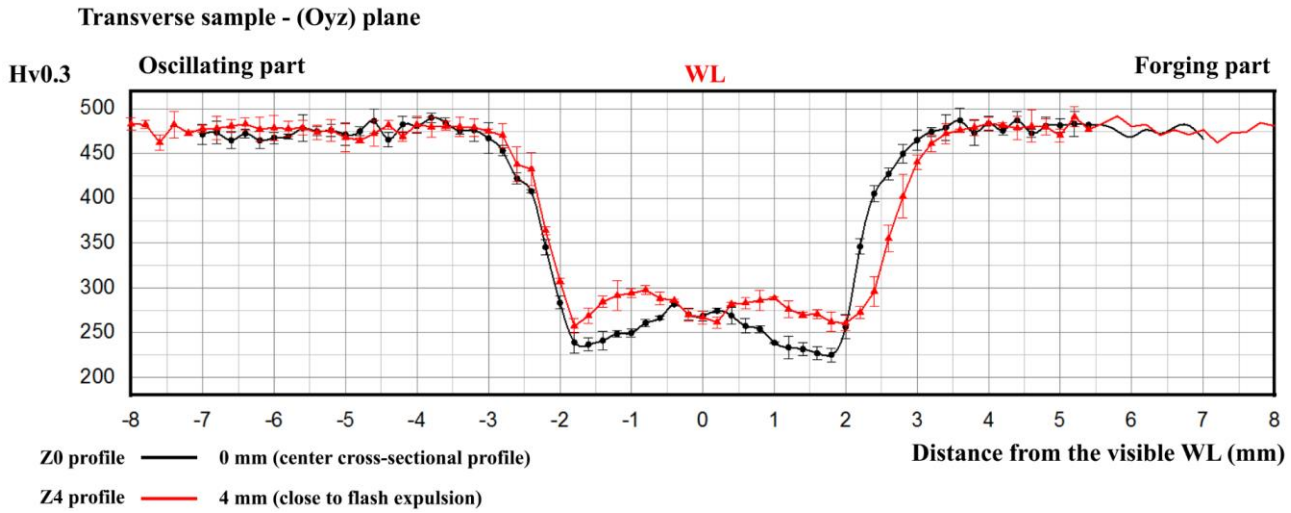


**Figure 18**: *Hv0.3 microhardness profiles measured along the Z direction on the transverse cross-sectional view (TD, ND).*

The base material hardness globally displays a substantial drop within the Process Affected Zone (PAZ). The local mechanical properties are affected over a band of about ± 3.5 mm in thickness starting from the welding line. Then, slight local hardening is noticeable on either side of the WL within the soft affected junction. The WL zone displays a slight but discernable softening. This phenomenon becomes even more remarkable on the Z4 profile. Lastly, a slight softening is perceptible in the WL and its neighboring zone on about ± 400 µm distance on both profiles.

### 5.4 Overall crystal orientation analyses

In complement with micrographs, deeper analyses were performed *via* crystal orientation characterizations across the weld. Three orientation maps were executed on the transverse cross-sectional plane of the joint by electron back-scattered diffraction (EBSD) technique. The resulting orientation maps are presented in Figure 19. It is recalled that the RD corresponds to the direction of friction and ND is aligned with the forge direction.

A slight but discernable crystal re-orientation is noticed in the middle of refined microstructure composing the junction zone on the IPF maps. Indeed, a remarkable proportion of grains manifests little texture presence the normal of the family of {001} crystallographic planes seems to be aligned with the RD direction of the map. In addition, these texture markers are concomitant with the welding line position previously determined by visible light microscopy. The fine central grain refined microstructure presents a quasi-symmetric aspect from one side to the other of the textured central zone.

A marked enlargement of the grain refinement phenomenon is observed as approaching the lateral expulsion zone. The thickness of the totally refined zone is about ± 250 µm from the center of the welding zone marker at the Z0 profile and goes to a ± 600 µm value at the Z4 profile.

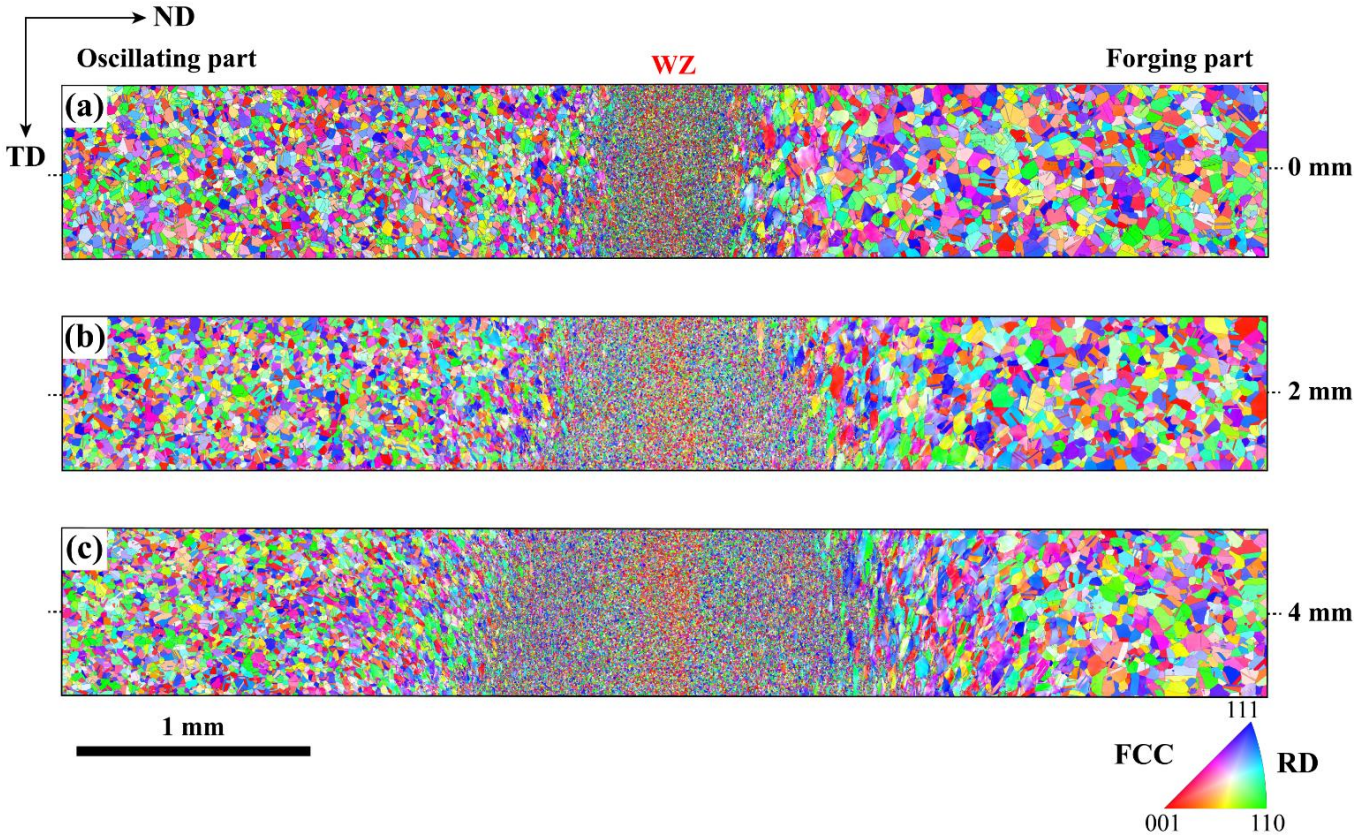


**Figure 19**: *Inverse pole figures obtained from EBSD analyses (0.5 µm step size) on the median transverse plane of the IN718 LFW joint showing three cross-sectional profiles at* **(a)** *0 mm,* **(b)** *2 mm,* **(c)** *4 mm distance from the longitudinal plane of symmetry cutting the welded blocks in half. The FCC indexed data are superimposed with the grain boundaries (15° orientation angle threshold); the colors represent the crystallographic direction of the indexed lattice along RD (friction direction).*

The Grain Orientation Spread (GOS) indicator was chosen in an attempt to visually picture the deformation state of the EBSD-mapped grain populations. Indeed, the GOS indicator is pertinent to evaluate the level of internal plastic deformation as it is strongly related with the internal orientation variations from the mean-crystal orientation of the grains. The GOS procedure is a grain based-method. For a considered grain *I*, it is computed as it follows:

$$\mathrm{GOS(i)} = \frac{1}{N(i)} \cdot \left[ \sum_{j} w_{ij} \right]$$

Where *N(i)* is the number of pixels composing the grain *i*, and the $\omega_{ij}$ term is the misorientation angle between the mean-orientation of the grain *i* and the *j*-pixels composing the grain. Consequently, grains that would display high GOS values would present important internal variations of orientation within its crystal structure. On contrary, grains displaying low GOS values would demonstrate low internal distortion levels, indicating low internal strain levels.

Global GOS cross-sectional maps are presented in Figure 20, these maps were computed from the EBSD data above presented (Figure 20). First of all, the results display a remarkable ± 250 µm thick band of

very low [0°, 1°] GOS value grains that goes across the affected microstructure following along the welding line. The characteristic thickness of this band totally covers the fully refined microstructure of the Z0 section profile; however, it is not an observed feature on the Z2 and Z4 profiles. In the latter, the finely refined microstructure additionally present distinct portion of grain population displaying little higher GOS value, ranging between [1°, 2°], which would be correlated with the presence of local residual internal plastic strain. This observation is particularly remarkable on the Z4 profile where about 50% of the fine-grained microstructure presents non-negligible internal misorientations.

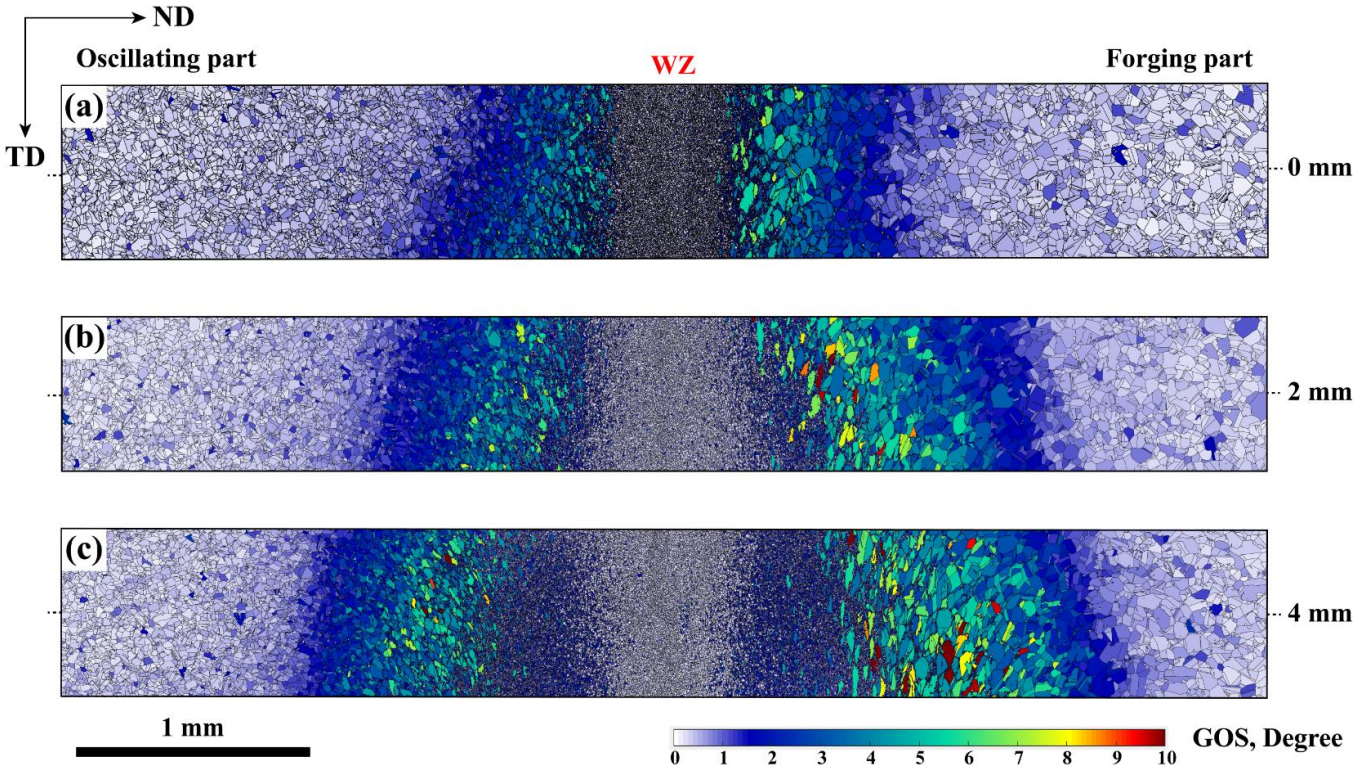


**Figure 20**: *Corresponding Grain Orientation Spread mapping on the transverse plane of the IN718 LFW joint showing three cross-sectional profiles at* **(a)** *0 mm,* **(b)** *2 mm,* **(c)** *4 mm distance from the longitudinal plane of symmetry that cut the welded blocks in half: the grain boundaries orientation angle threshold value is 2°.*

Beyond, a fragmented microstructure is readily discernable on both sides of the weld assembly. The GOS maps highlight the progressiveness of the fragmentation process that occurred in that region going from deformed grain structures exhibiting weak internal deformation values (GOS<2°), to heavily pancake-shape plasticized crystals presenting higher GOS values (GOS>2°) with the progressive appearance of necklace refined crystallites neighboring the deformed parent structures. The appearance of refinement is observed to be concomitant with an average global decrease of the GOS indicator within the deformed structures originating from the parent microstructure. In-between these regions, an outstanding GOS peak value is reached where the refinement phenomenon is rather limited and where some grains manifest tremendous internal misorientation gradients (GOS>6°!). Below the marked plasticized regions, some sparse deformed grains are observed.

The overall aspect of the deformed microstructure evidences a highly asymmetrical partition. In effect, the forge side notably demonstrates a wider band of plasticized grains than the oscillating side, with a higher proportion of markedly distorted grain structures. This phenomenon is notably remarkable as moving toward the transverse expulsion zone (Figure 20.c). These highly plastically deformed zones are forming the Thermo-Mechanically Affected Zone (TMAZ) and vary from ±1 mm at the median Z0 profile to an about ±2 mm at the Z4 profile bordering the lateral expulsion flash.

To sum-up, three main area presenting specific characteristics within the Thermo-Mechanically Affected Zone (TMAZ) may be distinguished:

(1) First, a progressive change in shape of the grain structures is observed and corresponds to the most distant part of the TMAZ from the joint center line *id est*: Zone III, Figure 16. The complementary EBSD analyses show the simultaneous and progressive appearance of gradual changes in orientation within the squashed individual crystallites.

(2) Second, a bimodal microstructure composed of aggregated grains displaying a uniform grain size surrounding large parent grains exhibiting important internal deformation features: Zone II, Figure 16.

(3) And third, the parent microstructure was completely consumed and transformed into a fine-grained microstructure presenting a uniform grain size distribution as well as low internal strain: Zone I, Figure 16.

### 5.5 Grain fragmentation & microstructure refinement

Detailed examinations of the grain fragmented region are exposed in the following section. A first EBSD overview focuses on the transitional zone between the completely fragmented microstructure and the partially fragmented band. The results are decomposed following two complementary parts: Figure 21 & 22.

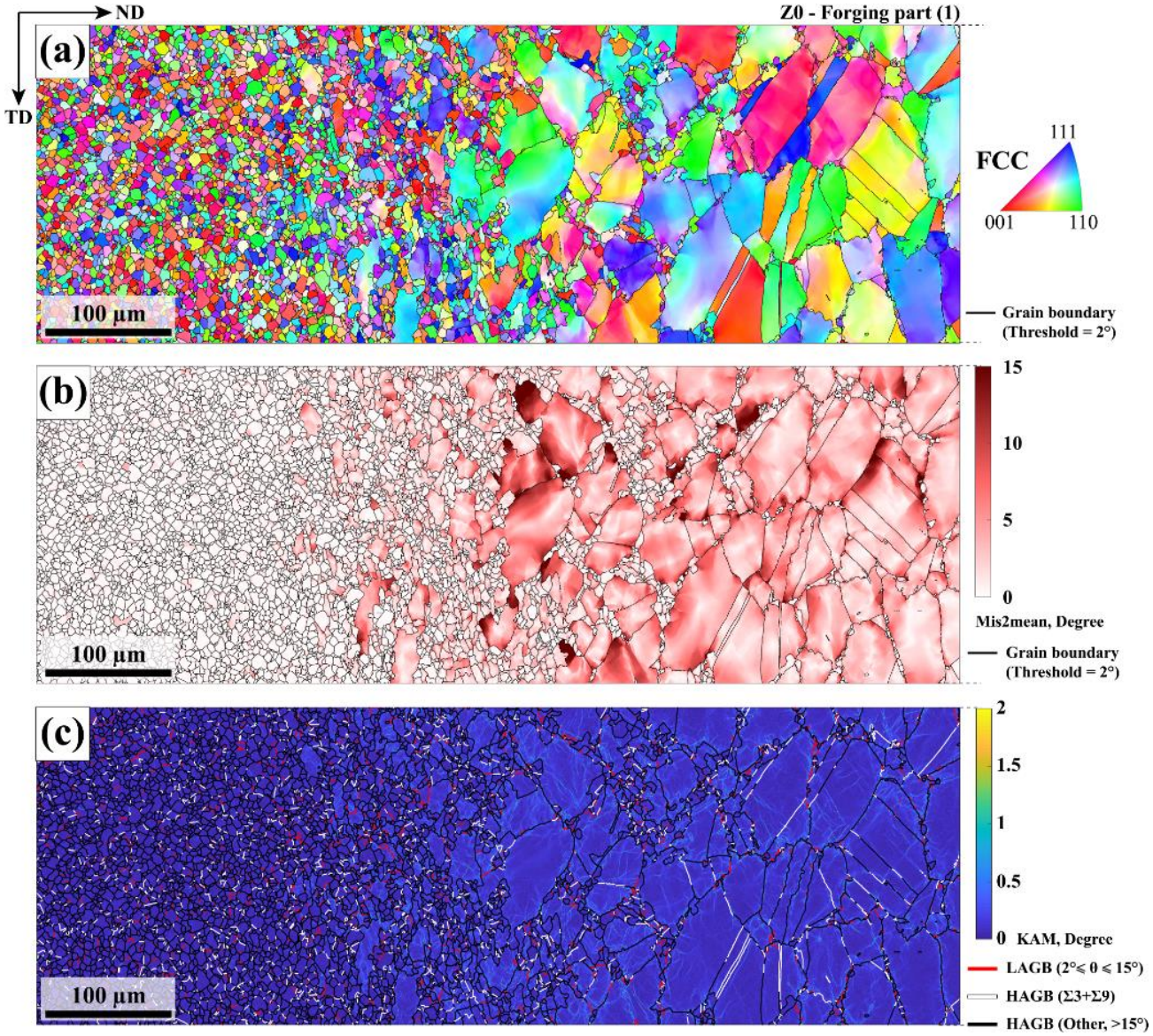


**Figure 21**: **(a)** *Inverse pole figures map from EBSD analyses focusing on the plasticized region along the Z0 profile of the forging part (150 nm step size), the FCC indexed data are superimposed with the grain boundaries (2° orientation angle threshold); the colors represent the crystallographic direction of the indexed lattice along RD (friction direction);* **(b)** *Misorientation to mean-grain orientation map (15° misorientation maximum value threshold) and 2° disorientation angle threshold for grain definition;* **(c)** *Kernel Average Misorientation (KAM) cartography combined with the grain boundary misorientation classification, order 1.*

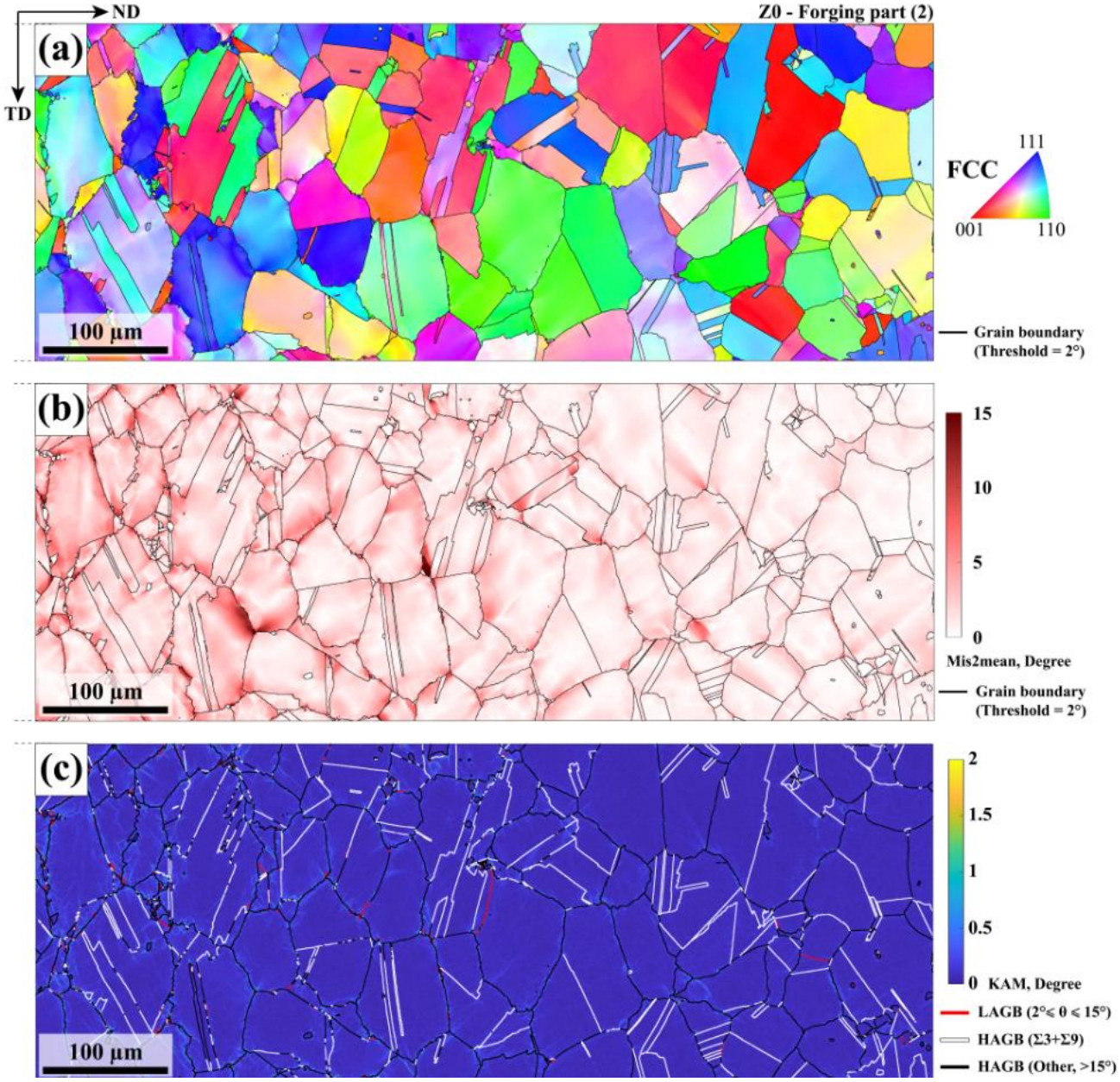


**Figure 22**: **(a)** *Inverse pole figures map from EBSD analyses following the previously exposed microstructure (150 nm step size), the FCC indexed data are superimposed with the grain boundaries (15° orientation angle threshold)*; **(b)** *Misorientation to mean-grain orientation map (15° misorientation maximum value threshold) and 2° disorientation angle threshold for grain definition;* **(c)** *Kernel Average Misorientation (KAM) cartography combined with the grain boundary misorientation classification, order 1*.

The mis2mean indicator computes the minimum rotation angle (taking into account the crystal symmetry) between each pixel composing the grain and the mean orientation of the grain and allows to assess the intragranular misorientation within the grain structures. The mis2mean signal plotted on the Figure 21.b & 22.b highlights that the most significant intragranular misorientation gradients within the deformed grain structures are preferentially situated near the grain boundary zones. By contrast, the adjacent fine-grained microstructure displays only weak to medium internal distortions.

A classification of the grain boundary misorientations and grain boundary character is also provided combined with a Kernel Average Misorientation (KAM) cartography (2° threshold), Figure 21.c & 22.c. The Kernel Average Misorientation value represents the average misorientation angle between a pixel and its neighbors (here the KAM value was evaluated at the first order *id est* taking into account the first neighboring pixels with a 2° local misorientation threshold).

The kernel average misorientation consequently is a measure of local grain misorientation, which means that it is highly sensitive to step-size and the global quality of the signal. Noting $o_{i,j}$ the orientation at the *(i, j)* pixel position and *n(i, j)* the set of all neighboring pixels, the kernel average misorientation at the *(i, j)* pixel position would be defined as:

$$\mathrm{KAM(i,j)} = \frac{1}{n(i,j)} \cdot \left[ \sum_{(k,l) \in n(i,j)} w_{(}o_{i,j}, o_{k,l}) \right]$$

Where *n(i, j)* is the number of all neighboring pixels and $\omega(o_{i,j}, o_{j,k})$ is the disorientation angle between the orientation $o_{i,j}$ at the *(i, j)* reference position and the *(k, l)* neighboring orientations $o_{j,k}$.

Such indicator notably highlights internal structuration leading to abrupt changes in orientation as sub-grain structures that locally fold crystal the lattice. Here, some internal sub-structures formations are observables within the deformed microstructure, notably near the boundary zones.

Indeed, low-angle grain boundaries are preferentially observed to develop near the deformed high angle crystal interfaces of their parent grains. Incidentally, the parent boundary structures locally present a relatively distorted geometry with a broken ripples aspect. Besides, most of these small *nuclei* locally exhibit quasi-homogeneous orientation with little to medium spatial orientation variations. However, the global proportion of low-angle grain boundaries within the fragmenting microstructure is weak and the refined microstructure is essentially constituted of a high-angle grain boundary network. Such a microstructure would indicate that extensive grain fragmentation occurred accompanied by important and rapid crystallites rotation.

Furthermore, it is observed that the Σ3 and Σ9 twin-boundaries (which are defined with a 5° misorientation tolerance threshold from the ideal orientation relationships) of the parent grain structures are progressively losing their special boundary character as moving toward the most distorted regions. Meaning that the local accumulated deviations of the lattice transformed these special boundaries into classical high-angle grain boundaries.

In addition, a Geometrically Necessary Dislocations (GND) map was computed on a part of the partially refined zone, extracted from Figure 21. The region of interest for GND mapping contains heavily deformed former parent grains surrounded by small crystallites nucleated around. The map was calculated considering the main FCC slip system *id.est*: a/2.<110>{111}, the results are presented in Figure 23:

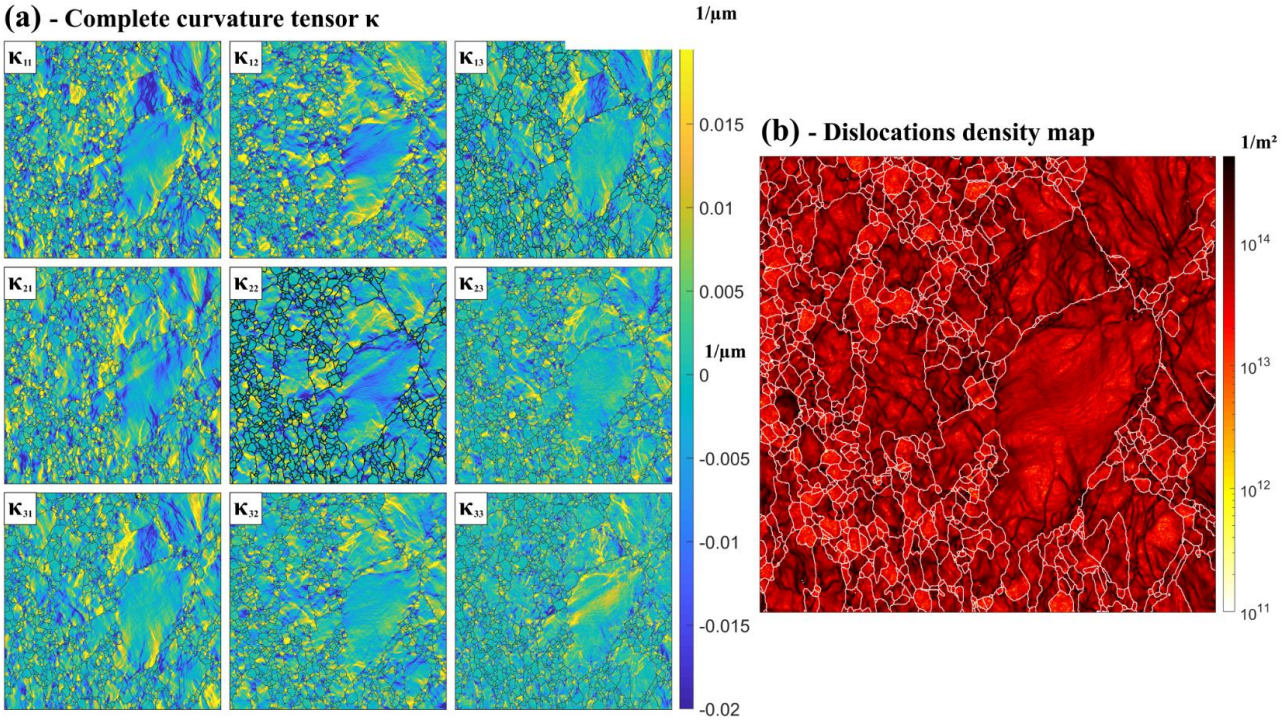


**Figure 23**: *Squashed grains near the WZ, acquisition zone of 150 x 150 µm² dimension* **(a)** *Complete lattice curvature tensor* **κ** *given along the sample directions.* **(b)** *Computed dislocations density map. The step-size is of 150 nm. The grain boundaries are defined by black continuous lines, with a 2° misorientation threshold.*

**S**tored dislocations are classically divided into two classes of defects: the statistically stored dislocations (SSDs) that accumulate due to statistical entanglements in random trapping processes during plastic deformation, and geometrically necessary dislocations (GNDs) that accommodate lattice curvature in response to strain gradient [84]. Even though GND density represents only a few percent of the total dislocation density, their presence have significant geometric consequences on the crystal lattice [85]. Indeed, knowing that a single dislocation induces a local lattice distortion, GNDs consequently arise from the spontaneous structuration of several individual dislocations resulting in measurable cumulated effects on the lattice. In other words, by generating a local misorientation. Hence, the intragranular misorientations can be used to estimate the GND density. The framework of geometrically necessary dislocations (GNDs) was genuinely introduced by Nye [86], describing the dislocated state of the crystal by a dislocation (or Nye) tensor field. The latter is expressed in the field of continuum mechanics as a function of the elastic curvature **κ**, which can itself be expressed as a function of local misorientations [87].

EBSD data are acquired on a single sample 2D section; consequently, they do not assess the orientation changes along the direction normal to the sample surface. The curvature tensor is then incomplete, and the out of plane components are usually unknown (here $\kappa_{13}$, $\kappa_{23}$, $\kappa_{33}$ in the Figure 23. a). The GND density tensor **α** (or Nye-Kröner tensor) can then be calculated through an energy minimization method [88] taking into account each possible dislocation system, here: a/2.<110>{111} and finally keeping the minimal energy configurations. From this fitting procedure is thus possible to restore a 'complete' curvature tensor, giving estimated values for the $\kappa_{13}$, $\kappa_{23}$, $\kappa_{33}$ components (Figure 23.a).

The associated dislocation density map is finally obtained by considering the elastic energy of the different dislocation systems resulting from the previous fitting computations (Figure 23.b). The GND density map highlights important lattice rotations in the inner structures of the strained grains. Such rotation gradients correspond to the formation of subgrain boundaries. The latter are markedly pronounced in the immediate vicinity of the deformed former parent grains. However visible lattice rotations are also observed in the core structure of these fragmenting grains. On another note, many already fragmented crystallites demonstrate clear internal strain gradients indicating in-progress subdivision in these grain structures.

### 5.6 Texture development analyses

The texture prospection focuses in the first instance on the slight crystal preferred orientation development observed in the grain refined central zone of the joint, neighboring the welding line. As the crystal re-orientation seems to only appear in the part of the microstructure displaying an advanced refinement stage. The grain population was consequently filtered to solely keep the most refined grain structures *id est*, the ones presenting low internal strains. To do so, the arbitrary chosen cut-off criterion was a GOS < 1° indicators value. The results are displayed in Figure 24 for the Z0, Z2 and Z4 profiles from the median transverse plane (TD, ND) of the weld. The RD corresponds to the friction direction.

Within the considered regions of interest (ROI), the Orientation Density Function (ODF) were first evaluated using the spherical harmonic method (with a 10° Euler space subdivision). Then, the associated 111, 100 and 110 pole figures were plotted for each region of interest. The stereographic projections were realized on the (TD, ND) cross-sectional plane, along the RD and according to the Schmidt equal-area convention.

These observations seems to highlight the formation of a weak {001}<100> cube micro-texture in the center of the welding zone concomitant with the appearance of a finalized grain fragmentation process (GOS < 0,5°).

However, it should be noted the description of texture by pole figures is incomplete. Indeed, the information provided refers only to the statistical distribution of a single direction and there is no way of using this information to obtain the complete orientation of individual grains or volume elements. A better description is given by the ODF, which describes the distribution of orientations of all the material in the sample.

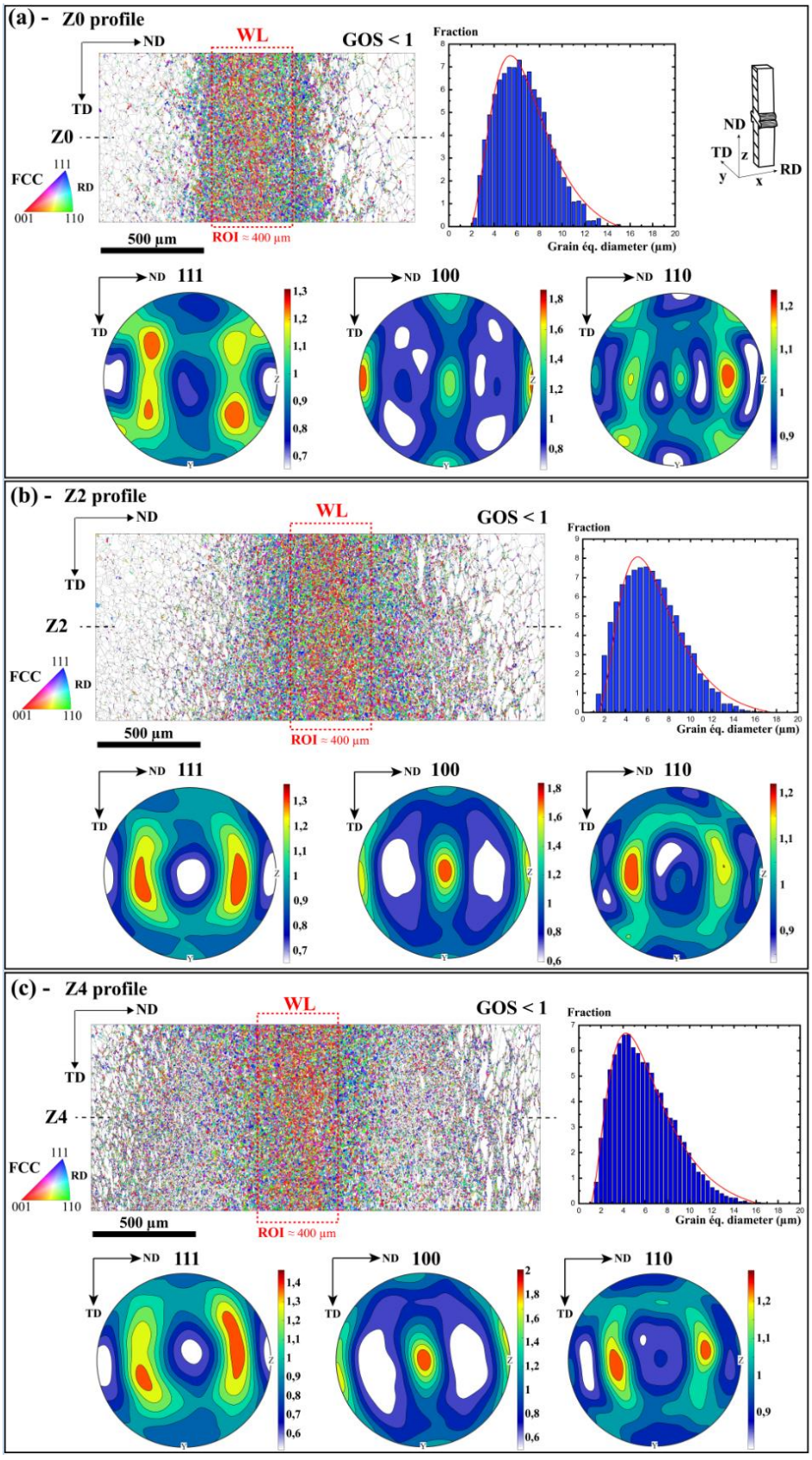


**Figure 24**: *Illustration of the texture development within the ROI of the WL and neighboring zone at the* **(a)** *Z0,* **(b)** *Z2 and* **(c)** *Z4 profiles with 111, 110, 100 equal-area stereographic pole figure projections; area-weighted grain equivalent diameter distribution in the grain refined WL neighboring zone, the grain population has been filtered to keep the low internal strain crystallites with a GOS<1° criterion.*

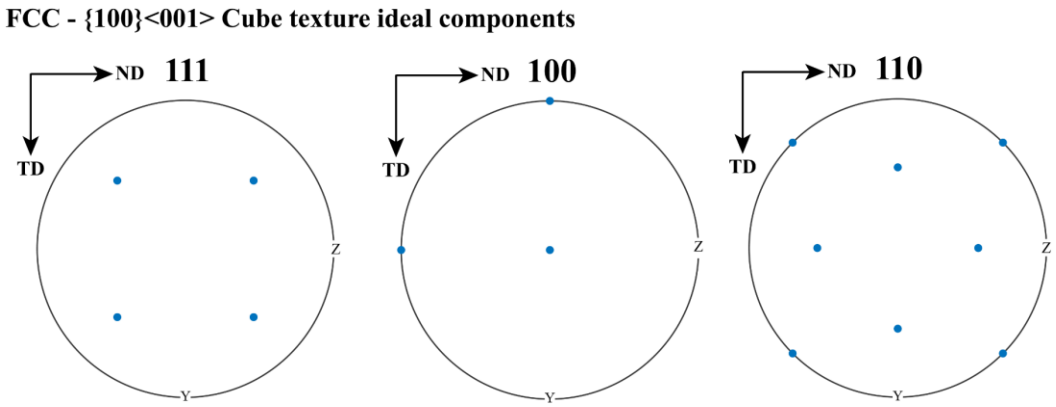


**Figure 25**: *Equal-area pole figure projection of the ideal cube texture components.*

The distributions of the misorientation angles in the FCC nickel (Figure 26.d) microstructure do not corroborate with the presence of a subsequent texture development. Indeed, in both microstructures, the spatially correlated and uncorrelated misorientation distributions are close to a random Mackenzie distribution.

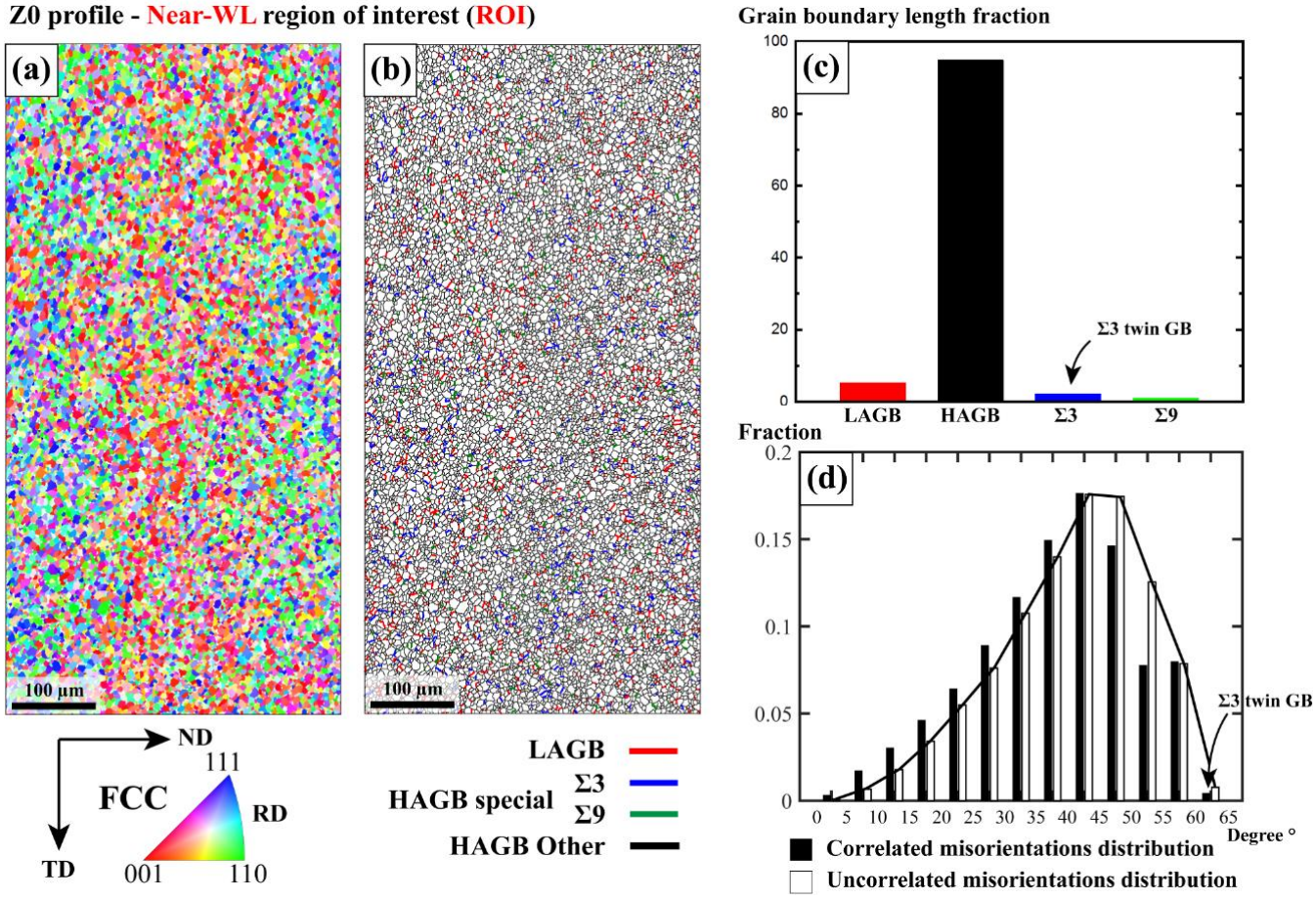


**Figure 26**: **(a)** *Magnified IPF map of the Z0 profile ROI for texture analyses;* **(b)** *plot of the corresponding boundary character map;* **(c)** B*oundary type length fraction distribution;* **(d)** *Misorientations distributions.*

### 5.7 Deformation texture near the expulsion zone

On another note, texture features were prospected in the deformed region and are presented in Figure 27, the grain population was filtered using a GOS >2° criteria to keep solely grains presenting subsequent plastic deformation (Figure 27.a and b):

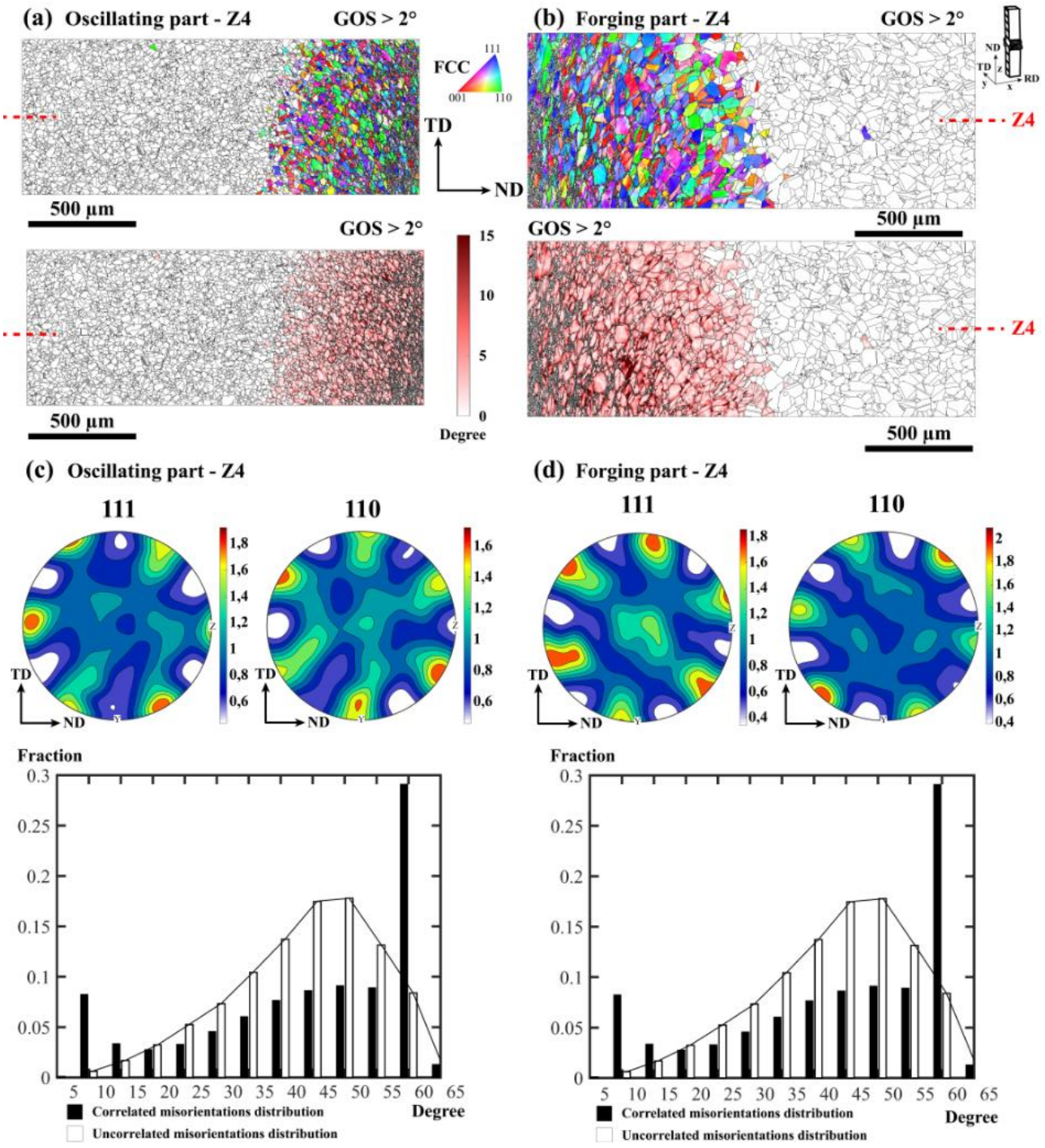


**Figure 27**: *Texture development within* **(a)-(b)** *the deformed microstructure neighboring the expulsion zone (Z4 profile), the grain population has been filtered to keep only highly strained grains with a GOS>2° criterion.* **(c)-(d)** *The associated 111, 110, 100 equal-area stereographic pole figure projections are displayed. The corresponding area-weighted grain equivalent diameter distributions are also plotted.*

Indeed, in both microstructures, the spatially correlated and uncorrelated misorientation distributions revealed the presence of a noteworthy but not significant statistical peak at the low angle boundaries values going from 5° to 20°. Such a feature would indicate that the grain fragmentation process is accompanied by rapid rotation of the nucleated crystallites from low-angle to high-angle grain boundaries within the deformed microstructure. The presence of twin boundaries Σ3 originating from the base microstructure is highlighted by the 55° to 60° peak in these distributions.

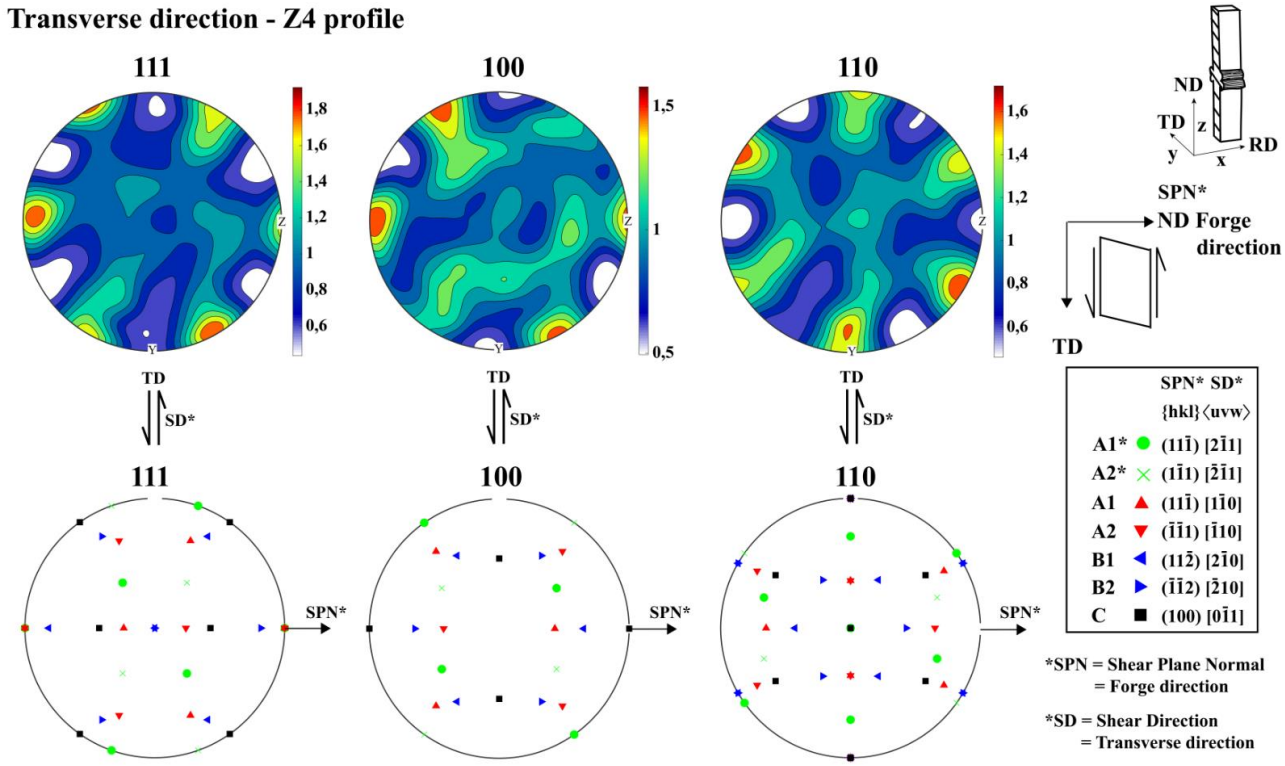


**Figure 28**: *Illustration of the texture development within the deformed microstructure in the shear reference frame.*

A superposition of various shear texture component seems to take place in the deformed material. The A1* & A2* twin-symmetric components and the C components seems to be the dominant expressing components (Figure 28).

### 5.8 Chemical investigations at the weld interface

SEM imaging carried out at high-magnification revealed the presence of local defects dispersed along the welding line zone in form of nano-particles. The latter are embedded in the γ-austenite matrix in the core of the junction. Such findings are characteristic markers of the WL zone and are present all along the joining plane. The results are displayed in Figure 29. Some nano-porosities are also distinguishable in the concerned zone.

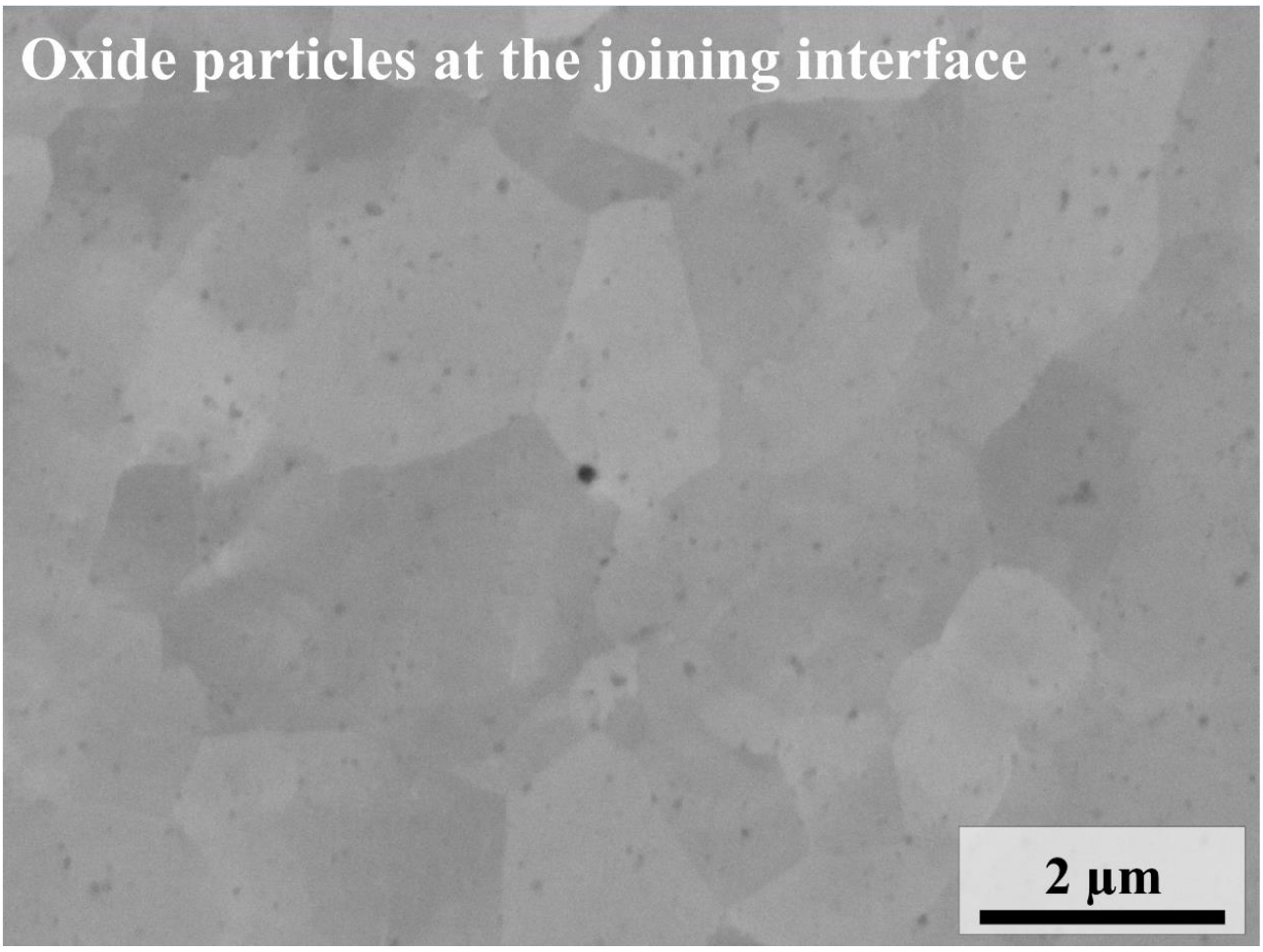


**Figure 29**: *SEM-SE2 imaging of entrapped particles near the weld interface zone.*

Additional inspections realized under TEM in the close weld center zone unequivocally confirmed the particle nature of the disseminated defects. Their presence may probably result from the former surface oxide interaction during the friction welding procedure. Indeed, two main hypotheses can be argued: whether these particles originate from intense mechanical fragmentation of the superficial oxide layers; whether they result from chemical transformation that may have been favored because of the elevated temperature reached in the core of the joint during the welding process.

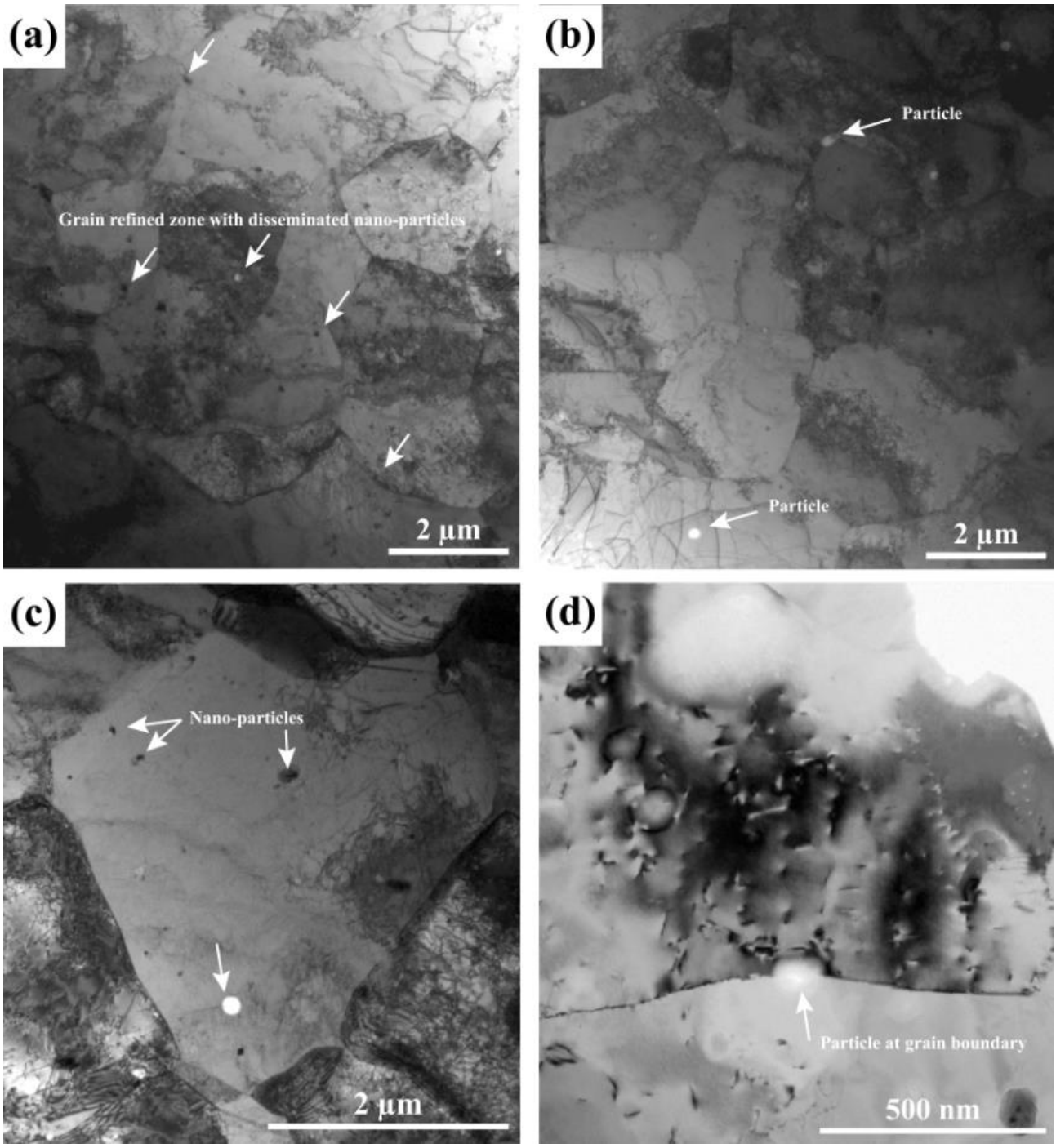


**Figure 30**: *TEM bright field imaging of the grain refined central microstructure of the weld junction.*

In order to clarify the chemical composition of those species, local distribution of substitutional elements was investigated through energy-dispersive X-ray spectroscopy in TEM; the corresponding qualitative element cartographies are presented in Figure 32.

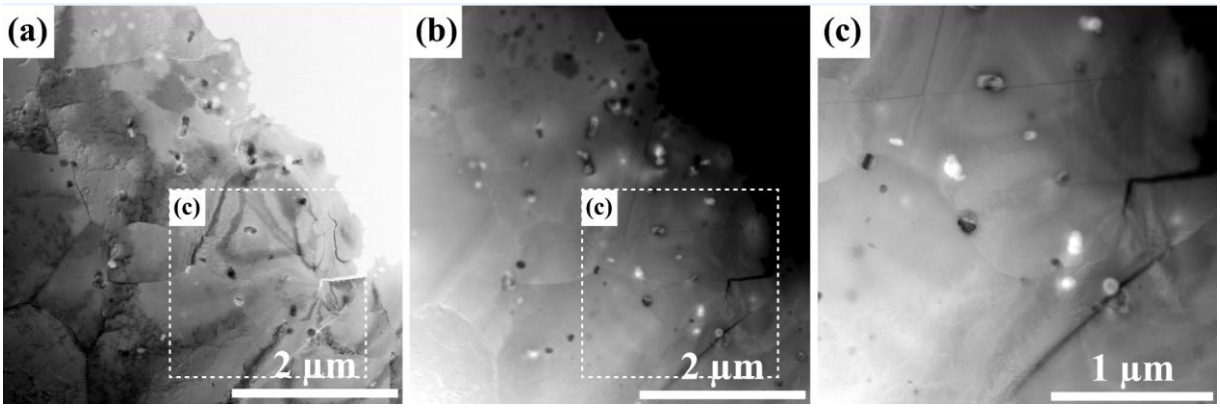


**Figure 31:** *HAADF imaging of the precipitated particles in the weld center zone.*

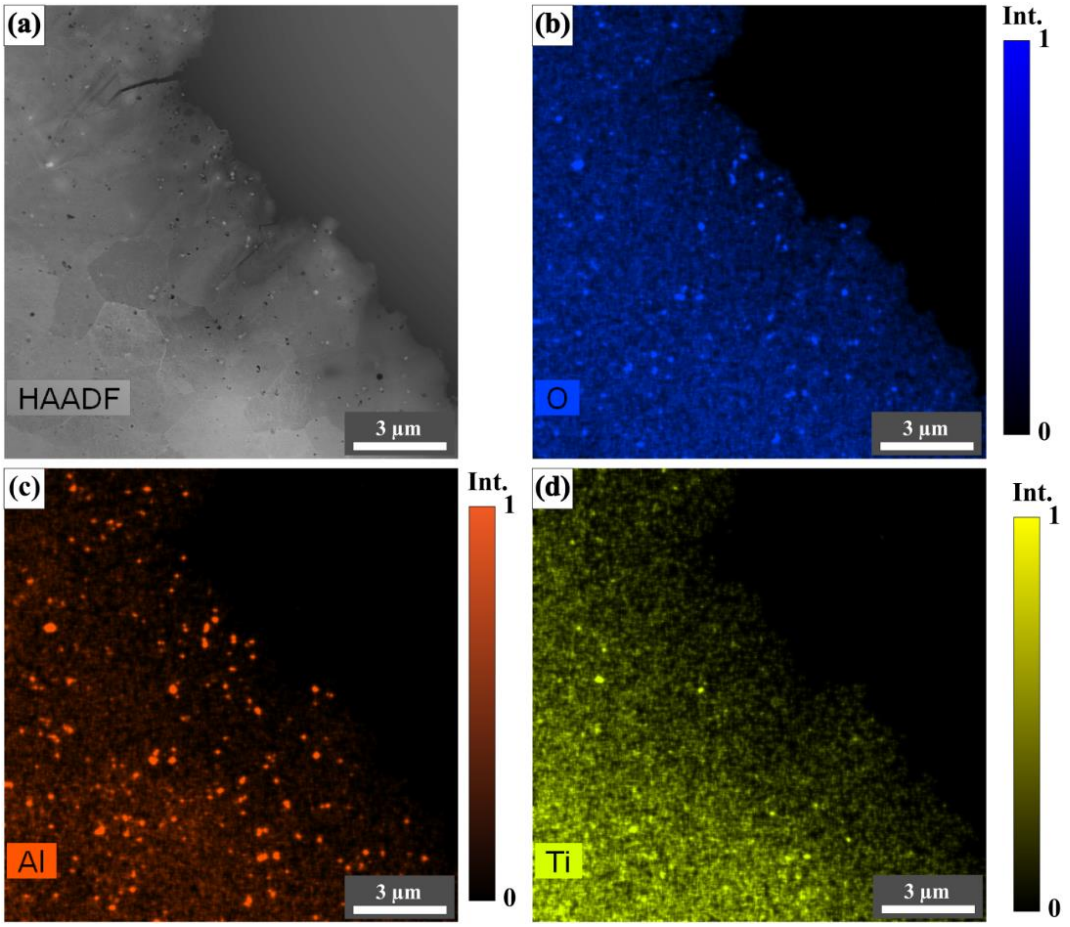


**Figure 32**: **(a)** *HAADF image at the interfacial zone, the EDX intensity maps of the solute elements:* **(b)** *Oxygen,* **(c)** *Aluminum, and* **(d)** *Titanium (intensity bar scaled on the local maximal concentration).*

EDX chemical maps (Figure 32) display a strong correlation between Al, Ti elements with O element respectively. The findings would correspondingly evidence the formation of nano-oxide particles composed of Al and Ti. The latter are regularly reparsed among the refined microstructure. In addition, their size is about ~10nm to ~30nm.

## 6. Discussion

In the first instance, the overall microstructural observations (Figure 15-17) are analyzed in comparison with the microhardness results (Figure 18). In light of that, clarifications about phase transformations that occurred during the friction welding process applied on precipitation hardened IN718 alloy blocks are deduced.

### 6.1 As-welded state, phase presence description across the assembly

The following description starts from the base material zone (Zone IV, Figure 16), then follows toward the weld center zone. In Zone IV, the local mechanical properties reflected by the conducted microhardness tests (Figure 18) form a plateau with high hardness values ranging around ≈ 475 ±20 $Hv_{0,3}$. The latter corresponds to the expected standards for base IN718 alloy in a precipitation strengthened metallurgical state. Moreover, the corresponding microstructure presents a visibly unaffected morphology. Then, the etching contrasts situated at about ±3.5 mm from either side of the joint are concomitant with a substantial drop in microhardness values within the weld junction. These markers indicate the extensive dissolution of the γ' and γ'' strengthening precipitates in that zone, suggesting that the thermal load reached temperature values above the γ' / γ'' *transus* during thermal cycle of the process. It consequently led to an important softening of the material in the joining zone. These features thus correspond to the limit between the Zones III and IV, Figure 16. The latter phase transformation markers therefore delimit the extent of the Process Affected Zone (PAZ) within the weld assembly. From a global perspective, one can remark that the limits of the PAZ match with the lateral and longitudinal material flashes thickness. The γ' / γ'' precipitates dissolution correspondingly caused a significant collapse of the yield stress facilitating subsequent plastic flow. It finally resulted in the formation of the observed expulsion flashes.

Unfortunately, *in-situ* temperature measurements could not be carried out in the PAZ during the assembling procedure. However, a detailed description of the spatial evolution of phase presence across the PAZ allow coarsely speculating on the maximal temperature values reached during the assembling. In effect, supposing that the influence of the mechanical load on the phase transformation temperatures of the strengthening precipitates is marginal; local isothermal values may then be roughly estimated from microstructural markers. Therefore, the beginning of the TMAZ, marked by a nascent hardness drop, would correspond to local temperature in the order of magnitude of the *equilibrium* starting γ' *solvus* temperature value (*id est* $T_{\gamma'\_solvus} \approx 650°C$) [19], [89]. Since, the γ' phase possesses the lowest phase decomposition temperature among the strengthening precipitates.

Thereafter, the measured microhardness drops until reaching values of about 220 to 230 $Hv_{0.3}$ at ±2 mm distance from the WL. This trend is notably observed on the Z0 profile, which is less affected by strain hardening effects. Such values are in the order of magnitude of the ones of the solution annealed metallurgical state, depleted from γ'/ γ", and would then indicate the complete dissolution of the hardening particles within

the matrix. The approximate γ" *solvus* temperature in close *equilibrium* conditions is about $T_{\gamma"\_solvus} \approx 880°C$ [19], [89] and also marks the complete dissolution of the γ'/ γ" strengthening precipitates in the austenitic matrix (Figure 33).

In addition to that, the austenitic microstructure in the hardness dropping zones did not extensively deformed during the process, even though some slip band traces are perceptible at the Zones III and IV delineations. The latter features most likely result from the local mechanical incompatibilities arising from the abrupt dissolution of strengthening phases in that zone. The local mechanical properties of the unaffected being much higher than the ones of the adjacent austenitic grains less dense in strengthening phases. However, the global shape of the parent grain structures remained weakly affected (Figure 16) in that zone. In the field of welding or joining technologies, zones undergoing local change in mechanical properties while their grain structures remain unchanged (or little plastically affected) are often designated as the Heat Affected Zones (HAZ). These variations are generally due to differences in phase composition resulting from the thermal loads induced by the process, such as the γ'/ γ" dissolution in the present case.

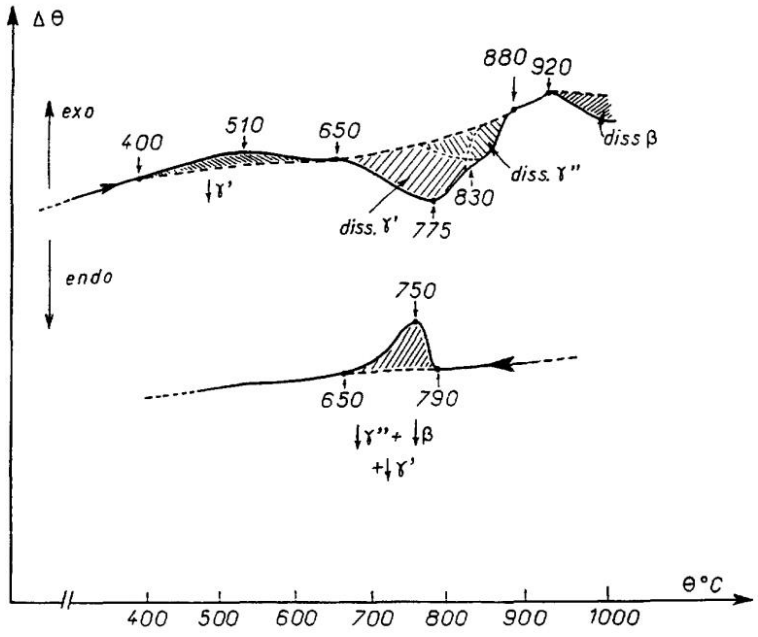


**Figure 33**: *Differential thermal analyses records while heating up a IN718 alloy grade at a 300°C/h heating rate, data extracted from* [19].

Besides, the progressive dissolution of γ' and γ" strengthening phases presumably caused the remarkable slope change observed on the axial shortening curve versus processing time (Figure 14), because of the abrupt mechanical properties alteration it entails. Indeed, the material consumption rate suddenly hastens passing from a $\alpha_1 \approx 0.35$ mm/s axial shortening speed to $\alpha_2 \approx 0.98$ mm/s. Such finding would corroborate with an abrupt collapse of the yield stress due to sudden extensive secondary phase dissolution over the processing time. Although hypothetical, the latter hypothesis seems reasonable in regard of the facts.

Eventually, visible light microscopy (Figure 16) completed with meticulous observations by SEM in back-scattered electron mode (Figure 17) highlighted the progressive dissolution of the intergranular δ phase platelets as approaching the weld center zone. A complete absence of interdispersed δ phase particles is notified in a ± 250 µm thick band of microstructure. The latter corresponds to a subsequently grain-refined region of the weld and marks the delimitation between the Zone I and the Zone II (identified in Figure 16). The *equilibrium* δ-*solvus* temperature for the studied IN718 grade is estimated to be within a 1025°C to 1030°C temperature range [79]. Therefore, the temperature values at the vicinity of the interfacial zone reached magnitudes above the δ-*solvus*.

Last, the successive changes of phases through the weld demonstrates a symmetrical aspect going from the center on the weld junction to the unaffected base materials. Therefore, the thermal field that arose during the friction process correspondingly developed the same spatial symmetry as the phase transformations it induced. Besides, the weld center zone experienced the highest temperature values, exceeding the δ phase *transus*. The latter zone also corresponds to the most mechanically solicited region, since heat generation in such processes originates from a plasticity-induced heating phenomenon.

### 6.2 Hot deformation process and plastic flow

At the beginning of the process, thermal energy arises from the frictional interactions between the faying blocks. It progressively yields to substantial temperature elevation in the close surface region. Such tribological conditions concomitantly lead to the collapse of the material yield stress due to thermally induced softening and strengthening precipitates dissolution. From that point of the process, the increasing onset of plastic deformation progressively prevails over the bulk materials until becoming the dominant operating mechanism through the junction. The resulting plastic deformation process is dominated by shear along the oscillating direction and pressure-driven compression along the Z-axis. Besides, the harmonic mechanical load continuously supplied by the welding machine led to a self-regulated plastic flow. Indeed, as plasticity is a highly dissipative process [90], the cyclic motion of the oscillating block sustains the deformation-induced heat source in the center of the junction. The induced thermo-mechanical coupling effects results in a consistent self-regulated response. The linear aspect of the axial shortening Figure 14 translates the latter phenomenon. Hence, the friction welding procedure results in a hot deformation process throughout the junction.

#### 6.2.1 Crystal plasticity and plastic flow

Specific carriers within the crystal lattice, namely the dislocations, mainly cause the plastic deformation in metals. When the load overpasses the flow stress of a crystal, dislocations are pushed over local energy barriers within which they were formerly trapped [5]. While moving, they also bring a small geometrical lattice distortion increment in their wake. The local displacement introduced in the lattice though their passage characterized by a Burgers vector, $\vec{b}$. The latter describes the local displacement introduced within the lattice after a dislocation has passed through it. The accumulation and the interaction of mobile

dislocations within crystals allows accommodating deformation at the grain scale. As a result, the deformed grains change shapes and accumulate lattice rotation to accommodate strain within the polycrystalline structure. In addition, dislocation movements is a thermally activated process meaning that an increase in thermal energy helps dislocations to overcome lattice resistance and facilitates dislocations glide. It gives rise to the emergence of a subsequent macroscopic plastic flow.

### 6.2.2 Specificities of FCC-ordered crystal structure regarding crystal plasticity

The IN718 austenitic phase deprived from secondary phases possesses an FCC crystal structure with a low to intermediate stacking fault energy ($\gamma_{SFE}$). A stacking fault is an interruption in the dense atomic layer stacking sequence. From a fundamental point of view, the stacking fault energy depends on the free electron density distribution within the crystal lattice, which in turn influences the lattice polarity and its bonding properties. The stacking fault energy consequently influences the materials properties at a fundamental level and notably regarding the dynamic of dislocations.

The usual features of crystal plasticity in FCC structures ideally occur by slip on the close-packed planes $\{111\}$, which all contain the $\vec{b} = a/2\,\langle 110\rangle$ with, $\|\vec{b}\| = a/\sqrt{2}$ Burgers vector (dominant slip direction) vector of the lowest energy dislocation. The second best option is $\vec{b} = a\,\langle 100\rangle$ with $\|\vec{b}\| = a$, the latter presents a much higher activation energy comparably to the first option (the slip distance is twice higher!) as a consequence they are generally rarely observed. The main slip system in the FCC crystal lattice is then: $a/2\,\langle \bar{1}10\rangle\{111\}$ with a Burgers vector length of $\|\vec{b}\| = a/\sqrt{2}$. Nevertheless, such perfect glide relationship rarely respects the micromechanical reality in FCC. Indeed, perfect dislocations are dissociated into partial dislocations introducing a stacking fault in the crystal structure.

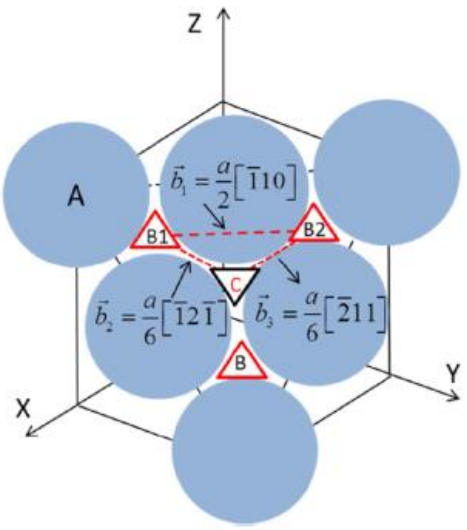


**Figure 34**: *Illustration of the classical Read-Shockley partial dislocation dissociation from* [91].

As an example, the Figure 34 illustrates a $/2\,\langle 1\bar{1}0\rangle\{111\}$ perfect dislocation splitting into two Read-Shockley partials: $\frac{a}{2}[\bar{1}10] = \frac{a}{6}\,[\bar{1}2\bar{1}] + \frac{a}{6}\,[\bar{2}11] + SF$ that glide on the same $(111)$ plane. After dissociation

reaction, a stacking fault ribbon connects the partial dislocations. When moving, the leading partial creates a stacking fault while the trailing one removes it.

The normalized stacking fault energy $\gamma_{SFE/(Gb)}$ controls the average width of the stacking fault ribbon, the smaller is the normalized stacking fault energy, the wider is the dissociation length. With increasing width of dissociation, cross slip of screw dislocations and climb of edge dislocations phenomena become more difficult. Thus, when the stacking fault energy is low perfect dislocations tend to dissociate. Such modifications on the glide properties of dislocations are notably of utmost importance when considering the hot deformation behavior of the IN718 alloy.

### 6.2.3 Consequences on the hot working microstructure of the IN718 alloy

Under hot working conditions, the structural defects accumulating in the austenitic matrix also acquire an increased mobility due to thermal agitation. Furthermore, dislocations do not obey the principles of equilibrium thermodynamics and form a class of metastable defects that are costly from an energetic point of view [92]. Therefore, while deforming, the material is brought far from thermodynamic equilibrium. Such system notably exhibits spontaneous forms of organization that tends to decrease its free energy by getting rid of stored dislocations *via* recovery [93]. The latter process is notably ensured through dislocation annihilation events (happening when dislocations with opposite Burger vector met and annihilate) that are known to be favored by cross-slip. In addition, cross-slip (but also climb) results from the interaction of dislocations with vacancies, as vacancy density exponentially increases with temperature (Arrhenius law), the probability for mutual interactions are statistically favored as temperature increases [5]. Such process is generally said to be thermally activated. Since partial dislocations have a mixed screw and edge character with a stacking fault in between, cross-slip events at high temperature becomes energetically difficult, so that recovery by cross-slip events of screw dislocations are limited in the lattice.

As a result, the dislocation density significantly increases during hot straining of IN718 with only limited recovery in the austenitic phase. Dislocation accumulation combined with high thermal energy give rise to short-range interaction between the cores of adjacent dislocations. Such system proceeds to decrease its free energy by spontaneous self-organization of the structural defects into lower energy metastable configurations. It finally results in dislocations re-arrangement into subgrain boundaries. Such structuration of dislocations into dislocation-walls is notably highlighted on the GND map presented in Figure 23. Dislocation accumulation, and in particular geometrically necessary dislocations (GND), are observed to preferentially develop at grain boundaries region. They accommodate in response to non-uniform straining and the geometrical incompatibilities resulting from the polycrystalline nature of the microstructure [84].

### 6.3 Detailed mechanisms of the grain fragmentation process

The materials response to the thermo-mechanical processing conditions is markedly heterogeneous regarding the position in the joint. Although the temperature reached elevated values exceeding the γ'/γ" *transus* in a ±3.5 mm band of microstructure surrounding the WL, the welded microstructure is only substantially affected on ±2 mm band near the expulsion zone (Z4 profile) and on ±1 mm band at the median position (Z0) (as indicated by the GOS>2° indicator on the map Figure 20). In the TMAZ, orientation gradients are observed to primarily develop in the vicinity of the former parent grain boundaries. Then, while approaching the weld center zone fine structurations forms along the initial grain boundaries and develop typical necklace structures (Figure 21 and 22). Such findings evidence the nucleation of new grain structures originating from previous subgrain structures that formed during the straining process.

Although slip process tends to produce high densities of dislocations on the active slip planes, energy considerations promote relaxation by progressive self-arrangement into grain boundaries by dynamic recovery [94]. The balance between dislocation slips and recovery processes exerts a huge influence on the nature of activated mechanisms accommodating deformation. The latter strongly depend on the rate of straining and the temperature as they control the mobility and the availability of crystal plasticity mechanisms. The nature of the activated deformation mechanisms consequently affects the degree to which the deformed microstructure exhibits crystallographic alignment and whether the arising internal boundaries are diffuse (cell structures) or sharp (subgrain walls) [91].

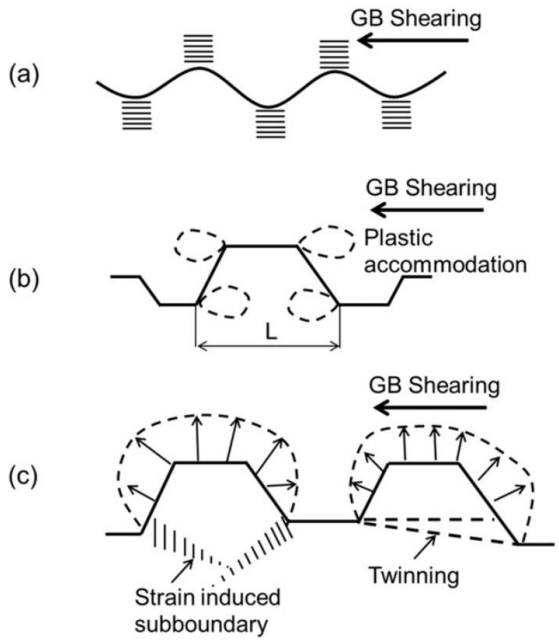


**Figure 35**: *Nucleation of new low-strained crystallites after grain boundary bulging mechanism extracted from* [95]. **(a)** *Boundary corrugation accompanied by the evolution of sub-boundaries.* **(b)** *Partial grain boundary sliding/shearing, leading to the development of inhomogeneous local strains.* **(c)** *Bulging of parts of a serrated grain boundary accompanied with the evolution of dislocation sub-boundaries or twinning, leading to the formation of a new crystallite.*

In such FCC-ordered crystal, planar slip restricted to the compact {111} planes is expected. Hence, the extensive development of planar slip with limited cross-slip events during straining logically lead to the pile-up of dislocations in the grain boundary zones. The observation of sizable internal misorientation gradients near the grain boundary region corroborate with that hypothesis. In addition, the local strain incompatibilities led to the formation of fluctuating grain boundary shapes (see Figure 22). Dislocation patterning near these corrugated boundaries led to the progressive building of low-angle grain boundary (>2° disorientation) that would eventually lead to the nucleation of refined grain structures with high-angle grain boundary (>15° disorientation). Such nucleation events from bulging of boundaries are accompanied by the sweeping of the excess of dislocations within their inner crystal structure due to recovery processes. It finally results in the appearance new low-strained crystallites in the boundary zone of the deforming parent grains.

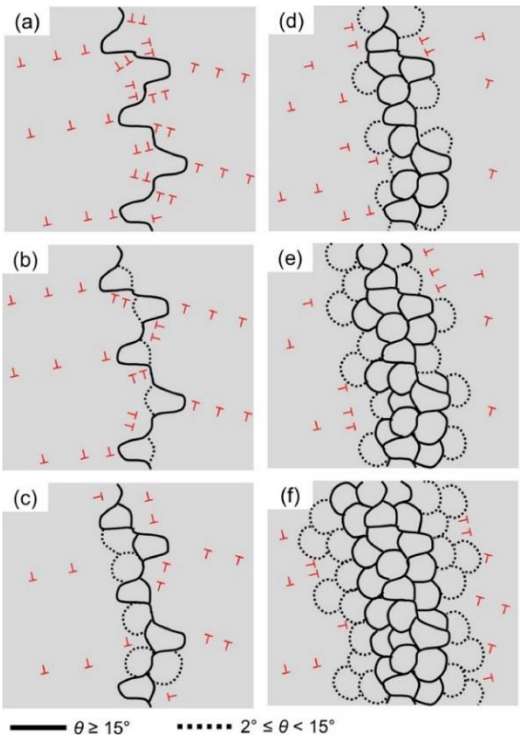


**Figure 36**: *Schematic illustration of necklace grain structures throughout discontinuous dynamic recrystallization (dDRX) during hot deformation process, extracted from* [96]. *The black bold lines indicate high angle grain boundaries (HAGBs) with misorientations (θ), $\theta \geq 15°$, while black dotted lines indicate low angle grain boundaries (LAGBs) with misorientations (θ), $2° \leq \theta < 15°$. Red symbols represent dislocations.* **(a)** *Grain boundary bulging causes activation of various slip systems near some corrugated grain boundaries.* **(b)** R*e-arrangement of dislocation lead to the formation of LAGBs.* **(c, d)** *The formed LAGBs progressively turn into HAGBs with increasing plastic strain, forming the first dDRX necklace layer*. **(e, f)** *New nucleation/rotation cycle by repetition of the process.*

After nucleation, the new-born *nuclei* interact with their surrounding while triggering grain rotation and growth as efficient accommodation mechanisms to overcome the strong local strain incompatibilities [97]. Grain growth arises from strain-induced grain boundary migration, where the difference in stored energy between adjacent crystallites due to local strain heterogeneities is believed to stimulate crystal interfaces motion [98], [99]. Although convincing at the first glance, the exact mechanism responsible for boundary

migration are still subjected to debate in the field [100]. The explanation seems however reasonable from a qualitative point of view. The grain boundary migration is accompanied by the dissociation of incoming lattice dislocations into grain boundary dislocations [101] as accommodating mechanism relaxing stress concentration. Such grain fragmentation process is referred to as a discontinuous dynamic recrystallization (dDRX) [102]. With the progress of deformation, the bulged boundaries eventually change to form equiaxed grain structures decorating the former parent grain boundaries, leading to necklace structures as illustrated in Figure 27.

The fraction of recrystallized grains increases as moving toward the weld center zone until reaching a fully recrystallized state in the middle of the joint (Figure 24). Such features suggest that the dynamic recrystallization phenomenon reached a steady state during the hot deformation process. It resulted in an equiaxed microstructure presenting a fine and homogeneous grain-size distribution on a ±400 µm band (Figure 24 and 26). In addition, the low-internal misorientation gradients corroborate the fact that the operating recrystallization reached its stable dynamic grain size with a saturation value of ~6 µm (grain equivalent diameter). Finally, because of the thermal inertia in the weld center zone, some post-dynamic recrystallization effects are also expected once the oscillation motion stops.

### 6.4 Microhardness / microstructure relationship

The steep fall in hardness at ± 3.5 mm marks the extensive dissolution of the γ' and γ'' strengthening precipitates (Figure 18). A soft plateau extends through the junction zone where the microhardness displays a balanced signal reflecting the competition between work hardening and thermally activated recovery. Indeed, the far thermo-mechanical affected zone first experiences dominating work hardening effects [103], [104] due to dislocation accumulation in the lattice. Then, the significant temperature elevation as approaching the weld center zone yields to the progressive enhancement of recovery processes that increasingly soften the material. A probable additional Hall-Petch strengthening effect is also expected due to extensive grain refinement toward the WL, notably within a ±1.5 mm band of microstructure.

### 6.5 Succinct texture analyses

A weak, however intriguing, {001}<100> cube micro-texture was characterized in the center of the welding zone (Figure 24). A pole figure projection of the ideal orientation is represented in Figure 25. This band of slightly textured microstructure traverses throughout the joint and correspond with the most solicited area of the joint (*id est* subjected to the highest thermo-mechanical loads due to thermo-mechanical coupling effects). Such findings are somewhat surprising since nickel-based alloys are known to substantially randomize recrystallizing microstructure without any preferential orientation selection. Although weak, the texture signal seems reliable and may correspond to a cube recrystallization texture [105].

Lastly, slight FCC simple shear deformation components developed in the deformed microstructure (GOS>2°) near the lateral expulsion zones (see Figure 27 & 28). The shear normal direction corresponds to the compression direction Z whereas the shear direction is aligned with the lateral expulsion direction. These characteristics are consistent with accommodation mechanisms developing from the kinematically admissible plastic flow taking place along the lateral direction. Furthermore, the high-relative proportion of low-to-medium disorientation angle on the spatially correlated misorientation distribution (Figure 27) evidences on-going grain fragmentation

### 6.6 Interface particle formation

As most Ni-based superalloys, the IN718 grade presents a complex element composition. Its chemical composition consists of Ni, Cr, Fe, Ti, Al, Nb, Ta and Mo as main elements, some of which are known to have particularly good chemical affinity with oxygen. Consequently, many different oxidation products are possible. The latter for instance include: NiO(s), $Fe_2O_3$(s), $Cr_2O_3$(s), $Al_2O_3$(s), $TiO_2$(s).

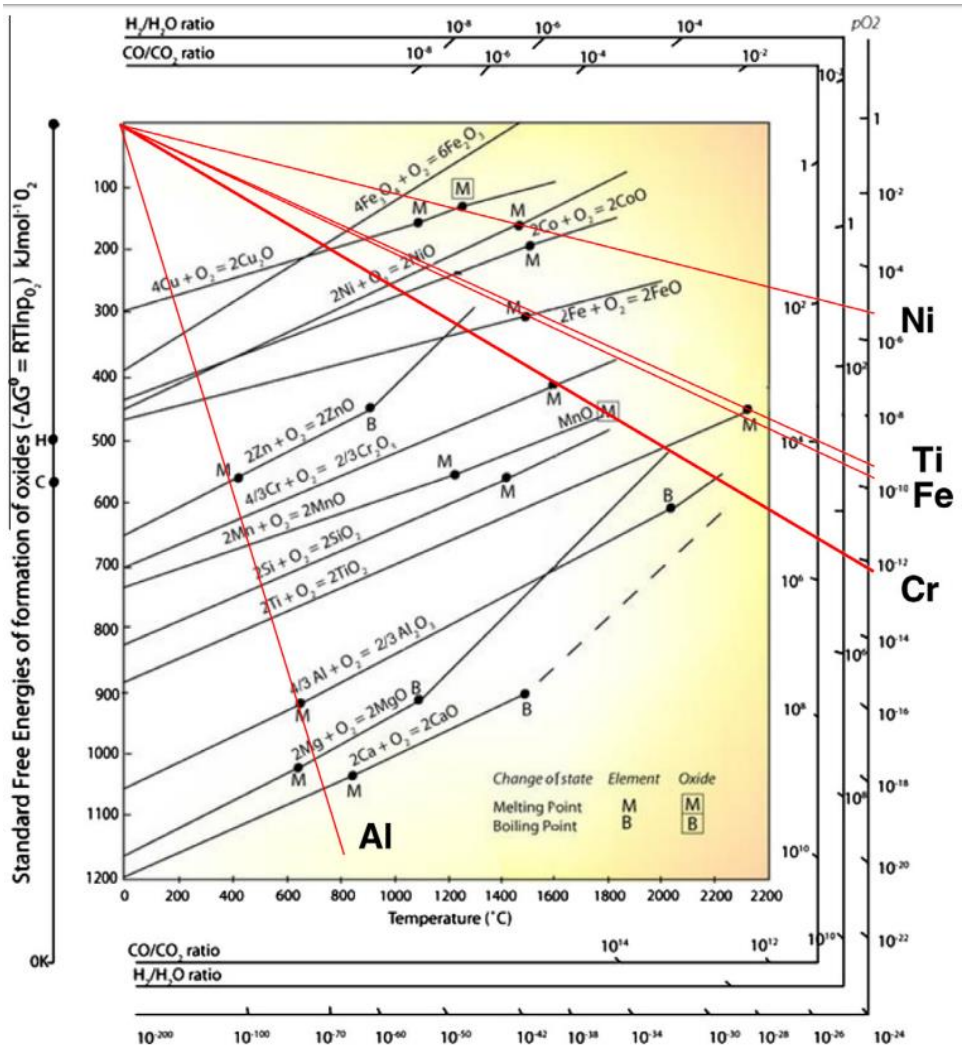


**Figure 37**: *Ellingham diagram extracted from* https://www.doitpoms.ac.uk/tlplib/ellingham_diagrams.

Ellingham diagram illustrates red-ox equilibria, where the standard Gibbs energies of formation of oxides per one mole of gaseous oxygen are represented as a function of temperature. The standard Gibbs energies of formation $\Delta G^0$ must then be negative in order for the oxidation reaction to proceed [106]. Thus, a simple look on an Ellingham diagram (Figure 37) allows qualitatively stating that the affinity of the Al and Ti elements for oxygen are the highest among the alloy element composition as their $\Delta G^0$ are the lowest among the alloys composition elements.

However, in ambient air conditions, the IN718 alloy develops a protective passivation layer made of chromia ($Cr_2O_3$) by selective oxidation of oxygen with chromium [107], two nickel spinel phases ($NiCr_20_4$ and $NiFe_{2-x}Cr_xO_4$, $0 < x < l$) are also reported *via* X-ray diffraction analyses, slight subsurface alumina ($Al_2O_3$) precipitation preferentially along the grain boundary are also reported. Taking into account the previous thermodynamic consideration, the more negative the formation energy of a metal oxide, the more favorable the oxidation of the metal. Thence, Alumina ($Al_2O_3$) would be expected to be the most plausible oxide to form and on the surface of the Ni-based superalloy 718, as it is the most stable possibility. Nevertheless, at ambient temperature, aluminum oxide does not form fast enough in comparison to chromium oxide, when the latter is present is sufficient portion in the alloy. Indeed, from kinetic point of view, the rate of a chemical reaction depends on the concentrations of the reactants and the higher the content of a metal in an alloy, the more favorable the oxidation of the metal. It is the reason why chromia spontaneously forms as a native oxide layer on the surface on IN718 alloy, because kinetically chromia is the primary oxide that forms. Therefore, the coupling effect of the thermodynamics and the kinetics determines which metal oxidizes preferentially in a complex alloy [108].

In the present case, no remnant chromia fragments were found on the post-welded microstructure, but evidences of nano-oxide particles formation composed of Al and Ti were highlighted (Figures 29 to 32). This finding suggests that an internal reaction [109] occurred during the assembling procedure causing the probable reduction of the native surface oxide with the help of elevated temperature condition (estimated at about 1100°C [83], [110]). Meanwhile, it is strongly suspected that the dissociated oxygen ions did not subsist long in solid solution within the crystal lattice and were selectively oxidized by Al and Ti elements. The latter being the strongest reducers available in the γ phase. An internal oxidation phenomenon then arises and yields to the precipitation of the nano-oxide particles observed.

Internal oxidation can occur if the oxygen solubility in the γ phase lattice is high enough and if the diffusion rate of oxygen in the γ phase is faster than the ones of the solute elements [106]. Generally, the diffusion rate is lower than the chemical reaction rate and the diffusion of solute elements and/or oxygen controls the internal oxidation. Thus internal oxidation most often follows a parabolic rate law [111].

Therefore, the hypothesis of rapid chromia dissociation triggering an internal Ti and Al selective oxidation phenomenon seems plausible. Furthermore, similar experimental observations were reported notably on LFWed GH4169 alloy [112] (which more or less correspond to the Chinese standard commercial equivalent

to IN718) or in IN718 powder metallurgy [113], where similar nano-oxidation features appear under comparable thermal loads, then seems to consolidate such hypothesis.

The physical mechanisms in play here are comparable to some extent with the ones on-going in powder metallurgy, notably in isostatic powder compression processes or in the elaboration of Oxide Dispersed Strengthened (ODS) alloys. As an example, some ODS-strengthened steel grades are fabricated by mechanical alloying with $Y_2O_3$ oxide powders. After initial mechanical mixing, the powders are subjected to a hot isostatic compression followed by an annealing stage. Under the latter thermal load, the dispersed $Y_2O_3$ oxide particles are known to decompose in the metallic matrix [114]. The dissolved Y and O elements then spontaneously recombine with transition metals contained in the metallic matrix [115]. The reaction crystallize into complex oxide phases that are favored thermodynamically [116]. For instance, the addition of titanium to ODS streels leads to the formation of fine Y-Ti-O types of oxides [116] (notably the cubic $Y_2Ti_2O_7$, which is the most stable form) dispersed in the austenitic or ferritic matrix (depending on the grade type). The latter bring a strengthening effect *via* dislocations/precipitates interactions in such steel materials [117], while allowing controlling grain size *via* boundary pining.

Lastly, interaction between the dispersed oxide particle with the dynamic recrystallization may have given rise to a particle stimulated nucleation phenomenon [118] in the weld center that may explain the finer grain size statistics in joining zone.

## 7. Conclusion

**(1)** Blocks of IN718 in a Precipitation Hardened (PH) initial metallurgical state were successfully linear friction welded. The temperature elevation across the weld led to extensive dissolution of the γ'/γ" strengthening precipitates within a sharp ±3 mm band of microstructure. It consequently resulted in a significant softening of the material properties in the joint. Besides, a progressive dissolution of the intergranular δ phase was shown with a complete decomposition on ±250 µm band around the weld center zone.

**(2)** The friction welding procedure resulted in a hot working process in the junction zone. The differences in local strain condition and temperature across the junction nobly resulted in a highly heterogeneous microstructure. A discontinuous dynamic recrystallization phenomenon was identified in the joining zone. In the weld center zone, the dynamic recrystallization process reached a steady state leading to a fine equiaxed microstructure with low internal misorientations extending on a ±400 µm band. The corresponding grain equivalent diameter saturation value is of about 6 µm. Then, a partially recrystallized zone consisting of strained parent grain structures alternating with freshly nucleated recrystallized crystallites was highlighted. Nucleation events shrink as moving toward base materials and visibly deformed grains marks the end of the thermo-mechanically affected zone.

**(3)** The global deformation process is roughly comparable to a simple shear deformation process; nonetheless no marked texture components were detected in the joint and the crystal orientations in the deformed or recrystallized grain structures are globally randomized. Only a slight cube texture has been identified in the weld center zone, which also is the most thermo-mechanically solicited region.

**(4)** The lateral material extrusions and the phase changes across the weld revealed a rather symmetrical behavior between the oscillating and the forging parts. The thermo-mechanically affected zone is thicker as approaching the expulsion zones than in the middle of the assembly demonstrating a significant spatial dependence of the process on the strain field.

**(5)** Precipitated nano-oxide particles made of titanium and aluminum were identified in the joining zone. These dispersed weld defects were likely generated *via* selective internal oxidation during the welding procedure. The elevated thermal load presumably yielded to the dissociation of the former native oxide layer, thus providing the excess oxygen in the austenitic matrix for internal oxidation. Lastly, alumina particles notably are extremely stable against solid state treatments, such property may be problematic for further homogenization treatments

## 8. Prospects

Further investigations testing different initial oxidized states (changing the thickness and the nature of the surface oxide phases) would be interesting to carry out. Such approach may bring some information about the influence of the surface oxide on the friction welding process. Notably, the chemical mechanisms involved during the joining process would worth more prospections. Concomitantly, thermodynamic-based modelling of the internal oxidation and kinetics of particle formation would also be interesting to carry out. The decisive influence and evolution of the former surface oxide during these types or weld procedures are often ignored in the current literature despite their crucial importance on the assembling.

The tribological conditions yielding to effective welding in friction assembling processes remain poorly known and difficult to prospects *via* experimental means. Indeed, the complexity and the variety of physical phenomena involved make the elaboration of reliable prediction model particularly harsh. Nevertheless, the experimental butt-weld tests carried out through this work demonstrated that the linear friction technique is robust meaning that same inputs lead to close outcomes in repeatable way. Therefore, wider experimental campaigns testing a greater variety of set of process parameters for a given geometry and surface state may allow achieving a consistent phenomenological law. The latter might help understanding the effect of process parameters on the resulting assembling procedure and guide further modelling developments.

Eventually, it is remarkable that successful weld procedures generally lead to a fully-recrystallized microstructure in the weld center zone that usually displays stationary grain size characteristics (for instance, see Figure 24 for the PH-Centre configuration). The build-up of a Derby diagram that connects the stationary flow-stress as a function of the mean stationary grain-size for different applied normal pressure while keeping constant the oscillating parameters may help understanding the rheological behavior of the material during hot deformation procedure. Such experimental procedure may notably help guiding modelling approaches in such challenging and complex processes.

## 9. References


[1] A. Kracke, « Superalloys, the Most Successful Alloy System of Modern Times-Past, Present, and Future », p. 38.

[2] P. M. Mignanelli *et al.*, « Gamma-gamma prime-gamma double prime dual-superlattice superalloys », *Scripta Materialia*, vol. 136, p. 136‑140, juill. 2017, doi: 10.1016/j.scriptamat.2017.04.029.

[3] R. C. Reed et C. M. F. Rae, « Physical Metallurgy of the Nickel-Based Superalloys », in *Physical Metallurgy*, Elsevier, 2014, p. 2215‑2290.

[4] M. Feidt, « Carnot Cycle and Heat Engine: Fundamentals and Applications », *Entropy*, vol. 22, nº 3, p. 348, mars 2020, doi: 10.3390/e22030348.

[5] D. Caillard et J.-L. Martin, *Thermally activated mechanisms in crystal plasticity*. Amsterdam ; Boston, Mass: Pergamon, 2003.

[6] A. Nowotnik, « Nickel-Based Superalloys », in *Reference Module in Materials Science and Materials Engineering*, Elsevier, 2016, p. B9780128035818025000.

[7] T. Gladman, « Precipitation hardening in metals », *Materials Science and Technology*, vol. 15, nº 1, p. 30‑36, janv. 1999, doi: 10.1179/026708399773002782.

[8] E. A. Loria, « The Status and Prospects of Alloy 718 », *JOM*, vol. 40, nº 7, p. 36‑41, juill. 1988, doi: 10.1007/BF03258149.

[9] J. W. Brooks et P. J. Bridges, « Metallurgical Stability of Inconel Alloy 718 », in *Superalloys 1988 (Sixth International Symposium)*, 1988, p. 33‑42, doi: 10.7449/1988/Superalloys_1988_33_42.

[10] D. Fournier et A. Pineau, « Low cycle fatigue behavior of inconel 718 at 298 K and 823 K », *MTA*, vol. 8, nº 7, p. 1095‑1105, juill. 1977, doi: 10.1007/BF02667395.

[11] Kh. A. Al-hatab, M. A. Al-bukhaiti, U. Krupp, et M. Kantehm, « Cyclic Oxidation Behavior of IN 718 Superalloy in Air at High Temperatures », *Oxid Met*, vol. 75, nº 3‑4, p. 209‑228, avr. 2011, doi: 10.1007/s11085-010-9230-6.

[12] D. F. Paulonis et J. J. Schirra, « Alloy 718 at Pratt & Whitney: Historical Perspective and Future Challenges », in *Superalloys 718, 625, 706 and Various Derivatives (2001)*, 2001, p. 13‑23, doi: 10.7449/2001/Superalloys_2001_13_23.

[13] F. D. Rizzo et J. D. Buzzanell, « Effect of Chemistry Variations on the Structural Stability of Alloy 718 », in *International Symposium on Structural Stability in Superalloys (1968)*, 1968, p. 501‑543, doi: 10.7449/1968/Superalloys_1968_501_543.

[14] R. Cozar, G. Rigaut, et A. Pineau, « Durcissement par precipitation d'un alliage Fe - 30 % Ni - 9 % Ta », *Scripta Metallurgica*, vol. 3, nº 12, p. 883‑886, déc. 1969, doi: 10.1016/0036-9748(69)90234-8.

[15] R. Cozar et A. Pineau, « Influence of coherency strains on precipitate shape in a Fe-Ni-Ta alloy », *Scripta Metallurgica*, vol. 7, nº 8, p. 851‑854, août 1973, doi: 10.1016/0036-9748(73)90277-9.

[16] J. M. Oblak, D. F. Paulonis, et D. S. Duvall, « Coherency strenghthening in Ni base alloys hardened by DO22 γ'' precipitates », *Metallurgical transactions*, vol. 5, p. 143‑153, 1974.

[17] M. Sundararaman, P. Mukhopadhyay, et S. Banerjee, « Deformation behaviour of γ'' strengthened Inconel 718 », *Acta Metallurgica*, vol. 36, nº 4, p. 847‑864, 1988.

[18] M. C. Chaturvedi et Y. Han, « Strengthening mechanisms in Inconel 718 superalloy », *Metal Science*, vol. 17, nº 3, p. 145‑149, mars 1983, doi: 10.1179/030634583790421032.

[19] C. Slama et G. Cizeron, « Étude du comportement structural de l'alliage NC 19 Fe Nb (Inconel 718) », *J. Phys. III France*, vol. 7, nº 3, p. 665‑688, mars 1997, doi: 10.1051/jp3:1997148.

[20] Liu, « Relationship between the lattive constant of γ phase and the content of δ, γ'' and γ' phases in Inconel 718 », *Acta Metallurgica et Materialia*.

[21] R. C. Hall, « The Metallurgy of Alloy 718 », *Journal of Basic Engineering*, p. 511‑516, sept. 1967.

[22] D. F. Paulonis, J. M. Oblak, et D. S. Duvall, « Precipitation in nickel-base alloy 718 », *ASM*, vol. 62, p. 611‑622.

[23] R. Cozar et A. Pineau, « Morphology of γ and γ" precipitates and thermal stability of Inconel 718 type alloys - CEMEF.pdf », *Metallurgical transactions*, vol. 4, p. 47‑59, 1973.

[24] M. Sundararaman, P. Mukhopadhyay, et S. Banerjee, « Some aspects of the precipitation of metastable intermetallic phases in INCONEL 718 », *MTA*, vol. 23, nº 7, p. 2015‑2028, juill. 1992, doi: 10.1007/BF02647549.
[25] M. Sundararaman et P. Mukhopadhyay, « Overlapping of γ'' Precipitate Variants in Inconel 718 », *Materials Characterization*, vol. 31, p. 191‑196, 1993.
[26] B. Dubiel *et al.*, « TEM, HRTEM, electron holography and electron tomography studies of γ′ and γ″ nanoparticles in Inconel 718 superalloy: STUDIES OF γ′ AND γ″ NANOPARTICLES IN INCONEL 718 SUPERALLOY », *Journal of Microscopy*, vol. 236, nº 2, p. 149‑157, nov. 2009, doi: 10.1111/j.1365-2818.2009.03283.x.
[27] W. T. Geng, D. H. Ping, Y. F. Gu, C. Y. Cui, et H. Harada, « Stability of nanoscale co-precipitates in a superalloy: A combined first-principles and atom probe tomography study », *Phys. Rev. B*, vol. 76, nº 22, p. 224102, déc. 2007, doi: 10.1103/PhysRevB.76.224102.
[28] L. Yang, K.-M. Chang, S. Mannan, et J. deBarbadillo, « A New DTA Approach for Verifying Precipitate Solvus in Inconel Alloy 718 », in *Superalloys 718, 625, 706 and Various Derivatives (1997)*, 1997, p. 353‑365, doi: 10.7449/1997/Superalloys_1997_353_365.
[29] R. Lawitzki *et al.*, « Differentiation of γ′- and γ″- precipitates in Inconel 718 by a complementary study with small-angle neutron scattering and analytical microscopy », *Acta Materialia*, vol. 163, p. 28‑39, 2019.
[30] B. H. Kear et J. M. Oblak, « Deformation modes in γ' precipitation hardened nickel-based alloys », *J. Phys. Colloques*, vol. 35, nº C7, p. C7-35-C7-45, déc. 1974, doi: 10.1051/jphyscol:1974702.
[31] B. H. Kear, J. M. Oblak, et A. F. Giamei, « Stacking faults in gamma prime Ni3(Al, Ti) precipitation hardened nickel-base alloys », *Metallurgical Transactions*, vol. 1, p. 2477‑2486, 1970.
[32] V. Paidar, M. Yamagushi, D. P. Pope, et V. Vitek, « Dissociation and core structure of <110> screw dislocations in L12 ordered alloys », *Philosophical Magazine A*, vol. 45, nº 5, p. 883‑894, 1982.
[33] D. P. Pope et S. S. Ezz, « Mechanical properties of Ni3Al and nickel-base alloys with high volume fraction of γ' », *International Metals reviews*, vol. 29, nº 3, p. 136‑167, 1984.
[34] M. C. Chaturvedi et Y. Han, « Effect of particle size on the creep rate of superalloy Inconel 718 », *Materials Science and Engineering*, vol. 89, p. L7‑L10, mai 1987, doi: 10.1016/0025-5416(87)90264-3.
[35] V. A. Vorontsov, C. Shen, Y. Wang, D. Dye, et C. M. F. Rae, « Shearing of γ′ precipitates by a 〈112〉 dislocation ribbons in Ni-base superalloys: A phase field approach », *Acta Materialia*, vol. 58, nº 12, p. 4110‑4119, juill. 2010, doi: 10.1016/j.actamat.2010.03.041.
[36] L. Kovarik *et al.*, « Microtwinning and other shearing mechanisms at intermediate temperatures in Ni-based superalloys », *Progress in Materials Science*, vol. 54, nº 6, p. 839‑873, août 2009, doi: 10.1016/j.pmatsci.2009.03.010.
[37] E. Nembach, « Order strengthening: recent developments, with special reference to aluminium–lithium-alloys », *Progress in Materials Science*, vol. 45, nº 4, p. 275‑338, juill. 2000, doi: 10.1016/S0079-6425(99)00009-2.
[38] R. W. Kozar, A. Suzuki, W. W. Milligan, J. J. Schirra, M. F. Savage, et T. M. Pollock, « Strengthening Mechanisms in Polycrystalline Multimodal Nickel-Base Superalloys », *Metall and Mat Trans A*, vol. 40, nº 7, p. 1588‑1603, juill. 2009, doi: 10.1007/s11661-009-9858-5.
[39] M. Yamaguchi, V. Paidar, D. P. Pope, et V. Vitek, « Dissociation and core structure of 〈110〉 screw dislocations in $L1_2$ ordered alloys I. Core structure in an unstressed crystal », *Philosophical Magazine A*, vol. 45, nº 5, p. 867‑882, mai 1982, doi: 10.1080/01418618208239909.
[40] V. Paidar, D. P. Pope, et V. Vitek, « A theory of the anomalous yield behavior in L12 ordered alloys », *Acta Metallurgica*, vol. 32, nº 3, p. 435‑448, 1984.
[41] M. H. Yoo, « Stability of superdislocations and shear faults in L12 ordered alloys », *Acta Metallurgica*, vol. 35, nº 7, p. 1559‑1569, 1987.
[42] P. B. Hirsch, « A model of the anomalous yield stress for (111) slip in L12 alloys », *Progress in Materials Science*, vol. 36, p. 63‑88, janv. 1992, doi: 10.1016/0079-6425(92)90005-R.
[43] Y. M. Wang-Koh, « Understanding the yield behaviour of $L1_2$ -ordered alloys », *Materials Science and Technology*, vol. 33, nº 8, p. 934‑943, mai 2017, doi: 10.1080/02670836.2016.1215961.

[44] P. J. Phillips *et al.*, « Nano *γ′⁄γ ″* composite precipitates in Alloy 718 », *Appl. Phys. Lett.*, vol. 100, nº 21, p. 211913, mai 2012, doi: 10.1063/1.4721456.
[45] R. Shi *et al.*, « Growth behavior of γ ’ / γ ’ ’ coprecipitates in Ni-Base superalloys », *Acta Materialia*, vol. 164, p. 220‑236, févr. 2019, doi: 10.1016/j.actamat.2018.10.028.
[46] E. Anisimov, A. K. Khan, et O. A. Ojo, « Analysis of microstructure in electro-spark deposited IN718 superalloy », *Materials Characterization*, vol. 119, p. 233 ‑ 240, sept. 2016, doi: 10.1016/j.matchar.2016.07.025.
[47] R. Shi *et al.*, « Growth behavior of γ ’ / γ ’ ’ coprecipitates in Ni-Base superalloys », *Acta Materialia*, vol. 164, p. 220‑236, févr. 2019, doi: 10.1016/j.actamat.2018.10.028.
[48] M. Sundararaman, J. B. Singh, et P. Mukhopadhyay, « Estimation of order strengthening in Inconel 718 type alloys containing all γ’’ precipitate variants », *Scripta Metallurgica et Materialia*, vol. 29, p. 557‑562, 1993.
[49] D. McAllister, D. Lv, B. Peterson, H. Deutchman, Y. Wang, et M. J. Mills, « Lower temperature deformation mechanisms in a γ″-strengthened Ni-base superalloy », *Scripta Materialia*, vol. 115, p. 108‑112, avr. 2016, doi: 10.1016/j.scriptamat.2015.11.026.
[50] D. C. Lv, D. McAllister, M. J. Mills, et Y. Wang, « Deformation mechanisms of D022 ordered intermetallic phase in superalloys », *Acta Materialia*, vol. 118, p. 350 ‑ 361, oct. 2016, doi: 10.1016/j.actamat.2016.07.055.
[51] D. McAllister *et al.*, « Characterization and Modeling of Deformation Mechanisms in Ni-Base Superalloy 718 », in *Proceedings of the 9th International Symposium on Superalloy 718 & Derivatives: Energy, Aerospace, and Industrial Applications*, E. Ott, X. Liu, J. Andersson, Z. Bi, K. Bockenstedt, I. Dempster, J. Groh, K. Heck, P. Jablonski, M. Kaplan, D. Nagahama, et C. Sudbrack, Éd. Cham: Springer International Publishing, 2018, p. 319‑338.
[52] F. Theska, S. P. Ringer, et S. Primig, « Atom Probe Microscopy of Strengthening Effects in Alloy 718 », *Microsc Microanal*, vol. 25, nº 2, p. 470‑480, avr. 2019, doi: 10.1017/S1431927618015611.
[53] Y. Ji *et al.*, « Predicting Coherency Loss of $$ \gamma^{\prime\prime} $$ γ ″ Precipitates in IN718 Superalloy », *Metall and Mat Trans A*, vol. 47, nº 6, p. 3235‑3247, juin 2016, doi: 10.1007/s11661-016-3480-0.
[54] S. Azadian, L.-Y. Wei, et R. Warren, « Delta phase precipitation in Inconel 718 », *Materials Characterization*, vol. 53, nº 1, p. 7‑16, sept. 2004, doi: 10.1016/j.matchar.2004.07.004.
[55] J. F. Barker, E. W. Ross, et J. F. Radavich, « Long Time Stability Of Inconel 718 », *JOM*, vol. 22, nº 1, p. 31‑41, janv. 1970, doi: 10.1007/BF03355624.
[56] A. Mitchell, A. J. Schmalz, C. Schvezov, et S. L. Cockroft, « The Precipitation of Primary Carbides in Alloy 718 », in *Superalloys 718, 625, 706 and Various Derivatives (1994)*, 1994, p. 65‑78, doi: 10.7449/1994/Superalloys_1994_65_78.
[57] M. Sundararaman, P. Mukhopadhyay, et S. Banerjee, « Carbide Precipitation in Nickel Base Superalloys 718 and 625 and Their Effect on Mechanical Properties », in *Superalloys 718, 625, 706 and Various Derivatives (1997)*, 1997, p. 367‑378, doi: 10.7449/1997/Superalloys_1997_367_378.
[58] J. S. Slaney, « A General Method for the Prediction of Precipitate Compositions », in *International Symposium on Structural Stability in Superalloys (1968)*, 1968, p. 67 ‑ 79, doi: 10.7449/1968/Superalloys_1968_67_79.
[59] H. M. Lalvani et J. W. Brooks, « Hot Forging of IN718 with Solution-Treated and Delta-Containing Initial Microstructures », *Metallogr. Microstruct. Anal.*, vol. 5, nº 5, p. 392‑401, oct. 2016, doi: 10.1007/s13632-016-0299-4.
[60] M. Zouari, R. E. Loge, O. Beltran, S. Rousselle, et N. Bozzolo, « Multipass forging of Inconel 718 in the delta-Supersolvus domain: assessing and modeling microstructure evolution », *MATEC Web of Conferences*, vol. 14, p. 12001, 2014, doi: 10.1051/matecconf/20141412001.
[61] F. Theska, A. Stanojevic, B. Oberwinkler, S. P. Ringer, et S. Primig, « On conventional versus direct ageing of Alloy 718 », *Acta Materialia*, vol. 156, p. 116 ‑ 124, sept. 2018, doi: 10.1016/j.actamat.2018.06.034.
[62] A. M. Hall et H. J. Wagner, « Physical metallurgy of alloy 718 », Defense metals information center, Columbus, DMIC Report 217, juin 1965.

[63] O. T. Ola, O. A. Ojo, P. Wanjara, et M. C. Chaturvedi, « Analysis of Microstructural Changes Induced by Linear Friction Welding in a Nickel-Base Superalloy », *Metall and Mat Trans A*, vol. 42, nº 12, p. 3761‑3777, déc. 2011, doi: 10.1007/s11661-011-0774-0.
[64] A. Chamanfar, M. Jahazi, J. Gholipour, P. Wanjara, et S. Yue, « Mechanical Property and Microstructure of Linear Friction Welded WASPALOY », *Metall and Mat Trans A*, vol. 42, nº 3, p. 729‑744, mars 2011, doi: 10.1007/s11661-010-0457-2.
[65] A. Chamanfar, M. Jahazi, J. Gholipour, P. Wanjara, et S. Yue, « Analysis of integrity and microstructure of linear friction welded Waspaloy », *Materials Characterization*, vol. 104, p. 149‑161, juin 2015, doi: 10.1016/j.matchar.2015.04.011.
[66] O. T. Ola, O. A. Ojo, P. Wanjara, et M. C. Chaturvedi, « Enhanced resistance to weld cracking by strain-induced rapid solidification during linear friction welding », *Philosophical Magazine Letters*, vol. 91, nº 2, p. 140‑149, févr. 2011, doi: 10.1080/09500839.2010.541164.
[67] M. Y. Amegadzie, O. T. Ola, O. A. Ojo, P. Wanjara, et Mc. Chaturvedi, « On Liquation and Liquid Phase Oxidation during Linear Friction Welding of Nickel-Base IN738 and CMSX Superalloys », in *Superalloys 2012*, E. S. Huron, R. C. Reed, M. C. Hardy, M. J. Mills, R. E. Montero, P. D. Portella, et J. Telesman, Éd. Hoboken, NJ, USA: John Wiley & Sons, Inc., 2012, p. 587‑594.
[68] F. Masoumi, D. Shahriari, M. Jahazi, J. Cormier, et B. C. D. Flipo, « On the Occurrence of Liquation During Linear Friction Welding of Ni-Based Superalloys », *Metall and Mat Trans A*, vol. 48, nº 6, p. 2886‑2899, juin 2017, doi: 10.1007/s11661-017-4067-0.
[69] A. Chamanfar, M. Jahazi, et J. Cormier, « A Review on Inertia and Linear Friction Welding of Ni-Based Superalloys », *Metall and Mat Trans A*, vol. 46, nº 4, p. 1639‑1669, avr. 2015, doi: 10.1007/s11661-015-2752-4.
[70] O. N. Senkov, D. W. Mahaffey, S. L. Semiatin, et C. Woodward, « Inertia Friction Welding of Dissimilar Superalloys Mar-M247 and LSHR », *Metall and Mat Trans A*, vol. 45, nº 12, p. 5545‑5561, nov. 2014, doi: 10.1007/s11661-014-2512-x.
[71] O. N. Senkov, D. W. Mahaffey, S. L. Semiatin, et C. Woodward, « Site-Dependent Tension Properties of Inertia Friction-Welded Joints Made From Dissimilar Ni-based Superalloys », *J. of Materi Eng and Perform*, vol. 24, nº 3, p. 1173‑1184, mars 2015, doi: 10.1007/s11665-014-1379-8.
[72] D. W. Mahaffey, O. N. Senkov, R. Shivpuri, et S. L. Semiatin, « Effect of Process Variables on the Inertia Friction Welding of Superalloys LSHR and Mar-M247 », *Metall and Mat Trans A*, vol. 47, nº 8, p. 3981‑4000, août 2016, doi: 10.1007/s11661-016-3600-x.
[73] R. Damodaram, S. G. S. Raman, et K. P. Rao, « Microstructure and mechanical properties of friction welded alloy 718 », *Materials Science and Engineering: A*, vol. 560, p. 781‑786, janv. 2013, doi: 10.1016/j.msea.2012.10.035.
[74] R. Damodaram, S. Ganesh Sundara Raman, et K. Prasad Rao, « Effect of post-weld heat treatments on microstructure and mechanical properties of friction welded alloy 718 joints », *Materials & Design*, vol. 53, p. 954‑961, janv. 2014, doi: 10.1016/j.matdes.2013.07.091.
[75] C. Mary et M. Jahazi, « Linear Friction Welding of IN-718 Process Optimization and Microstructure Evolution », *AMR*, vol. 15‑17, p. 357‑362, févr. 2006, doi: 10.4028/www.scientific.net/AMR.15-17.357.
[76] C. Mary et M. Jahazi, « Multi-Scale Analysis of IN-718 Microstructure Evolution During Linear Friction Welding », *Adv. Eng. Mater.*, vol. 10, nº 6, p. 573‑578, juin 2008, doi: 10.1002/adem.200700361.
[77] M. Smith, J.-B. Levesque, L. Bichler, D. Sediako, J. Gholipour, et P. Wanjara, « Residual stress analysis in linear friction welded in-service Inconel 718 superalloy via neutron diffraction and contour method approaches », *Materials Science and Engineering: A*, vol. 691, p. 168‑179, avr. 2017, doi: 10.1016/j.msea.2017.03.038.
[78] F. Bachmann, R. Hielscher, et H. Schaeben, « Texture Analysis with MTEX – Free and Open Source Software Toolbox », *Solid State Phenomena*, vol. 160, p. 63‑68, févr. 2010, doi: 10.4028/www.scientific.net/SSP.160.63.
[79] S. Azadian, L.-Y. Wei, et R. Warren, « Delta phase precipitation in Inconel 718 », *Materials Characterization*, vol. 53, nº 1, p. 7‑16, sept. 2004, doi: 10.1016/j.matchar.2004.07.004.

[80] P. J. P. Kañetas, L. A. R. Osorio, M. P. G. Mata, M. D. L. Garza, et V. P. López, « Influence of the Delta Phase in the Microstructure of the Inconel 718 subjected to “Delta-processing” Heat Treatment and Hot Deformed », *Procedia Materials Science*, vol. 8, p. 1160‑1165, 2015, doi: 10.1016/j.mspro.2015.04.180.
[81] V. Horálek, « ASTM grain-size model and related random tessellation models », *Materials Characterization*, vol. 25, nº 3, p. 263‑284, oct. 1990, doi: 10.1016/1044-5803(90)90057-Q.
[82] H. Bunge, *Texture analysis in materials science: mathematical methods*. London: Butterworths, 1982.
[83] C. Mary et M. Jahazi, « Linear Friction Welding of IN-718 Process Optimization and Microstructure Evolution », *Advanced Materials Research*, vol. 15 ‑ 17, p. 357 ‑ 362, févr. 2006, doi: 10.4028/www.scientific.net/AMR.15-17.357.
[84] A. Arsenlis et D. M. Parks, « Crystallographic aspects of geometrically-necessary and statistically-stored dislocation density », *Acta Materialia*, vol. 47, nº 5, p. 1597‑1611, mars 1999, doi: 10.1016/S1359-6454(99)00020-8.
[85] P. J. Konijnenberg, S. Zaefferer, et D. Raabe, « Assessment of geometrically necessary dislocation levels derived by 3D EBSD », *Acta Materialia*, vol. 99, p. 402 ‑ 414, oct. 2015, doi: 10.1016/j.actamat.2015.06.051.
[86] J. F. Nye, « Some geometrical relations in dislocated crystals », *Acta Metallurgica*, vol. 1, nº 2, p. 153‑162, mars 1953, doi: 10.1016/0001-6160(53)90054-6.
[87] A. Seret, C. Moussa, M. Bernacki, J. Signorelli, et N. Bozzolo, « Estimation of geometrically necessary dislocation density from filtered EBSD data by a local linear adaptation of smoothing splines », *J Appl Crystallogr*, vol. 52, nº 3, p. 548‑563, juin 2019, doi: 10.1107/S1600576719004035.
[88] W. Pantleon, « Resolving the geometrically necessary dislocation content by conventional electron backscattering diffraction », *Scripta Materialia*, vol. 58, nº 11, p. 994 ‑ 997, juin 2008, doi: 10.1016/j.scriptamat.2008.01.050.
[89] A. Niang, « Contribution à l’étude de la précipitation des phases intermétalliques dans l’alliage 718 », p. 158.
[90] A. Zubelewicz, « Century-long Taylor-Quinney interpretation of plasticity-induced heating reexamined », *Sci Rep*, vol. 9, nº 1, p. 9088, déc. 2019, doi: 10.1038/s41598-019-45533-0.
[91] K. Huang et R. E. Logé, « A review of dynamic recrystallization phenomena in metallic materials », *Materials & Design*, vol. 111, p. 548‑574, déc. 2016, doi: 10.1016/j.matdes.2016.09.012.
[92] D. Weygand, Y. Brechett, et J. Lépinoux, « On the nucleation of recrystallization by a bulging mechanism: A two-dimensional vertex simulation », *Philosophical Magazine B*, vol. 80, nº 11, p. 1987‑1996, nov. 2000, doi: 10.1080/13642810008216521.
[93] J. Humphreys, G. S. Rohrer, et A. D. Rollett, *Recrystallization and related annealing phenomena*, Third Edition. Elsevier, 2017.
[94] T. Sakai, A. Belyakov, R. Kaibyshev, H. Miura, et J. J. Jonas, « Dynamic and post-dynamic recrystallization under hot, cold and severe plastic deformation conditions », *Progress in Materials Science*, vol. 60, p. 130‑207, mars 2014, doi: 10.1016/j.pmatsci.2013.09.002.
[95] A. M. Wusatowska-Sarnek, H. Miura, et T. Sakai, « Nucleation and microtexture development under dynamic recrystallization of copper », *Materials Science and Engineering: A*, vol. 323, nº 1‑2, p. 177‑186, janv. 2002, doi: 10.1016/S0921-5093(01)01336-3.
[96] R. R. Eleti, A. H. Chokshi, A. Shibata, et N. Tsuji, « Unique high-temperature deformation dominated by grain boundary sliding in heterogeneous necklace structure formed by dynamic recrystallization in HfNbTaTiZr BCC refractory high entropy alloy », *Acta Materialia*, vol. 183, p. 64‑77, janv. 2020, doi: 10.1016/j.actamat.2019.11.001.
[97] M. Upmanyu, D. J. Srolovitz, A. E. Lobkovsky, J. A. Warren, et W. C. Carter, « Simultaneous grain boundary migration and grain rotation », *Acta Materialia*, vol. 54, nº 7, p. 1707‑1719, avr. 2006, doi: 10.1016/j.actamat.2005.11.036.
[98] H. Gleiter, « Theory of grain boundary migration rate », *Acta Metallurgica*, vol. 17, nº 7, p. 853‑862, juill. 1969, doi: 10.1016/0001-6160(69)90105-9.
[99] H. Miura, T. Sakai, R. Mogawa, et G. Gottstein, « Nucleation of dynamic recrystallization at grain boundaries in copper bicrystals », *Scripta Materialia*, vol. 51, nº 7, p. 671 ‑ 675, oct. 2004, doi: 10.1016/j.scriptamat.2004.06.015.

[100] H.-W. Son, J.-W. Lee, et S.-K. Hyun, « Mechanism of grain boundary serration during hot deformation of AZ31 alloy: Role of grain boundary dislocations and grain boundary sliding », *International Journal of Plasticity*, vol. 125, p. 118‑132, févr. 2020, doi: 10.1016/j.ijplas.2019.09.003.
[101] D. A. Smith, « Interaction of dislocations with grains boundaries », *J. Phys. Colloques*, vol. 43, nº C6, p. C6-225-C6-237, déc. 1982, doi: 10.1051/jphyscol:1982621.
[102] F. Montheillet, O. Lurdos, et G. Damamme, « A grain scale approach for modeling steady-state discontinuous dynamic recrystallization », *Acta Materialia*, vol. 57, nº 5, p. 1602‑1612, mars 2009, doi: 10.1016/j.actamat.2008.11.044.
[103] U. F. Kocks et H. Mecking, « Physics and phenomenology of strain hardening: the FCC case », *Progress in Materials Science*, vol. 48, nº 3, p. 171‑273, janv. 2003, doi: 10.1016/S0079-6425(02)00003-8.
[104] R. B. Sills, N. Bertin, A. Aghaei, et W. Cai, « Dislocation Networks and the Microstructural Origin of Strain Hardening », *Phys. Rev. Lett.*, vol. 121, nº 8, p. 085501, août 2018, doi: 10.1103/PhysRevLett.121.085501.
[105] I. Samajdar et R. D. Doherty, « Cube recrystallization texture in warm deformed aluminum: understanding and prediction », *Acta Materialia*, vol. 46, nº 9, p. 3145‑3158, mai 1998, doi: 10.1016/S1359-6454(97)00492-8.
[106] N. Birks, G. H. Meier, et F. S. Pettit, *Introduction to the high temperature oxidation of metals*. .
[107] M. Lenglet, R. Guillamet, J. Lopitaux, et B. Hannoyer, « Caracterisation des premieres etapes de l'oxydation de l'alliage inconel 718 par spectrometrie I.R.F.T. », *Materials Research Bulletin*, vol. 25, nº 6, p. 715‑722, juin 1990, doi: 10.1016/0025-5408(90)90199-C.
[108] « Constrained Growth of Creep Cavities », in *High Temperature Deformation and Fracture of Materials*, Elsevier, 2010, p. 230‑238.
[109] R. A. Rapp, « Kinetics, microstructure and mechanisms of internal oxidation its effect and prevention in HT alloy oxidation », *Corrosion*, vol. 21, p. 382‑401, déc. 1965.
[110] S. Okeke, N. Harrison, et M. Tong, « Thermomechanical modelling for the linear friction welding process of Ni-based superalloy and verification », *Proceedings of the Institution of Mechanical Engineers, Part L: Journal of Materials: Design and Applications*, vol. 234, nº 5, p. 796‑815, mai 2020, doi: 10.1177/1464420719900780.
[111] « Constrained Growth of Creep Cavities », in *High Temperature Deformation and Fracture of Materials*, Elsevier, 2010, p. 230‑238.
[112] P. Geng, G. Qin, T. Li, J. Zhou, Z. Zou, et F. Yang, « Microstructural characterization and mechanical property of GH4169 superalloy joints obtained by linear friction welding », *Journal of Manufacturing Processes*, vol. 45, p. 100‑114, sept. 2019, doi: 10.1016/j.jmapro.2019.06.032.
[113] Y. N. Zhang, X. Cao, P. Wanjara, et M. Medraj, « Oxide films in laser additive manufactured Inconel 718 », *Acta Materialia*, vol. 61, nº 17, p. 6562‑6576, oct. 2013, doi: 10.1016/j.actamat.2013.07.039.
[114] M. Brocq, B. Radiguet, J.-M. Le Breton, F. Cuvilly, P. Pareige, et F. Legendre, « Nanoscale characterisation and clustering mechanism in an Fe–Y2O3 model ODS alloy processed by reactive ball milling and annealing », *Acta Materialia*, vol. 58, nº 5, p. 1806‑1814, mars 2010, doi: 10.1016/j.actamat.2009.11.022.
[115] H. Kishimoto, R. Kasada, O. Hashitomi, et A. Kimura, « Stability of Y–Ti complex oxides in Fe–16Cr–0.1Ti ODS ferritic steel before and after heavy-ion irradiation », *Journal of Nuclear Materials*, vol. 386‑388, p. 533‑536, avr. 2009, doi: 10.1016/j.jnucmat.2008.12.169.
[116] S. Yamashita *, S. Ohtsuka, N. Akasaka, S. Ukai, et S. Ohnuki, « Formation of nanoscale complex oxide particles in mechanically alloyed ferritic steel », *Philosophical Magazine Letters*, vol. 84, nº 8, p. 525‑529, juill. 2004, doi: 10.1080/09500830412331303609.
[117] A. Chauhan *et al.*, « Microstructure characterization and strengthening mechanisms of oxide dispersion strengthened (ODS) Fe-9%Cr and Fe-14%Cr extruded bars », *Journal of Nuclear Materials*, vol. 495, p. 6‑19, nov. 2017, doi: 10.1016/j.jnucmat.2017.07.060.
[118] J. D. Robson, D. T. Henry, et B. Davis, « Particle effects on recrystallization in magnesium–manganese alloys: Particle-stimulated nucleation », *Acta Materialia*, vol. 57, nº 9, p. 2739‑2747, mai 2009, doi: 10.1016/j.actamat.2009.02.032.

# Chapter IV

## Microstructural characterization of an IN718 weld - SA state

### *Parameter prospection toward the welding of the solution annealed IN718 state*

### Background

The possibility to assemble IN718 alloy blocks under a precipitation hardened metallurgical starting state was explored throughout the previous chapter. A consistent window of parameters has been determined for the considered: (1) 10 x 80 mm² rectangular contacting surface geometry, with (2) a 120p grit paper polished initial state of surface (which correspond to a 125 µm average particle diameter for the abrading particles). Among the tested sets of parameters for the precipitation hardened metallurgical state, the 'Centre' configuration: **270 MPa** of forging pressure, **1 mm** of friction amplitude at a **50 Hz** frequency stood out by its ability to reach the 3 mm targeted axial shortening value with the shortest friction processing time. This 'Centre' friction welding conditions was consequently chosen as a 'reference' set of parameters; because it led to the most-efficient rate of deformation-induced plastic flow of matter in order to reach the aimed axial-shortening value of 3 mm in height. This, only considering the tested sets of parameters carried out during the experimental procedures.

Nevertheless, the thermomechanical conditions induced by the friction welding process notably led to an unavoidable and extensive dissolution of the γ"/γ' strengthening precipitates within the joining zone resulting in an inoperable assembling in such As-Welded (AW) state. Indeed, the local softening induced by the process harshly deteriorate the resulting mechanical properties of such joint making it unusable for any practical engineering application. To do so, an integral re-precipitation heat treatment strategy must be carried out in order to re-form these essential strengthening phase and obtain an operating joint.

Consequently, it would be interesting to explore the possibility to weld the IN718 superalloy in a starting solution annealed (SA) condition (*id est* without γ"/γ' strengthening precipitates in the initial microstructure) in order to save a useless precipitation strengthening heat treatment prior the linear friction welding procedure. **The claimed objective here is to prospect for new sets of parameters that would allow the joining of solution annealed IN718 workpieces by linear friction welding. Then, this work will also aim to characterize the resulting microstructures of the viable obtained configurations and compare them with the results obtained on the precipitation hardened configuration.**

## 1. Introduction and parameter prospection method

In this part of the work, a basic prospection for a set of parameters allowing the solid state assembling of IN718 blocks in a solution annealed (SA) metallurgical state. Similarly to the previous work done on the precipitation hardened configuration, the extracted specimens were linear friction welded following the same procedure described in the previous chapter. The weld surface dimensions are still: 10 x 80 mm² and the oscillation direction still correspond with the $\langle x \rangle$ direction (largest edge dimension of the parallelepipedic block).

### 1.1 Friction assembling process, first step and basic observations

Before the welding procedure, the raw assembling surfaces, which underwent marked surface oxidation originating from the electrical discharge (EDM) cutting process, were manually polished by means of P120 grade SiC grinding paper in order to remove the polluted oxidized layer and avoid perturbations and limit adverse effects during the frictional procedure. The declared objective was also to control the surface characteristics at least in term of chemical composition as this parameter is mostly suspected to have a huge influence on the frictional behavior and the initiation step of the process*. The key point here was to apply the friction welding procedure on IN718 surfaces presenting their native passivation layer under standard conditions of temperature and pressure, and under an ambient atmosphere.

As a first step, an intuitive hypothesis would suggest to use the 'PH-Centre' set of parameters that led to successful frictional condition and robust workpieces assemblies. The set of parameters is recalled in the following table:

| Parameters (Units) | Pressure (MPa) | Frequency (Hz) | Amplitude (mm) | Axial shortening, measured (mm) | Total oscillations duration (s) | |
|---|---|---|---|---|---|---|
| **Try 1** | 270 | 50 | 1 | **0** | 15 (limit time) | No weld |

**Table 1**: *Step 1, initial set of process parameters.*

Paradoxically, no weld occurred under these processing conditions. Only little marks of local adhesion then bond breaks and matting are discernable on the contacting surfaces of the workpieces (see Figure 1). The contact surfaces remained globally unaffected and the matting traces were probably caused by the vibrational shocks induced by the alternate frictional motion during the process. Also, no traces of mutual adhesion, material exchange or important frictional heating were observed (no evidence of coloration due to material oxidization which usually are classical features in such processes).

These observations suggest that the processing condition did not lead to an extensive conversion of the mechanical energy supplied by the friction-welding machine into thermal energy during the alternate sliding motion. Consequently, the process remained closed to a low-friction gliding motion sequence, with only little frictional interactions between the contacting surfaces that did not lead to extensive softening of the in-contact materials due to a subsequent temperature elevation in the junction zone.

In addition, the noisy and chaotic vibrational behavior qualitatively observed during the frictional process suggest that the selected set of parameters led to an unstable.

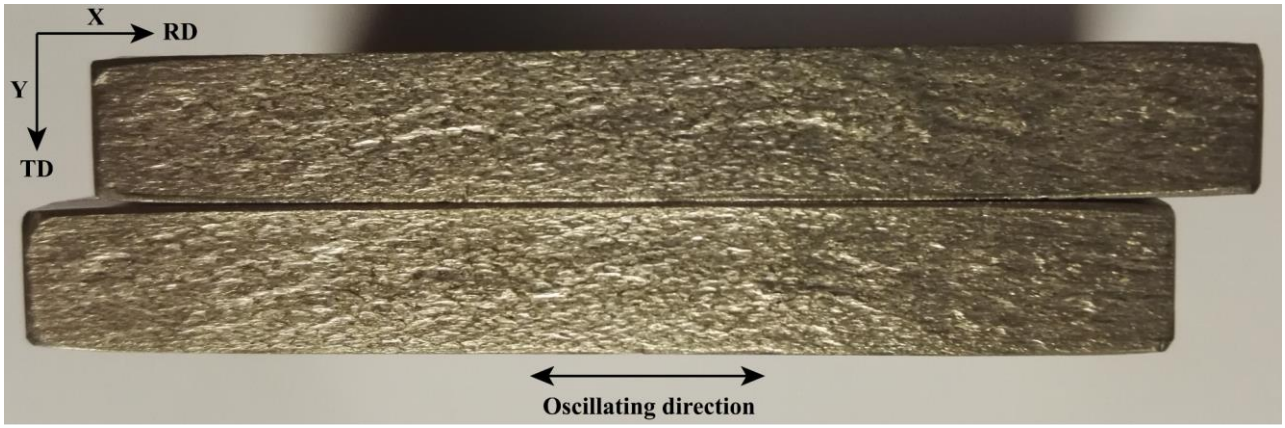


**Figure 1**: *Photograph of the matting surfaces after the assembling, 'try 1' set of parameters.*

The objective is now to try to find a set of parameters allowing to fulfill the following conditions: (1) obtain frictional heating conditions during the initiation stage of the process that would lead to an adhesive bond of the in-contact surfaces; (2) obtain hot deformation conditions in the joining zone that would allow a progressive axial shortening by the appearance of plasticized lateral expulsion flashes; (3) reach the standard set axial shortening condition of 3 mm or at least to approach it.

---

*The influence of the electrical discharge oxidized surface condition on resulting behavior of the solution annealed IN718 during the friction welding procedure had indirectly been verified along the project. Indeed, contrary to the surface grinded IN718 blocks, EDM surface oxidized blocks were successfully linear friction welded under these parameters *id est* a forging pressure of 270 MPa, an oscillation amplitude of 1 mm and a 50 Hz oscillation frequency.

**The results notably demonstrated a drastic influence of the chemical nature of the close contacting surfaces on the frictional behavior of the processed solution annealed IN718 alloy (notably during the initiation stage of the process). However, these results, although interesting, also poses serious methodological issues by the lack of scientific rigor that they implied: the exact chemical nature of the contaminated layer is uncontrolled and difficult to characterize, furthermore, such assembling procedure has only little interest regarding the in-use applicability. The reader is referred to the associated supplementary materials summing up the results obtained on that peculiar configuration.

### 1.2 Experimental prospection of assembling parameters for the solution annealed state

Now that the targeted requirements are specified, it is still necessary to find a set of process parameters that would lead to the solid-state welding of the SA-IN718 workpieces. The results determined on the linear

friction welding procedures applied on titanium alloys and on the precipitation hardened IN718 configuration demonstrated the importance of hot deformation induced phenomena for the establishment of the cohesive joining between the rubbing workpieces. These results notably highlighted the predominant role of high temperature deformation induced mechanisms in the cohesive bond formation in linear friction welding. Therefore, it is important to devote a specific attention on the process parameter conditions that would lead to efficient high temperature deformation condition in the joining interface. Thence, a first particular attention will be given to the frictional conditions that would allow initiating the local plasticization of the sliding materials in the vicinity of the contacting zone induced by an extensive thermal softening of the materials.

Indeed, while it appears obvious that the tribological behavior of the contacting materials presents major effects during the initiation stage of such friction welding process, the qualitative evaluation of their associate parameters would necessary imply a solid and considerable experimental coverage. This, in order to potentially achieve a phenomenological understanding of the initiation stage. Even though highly interesting, this type of approach is not in the scope of the work exposed here. However, it is important to keep in mind some classical conceptions coming from the tribological field in the process parameter prospecting approach. Indeed, contrary to most of the galling and wear problematic in usual engineering applications, the objective in friction assembling processes is to optimize the frictional conditions that would generate a global seizure effect in the joining zone [1].

In order to reduce the potential influence of the roughness properties of the contacting surfaces on the resulting frictional behavior, a simple polishing procedure was applied by the use of 120p grade SiC grinding paper (125 µm average particle diameter for the abrading particles). A medium grade was chosen to mimic starting surface roughness characteristics close to a post-machined state. Even if it does not take into account the complementary morphological parameters of roughness, this procedure allowed to grossly standardize the initial surface in term of global roughness characteristics and also in term of sub-surface chemical composition. The initial superficial oxidized layer of the SA-IN718 rubbing blocks is then composed of the passive that quasi-instantly develops under ambient air exposure and under standard conditions of temperature and pressure.

The significant and chaotic vibratory response during the ‘try 1’ suggested that the set forging pressure was too elevated and conducted to an instable motion behavior thus limiting the sliding contact interactions between the workpieces. Moreover, knowing that the solution annealed metallurgical state of IN718 is much softer that its classical precipitation strengthened one, it has been decided to downgrade the processing parameters to set starting values close to the one determined for titanium alloys as described in the chapter II:

| Parameters (Units) | Pressure (MPa) | Frequency (Hz) | Amplitude (mm) | Axial shortening, measured (mm) | Total oscillations duration (s) | Observations |
|---|---|---|---|---|---|---|
| **Try 2: ‘SA0’** | 90 | 50 | 2 | 0 | 15 (limit time) | Cohesive, but no axial shortening |

**Table 2**: *Set process parameters, try 2.*

The latter processing parameters led to an apparently cohesive junction between the workpieces. However, the measured post-assembling axial shortening remained close to a null value with no significant expulsion flashes formation observed on the bonded structure. Nevertheless, the intense red glow that radiated from the close interfacial zone during the rubbing procedure allows qualitatively confirming that such the frictional conditions led to an effective temperature elevation at the joining interface between the mutually sliding bodies.

So, starting from the 'try 2' configuration as a reference point, a simple trial-and-error methodology was applied to try to improve the reached final axial shortening height and satisfy the 3 mm set point condition. The main idea throughout that procedure is (1) to increase the applied forging pressure in order to trigger the plastic flow yielding of the in-contact materials and finally result to an axial shortening by the lateral expulsion flashes formation; (2) then adapt the oscillation parameters (amplitude and frequency) for purposes of generating local high temperature conditions that would soften their mechanical properties.

Finally, the value of the forging effort has been chosen considering the classical thermo-mechanical processing maps notably reported in the literature [2]–[6] and knowing that the expected strain-rate value in such assembling technique is expected to range between 0.1 $s^{-1}$ to 10 $s^{-1}$ in the near-assembling zone with estimated temperature going up from 950°C to 1100 °C.

The forge pressure and the oscillating conditions were adapted in an incremental manner which is detailed in the table below:

| Parameters (Units) | Pressure (MPa) | Frequency (Hz) | Amplitude (mm) | Axial shortening, measured (mm) | Total oscillations duration (s) | Observations |
|---|---|---|---|---|---|---|
| **Try 2: 'SA0'** | 90 | 50 | 2 | 0 | 15 (limit time) | Cohesive, but no axial shortening |
| **Try 3** | 150 | 50 | 2 | 1.51 | 15 (limit time) | Cohesive and flash formation, unreached set axial shortening |
| **Try 4** | 150 | 50 | 3 | 0.6 | 15 (limit time) | Little axial shortening |
| **Try 5** | 150 | 30 | 1 | 0 | 15 (limit time) | Cohesive but no axial shortening nor flash formation |
| **Try 6** | 150 | 60 | 2 | 0 | 15 (limit time) | Strong vibrations, no weld |
| **Try 7** | 160 | 50 | 1 | 2.46 | 15 (limit time) | Bond formation, unreached set axial shortening |
| **Try 8** | 180 | 50 | 1 | 0 | 15 (limit time) | Cohesive bond, then fracture at the interface |

| | | | | | | |
|---|---|---|---|---|---|---|
| **Try9** | 160 | 60 | 1 | 0.87 | 15 (limit time) | Strong vibrations, slight axial shortening |
| **Try 10: 'SA1'** | 160 | 70 | 1 | 2.91 | 15 (limit time) | Bond formation, best try, closest try to 3mm of axial shortening |
| **Try 11** | 170 | 70 | 1 | 2.38 | 15 (limit time) | Bond formation, unreached set axial shortening |
| **Try 12** | 180 | 70 | 1 | 1.71 | 15 (limit time) | Bond formation, unreached set axial shortening |

**Table 3**: *Window of process parameters explored for the solution annealed configuration*.

The total oscillation duration during these weld campaigns was pushed to 15 s which is the maximal duration value for the frictional stage of the machine set, as a consequence it was not possible to reach the aim value of 3 mm of axial shortening. However, throughout that parameter prospection procedure, it seemed that the 'try 10' also denominated '**SA1**' led to friction welding conditions close enough to the 3 mm burn-off criterion to make viable comparison with the welded precipitation hardened configurations. This configuration is then logically chosen for in-depth microstructural characterization on the one hand.

On another hand, the '**SA0'** configuration demonstrated a cohesive aspect despite much lower forging pressure values with no extensive burn-off formation. **Hence, the interest for that weld configuration is that the quasi-absence of axial-shortening may allow getting a better insight on the joining formation mechanism between the contacting materials that occurred during the process**. Regarding these prospects, the 'SA0' appears as an interesting configuration that would also deserve deepened microstructural observations.

Lastly and to sum up, two configurations were selected for further microstructural characterizations:

| **Parameters (Units)** | **Pressure (MPa)** | **Frequency (Hz)** | **Amplitude (mm)** | **Axial shortening (mm)** | **Total oscillations duration (s)** | |
|---|---|---|---|---|---|---|
| **'SA0'** | 90 | 50 | 2 | 0 | 15 (limit time) | Cohesive but no axial shortening |
| **'SA1'** | 160 | 70 | 1 | 2.91 | 15 (limit time) | No weld, but cohesive start |

**Table 4**: *Selected process parameter sets for microstructural characterization*.

## 2. Result and discussion on the 'SA0' set of parameters

Microstructure observations were first performed on the SA0 assembled configuration. These observations were carried out to study the bond formation mechanisms on an apparently cohesive solution annealed IN718 weld that do not present extensive lateral flashes formation. The processing parameters to obtain the junction are recalled in the table below:

| Parameters (Units) | Pressure (MPa) | Frequency (Hz) | Amplitude (mm) | Axial shortening (mm) | Total oscillations duration (s) | |
|---|---|---|---|---|---|---|
| **'SA0'** | 90 | 50 | 2 | 0 | 15 (limit time) | Cohesive but no axial shortening |

### 2.1 Materials & methods for microstructural description

The microstructural observations were carried out on the median cross-sectional interfaces has illustrated in the Figure 2. The sample was extracted at the median position of the assembly.

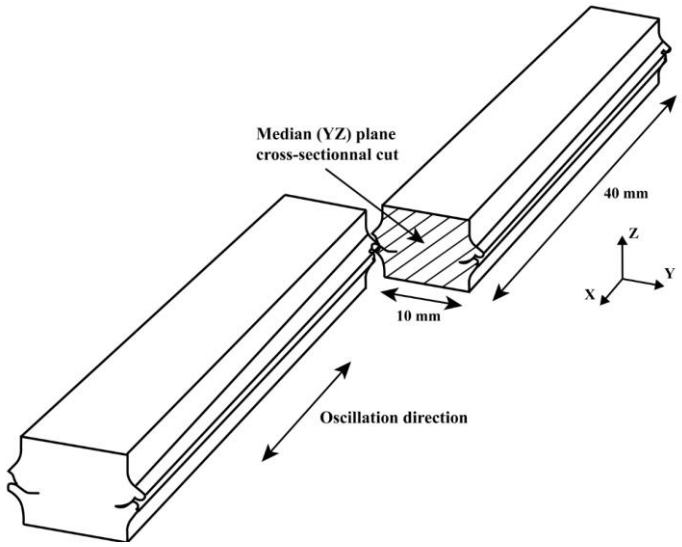


**Figure 2**: *Schematic illustration of the extraction sample strategy on the alloy 718 linear friction assembled blocks for further characterizations.*

As for the 'PH-IN718' configurations, the specimen was first mechanically polished through standard abrasive polishing procedures using SiC abrasive grinding papers until a P4000 grit size. The grind finishing procedure is done using successive polishing with standard diamond solution from 3 µm to 1 µm particle mean diameter on a polyester cloth. The final surface finishing is done using a 50% oxide polishing suspension (OPS) solution and 50% in volume of $H_2O$ on a Buehler VibroMet™ 2 vibratory polisher.

Microstructural observations were done using a tungsten field emission gun Zeiss Σigma scanning electron microscope (FEG-SEM). The orientation maps were obtained by electron back-scattered diffraction (EBSD) technique. A Nordiff OptiPlex 7040 detector was used for the Kikuchi pattern images capture and the orientation maps were calculated through the use of the TSL OIM data collection™ software. During the

acquisition, the specimens were mounted onto a 70° tilted holder fixed at a 20 mm working distance from the electron gun outlet. The Matlab© open source toolbox Mtex [7] v5.1.1 is used for the EBSD post-processing procedures.

### 2.2 Analyses of the microstructure changes across the joint

The position of the welding line is first localized within the welded microstructure by optical microscope observations on a cross-sectional sample taken from the (TD, ND) plane, the oscillating direction (RD or X) is normal to the observation plane. The corresponding micrographs are exposed in Figure 3.a and b. The rectilinear band of fine-grained microstructure marks the position of the welding (WL). The oscillating part (below) displays a finer initial average grain size that the forging workpiece (upper).

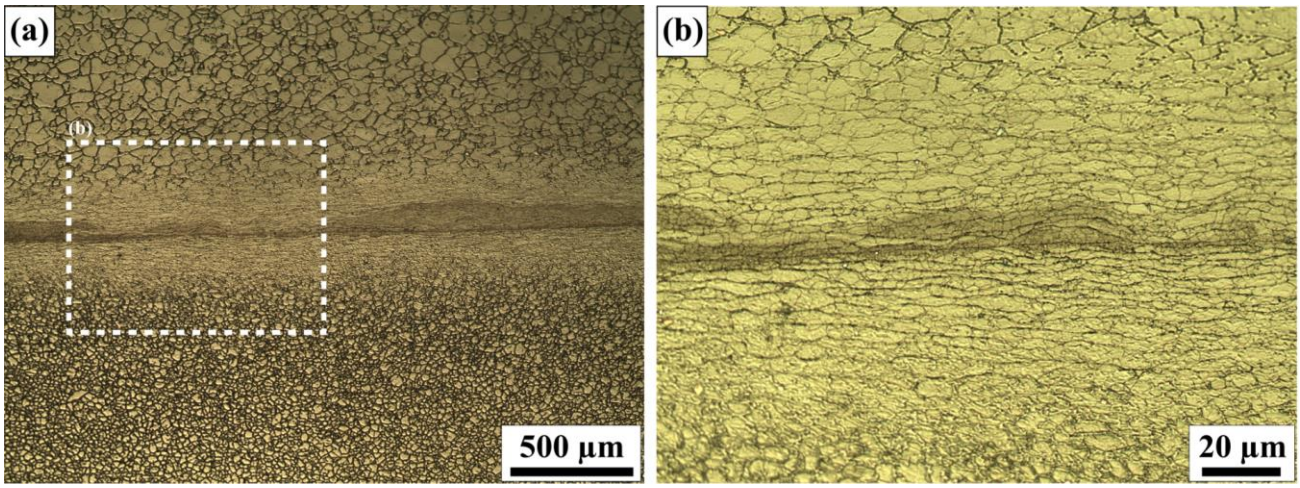


**Figure 3**: *Visible light micrographs of the welding junction in the (TD, ND) plane*.

Around the weld center zone, a severely deformed microstructure forms a 500 µm thick band of squashed grains presenting visible internal sub-grain formations. These fragmented and elongated crystallites form continuous layer-like grain structures parallel to the friction plane (RD, TD) eventually forming lamellar boundary structures. Such alignments of grain boundaries are classically linked to intense slip activity coupled with dynamic recovery under applied plane strain compression (here the forging pressure provided by the assembling machine). This phenomenon is often described with accuracy in the hot rolling and forging literature [Réfs] of Ni-alloys and Al-alloys.

The microstructure at the weld interface was additionally tracked by EBSD analyses; the associated inverse pole figure map presented in Figure 4.a. The position of the welding line stands out by its fine equiaxed microstructure. Furthermore, the associated Grain Orientation Spread (GOS) map (Figure 4.b) shows that the microstructure composing the WL exhibits very low internal misorientation. These findings corroborate with a complete recrystallization phenomenon in the WL zone. The latter may have been stimulated first by the intense accumulation of structural defects due to cold working and shear deformation within the subsurface

zone during the dry sliding contacts, and then by the high thermal energy provided by the friction related interactions. Both combined may have acted as a driving force favoring a complete recrystallization phenomenon in this localized area.

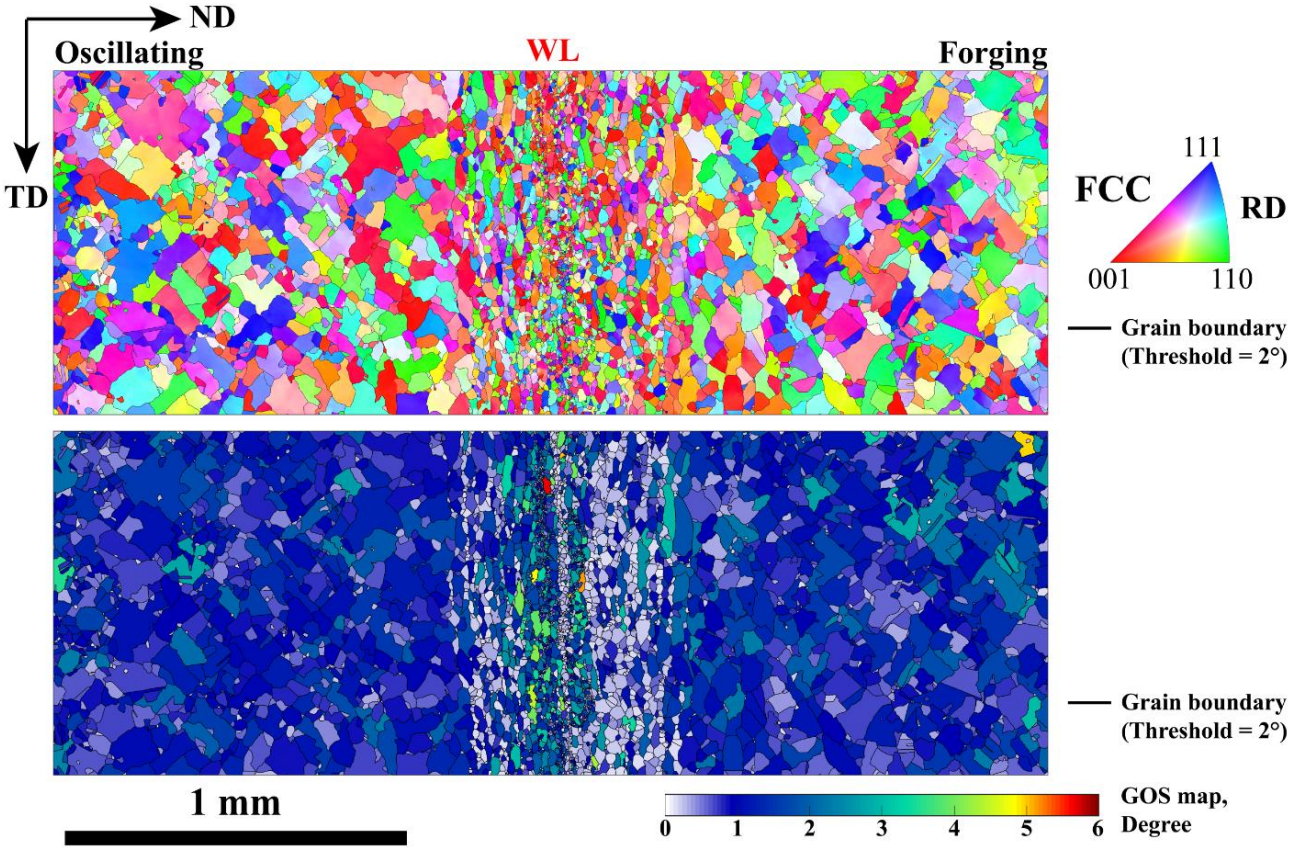


**Figure 4**: **(a)** *Inverse pole figures obtained from EBSD analyses (0.2 µm step size) on the median transverse plane of the SA0 sample. The FCC indexed data are superimposed with the grain boundaries (2°disorientation angle threshold); the colors represent the crystallographic direction of the indexed lattice along RD (friction direction);* **(b)** *the grain orientation spread map in displayed with 6° threshold.*

Then, the microstructure surrounding the WL is visibly plastically deformed. On the one hand, a significant population of the observed layer-like grain structures present low-internal misorientation (< 0,5° on the GOS signal). These features indicate that thermally activated phenomena of restoration and recrystallization (if mobile high angle grain boundaries are implied in the process) structured and swept the dislocations in excess during the plastic deformation. Whereas on the other hand, portion of the deformed microstructure presents intermediate to high level of internal misorientations. In the latter grain structures, the deformation is also accommodated by accumulation of dislocations; nevertheless, the critical strain for a local grain fragmentation process was not reached in this concern. The progressive structuration of these dislocations notably near the grain boundaries led to the observed internal orientation gradients and would eventually have yielded to a grain fragmentation process either by grain subdivision *via* the progressive building of low-angle grain boundaries or by nucleation of new crystallites by bulging mechanism from distorted grain boundaries if the hot deformation process had continued. Furthermore, it is notably remarked that the region close to the

WL locally exhibits a higher density of low-angle grain boundaries (LAGB) compared with the rest of the microstructure suggesting such in-going grain fragmentation process (Figure 5).

From these observations, it can be concluded that the microstructure close to the WL most-likely experienced deformation under local elevated temperature conditions. The ensemble forms alternate bands of lamellar grain structures frozen at different stages of a grain fragmentation process because the junction underwent a critical cooling once the oscillation motion stopped.

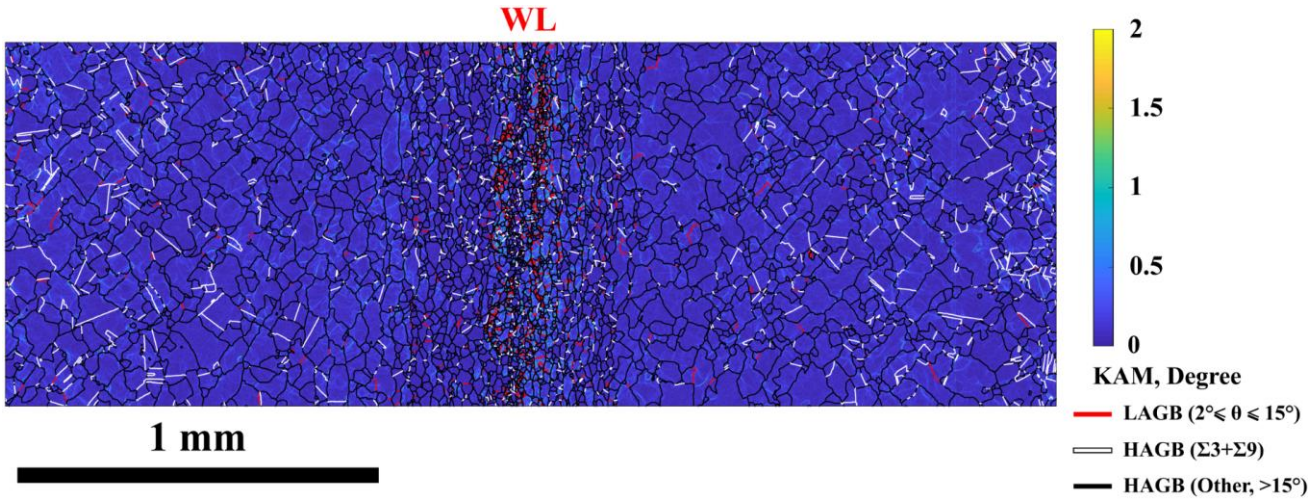


**Figure 5**: *Kernel Average Misorientation (KAM) cartography combined with the grain boundary disorientation classification, the threshold for KAM is fixed at a 2° value and the order is of 1. The disorientation threshold for the special boundary character deviation is fixed a 5°-degree value.*

Further away, the influence of the thermally activated restoration mechanisms is fading away even if some traces of low-angle grain boundary structuration are perceived on the Kernel Average Misorientation (KAM) map (Figure 5). A moderate change of shape of the grains is observed compared with the parent microstructure; however, the GOS map highlights some consistent internal misorientation gradients in their inner structure. At the vicinity of the severely deformed zone, the annealing twin boundaries (Σ3 and Σ9) from the parent microstructure are observed to deviate from their ideal coincidence site lattice (CSL) orientation relationships and lost their special character due to the high misorientation gradients accumulated under straining. Finally, the plastic deformation markers are expected to decrease progressively as moving away from the welding zone.

### 2.3 Global analyses along the transverse interfacial zone

A general imaging of the microstructure by SEM is displayed in Figure 6. The inferior part in the image corresponds to the oscillating block and the superior part corresponds to the forging part. The strongly affected microstructure is readily visible in the junction zone in-between, and displays a marked grain refinement. Despite the presence of noticeable cavities and voids in the cohesion zone, the global aspect of the

junction appears continuous and as a sound-weld. The lateral expulsion flashes are little developed; however, a layer of extensively plasticized material is readily discernable in the junction zone. The plasticized layer forms an intermediate band of microstructure between the frictional parts.

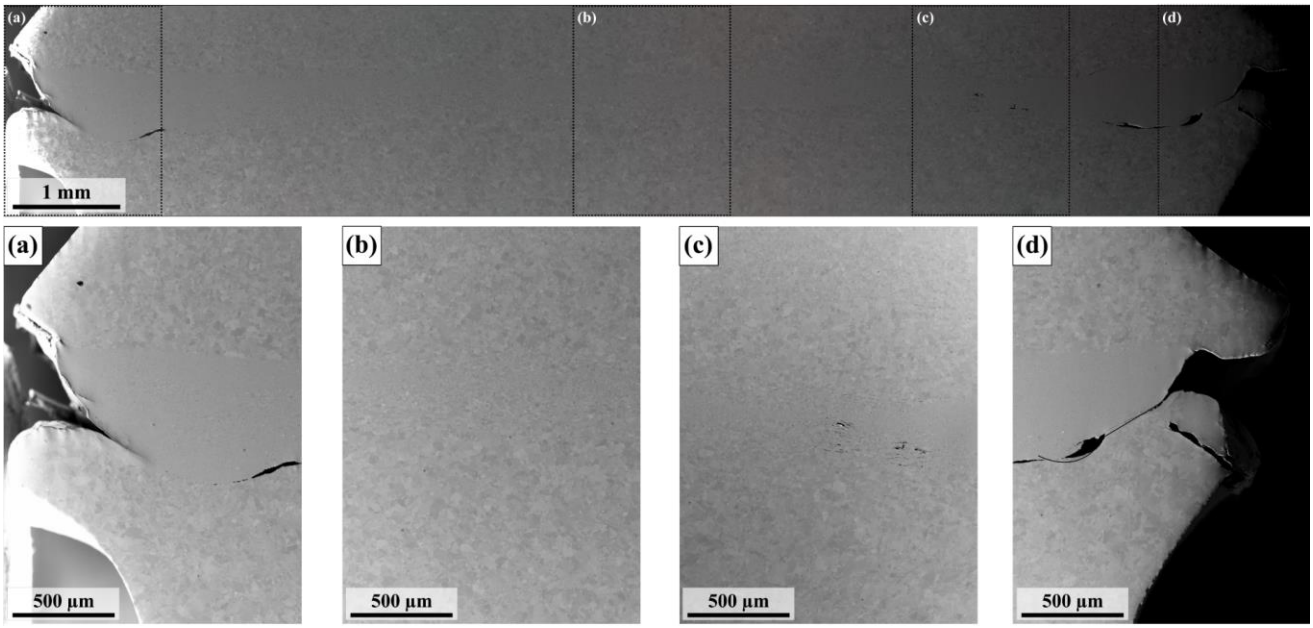


**Figure 6**: *Transverse secondary electron imaging of the extracted SA0 weld sample. The inferior part is the oscillating block and the superior part the forging block. Detailed views of the lateral expulsion flashes formation are displayed in (a) and (d). The microstructure near the median position of the weld is shown in (b); a view on voids formation is displayed in (c), near the expulsion zone.*

Near the lateral expulsion zones, the intermediate layer of plasticized material marks a continuous delineation with the upper forging part. In contrast, a clear discontinuity is observed between the grain refined microstructure of the intermediate layer on one side and a little plastically affected microstructure close to the parent material on the other side, the whole forming unbounded lips of material at the weld extremities.

Now as moving along these unbounded lips from the expulsion zone toward the core of the junction (Figure 6.c.), bands of intergranular voids are observed at the edge of the material discontinuity. The detailed imaging of the voids formation zone displayed in Figure 4.a and b unequivocally confirms the intergranular nature of these voids. In addition, the microstructure at the vicinity of these void formations has a refined aspect with low intragranular misorientation gradients which are usually associated with dynamic restoration/recrystallization mechanisms (Figure 6.b). The later are thermally-activated and are effective under hot thermo-mechanical conditions ($T > 0.6\ T_m$). These findings consequently suggest that the voids formation concomitantly occurred with the grain fragmentation mechanisms under high temperature conditions.

In that respect, a reasonable hypothesis for the appearance of the observed intergranular voids would suggest that the severe local straining conditions could not be accommodated by the fragmenting microstructure which eventually led to cavity nucleation by decohesion at the grain boundaries. The strain incompatibilities between the lamellar boundary structures of the fragmenting grains progressively yield to

damage cavities nucleation in the grain boundary vicinity. Then, classical mechanisms of cavity growth and coalescence finally yielded to the observed high temperature ductile damage development.

Lastly, it is strongly suspected that these observed unbounded lips result from a crack formation phenomenon. The crack propagation most likely occurred between the intermediate plasticized layer and the little affected parent material from the oscillating part due to the extreme thermo-mechanical conditions caused by the shear/frictional motion of the oscillating part. In any case, these observations indicate intense stress concentration in that zone of the microstructure during the welding procedure.

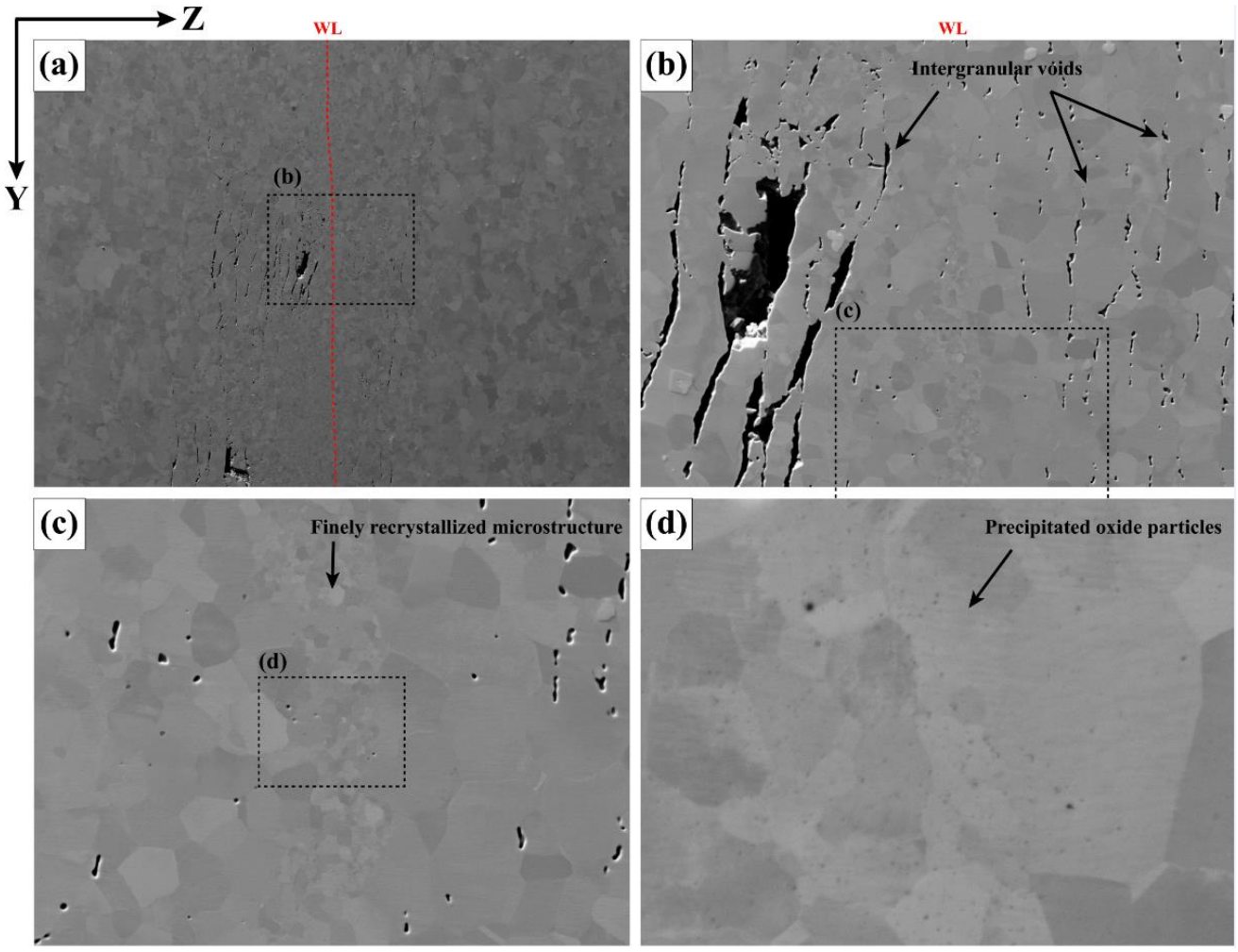


**Figure 7**: *Magnified secondary electron imaging of near the expulsion zone also depicted in Figure 3.c; the images in (a) and (b)display the intergranular voids formations and the (c) and (d)images picture the WL. Scale bars missing!*

### 2.4 Bond localization and junction formation

The observations will now focus on finding the position of the adhesive bond formation between the blocks in-contact. The previous work on the precipitation hardened IN718 configurations allows to state that looking for the position of the welding line is equivalent to search for remaining traces originating from the native surface oxide of the blocks.

Thus, an attentive look in the joint highlights the presence of finely inter-dispersed particles entrapped within a fine band of recrystallized microstructure. Furthermore, the EBSD analyses provided in Figure 4 and 5 highlighted demonstrated recrystallization phenomenon in that zone. The precipitated particles present a round shape aspect of a few dozen of nm average grain size diameter. The concomitant observation of particle and finely recrystallized microstructure would corroborate that a particle assisted nucleation recrystallization mechanism [8] occurred in the junction zone leading to the observed microstructure.

These particles are highly suspected to result from the surface oxide interactions between the faying frictional surfaces. They are observed all along the joint. In that respect, it is possible to follow the extent of these dispersed particles from the core of the weld to the expulsion lips which would consequently mark the effective position of the welding line (WL). The WL location is highlighted in the Figure 6.

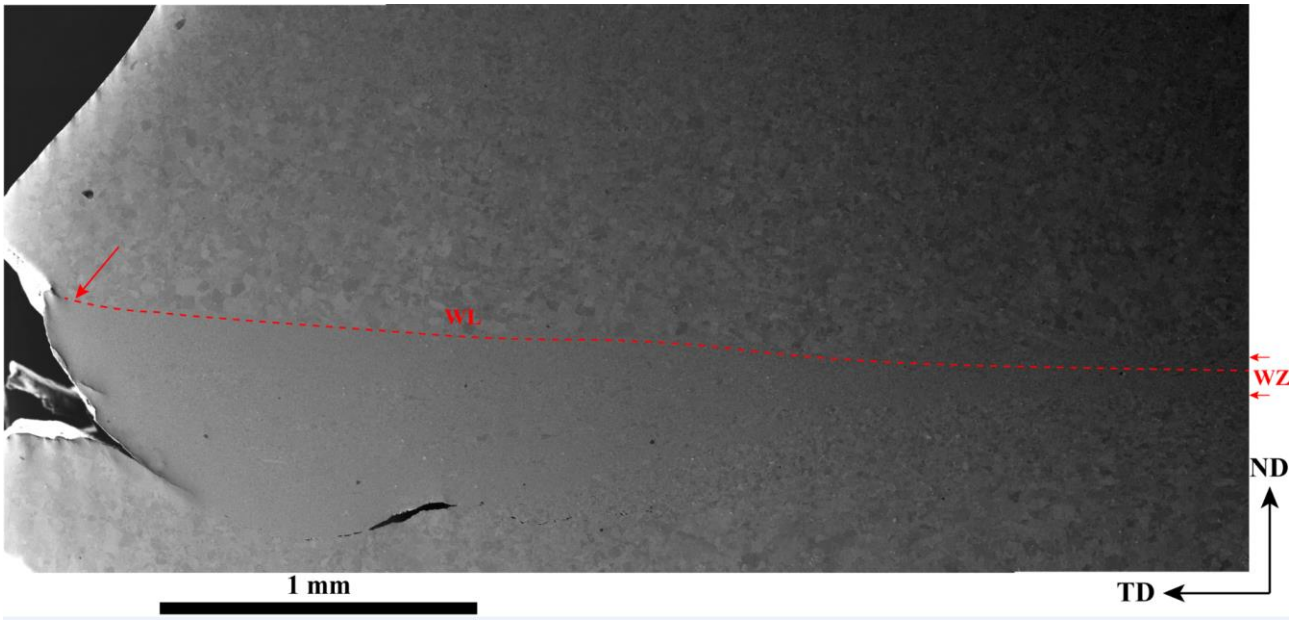


**Figure 8**: *SEM-SE2 imaging of the welding line (WL) indicated by a red dashed-line on the micrograph.*

It is remarkable to notify that these WL markers become thicker as approaching the expulsion zone. Interestingly, the WL position appeared to be in direct contact with the upper forging part and do not connect with the lips-shaped crack developing in the intermediate zone. Hence, deeper observations were executed at the vicinity of the expulsion zone, on the upper part of the burn-off flash; the corresponding micrographs are presented in Figure 9. Again, the presence of the precipitated nanoparticles allows localizing the former bonding zone, and remaining traces of surface oxides are also detected.

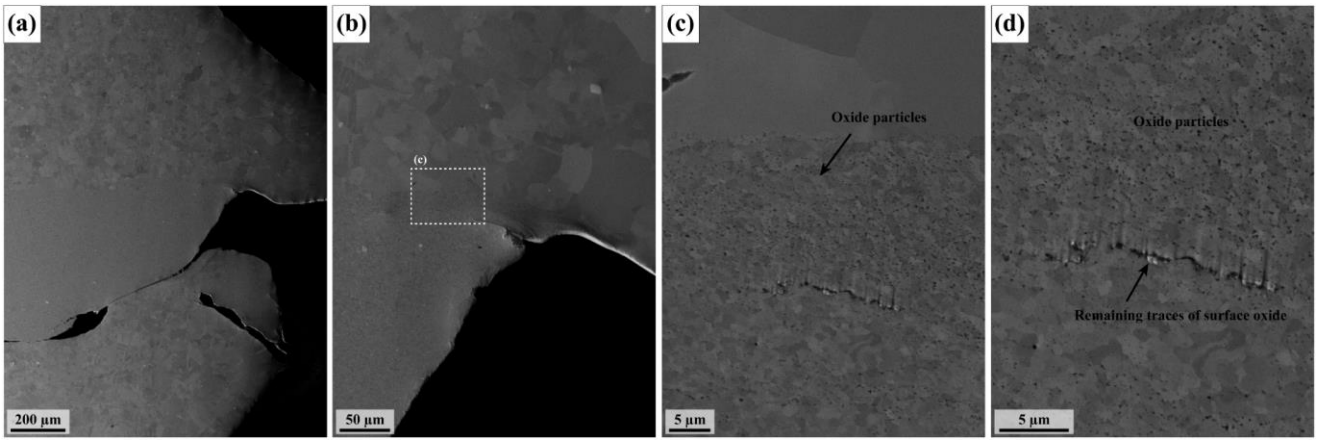


**Figure 9**: *SEM-SE2 detailed imaging of the microstructure near expulsion formation.*

In order to clarify the latter observations, additional chemical analyses were realized by EDX on the zone corresponding to the micrograph presented in the Figure 9.d:

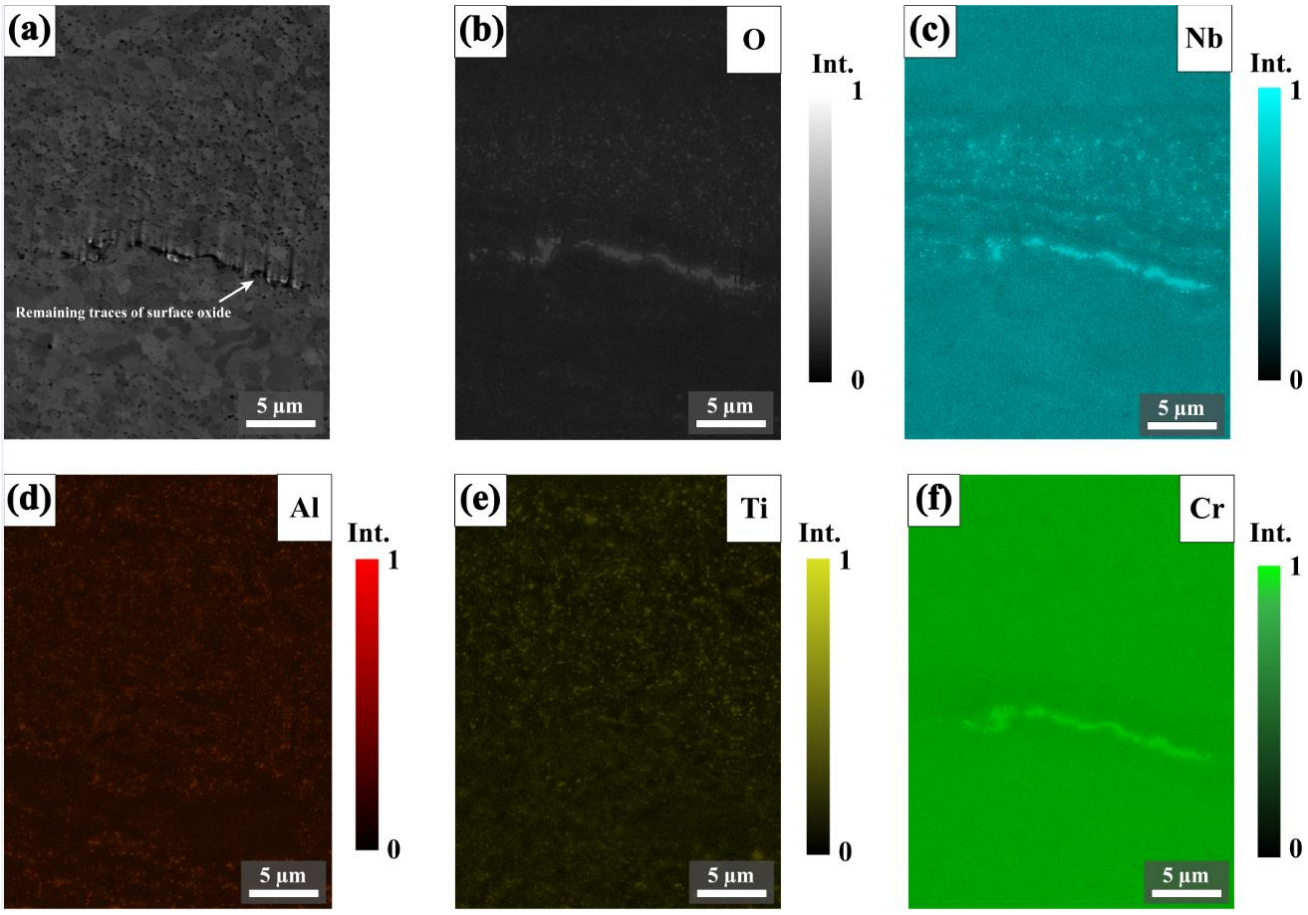


**Figure 10**: **(a)** *SEM-SE2 image of the EDX-mapped zone; the EDX intensity maps of the solute elements:* **(b)** *Oxygen,* **(c)** *Niobium,* **(d)** *Aluminum,* **(e)** Titanium and **(f)** Chromium *(intensity bar scaled on the local maximal concentration).*

The Cr signal superimposed with oxygen signal Figure 10.f and b. highlights traces of the chromia native surface oxide. Indeed, IN718 is known to develop a dense and adherent chromia native oxide barrier

with ambient air environment. In addition to that, Al and Ti elements are commonly found to precipitate as internal oxides beneath the external chromia scale.

Consequently, the presence of these oxide particles may be explained either because of the selective oxidation of the Al and Ti elements following an excess of oxygen atom introduce in the lattice following the decomposition of the former chromia layer under the elevated temperature condition under welding; either by the dispersion of these already present oxide species in the parent microstructure, the latter being more stable at high temperature.

### 2.5 Conclusion on the SA0 weld

From these observations, the following major findings may be drawn:

**(1)** The presence of interspersed oxide particles marks the position of the effective welding line between the faying surfaces of the block. The microstructure neighboring the weld center line is recrystallized and present low-internal misorientations. The latter fact suggests that a particle assisted recrystallization mechanism stimulated the grain refinement phenomenon in that region. In addition, it is probable that the high density of dislocations stored because of the cold work induced by the friction interactions brought a supplementary driving force for recrystallization. The finer grain size in that zone most likely originates from a Zener-Smith drag phenomenon.

**(2)** These findings would correlate with an early adhesive bond formation of the oscillating part on the forging part at the premises of the oscillating stage. The high temperature intermediate plasticized layer developed thereafter, once the metallic adhesion established between the parts.

**(3)** The high temperature damaging phenomena observed near the expulsion zone at the oscillating side reveals that the occurrence of intense stress concentration. The latter may be due to the global shear deformation of the junction because of the mutual adhesion and the softened plastic flow formation with the forging part and the local strong incompatibilities would form the proto-expulsion lips.

In addition, the following scenario may be drawn for weld junction formation:

**(1)** First, the dry sliding friction locally induces a temperature increase in the vicinity of the friction surfaces. Indeed, the energy dissipation originating from the friction interactions is substantially transformed into thermal energy [29]-[30], and the rest is mostly stored in the materials in a form of crystal lattice defects.

**(2)** The occurrence of adhesion sites then gradually increases between the faying surfaces of the blocks. The local thermal softening of the materials enhances the contact interaction area between the frictional workpieces and increases the probability for local adhesion phenomena by seizure effects. Furthermore, the

mutual plastic deformation of materials is expected to be the main mechanism in closing the interfacial voids between the mating surfaces. The steep temperature elevation in the interfacial zone creates an intermediate layer of softened material between the rubbing blocks.

**(3)** At one point of the process, the adhesive effects become dominant for global a mutual adhesion between the faying surfaces. From here, the dry sliding friction process progressively turns into an internal friction-dominated process for the heat-source sustainment. The latter is due to the subsequent degeneration of the deformation energy into thermal energy within the lattice.

**(4)** The microstructural observation in the joint showed that the highly plasticized layer in the weld center zone was subjected to critical thermo-mechanical conditions for triggering a dynamic recrystallization phenomenon. The latter expectedly soften the materials in that zone which allows accommodating large plastic deformations. Consequently, once a sufficient metallic adhesion contact is reached between the contacting surfaces, a global shear of the material may occur around the adhesion plane.

**(5)** A population of intergranular voids was noticed near the lateral expulsion flow and would correspond with a high-temperature damage mechanism. Such features probably originate from local mechanical incompatibilities between the part of the microstructure where recrystallization is triggered and the strained non-recrystallizing one.

## 3. Results on the 'SA1' set of parameters

### 3.1 Introduction

From a naive conception, it may have been expected that welding the much softer solution annealed metallurgical state of IN718 would have been much easier than for the precipitation hardened one. Furthermore, it has been previously demonstrated that the extreme thermal conditions in the joint always yielded to the complete dissolution of the γ'/γ" strengthening precipitates within the precipitation hardened configurations. Regarding that, and from a technological point a view, the two successive strengthening annealing stages at 720°C then 620°C are always to apply on the as-welded configuration after the assembling procedure in order to recover viable in-use strength in the joint. Consequently, welding solution annealed configurations would avoid the useless application of two successive strengthening annealing procedures: one before assembling and the other after, during the post-weld heat treatment procedures.

The weld experimental procedures carried out demonstrated that the solution annealed configuration is particularly demanding. The realized weld campaign suggests that the window of process parameter is tiny. Nevertheless, some interesting configurations could have been realized.

Among the solution annealed joined configuration, the '**SA1**' set of parameters was chosen for further microstructural characterizations. Indeed, the axial shortening (2,9 mm) reached during the friction welding process is close to the 3 mm set value to aim. Although not identical, it is presumed that similar total axial shortening would result on similar macroscopic level of deformation. The latter parameter would allow pertinently comparing the resulting microstructures with the ones obtained on the precipitation hardened configurations. But it still should be highlighted that the comparison stops here. Indeed, if the final deformed state may be relatively comparable, their thermo-mechanical historicity to reach that comparable level of deformation is different.

**The aim in that part is more to point out the microstructural differences with regard to the 'PH-Centre' configuration and try understanding the consequences of the linear friction welding procedure on a solution annealed IN718 initial microstructure.**

### 3.2 Friction assembling procedure

The process parameters on the herewith work are recalled: a **forging pressure** of **160 MPa**, a **frequency** of **70 Hz**, the oscillation amplitude is of **1 mm**. The set and aimed **axial shortening** correspond to a **3 mm** material burn-off width nevertheless only a 2.9 width value was reached. The total oscillation phase duration was of 15 s (maximal possible duration), then; when the relative motion between the blocks stopped, the forging pressure of 160 MPa was maintained for 5 s to consolidate the joint. A comparison between the set-signals and the response signals of the MDS30 welding machine is examined and presented in Figure 11.

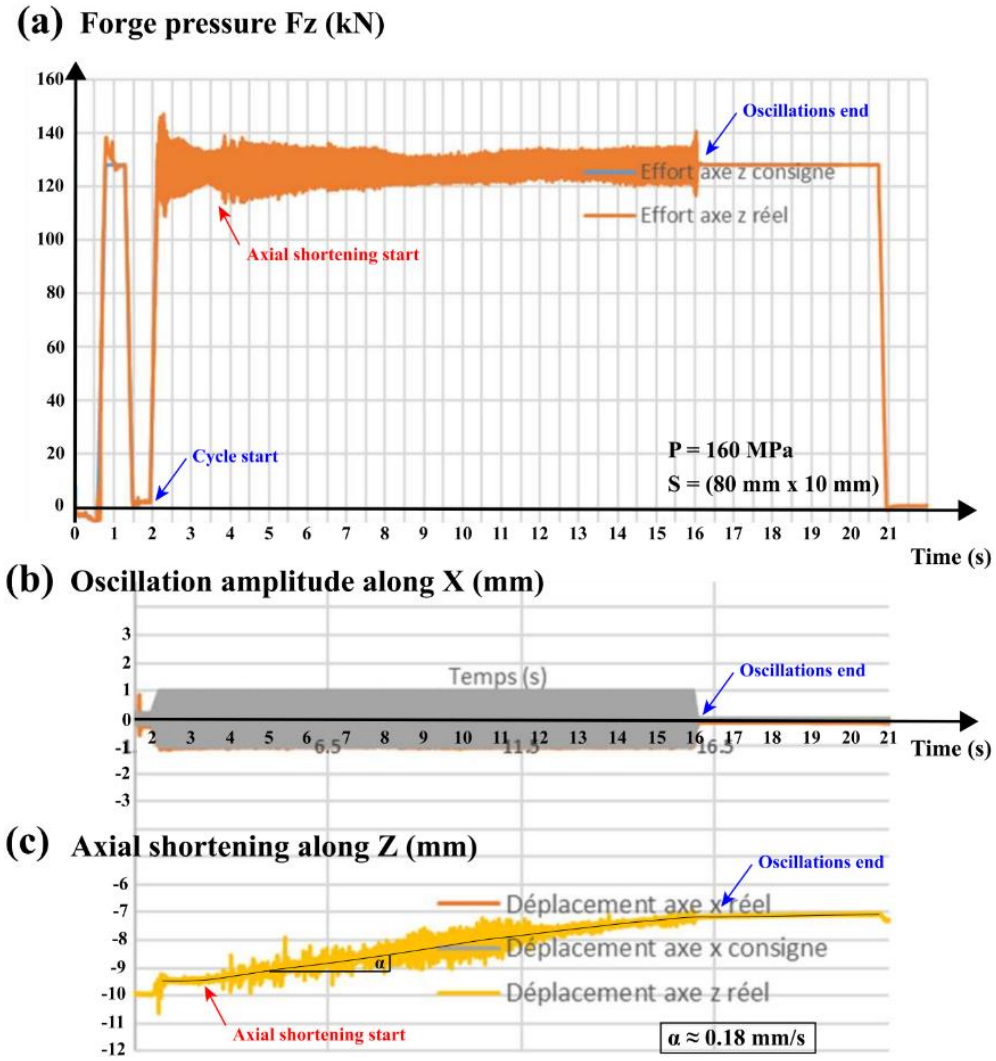


**Figure 11**: ***(a)*** *Forging pressure signal evolution vs time ;* ***(b)*** *amplitude response signal,* ***(c)*** *pressing force application set-point (kN),* ***(d)*** *pressing force machine signal,* ***(e)*** *Z-axial shortening evolution during the processing time.*

During the experimental welding procedure, the SA1 set of parameters demonstrated a peculiar and particularly noisy behavior (Figure 11.c). This perceived vibrational trend was notably recorded on the forge pressure and the axial shortening output signals (Figure 11.a and b). Indeed, the latter demonstrates noisy trends with chaotic envelope variations with time. These trends are noticeable all along the friction process duration. A noise envelope variation on the forge pressure output correlates with the beginning of the increase of the axial-shortening signal.

The average trend of the axial shortening output signal presents a quasi-linear aspect and the average axial shortening velocity is of about 0,18 mm/s. The latter upholds at quasi-constant value from the beginning of the burn-off formation until the end of the frictional process. Then, the oscillation movements ended because the machines accumulators cannot deliver more power. It is remarkable that the noisy trends on the axial shortening signals outputs were observed on every tested solution annealed configuration. This finding may originate from a specific frictional behavior under the tested.

### 3.3 Macroscale description of the microstructural changes in the junction

The observation strategy is the same as for the 'PH-Centre' weld configuration description; the sample extraction method is recalled in the Figure 12 below:

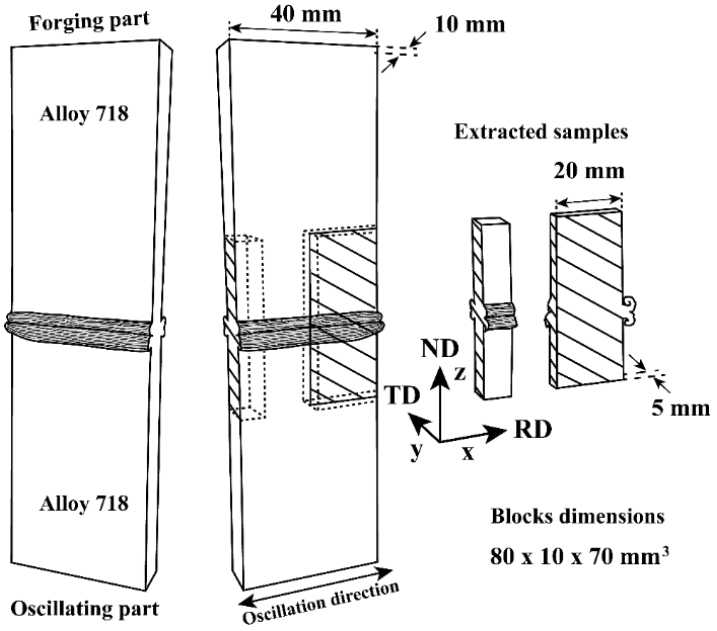


**Figure 12**: *Schematic illustration of the extraction sample strategy on the alloy 718 linear friction assembled blocks for further characterizations.*

An overall visible light macrograph after chemical etching is displayed in Figure 13 on two selected representative cross-sectional cut. The cutting procedure for microstructural analyses is identical to the one described for the 'PH-Centre' weld configuration with a transverse cross-sectional view in the median plane of the weld along the friction direction (RD) and a longitudinal cross-sectional view in the median plane of the joint.

Similarly to the precipitation hardened configurations, the macroscopic observation of the joint highlights gradual changes in microstructure as moving toward the weld center zone (Figure 13). Indeed, a progressive grain fragmentation phenomenon is observed across the affected microstructure. Similar features of parents grains increasingly deformed and squashed as approaching the weld junction zone are observed. Identically, the visibly plastically deformed microstructure is thicker close the material expulsion zone than in the core of the junction, even if less marked than for the precipitation-strengthened configurations.

A regular band of refined microstructure displaying an equiaxed aspect marks the position of the cohesion zone. The expected position of the welding line is determined from the slight traces of most-likely remaining contaminants than get entrapped at the vicinity of the weld interface. The weld interface displays a rectilinear aspect particularly regular on the transverse/longitudinal directions and connects the weld expulsion lips from one to the other. These observations suggest that the cohesion zone geometrically corresponds with the center of the most thermo-mechanically affected zone.

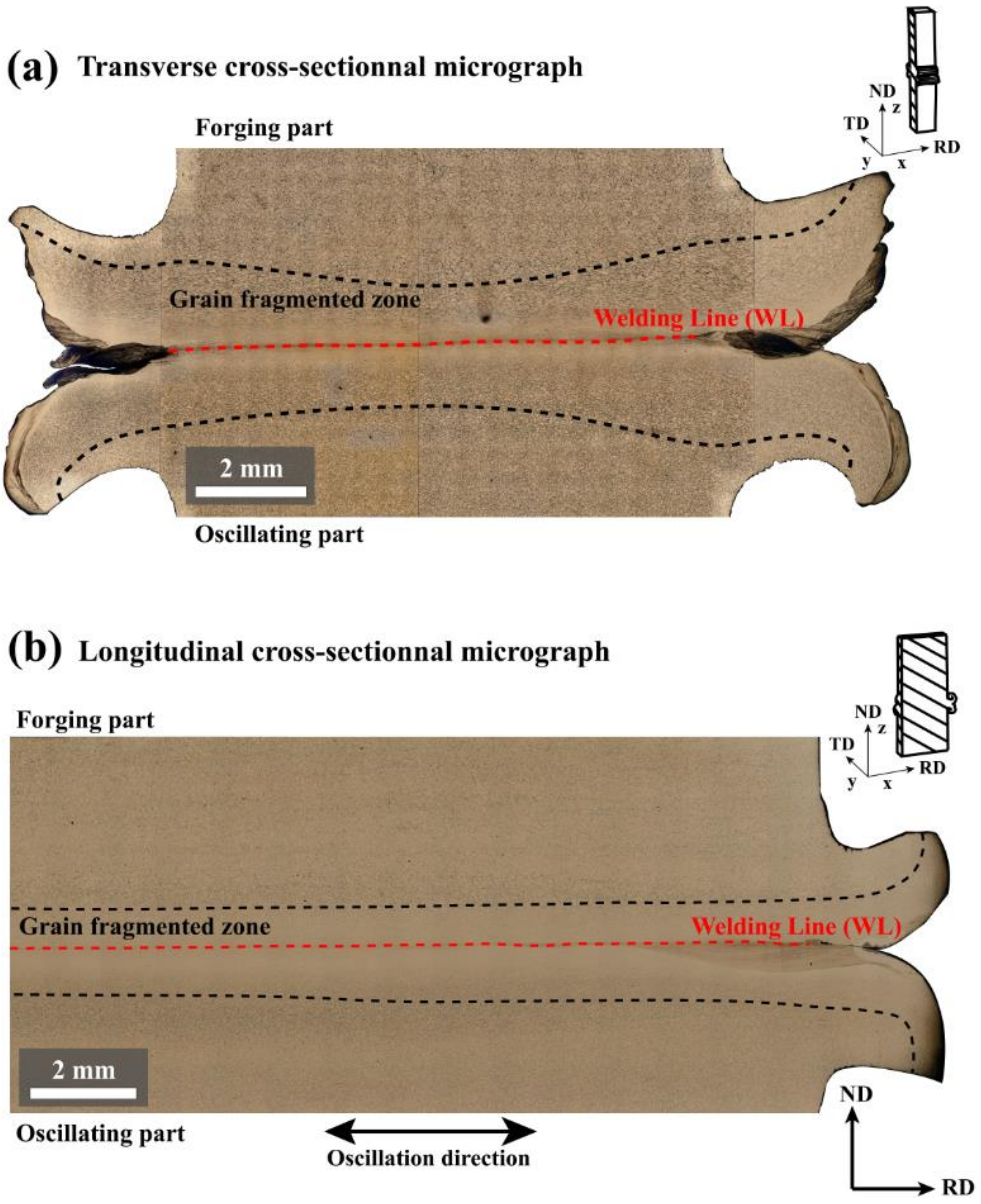


**Figure 13**: *Visible light microscope imaging of selected cross-sectioned weld samples with,* **(a)** *transverse cross sectional micrograph;* **(b)** *longitudinal cross-sectional micrograph.*

The flash morphology that developed during the material flow is disjoint (see Figure 13). The lateral flashes are well formed but did not unify each other during the extrusion process, this is notably visible on the transverse (RD, ND) cross-sectional view (Figure 14); whereas the longitudinal flashes are only partially continuous on an about 1 mm distance before having a divergent aspect. These morphological characteristics are sometimes reported in the literature as qualitatively important for the mechanical integrity of the joints. Indeed, some studies [11], [12] report that higher axial shortening set-value generally lead to longer continuous expulsion flashes and corroborate with better strength performance.

Deeper observations on the weld-flashes microstructure indicate subsequent δ phase dissolution at the edge of the extruded material (Figure 14.a). Knowing that the *equilibrium* δ-*solvus* temperature is estimated

within a 1025°C to 1030°C temperature range, this finding suggests that elevated temperature ranging about this order of magnitude were reached at the early formation of the flashes.

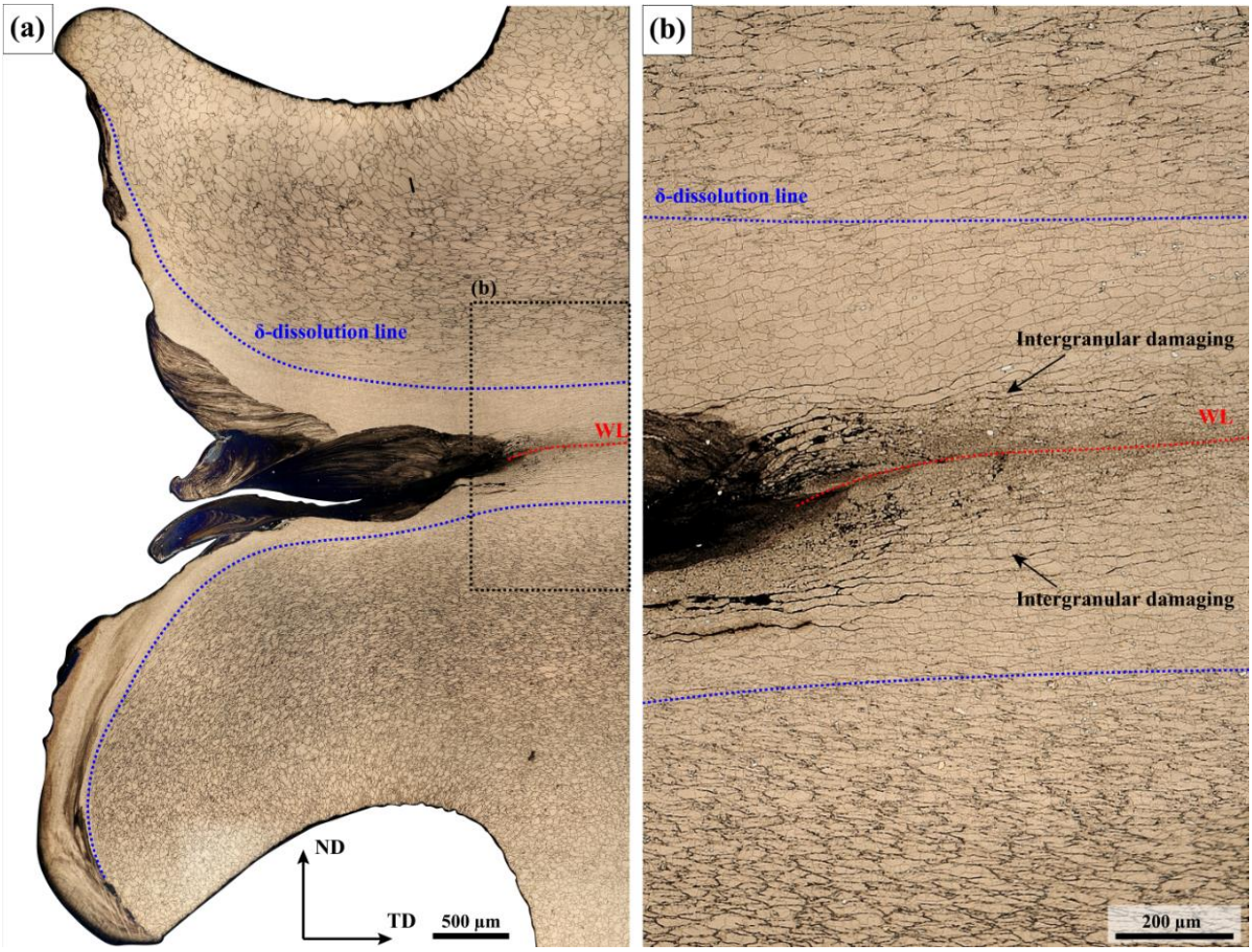


**Figure 14**: *Visible light microscope imaging of the lateral expulsion flash,* **(a)** *half-imaging of the flash formation on the transverse cross-sectional micrograph;* **(b)** *high magnification imaging of the WL zone.*

Intergranular damaging is observed on the close WL microstructure at the foot of the extruded flashes (see Figure 14.b). Such intergranular voids resemble the 'SA0' case and also probably originated from extreme local thermo-mechanical loads yielding to a high temperature ductile damage development. The latter is most likely attributable to the plastic flow generated at the confluence between the WL extremities and the extruded flashes formation. Similarly, the plastic flow could not be accommodated by the fragmenting microstructure which eventually led to the observed decohesion at the grain boundaries.

The near-WL zone presents a fragmented and refined microstructure forming characteristic lamellar grain boundary structures. These refined crystallites form regular ribbon-like structures parallel to the friction plane (RD, TD). Then, this layer-like aspect progressively vanishes as moving away the WL and gives way to squashed deformed grain structures (Figure 15).

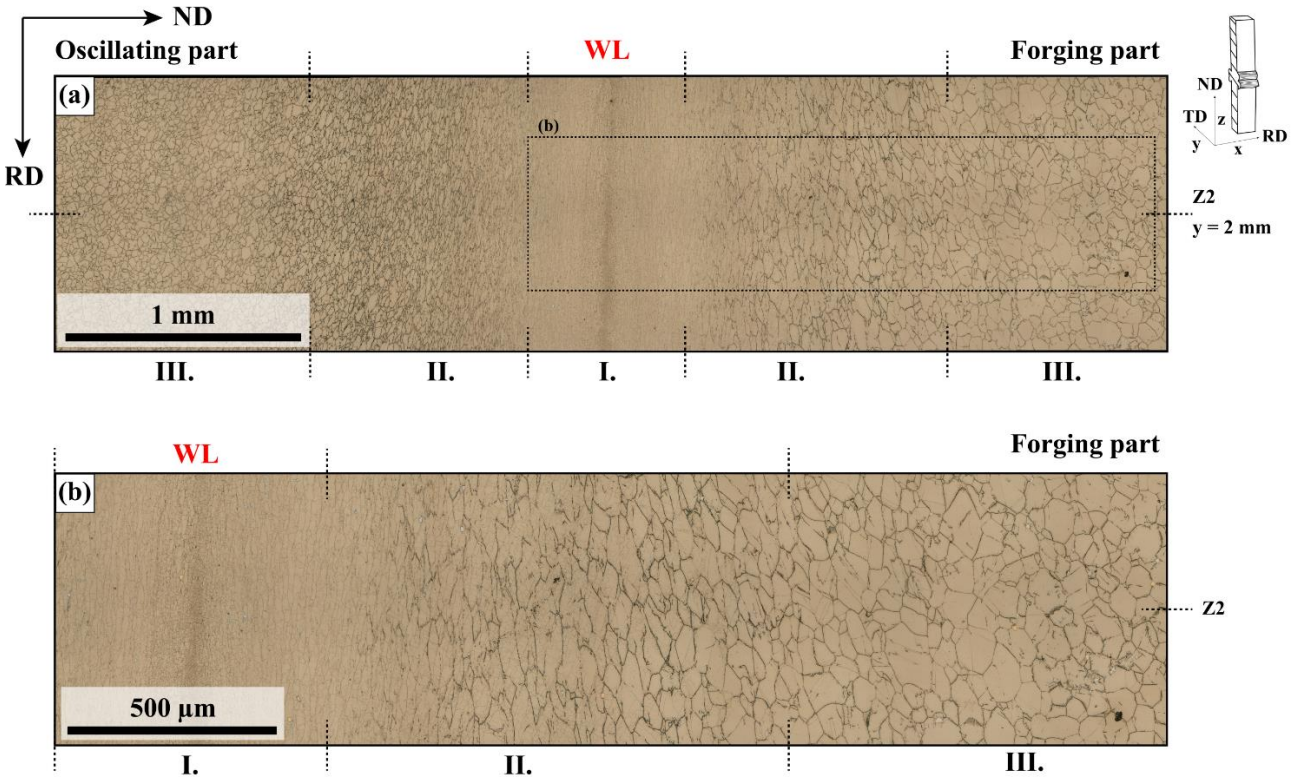


**Figure 15**: *Detailed visible light microscope imaging of the microstructural change at y =2 mm away from the geometric center of the weld, in the (RD, ND) plane;* **(a)** *global cross-sectional micrograph;* **(b)** *focus on the microstructural changes within the forging part.*

Lastly, the intergranular δ-phase is absent along a ± 350 µm thick band of microstructure neighboring the WL which tends to indicate that above the δ-*transus* temperature were reached in the joint during the assembling process. The combination of δ-phase dissolution and subsequent grain refinement is identified as the Zone I on the micrograph above, Figure 15. The transition zone from the refined layer-like microstructure close to near-WL zone to the little plastically deformed zone (which marks the Zone III) demonstrates internal subgrain structuration and constitutes the Zone II, Figure 15.

The exact extent of the Thermo-Mechanical Affected Zone is difficult to evaluate by only visual markers. However, it is generally expected that the thermo-mechanical route experienced by the materials during the friction welding process yields to changes on the local mechanical properties measurable by simple micro-hardness tests.

### 3.4 Microhardness evolution across the joint

Two microhardness profiles were measured across the joint along the Z direction in the transverse median plane (TD, ND) of the welded specimens. The microhardness tests were carried out on about 16 mm length: one (Z0) evaluated at the median position in the transverse plane (TD, ND) and the other measured at 1 mm from the foot of the extrusion zone (Z4). The results are illustrated in the Figure 16 below.

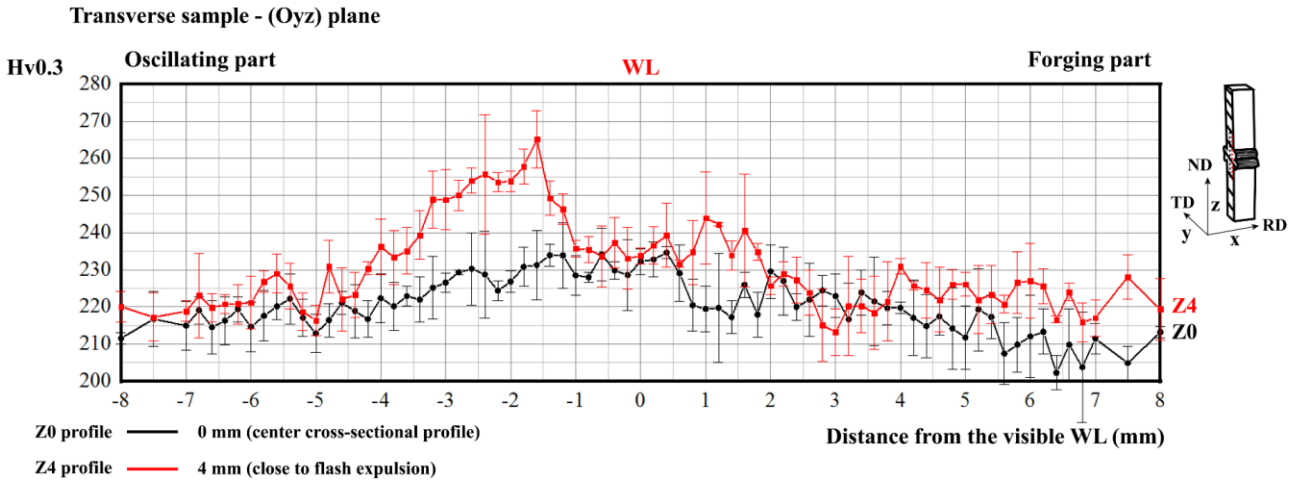


**Figure 16**: *Hv0.3 microhardness profiles measured along the Z direction on the transverse cross-sectional view (TD, ND).*

The materials hardness globally displays a global hardening which approximately marks the extent of the Process Affected Zone (PAZ). The local mechanical properties are affected over a band of about ± 5 mm in thickness starting from the welding line. A dissymmetric trend is observed between the oscillating and forging sides. The zone neighboring the expulsion zone exhibits wider hardness variations than the central zone. The latter remains globally faintly affected with variations on only a few dozens of Hv.

Far from the WL, the dislocations which are responsible for plastic flow and that accumulated during the deformation process remained in subsequent portion in the crystal lattice. The influence of thermally activated processes of restoration for dislocation annihilation in these zones is negligible and the strong interactions between the multiplying dislocations tend to create efficient obstacles to their motion. The latter fact ultimately led to the work hardening phenomenon well-observable on the above-exposed hardness trends, notably on the Z4 profile. The difference in work hardening between the oscillating side and the forging side is most likely due to the finer parent grain size distribution in the initial microstructure of the oscillating part. Indeed, the higher density of grain boundaries is a supplementary obstacle for the mobility of dislocations and consequently enhances the work hardening effect in the corresponding microstructure.

Then, the progressive decrease in hardness as approaching the WL is due to the increasing influence of thermally activated restoration processes that swept the lattice of portions of dislocations eventually leading to a softer microstructure. This trend also qualitatively marks the significant temperature increase as approaching the welding zone.

In the welding zone, the hardness values reach a plateau for both profiles in the zone ranging between -1 mm and +1 mm from the WL position. This is probably due to the important grain-refinement phenomenon that occurred in the core of the joint. A slight Hall-Petch hardening effect is attributable for the higher local hardness values. Local variations in dislocation density difference may be present in that zone of the microstructure but their influence is weak and imperceptible on the measured microhardness profiles.

### 3.5 Overall crystal orientation analyses

As for the 'PH-Centre' configuration, the microstructure in the core of the junction manifests clear indications of hot-working and dynamic restoration mechanisms. However, the much slower axial-shortening rate indicates that the global deformation route proceeded in a different manner. In order to characterize these features, three orientation maps were executed on the transverse cross-sectional plane of the joint by electron back-scattered diffraction (EBSD) technique. The resulting orientation maps are presented in Figure 17, where the RD corresponds to the direction of friction and ND is aligned with the forge direction. The orientation maps are displayed with their associated Grain Orientation Spread (GOS) map in Figure 18; the latter allows evaluating the level of internal misorientation reached within the grains.

The welding zone (WZ) is characterized by fine equiaxed grains free from any markers of internal misorientation gradients (GOS indicator close to a null value). Its extent forms a regular 400 µm thick band of low-misorientated microstructure all along the weld junction and would indicate a complete recrystallization process in the WZ. On the contrary, the refined microstructure neighboring the WZ exhibits moderate traces of plastic deformation. This is revealed by intermediate GOS values ranging from 1° to 3° degree within the grain structures. Although, some crystallites presenting very low-intragranular misorientations are also discernible. This part of the joint microstructure is observed to form layer-like grain structures aligned with the (RD, TD) friction plane. These features are usually characteristic from important dynamic recovery effects on the local fragmenting microstructure and results in a band arranged sub-structuration aligned on planes of high shear stress [13]. Owing to the global simple shear deformation mechanism imposed during this type of assembling procedure on the rubbing materials, the plane of high shear stress would logically corroborate with the plane of friction. However, such dynamic recovery features are intriguing and are not usually found in nickel-based superalloys. Indeed, nickel superalloys presents low to intermediate stacking fault energy meaning that their dislocation mobility is quite limited and confined to the dense glide planes of the FCC lattice. The ease decomposition of perfect dislocations into partials ones connected each other by a stacking fault ribbon limits the influence of thermally activated mechanisms such as dislocation climb, or cross-slip which limit in the same time the possible occurrences of recovery by dislocation annihilation events. In low to intermediate stacking fault alloys the recovery rate is then slow.

Beyond, the microstructure displays a marked change with squashed parent grains presenting subsequent internal orientation gradients (highest GOS values of the map). Some serration events are noticeable at grain boundaries and lays out the premises for discontinuous dynamic recrystallization whereas recrystallized *nuclei* are in the same observed at the vicinity of the grain boundary of the remaining heavily deformed and already fragmented parent grains. This is particularly remarkable on the Z2 and Z4 profiles. Consequently, a discontinuous dynamic recrystallization process led to the partial fragmentation of the microstructure in that zone which also mark the limit between the Zone II and the Zone III (Figure 15).

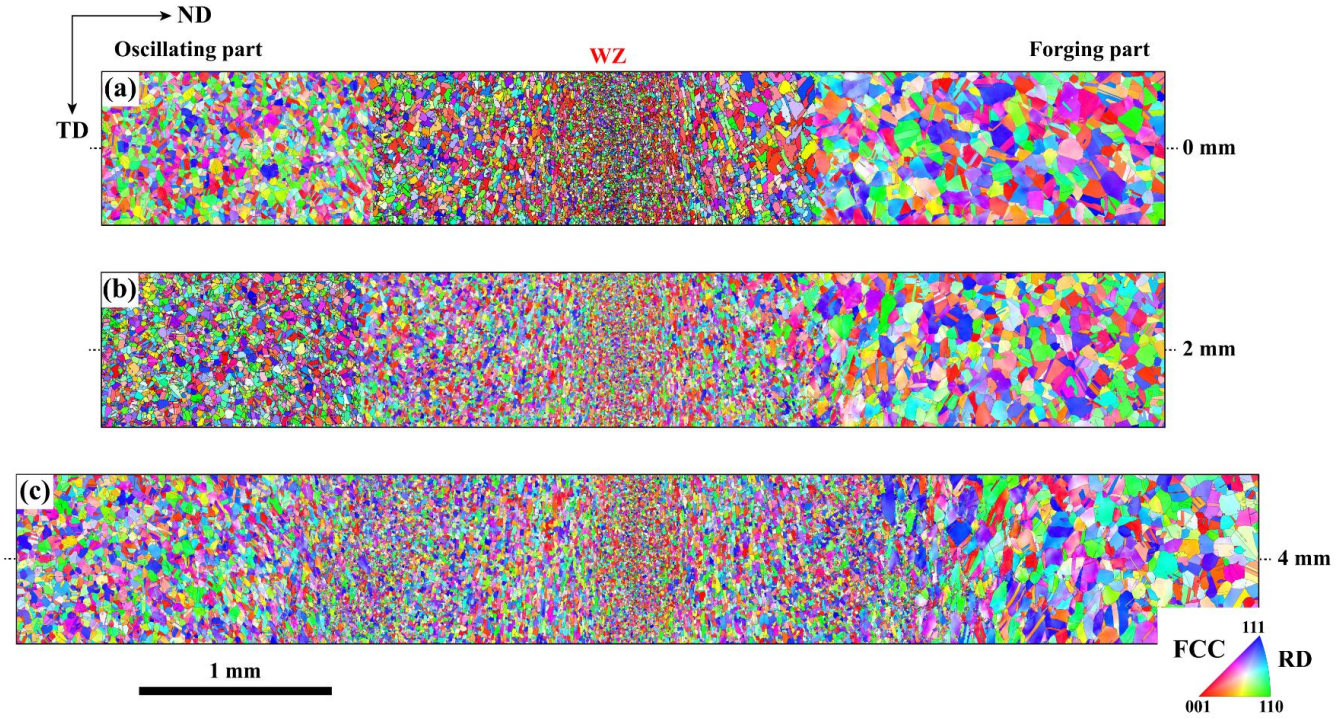


**Figure 17**: *Inverse pole figures obtained from EBSD analyses (0.5 µm step size) on the median transverse plane of the IN718 LFW joint showing three cross-sectional profiles at* **(a)** *0 mm,* **(b)** *2 mm,* **(c)** *4 mm distance from the longitudinal plane of symmetry cutting the welded blocks in half. The FCC indexed data are superimposed with the grain boundaries (15° orientation angle threshold); the colors represent the crystallographic direction of the indexed lattice along RD (friction direction).*

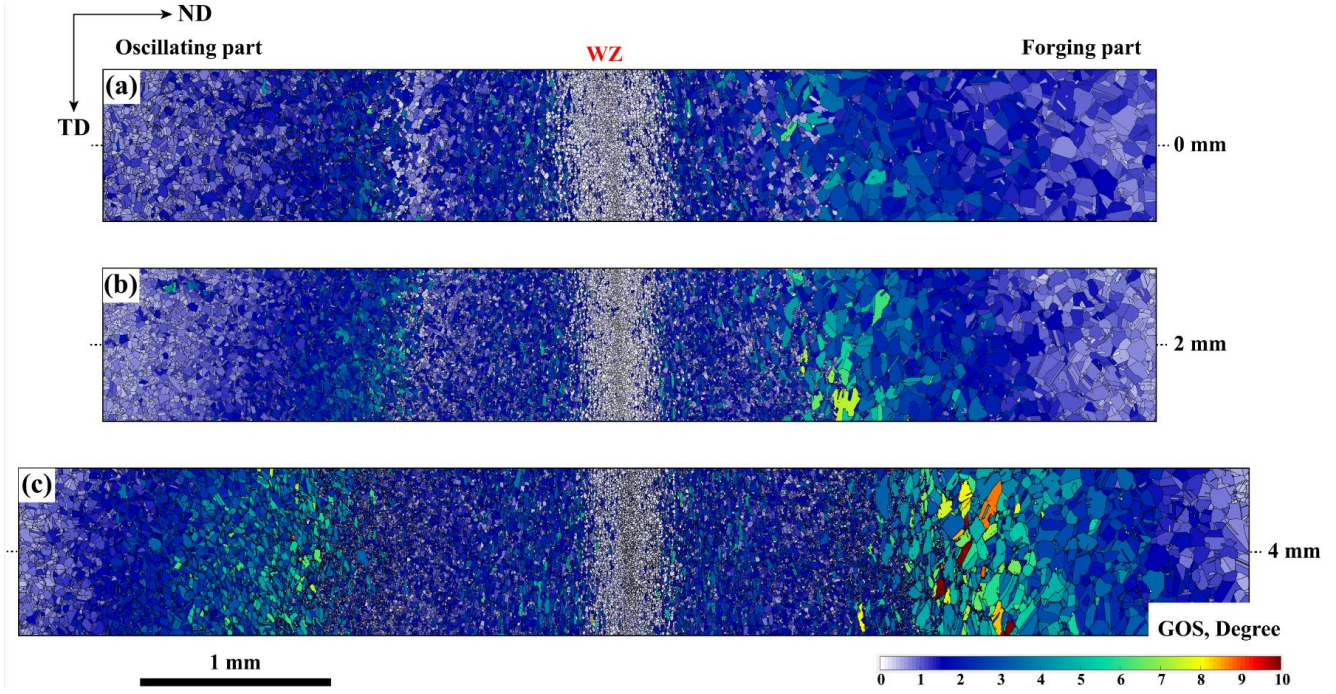


**Figure 18**: *Corresponding Grain Orientation Spread mapping on the transverse plane of the IN718 LFW joint showing three cross-sectional profiles at* **(a)** *0 mm,* **(b)** *2 mm,* **(c)** *4 mm distance from the longitudinal plane of symmetry which cut the welded blocks in half: the grain boundaries orientation angle threshold value is 2°.*

Two propositions may be formulated for the layer-like microstructure formation constituting the Zone II: The morphology indicate alternate composition of dermormed restored parents cristalllite with DDRX nucleated ones.

(1) Whether, the materials locally underwent successive stages of fragmentation then growth during the process. Indeed, it is strongly suspected that a first generation of crystallites nucleated from a former discontinuous dynamic recrystallization process. The fine nucleated crystallites then grew at the expense of the surrounding deformed regions. Depending on the local thermo-mechanical conditions, these grown grains went under a new deformation cycle and started again to store geometrically necessary dislocation within their lattice to accommodate the deformation. This process resulted in the layer-like and elongated structures detailed in the Figure 19.

(1) Whether the materials underwent high recovery rate during deformation yielding to the observed elongated grains.

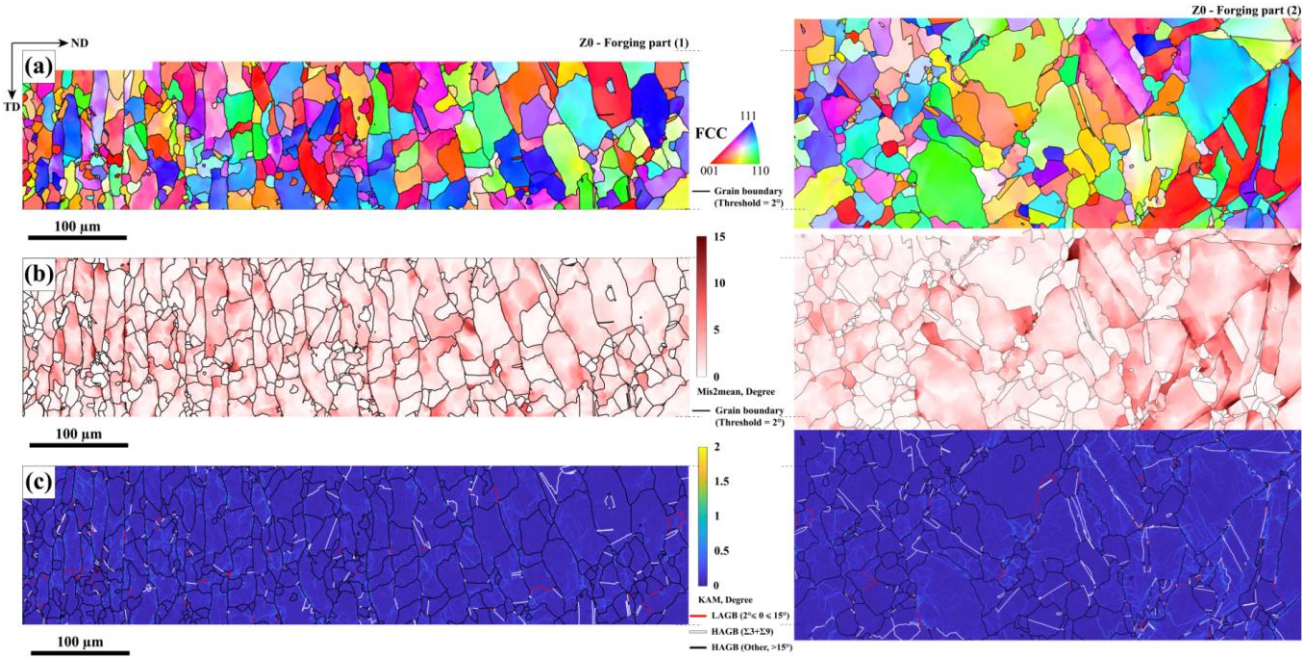


**Figure 19**: **(a)** *Inverse pole figures map from EBSD analyses focusing on the plasticized region (Zone II and Zone II) along the Z0 profile of the forging part (150 nm step size), the FCC indexed data are superimposed with the grain boundaries (2° orientation angle threshold); the colors represent the crystallographic direction of the indexed lattice along RD (friction direction);* **(b)** *Misorientation to mean-grain orientation map (15° misorientation maximum value threshold) and 2° disorientation angle threshold for grain definition;* **(c)** *Kernel Average Misorientation (KAM) cartography combined with the grain boundary misorientation classification, order 1*. (Both scans are continuous).

The KAM map (Figure 19.c) shows some substructurations within the deformed crystallites and emphasize the mechanisms of recovery that takes place during the incubation time preceding the nucleation of recrystallized *nucleus*. Strong misorientations gradients are observed close to the grain boundary, these

heterogeneities tend to self-structure into low-angle grain boundaries that quickly acquires high misorientation with its former parent crystal orientation.

### 3.5 Chemical analyses of the interfacial defects

EDX analyses were carried out near the expulsion zone region. The latter displays the highest density of defects which allows accurately capturing the compositional nature of the precipitated particles observed in the weld center zone

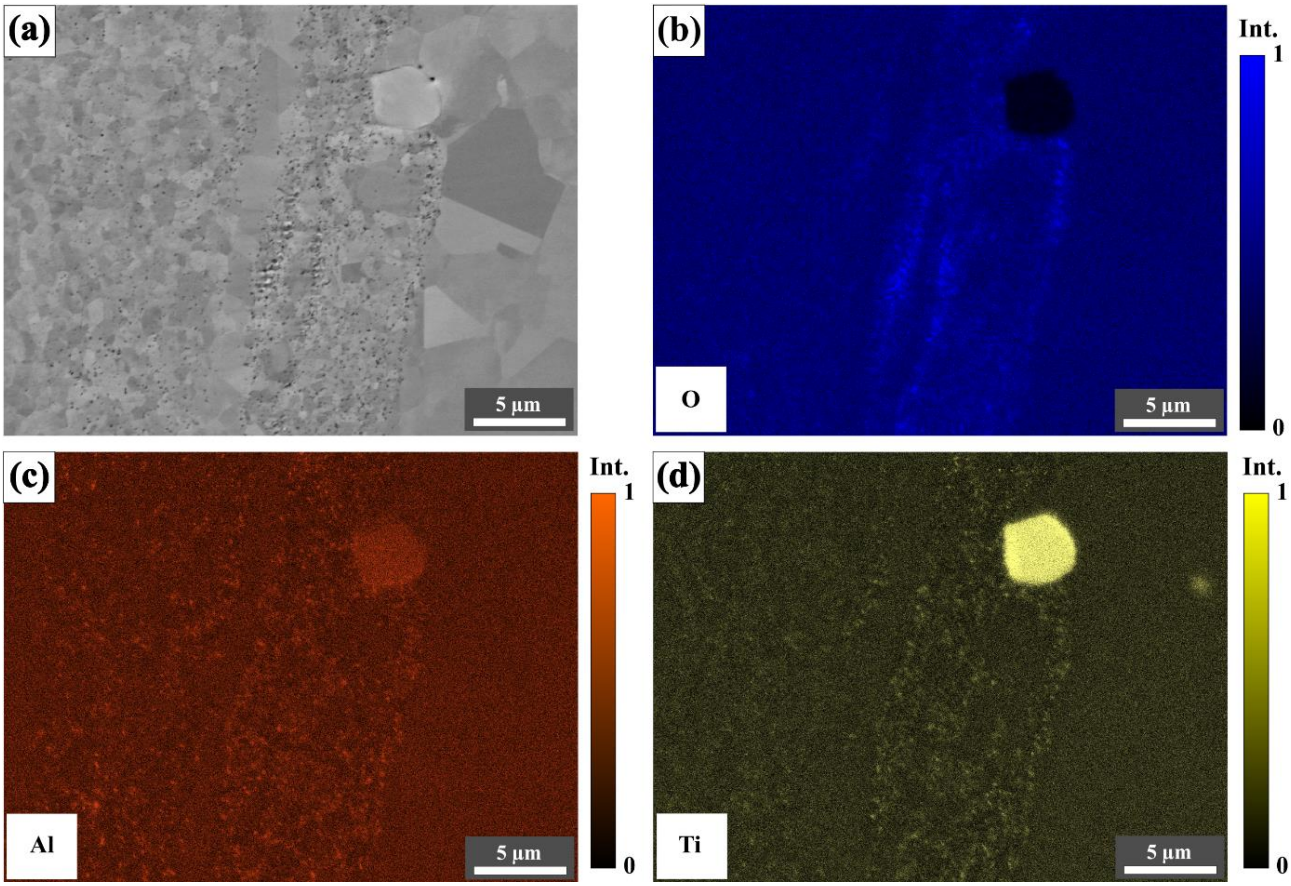


**Figure 20**: **(a)** *SEM-SE2 imaging at the interfacial zone near the expulsion zone, the EDX intensity maps of the solute elements are given with:* **(b)** *Oxygen,* **(c)** *Aluminum, and* **(d)** *Titanium (intensity bar scaled on the local maximal concentration).*

Again, EDX chemical maps (Figure 20) display a strong correlation between Al, Ti elements with O element respectively. The findings evidence the formation of nano-oxide particles composed of Al and Ti. The latter are regularly reparsed among the refined microstructure. In addition, their size is about ~10nm to ~30nm.

## 4. Conclusion on the microstructural observations

From these observations, the following major findings may be drawn:

**(1)** δ phase dissolution on a ± 350 µm band neighboring the WL due to elevated temperature reached in the weld center zone. Knowing that the δ-*transus* temperature is about 1030°C, this microstructural marker indicates that higher temperature values were reached in the weld center zone. The δ phase dissolution band is approximately symmetrically distributed along the WL. This finding indicates that the peak temperature in the weld corresponds with the WL locations.

**(2)** A complete dynamic recrystallization phenomenon on a fine 200 µm band resulted in a regular equiaxed microstructure with low internal misorientation in the center of the junction. The presence of a finer band of recrystallized microstructure indicates the presence of defects partitioned in the microstructure that probably led to particle-assisted recrystallization. The finer grain size in that zone is most-likely due to a Zener-Smith drag-pining phenomenon. As for the other weld configuration, these defects result from the native surface oxide interaction during the process and result in stable nano-particles dispersed around the original contacting zone.

**(3)** The extent of the plastically affected microstructure is much wider that for the precipitation hardened configurations. On the contrary, the solution annealed as-welded microstructure globally displays lower internal misorientation gradients within the deformed grains even though a zone of intense deformation is observed on both sides. The latter was identified as a DDRX zone.

**(4)** Markedly fragmented microstructure with layer-like and elongated structures extends forming sorts of deformation bands. The elongation directions are parallel with the friction plane. The occurrence of subsequent restoration mechanisms is hypothesized and would have resulted in the formation of such elongated grain structures while accommodating compression.

**(5)** In term of defects, intergranular damaging is observed in the strained microstructure near the extrusion zones probably arising from strong local incompatibilities during the plastic flow. An internal oxidation mechanism, identical to the one identified on the PH-Center configuration (Chapter III), led to the formation of disseminated Ti and Al based nano-oxide particles along the junction.

## 5. Prospects

The window of parameter for the LFWing of IN718 in a solution-annealed state remain inchoate. Notably, the tribological condition leading to the establishment of an effective axial shortening are still poorly understood. A wider experimental campaign appears necessary to further prospect the window of parameters. In particular, welding with applied forge pressure beyond a 180 MPa value remained unsuccessful and could not be explained.

The tested set of parameters led to particularly unstable welding conditions, notably displaying high level of vibration during the axial shortening process. The origin of such peculiar vibrational behavior is unclear and may arise from mechanical vibrations issues coming from the welding machine or because of the discontinuous aspect of dynamic recrystallization process trigged during straining. Indeed, in low-stacking fault metal, a jerky flow stress is often during the transient regime of dynamic recrystallization. Such phenomenon originates from successive strain hardening and softening due to nucleation events when the critical value of stress is reached during high temperature deformation. The flow stress therefore oscillates in function of the nucleation events frequency eventually resulting in a jerky behavior.

The tribological conditions allowing the transition from a dry sliding friction phenomenon to an alternate and global shear deformation process remain far from understood. Since reliable modelling on such tribological problems remain utopian, an exhaustive experimental work focusing on a specific block geometry with controlled surface state appears necessary in an attempt to clarify this essential issue.

## 6. References


[1] A. P. Semenov, « The phenomenon of seizure and its investigation », *Wear*, vol. 4, nº 1, p. 1‑9, janv. 1961, doi: 10.1016/0043-1648(61)90236-8.

[2] Y. Wang, W. Z. Shao, L. Zhen, L. Yang, et X. M. Zhang, « Flow behavior and microstructures of superalloy 718 during high temperature deformation », *Materials Science and Engineering: A*, vol. 497, nº 1‑2, p. 479‑486, déc. 2008, doi: 10.1016/j.msea.2008.07.046.

[3] S. L. Thomas, K. Chen, J. Han, P. K. Purohit, et D. J. Srolovitz, « Reconciling grain growth and shear-coupled grain boundary migration », *Nature Communications*, vol. 8, nº 1, déc. 2017, doi: 10.1038/s41467-017-01889-3.

[4] M. Azarbarmas, M. Aghaie-Khafri, J. M. Cabrera, et J. Calvo, « Microstructural evolution and constitutive equations of Inconel 718 alloy under quasi-static and quasi-dynamic conditions », *Materials & Design*, vol. 94, p. 28‑38, mars 2016, doi: 10.1016/j.matdes.2015.12.157.

[5] Y. C. Lin, S.-C. Luo, M.-S. Chen, D.-G. He, et C.-Y. Zhao, « Effects of pressure on anisotropic elastic properties and minimum thermal conductivity of D022-Ni3Nb phase: First-principles calculations », *Journal of Alloys and Compounds*, vol. 688, p. 285‑293, déc. 2016, doi: 10.1016/j.jallcom.2016.07.204.

[6] F.-L. Sui, L.-X. Xu, L.-Q. Chen, et X.-H. Liu, « Processing map for hot working of Inconel 718 alloy », *Journal of Materials Processing Technology*, vol. 211, nº 3, p. 433‑440, mars 2011, doi: 10.1016/j.jmatprotec.2010.10.015.

[7] F. Bachmann, R. Hielscher, et H. Schaeben, « Texture Analysis with MTEX – Free and Open Source Software Toolbox », *Solid State Phenomena*, vol. 160, p. 63‑68, févr. 2010, doi: 10.4028/www.scientific.net/SSP.160.63.

[8] J. D. Robson, D. T. Henry, et B. Davis, « Particle effects on recrystallization in magnesium–manganese alloys: Particle-stimulated nucleation », *Acta Materialia*, vol. 57, nº 9, p. 2739‑2747, mai 2009, doi: 10.1016/j.actamat.2009.02.032.

[9] F. E. Kennedy, « Thermomechanical phenomena in high speed rubbing », *Wear*, vol. 59, nº 1, p. 149‑163, mars 1980, doi: 10.1016/0043-1648(80)90276-8.

[10] F. E. Kennedy, « Thermal and thermomechanical effects in dry sliding.pdf », *Wear*, p. 453‑476, 1984.

[11] A. Chamanfar, M. Jahazi, J. Gholipour, P. Wanjara, et S. Yue, « Maximizing the integrity of linear friction welded Waspaloy », *Materials Science and Engineering: A*, vol. 555, p. 117‑130, oct. 2012, doi: 10.1016/j.msea.2012.06.041.

[12] P. Geng, G. Qin, J. Zhou, et Z. Zou, « Hot deformation behavior and constitutive model of GH4169 superalloy for linear friction welding process », *Journal of Manufacturing Processes*, vol. 32, p. 469‑481, avr. 2018, doi: 10.1016/j.jmapro.2018.03.017.

[13] J. Humphreys, G. S. Rohrer, et A. D. Rollett, *Recrystallization and related annealing phenomena*, Third Edition. Elsevier, 2017.

# Chapter V

## Comparative evaluation of Post-Weld Heat Treatments on the Precipitation Hardened ('PH-Centre') and the Solution Annealed ('SA1') IN718 weld configurations

***Microstructure stability under post-weld heat treatment for re-homogenization***

***&***

***Monotonic tensile tests***

### Background

From a practical point of view, the joints in the As-Welded (AW) state are unusable for further applications, whether precipitation hardened or solution annealed. Indeed, the welded microstructures are markedly heterogeneous in both material configurations, displaying gradual phase transformations and progressive grain fragmentation stopped at different level. The re-homogenization procedure aims at triggering recovery to sweep the deformed structures and stimulating grain growth in order to recover grain size statistics close to the parent materials. To this end, 1h aging treatments were applied on the welded samples. Such possibility has already been prospected elsewhere [1], [2] on inertia friction welded samples. The homogenization treatment is eventually followed by conventional annealing for intergranular δ phase precipitation and double aging for γ'/γ" strengthening phase precipitation.

The annealing temperature values were chosen around the δ-*transus* temperature (~1027°C) *id est*: 1020°C, 1030°C and 1035°C. The experimental procedure aimed at roughly evaluating the possible beneficial effects of these heat treatments on the as-welded microstructures. The evolution and the stability of the as-welded microstructure under such thermal loads has been inspected with attention. The response of the precipitation hardened and solution annealed welded states to the homogenization treatments are compared.

Finally, the mechanical viability of these configurations will eventually be tested *via* monotonous tensile tests followed by a DIC procedure.

# 1. Introduction

Simple prospections were carried out on the stability of the IN718 welded microstructures toward Post-Weld Heat Treatments (PWHT). Both configurations, the precipitation strengthened 'PH-Centre' and the solution annealed 'SA1' are tested through identical experimental protocols. The ultimate ideal goal for such strategy would be to recover the base material microstructure and erase the consequence of the eventful thermo-mechanical history the materials underwent in the junction zone. However, this task is extremely challenging. Indeed, the friction welding procedure intrinsically leads to sharp and progressive changes on the microstructural features across the joint. These variations result from the gradual thermo-mechanical loads that the materials endure during the process which in turn yield to considerably heterogeneous microstructures on a quite short-range distance (millimetric gradients). As a matter of consequence, imagining a heat treatment that would allow compensating the microstructural change within the affected zone without losing the specificities of the unaffected parent material appears quite idealistic and some compromises seem inevitable.

Contrary to titanium alloys where the precipitation kinetics from the β domain are complex and often necessitate alternate mechanical passes and controlled heating /cooling rates to obtain various types of microstructures. The nickel superalloys microstructure is quite simple: austenitic grains are pinned by an intergranular intermetallic phase (the δ phase), and strengthening secondary phases (the γ'/γ" phases) can be precipitated thereafter without noticeable influence on the grain characteristics.

Consequently, simple annealing procedures may be prospected in the first instance in order to shape the affected and plasticized austenitic grains by triggering grain growth and to try understanding the response of the microstructure toward bringing some thermal energy to the welded samples.

## 1.1 Sum-up on the microstructural changes within the PH and SA welded samples

The thermo-mechanical loads locally experienced by the materials during LFW yielded to remarkable microstructural changes that may be summarized as it follows:

On the one hand, the precipitation strengthened materials underwent a substantial γ'/γ" dissolution on ± 2 mm band within the junction zone. Then, the austenitic microstructure indicates progressive markers of plastic deformation with increasingly squashed-like grains displaying more and more intense internal misorientation gradients. As approaching the weld center zone, the influence of the temperature elevation triggered a thermally activated grain fragmentation process identified as a discontinuous dynamic recrystallization phenomenon; the microstructure thus displays a bimodal aspect composed of deformed parent austenitic grains and small recrystallized crystallites with a progressive global grain refinement as getting closer to the welding line. The weld center zone is characterized by a fine equiaxed microstructure (with a ~6 µm grain equivalent diameter), the low-internal misorientation gradients indicate that the recrystallized process operating reached its stable dynamic grain size. Lastly, a progressive dissolution of the intergranular δ phase

was found in the zone comprise from ±250 µm and ±500 µm to the WL. The ±250 µm band of microstructure neighboring the WL appears to be completely free of δ-phase compounds.

On another hand, the solution annealed configuration does not present γ'/γ" phases since they are not present in the initial microstructure. However, a wider portion of the austenitic microstructure demonstrates a marked plastic deformation in the joint. These markers extend on a ± 5 mm thickness from the WL position and are most likely due to the combination of a softer mechanical behavior for the IN718 depleted from its usual strengthening precipitates and a longer processing time. The latter presumably yielded to the establishment of a thicker temperature gradient across the joint. This is notably reinforced by the observation of a wider δ-phase depleted zone of ±400 µm on both sides of the WL. Contrary to the precipitation hardened configuration, the misorientation gradients intensity that usually reveal the extent of plastically deformed zone are smoother and quite moderate across the junction. Similarly, the hot deformation process also led to a discontinuous dynamic recrystallization. This is readily discernible on a characteristic zone of the affected microstructure presenting deformed parent grains with locally higher internal misorientations. The observed necklace structures formed by nucleated crystallites with low density of dislocation confirmed such hypothesis. Large bands of layer-like grain structures characterized by low to intermediate internal misorientations neighbors the WL on both sides. Finally, the weld center zone also displays a fine equiaxed recrystallized microstructure on a ±250 µm thickness.

To summarize, the gradual thermo-mechanical loads resulted in a heterogeneous affected microstructure frozen at different stages of plastic deformation. The response of the materials is function of the mechanical load and the level of thermally activated mechanisms ongoing in the local microstructure. The intergranular δ phase is shown to progressively decompose until a total dissolution in the weld center zone.

### 1.2 Specifications and objectives of the PWHT procedure

Knowing these facts, some basic specifications may be enumerated for the re-homogenizing of the microstructure in the friction welded joints:

(1) After PWHT, the resulting austenitic microstructure should ideally present the same general characteristics as the parent materials one, *id est*: grain size distribution and grain boundary types fraction in similar or comparable order of magnitude.

(2) In term of phase presence, similar fraction of δ phase would be expected between the parent and the affected materials to consolidate the grain boundary stability of the austenitic microstructure. An over-precipitation of δ phase is to avoid because it would notably consume the Nb and Al which are key elements for the strengthening precipitates formation responsible and lead to a global deterioration of mechanical properties.

(3) The γ'/γ" strengthening phases can be precipitated afterward once the γ austenitic characteristics of the microstructure are stabilized.

(4) A residual stress relieves in the joint (even if this matter will not be prospected in this work).

### 1.3 Constraints on the PWHT elaboration procedure

Now that the ideal objectives are established and in accordance with the microstructural observations, the following constraints may be formulated:

(1) When the oscillating motion stops, the materials undergo a critical cooling. The deforming microstructure was consequently frozen in a complete out of equilibrium state. Regarding that, the austenitic γ grains not only display heterogeneous size and shape statistics in function of their position in the joint but also way different level of internal stored energy in form of structural defects. The latter fact signifies that huge discrepancies may be expected toward grain growth behavior under the intake of thermal energy when these grain structures are annealed.

(2) In addition, nickel-based alloys are known to present some deviations from the usual standard grain growth behavior under specific conditions. These features are often referred as "abnormal grain growth" or "critical grain growth" in the literature [3]. Such phenomenon yields to the excessive and localized growth of a few grains at the expense of others during grain growth annealing procedure. It results in important grain size heterogeneities among the final microstructure.

(3) The presence of residual defects in form of nano-oxides and porosities at the weld interfaces will presumably influence the grain growth behavior in the weld center zone microstructure and will be attentively followed up. Their pinning influence on grain further grain growth behavior is suspected to be strongly depending on their stability toward the annealing temperature loads.

(4) The partial then complete dissolution of the δ phase in the weld junction is also of matter of importance; because of the possible pining and drag effect on the microstructure to re-homogenize it brings. Furthermore, as the microstructure was squashed under the action of the compressive strain, the δ phase particle are reproached each other as moving toward the weld center zone creating denser zone of δ compounds. Nevertheless, the latter effect must be balanced out because of the concomitant progressive dissolution of the δ intermetallic phase. These heterogeneities in term phase presence may create a delayed and space-dependent drag effect according to the chosen annealing strategy.

(5) Lastly, in the perspective of industry applicability, the heating kinetics and holding time for heat treatments must ideally be applicable on massive workpieces which implies long exposure time to the thermal load.

Regarding that, two post-weld heat treatment strategies are envisaged in the first instance:

> On the one hand, *super*-δ-*transus* strategies would be attractive because it would allow a complete reset on the phase presence within the alloys. Simultaneously, the triggering of the grain growth mechanisms may allow recovering a homogeneous microstructure, indeed; the quicker growth kinetics of the refined and fragmented part of the affected microstructure may bridge the gap with the large parent grains while they display much slower growth kinetics. The δ phase may be recovered afterward by a simple precipitation annealing stage. Nevertheless, such a procedure would in counterpart imply grain growth rate that would be difficult to control, eventually leading to a coarse grains microstructure. The latter would probably demonstrate important decrease of its mechanical performance, notably on the elastic/plastic domain yield point that would most likely subsequently decrease. Nonetheless, super-δ-transus strategies may be interesting for in-use applications that would require coarse austenitic grain structures. Furthermore, such procedure would also be of scientific interest for purpose of testing the stability of the interfacial defects regard high annealing temperature loads and test their viability regarding this major issue.

< On the other hand, *sub*-δ-*transus* strategies would allow a better control on the grain growth rate within the affected microstructure without significant consequences on the parent microstructure. However, the precipitation of additional δ phase may globally weaken the mechanical integrity of the joint. In addition, the precipitation of ancillary δ phase particles may induce an additional drag effect and act as supplementary obstacles for grain boundary migration. Thus, considering these retardation effects and the heterogeneous state of the as-welded microstructure (both, in term of grain size distribution and density of internal defects), obtaining a spatially homogeneous grain size after *sub*-δ-*transus* annealing would still be a harsh task. Nevertheless, such a strategy may require a compromise in order to get a close to homogenized microstructure with properties close to the parent materials.

## 2. Materials & methods for microstructural characterizations

Considering the previously enumerated issues, annealing ramps were applied on selected As-Welded specimens (AW). The post-weld heat treatments were applied on extracted specimen from the welded workpieces. The extraction method is schematically illustrated in the Figure 1 below. The position of the extracted samples for microstructural analyses is situated between the x=5 to x =20 mm within the welded workpieces.

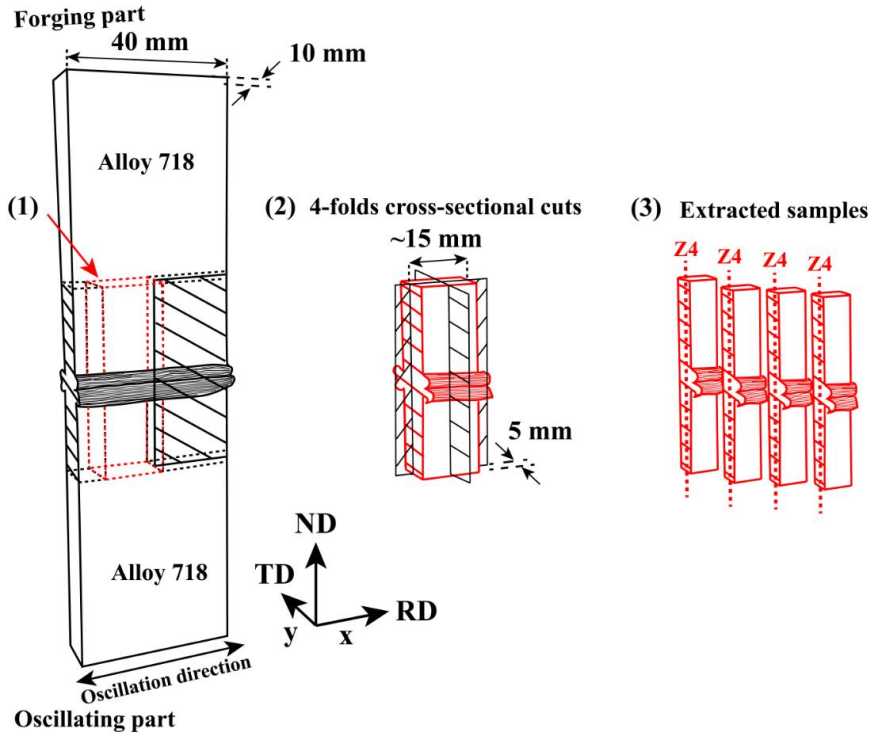


**Figure 1**: *Sample extraction strategy for the post-weld heat treated samples.*

The microstructural analyses were carried out on the "Z4" profiles *id est* along the Z direction (or ND) at 1 mm from the weld expulsion zone. The latter zone was chosen because it is suspected to still present a consequent amount of defect in the weld center line zone as one of the objectives is to test their influence and their possible detrimental effects on grain growth during the post-weld heat treatment procedures.

After heat-treatments, the specimens were first mechanically polished on few hundred of µm through with standard abrasive procedures, this in order to prevent disruptive effects due to the interaction of the sample with oxygen during the heat treatment procedure. For metallographic observation, the polishing procedures were then carried on until a P4000 grit size and using SiC abrasive grinding papers. The finishing procedure is then the same as for the as-welded samples with successive polishing using a standard diamond solution from 3 µm to 1 µm particle mean diameter on a polyester cloth. The final surface finishing is done using a 50% oxide polishing suspension (OPS) solution and 50% in volume of $H_2O$ on a Buehler VibroMet™ 2 vibratory polishing machine.

Now, for the delicate choice of the annealing temperatures, an interesting compromise to test would be to try annealing temperature close to the δ-*transus* point. The point would be to try to provoke an extensive grain growth in the affected and refined microstructure only, and contain the latter in the non-affected parent materials microstructure. Regarding that, the presence of the δ-phase is necessary and effective to keep control on the parent austenitic microstructure. Nevertheless, further δ-phase precipitation may also impinge grain growth in the affected zone and deteriorate the strength performance in the parent materials because of the supplementary Nb element consumption it causes (Nb elements are essential for γ" precipitation formations, which is the main material's strengthener).

Thus, an ideal compromise then would be: on the one hand, to initiate the slow dissolution of the δ-phase in the parent material zone, in order to preserve the original microstructure characteristics. On another hand, to stimulate a static recrystallization and a grain growth phenomenon in the affected zone, in order to regularize the grain size distribution characteristics across the junction. However, the latter issue would still be difficult regarding the important and gradual heterogeneities of stored energy, grain size and residual phase presence within the affected microstructure that may be tough to monitor. Ideally after this stage a grain size distribution in the order of magnitude of the one of the parent materials is reached (or let us pretend as if that were the case). A δ-precipitation annealing procedure can then be carried out in order to 'freeze' the resulting microstructure. The role of the slow δ-phase dissolution previously done is to avoid a δ-phase over-precipitation afterward. Lastly, the double-aging annealing procedure can be performed for γ'/γ"-precipitations within the austenitic matrix and to confer its final in-use mechanical properties to the joint.

Knowing that the expected δ-*transus* is supposed to be within a [1025°C, 1030°C] temperature range, the annealing prospections were made around this value. Consequently, three holding annealing temperatures were chosen for extensive microstructure characterizations. A holding time of 1 hour was chosen (which is quite enough for massive pieces). The chosen annealing temperatures are presented as it follows:

(a) **1020 °C**

(b) **1030 °C**

(c) **1035 °C**

Every annealing stage is followed by an air quenching procedure (AQ). After that, the standard IN718 heat treatment was carried out. The latter consists in a δ-precipitation annealing procedure applied for 2 hours at a 990°C holding temperature and followed by an air quenched. Then, the sample were strengthened through the classical double stage γ'/γ"-precipitation annealing procedure: 8h at 720°C followed by 8h at 620°C with a controlled cooling rate of 50°C/h in between. The samples were finally left to cool down in the furnace until room-temperature.

In short:

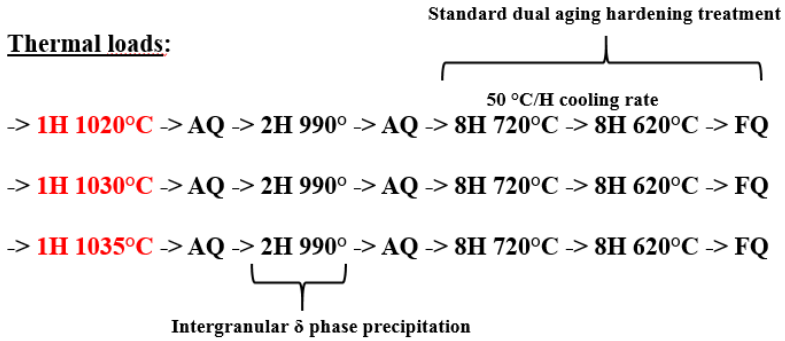


## 3. Results on the Post-Weld Heat Treated (PWHT) microstructures: PH & SA1

### 3.1 Observations in the near-WL zone

First, EBSD analyses were carried out first around the weld center zone for each post-weld heat treated samples. Both material configurations, the precipitation hardened one ('PH – Centre') and the solution annealed one ('SA1') were examined. The comparative results are exposed in Figure 2 for the PH configuration and Figure 3 for the SA configuration.

The position of the WL is clearly identifiable due to the persistent fine microstructure retained in the interfacial zone. An important portion of the WL recrystallized grains displays a fine and little to ungrown microstructure in all extracted samples. Such finding outlines that an important drag effect most-likely occurred in that zone and strongly hindered the grain growth phenomenon. The drag effect is probably imputable to the presence of disseminated contaminant that remained stable under the applied thermal loads.

In term of grain boundary types, it is globally remarked that the resulting microstructure after annealing treatment is essentially composed of High-Angle Grain Boundaries (HAGB) with a general boundary character similar to the parent microstructure id 97% of HAGB of which about 43% are ∑3 special boundaries and 3% are Low-Angle Grain Boundaries (LAGB). Those numbers are comparable with the ones of the parent microstructures.

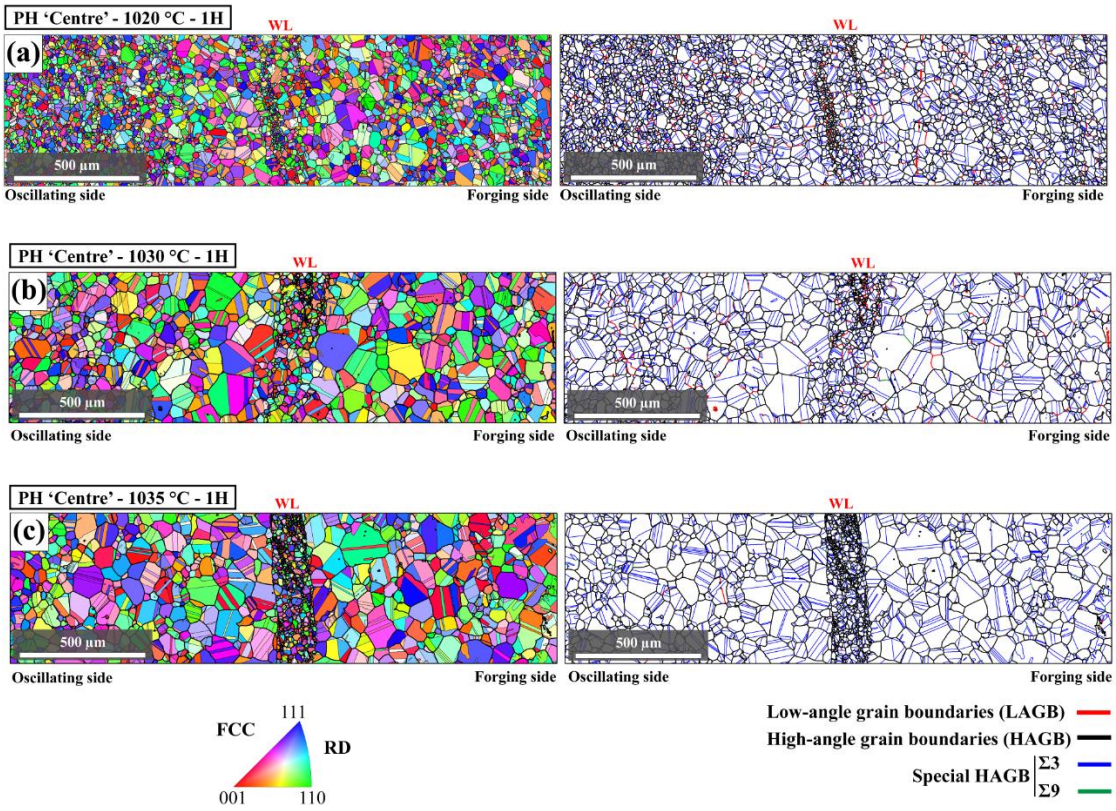


**Figure 2**: *PH microstructure evolution near the WL zone at the Z4 position after 1h annealing at* **(a)** *1020°C;***(b)** *1030°C and* **(c)** *1035°C followed by an air quenching procedure.*

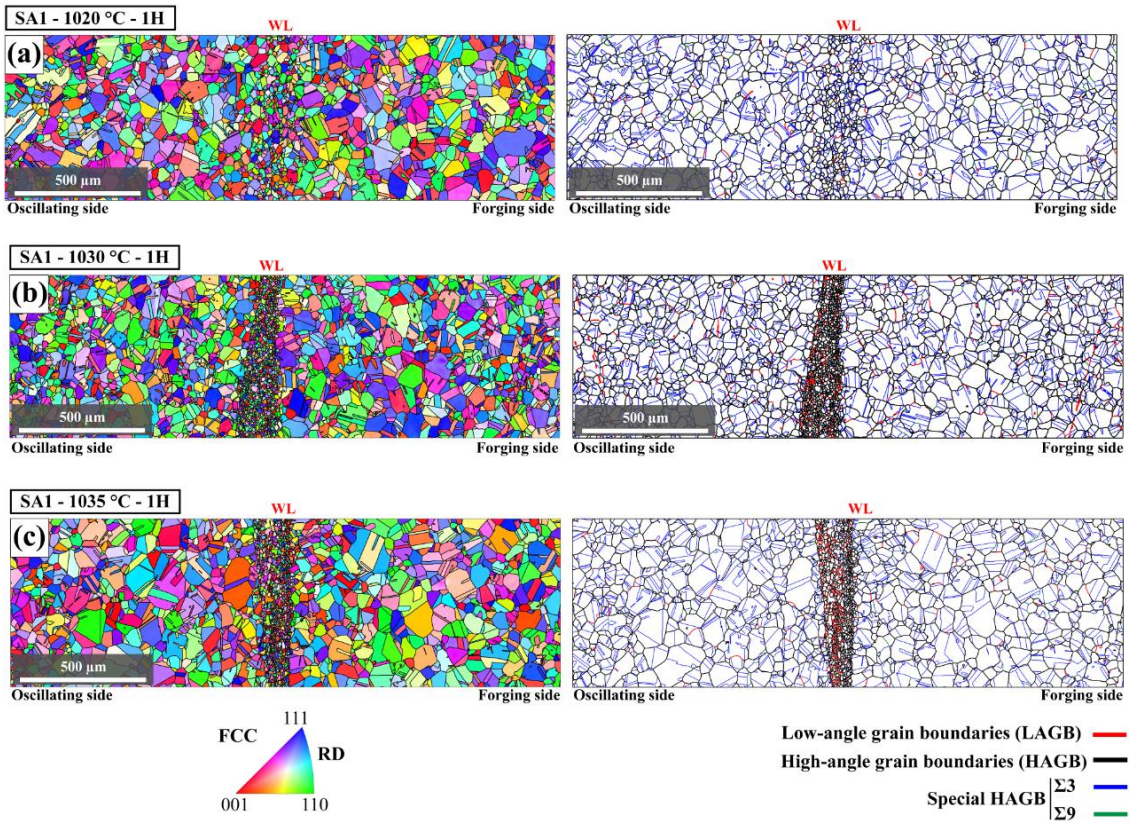


**Figure 3**: *SA1 microstructure evolution near the WL zone at the Z4 position after 1h annealing at* **(a)** *1020°C;* ***(b)*** *1030°C and* **(c)** *1035°C followed by air quenching.*

The corresponding grain equivalent diameter maps are plotted in Figure 4. The 1020°C/1h annealed microstructure is quite fine and regular with slightly higher grain size in a ±400 µm band neighboring the WL. The latter observation is most likely due to the subsequent to complete dissolution of the δ phase in the close-WL microstructure during the friction welding process.

The 1030°C/1h and 1035°C/h microstructures display significant grain growth that would corroborate with a weaker pining influence of δ-phase on it in the affected zone combined with a slightly higher thermal energy brought by the external medium.

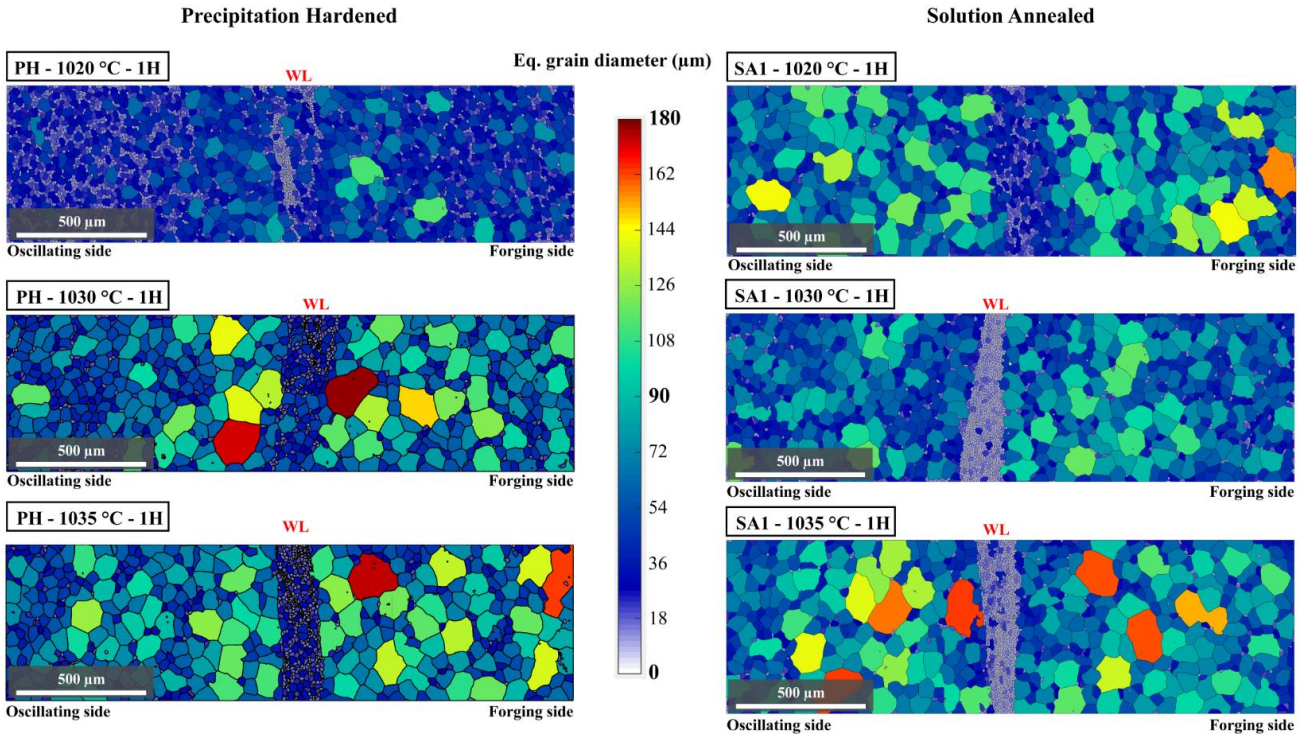


**Figure 4**: *Grain size equivalent diameter map near the WL zone at the Z4 position after 1h annealing followed by air quenching; the results are displayed for the PH-Centre and SA1 configurations.*

The welding line demonstrates an important density of defect in the weld junction zone (Figure 5). The presence of defect apparently limited the motion of the crystal interfaces from on side of the defect line to the other, probably due to a strong Zener-Smith pining effect. The latter hindered the grain boundary mobility across the weld interface.

Further prospections by SEM analyses (Figure 6) prove that an important population of nano-oxide particles remained stable along the WL zone despite the annealing procedure; the SEM observations also evidence the appearance of fine sub-micrometric spherical voids in the junction zone. Such spherical-shape aspect may indicate these voids they reached a thermodynamic equilibrium with the adjacent solid matter.

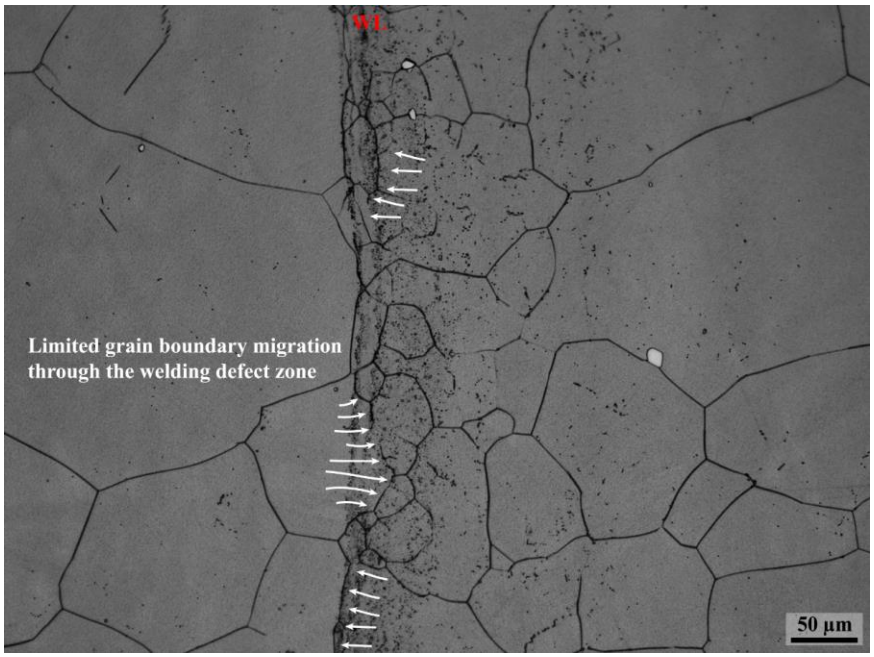


**Figure 5**: *Visible light micrograph at the WL of the 'PH-Centre', 1030°C/1h annealed sample, Z4 profile.*

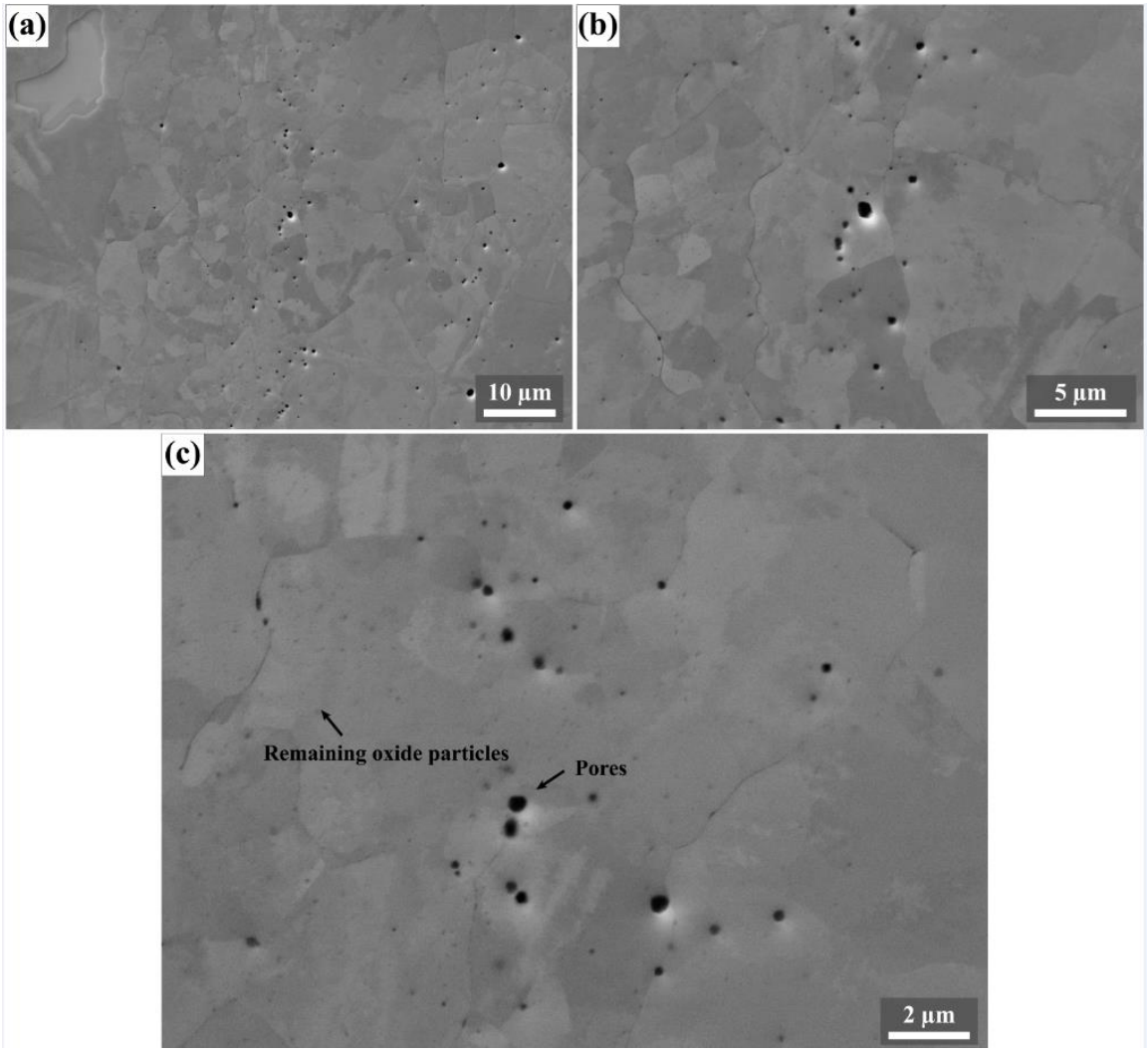


**Figure 6**: *SEM micrographs at the WL of the 'PH-Centre', 1030°C/1h annealed sample, Z4 profile.*

### 3.2 Critical grain growth in the affected zone

A global overview of the microstructural changes induced by the annealing heat treatment on the process affected microstructure is illustrated in the Figure 7 below for the precipitation hardened configuration: 'PH-Centre'.

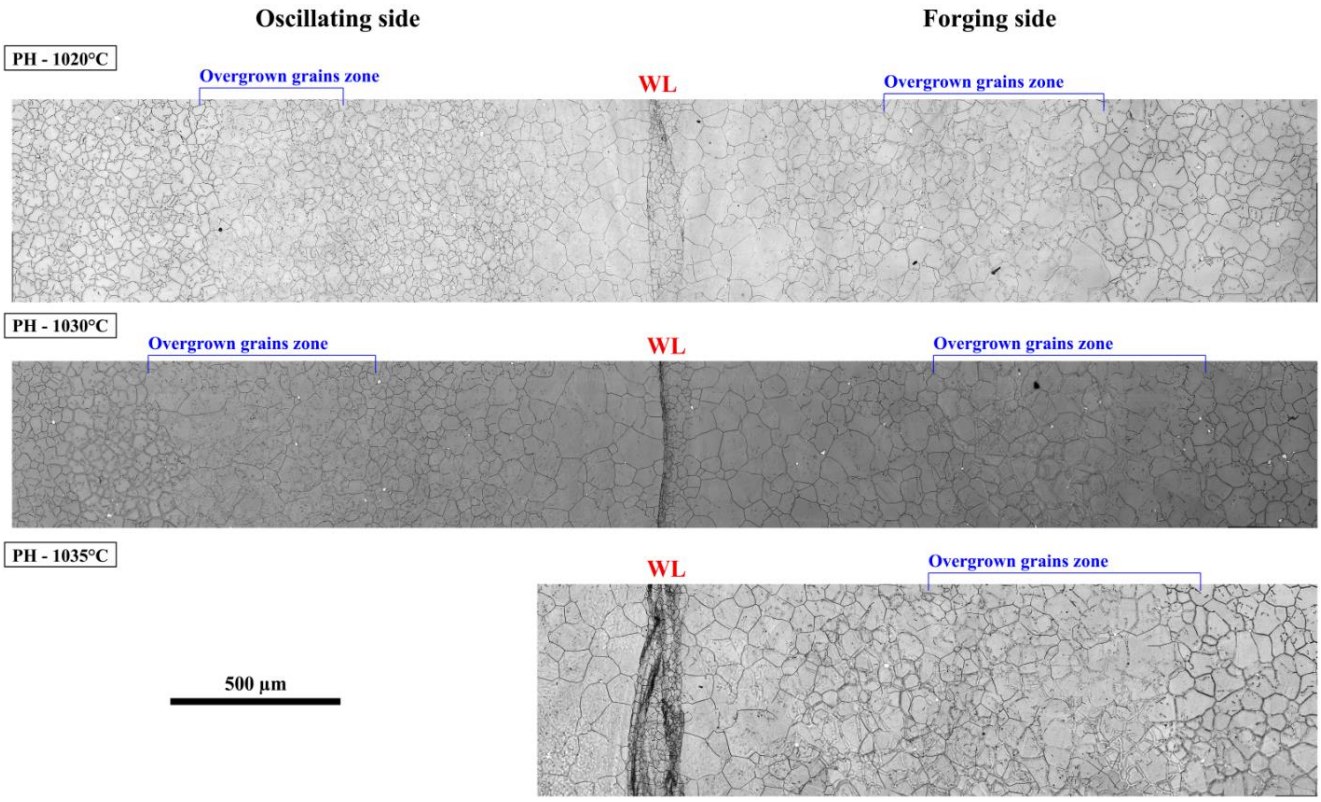


**Figure 7**: *Visible light overview of the 'PH-Centre' configuration after 1h annealing, Z4 profile.*

The overmatch of intergranular (mostly) δ phase presence with grain boundaries allow to identify the parent grain structures. The latter remained remarkably stable during the three conducted annealing procedures. Then, the microstructure demonstrates clear morphological changes. In the far-thermo-mechanically affected zone, it is suggested that the δ phase did not completely decomposed into the γ austenitic matric. The white local traces visible in the optical micrographs mark the remnant presence δ phase because of the local niobium enrichment it implies. An important fraction of remnant δ phase is observed to disjoin form the grain boundary interfaces. As getting closer to the WL, the remnant δ phase markers eventually blur away indicating a complete δ phase decomposition into the metallic matrix. Thus, the element composition tends to homogenize in the weld center zone.

In the far-thermo-mechanical affected zone the parent microstructure is shown to be in direct contact with particularly remarkable and peculiar grain structures. Indeed, a coarse microstructure composed gigantic crystallites of the size of several parent grains grouped upon each other are evidenced. A closer insight is given in Figure 8, focusing on the forging side annealed microstructures. The critical grain growth phenomenon is notably highlighted by the visible presence of remnant δ phase markers. The latter originates from the initial

microstructure within their austenitic structure. Such features are observed on both sides of the junction and for the three tested annealing temperatures. They are highlighted as the “overgrown grains zones’ in Figure 7.

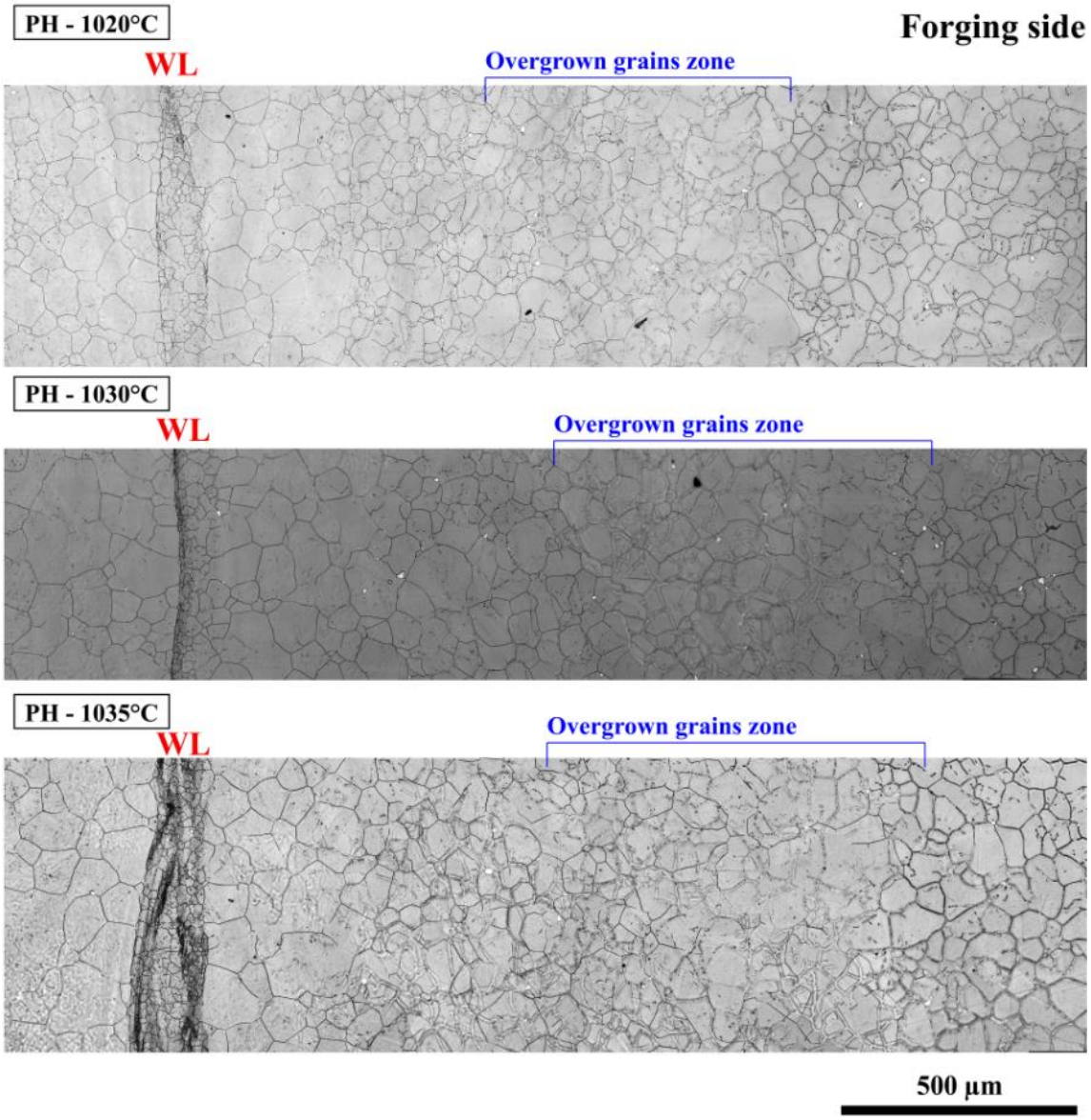


**Figure 8**: *Optical micrograph focusing on the forging side microstructure of the ‘PH-Centre’ configuration after 1h annealing, Z4 profile.*

To demonstrate the spatial coherence in term of crystallographic orientation of these super-grain structures, complementary analyses were carried out by EBSD in the far-thermo-mechanical zone. The crystal orientation analyses unequivocally strengthened the overgrowth phenomenon evidenced by the above visible light observations. The phenomenon is particularly remarkable on the PH-center 1020 °C/1h annealed sample given as an illustration in Figure 9, where the overgrown zone denotes from the neighboring microstructure.

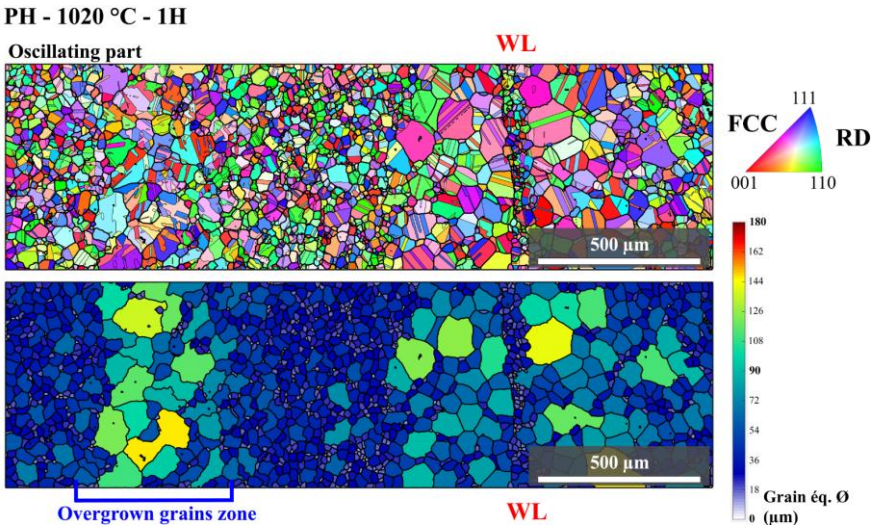


**Figure 9**: *EBSD analyses focusing in the 'overgrown grains zone" of the PH-center 1020 °C/1h annealed sample, oscillating side. The inverse pole figure map is provided with its associated equivalent grain diameter map.*

The critical growth phenomenon observed is intriguing and seems to happen in very specific zones of the thermo-mechanically affected microstructure of each tested sample. This finding means that specific conditions must be reunited within the local plastically deformed microstructure to trigger the phenomenon. Regarding that, it would then be interesting to compare the 'As-Welded' microstructures with the Post-Weld Heat treated ones. Consequently, the Figure 10 compares the post-weld heat treated microstructure of the 'PH-1030°C/1h annealing' with the GOS signal of a former comparable as-welded microstructure. Interestingly, the critical grain growth location seems to corroborate with a zone presenting intermediate to low GOS values. Furthermore, the local microstructure outlines the features of partial dynamic recrystallization with an unachieved subdivision/rotation process among the deformed crystallites and limited nucleation events along the former parent grain boundaries.

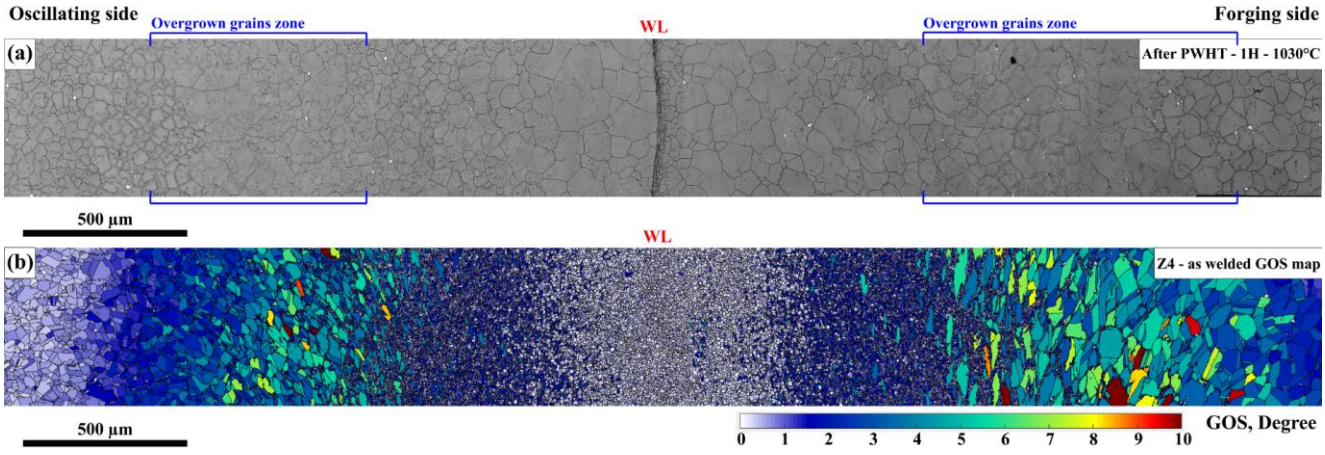


**Figure 10**: *Comparison between* **(a)** *the PH-center Z4 profile after a 1030 °C/1h long annealing homogenization treatment and* **(b)** *the Grain Orientation Spread indicator of the As-welded microstructure at the Z4 position (10° threshold). The superimposed grain boundaries are displayed (2° threshold).*

The PWHT on the SA1 configuration resulted in similar microstructural features (Figures 11 & 12):

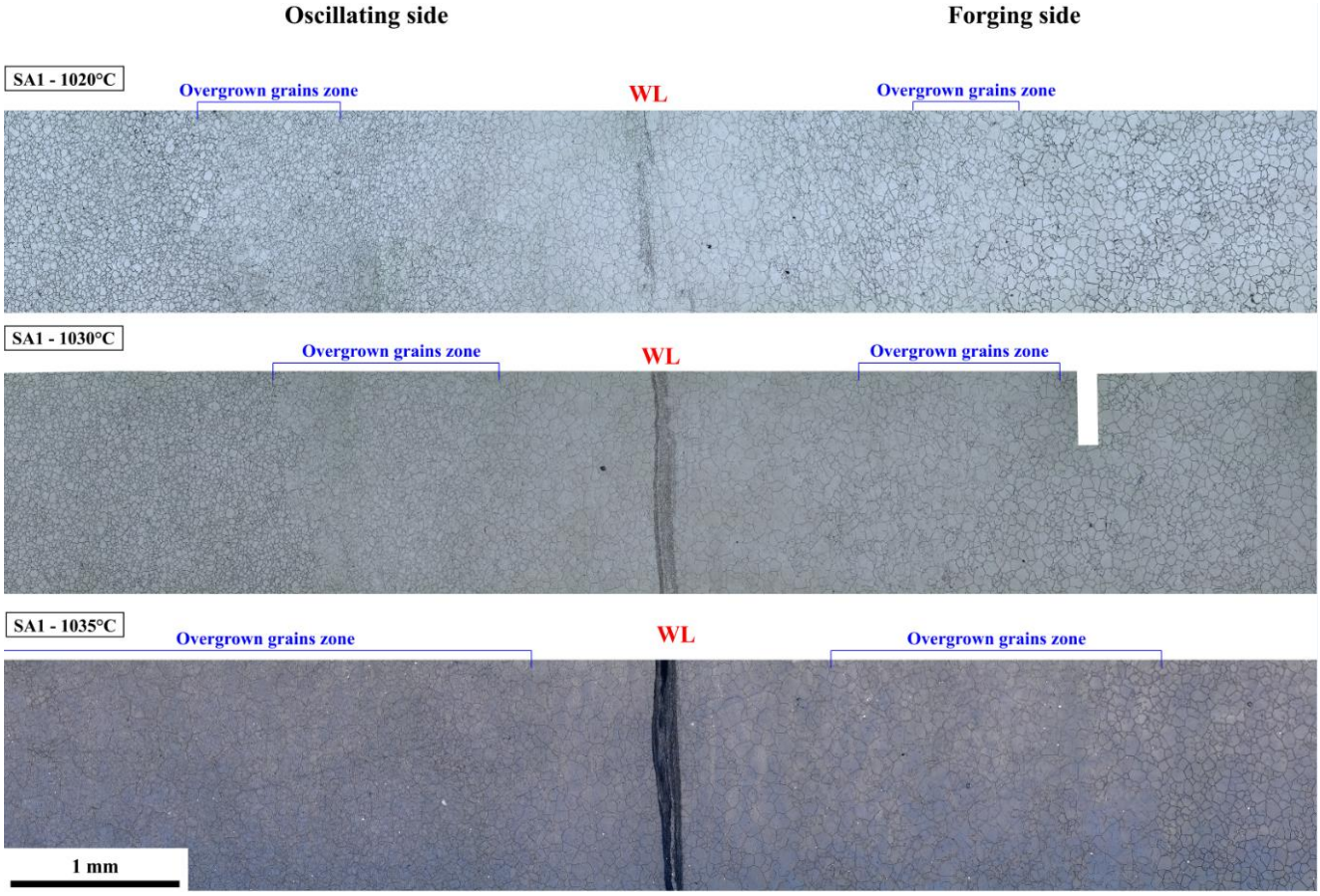


**Figure 11**: *Visible light micrograph at the WL of the 'SA1', 1030°C/1h annealed sample, Z4 profile.*

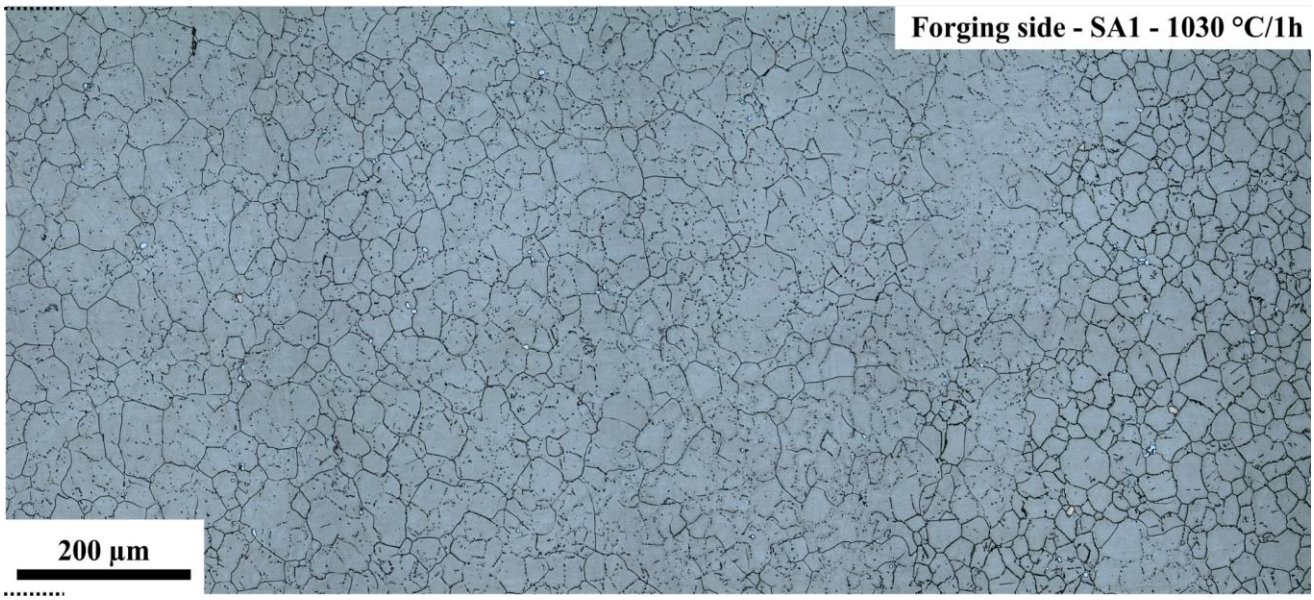


**Figure 12**: *Optical micrograph focusing on the 'overgrown grains' zone of the SA1 configuration after PWHT (1030°C/1h annealing then air quench), the left part of the image is about 800µm away from the WL.*

Overgrown grains were also observed on each tested SA1-annealed configuration. The global intensity of grain overgrowth phenomena seems higher than for the 'PH-Centre' weld configuration. The comparative observation of the annealed microstructure with the prior as-welded microstructure (Figure 13) seems to corroborate than the overgrowth phenomenon tends to occur in the far-thermo-mechanically affected zone.

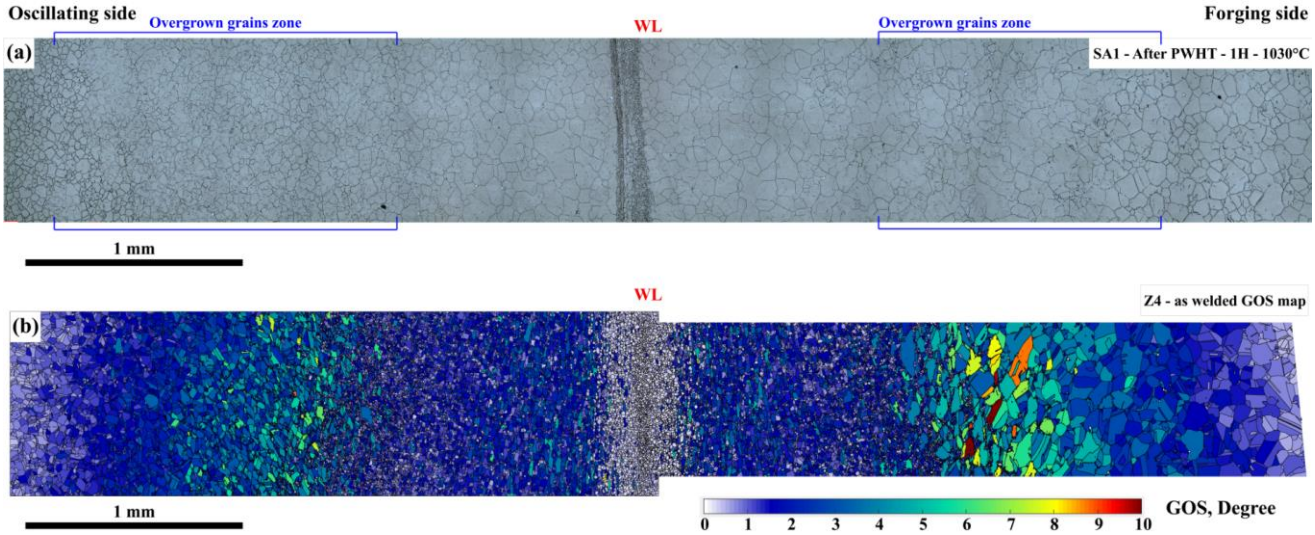


**Figure 13**: *Comparison between* **(a)** *the SA1, Z4 profile after a 1030 °C/1h long annealing homogenization treatment and* **(b)** *the Grain Orientation Spread indicator of the As-Welded SA1 microstructure at the Z4 position (10° threshold). The superimposed grain boundaries are displayed (2° threshold).*

Identically to the PWHTed 'PH-Centre' configuration, the near weld center zone displays coarser austenitic grain size on a ±400 µm band of microstructure adjacent to the WL. The WL zone also presents a fine microstructure with evidences of defects within.

## 4. Discussion

From a global point of view, the grain size statistics after homogenization post-weld heat treatment attempts remain quite heterogeneous and the severe microstructural changes induced by the linear friction welding procedure could not be compensated. This; regardless the tested annealed configuration. Indeed, despite the thermal load, the weld center zone microstructure remained quite fine and displays a similar aspect to the as-welded state without significant grain growth.

On the contrary, the bands of microstructure adjacent to the WL and extending on a ± 400 µm width present prominent grain growth. The latter zone corresponds to the former as-welded microstructure displaying advanced stages of discontinuous dynamic recrystallization accompanied with subsequent δ phase dissolution. As a result, the local microstructure underwent an unconstrained grain growth behavior starting from a fine recrystallized microstructure under annealing. The absence of δ phase could not hinder grain growth yielding to a coarse final microstructure.

Afterward, a lower grain size was noticed, remnant traces to δ phase were observed and mostly do not match with the current grain boundary position after annealing. It is then strongly suspected that the partially recrystallized and heavily deformed as-welded microstructure corresponding to that zone got through a static recrystallization process leading first to a refined microstructure, then to a "normal" grain growth phenomenon. The lower grain size compared to the close WL microstructure is most likely due to the drag effect induced by the remaining stable δ phase particles on the growing microstructure.

Then, a particularly coarse microstructure is observed with a grain equivalent diameter reaching and unusually irregular grain boundary shapes, as if several grains have been merged together. The formation mechanisms for such grains super-structures will be discussed further on in details in the section 4.2.

Lastly, it is noticed that the parent austenitic microstructures in the unaffected zone remained stable with apparent grain size statistics similar to the pre-heat-treated state. However, it is probable that slight changes on the δ phase fraction occurred during the annealing procedures depending on the *sub* or *super* δ - *solvus* applied thermostat.

### 4.1 Zener-Smith drag phenomenon in close interfacial zone

Despite the high temperature post-weld annealing procedures carried out, the abundant presence of defects totally hindered further grain growth and resulted in the formation of a very fine austenitic microstructure in the junction zone. Remnant dispersed nano-oxide particles were observed in the weld junction proving that these entrapped species are particularly stable and that they could not be dissolved in the metallic matrix despite quite high applied annealing temperatures.

It is consequently suggested that a Zener-Smith particle pining phenomenon [4] heavily affected the mobility of grain boundaries by exerting a strong antagonistic anchoring resistance to the displacement of the crystal interfaces. When migrating a grain boundary is then susceptible to be pinned at some portion under the action of the surface tension differences with particles. The particle/boundary interaction results in a force $F_z$ which opposes the driving force. The calculation of the maximum pining pressure (Fz) due to a random population of spherical particles exerting a drag force on a grain boundary is given by the following relation [4]:

$$F_Z = \frac{3\gamma F_V}{2r}$$

Where $\gamma$ is the surface energy of the grain boundary, *r is* the mean particle radius and *Fv* the volume fraction of the precipitate.

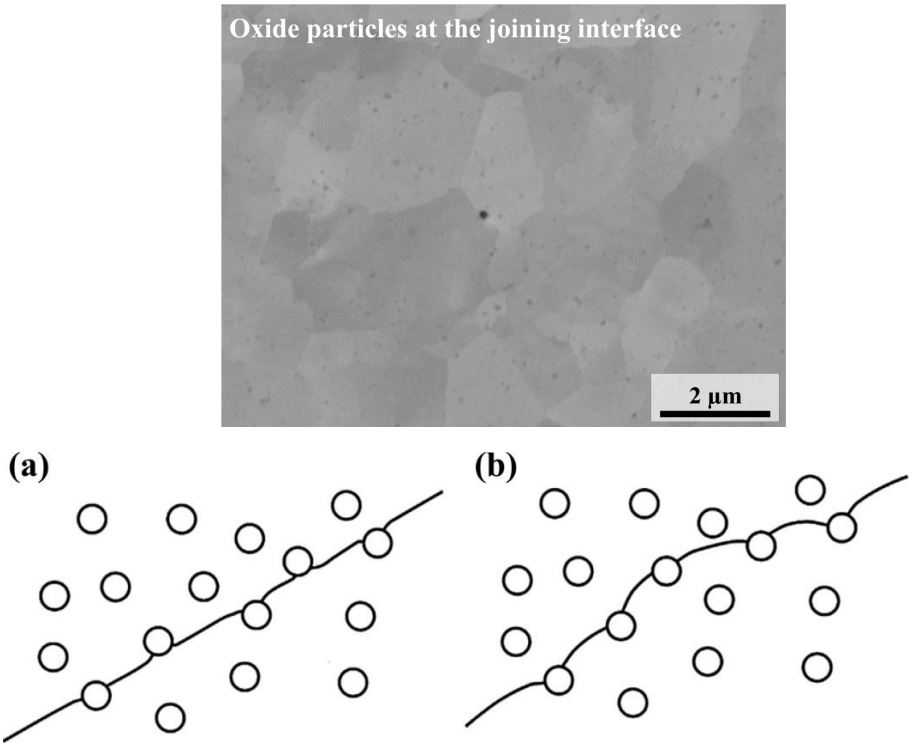


**Figure 15**: *SEM images of the precipitated oxide particles at the weld interface embedded in a fully recrystallized austenitic microstructure.* **(a)-(b)** *Schematic representation of the drag effect induced by disseminated spherical particles on a moving crystal interface as modeled by Zener-Smith.*

Furthermore, a remarkable and concomitant presence of sub-micrometric voids was also observed in the close interfacial zone. Such a large proportion of void was not detected on the as-welded configurations. Consequently, these observations are quite intriguing and their appearance does not find a straightforward physical explanation. So, only hypotheses may be formulated. The round shaped aspect of the voids suggests that they reached kind of thermodynamic equilibrium with the surrounding medium. Their formation may result from the coalescence of undetected nanovoids during the annealing treatment. Or, it can be suggested

that they may result from the decomposition of some entrapped oxide species into gaseous reactional products through time leading to these observed round shaped porosities. Notably, the passivation layer mainly composed of chromia ($Cr_2O_3$) may sublimate into the gaseous: CrO3(g) under high temperature condition, leading to the formation of internal porosities.

### 4.2 Critical grain growth mechanism

After the annealing procedures, a few grains are observed to selectively grow far more on average that others in the far-thermomechanical affected zone [3], despite the presence of residual δ phase particles. Similar cases of excessive growth of grains in nickel based alloys (but not only) are abundantly reported in the scientific and technical literature [5]–[7]. They notably pose serious issues in forge processing and powder metallurgy. The phenomenon is often referred with different terminologies such as “abnormal grain growth” (AGG), “critical grain growth” (CGG) [8], “large grain growth” (LGG) or “inhomogeneous grain growth” (IGG). All these terms designate a general microstructural evolution where a few grains excessively grow at the expense of their neighbors under the application of a thermal load. Regarding these general observations, many efforts were realized in the field aiming at; first, evaluating the influence of deformation and annealing temperature on the triggering of the phenomenon and second, understanding the exact underlying mechanism that would yield to the formation of overgrown grains in a deformed microstructure.

It is first noted that the “abnormal grain growth” designation most often refers to particular grain growth conditions that usually take place in highly textured materials [8]. In the latter case, the combination of strong anisotropy in terms of grain boundary mobility and grain boundary energy can lead to peculiar growth behavior during annealing where some grains with favorable configuration may grow at the expense of their neighbors. Nevertheless, this hypothesis can here be eliminated, as marked textures were not exhibited in the thermo-mechanically affected zone. Only slight simple shear texture components with intensities that are in the order of magnitude of 2 M.R.D. (Multiples of the Random Distribution) were measured on the deformed microstructure near the expulsion zone (cf. Chapter III). On another note, the relevance of the use of “abnormal” terminology to describe such phenomenon in the field is quite debatable since its mechanisms are rigorously explainable and do not nullify any physics law. The critical grain growth terminology appears preferable and will be employed from now in the discussion part.

The critical grain growth phenomena reported in the literature have in common to get triggered after annealing on former deformed microstructures that exhibit quite moderate strain values [6], [9], [7]. The exact critical strain window may vary from one alloy to the other regarding its composition, its preparation or the heat treatment applied. However, the different experimental works that have been carried out broad a solid consensus on the issue and estimate that the critical nominal compressive strain range lies between a $\varepsilon \sim 0{,}01$ value and a $\varepsilon \sim 0{,}1$ value [7].

The microstructural observations conducted on the different IN718 samples demonstrate that the linear friction welding procedure intrinsically generates a progressive strain gradient through the junction zone. It extends from a close to null value far from the WL and is estimated to reach values of several order of magnitude higher than $\varepsilon \sim 0{,}1$ in the WCZ. Consequently, the generated strain gradient inevitably overlaps the critical strain range. As shown on the comparative GOS map/post-heat-treated microstructure comparison displayed in Figure 9, such critical strain levels were reached in the far-thermomechanical affected zone which presents low deformation features.

The purported physical mechanisms for such critical growth phenomenon are two-folds:

**Assumption (1): the heterogeneous deformation at the grain scale led to local important heterogeneities in stored energy distribution:**

Indeed, when the external stress is raised above the yield stress, crystalline materials store structural defects in their lattice and plastic deformation arises. These defects, essentially dislocations, are responsible for the macroscopic plastic flow and carry the plastic deformation at the atomic scale level in form of successive plastic slip events mostly extending along slip bands. Such dislocation avalanches manifest a collective behavior and locally increases the dislocation density in their immediate environment, raising the local stress needed to produce further deformation because of work hardening. It is consequently outlined that the slip distribution within the crystal lattice is highly heterogeneous by nature.

Now at the grain scale, the multiplication, annihilation, rearrangement, entanglement and various interactions of these mobile dislocations allow adapting the grain shapes to the imposed external loads by introducing some grain rotation and lattice distortion in order to mediate the plastic deformation. In polycrystalline aggregates, the local grains behavior regarding deformation is highly constraint by its neighborhood, composed of different in-contact crystallites presenting anisotropic mechanical properties. Thus, as deformation proceeds the local constraints result in a highly heterogeneous partition of strain through the microstructure. In turn, the accumulation and self-structuration ability of dislocations spontaneously result in the formation of local lattice rotation by curvature introduction, eventually yielding to the formation of orientation gradients through the crystal. The latter introduced geometrically necessary defects are costly from an energetic point of view ($1/2.Gb^2$ where G is the lattice shear modulus and b the Burgers vector norm) and represent an important potential energy source stored within the lattice.

Knowing that, it is highly suspected that the critical strain conditions, even though moderate, lead to a particularly heterogeneous stored energy distribution within the deformed crystallites, where some part of the grains display strong orientation gradients and other remained close to an undeformed state. These features where notably described in the far-thermomechanically affected zone, where important orientation gradients observed to coexist with much slighter ones (to illustrate this statement, the Figure 10 provided below demonstrates such heterogeneous local lattice distortions in the far-TMAZ on the ‘PH – Centre’ configuration,

notably noticeable on the mis2mean signal). Nevertheless, such microstructural characteristics alone appear insufficient to explain critical grain growth and another factor must take place.

**Assumption (2): On such critically strained microstructure, a static recrystallization phenomenon can only be triggered at a limited number of nucleation sites during annealing:**

On another note, when such deformed microstructure is brought to an elevated temperature, the density of vacancies becomes several orders of magnitude higher. Simultaneously, the thermally induced vibrational energy substantially increases within the lattice. Hence, the dislocation mobility is significantly enhanced. On this basis, the deformed material processes to decrease its free energy by collective and spontaneous reconfigurations of its structural defects into lower energy structures such as dislocation walls, then low angle grain boundaries [10]; or simply by getting rid of portions of stored dislocations through annihilation events. Such recovery processes take place during the early stages of annealing and relieve the internal stresses. In some regions of the deformed material, the local conditions are reunited for the nucleation of new crystallites that present extremely low to none internal misorientations [11], [12].

In low/intermediate stacking fault energy alloys, as IN718, these nucleation events preferentially form by bulging mechanism [13] close to serrated grain boundaries (see Figure 13). Their formation necessitate an incubation time during which the nucleating crystallites first develop inner low-angle grain boundaries with the former parent matrix [14]. Once stabilized, they rapidly acquire a high disorientation toward the parent structure by grain rotation [15], while recovery processes self-clean the excess dislocations within the new-born *nuclei*. The resulting crystallites display fairly homogeneous orientations and are separated from their original deformed parent grains by high angle grain boundary types [16].

Yet, these fine *nuclei*, deprived of excess dislocations, start to grow at the expense of the deformed surrounding regions. The driving force for such grain boundary migration is qualitatively explained by the difference in potential energy between the *nucleus* which displays low dislocation density therefore low free energy and the deformed region of the microstructure with much higher densities of structural defects. Thus, the latter are swept away through the passage of the migrating crystalline interface (see Figure 15, classical Bailey & Hirsh nucleation criterion for recrystallization). Consequently, the heterogeneous partition of stored energy distribution triggers a static recrystallization phenomenon by strain induced grain boundary migration.

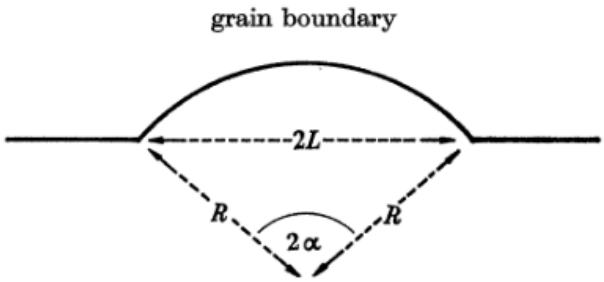


The model considered for the grain boundary migration process.

$$R_{\text{crit}} > \frac{2\gamma_b}{\Delta E}$$

**Figure 15**: *Bailey & Hirsh model* [17]. $R_{crit} > (2.\gamma_b / \Delta E)$*; where* $\Delta E$ *is the difference in stored energy between the two grains and* $\gamma_b$ *is the energy of the high angle grain boundary. It is noted that if the difference in stored energy increases, the critical radius for grain boundary bulging* $R_{crit}$ *decrease.*

To summarize, it is important to outline that local specific conditions must necessary be fulfilled to trigger a nucleation event by bulging mechanism. The latter would afterward lead to an effective recrystallization phenomenon by strain induced boundary migration. Various experimental works highlight that when the number of active nucleation sites is limited in a deformed microstructure, the recrystallization can produce exceptionally coarse grain structures Indeed, if the regions neighboring a recrystallized *nucleus* do not also complete the conditions for nucleation, they are prone to be devoured by the boundary migration during the growth phase of the recrystallization. Thus, there are strong evidences that inhomogeneous deformation condition leading to limited nucleation sites would correlate with the critical nominal compressive strain range lies between a $\varepsilon \sim 0{,}01$ value and a $\varepsilon \sim 0{,}1$ for critical grain growth. Once the strain induced boundary migration achieved, the further growth would shift to a capillarity driven mechanism assisted by capillarity force until mutual impingement with other overgrown structures presenting similar size and morphologic characteristics. In addition, it was elsewhere [6] remarked that that boundaries displaying $\Delta(\text{GOS}) > 1{,}5°$ between neighboring grains would be particularly favorable nucleation sites for bulging nucleation and strain induced boundary migration.

Differences in ‘overgrown grains’ intensity are noticeable between the welded configurations. The global trend observed is globally highly favored in higher temperature heat treated sample such as 1035°C/1h configurations. The solution annealed welded configuration is also observed to be more prone to ‘overgrown grains’ triggering phenomenon, probably because the resulted as-welded microstructure present higher fraction of low to intermediate grain deformation that would correspond to the critical strain range already highlighted in the nickel alloy forging literature [6], [9].

It is remarked that the driving force for crystal interface migration was strong enough to pass through residual non diluted δ phase particle which shows that the driving force for migration was high enough to pass through the residual phases pining effect.

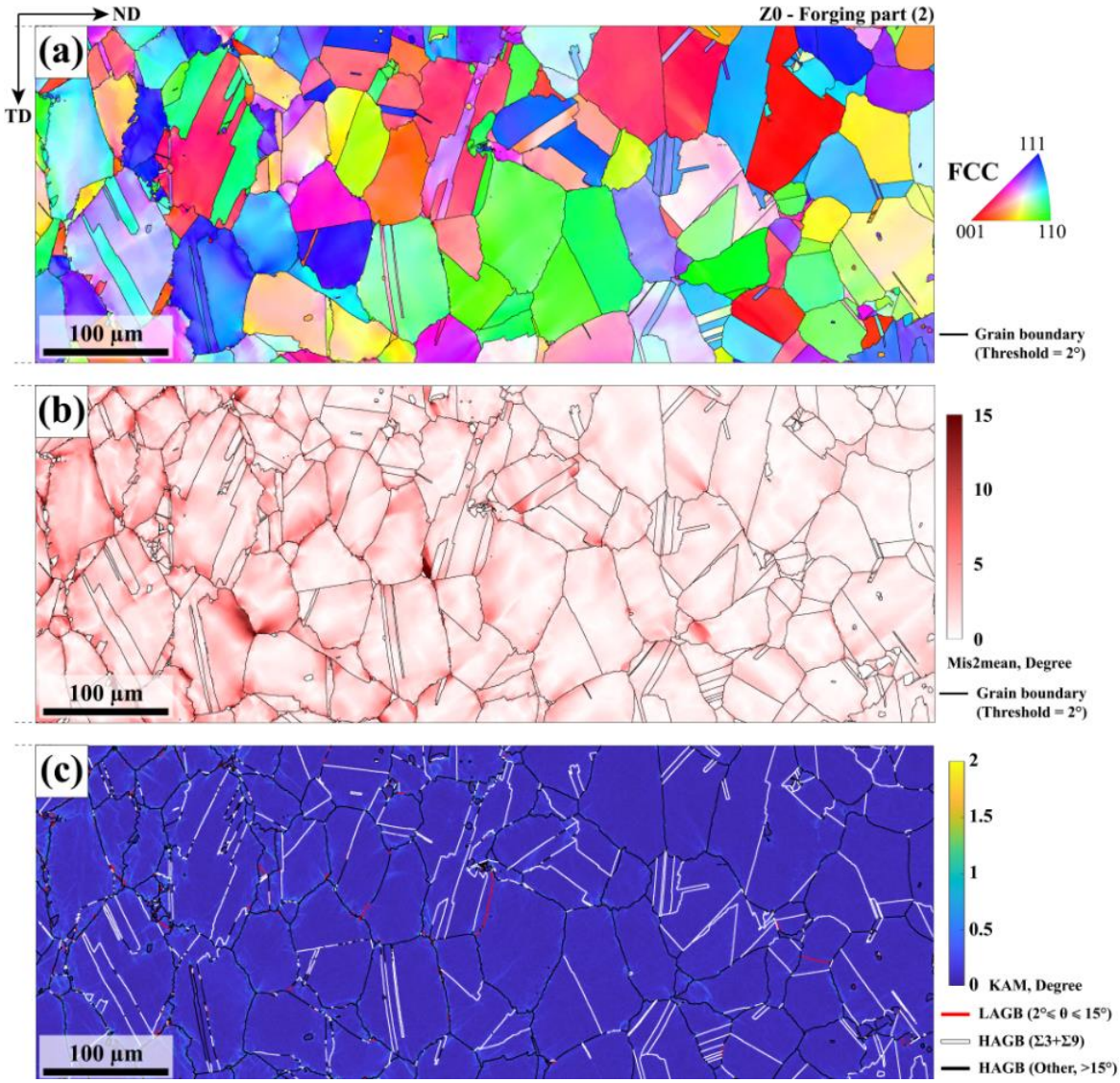


**Figure 16**: ***Far-TMAZ of the 'PH – Centre configuration', forging side, Z0 profile*** **(a)** *Inverse pole figures map from EBSD analyses following the previously exposed microstructure (150 nm step size), the FCC indexed data are superimposed with the grain boundaries (15° orientation angle threshold)*; **(b)** *Misorientation to mean-grain orientation map (15° misorientation maximum value threshold) and 2° disorientation angle threshold for grain definition;* **(c)** *Kernel Average Misorientation (KAM) cartography combined with the grain boundary misorientation classification, order 1*.

## 5. Conclusion on the microstructural changes

**(1)** The gradual thermo-mechanical loads imposed during the process resulted in a highly heterogeneous austenitic microstructure where low to highly deformed grain structures successively coexist through the affected zone. In addition to that, the severe thermomechanical conditions triggered a dynamic recrystallization process. The latter become increasingly active as approaching the weld center zone. The progressive effect of restoration phenomena resulted in successive zones of partially, then totally recrystallized austenitic microstructures. Lastly, extensive phase dissolution phenomena were observed. Notably on the γ'/γ" strengthening precipitates for the precipitation hardened welded configuration 'PH-Centre'. And on the intergranular δ phase which progressively dissolves as getting closer to the weld center zone.

**(2)** As significant microstructure changes operated through the weld interface, simple annealing procedures were applied in order to re-homogenize the affected microstructure. Both representative weld configurations were tested: the precipitation hardened PH-Centre and solution annealed SA1. The objectives for such thermal treatments were two-fold: re-homogenize the austenitic grain characteristics/phase presence across the weld junction and evaluates the microstructure stability regarding the applied thermal loads.

**(3)** In all configurations, the stored energy distribution heterogeneity within the grain structures in the low-deformed region of the far-thermo-mechanical affected zone were shown to be prone to a strain induced selective grain growth. Indeed, a critical grain growth phenomenon was observed in the latter zone, where a few lower stored energy grains grew at the expense of high stored deformation energy ones. A nucleation site limited recrystallization would corroborate with such overgrown grains phenomenon triggering. These observations allow to state that such annealing procedures within the tested temperature range intrinsically led to heterogeneous microstructures. It is strongly suspected that higher annealing temperature (notably in the *super*-δ-*transus* domain) would most likely enhance the critical grain growth phenomenon by bringing additional thermal energy for grain growth.

**(4)** Despite such elevated annealing temperature range, the WL microstructure remained fine (in an order of magnitude comparable with the as-welded condition) and demonstrated only limited grain growth. The presence of stable nanoscaled oxide particles entrapped and nanoporosities in the weld center zone presumably hindered grain growth by a Zener-Smith particle pining phenomena.

**(5)** On the contrary, the complete dissolution of δ phase particle in the near weld center zone (this, on a ± 400 µm thick band adjacent to the WL) corroborates with extensive grain growth from a complete or close to complete recrystallized post-welded microstructure to a coarse grain austenitic microstructure with grain size characteristics above the microstructure average. Therefore, the grain growth behavior in the near weld center zone is attributable to the absence of pining pressure due to residual δ phase particle yielding to unrestricted grain growth.

**(6)** The 1020°C/1h annealing treatment demonstrated the best results in term of grain characteristics (size partition) homogenization among the tested configurations.

## 6. Prospects on the microstructural changes

The choice for such high annealing temperatures was primarily guided by the will of triggering grain growth within the fine-grained microstructure close welding line. Indeed, the remnant presence of nanometric oxide particles and nanopores in that zone appears as a major issue for further efficient re-homogenization strategy. The point here was to test the upper limit of temperature and observe the impingement effects resulting from the drag phenomenon that their presence induces.

Further work on the microstructure stability regarding critical grain growth phenomenon is clearly needed. The trend deduced from these basic experimental tests seems to indicate that lower annealing temperature may give better results on this issue. A balance must then be found between the grain growth phenomenon triggered in the different section of the affected microstructure and the δ phase precipitation that would interfere with the latter. It is noted that the δ precipitation kinetic is variable with temperature and is generally estimated to reach its highest precipitation rate when approaching values of about 950°C.

From a personal viewpoint, it seems that the influence of the former surface contaminants and notably of the sub-surface oxide layers on the weld integrity has only caught a minor interest within the friction welding field; while they probably are the major issue in such assembled microstructures, even more when considering in-use fatigue life cycle. Indeed, these weld defects appear as intrinsic and unavoidable side effects in such deformation assembling techniques. Their influence and a better description of the actual mechanical fragmentation mechanisms, reactional behavior regarding the materials element composition and stability would deserve deeper treatments in the scientific literature. From a technological point of view, the prospection of windows of parameters allowing optimized dispersion of these defects within the weld center zone is of high interest. This, notably to limit their detrimental influence regarding re-homogenization treatment strategies. Eventually, the origin of the observed porosities in the weld center zone remains difficult to explain. Nevertheless, similarly to hot isostatic compression applied on compacted metallic powders, the concomitant application of a slight compression while applying post-weld heat treatment may resorb the disseminated pores at the weld interface. The latter hypothesis would be interesting to prospect.

# 7. Monotonic tensile tests

## 7.1 Introduction

Monotonic tensile tests aiming at prospecting the effect of post-weld heat treatments on the global and local mechanical properties were carried out. The analyses are combining tensile tests on standard plate samples with full-field measurements to obtain the local materials response regarding tensile solicitation. The idea is to inspect the potential beneficial effects or detrimental effects of the tested post-weld annealing treatments on the macroscopic mechanical behavior of the weld assembly. In addition, monotonic tensile tests are a simple way to investigate the mechanical strength and roughly evaluate the quality of a weld assembly.

The gradients of thermo-mechanical loads experienced by the materials during the process resulted in significant microstructural changes affecting the crystallographic phases and the grains morphology. Despite post-weld annealing treatments, the progressiveness of the microstructural change through the weld junction would probably result in remarkable effects on the local mechanical properties of PWHTed microstructure. Regarding that, the objective behind full-field measurements is, as always, to relate the local microstructure with the local mechanical properties.

## 7.2 Materials & methods: monotonic tensile tests and DIC set-up

The monotonic tensile tests were conducted up to failure on each examined configurations: 'PH-Centre' and 'SA1', in the As-Welded (AW) state and in three Post-Weld Heat Treated (PWHTed) states. The local displacement fields during the tests were determined through Digital Image Correlation (DIC) from the black and white speckle [18]. The latter speckle was obtained by airbrushing fine droplets on a black background layer [19].

The DIC was performed using an open access Matlab© codes available at Digital Image Correlation and Tracking [20] a step size of 10 pixels and a median filter to the first neighbors were used. In all configurations, the process affected zone covers about ~25% to ~30% of the total gauge length $L_0$ which is about $L_0 \approx 25$ mm. The local displacements were acquired over a rectangular region of interest of approximately 5 x 25 mm² surface (see Figure 1). The expected position of the welding line is situated in the Z-median position of the tensile sample.

The sample extraction procedure is schematically detailed in Figure 1 as well as the extracted specimen geometry. The monotonic tensile tests were performed on a conventional tensile test machine driven through displacement up to failure.

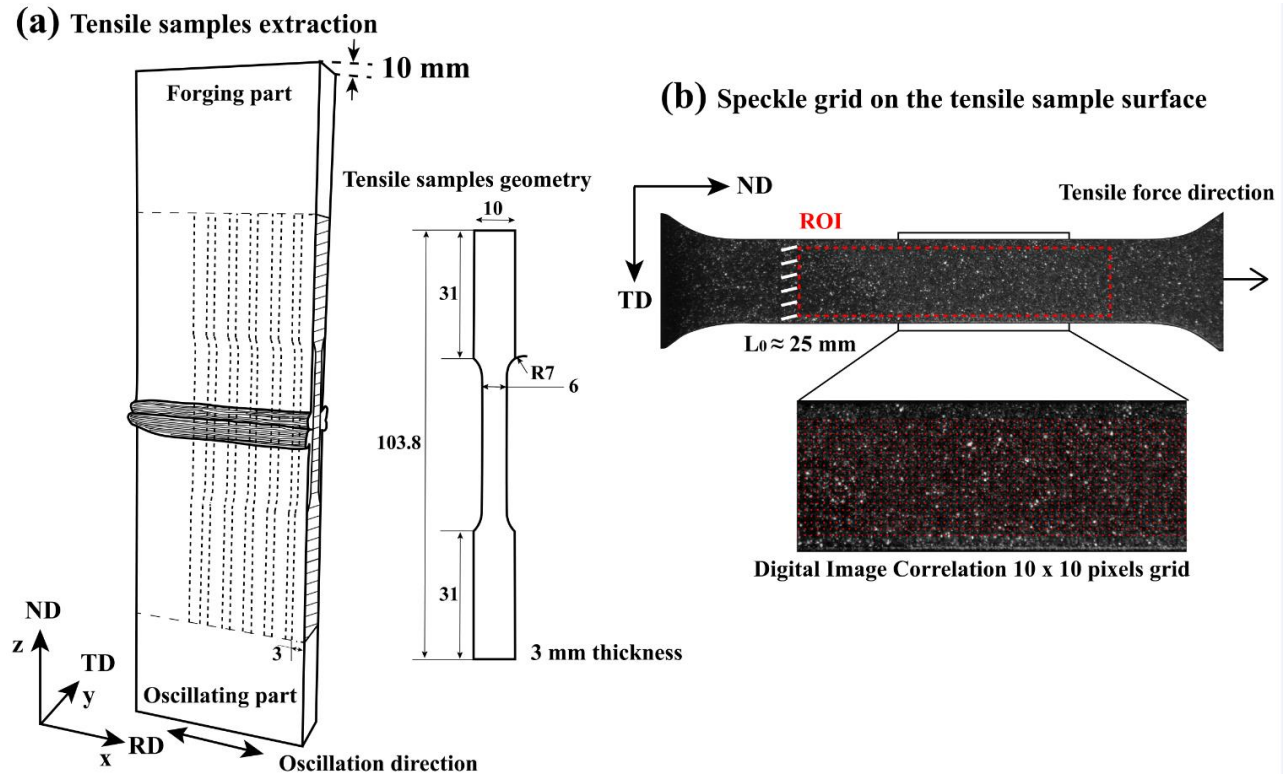


**Figure 1**: *DIC image correlation schematic presentation of the procedure with; (a) illustration of the sample extraction and tensile sample geometry.*

Overviews on as-welded tensile configurations are displayed in Figure 2:

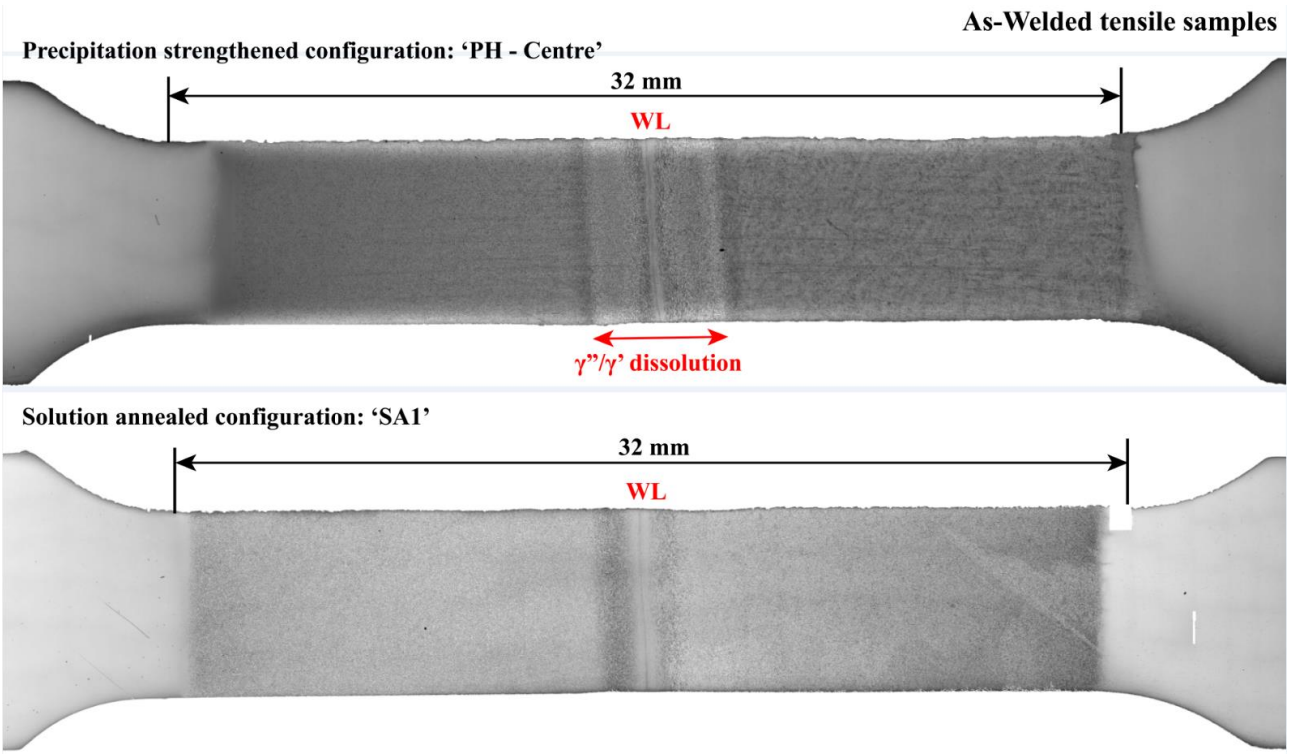


**Figure 2**: *Overview of the microstructure of the 'as-welded' tensile samples after chemical etching, the 'PH-Centre' and 'SA1' configurations are displayed.*

The mechanical properties of the parent material after standard staged precipitation hardening are exposed in the Table 1 below:

| Temperature | Direction | $\sigma_{0.2\%}$ | UTS | A% | Z% |
|---|---|---|---|---|---|
| **20°C** | ***Radial*** | 1173 MPa | 1384 MPa | 17 % | 34 % |
| **20°C** | ***Longitudinal*** | 1177 MPa | 1410 MPa | 20.5 % | 43 % |
| 650°C | ***Radial*** | 973 MPa | 1090 MPa | 17.5% | 28 % |
| 650°C | ***Longitudinal*** | 953 MPa | 1093 MPa | 28 % | 33 % |

**Table 1**: *Inspection certificate type 3.1 of the wrought IN718 alloy used in the below exposed work, according to NF-EN-10204 and NF-L-00-015C.*

Concerning the digital image correlation tracking, only the displacement data along the Z direction (tensile direction) was considered. The transverse displacement data were quite noisy with only limited reliability for further exploitation, they were consequently eliminated from the analyses. The Region Of Interest (ROI) is represented on each tested samples by a red-dashed rectangular box. The expected position of the WL is set as the reference position for the Z-coordinate system. During the image correlation procedure, the measured Z displacements are averaged along the transverse direction Y and reported to the Z-median profile. Therefore, the corresponding strain $\varepsilon_{zz}$ along the Z direction is actually computed as the mean strain value along the corresponding Y transverse coordinates (see graphical representation on Figure 3 (1)).

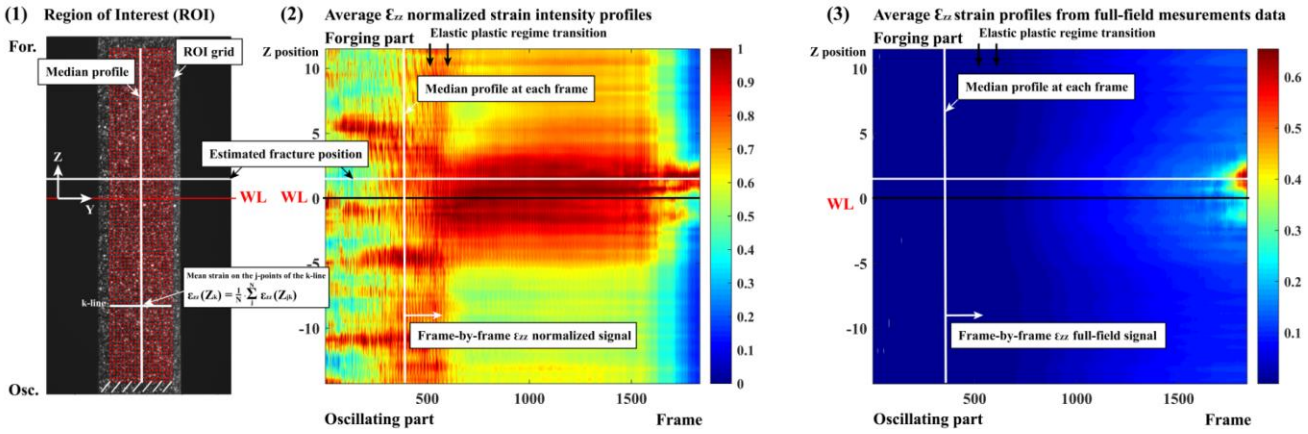


**Figure 3**: *Schematic representation of DIC results with:* **(1)** *the depiction of the region of interest and the data averaging method along the Y-direction on the Z-median profile;* **(2)** *spatio-temporal graphical representation of the instantaneous $\varepsilon_{zz}$ strain activity normalized on each frame by the local maximal $\varepsilon_{zz}$ value;* **(3)** *full-field representation of the Y-direction averaged $\varepsilon_{zz}$ signal on the Z-median profile.*

From the latter measurement procedure, two spatio-temporal graphical indicators [21] were used to highlight the strain heterogeneities during the monotonic tests:

< A space-time graphical representation was first used in order to picture the instantaneous local deformation heterogeneities during the different tensile tests (See Figure 3, (2)). The principle of the method is to normalize the averaged $\varepsilon_{zz}$ correlated signal measured along the Z-median profile by the maximal strain intensity for each frame of time. The frame-by-frame relative strain intensity signal is then represented on a

[0, 1] scaled color map, where 1 corresponds to the most 'active' deforming zone at each individual frame. Therefore, such graphical representation allows visualizing potential strain localization events and highlights the instantaneous plastic activity while loading.

> In complement, a frame-by-frame graphical representation of the averaged $\varepsilon_{zz}$ full-field correlated signal is also displayed. The latter is measured along the Z-median profile and represent the local instantaneous $\varepsilon_{zz}$ strain in dependence with the Z position during time.

### 7.3 Results & discussion on the mechanical properties of the weld

Monotonic tensile tests were first applied on as-welded configurations and aimed at verifying the mechanical integrity of the friction welded joints before the application of any thermal loads. The macroscopic engineering stress/strain curves plotted in Figure 4 indicates that the as-welded configurations are cohesive and displays some plastic deformation with necking before breaking. The as-welded 'PH-Centre' configuration displays a global mechanical response close to the 'SA1' as-welded configuration indicating that the strain mainly localized in the γ'/γ" free zone of the affected microstructure. This observation is also consistent with the lower stiffness and yield stress at 0,2% observed.

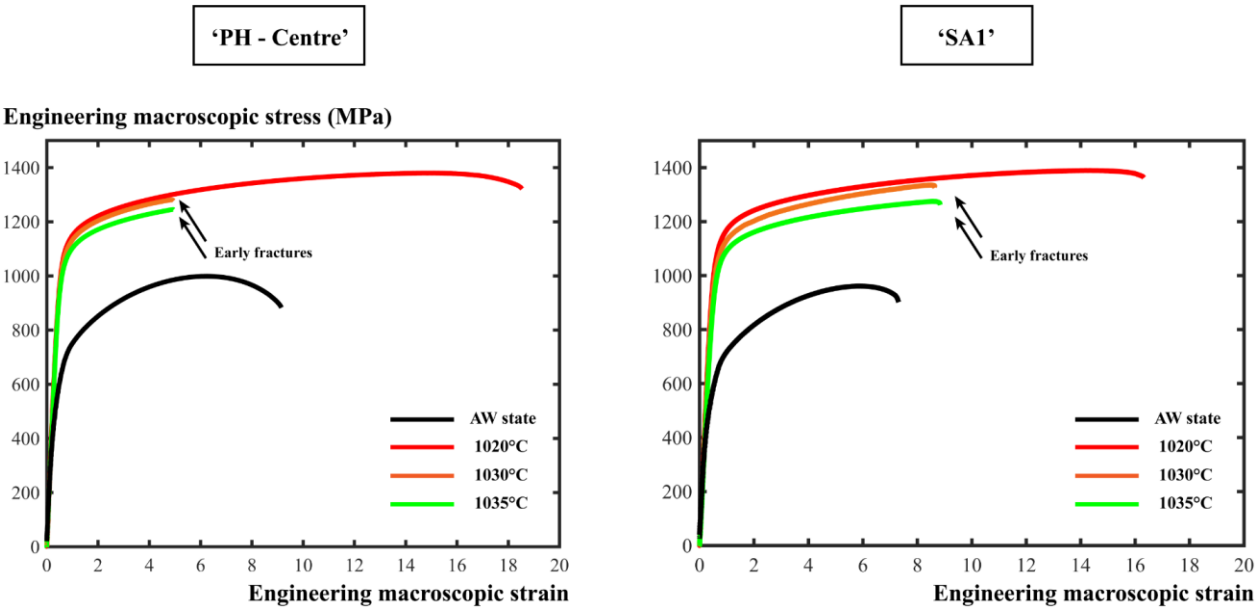


**Figure 4**: *DIC-calculated macroscopic engineering stress/strain responses of the tested configurations.*

Concerning the post-weld heat treated configurations, interesting mechanical characteristics are observed. Globally, the macroscopic mechanical responses display similar elastic stiffness close to the expected value for IN718 alloy, *id est*: ~210 GPa. Such behavior was expected because of the application of the precipitation strengthening heat treatments that put the materials back to a standard in-use metallurgical condition *via* the γ'/γ double staged annealing precipitation procedure. Among the tested samples, two main behaviors are observed: whether the tensile sample passed the necking point and reached an elongation to

break in the order of magnitude of the expected values for the employed IN718 alloy (see Table 1); or a premature and brutal rupture occurred after an only limited elongation. Thus, the 'SA1/PH-Centre' 1020°C/1h solution annealed samples demonstrate the highest macroscopic elongation; in contrast, the 'SA1/PH-Centre' 1030°C/1h and 1035°C/1h solution annealed configurations display early fracture.

Such discrepancies in term of mechanical behaviors are intriguing and local information brought by DIC analyses may give some interesting insights about it. Indeed, given the heterogeneity the PWHTed microstructures, it may be expected that the former affected microstructure influences the local mechanical response of the weld assembling.

### 7.3.1 Results for the precipitation strengthened configuration: "PH – Centre"

The monotonic tensile tests outcomes for the 'PH-Centre' configuration are displayed in the following section. For each configuration, the results are plotted with:

**(a)** The imaging of the samples at the beginning of the tensile procedure with the superimposed region of interest for correlation, then the imaging of the sample at the frame preceding failure and at the failure frame. The approximate position of the WL and the fracture position are also outlined.

**(b)** The macroscopic engineering stress/strain curves are then displayed.

**(c)** The detailed depiction of the region of interest with the expected WL and breaking positions.

**(d)** The frame-by-frame space-time representation of the instantaneous $\varepsilon_{zz}$ strain normalized to the local maximal strain value.

**(e)** The instantaneous $\varepsilon_{zz}$ full-field signal is finally represented.

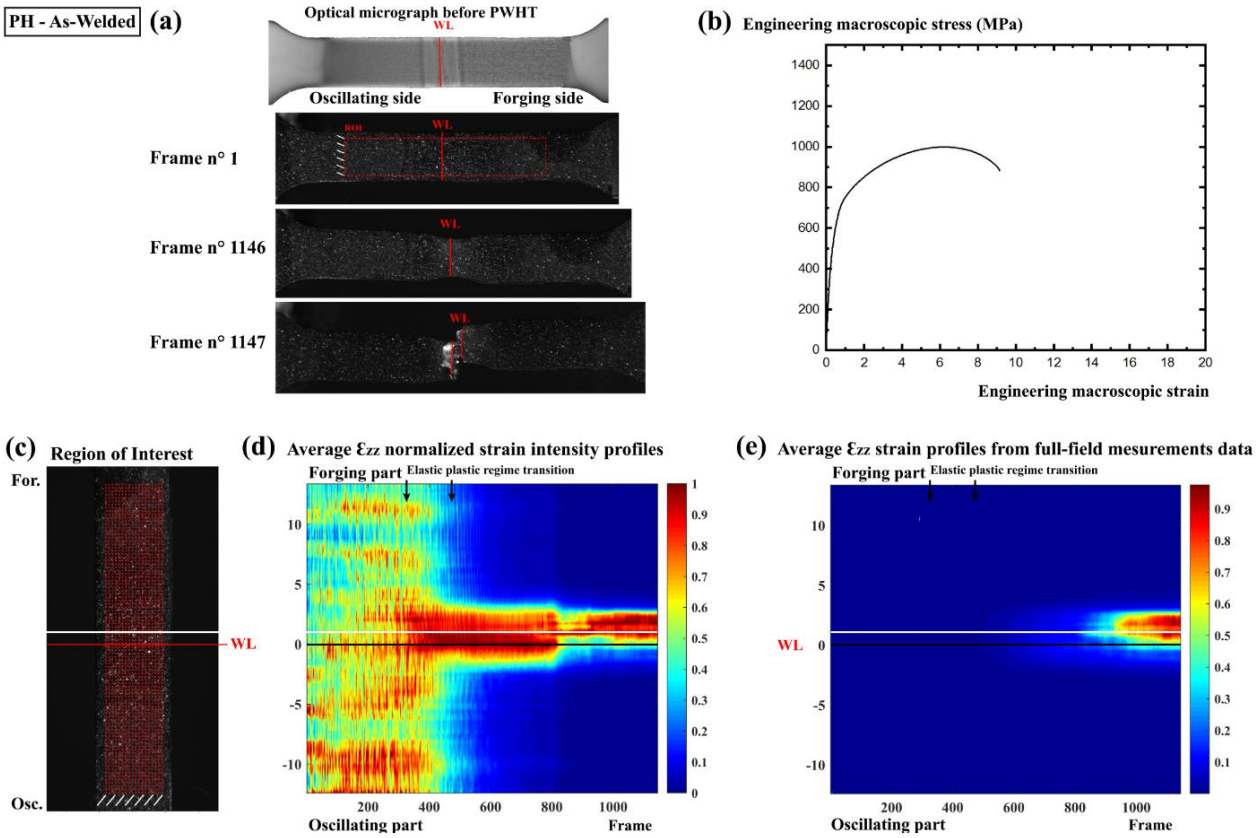


**Figure 5**: *DIC-results for the 'PH-Centre', As-Welded configuration.*

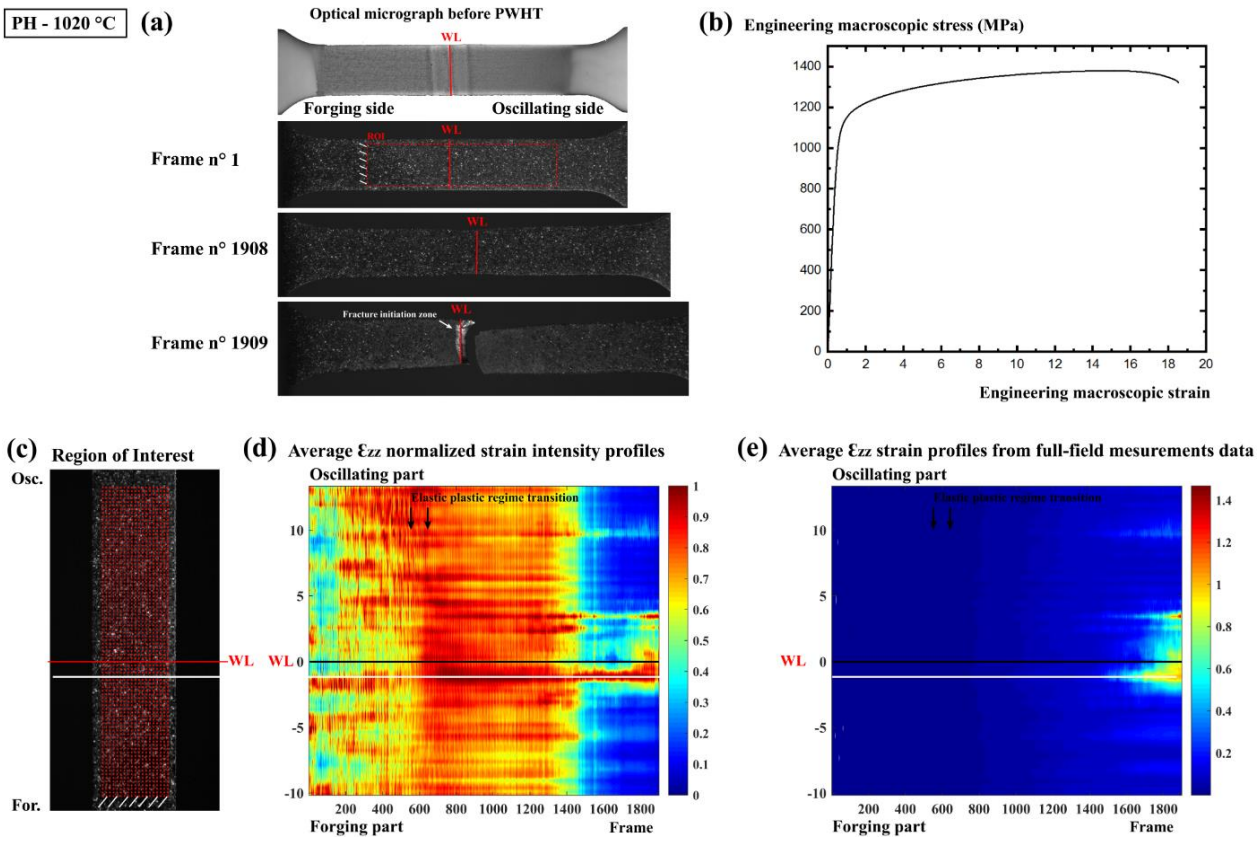


**Figure 6**: *DIC-results for the 'PH-Centre', after 1020°C/1h annealing then δ and γ'/γ'' precipitation stages.*

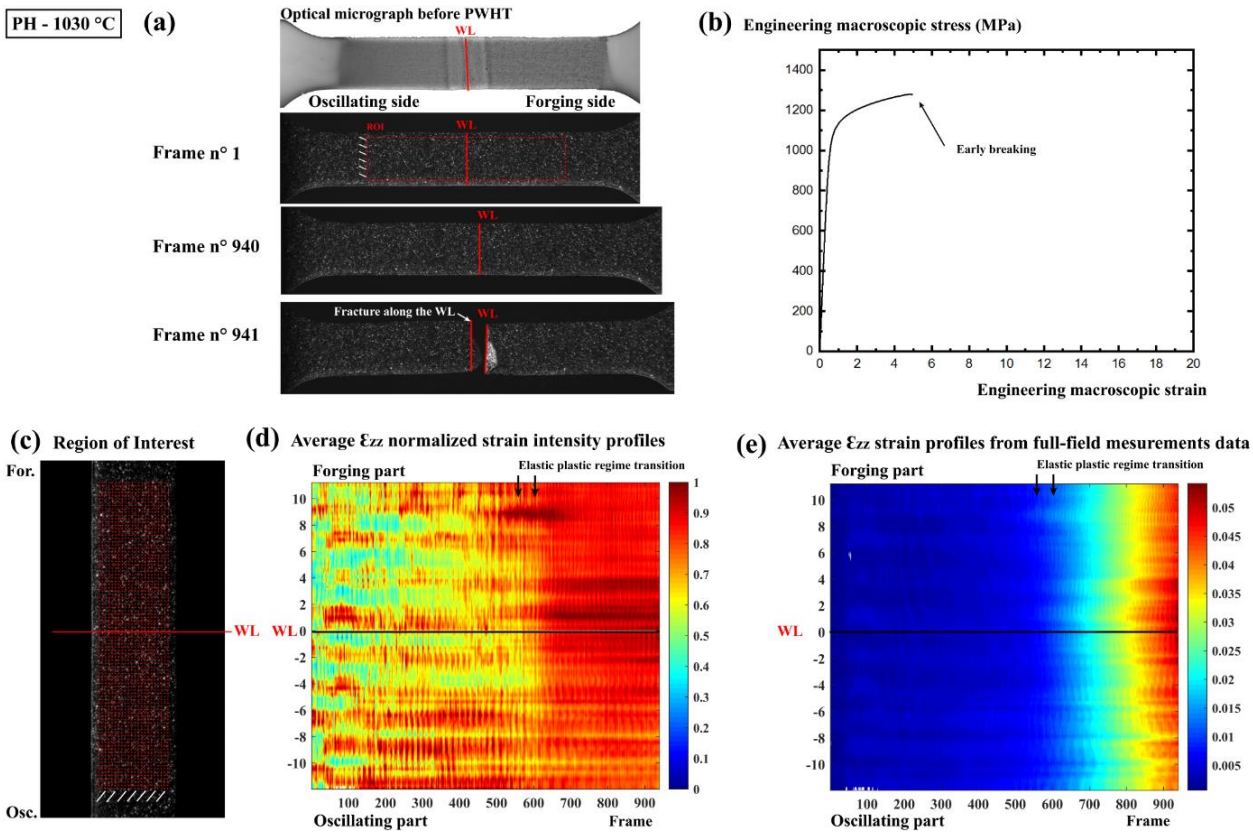


**Figure 7**: *DIC-results for the 'PH-Centre', after 1030°C/1h annealing then δ and γ'/γ'' precipitation stages.*

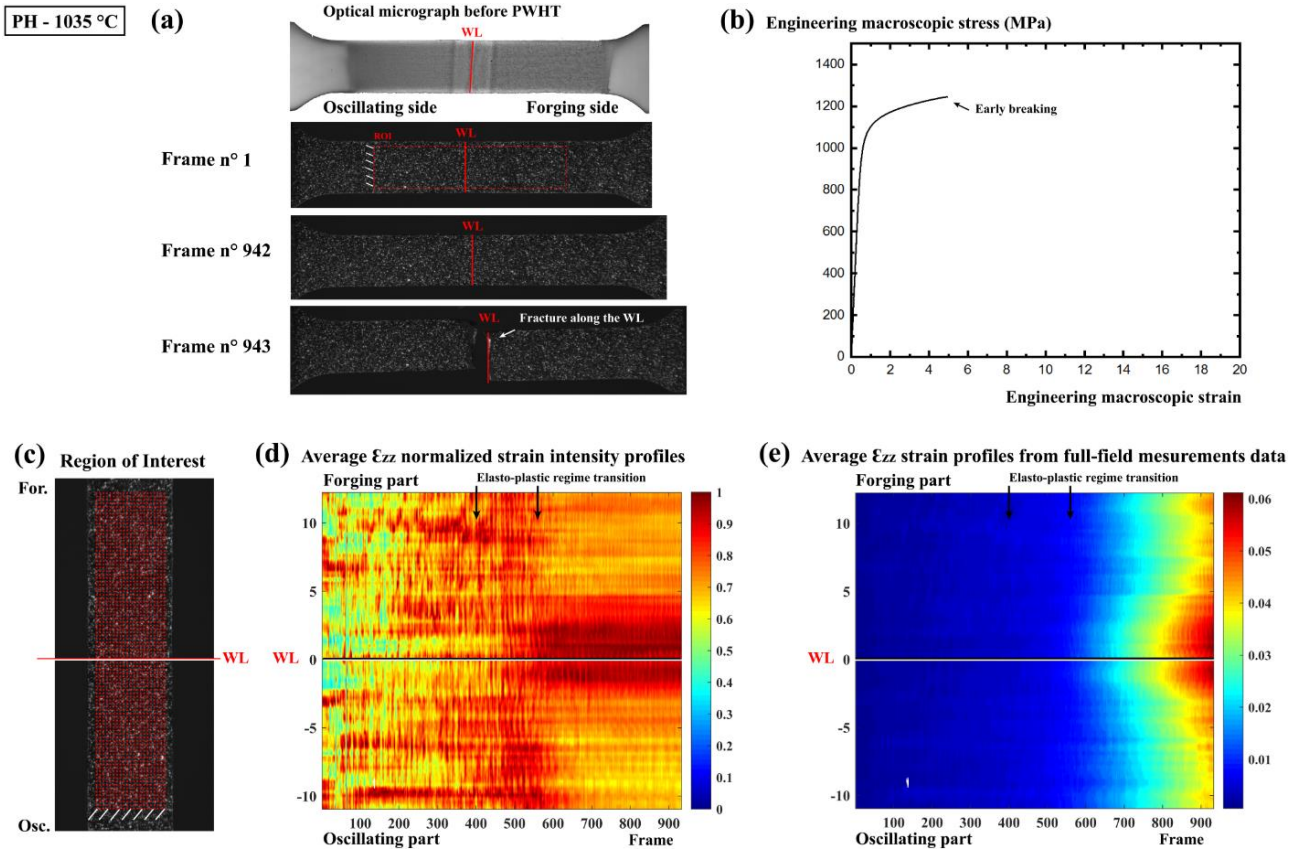


**Figure 8**: *DIC-results for the 'PH-Centre', after 1035°C/1h annealing then δ and γ'/γ'' precipitation stages.*

As expected, the plastic activity within the as-welded configuration directly localizes in the process affected microstructure. It is noted that the mechanical characteristics of the extensively affected material in the weld junction is much softer than the adjacent precipitation hardened parent materials. In all configurations, the elastic part of the signal presents a quite poor signal/noise ratio. Thereafter, the latter tends to stabilize once the plastic deformation domain is reached.

The location of the breaking point in both early fractured configurations, the 1030°C/1h and 1035°C/1h solution annealed samples, is situated in the close weld center zone. A comparative observation on the spatio-temporal graphs allow identifying the local stain partition across the samples. Indeed, while the plastic deformation partition appears quite homogeneous at the first sight through the welds; a slightly higher plastic activity is observed to develop within a ±4 mm band of microstructure around the WL. The latter zones corroborate with the characteristic length of the heterogeneously grown microstructure described within the PWHTed microstructures in the previous section. Indeed, the development of heterogeneous grain growth phenomenon led to local microstructures with globally higher grain size statistics and some important local contrasts in term of grain size distribution. This is notably the case between the critical grain grown zones that developed in the far thermo-mechanically affected zone and the adjacent microstructures. These phenomena are known to affect the plastic behavior of the material since higher grain size statistics are correlated with lower 0,2 % yield stress value [22]. In addition, the critical grain growth phenomenon was shown to get favored when the annealing temperature increased. Therefore, these findings corroborate with the lower mechanical characteristics observed on the macroscopic response (Figure 3) of the 1030°C/1h and 1035°C/1h solution annealed samples. In both samples, the WL zone is the weakest point of the assembly. It is hypothesized that the strong local strain incompatibilities probably developed between the fine ungrown interfacial microstructure and the coarse grain neighboring ones that developed during PWHT resulted in such premature breaking behavior. The close to rectilinear aspect of the fracture developments would suggest that the damage mechanisms mainly extended along the WL zone.

On the contrary, the 1020°C/1h solution annealed configuration displays much better mechanical properties in term of 0,2% yield stress and elongation to break. In addition, the latter configuration also presents the highest Ultimate Tensile Stress (UTS) value among the tested weld configurations and it is the only PWHTed configuration displaying necking. The spatio-temporal analyses allow concluding that the sample failed in zone corresponding to the far thermo-mechanically affected zone, where a strong localization of the deformation is observed. Such location within the microstructure corresponds to the overgrown grains zone. The latter demonstrates a high plastic activity in the late tensile process, after passing the necking point. The overgrown grains zone appears here as the weak point where the final fracture developed until breaking. The 1020°C/1h solution annealed configuration also displays a higher strain activity in the former process affected zone. Local heterogeneities in term of grain statistics are probably responsible for such behavior leading to strain incompatibilities. Strain hardening differs from one zone to the other

It is lastly remarked that all configurations failed in the forging side. The higher grain size statistics, so lower expected mechanical properties in term of 0,2% yield stress of the forging side material may correlate with that observed trend.

### 7.3.2 Results for the precipitation strengthened configuration: “SA1”

The global trends on the results obtained on the PWHTed ‘PH-Centre’ configuration are transposable to ‘SA1’ configuration similar conclusion may be drawn. Indeed, similar behavior toward monotonic tensile tests are observed with: the former process affected microstructure displays more intense plastic strain activity. In all configurations, the onset of plastic strain activity shifts from the process affected zone to the forging side.

Again, the 1020°C/1h solution annealed configuration also displays the best mechanical characteristics with the highest 0,2% yield point.

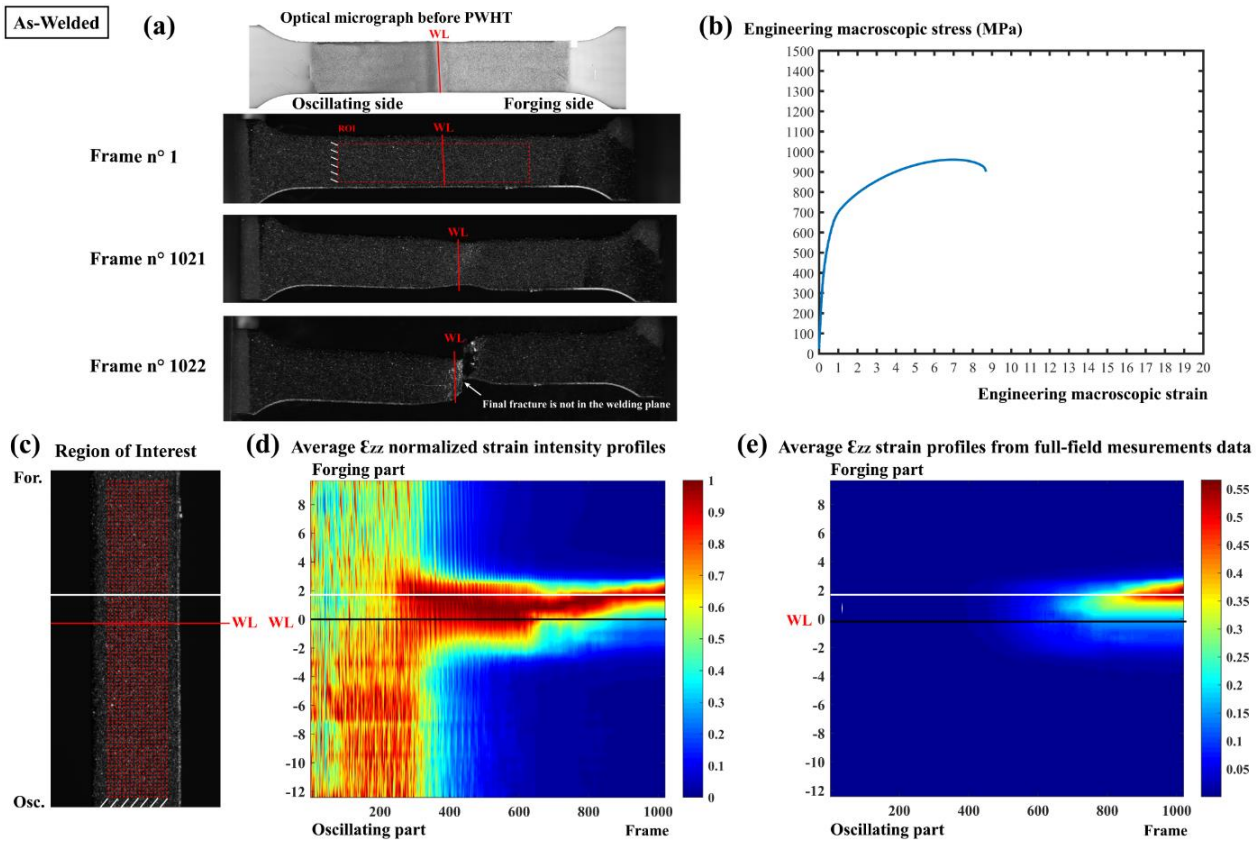


**Figure 9**: *DIC-results for the 'SA1 - As-Welded' configuration.*

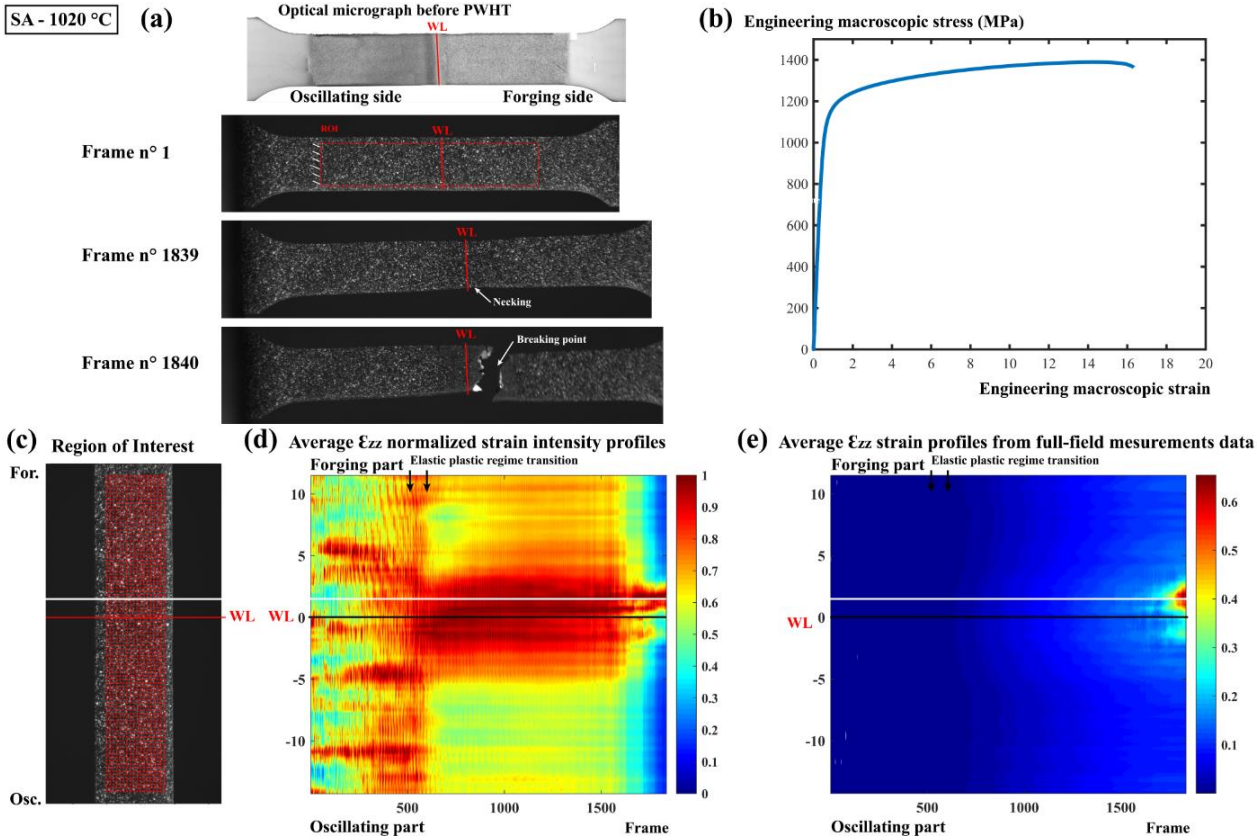


**Figure 10**: *DIC-results for the 'SA1, after 1020°C/1h annealing then δ and γ'/γ" precipitation stages.*

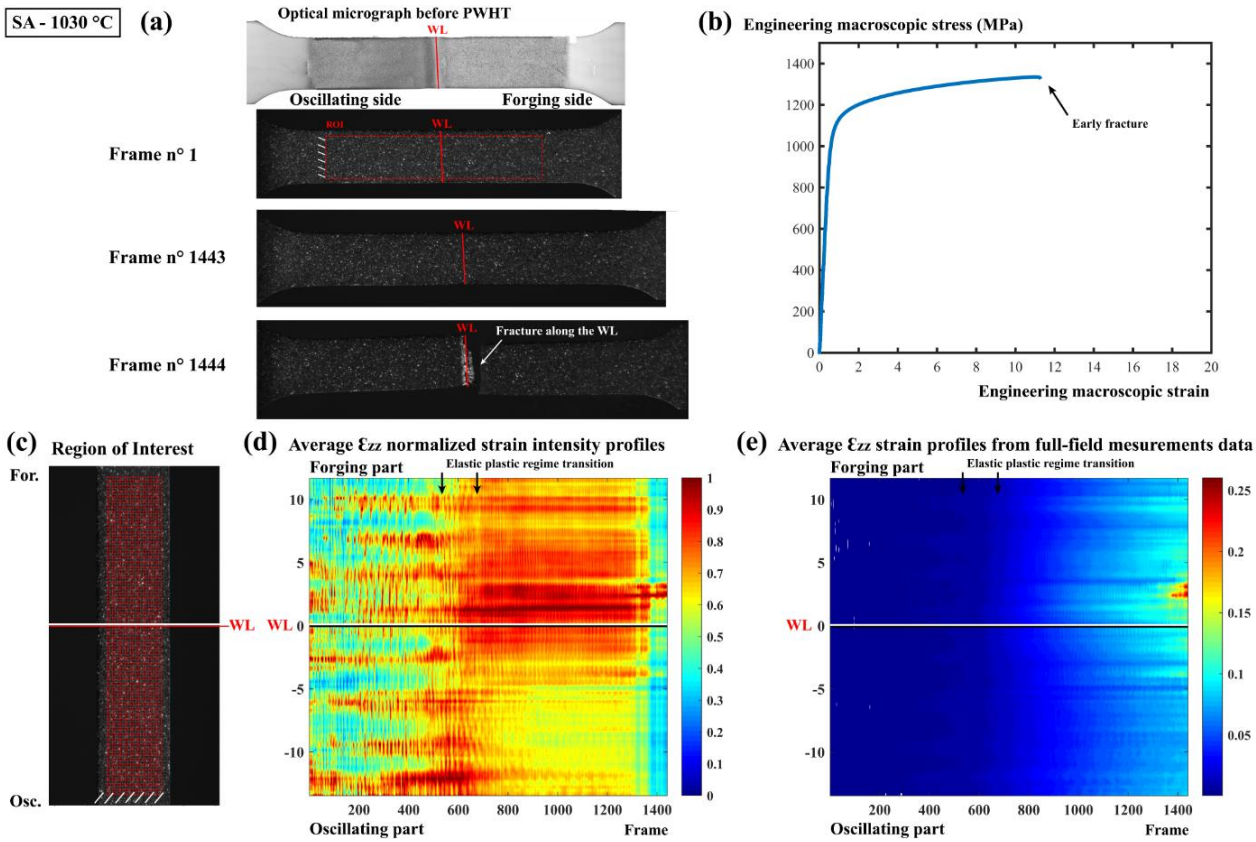


**Figure 10**: *DIC-results for the 'SA1, after 1030°C/1h annealing then δ and γ'/γ" precipitation stages.*

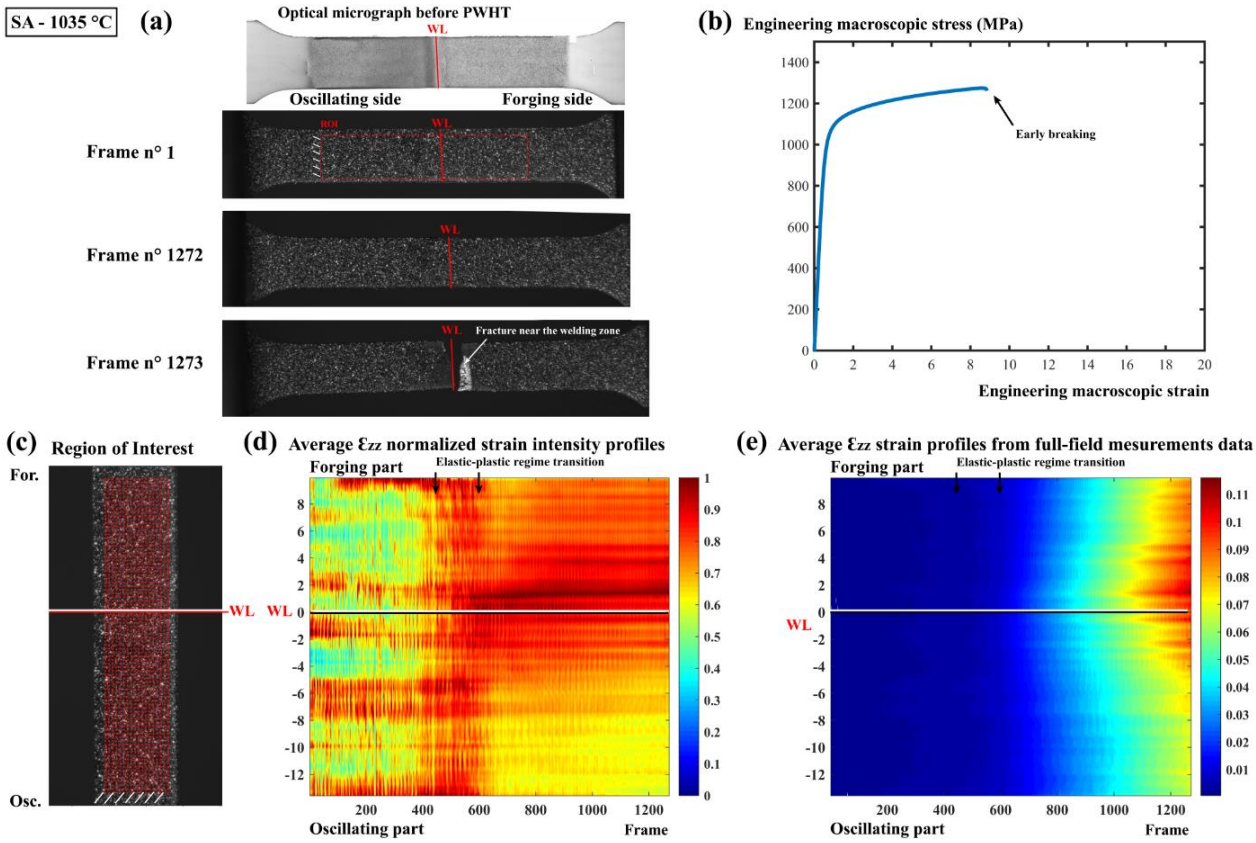


**Figure 10**: *DIC-results for the 'SA1, after 1035°C/1h annealing then δ and γ'/γ" precipitation stages.*

## 8. Conclusion

**(1)** Brutal failures without extensive elongation are localized in the weld center zone. The difference in mechanical properties between the fine grain size WL zone and the wide grain sized microstructure surrounding the joint is suspected to have favored failure. Such early breaking phenomena without further elongation are catastrophic considering the joint integrity. This effect is noticed to be enhanced with temperature, notably when the annealing temperature overpasses the δ-*transus*.

**(2)** A specific plastic activity is observed within the thermo-mechanical affected zone after PWHT. The plastic activity is concentrated in the forging side in the process affected zone. As the yield point decrease when grain size coarsens, it is probable that the plastic activity initiates prematurely in the zones displaying critical growth events.

**(3)** Lower annealing temperature led to better strength performances of the joint integrity. Heat treatments carried out under the δ-*transus* temperature seem to be the best strategy. Both annealing treatments beyond the δ-*transus* temperature led to extensive deformation in the former TMAZ before early breaking. It is likely that the triggering of critical grain growth event in the far-TMAZ significantly lowered the local mechanical properties. Meanwhile, the WL region kept a fine-grained microstructure due to the pinning action of stables and dispersed nano-oxide particles. Such local heterogeneities in material properties most probably caused the early breaking event in the weld center zone.

**(4)** The number of test samples by PWHT configurations is insufficiently representative and would deserve extensive tests campaigns. Notably, the campaign did not take in account the sample removal position in the welded block. Indeed, the microstructural transformation and the defect density distribution are spatially dependent and most probably have non-negligible influence on the microstructural evolution occurring through PWHT and the resulting mechanical strength of the treated sample.

**(5)** Better quality joints in term of interfacial contamination are necessary, a 5 mm axial shortening would be interesting to test. Since the latter has a huge influence on grain growth during the annealing stages and on the joint integrity.

**(6)** Fatigue tests would be interesting to carry out to clarify the damage behavior of the assemblies as the sensitivity to microstructure heterogeneities notably become a key factor during such testing procedure.

## 9. Prospects

Interesting results were obtained on sub-δ-*transus* treated tensile samples in both, the SA and PH metallurgical states. Indeed, the latter notably exhibit a combination of high strength and large elongation to break value. The 990°C annealing temperature most likely did not trigger critical grain growth phenomenon. It probably resulted in a finer austenitic microstructure in weld region.

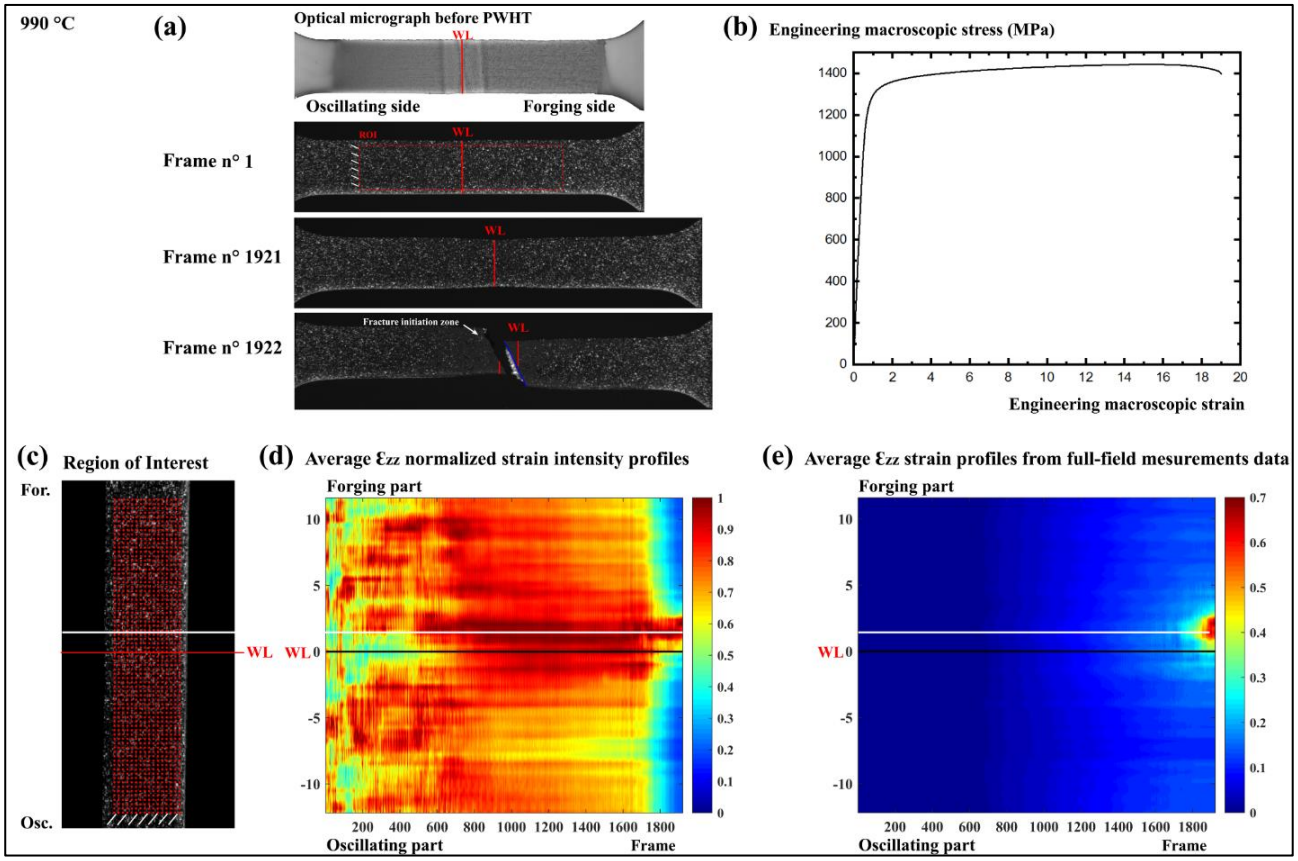


Lastly, it is interesting to note that applying direct ageing procedures most likely result in quite interesting strength properties in the assemblies as the direct ageing temperatures remain low enough to limit the triggering of some critical grain growth phenomena. Such procedures may then be viable options for interesting in-use properties despite the resulting grain size heterogeneities in the weld center zone. However, it is again strongly suspected that the presence interfacial defects may greatly influence the mechanical strength of these joints. Such findings would need further clarifications notably *via* fatigue tests in order to test the influence of the weld defect on the fatigue life of the assemblies.

## 10. References


[1] R. Damodaram, S. G. S. Raman, et K. P. Rao, « Microstructure and mechanical properties of friction welded alloy 718 », *Materials Science and Engineering: A*, vol. 560, p. 781‑786, janv. 2013, doi: 10.1016/j.msea.2012.10.035.

[2] R. Damodaram, S. Ganesh Sundara Raman, et K. Prasad Rao, « Effect of post-weld heat treatments on microstructure and mechanical properties of friction welded alloy 718 joints », *Materials & Design*, vol. 53, p. 954‑961, janv. 2014, doi: 10.1016/j.matdes.2013.07.091.

[3] M. Hillert, « On the theory of normal and abnormal grain growth », *Acta Metallurgica*, vol. 13, nº 3, p. 227‑238, mars 1965, doi: 10.1016/0001-6160(65)90200-2.

[4] E. Nes, N. Ryum, et O. Hunderi, « On the Zener drag », *Acta Metallurgica*, vol. 33, nº 1, p. 11‑22, 1985, doi: https://doi.org/10.1016/0001-6160(85)90214-7.

[5] O. Underwood, J. Madison, R. M. Martens, G. B. Thompson, S. Welsh, et J. Evans, « An Examination of Abnormal Grain Growth in Low Strain Nickel-200 », *Metallogr. Microstruct. Anal.*, vol. 5, nº 4, p. 302‑312, août 2016, doi: 10.1007/s13632-016-0290-0.

[6] V. M. Miller, A. E. Johnson, C. J. Torbet, et T. M. Pollock, « Recrystallization and the Development of Abnormally Large Grains After Small Strain Deformation in a Polycrystalline Nickel-Based Superalloy », *Metall and Mat Trans A*, vol. 47, nº 4, p. 1566‑1574, avr. 2016, doi: 10.1007/s11661-016-3329-6.

[7] X. Wang *et al.*, « Formation mechanism of abnormally large grains in a polycrystalline nickel-based superalloy during heat treatment processing », *Acta Materialia*, vol. 168, p. 287‑298, avr. 2019, doi: 10.1016/j.actamat.2019.02.012.

[8] G. H. Fan, Y. B. Zhang, J. H. Driver, et D. Juul Jensen, « Oriented growth during recrystallization revisited in three dimensions », *Scripta Materialia*, vol. 72‑73, p. 9‑12, févr. 2014, doi: 10.1016/j.scriptamat.2013.09.031.

[9] M.-A. Charpagne, J.-M. Franchet, et N. Bozzolo, « Overgrown grains appearing during sub-solvus heat treatment in a polycrystalline γ-γ' Nickel-based superalloy », *Materials & Design*, vol. 144, p. 353‑360, avr. 2018, doi: 10.1016/j.matdes.2018.02.048.

[10] J. Humphreys, G. S. Rohrer, et A. D. Rollett, *Recrystallization and related annealing phenomena*, Third Edition. Elsevier, 2017.

[11] D. J. Srolovitz, G. S. Grest, et M. P. Anderson, « Computer simulation of recrystallization—I. Homogeneous nucleation and growth », *Acta Metallurgica*, vol. 34, nº 9, p. 1833‑1845, sept. 1986, doi: 10.1016/0001-6160(86)90128-8.

[12] D. J. Srolovitz, G. S. Grest, M. P. Anderson, et A. D. Rollett, « Computer simulation of recrystallization—II. Heterogeneous nucleation and growth », *Acta Metallurgica*, vol. 36, nº 8, p. 2115‑2128, août 1988, doi: 10.1016/0001-6160(88)90313-6.

[13] D. Weygand, Y. Brechet, et J. Lépinoux, « On the nucleation of recrystallization by a bulging mechanism: A two-dimensional vertex simulation », *Philosophical Magazine B*, vol. 80, nº 11, p. 1987‑1996, nov. 2000, doi: 10.1080/13642810008216521.

[14] K. Huang et R. E. Logé, « A review of dynamic recrystallization phenomena in metallic materials », *Materials & Design*, vol. 111, p. 548‑574, déc. 2016, doi: 10.1016/j.matdes.2016.09.012.

[15] T. Chauve, M. Montagnat, F. Barou, K. Hidas, A. Tommasi, et D. Mainprice, « Investigation of nucleation processes during dynamic recrystallization of ice using cryo-EBSD », *Phil. Trans. R. Soc. A*, vol. 375, nº 2086, p. 20150345, févr. 2017, doi: 10.1098/rsta.2015.0345.

[16] T. Sakai, A. Belyakov, R. Kaibyshev, H. Miura, et J. J. Jonas, « Dynamic and post-dynamic recrystallization under hot, cold and severe plastic deformation conditions », *Progress in Materials Science*, vol. 60, p. 130‑207, mars 2014, doi: 10.1016/j.pmatsci.2013.09.002.

[17] N. Bailey et P. B. Hirsch, « The recrystallization process in some polycrystalline metals », *Proc. R. Soc. Lond. A*, vol. 267, nº 1328, p. 11‑30, avr. 1962, doi: 10.1098/rspa.1962.0080.

[18] International Digital Image Correlation Society *et al.*, « A Good Practices Guide for Digital Image Correlation », International Digital Image Correlation Society, oct. 2018. doi: 10.32720/idics/gpg.ed1.

[19] M. Grédiac, F. Hild, et A. Pineau, Éd., *Full-Field Measurements and Identification in Solid Mechanics: Grédiac/Full-Field Measurements and Identification in Solid Mechanics*. Hoboken, NJ USA: John Wiley & Sons, Inc., 2013.

[20] C. Ebert, R. Thompson, D. Gianola, et Bundschuh, *Digital image correlation and tracking with Matlab*. 2010.
[21] G. Besnard, S. Guérard, S. Roux, et F. Hild, « A space–time approach in digital image correlation: Movie-DIC », *Optics and Lasers in Engineering*, vol. 49, nº 1, p. 71‑81, janv. 2011, doi: 10.1016/j.optlaseng.2010.08.012.
[22] S. C. Medeiros, Y. V. R. K. Prasad, W. G. Frazier, et R. Srinivasan, « Modeling grain size during hot deformation of IN 718 », *Scripta Materialia*, vol. 42, nº 1, p. 17‑23, déc. 1999, doi: 10.1016/S1359-6462(99)00316-4.

# Conclusion chapter

The research work aimed at characterizing the effect of the linear friction welding procedure on the local microstructure of different aeronautical alloys weld configurations. Two types of alloys were inspected: two titanium alloy grades Ti6242 and Ti17 and one nickel-based alloy grade Inconel 718 and three weld configurations were investigated: (1) one dissimilar but mutually soluble Ti17 and Ti6242 alloy couple; (2) the IN718 in the precipitation hardened state: and (3) the IN718 alloy in the solution annealed metallurgical state. Prospective tests were also realized on the welding of Ti-alloys with Inconel 718 but were not conclusive or convincing; an overview of these results is given in supplementary material (Suppl. Mat. C).

The friction welding procedure imposes severe thermo-mechanical loads on the materials, regardless of the configuration. In turn, the energy delivered during the process causes remarkable microstructural transformations on the parent microstructure. These changes notably include phase transformations and plastic deformation induced phenomena such as grain-fragmentation, recrystallization and recovery. Once achieved, the welds display significant microstructure heterogeneities in term of phase presence and grain characteristics resulting in discontinuous mechanical properties. The effects of the linear friction welding process on the microstructure of the different material configurations have been extensively described and reported through that work. From the results exposed along the manuscript and the successive analyses and discussions, the main following conclusions may be drawn:

## 1. Synthesis on the understanding of the joining mechanism taking place during LFW

The dissimilar Ti6242 / Ti17 LFWed configuration has been advantageously exploited to elucidate the joining mechanism that takes place at the microstructural level in the weld interface. Indeed, both alloys display divergent phase transformation kinetics regarding rapid cooling from the high temperature β-domain. Under such cooling conditions, the quasi-α Ti6242 grade is prone to precipitate α'-HCP martensite phase, while the β-metastable grade, Ti17, is prone to stabilize a room-temperature β-metastable phase. Besides, both alloys are mutually soluble and are not subject to intermetallic compound formation at the weld interface. The exchange of elements at the weld interface formed a 5 µm thick interdiffusion gradient band was measured.

The LFW process led to a hot straining process with significant α→β transformation in the joint, a complete dissolution of the α phase occurred on a 1 mm band on the Ti6242 side and a 2.5 mm band on the Ti17 side. The local thermomechanical conditions yielded to large plastic deformation in the junction zone. The strain was notably accommodated *via* a β-grain fragmentation process assisted by a continuous dynamic recrystallization phenomenon. Furthermore, the shear dominant deformation mode imposed by the harmonic

mechanical load gave rise to a marked BCC simple shear deformation texture in the joining zone, where the shear direction corresponds to the friction direction and the normal shear direction corresponds to forging axis.

The welding process resulted in a remarkable phase contrast in the interfacial zone. β recrystallized grains sharing both, α'-HCP martensitic phase on the one hand and a room-temperature β-BCC metastable phase on another hand, in their inner structure was observed. Such interfacial grain structures were demonstrated to originate from identical high temperature β-parent crystal orientation *via* the Burgers orientation relationship. The thermomechanical loads yielded to subsequent straining in the single-phase β domain therefore stimulating the active migration of the crystalline interfaces from one material to another across the junction zone by a continuous dynamic recrystallization process.

Such work highlights the crucial role of grain boundary motion stimulated by the hot deformation process as a key mechanism for bond formation within mutually soluble during such solid-state welding.

## 2. Synthesis on the linear friction welding of IN718 taking place during LFW

The IN718 nickel-based alloy microstructure in a solution-annealed state consists of face-centered cubic (FCC) γ austenitic grains presenting an equiaxed grain shape decorated with δ phase micron-sized platelets of $Ni_3Nb$. The usual in-use metallurgical state of the material is achieved by the precipitation of the finely inter-dispersed nanoscale intermetallic compounds within the γ austenitic matrix grains.

During the experimental campaign, blocks of IN718 were successfully LFWed in two different initial metallurgical states: first in a Precipitation Hardened (PH) state and second in a Solution Annealed (SA) state. Again, the friction welding process led to a hot straining process resulting in important transformations on the parent microstructures

On the precipitation hardened configuration, the temperature elevation across the weld led to extensive dissolution of the γ'/γ" strengthening precipitates within a sharp ±3 mm band of microstructure. It consequently resulted in a significant softening of the material properties in the joint. Besides, a progressive dissolution of the intergranular δ phase was shown with a complete decomposition on ±250 µm band around the weld center zone. While, on the solution-annealed configuration, the temperature elevation led to a δ phase dissolution on a ± 350 µm band neighboring the WL.

The imposed thermomechanical loads yielded to extensive plastic deformation in both joints. The ensuing hot deformation process gave rise to a discontinuous dynamic recrystallization phenomenon in the junction zone. The latter favored grain boundary migration across the interface and presumably play a key role in the solid-state weld formation. The heterogeneous strain and temperature fields arising from the straining process resulted in a highly heterogeneous post-weld microstructure. The dynamic recrystallization process reached different level going from a complete recrystallization state in the weld center zone, then the

recrystallization rate progressively decreases as moving away. The post-welded microstructure do not display marked crystallographic texture. Although a slight cube texture component was noted in the weld center zone, where the level of strain and temperature reached the highest values.

In both IN718 weld configurations, precipitated nano-oxide particles of titanium and aluminum were identified in the joining zone. These dispersed weld defects presumably originate from a selective internal oxidation mechanism that occurred during the welding procedure.

## 3. Synthesis on the re-homogenization of the post-welded microstructure of IN718

The post-weld heat treatment strategies prospected on the IN718 weld samples, precipitation hardened and solution annealed, consisted in a 1h annealing treatment followed by air quenching. The annealing temperature values were chosen around the δ-*transus* temperature (~1027°C) *id est*: 1020°C, 1030°C and 1035°C. These annealing holds aim at triggering grain growth within the refined grain structures and recover the parent grain statistics.

However, in all tested configurations, the heterogeneous nature of the post-welded microstructure and notably the heterogeneity in stored energy distribution in the low-deformed grains of the far-thermo-mechanical affected zone were shown to be prone to a strain induced selective grain growth. The intensity of the critical grain growth events was observed to decrease with the annealing temperature.

The nano-oxide particles dispersed in the joining zone remained stable under the thermal loads. The abundant presence of defects totally hindered further grain growth and resulted in the formation of a very fine austenitic microstructure in the weld center zone.

In addition to that, the residual presence of δ phase particles in variable density in the post-weld microstructure perturbed the grain growth kinetic during annealing notably resulting in coarser grain size in the δ depleted zones neighboring the WL.

The combination of these factors resulted in heterogeneous post-weld heat-treated microstructures, notably in term of grain size distribution. Such heterogeneities had distinct consequences on the mechanical properties of the joints. The critical grain growth events lowered the local mechanical strength in the joint yielding to premature plastic deformation in the thermomechanically-affected zone (TMAZ). Such trend was observed to decrease when the annealing temperature decreased beyond the δ-*transus* temperature (~1027°C). Indeed, the 1020°C annealed samples displayed a marked reduction of the critical grain growth events concomitantly going with a greater microstructure homogeneity and superior tensile strength properties (higher yield point, best elongation to break). Besides, the stable nano-oxide particles present in the weld center zone constrained the local microstructures by substantially hindering grain growth during the annealing procedures. The resulting difference in mechanical properties between the ungrown microstructure from the WL and the overgrown

microstructure in the neighboring TMAZ presumably favored the early brutal fractures observed on the *super*-δ-*transus* treated samples.

### Prospects concerning the LFWing of IN718 alloy

**(Oxide formation in the welding zone)**: The spontaneous formation of detrimental nano-oxide particles in the weld interfacial zone appears unavoidable. Eventual decomposition of the latter through heat treatments is unrealistic regarding the high temperature stability of the precipitated compounds. Stimulating plastic flow by increasing the axial shortening set value may help enhancing the mechanical dispersion of such particles in the weld center zone.

**(Interfacial porosities)**: The origin of the interfacial porosities observed in the cohesion zone after post-weld heat treatments remain unclear. The application of an axial isostatic compression on the weld is suggested as it may have a beneficial effect to disrupt such defects.

**(Homogenization annealing temperature)**: The main requirement is avoiding critical grain growth phenomena. Annealing in the *sub*-δ-*transus* domain would probably allow re-homogenizing the grain size statistics in the process-affected zone.

**(Window of process parameters)**: The behavior of IN718 regarding friction welding sets of parameters is still little known. The solution-annealed metallurgical state was particularly difficult to weld despite its 'softer' mechanical properties compared with the hardened state. The tribological condition yielding to effective assembling remain poorly known and difficult to prospects *via* experimental means. Notably, the passage from a dry sliding friction dominated phenomenon to a bulk deformation dominated phenomenon remain a grey zone. The complexity of physical phenomena involved make the elaboration of reliable prediction model particularly harsh. Nevertheless, the experimental butt-weld tests carried out through this work demonstrated that the linear friction technique is robust: the same experimental inputs lead to similar outcomes in repeatable way. Therefore, wider experimental campaigns testing a greater variety of set of process parameters for a given geometry and surface state may allow achieving a consistent phenomenological law.

## 4. Global key points on LFW applied on metallic materials

**(1)** The linear friction welding process actually belongs to the class of the hot deformation assembling processes. The plasticity-induced phenomena triggered during intense straining at elevated temperature play a key role in the metallurgical joining of mutually soluble metallic alloys. Strain-induced grain boundary motion was highlighted as a crucial metallurgical mechanism for solid-state bond formation.

**(2)** The linear friction welding process may be decomposed into two basic regimes: a dry sliding friction dominated state and an alternate simple shear bulk deformation dominated state. The frontier from one regime to the other is blur. Besides, the connections between the set of parameters, block geometry, surface state and the effective establishment of a self-regulated plastic flow still remain poorly understood. Nevertheless, the technology is remarkably robust, similar initial surface conditions lead to similar weld outputs in statistically repeatable way.

**(3)** During friction welding procedure, severe thermo-mechanical loads are applied on the materials resulting in serious consequences on the microstructure of the materials. The latter must be attentively characterized in order to determine the appropriate post-welding procedure to adopt to obtain a reliable joint.

# Supplementary Material A

## Tested parameters on the Precipitation Hardened ('PH-Centre') weld configurations

***Microstructure stability under post-weld heat treatment for re-homogenization***

Variations on the weld parameters were introduced during the weld campaign in the manner of an experiment plan. IN718 blocks were linear friction welded under a precipitation strengthened metallurgical state at different weld parameter sets. The 'Centre' value was taken as the reference set (as its name indicates), the latter value was determined *via* previous experimental procedures carried out on precipitation hardened IN718 blocks with similar geometry. Parameter variation were introduced around the 'Center' value, varying first the forging pressure of +30 MPa then -30 MPa values, then the amplitude of oscillation by a ±0.5 mm value and finally, by modifying the oscillation frequency by a ±20 Hz value. All tested set of parameters are recalled in Table 1 below.

| **Parameters (Units)** | **Pressure (MPa)** | **Frequency (Hz)** | **Amplitude (mm)** | **Axial shortening (mm)** | **Total oscillations duration (s)** | |
|---|---|---|---|---|---|---|
| **'Centre'** | 270 | 50 | 1 | 3,13 | 5,68 | Nominal weld |
| **P+1** | 300 | 50 | 1 | 3,07 | 6,23 | Nominal weld |
| **P-1** | 240 | 50 | 1 | 3,07 | 5,97 | Nominal weld |
| **A+1** | 270 | 50 | 1,5 | 3,07 | 5,97 | Nominal weld |
| **A-1** | 270 | 50 | 0,5 | 0 | 10 (limit time) | No weld |
| **F+1** | 270 | 70 | 1 | 0 | 10 (limit time) | No weld, an observed cohesive start, then the bond fractured |
| **F-1** | 270 | 30 | 1 | 3,11 | 6,49 | Nominal weld |

**Table 1**: *Window of process parameters explored during the study*.

As for the 'Centre' configuration analyses, microstructural characterizations were carried out on the set of parameters resulting in actual welding. When successful, the welding procedures here resulted in similar weld junctions, with comparable microstructural characteristics. Indeed, the affected zones extents are quite similar from one set of parameters to the other; these features were notably highlighted through microhardness tests realized on cross-sectional sample extracted from the welded blocks (Figure 2). The similar hardness drops due to strengthening precipitates dissolution demonstrates comparable trends meaning that the resulting thermal fields were comparable between the P+1, P-1, A+1 and F-1 configurations when the axial shortening reached a 3 mm value. Variations between the configurations are nevertheless observable within the thermo-mechanically affected zone were strain hardening phenomena appear to differ between the tested configurations.

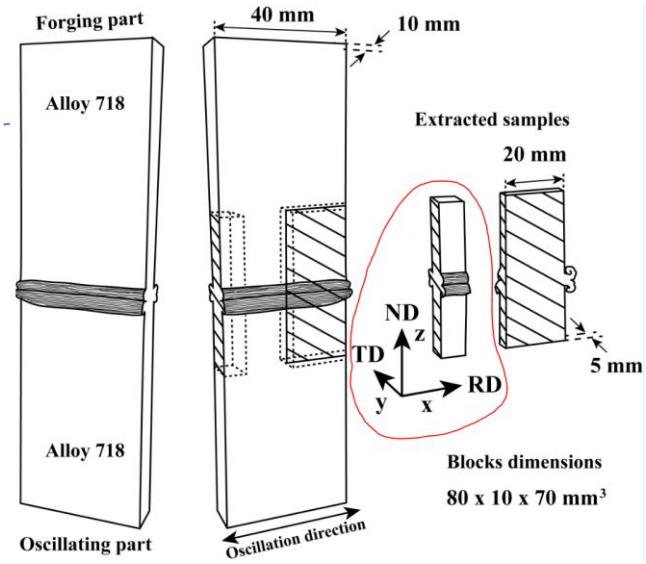


**Figure 1**: *Sample cutting strategy, the microstructural analyses were realized on the cross-sectional sample extracted from the median position (the test sample is highlighted in red).*

**Microhardness analyses**

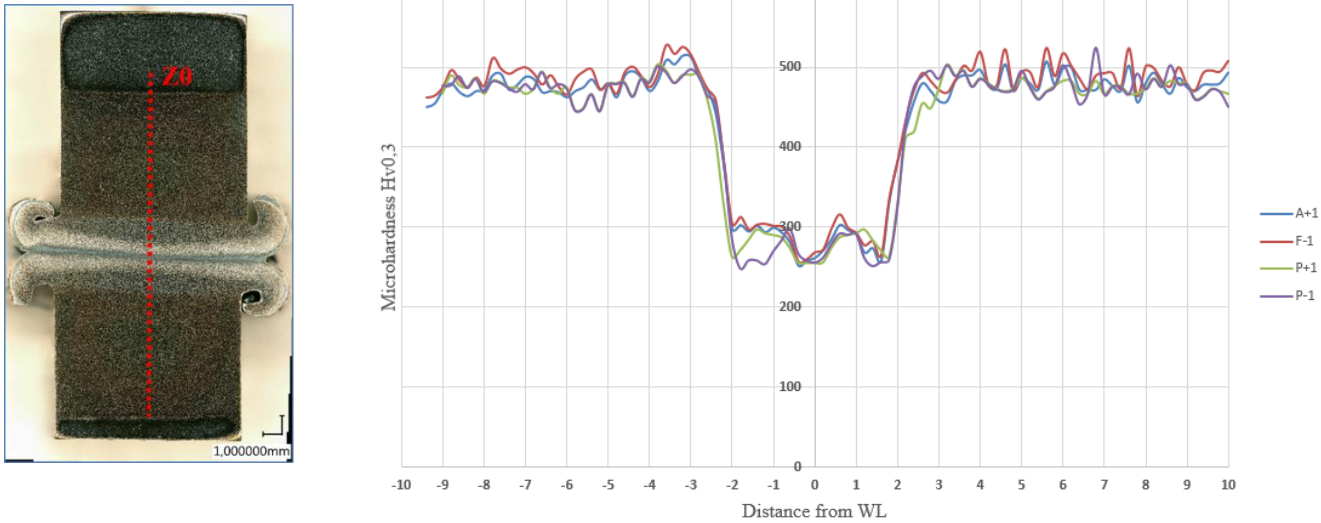


**Figure 2**: *Hv0.3 microhardness tests were carried out along the Z0 line with a 200 µm step-size in between the indents. A+1 transverse cross-section micrograph (left) with Z0 profile is schematically represented. The Hv0,3 micro-indentation profiles along the Z0 profile are plotted for the different configurations.*

Detailed local crystal orientation analyses were carried out using the grain orientation spread indicator (GOS) in order to quantify the internal misorientation within the strained microstructure neighboring the WL. However, the microstructural characteristics from one configuration to the other appear to demonstrate very similar and comparable features suggesting that despite the set of parameters differences, their consequences did not result in wide variations on the resulting microstructures. The latter all highlight similar features with: a low-misoriented recrystallized region in the weld center zone neighbored by a partially recrystallized microstructure with deformed parent grains and a low plastically affected microstructure thereafter (Figure 3).

**P+1 configuration:**

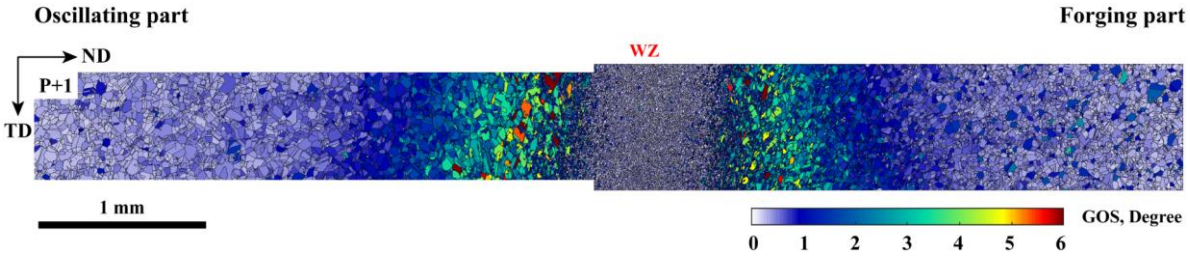


**P-1 configuration:**

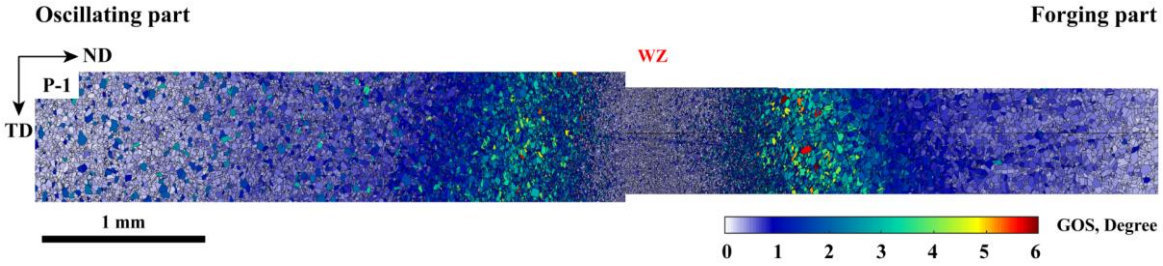


**A+1 configuration:**

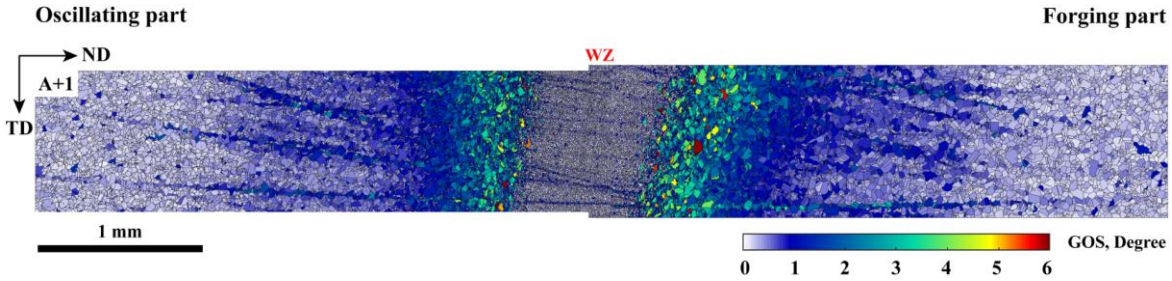


**A-1 configuration:**

The procedure led to insignificant heat generation and slight wear effects on the surface of the contacting blocks. No cohesion start happened during the procedure; the A-1 may be excluded from the analyses.

**F+1 configuration:**

Important temperature elevation was generated during the procedure (the weld interface became red-hot in the weld center zone), a bond was created between the faying surfaces leading to material transfer and adhesion between the parts, then immediately broke afterwards.

**F-1 configuration:**

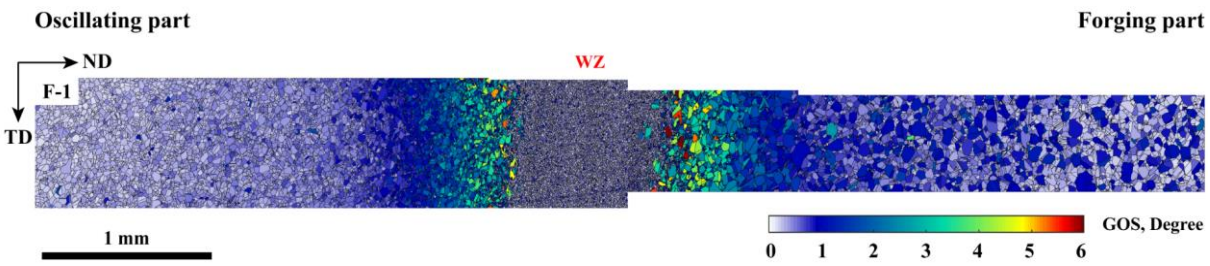


**Figure 3***: Grain Orientation Spread maps (6° threshold) of the tested configurations.*

Nevertheless, noticeable difference in axial shortening behavior were identified between the different tested configurations (Figure 4). First, the total processing duration changes from one set to the other. Some counter-intuitive behaviors are observed: for instance, the P+1 set of parameters led to longer processing time despite the higher forging pressure brought on the materials with a 6.23 s process duration. Whereas the P-1 set led to a 5.97 s total process duration. Such behavior may probably be explained by the complex relationship between applied forces and time-dependent material reaction during the friction welding procedure. The latter notably lead to complex time-dependent visco-plastic behavior that are not trivial to conceive by intuition. The F-1 configuration led to the slowest axial shortening rate with 6.49 s process duration.

In all realized and successful configurations, a slope change was identified during the axial shortening procedure. The axial shortening regime was then divided into two parts, both demonstrate a quasi-linear behavior. The physical causes of such slope changes remain difficult to interpret. However, the hypothesis of a switchover from a dry sliding friction regime to a bulk deformation dominated regime seems plausible at such point of the process. Regardless of its origin, such change reflects a global change in the bulk response of the materials being welded. The second regime (steady-state 2) always presents a slower axial-shortening rate compared with the first quasi-linear regime. Interestingly, despite a slower departure, the F-1 set of parameters demonstrated the highest axial shortening rates among the tested weld configurations, whether for the steady state regime 1: 1,10 mm/s or the steady state regime 2: 0,74 mm/s. In comparison the P+1 set of parameters, which theoretically presents the higher process input among the tested parameters respectively reached a axial shortening rate of: 0,78 mm/s on the first steady-state regime and 0,60 mm/s on the second. Such features further underline the non-intuitive character of the friction welding procedure applied on IN718 since the F-1 set of parameters seems to lead to more efficient axial-shortening rate than any other tested parameters, including P+1.

The axial-shortening output signal appears to be the most-reliable element in order to identify the effect of the set of initial process parameters on the friction welding behavior of a considered IN718 weld couples. Each tested set of parameters seems to present its own characteristic response to the weld procedure. Considering the window of parameters here evaluated, it may be concluded that the different tested set of parameters led to comparable global microstructural features when the aimed axial shortening value is reached (3 mm here). Nevertheless, each configuration follows a different and characteristic path with more or less efficiency regarding the global and initial plastic collapse of the materials and the axial-shortening rate regimes.

It is consequently interesting to note that a reliable modelling of the process should allow predictive results on such non-trivial axial shortening behavior. On another note, a wider experimental campaign seems necessary in order to characterize and bring some necessary further understanding on the friction welding behavior of the IN718 weld couple.

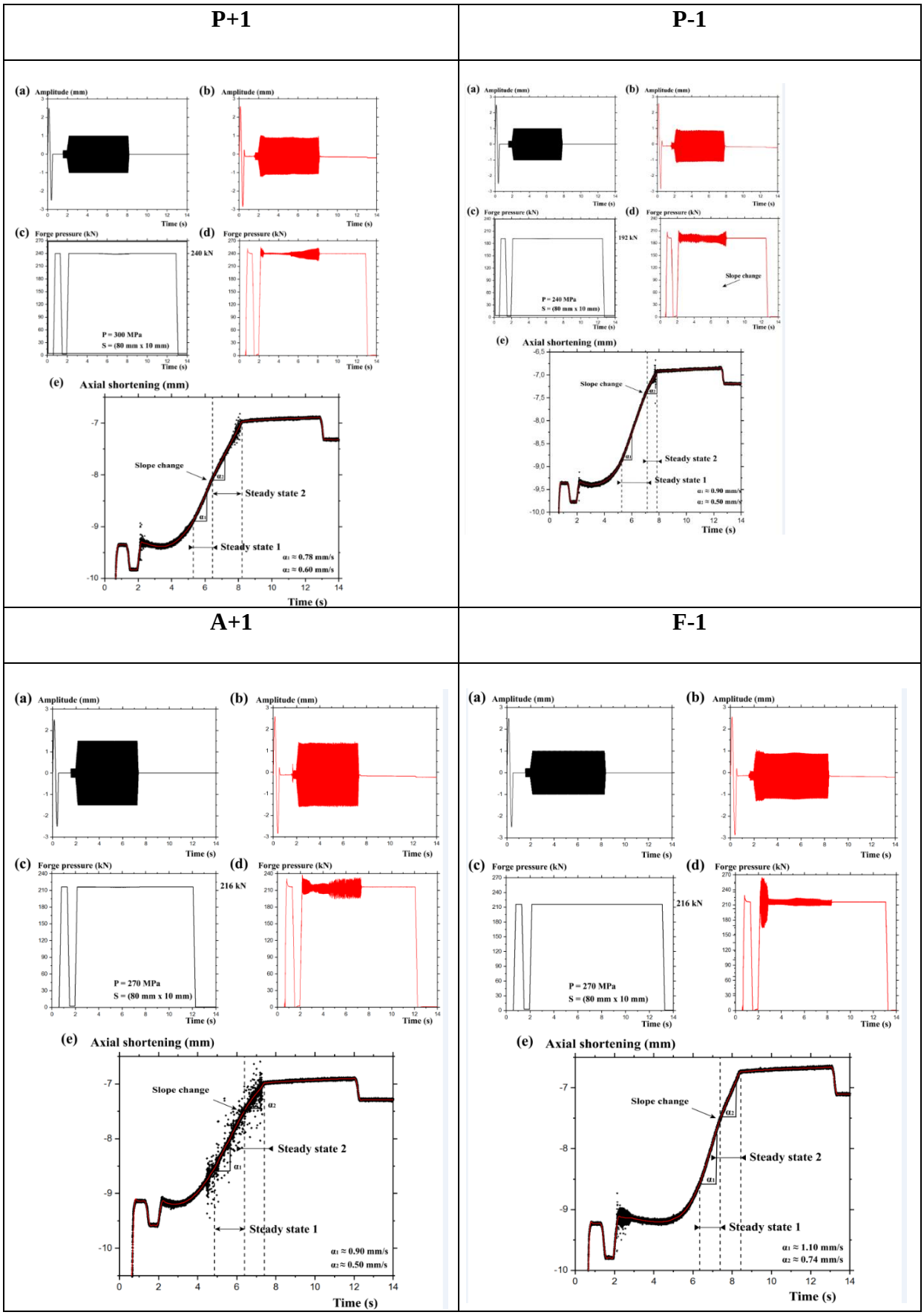


**Figure 4**: ***(a)*** *Amplitude set-point signal (± 1mm),* ***(b)*** *amplitude response signal,* ***(c)*** *pressing force application set-point (kN),* ***(d)*** *pressing force machine signal,* ***(e)*** *Z-axial shortening evolution during the processing time.*

Lastly, concerning the F+1 set of parameters, further micrographic analyses were carried out on the fractured weld. The results are illustrated in Figure 5. Interestingly, the specific characteristics of the welding line position was identified with a fine-grained fully-recrystallized microstructure that presumably formed between the frictional blocks during welding. Notably, a remnant parts originating from the forging block were clearly identified on the surface of the former oscillating part (here illustrated Figure 5.a, right part of the micrograph).

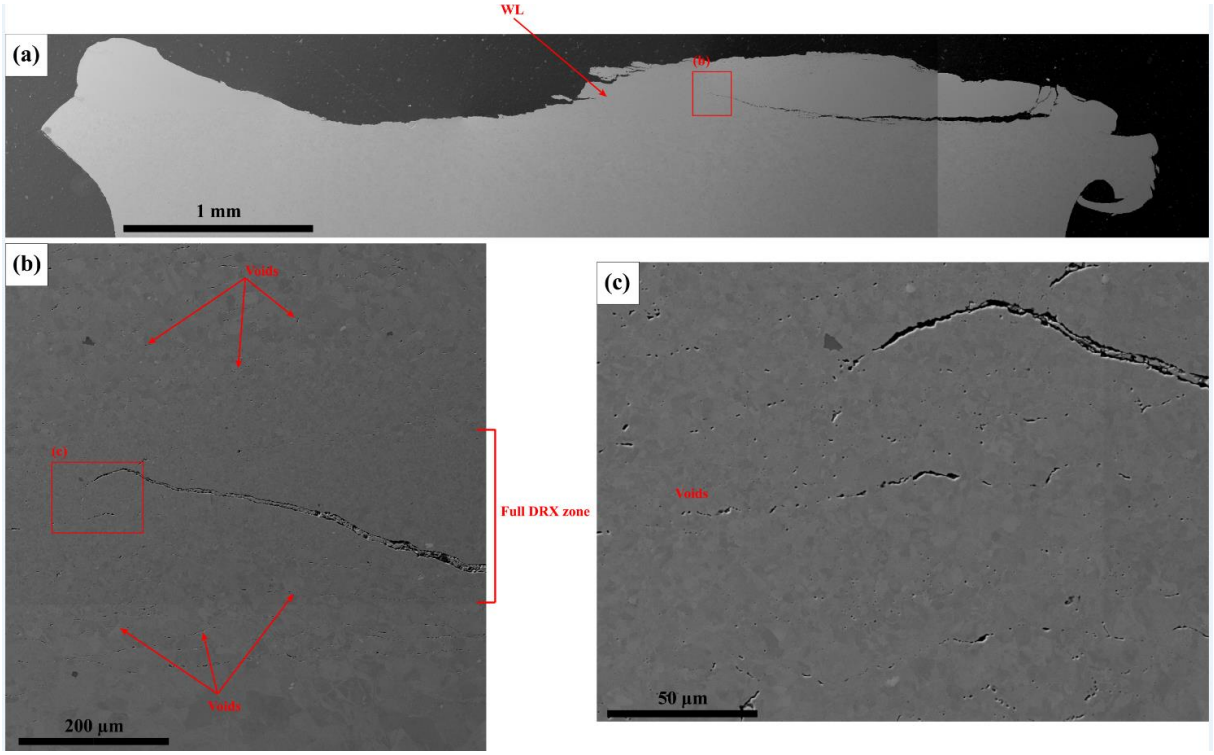


**Figure 5***: Transverse cross-sectional micrographs realized on the former oscillating part of the F+1 set of parameters by SEM imaging (SE2 observation mode).*

A numerous population of intergranular voids was also identified around the near weld center zone and at the vicinity of the fracture surface. Such elements indicate that local adhesion occurred between the faying surfaces during the weld procedure, then the extreme local thermomechanical conditions led to a high-temperature damage mechanism. Such scenario would correspond with the intergranular voids features observed in the former joining zone. The extreme deformation condition imposed by the F+1 external loads finally resulted in a high temperature fracture mechanism at the weld interface.

**Conclusion**

**(1)** Despite the difference in set of parameters, successful welds yielded to similar final microstructural features composed of a fine grained full-dynamically recrystallized microstructure in the weld center zone, a deformed and partially recrystallized surrounding the WCZ, and thereafter, a deformed microstructure demonstrating decreasing internal misorientation gradients as mowing away from the WL.

**(2)** The axial-shortening curves through processing time highlighted the signature of the effect of the process parameters on the friction welding behavior of the IN718 blocks. Each configuration displays a specific axial-shortening characteristic retracing the thermomechanical history during the friction welding process.

**(3)** If the 'Centre' set of parameters led to the quickest processing time, it is interesting to note the F-1 set of parameters led to the most efficient axial-shortening rat. This, despite the application of 'weaker' process parameter during the friction procedure.

**(4)** From this experimental work, the axial-shortening evolution through time appears to be the most reliable process output to evaluate the efficiency of the friction welding procedure. Wider experimental work seems however necessary for a clearer understanding of the effect on the process parameter inputs on the friction welding behavior. A process optimization approach considering the axial-shortening rate with care might help determining the most efficient set of process parameters to obtain sound-welds. The efficiency criteria are yet to be determined: shortest total processing time? or rapidest axis-shortening rate?

# Supplementary Material B

## Tested parameters on the Precipitation Hardened ('PH-Centre') weld configurations

### *On the influence of the initial surface layer on the linear friction assembling procedure*

This complementary part revisits the results from the first weld campaign implying the joining of the Ni-Fe-Cr IN718 superalloy by linear friction welding. Here, the base materials to assemble were both in a solution annealed (SA) initial metallurgical state. Consequently, the initial microstructure consisted of γ-FCC (Face-Centered Cubic) austenitic grains accompanied with δ-orthorhombic inter-granular platelets of $Ni_3Nb$ phase. Therefore, the two successive annealing at 720°C then 620°C for strengthening phase precipitation were not applied. The base materials to join were then in a 'soft' state.

The butt-weld campaigns implied the joining of 10 x 80 x 70 $mm^3$ parallelepipedic blocks. The assembling face corresponds to the 10 x 80 $mm^2$ surface. In term of method, the assembling procedures were similar to the other welding tests carried out along that work on Inconel 718. The solid blocks were extracted by electrical-discharge machining from a Ø115 mm diameter and 390 mm length standard wrought IN718 billets provided by Aubert&Duval, Les Ancizes, S.A. At this stage, it is important to note that the cutting wire was composed of a brass alloy. Nevertheless, the surface layers affected by the electrical-discharge machining (EDM) procedure were not removed after that, and the friction welding procedure was directly executed on the raw EDM cut oxidized surfaces.

Indeed, it is often commonly assumed in the linear friction welding literature that the welding procedure would be "self-cleaning". This hypothesis relies on the intuition that the friction welding procedure induces significant plastic deformation of the initial contacting surfaces leading to a significant stretch of the latter. Such deformation induced phenomenon would fragment and disperse the surface oxide layers by the action of the deformation induced along the joining process. However, no clear experimental evidence was carried to comfort and support unambiguously this statement. It was here observed that the complex nature of the surface oxides created during electrical discharge machining procedure led to significant consequences upon the weld procedure. The latter will be detailed further on in the associated results/discussion part.

In retrospect, and from a critical point of view, the lack of rigor concerning the frictional surface preparation introduced an important methodological bias on that first weld campaign. This finally led to huge deviations of the material behavior during the welding procedure notably during the alternate friction initiation step of the process.

Due to that fact, the results obtained from that weld campaign were not rigorous enough to be integrated among the main results discussed along that work. However, some interesting conclusion may be drawn, notably regarding the joining mechanism that operates in this particular study-case.

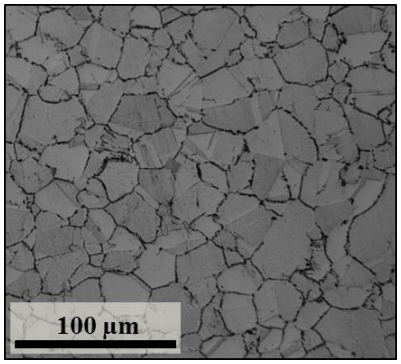


**Figure 1**: *Optical micrograph of the base material, solution annealed treatment*.

The Figure 1 illustrates, the base material microstructure in SA condition, it consists in a microstructure composed of D ≈ 50 µm γ-FCC austenitic grains with δ-orthorhombic inter-granular $Ni_3Nb$ phase.

## 1. Results & discussions

The friction assembling process was done in open air on the raw 10 x 80 mm² surface with the 80 mm edge parallel with to the oscillation direction. The process parameters selected in this study-case are: a **forging pressure** of **270 MPa**, **a frequency** of **50 Hz**, a **1 mm** of **oscillation amplitude**, and the axial-shortening was fixed to a 3 mm value.

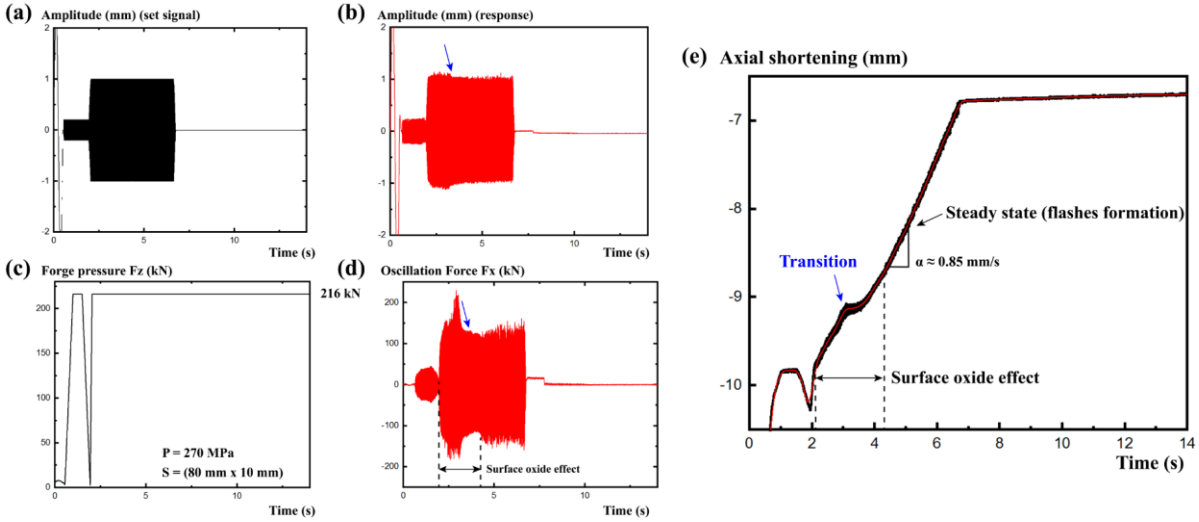


**Figure 2**: ***(a)*** *Amplitude set-point signal (± 1mm),* ***(b)*** *amplitude response signal,* ***(c)*** *pressing force application set-point (kN),* ***(d)*** *Oscillation force along the X direction,* ***(e)*** *Z-axial shortening evolution during the processing time.*

After an about 6 s of friction time, the aimed 3 mm material burn-off width was reached. The relative motion between the blocks thus stopped and the forging pressure of 270 MPa was then maintained for a duration of 10 s.

Six successive welds were realized under this protocol. It is interesting to note that they all resulted in comparable weld procedure characteristics with similar: total processing time, weld morphology and only minor deviations were remarked on the process signal outputs (amplitude, oscillation force, axial shortening) from one to another. The work presented below focuses on one representative specimen weld campaign.

The axial shortening signal (Figure 2.e) demonstrates a peculiar two-staged aspect. At the beginning of the frictional process, a rapid shortening is observed. It stands at a constant axial shortening rate until a transitional point, where the axial shortening rate slow down and reach a close to null value. The X-oscillation force signal is concomitantly observed to a reach a maximum amplitude plateau. The transition point marks an abrupt decrease of the X-oscillation force. After that, the axial shortening rate rises up again until it reaches a steady state value (of about $\approx 0.85$ mm/s), while in the same period the X-oscillation force also progressively reaches a constant amplitude. This steady state is finally sustained until the axial-shortening set-point of 3 mm is reached, marking the end of the frictional process.

Such axial shortening regime appears to be specific to the welding procedures implying workpieces with initial EDM oxidized surfaces. The observed quick initial increase of the axial shortening rate followed by a sudden double change in slope demonstrates a drastic change in the frictional behavior during the dry sliding friction stage of the process. None of these features were observed on any other IN718 friction welded configurations where the EDM-oxidized layers were polished away using P240 SiC grinding papers. Indeed, in the latter cases, the starting dry solid friction interactions developed on the native passive layer of the contacting blocks (and adsorbed residual contaminants resulting from the ambient environment).

However, once the transition point is passed and when the 'steady-state' is broached, the axial shortening trend becomes similar to the one of other IN718 weld procedures carried out under those parameters. For instance, the axial shortening rate here ($\alpha \approx 0.85$ mm/s) is rather comparable with the one of the 'PH-Center' condition (also 270 MPa forging pressure, 1 mm of amplitude, and 50 Hz of oscillating frequency). Indeed, despite the initial presence of the γ'+ γ" strengthening precipitates in the parent microstructure of the 'PH-center' weld parameter; it was shown that most of them dissolved in the thermally affected zone of the junction during the process. The shortening rate then reached a $\alpha_2 \approx 0.98$ mm/s value. The rate difference may be explained by the global stiffness difference between the precipitation hardened state and the soft solution annealed state pushing on the softened and plastically deformed material away during the frictional process.

This observation seems to indicate that the presence of the complex surface oxide layer coming from electrical discharge machining had a huge influence on the dry sliding friction behavior at the initiation stage of the process. This, until a transition point in the process where the nature of the outermost surface layer becomes negligible with respect to the mutual plastic flow established between the faying surfaces.

The latter hypothesis would support the idea that the friction welding process may be divided into two parts: a surface friction dominated part that allows initiating a bulk plastic deformation dominated part. **The problematic here is to clarify the influence of this specific EDM-oxidized layer on the friction welding procedure and its resulting microstructure**. To do so, deeper microstructural analyses were done within the assembled specimen.

### 1.1. Microstructure analyses *via* visible light microscope

The microstructural characterization of the assembling interfaces was carried out on selected cross-sectioned metallographic samples. The sample extraction strategy is detailed in Figure 3 below.

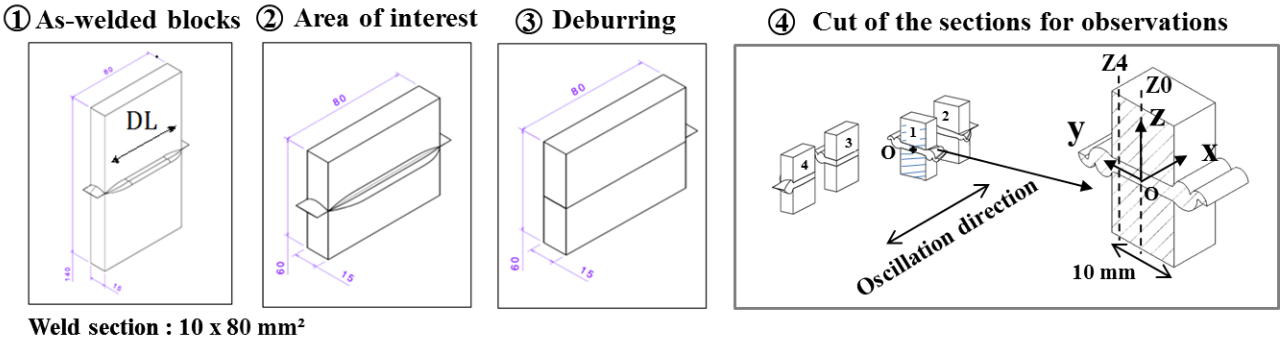


**Figure 3**: *Sample extraction strategy for microstructure characterization.*

For microstructural examinations, the specimen was first prepared by mechanical polishing through standard abrasive polishing procedures using SiC abrasive grinding papers until a P4000 grit size. The grind finishing procedure is done using successive polishing with standard diamond solution from 3 µm to 1 µm particle mean diameter on a polyester cloth. The final surface finishing is done using a 50% oxide polishing suspension (OPS) solution and 50% in volume of $H_2O$ on a Buehler VibroMet™ 2 vibratory polisher.

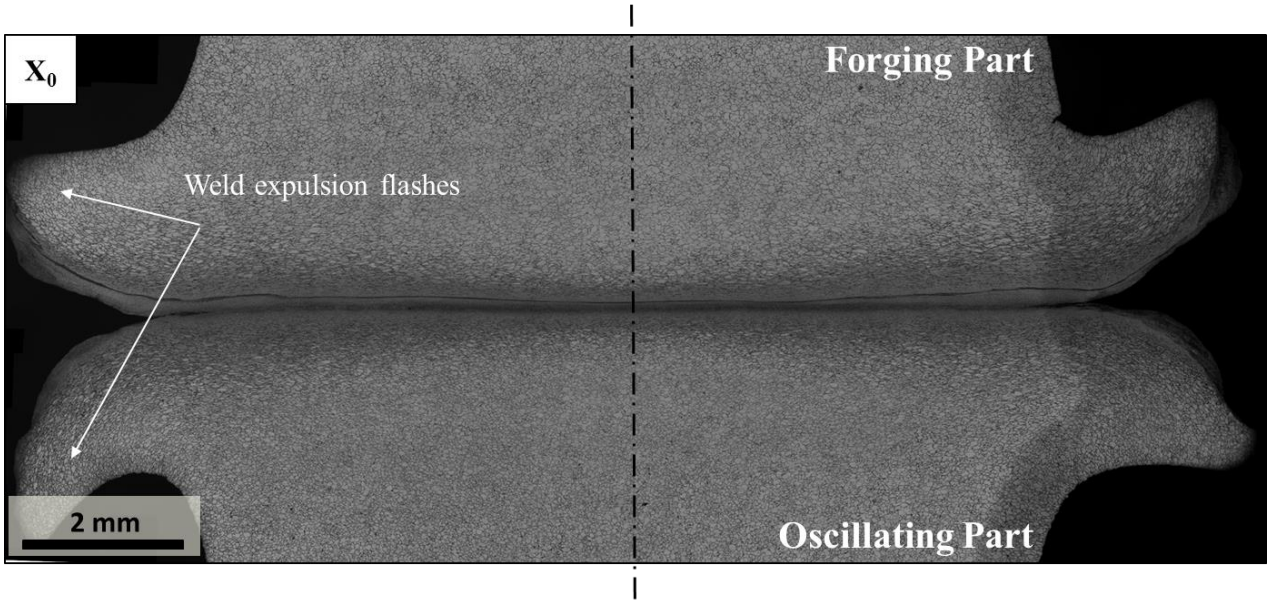


**Figure 4**: *Optical microscopy imaging of the transverse median cross-section of the IN718 linear friction weld.*

The global transverse optical micrograph presented in Figure 4 is extracted from the median position in the weld. Evidences of progressive grain fragmentation phenomena are observed within the apparent junction zones. The thickness of the fragmenting microstructure gradually increases as going toward the plasticized and expulsed material forming the lateral flashes.

A closer look on the Thermo-Mechanical Affected Zone (TMAZ) is presented in Figure 5. The TMAZ composed of: (1) a finer full-equiaxed microstructure in the core center of the junction. The latter connects the slies of the explusion lips from one to the opposite other. Additionally, It is observed that the microstructural changes within the oscillating and the forging sides are symmetrical about the zone (1) and spread along the Z direction. Such observation would suggest that the zone (1) corresponds to the center of the thermo-mechanically induced phenomena during the high temperature deformation process. Lastly, the zone (1) is part of a thicker grain refined microstructure delimited by the zone (2).

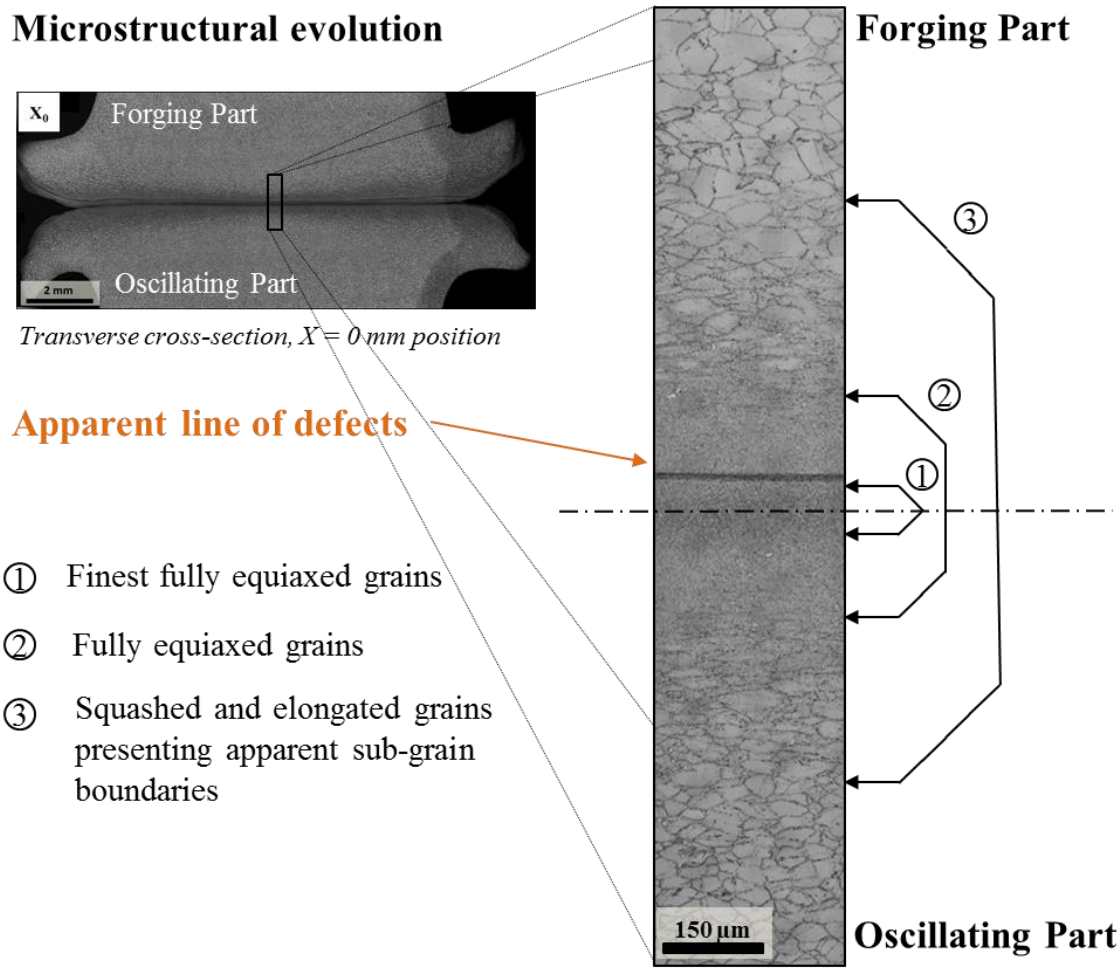


**Figure 5**: *Optical micrograph of the centerline of the cross-sectionned PH welded sample*

Further on, a partially refined microstructure is observed until the marker (3) with the appearance of squashed and elongated grains surrounded by typical necklace grain strucures. Substructure formation are also

observed inside severely deformed parent grain. Such markers are characteristic from a discontinuous dynamic recrystallization process. Nucleation and growth stage

The presence of a pecular line of defect is highlighted inside the TMAZ. It seems logical to suggest that these weld defects would originate from the interactions between the initial oxidized surface layers during the rubbing process. The resulting defects then remained entrapped within the joint. Regarding that fact, this hypothesis would imply that the cohesive junction between the block occurred through the defect line. Following this reasoning, the defect line also marks position of the Welding Line (WL). Paradoxically, the position of the line of defects do not correspond with the geometric center of the thermo-mechanically affected zone, but is slightly shifted toward the forging part side.

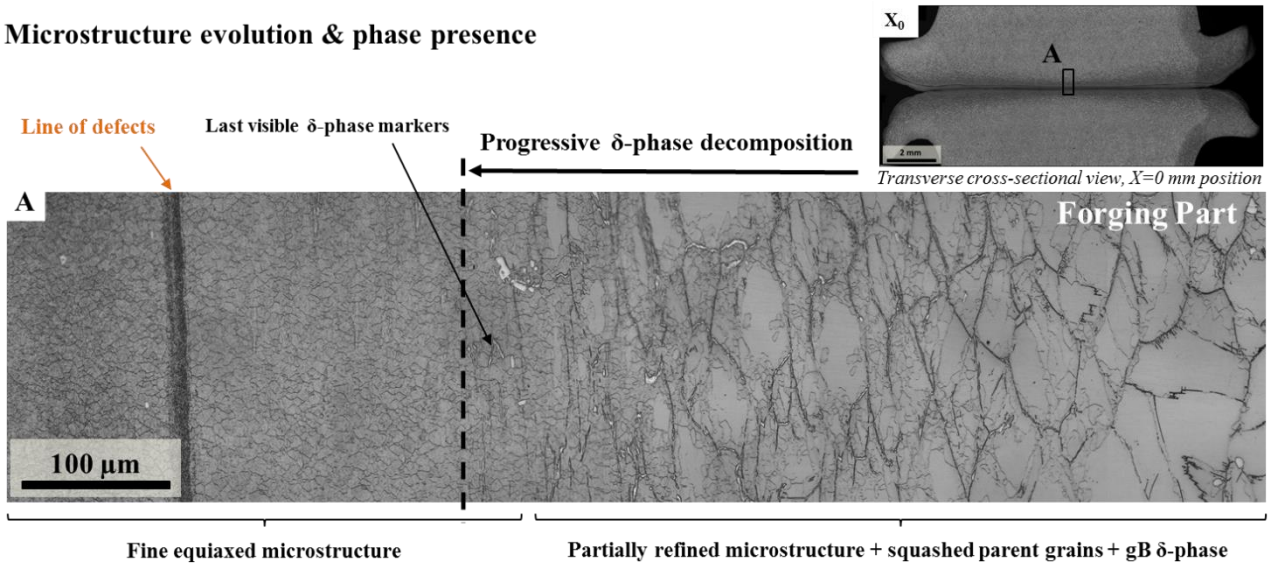


**Figure 6**: *Forging part side, transverse cross-section, optical micrograph in the center of the joining zone*.

As highlighted in the detailed micrograph presented in Figure 6, intergranular δ phase dissolution arose in the core region of the thermo-mechanical affected zone (2). It may be deduced that the local temperature conditions were high enough to induce the complete decomposition of the δ phase in that zone.

The *equilibrium δ-solvus* temperature is estimated to be in the range of 1025°C to 1030°C [2], [3]. It is difficult to ascertain an accurate estimate of the effective temperature reached in the core of the weld junction, notably because of the influence of the mechanical load and the effect of recrystallization on the local phase transformation kinetics. However, the thermal conditions were high enough to provoke the collapse of the yield strength conducing to important local plasticization of the 718 alloy.

Then, it seems plausible to assume that the local temperature range attained values at least slightly higher than these magnitudes in the core region of the junction. Finally, the δ-dissolution is also observed to be symmetric about the Zone (1) which is supplementary evidence corresponds to the thermal center.

### 1.2 Micro-hardness

In order to characterize the extent of microstructure affected during the solid-state joining process, $Hv_{0.3}$ micro-hardness profiles were done across the junction. The measurements were accomplished along the Z direction of the central transverse sample (extracted at the X = 0 mm position). Two profiles were measured, one in the median position Z0 and the other near the expulsion zone Z4. The visible line of defects marking the WL and illustrated in the previous micrographs was used as the starting point for the micro-hardness profiles.

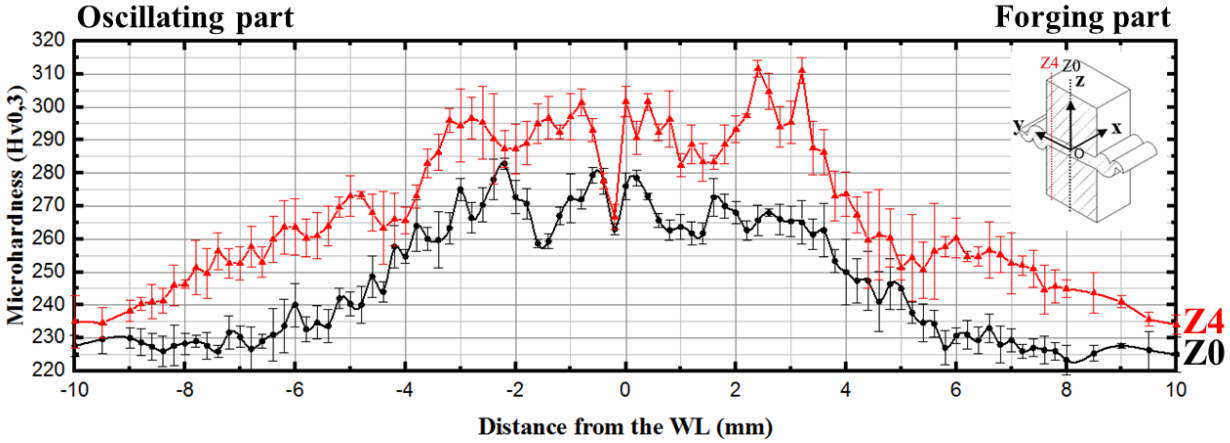


**Figure 7**: *Microhardness profiles on the transverse cross-section. The base material hardness in solution annealed state is about 220 to 230 $Hv_{0.3}$.*

A global hardening trend is observed through the joint and marks the spread of the Process Affected Zone (PAZ). As expected, the PAZ is wider near the expulsion zone where it reaches a ±10 mm in thickness compared with ±7 mm at the median profile Z0. First, the measured hardness values progressively increase as moving from the unaffected parent material zone toward the TMAZ. This evolution is consistent with a progressive strain hardening by the accumulation of lattice defects in form of dislocations within the microstructure. Concomitantly, the temperature elevation facilitates dislocation multiplication and mobility but also favors the activation of recovery mechanisms. The increasing importance of these recovery effects notably counterbalances the strain hardening effects as approaching the weld center zone resulting in a hardness plateau as shown in Figure 7.

### 1.3 Crystal orientation analyses in the joint

During the process, the thermo-mechanical loads led to severe temperature and strain gradients near the interfacial zone leading the important microstructural refinement. The identified mechanism responsible for grain fragmentation is here identified as a discontinuous dynamic recrystallization phenomenon. When the

friction welding process stops, the material undergoes a quick cooling similar to a quenching “freezing” the recrystallization phenomena at different stages of development.

As a matter of consequence, a progressive historicity of the recrystallization process is created by distance from the welding interface.

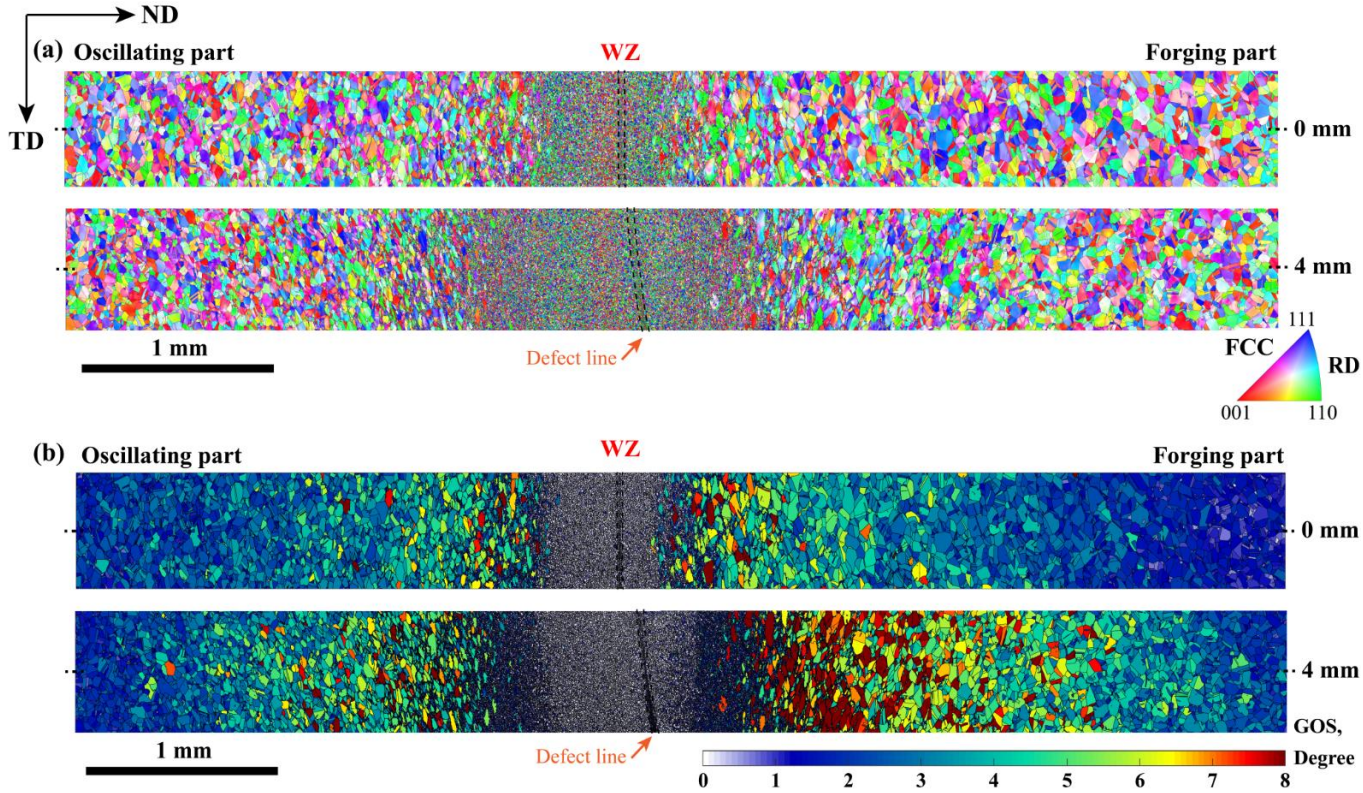


**Figure 8**: **(a)** *Inverse pole figure map across the central junction of the central transverse cross-sectional sample, two profiles were acquired at 0 mm* and *2 mm distance from the longitudinal plane of symmetry cutting the welded workpieces in half, the acquisition step-size is 0.5 µm. The FCC indexed data are superimposed with the grain boundaries (15° orientation angle threshold)*; *the colors represent the crystallographic direction of the indexed lattice along RD (friction direction)*; **(b)** *Grain orientation spread, 8° threshold.*

The IPF map in Figure 8 reveals a gradual microstructural change as getting closer to the cohesion line (WL). The slight cube texture identified in detail on the ‘PH-Centre’ configuration. The GOS map reveals low-internal misorientation level in the weld center zone made of fully-recrystallized grain structures. A wide partially recrystallized and deformed microstructure presenting strong intra-granular misorientation gradients extends on both side of the weld center zone WZ.

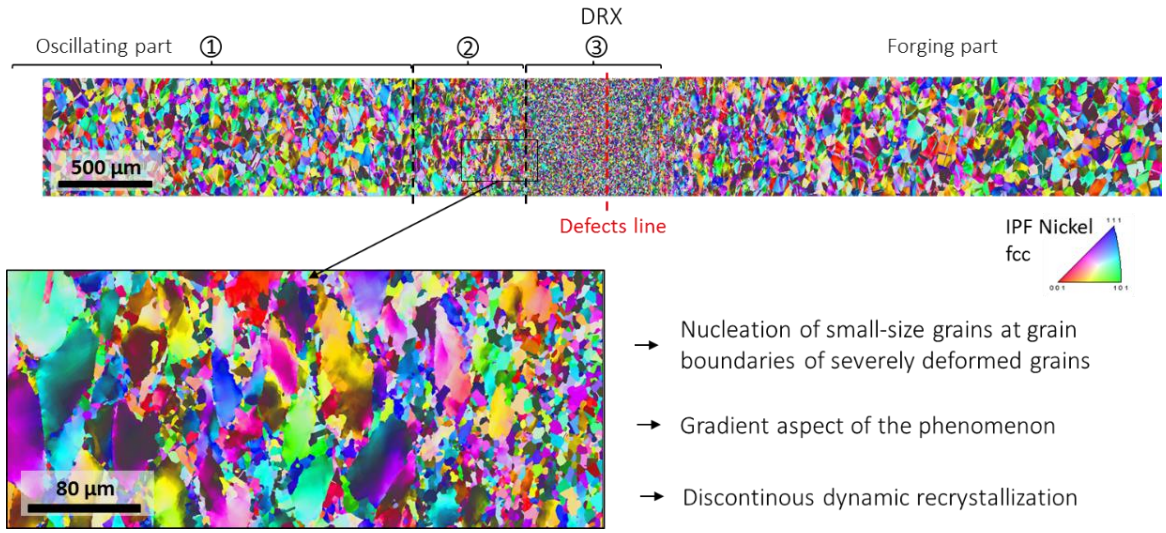


**Figure 9**: *Discontinuous dynamic recrystallization description in the transitional zone.*

Clear features of discontinuous dynamic recrystallization are distinguishable in the transitional zone. The Figure 9 illustrates the nucleation of new grains by bulging form deformed grains presenting high gradients of misorientation inside de parent crystal structures. The heterogeneity local density of dislocation of the near interfacial grain boundary zone (preferred region of dislocation pile up and interactions) yields to grain boundary serration phenomena. The quick evolution of the substructures that quickly present a high incoherence with the parent crystal lattice by grain rotation is a typical and characteristic feature of the discontinuous dynamic recrystallization phenomenon (illustration in Figure 10).

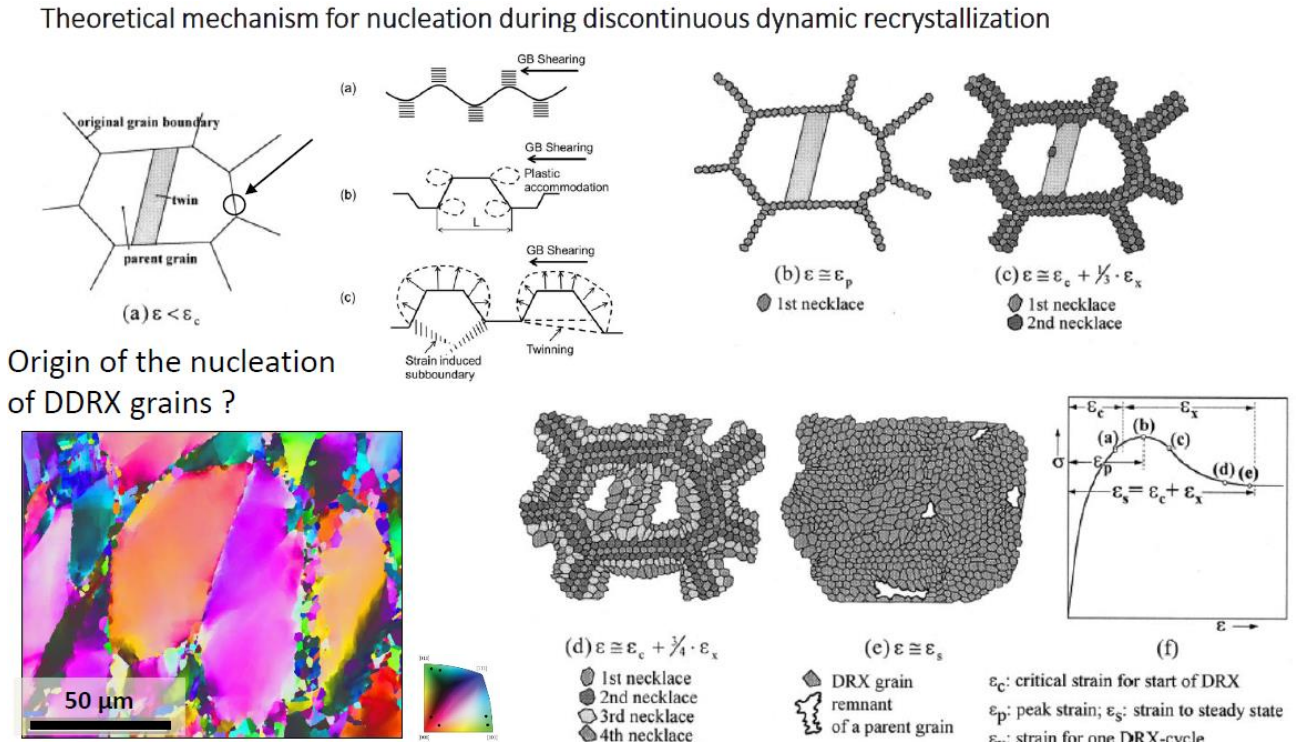


**Figure 10**: *Detailed progressive states yielding to discontinuous dynamic recrystallization DDRX in a low to intermediate SFE alloy.*

When deformation proceeds during the friction welding, the fraction of recrystallized grains increases by both nucleation of new grains and growth event in the previously nucleated grains.

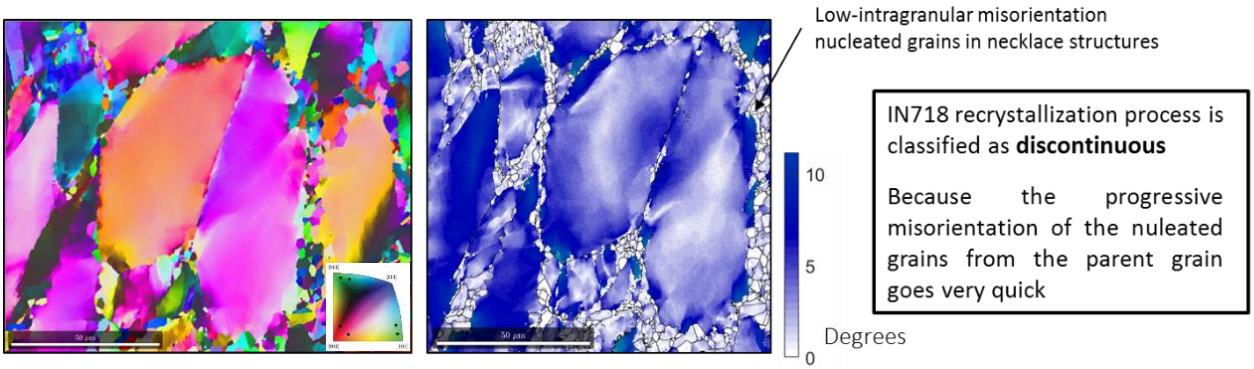


**Figure 11**: *Necklace DDRX formation of low misorientation and low density of dislocations nuclei resulting from parent grain boundary bulging and growth.*

As getting closer to the welding line, the recrystallized fraction increases with the strain until reaching a fully recrystallized microstructure. The difference in growing rate between nucleated grains and parent grains is due to the induced grain boundary mobility. The latter is the consequence of the difference of stored energy between neighboring crystallites. As high temperature deformation develops in the near interfacial zone, the nucleated grains see their dislocation density increase progressively. The interaction with the other grains eventually leads to the total disappearance of the parent structures.

The competition between growth and shrinkage of the newly recrystallized nuclei influences the final mean grain size. The local high temperature values increase the mobility of the boundaries. The latter are thermally dependent. An equilibrium situation is then reached with on the one hand the recovery rate that is high enough to sustain low density of incidental dislocation in the recrystallizing nuclei and the driving force for nucleation by local and progressive curvature of the parent structures. Both are balanced in between by the migration of the crystal boundaries that consume also part of the stored energy in forms of crystal defects. This is notably the case in the weld center zone WCZ.

In the deformed parent structures, the nucleation is observed to take exclusively place in near parent grain boundary zone and are characterized by their low dislocation density values. The growth of the recrystallized grains is driven by the difference in stored energy between adjacent boundaries (bulging mechanism). Bulging mechanism preferentially occurs near the grain boundary zone of the parents structures, where substructurations preferentially develops. Such features are notably illustrated in Figure 12 using a kernel average misorientation indicator (KAM) calculated from on EBSD map.

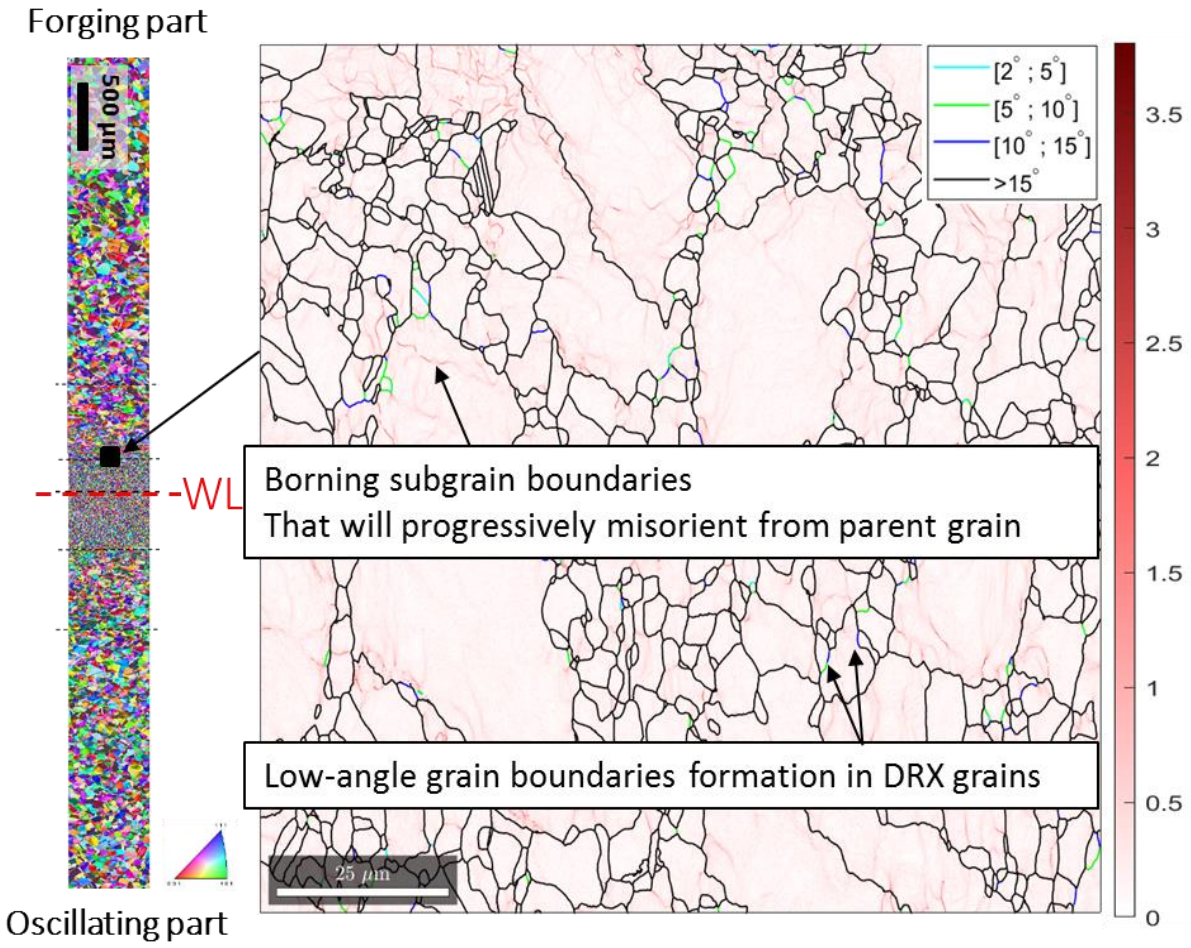


**Figure 12**: *Nucleation of recrystallized subgrain structures in the parent grains highlighted by a Kernel average misorientation map, with angle grain boundaries highlighted (<15°) and a 150 nm step size.*

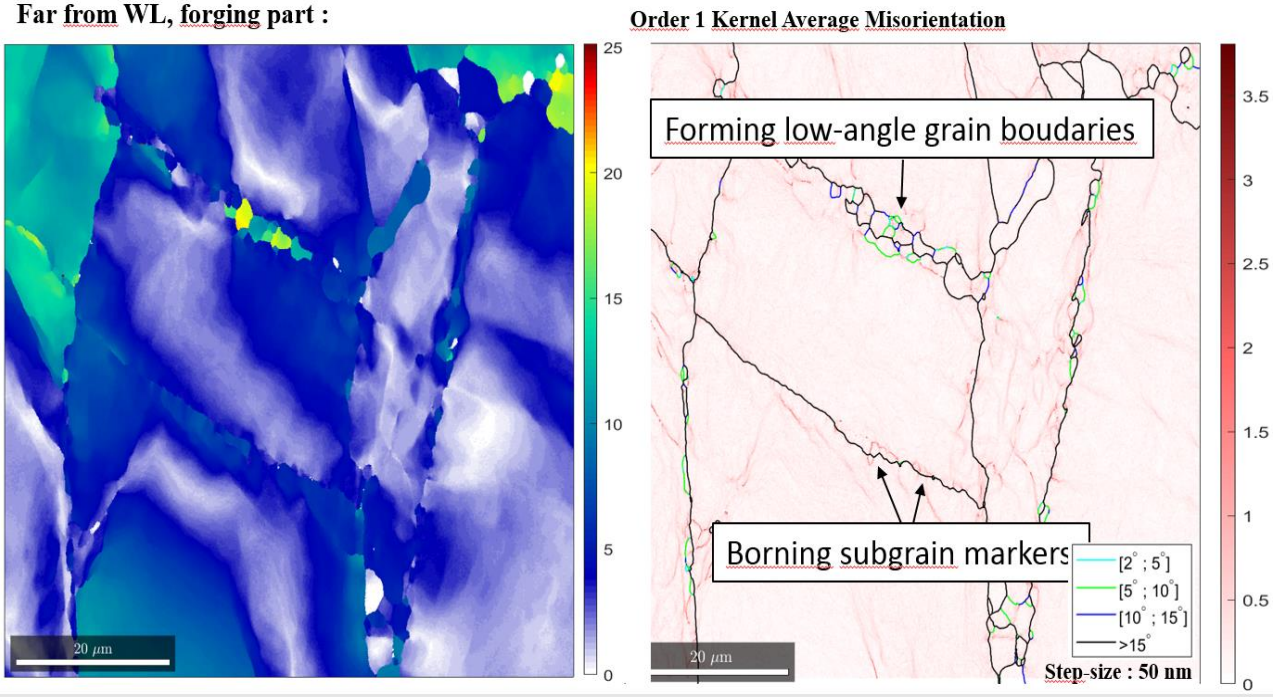


**Figure 12 (bis)**: *Nucleation of recrystallized subgrain structures in the far-TMAZ, (left) misorientation to mean orientation (25° angle threshold), (right) kernel average misorientation map, order 1, 50 nm step size.*

Close observations were done in the near interfacial zone to prospect the presence of assembling defects in the weld junction. A peculiar microstructure signature was noticed, and is of particular interest. A line of very finely recrystallized grains is observed around the theoretical welding line (Figure 13).

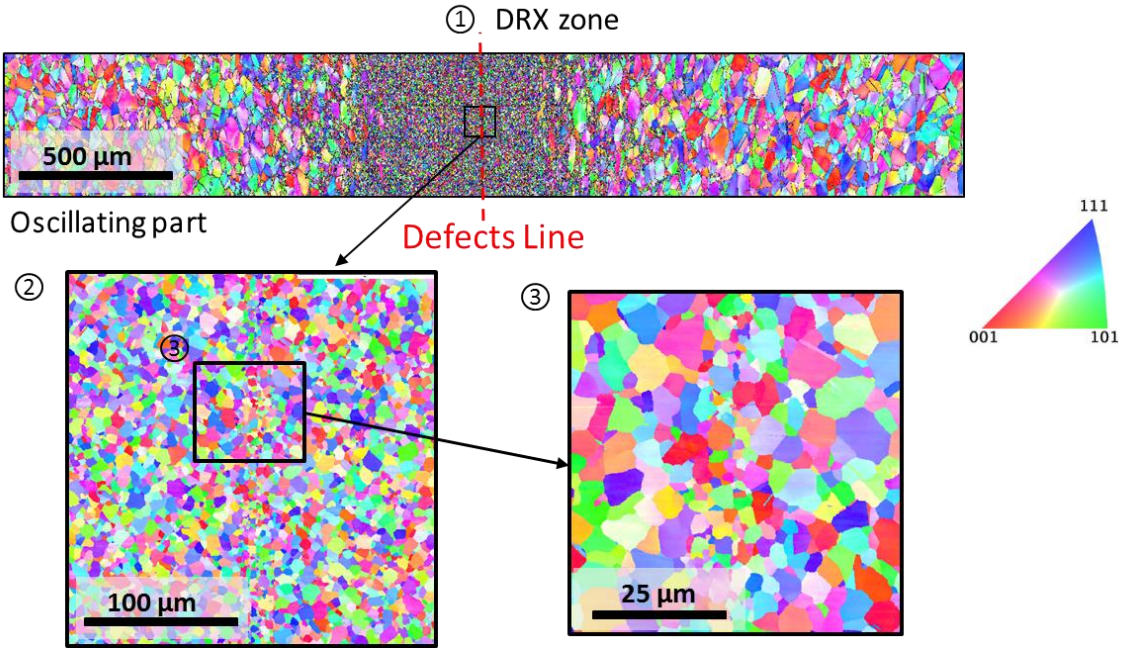


**Figure 13**: *EBSD mapping and IPF maps of the welding interfacial zone, the crystal orientation is displayed along the normal direction of the maps; a closer look in the interfacial zone clearly demonstrates the presence of thinner grains.*

### 1.4 Chemical analyses in the weld center zone

Further observations were carried out to investigate the origin for such local microstructural heterogeneities. First, SEM observations were done in back-scattered electrons mode, in an attempt to visualize the defects. The results are displayed in Figure 14; however, the exact nature of the observed defects is difficult to identify accurately.

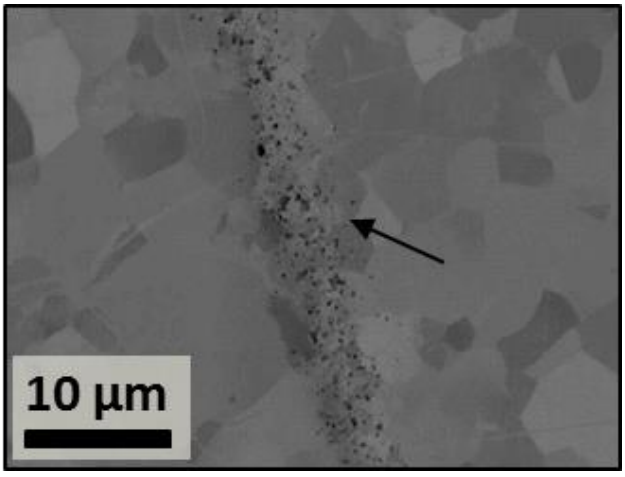


**Figure 14**: *BSE imaging of the line of defects in the weld center zone.*

To clarify the latter point, further chemical analyses through EDX were realized in order to identify the nature of the observed defects:

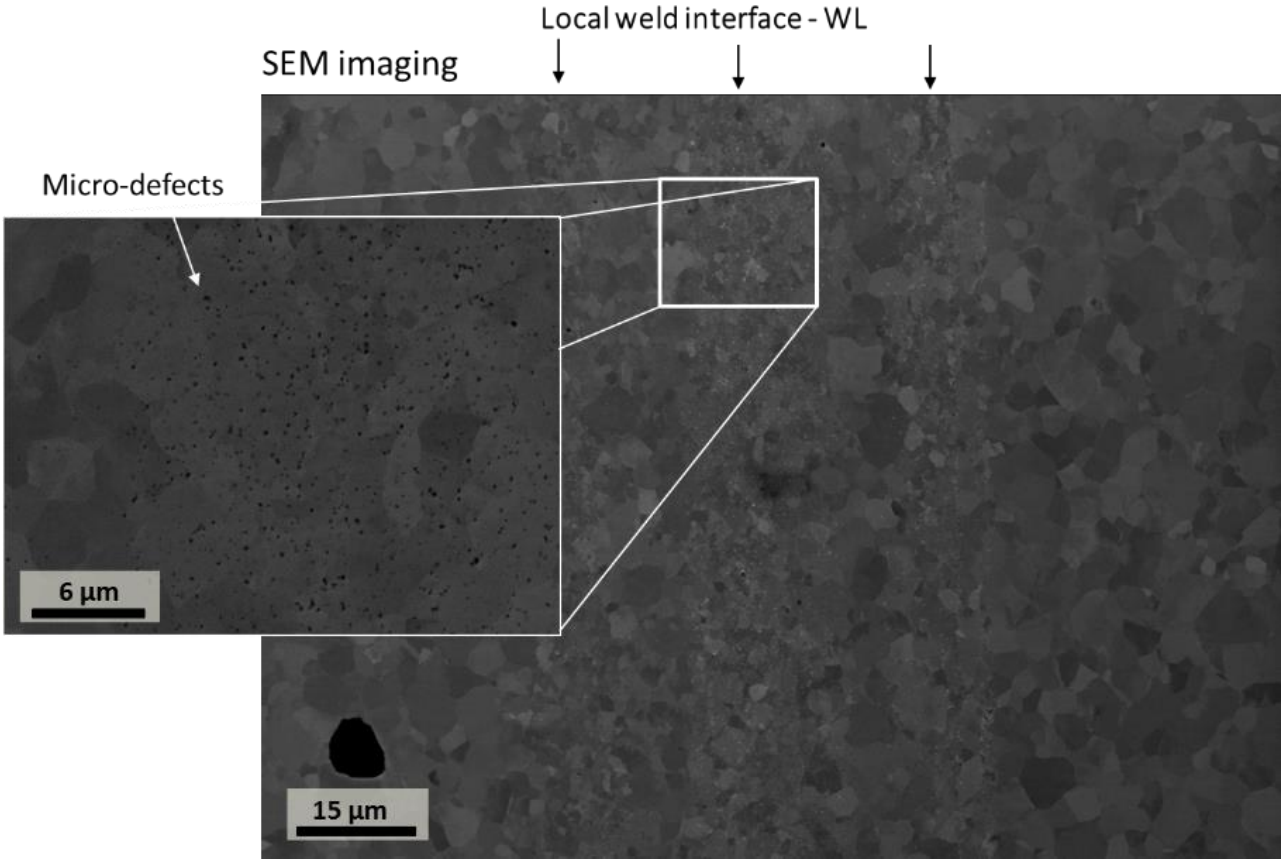


**Figure 15**: *BSE imaging of the EDX inspected zone*.

Defects were identified in the weld center zone and display a disseminated particles aspect in the fine-grained recrystallized microstructure in the center of the weld junction. Chemical investigations demonstrated the position on the defect line would first correspond with local enrichment of copper element (Figure 16). In addition to that, closer analyses highlighted the formation of numerous particles displaying a concomitant Al and O chemical signature that correspond with the position of the observed particles disseminated in the region. Such findings would most likely corroborate with the precipitation of nanometric alumina oxide particles at the vicinity of the weld junction during the friction welding procedure.

Such results were first unexpected considering the standard chemical composition of IN718. Indeed, the latter display only traces of Cu in its standard composition. Nevertheless, during the welded blocks were formerly cut through an electrical discharge machining procedure using a brass (Cu+Zn) wire. A copper oxide deposit probably formed on the surface of the block during the machining procedure. The latter finally remained trapped in the weld interfacial zone during the friction welding procedure. The cloudy and disseminated aspect of the Cu partition in the weld tend to demonstrate that the copper oxide probably decomposed on solid solution into the nickel alloy austenitic matrix during the welding procedure. Such oxide decomposition presumably enriched the local material composition in oxygen thus favoring an internal

oxidation mechanism. The most reactive element of the IN718 chemical composition is aluminum which possess the highest affinity with oxygen (see Ellingham diagram, Figure 18). During the welding procedure, the material local undergoes to elevated temperature (at least 1100°C), under such thermal conditions, the local oxygen composition went beyond the critical concentration for the spontaneous precipitation of alumina oxide particles in that region of the weld.

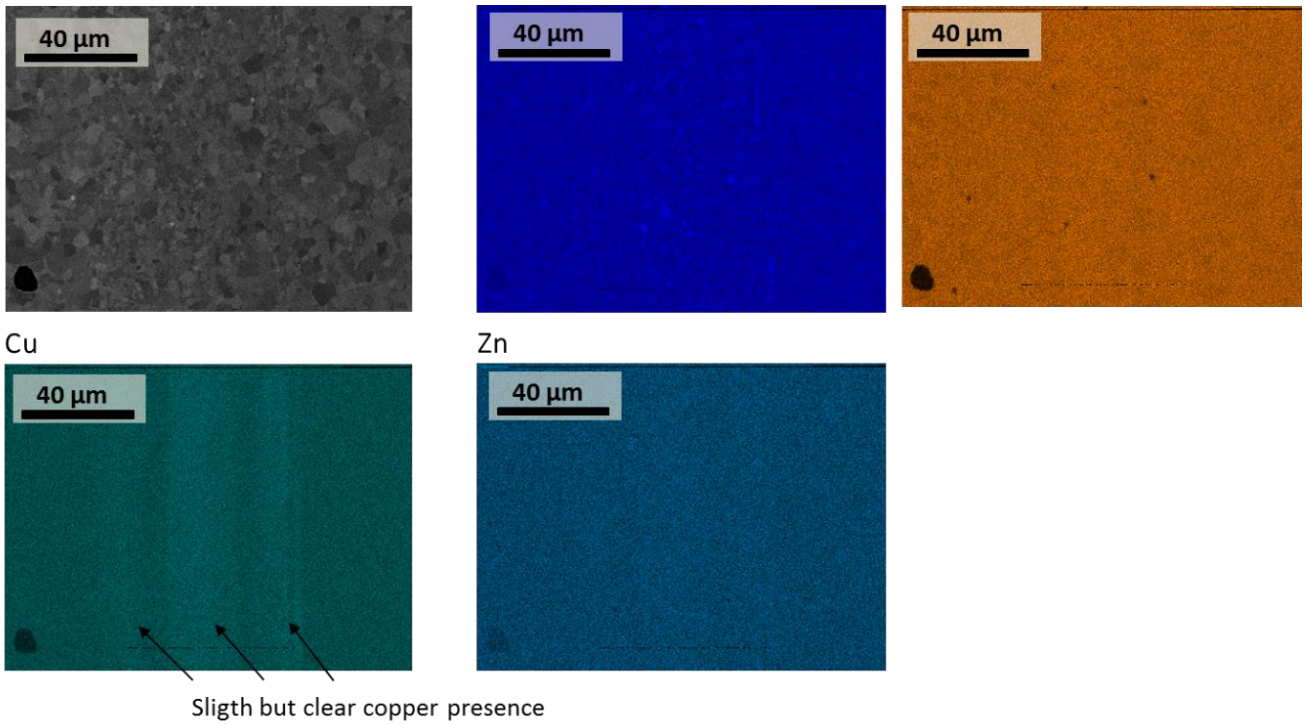


**Figure 16**: *EDX signals in the near interfacial zone.*

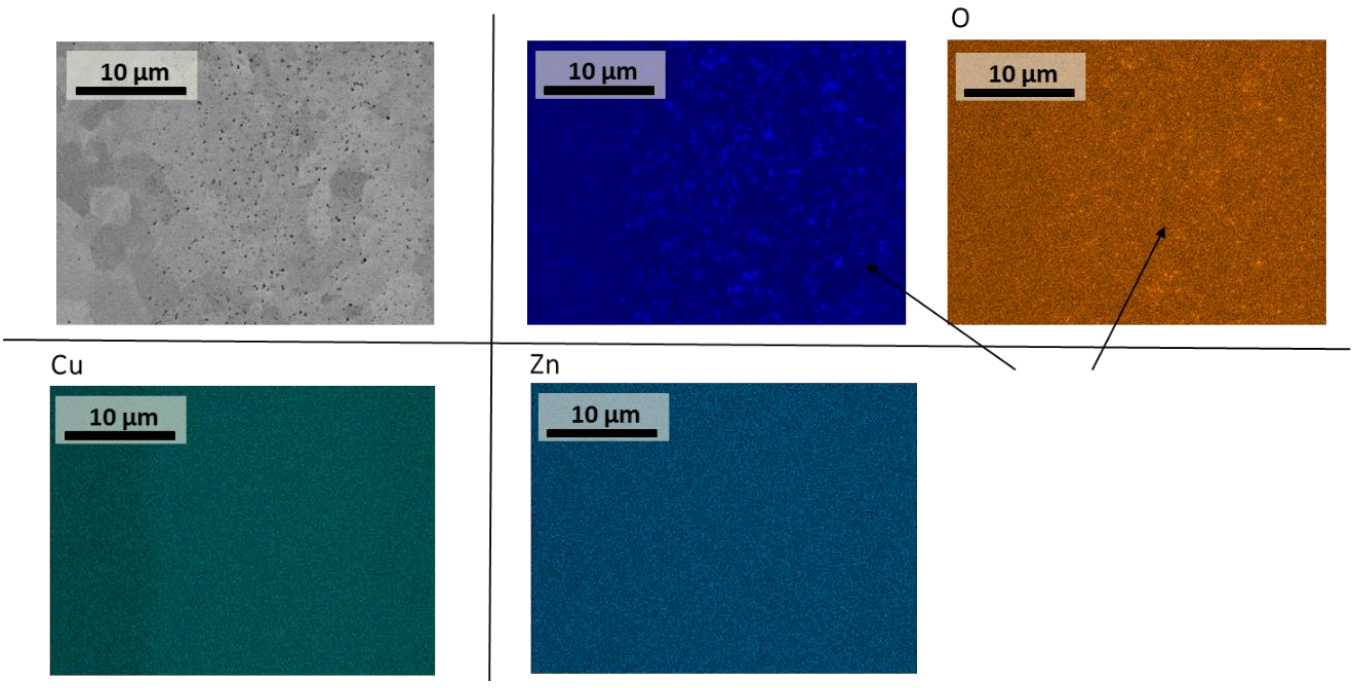


**Figure 17**: *Closer EDX signals in the near interfacial zone.*

These alumina particles are strongly suspected to exert a pinning effect (Zener-Smith pinning effecton the refined microstructure around resulting in a locally finer grain size nearby.

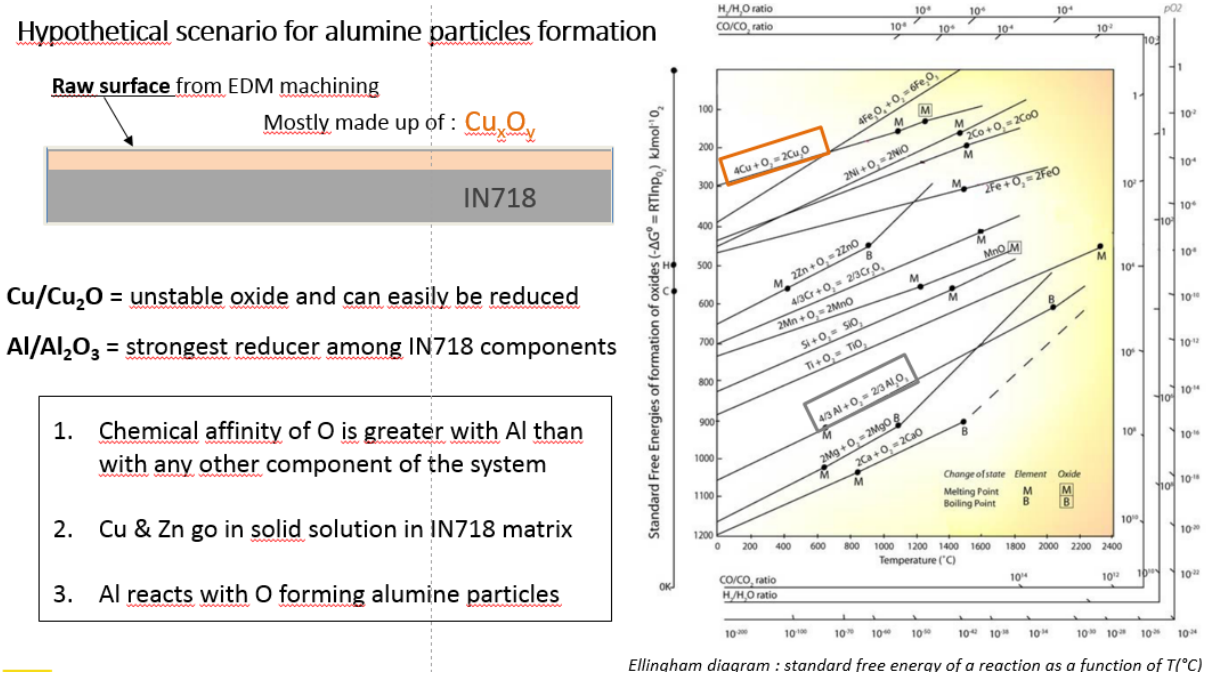


**Figure 18**: *Hypothetical scenario for alumina formation in the weld interface.*

The presence of such defects demonstrated catastrophic consequences on the mechanical strength of the assembly during monotonic tensile tests. It notably led to brutal failures in the elastic to plastic yield point thus demonstrating a fragile behavior. The mechanical behavior of the assembly is illustrated in the Figure 19 below.

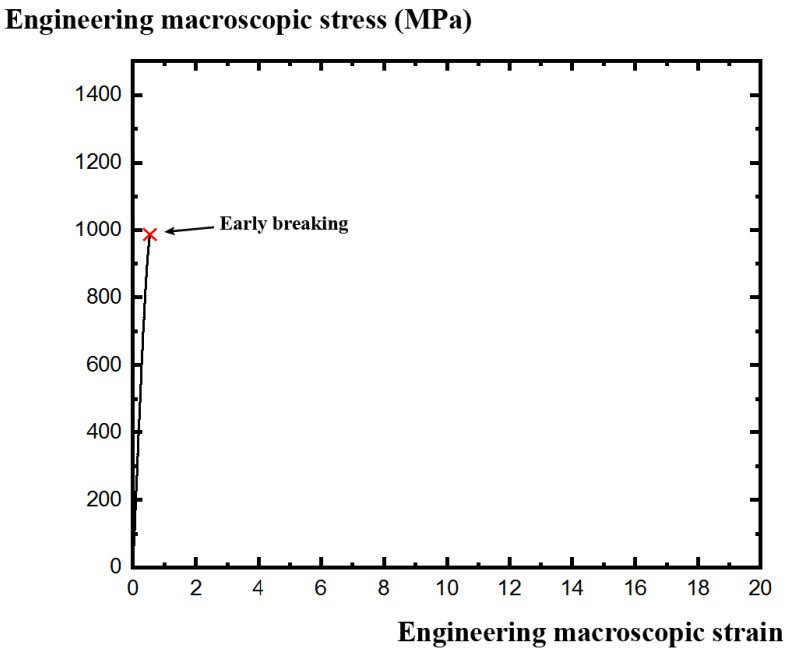


**Figure 19**: *Macroscopic engineering stress/strain curve during monotonic tensile test on the assembly.*

**Conclusion**

**(1)** The results obtained on the polluted join showed that the surface oxide decomposition phenomenon remained confined to a continuous <100 µm layer of material within the joint, no characteristic features with significant interfacial mixing were observed.

**(2)** The welded microstructure of linear friction assembled IN718 have been characterized. The microstructure is affected regarding the weld center position. A discontinuous recrystallization process occurred during the process. Around the bond line, the microstructure in fully recrystallized. The total effected zone in bot compared configurations is about 6 mm on each side of the welded block as identifies by Microhardness tests. The texture resulting is near random value. The geometric center of the thermomehcanical zone corresponds to the most affected zone thermomechanically. When the global shear of the weld junction occurred the mawiman internal friction occurred in the friction shearing zone leading to the formation of a main heat source by deformation energy dissipation (internal dissipation process).

**(3)** Concerning the bond mechanism, it can be concluded that a detrimental interfacial occurred in the near interfacial zone. The weakening of the bond is due to the presence and the formation of alumina particles at the primal bonding. This experimental fact proves that a chemical reaction is a possible mechanism occurring during the friction bonding process. As a matter of consequence, the motion of the moving boundaries of the recrystallized and growing grains was inhibited by Zener drag and pining effect. Nickel base alloys are well-known for their high sensitivity to such effect. Thus, the persistent presence of alumina particles, in quite high density, is strongly suspected to locally weaken the joint leading to a poor cohesive ability.

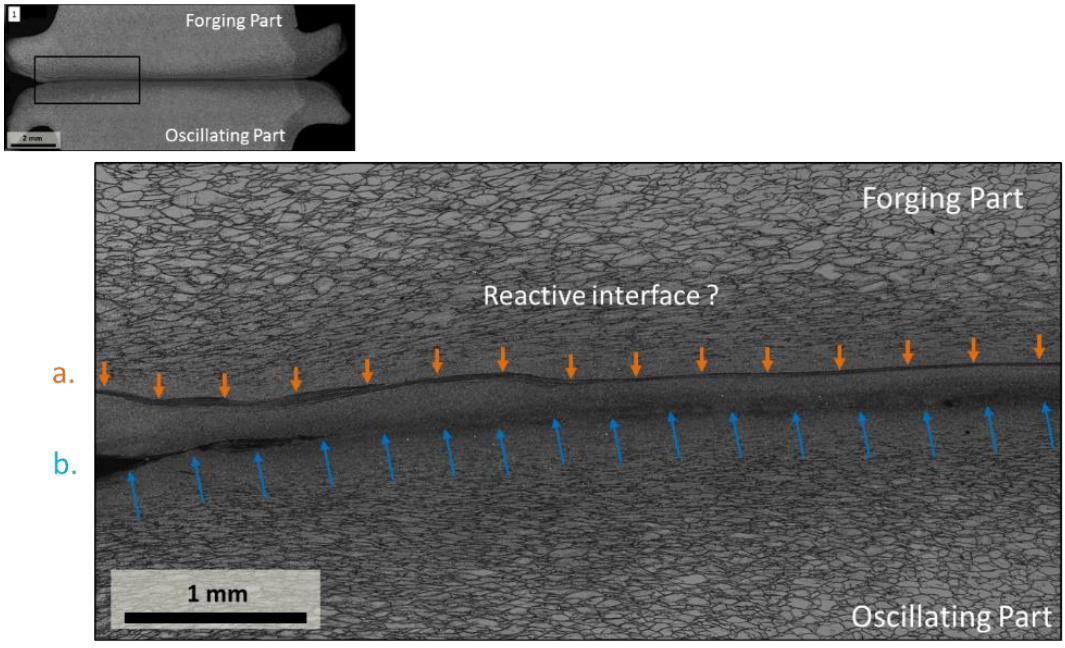


**Figure 20**: *Visible light micrograph of the bond line with the highlighted presence of defects,* **(a)** *position of the defect line;* **(b)** *position of the geometrical center of the thermo-mechanically affected zone.*

**(4)** The position of the line of defects do not correspond with the geometric center of the thermo-mechanical changes across the junction! (Illustration Figure 20). It suggests that bonding phenomenon and bulk deformation are decoupled. In the weld flash zone, it is noted that the defect line is not aligned with the bondline (or welding line WL). But, the defectline is going up in the forging part.

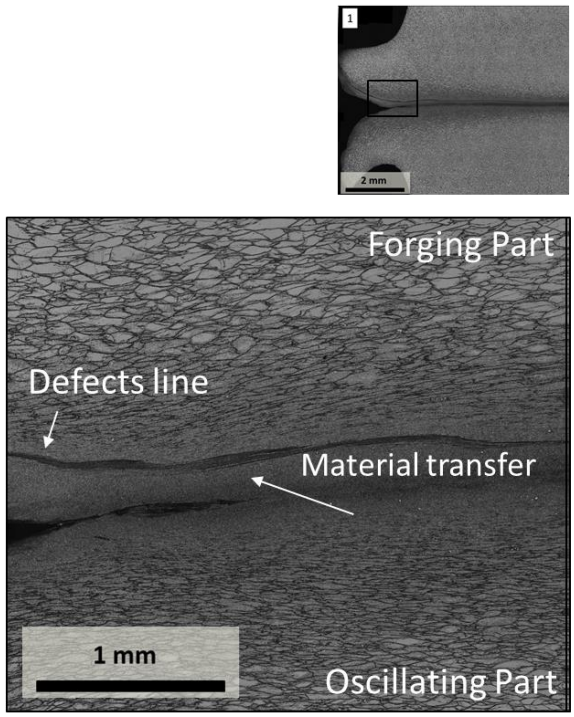


**Figure 21**: *Visible light micrograph focusing on the weld flash in the near expulsion zone.*

**(5)** The hypothetic scenario may be deduced: (1) a first metal-metal cohesion occurred through the initial weld interface; (2) a material transfers occurred from the oscillating part to the forging part during the friction process; (3) the maximum shearing zone coincide with the welding line near the expulsion zone and correspond to the geometric center of the weld.

# Supplementary Material C

## Ti-alloy / IN718 linear friction welding attempt

One of the side objectives of this work was also to evaluate the possibility of assembling together nickel based alloy with titanium alloy grades. Such configuration hypothetically poses serious issues in term of: mechanical compatibility considering a mutual bulk material plastic collapse during the friction welding procedure, sliding friction behavior and foremost, considering the complex chemistry of each of these alloys and their probable chemical reactivity at the weld interface.

As a prospective test, a IN718 (in a solution annealed metallurgical state) was 'welded' with a Ti6242 block. The weld surface geometry is of 10 x 80 mm², both surfaces were grinded with a 120p standard grind paper prior welding. The set of parameters is described in the following table:

| **Parameters (Units)** | **Pressure (MPa)** | **Frequency (Hz)** | **Amplitude (mm)** | **Axial shortening (mm)** | **Total oscillations duration (s)** | **Result** |
|---|---|---|---|---|---|---|
| **Test dissimilar** | 270 | 50 | 1 | 0 | 15 | Superficial bonding |

The associated visible light aspect of the dissimilar bond is given in Figure 1, below.

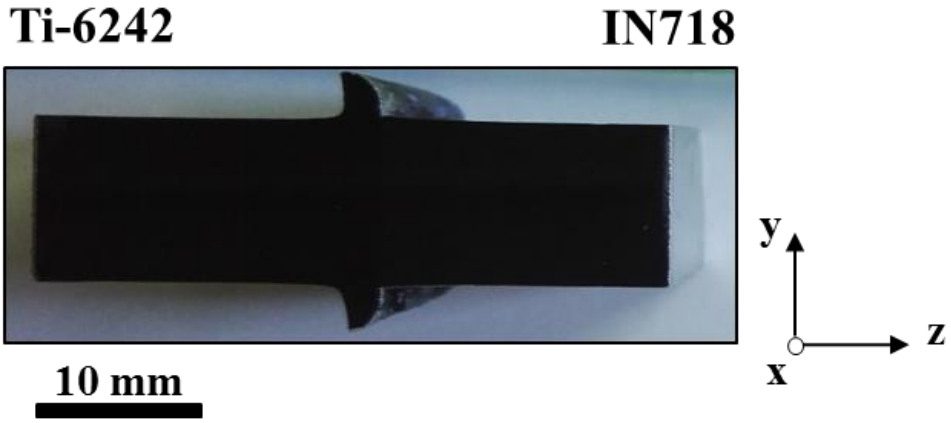


**Figure 1**: *Photograph of the Ti-6242 / IN718-SA after transverse cross-sectional cutting procedure.*

Only the Ti6242 alloy collapsed during the welding procedure, the IN718 part remained only little plastically affected by presenting a slight 'elephant foot' vertical squeezing due to the action of the forging force. During the procedure, the material local reached a hot-red aspect at the weld interface, nevertheless the thermo-mechanical condition was not severe enough to induce subsequent plasticization of the IN718 part (even considering its 'soft' initial metallurgical state).

Further observations were realized by SEM imaging at the weld interface of such a joint (Figure 2). The Ti6242 (left) underwent important morphological modification, the white cloudy aspect within its microstructure indicates important β-stabilizer elements diffusion toward the α nodular microstructure due to high temperature condition. On another note, the IN718 (right) remained little affected by the weld procedure and only display slight intragranular misorientation gradient testifying the occurrence of local plastic deformation. Nevertheless, the global shape of the IN718 grains remained quasi-unchanged. Between the parent materials, a peculiar intermediate microstructure developed presenting a quite heterogeneous aspect. The white / dark grey contrast seems to indicate bimodal microstructure.

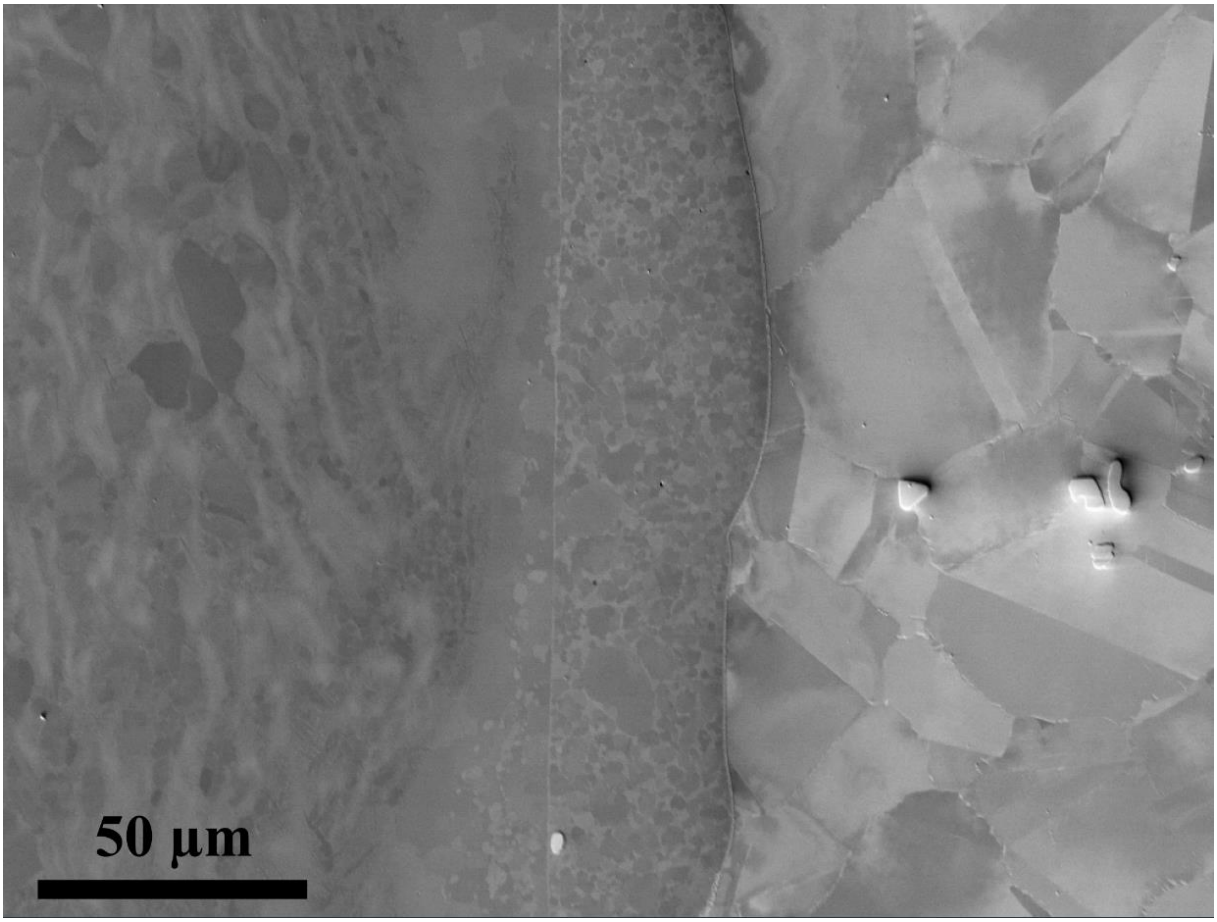


**Figure 2**: *SEM-SE2 micrograph at the welding interface (transverse cross-section).*

The global aspect of the intermediate phase presents a 50 µm total thickness with the remarkable occurrence of punctual irregularities in thickness and aspect along the bonding line. These irregularities are often accompanied by local excavation of the IN718 material, as if the austenitic phase of the IN718 had been locally dissolved within the intermediate phase. In addition to that, the intermediate layer locally takes the form of a fluid aspect flowing into the formed cavities (see Figure 3).

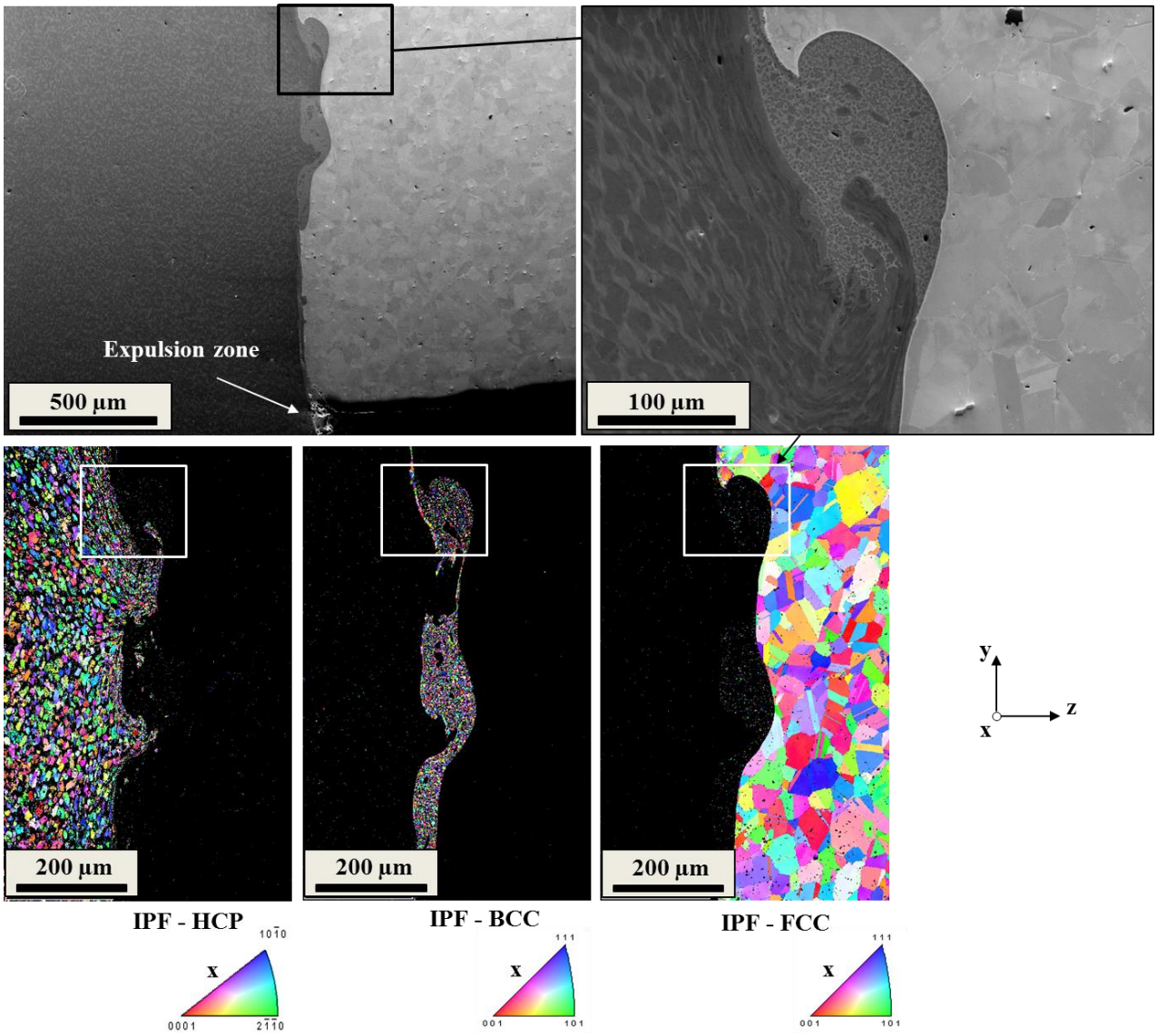


**Figure 3**: *SEM-SE2 micrograph at an interfacial irregularity, the associated crystal orientation signals are also provided on the HCP (Ti-α, phase), BCC (Ti-β phase) and FCC-γ (IN718) phases. The orientations are expressed along the friction direction x, normal direction of the maps.*

### Phases identification

The identification of the intermediate layer of material has been carried out *via* EDX analyses. This, in an attempt to identify the chemical composition and the nature of the phase in presence at the weld interface. First, a cross-sectional profile was realized through the interfacial layer. The chemical results are combined with crystal orientation analyses and are presented in Figure 4 and Figure 5, respectively. Considering the potential reactivity between the alloys in contact, the occurrence of intermetallic compounds precipitation is highly suspected in the interfacial zone.

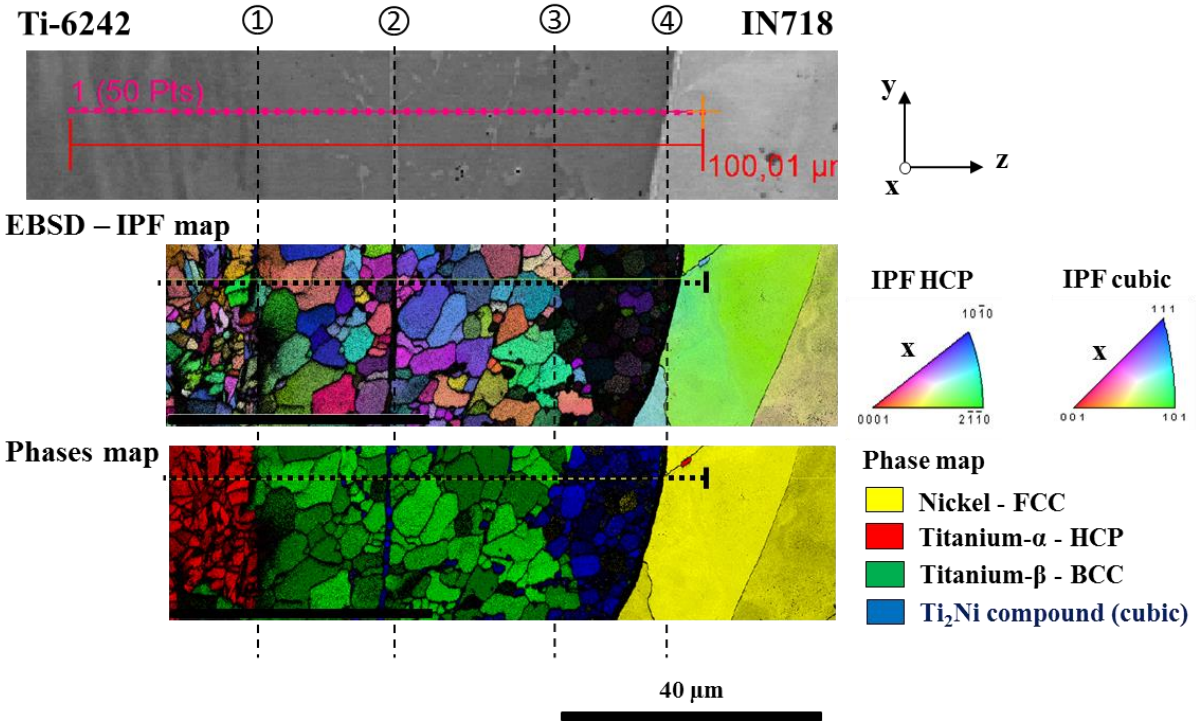


**Figure 4**: IPF-*crystal orientation map combined with the phases map of the HCP (Ti-α, phase), BCC (Ti-β phase); FCC-γ (IN718) phases and $Ti_2Ni$ (intermetallic phase) signal; CI index superimposed. The orientations are expressed along the friction direction x, normal direction of the maps.*

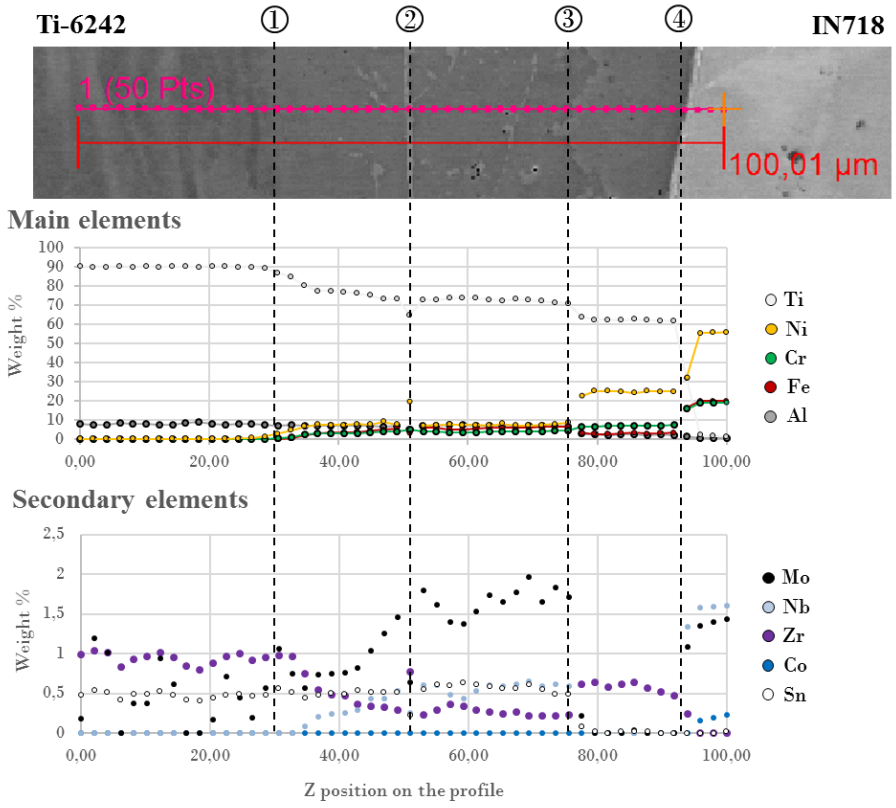


**Figure 5**: Weight % composition analyses, 50 points of measure on a 100 µm length, 2 min acq/pts.

In Figure 5, the position 1 marks the delineation between the Ti6242 base material composition and progressive enrichment by IN718 elements. The stable chemical composition of the structures observable between the markers 3 and 4 indicate the formation of a $Ni_2Ti$ intermetallic phase in the interfacial zone. Such intermetallic compounds were also identified with the help of kikuchi diffraction patterns. The latter notably matched with high confidence indexes with a cubic-$Ni_2Ti$ crystal structure. The marker 2 also possesses the same local composition has the intermetallic $Ni_2Ti$ phase. In addition to that, the subsequent element migration originating from the IN718 alloy composition locally enriched the Ti-alloy side in strong β-stabilizing elements. It resulted in the formation of a β phase at the weld interface. Thus, the interfacial microstructure is mainly composed of by a $Ni_2Ti$ and the Ti-β two-phase compound. The local elements are then partitioned between a Ti-β (strongly) enriched phase and a $Ti_2Ni$ intermetallic compound in a bimodal manner. The chemical analyses revealed quite stable local composition across the latter structures with well-defined composition once stabilized. The absence of chemical gradient indicate that a local thermodynamic equilibrium was reached in such structures, thus allowing to define them as phases.

The intermixing zone is particularly heterogeneous and some peculiar microstructural features were also regularly observed within such intermediate microstructure. As an example, some isolated α-HCP nodules were identified in the interfacial junction with composition close to the Ti6242 base material composition in the center of the nodule (Figure 6).

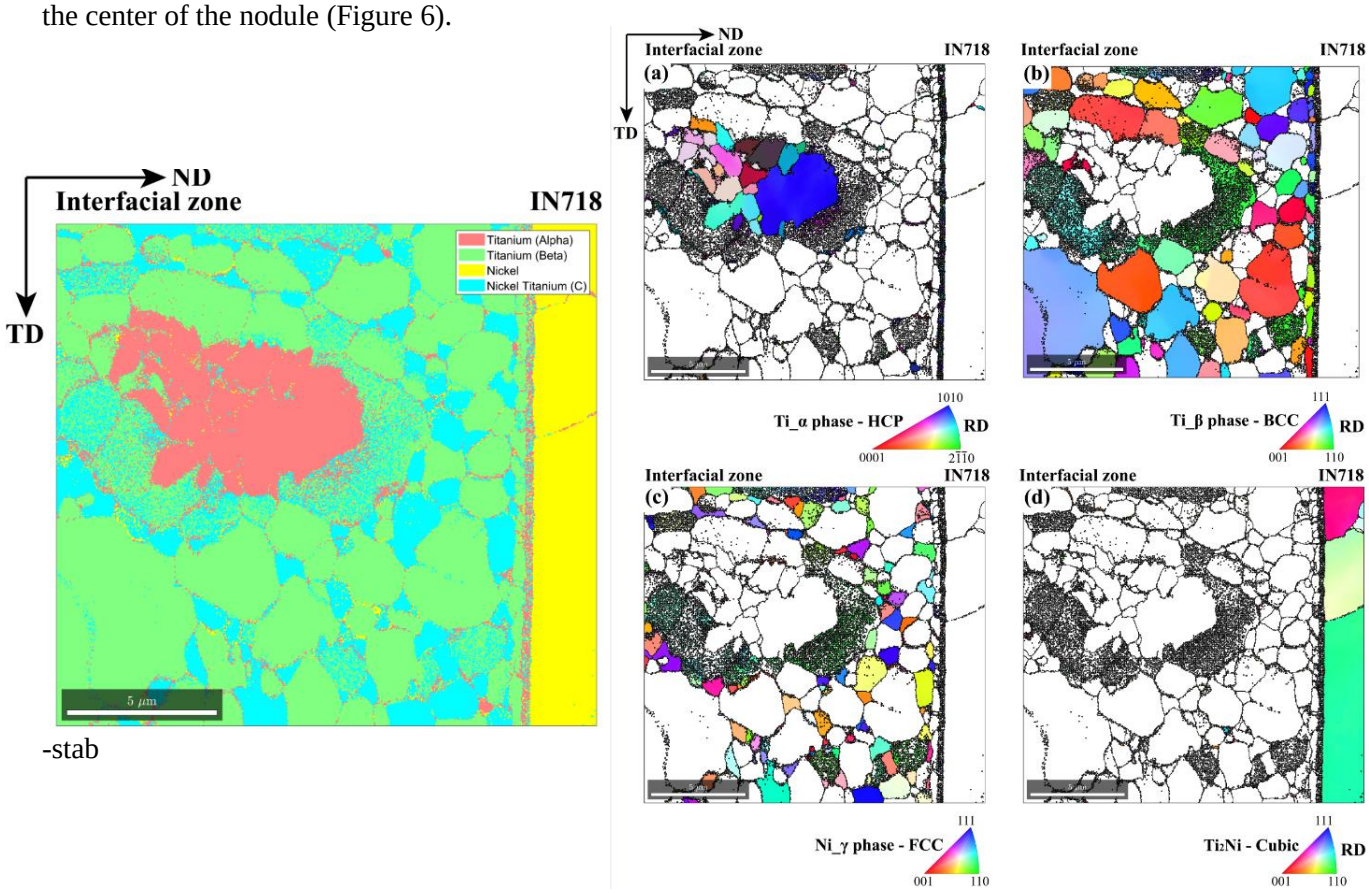


**Figure 6**: *(Left) phase map at the interfacial zone; (right) IPF-map for each phases indexed, 60 nm step-size. The grain boundaries (if between same phase, 15° threshold) and phase boundaries are superimposed in black.*

Such nodules were found in the middle of Ti-β enriched / $Ti_2Ni$ regions, subsequent chemical gradient is observed with the surrounding region, strongly enriched in IN718 additional elements (Figure 7). Such structures most likely remained in a far-from equilibrium state. Indeed, once the process stopped, the reaction kinetics most likely experienced a significant slowdown due to the critical cooling conditions, thus freezing the undergoing reaction. If the process had followed up, the important β-stabilizing effect brought by the IN718 elements would most likely favor the progressive stabilization of a room-temperature β metastable phase with the alternate and concomitant precipitation the$Ti_2Ni$ intermetallic compound in a bimodal (depending on the local thermodynamic conditions).

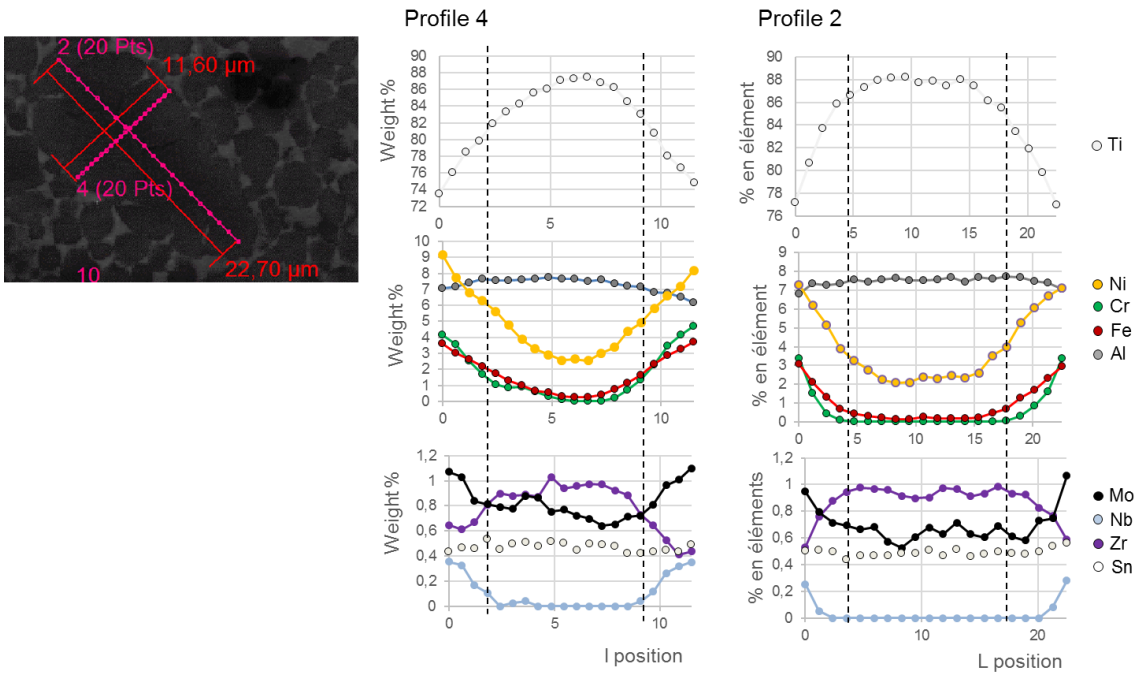


**Figure 7**: *Island of HCP phase nodule in the middle of the intermetallic $Ni_2Ti$ / Ti-β microstructure.*

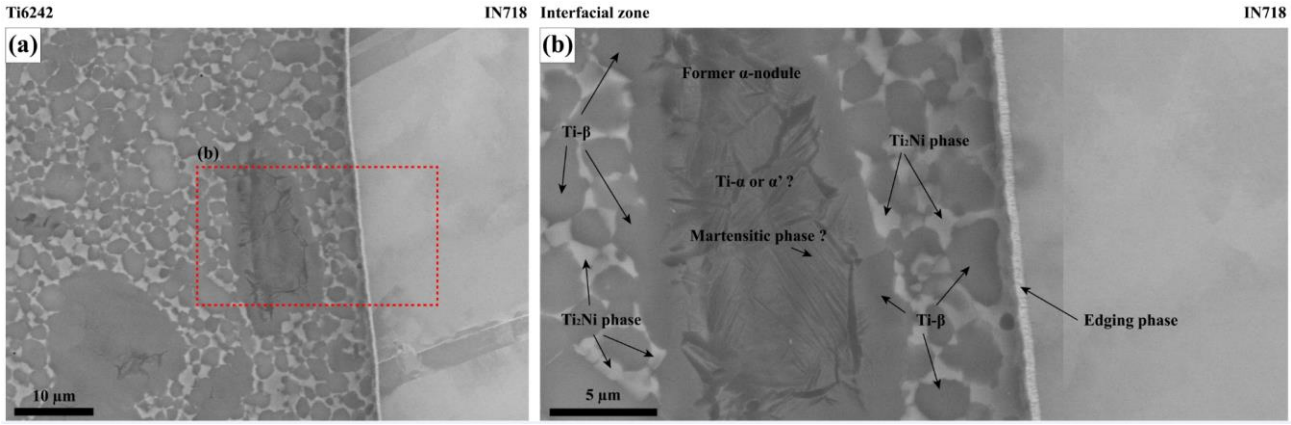


**Figure 8**: *Detailed micrographs on a former α-nodule trapped in the intermediate $Ni_2Ti$ / Ti-β microstructure.*

Closer observation carried out on such entrapped *α*-nodules revealed internal structures with morphology close to HCP α' martensitic laths (Figure 8). The latter may have precipitated under critical cooling conditions once the friction welding process stopped. It also means that during the process, such nodule also underwent a α to β phase transformation during the thermomechanical processing. Then, a β→α' was triggered under cooling while the process stopped.

In addition to that, a marked edging phase was observed at the interface between the precipitated reactive phases and the IN718 base microstructure forming a whitish border in-between (Figure 8). Such features may correspond to the existence of another intermediate phase. The latter, however, could not be identified *via* Kikuchi diffraction pattern analyses. Nevertheless, the SEM-imaging color contrast seems to indicate a fairly homogeneous chemical element partition that would suggest a phase precipitation occurrence.

Lastly, the microhardness of the intermetallic phase reached high values, in the order of magnitude of 500 to 600 Hv0,3 and demonstrated a frail mechanical behavior (easy propensity to form cracks at the weld interface when indenting through hardness procedures). Cracks are notably observables near the weld expulsion zones (as illustrated in Figure 9).

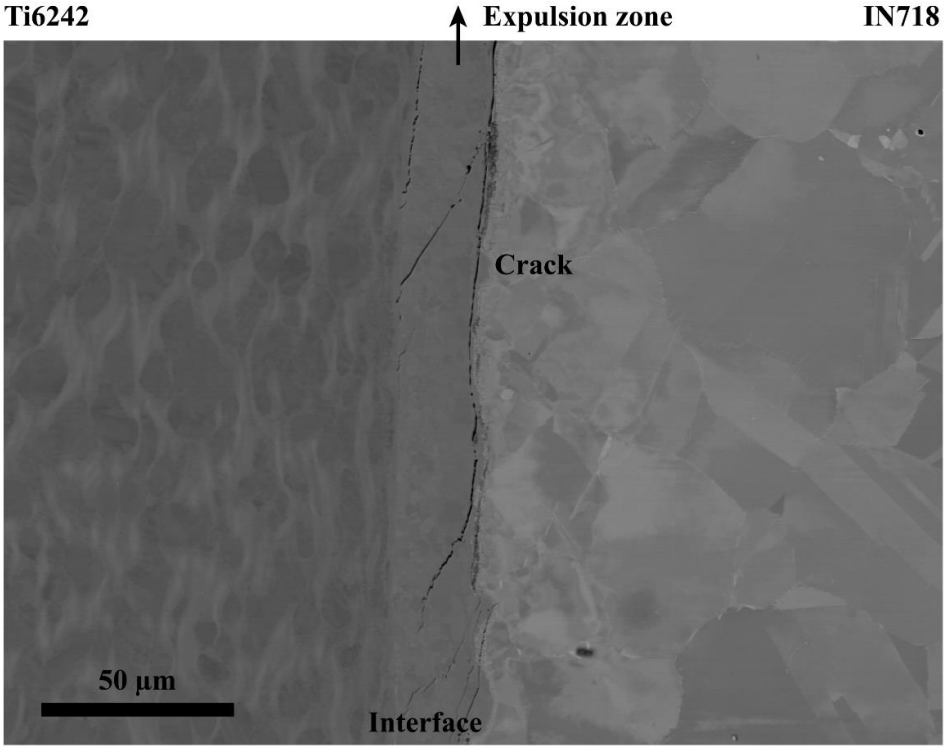


**Figure 9**: *Islands of HCP phase nodules in the middle of the intermetallic $Ni_2Ti$ / Ti-β microstructure.*

## Conclusion

**(1)** The local intermixing at the weld interface led to the formation of a reactive interface between the friction-welded materials. Only the Ti6242 alloy collapsed during the process, the IN718 part remained slightly affected.

**(2)** An intermediate microstructure develops; the latter presents a bimodal aspect and is mainly composed of Ti-β phase (rich in β stabilizing elements originating from IN718) and an intermetallic phase identified has a $Ti_2Ni$ phase (cubic) between the contacting materials.

**(3)** Only the Ti6242 / IN718 weld couples led to 'successful' bonds. Ti17 could not be weld with IN718. Such assembly are very fragile, and display very low mechanical resistance (some spontaneous debonding after the weld procedure were notably observed on Ti17 / IN718 configurations.

**(4)** Such configuration does not appear feasible nor interesting from a practical and technical point of view. The unavoidable and spontaneous formation intermetallic structure at the weld interface was shown to be detrimental for the joint integrity.